MECHANISTIC INVESTIGATIONS ON TRANSITION METAL-CATALYZED ASYMMETRIC ALLYLIC AND PROPARGYLIC SUBSTITUTION REACTIONS

Alèria Garcia Roca

UNIVERSITAT ROVIRA i VIRGILI

Mechanistic Investigations on Transition Metal-Catalyzed Asymmetric Allylic and Propargylic Substitution Reactions

ALÈRIA GARCIA ROCA

DOCTORAL THESIS

2023

PhD Thesis

“Mechanistic Investigations on Transition Metal-Catalyzed Asymmetric Allylic and Propargylic Substitution Reactions”

Alèria Garcia Roca

Supervised by Prof. Dr. Arjan W. Kleij

Tarragona

June 2023

UNIVERSITAT ROVIRA i VIRGILI

ICIQ

Prof. Dr. Arjan W. Kleij, Group Leader at the Institute of Chemical Research of Catalonia (ICIQ) and Research Professor at the Catalan Institution for Research and Advanced Studies (ICREA):

I STATE that the present Doctoral Thesis, entitled "**Mechanistic Investigations on Transition Metal-Catalyzed Asymmetric Allylic and Propargylic Substitution Reactions**" presented by Alèria Garcia Roca to receive the degree of Doctor, has been carried out under my supervision at the Institute of Chemical Research of Catalonia (ICIQ).

Tarragona, June 2023

Doctoral Thesis
Supervisor

Prof. Dr. Arjan W. Kleij

Alèria Garcia Roca, PhD Candidate at the Institute of Chemical Research of Catalonia (ICIQ) and Universitat Rovira i Virgili (URV):

I STATE that the present Doctoral Thesis, entitled "**Mechanistic Investigations on Transition Metal-Catalyzed Asymmetric Allylic and Propargylic Substitution Reactions**" has been written without the use of Artificial Intelligence.

Tarragona, June 2023

PhD Candidate

Alèria Garcia Roca

To my Gods and Goddesses

Curriculum Vitae

Alèria Garcia Roca was born on November 11 in 1994 in Barcelona, Spain. She obtained her BSc degree in Chemistry in September 2016 at the Autonomous University of Barcelona. During that time she carried out research abroad with the support of an Erasmus Grant defending her Bachelor Thesis at the Uppsala University in Sweden under the supervision of Prof. Lukasz Pilarski. She started her MSc degree that same year at the Universitat Rovira i Virgili, in joint collaboration with the Catalan Institute of Chemical Research (ICIQ) and supervised by Prof. Mónica H. Pérez Temprano. During her project, she worked on cobalt-catalyzed C-H functionalization reactions, and she obtained her MSc degree in September 2017. After volunteering abroad and working in the chemical industry, in 2018 she joined the Okinawa Institute of Science and Technology (OIST, Japan) to pursue a research project in the group of Prof. Julia Khusnutdinova, working on coordination chemistry and catalysis for the activation of small molecules.

In May 2019, Alèria started her doctoral studies under the supervision of Prof. Arjan W. Kleij focusing on the mechanistic evaluation of different methodologies developed in the Kleij group in the field of metal-catalyzed allylic substitutions. The results of these efforts are presented in this thesis. During her PhD, she spent a short research stay at the NYU (USA) under the supervision of Prof. Tianning Diao, working on new methodologies to investigate cross-coupling reactions catalyzed by nickel. Part of this PhD research has been communicated either as a poster or oral contribution at different international events including the 13th CaRLa Winter School in Heidelberg (Germany, 2020), the Roshchino EPR School in 2020 (online), the 13th International School on Organometallic Chemistry MMM in Santiago de Compostela (Spain, 2022), the XXXVIII Bienal meeting of the RSEQ in Granada (Spain, 2022) and the 1st Organometallic and Inorganic meeting of the SCQ in Barcelona (Spain, 2023).

Acknowledgments

First and foremost, I would like to thank Prof. **Arjan Kleij** for giving me the opportunity to join his group as a PhD candidate. I attended Arjan's classes during my Master and one year after I graduated, we both decided to start –as he likes to refer to the PI/PhD mentorship– our 4 year-long collaboration. During these past years, in which we faced a worldwide pandemic, I have managed to develop 3 different research projects hoping to shed light on the mechanistic aspects of some of the group's previously reported transition metal-catalyzed transformations. I would like to point out that from the very beginning, Arjan gave me absolute freedom to develop these projects according to my most preferred approaches. Being able to take my own decisions and choosing the techniques and methods I had envisioned for a particular study made me feel confident, valued and appreciated in the group. This allowed me to develop my own methods, formulation of hypothesis, experimental design, data analysis and drawing conclusions. I would like to point out the patience and the amiability that my supervisor provided me during this period of time and thank him for this beautiful experience. I hope we can continue celebrating scientific achievements in the future and remember the good moments that these last 4 years has brought us.

I would like to thank all the former group members in Arjan's Lab with a special mention for my current group colleagues: **Debasish Ghorai**, **David Lamparelli**, **Dimitrios Skoulas**, **Matteo Lanzi**, **Thiru Senthamarai**, **Balázs Tóth**, **Alba Villar**, **Jixiang Ni**, **Xuetong Li**, **Qian Zeng**, **Wangyu Shi**, **Fengyun Gao**, **Alex Delgado**, **Diego Meneses**, **Lorenz Dittrich** and **Chenyang Chang**. I really appreciate the time spent together: the food gatherings, the calçotades and the nights out in Cau.

I would particularly like to thank my co-authors and collaborators from my PhD including **Raúl Pérez**, **Dr. Debasish Ghorai** and **Hongli Wu**. We have spent a lot of time and effort developing our chemistry together and I am extremely proud of the results obtained. I want to thank you for all the lessons and knowledge acquired during this time and I believe that working in a team and collaborate is always better than doing it alone.

It makes me happy to acknowledge the help and care I received from **Prof. Mónica H. Pérez Temprano** being one of our collaborators and a personal friend, who not only assisted us in one of the objectives pursued during this thesis, but she has also

comforted and checked on me occasionally. I am also glad to thank Prof. **Rubén Martín** for the useful discussions we had for the Ni-based project presented in this thesis.

Both **Dr. Jordi Benet-Buchholz** (X-ray Manager) and **Dr. Georgiana Stoica** (EPR and UV-Vis spectroscopy manager), I want to particularly recognize their efforts and the good moments spent together while measuring my samples. I am always very careful treating my samples and highly ambitious –when it comes to obtaining results– and you have helped me realizing my goals throughout my PhD.

I want to specially celebrate the new friendships I started during these last years. We spent quality time outside the lab and you have not only experienced my good news and achievements, but also listened to my worries and fears. Thank you for being there **Ingrid Mateu**, **Qian Zeng**, **Clara Pagès**, **Kun Guo**, **Cristina Maquilón**, **Josefine Sprachmann**, **Marta Romero** and **Sarika Kumari**.

I would like to express my gratitude to various departments of ICIQ including IT, Human Resources, Maintenance, SHEQ and various research support units. Especially, I would like to express my gratitude to **Israel Macho** (NMR unit) for helping me with the NMR low temperature and 2D analyses and **Noemí Cabello** (HRMS unit) for her willingness to measure reaction samples in the spectrometers. Many thanks to our administrative support including **Ingrid, Cristina, Eva, Elena** and **Bea**.

I would like to acknowledge the financial support from the Ministerio de Ciencia e Inovación and AGAUR to cover my PhD expenses. Special thanks to the Severo Ochoa Funding that supported my research abroad in NYU when I worked under the supervision of Prof. **Tianning Diao**. I would like to take this opportunity to thank her for accepting me as a visiting PhD student in her lab. Also, I am very grateful to having been able to meet such a charming and welcoming group; I would like to mention the students from Diao Lab and the other visiting student I shared the best memories with: **Aoife Donohoe**, **Luchuan Ju**, **Gregory Dawson**, **Mason Chin**, **Benjamin Ben-Zvi**, **Sam Suh**, **Jenny Lam**, **Ethan Spielvogel**, **Elliot Silk**, **Zhenyan Guo** and **Jonathan Yuan**.

I also want to express my kindness to Prof. **Julia Khusnutdinova**, who supervised my Research Internship at the Okinawa Institute of Science and Technology (OIST) in 2018. I appreciate the lessons learnt from the projects I have been involved.

Remembering other good times in Tarragona, I cannot forget the cheerful moments we had playing football with my ICIQ fellows, playing padel with my friends in Viding Club and playing the cello in the ♪♫ URV Orquestra ♪♫ with **Suyun Sun** and **Edu García** from ICIQ.

Finally, I would like to dedicate some words recognizing the help, motivation and recognition I have received from my parents, always caring for me, believing in me: **Rosa** i **Ramon**. My siblings which I deeply love: **Judit** i **Ramon**, my beloved cousin **Raimon**, my grandparents that love me with all their heart and take care of me and feed me with real good food: **Mercè**, **Ramon**, **Mª Josep** i **Ramon**. My uncles, who when I was 19 years old mentioned for the first time about ICIQ to my persona. Little did I know I would be spending 5.5 years of my life in this Institute 4 years later: **Dr. Tomàs Roca** i **Anna Gràcia**. And to my cheerleader team, my loving uncles: l'**Àlex**, l'**Oriol** i l'**Antònio**. I love you all and I cannot imagine going through a PhD without any of you.

Reaching this point, I am sure my fiancée must be feeling a bit envious. But being the last does not mean that he is less important to mention, totally the contrary. Becoming a Doctor in Philosophy would not have been possible without him: **Dr. Shubham Deolka**. Being 4 years apart from the person you love is not easy. I am sure there have been similar stories like ours, nonetheless I like to refer to our relationship as one of a world record breaker. We have spent hours on the phone, talking about chemistry and us. You helped me going through my PhD like no one else, giving me advice and motivating me while being 11.000 Km away from each other. We laughed and cried and we kept our hopes high that we would be able to meet once the pandemic would finish; our story should be film-inspiring. We will soon graduate at around the same time, and the most important thing of all is that our next adventure we will be together.

I love you with all my heart.

Alèria, 2023

List of Publications

The results described in this doctoral thesis are based on the following publications:

- **Garcia-Roca A.**,‡ Pérez-Soto R.,‡ Stoica G., Benet-Buchholz J., Maseras F. Kleij A. W., *A Comprehensive Mechanistic Scenario for the Cu-Mediated Asymmetric Propargylic Sulfonylation forging Tertiary Carbon Stereocenters*, *J. Am. Chem. Soc*. **2023**, *145*, 6442-6452. https://doi.org/10.1021/jacs.3c00188

- **Garcia-Roca A.**,‡ Wu H.,‡ Pérez-Temprano M. H., Huang G., Kleij A. W., *Inner-Sphere Pd-Catalyzed Allylic Amination: A Comprehensive Computational and Experimental Mechanistic Study*, *J. Am. Chem. Soc*. **2023**, *submitted* - under review (ja-2023-039833)

- Ghorai, D.,‡ **Garcia-Roca A.**,‡ Kleij A. W., *Ni-Catalyzed Regio- and Enantioselective Homoallylic Coupling: Access to Chiral Branched 1,5-Dienes featuring a Quaternary Stereogenic Center*, *submitted.*

Other publications not presented in this thesis:

- Dinh H. M., Gridneva T., Karimata A., **Garcia-Roca A.**, Khanthapura J., Patil P. H., Petrov A., Sarbajna A., Lapointe S., Khaskin E., Fayzullin R. R., Khusnutdinova J. R., *Single and double dearomatization of N,S-donor pyridinophane ligand in ruthenium complexes, Dalton Trans.* **2022**, *51*, 14734.

- Karimata A., Gridneva T., Patil P. H., Fayzullin R. R., Khaskin E., S. Lapointe, **Garcia-Roca A.**, Khusnutdinova J. R., *Ethylene binding in mono- and binuclear Cu^{I} complexes with tetradentate pyridinophane ligands, Dalton Trans.* **2022**, *51*, 13426.

List of Abbreviations

In this doctoral thesis, the abbreviations and acronyms most commonly used in organic chemistry are based on the recommendations of the ACS “Guidelines for authors” which can be found and consulted at:

https://www.cas.org/support/documentation/references/cas-standard-abbreviations#listinga.

Abstract

Forging highly congested stereocenters in an asymmetric manner is of high interest to the fine chemical and pharmaceutical industry as these sterically stressed motifs (typically being tertiary or quaternary stereocenters) are found within the structures of many bio-active molecules and synthetic drugs. In the last couple of decades, new converging strategies have been developed using transition metal (TM) based catalytic methods providing a convenient way to form compounds featuring such appealing stereogenic centers. While transformations leading to these targets have long been dominated by the use of 2nd 3rd row transition metals such as Pd and Ir, recent work has uncovered the significant potential of first-row transition metals such as Cu, Ni and Co, which represent more sustainable and less expensive alternatives.

Our group has developed various asymmetric allylic substitution processes mediated by TMs during the last 8 years, spanning the use of 2nd and 3rd row to 3d (transition) metals. In order to design more and novel sustainable methodologies for the synthesis of scaffolds that feature stereogenic tertiary/quaternary carbon centers, an accurate analysis of the selectivity and activity parameters controlling these transformations is desired.

This thesis presents three different case studies that focus on a comprehensive mechanistic rational of allylic and propargylic substitution reactions developed in our group over the years. In each of these cases, a different metal catalyst was used and our efforts allowed us to investigate both more classical 2-electron but also less explored 1-electron pathways in transition metal catalysis. A range of techniques were applied to gather a complete mechanistic picture of the selected transformations including NMR, EPR, kinetics, UV-Vis spectroscopy, X-ray crystallography, MS, React-IR and computational methods. This thesis illustrates the value of mechanistic studies to reveal unexpected reaction intermediates and manifolds controlling the overall efficiency of protocols that furnish sterically frustrated stereocenters.

Table of Contents

Chapter 1. Introduction

1.1 Transition metals used by humankind

Humanity has used metals for technology and engineering advances for over the last 11.000 years.[1] There is evidence that back in the Stone Age the *Homo Sapiens* already used unprocessed copper and gold ores for decoration and bulk gold/silver for trade.[2] During the Bronze and the Iron Age, metallurgy raised in society as the main reason to search and explore useful tools and materials based on transition metals (TMs).[3] Newly discovered metals such as iron, copper and tin were utilized for stone device up-grading, food hunting, vivers processing and warfare.[4] While other ores based on gold and lead were applied in ritual ornaments and jewelry, silver and copper ones were employed for monetary systems.[5,6] Since then, different alloys have been discovered evolving these technologies used towards handcraft-utile gadgets (Figure 1.1).[7,8] Millennia later, iron and steel fueled the rise of the Industrial Revolution advancing the machinery employed in manufacturing processes.[9] Until then, transition metals has accompanied human technological advances, achieving milestones such as technical materials improvement used in medicine, engineering and energy storage among others. The use of transition metals has been crucial for our society being employed in important areas such as energy and transport of resources (water, electricity, gas), the construction of materials (alloys and blends) and in drug synthesis (metabolic complexes and vitamins). The chemical industry has used TMs in the last 100 years in the form of metal catalysts used primarily in hydrogenation, hydrogenolysis, isomerization and oxidation reactions, among others types of useful transformations.[10]

---

[1] Reardon, A. C., *Metallurgy for the Non-Metallurgist*. ASM International, 2012.

[2] Omondi, S. *What was the first metal used by humans?* https://www.worldatlas.com/articles/what-was-the-first-metal-used-by-man.html

[3] Biddulph, K. *Why prehistory? Why not Stone Age, Bronze Age, Iron age?* https://www.schoolsprehistory.co.uk/2013/11/24/why-prehistory/.

[4] University of Sydney, *Materials that shaped history*, https://www.unsw.edu.au/science/our-schools/materials/engage-with-us/high-school-students-and-teachers/materials-shaped-history.

[5] Bisson, M. S., *Ancient african metallurgy: The socio-cultural context*. Altamira Press, 2000.

[6] Bank of Thailand, *The first monetary currencies of the world.* https://www.bot.or.th/English/MuseumAndLearningCenter/BOTMuseum/Northern/Pages/T1stcoin.asp.

[7] Collis, J., *The European Iron Age*. Routledge, 1997.

[8] Ramage, A., Craddock P. T., *King croesus' gold: Excavations at sardis and the history of gold refining.* Harvard University Press, 2000.

[9] Britannica, T. *Industrial revolution*, Encyclopedia Britannica. https://www.britannica.com/event/ Industrial-Revolution

[10] David, J. M. R., History of the Chemical Industry 1750 to 1930 – an Outline, University of York, 1998.

The next section will explain why TMs have been often employed in the chemical industry, more precisely in the field of organic synthesis empowered by homogeneous catalysts.

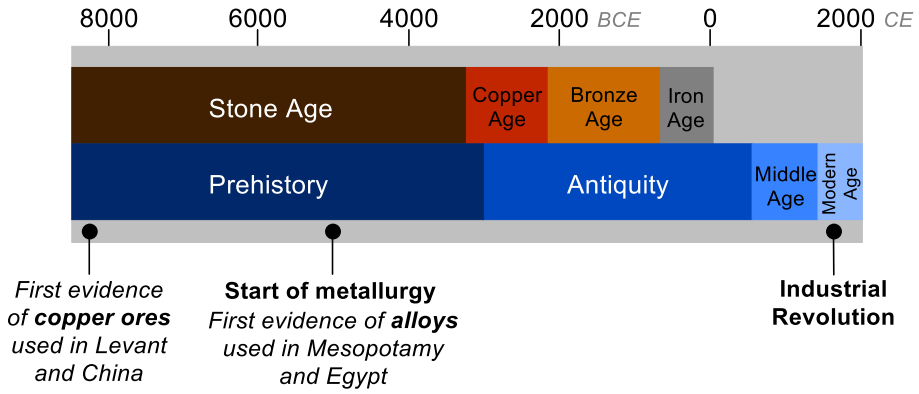

Figure 1.1: Initial discoveries of TMs and their use by the human race.

1.1.1 Transition metals used in organic synthesis

Organic synthesis is a key method for the preparation of pharmaceuticals, fine chemicals, agrochemicals, food additives, pigments and dyes, which are important compounds needed in every-day life.[11,12] In the last century, organic synthesis has extended its tools in order to achieve a higher synthetic efficiency related to two different objectives: [a] to accomplish higher selectivity and [b] to attain higher atom economy. There are four major types of selectivities: (*i*) chemo-selectivity, (*ii*) regio-selectivity, (*iii*) diastereo-selectivity and (*iv*) enantio-selectivity.[13] Figure 1.2 displays some typical examples related to the field of TM-catalyzed allylic substitutions to illustrate each concept. A chemo-selectivity example is provided for the Pd-catalyzed transformation of vinyl boronate esters. This reagent can be selectively activated with the same Pd catalyst under different reaction conditions achieving either an allylic substitution, a Suzuki–Miyaura cross-coupling or a base-driven elimination (Figure 1.2a).[14] To illustrate regio-selectivity, an Ir-catalyzed allylic substitution reaction involving cinnamyl carbonate is illustrated. In this case, the reaction was optimized towards the **branched** regio-isomeric product, avoiding (***E***) and (***Z***) configured **linear**

[11] Beller, M.; Bolm, C., *Transition Metals for Organic Synthesis,* Wiley-VCH, 2004.
[12] Mistri, R.; Kumar, B., *Asian J. Chem.* 2021, 33, 489.
[13] Tsuji, J., *Transition Metal Reagents and Catalysts: Innovations in Organic Synthesis,* John Wiley & Sons, 2000.
[14] Kim, B.-S.; Hussain, M. M.; Hussain, N.; Walsh, P. J., *Chem. Eur. J.* 2014, 20, 11726.

regio-isomers (1.2b).[15] Another example of an allylic substitution reaction explains the concept of diastereo-selectivity (1.2c).[16]

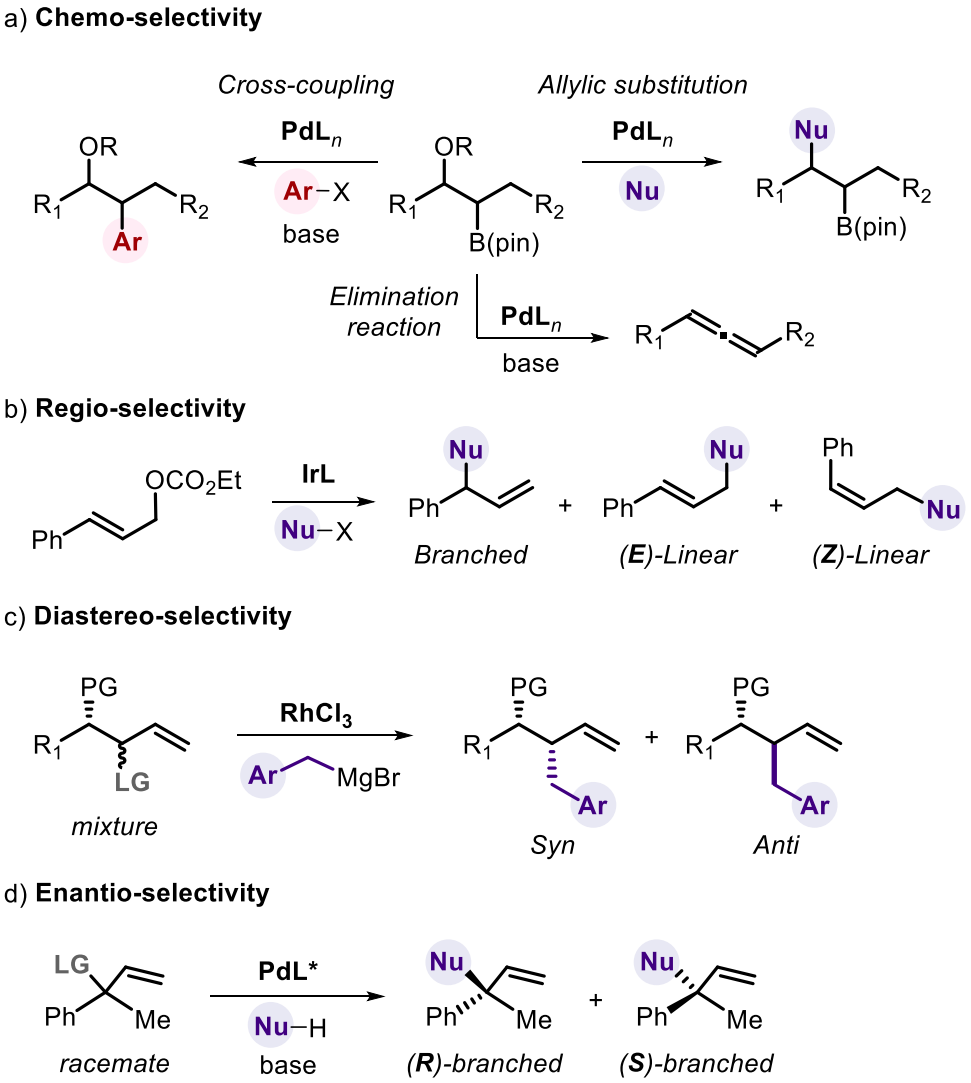

Figure 1.2: Types of selectivities defined in the area of organic chemistry and selected examples of TM-catalyzed (allylic substitution) reactions.

Here, a tertiary allylic surrogate bearing two different stereocenters (a chiral protecting group PG chain and a racemic leaving group LG) undergoes an alkylation reaction with a Grignard reagent. This reaction provokes the formation of the ***syn*** product. Finally, an example from our own group shows how a Pd-based chiral catalyst

[15] Madrahimov, S. T.; Li, Q.; Sharma, A.; Hartwig, J. F. *J. Am. Chem. Soc.* 2015, 137, 14968.
[16] Pal, D.; Wright, T. B.; O'Connor, R.; P. Evans, A. *Angew. Chem. Int. Ed.* 2021, 60, 2987.

activates a racemic allylic precursor and selectively delivers a functionalized (***S***)-configured product (1.2d).[17]

Overall, by exerting selectivity, product formation with high preference towards a specific reactivity is achieved avoiding by-products that hamper the yield and the isolation of the product of interest. Additionally, referring to the second objective mentioned above ([b]), the atom economy describes the amount/percentage of starting compounds converted into desired products. Unfortunately, this aspect is often sacrificed to enhance the process selectivity, for example when using a catalyst and/or additives.

Having discussed the main objectives of organic chemists while focusing on metal-based catalysts, it is worth mentioning in more detail some of the first examples of the use of metal complexes in the chemical industry.

One of the earliest examples dates back to 1925 when Fischer and Tropsch used heterogeneous Fe and Co catalysts to transform *syngas* (a carbon monoxide/hydrogen gas mixture) to hydrocarbons (i.e., synthetic oil, Figure 1.3a). Few years later, Rölen developed a hydroformylation reaction using *syngas* and propene as reagents $Co_2(CO)_8$ as a homogeneous catalyst (1.3b). Around the same time, Reppe established a new protocol for the catalytic formation of carboxylic acids and esters from acetylene, carbon monoxide and methanol (1.3c). The discovery of these carbonylation processes also permitted to access aldehydes and alcohols through Fe, Co and Ni carbonyl catalysis. Other types of selective and mild catalytic processes have been developed utilizing noble metals such as Rh and Ru.[13]

After these discoveries, chemists have sought to recycle these metals to avoid large amounts of chemical waste in industry, reduce costs and to enable more effective reactions. Inspired by enzymes found in nature, the field of organic chemistry has long focused on the development of metal catalysts that can be recycled and minimize the activation barrier of reactions thereby simplifying reaction routes. Massive efforts are currently put into (*i*) the development of new catalysts based on earth-abundant transition metals and (*ii*) understanding the mechanisms through which these complexes perform. The focus of this thesis is mainly on this latter aspect.[11]

[17] Pamies, O.; Margalef, J.; Canellas, S.; James, J.; Judge, E.; Guiry, P. J.; Moberg, C.; Backvall, J. E.; Pfaltz, A.; Pericas, M. A.; Dieguez, M. *Chem. Rev.* 2021, 121, 4373.

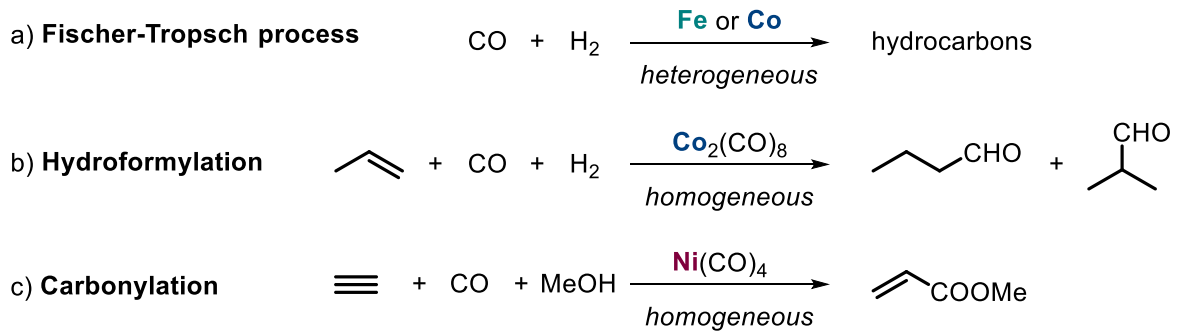

Figure 1.3: Early examples of the use of TMs in catalytic industrial processes.

1.1.2 The constant evolution of synthetic chemistry

The fields of organic and organometallic chemistry are constantly developing new concepts and methodologies for the preparation of organic compounds, metal catalysts and asymmetric synthesis strategies. In the last half century, these fields have evolved tremendously and as a testament of their importance, various researchers active in these areas have been awarded the Nobel Prize.[18] Figure 1.4 summarizes the recognitions given in four different fields of chemistry: **Organic** and **Organometallic** syntheses, **Asymmetric** chemistry applied in organic chemistry and **Physical** chemistry. Among the awarded work, the development of metathesis reactions through organometallic carbene complexes in **2005**, by Chauvin, Grubbs and Schrock is regarded an important milestone. Another example is the discovery of metal-catalyzed cross-coupling reactions (awarded in **2010**), which was initially explored with Pd-salts by Heck, Negishi and Suzuki, and in each case with a different coupling partner. These two discoveries revolutionized traditional organic chemistry approaches needed to access pharmacological compounds or agrochemicals, for example, and to allow their adaptation in an industrial context. In addition, two more Nobel Prizes were awarded to the field of asymmetric catalysis. In **2001**, the Swedish Academy recognized the use of chiral complexes in transition-metal catalyzed asymmetric reactions, and more specifically for enantioselective oxidation and hydrogenation reactions. 20 Years later in **2021**, the field of asymmetric organo-catalysis was awarded with this prestigious recognition. Both List and MacMillan found

[18] Novel Prize Outreach, https://www.nobelprize.org/prizes/chemistry/.

inspiration in the efficiency of chiral enzymes to develop simpler organic systems that could act as chiral auxiliaries in organic reactions.

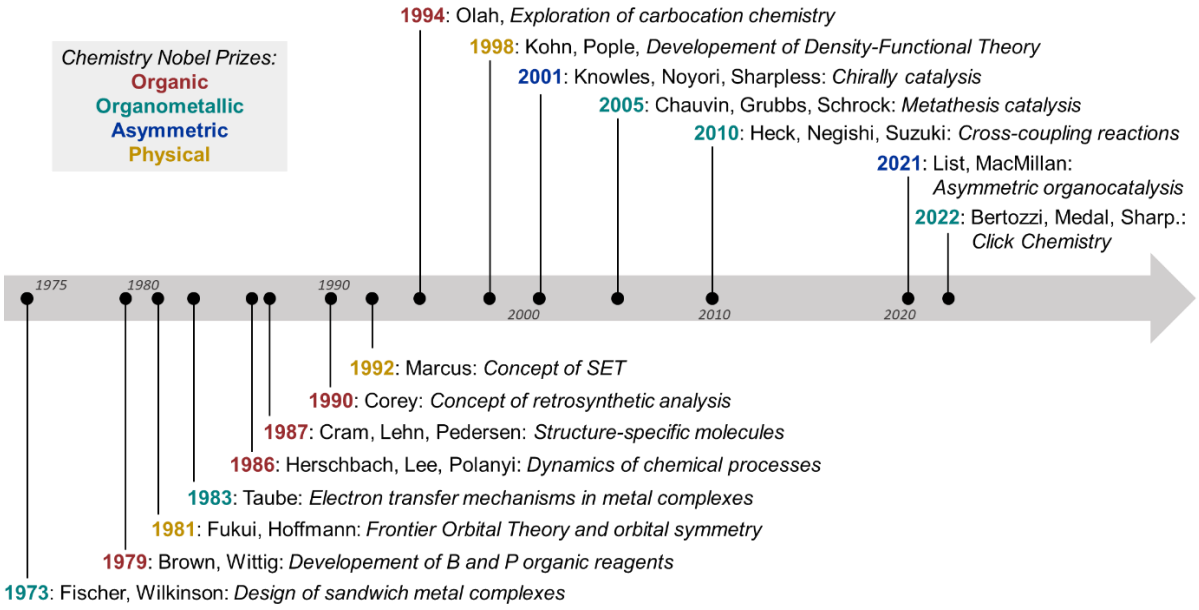

Figure 1.4: Chemistry Nobel prizes awarded from 1970 up to present in selected fields of chemistry.

Before moving to a more defined description of the reactivity patterns described in this PhD thesis, we should consider the degree of complexity that organic synthesis has accomplished in the last decades through different approaches. The areas of organic, organometallic and analytical science have together achieved both the synthesis and characterization of highly sophisticated molecules featuring densely substituted sp^3-carbon centers.

1.1.3 Forging quaternary and tertiary substituted stereocenters

Highly substituted carbon centers are found in a wide range of natural products, thus the interest of the fine chemical and pharmaceutical industry in the last decades has been on finding converging strategies for the formation of such congested stereocenters.[19,20] Quaternary stereocenters are defined as those sp^3-carbon centers in which all four-substituents are carbon atoms. Likewise, the replacement of one of these carbon-substituents by a heteroatom (or H) leads to a different definition as these are typically denoted as tertiary stereocenters (Figure 1.5a).

[19] Quasdorf, K. W.; Overman, L. E. *Nature* 2014, 516, 181.
[20] Liu, Y.; Han, S. J.; Liu, W. B.; Stoltz, B. M., *Acc. Chem. Res.* 2015, 48, 740.

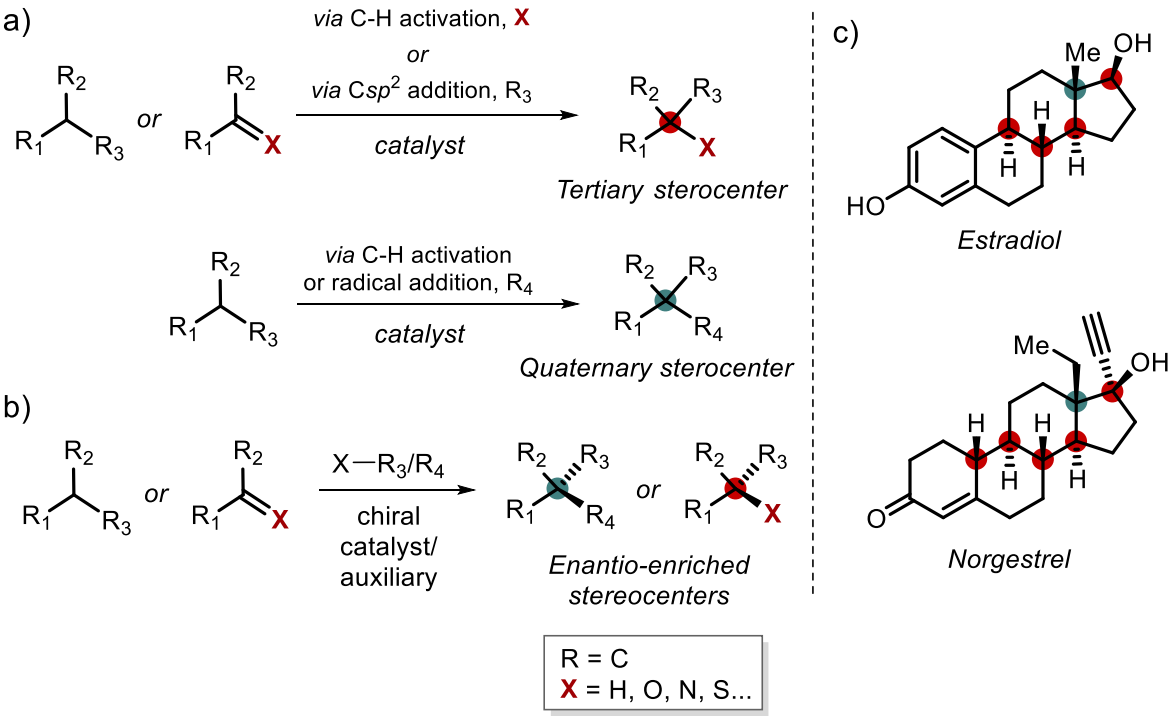

Figure 1.5: a) Formation of tertiary and quaternary substituted stereocenters, b) enantio-induction by chiral catalysts and c) examples of biologically active molecules with chiral tertiary (marked in **red**) and quaternary stereocenters (in **green**).

Moreover, as already briefly mentioned above, an absolute mutual arrangement of substituent represents a type of structural complexity, which can be achieved when the new bond formation process is subjected to a chiral environment (a chiral auxiliary, solvent or catalysts). Thus, conversions can be done enantio-selectively, with the chiral product often possessing higher and more directional biological activity than the corresponding racemate being of importance for effective pharmaceuticals (Figure 1.5b).[21,22]

Among the most used enantio-selective methods, organocatalysis,[23,24,25] biocatalysis [26,27] and TM-mediated transformations[28,29] have been shown to be effective and

[21] Susse, L.; Stoltz, B. M. *Chem. Rev.* 2021, 121, 4084.
[22] Cozzi, P. G.; Hilgraf, R.; Zimmermann, N. *Eur. J. Org. Chem.* 2007, 5969.
[23] Trowbridge, A.; Walton, S. M.; Gaunt, M. J. *Chem. Rev.* 2020, 120, 2613.
[24] Wang, J.; He, F.; Yang, X. *Nat. Commun.* 2021, 12, 6700.
[25] Kim, B.-S.; Hussain, M. M.; Hussain, N.; Walsh, P. J., *Chem. Eur. J.* 2014, 20, 11726.
[26] Marin-Valls, R.; Hernandez, K.; Bolte, M.; Parella, T.; Joglar, J.; Bujons, J.; Clapes, P. *J. Am. Chem. Soc.* 2020, 142, 19754.
[27] Gaggero, N. *Eur. J. Org. Chem.* 2019, 7615.
[28] Hawner, C.; Alexakis, A. *Chem. Commun.* 2010, *46*, 7295.
[29] Douglas, C. J.; Overman, L. E. *Proc. Natl. Acad. Sci. USA* 2004, 101, 5363.

versatile methods. This last category of transformations is very diverse including the sub-areas of TM-mediated photo-redox chemistry, C–H activation, cross-coupling reactions, allylic alkylations and propargylic substitution reactions that have created access to biologically active molecules containing quaternary or tertiary stereogenic centers.

Asymmetric allylic substitutions mediated by TMs provides a well-studied strategy to form highly congested centers. While this transformation has been dominated by the use of second- and third-row transition metals like Pd and Ir, recent work has uncovered the significant potential of first-row transition metals such as Cu, Ni and Co, which furnish a more sustainable and less expensive alternative. Their use also opens a doorway to single-electron transfer steps unlike the conventional two-electron redox pathways known for Pd and Ir. [21]

1.1.4 Atom configuration and active orbitals of transition metals

As the importance of transition metals for the transformation and synthesis of high valuable compounds has been described, it is essential to have a look at the atomic structure of such elements.

Transition metals, also referred as d-block metals, represent a family of elements that have “chemically active” electrons distributed over their d-orbitals (Figure 1.6a). Chemically active electrons are defined as electrons that can participate in chemical bonding with other molecules, for example, ligands and substrates. As there is a relatively small difference in the energy of the different d-orbital electrons, the number of electrons participating in chemical bonding can also vary.[30] It should be mentioned that s-orbitals of the same energetic period are also involved in chemical bonding. While in most cases the s-level electrons have a higher energy than the ones present in the d-orbitals, there are some examples where this situation is reversed. This is the case for Pd(0), which has $4d^{10}5s^{0}$ as an electronic configuration.[31]

[30] Ernest, Z. *Electronic configuration: s,p,d,f orbitals.* https://socratic.org/chemistry/the-electron-configuration-of-atoms/arrangement-of-electrons-in-orbitals-spd-and-f.
[31] Hartwig, J. F, *Organotransition Metal Chemistry – From Bonding to Catalysis,* University Science books, 2009.

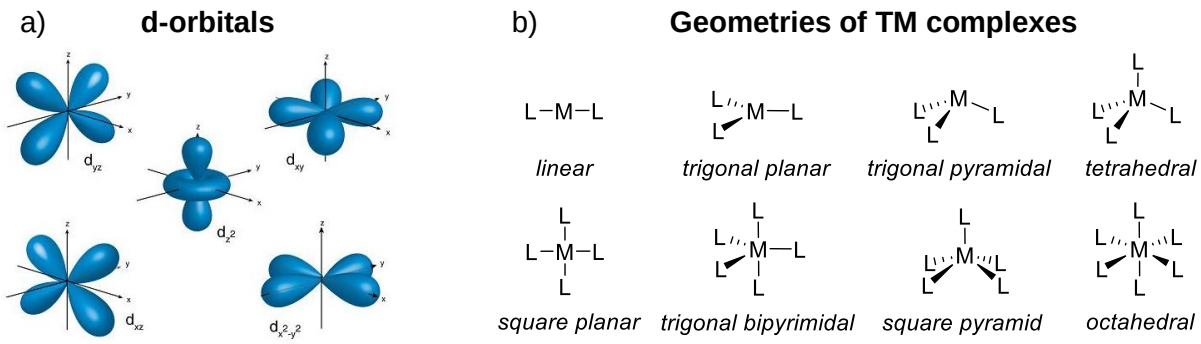

Figure 1.6: a) Lobular representation of the 5 types of d-orbitals and b) typical geometries adopted my TM complexes.

TMs that bind with ligands form coordination complexes. These compounds have different geometries depending on the atomic number of the metal, number of ligands involved and the oxidation state of the metal center (Figure 1.6b). Generally, a d-electron count – following the 18-electron rule – is an effective way to understand the geometry and reactivity of transition metal complexes. This formalism has been integrated into two more accurate models, the crystal field theory (CFT) and the ligand field theory (LFT), which both are more advanced versions based on molecular orbital theory (MOT). MOT reshaped the study of chemical bonding by approximating the states of bonded electrons (the molecular orbitals) as linear combinations of atomic orbitals (LCAO). These approximations can be achieved by the use of density functional theory (DFT) or Hartree-Fock (HF) models for the Schrödinger equation.

According to these terminologies, we can generally classify metal complexes into two categories: those complexes that have unpaired electrons which are described as paramagnetic substances, and complexes with paired electrons in all their highest occupied molecular orbitals (HOMOs) and are considered as diamagnetic species. In this thesis, each experimental chapter intends to resolve the challenge of determining the oxidation state of the metal catalyst and whether there are dia/paramagnetic species involved.[31]

In the following division, we will dive into the world of allylic and propargylic chemistry. Exploring the chemistry and structure of these compounds and understanding how they interact with transition metals can help to develop new carbon-carbon and carbon-heteroatom bond formation reactions.

1.2 Allyl and propargyl groups in organometallic complexes

1.2.1 Structure and properties

The allyl motif is present in many biologically active compounds, polymers and materials. Similarly, the propargyl group is also encountered often and as for allyl fragments, synthetically useful. The allyl group is a $–CH_2-CH=CH_2$ chain (Figure 1.7 right), while the propargyl moiety bears a higher level of unsaturation featuring a $–CH_2-C\equiv CH$ atom connection (Figure 1.7 left). It is important to differentiate the intermediates derived from hydride loss (forming an allylic/propargylic cation), radical abstraction (generating a radical in the allylic/propargylic chain) and proton abstraction (obtaining an allylic/propargylic anion).

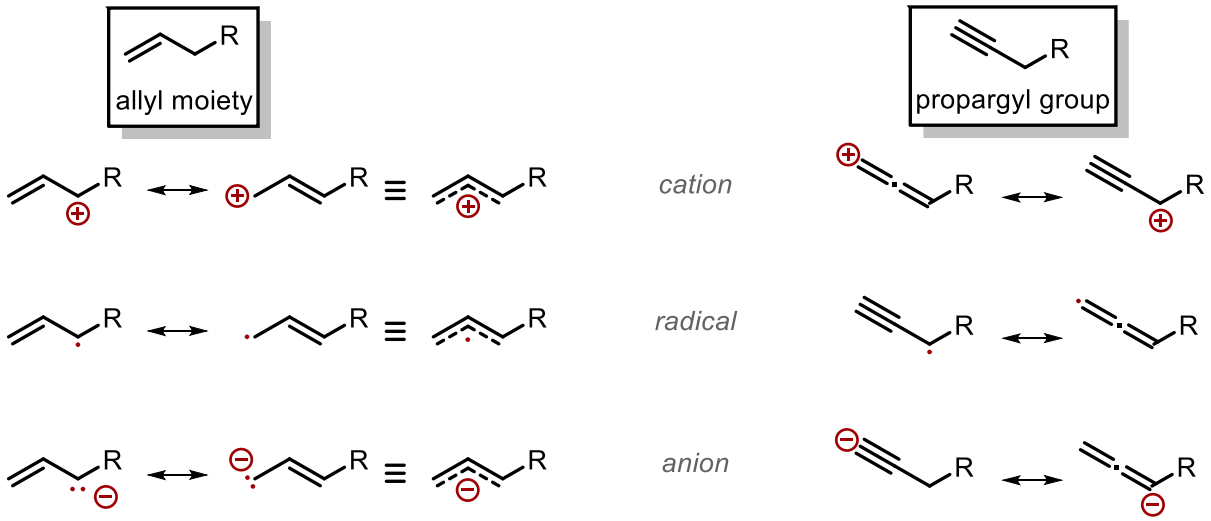

Figure 1.7: Allyl and propargyl groups and their resonance structures.

1.2.2 Allyl and propargyl moieties as ligands for metal bonding

To understand the structure and bonding of allyl and propargyl ligands with transition metals it is imperative to consider that these ligands generally coordinate to the positively charged metal center as anions, and although sometimes in their radical form.[31] The oxidation states of the metal can range from neutral to +6 and only in rare occasions catalytically active, negatively charged centers are involved. If we draw the molecular orbitals of these moieties, a better view on which d-orbitals of the metal will optimally combine. The allyl anion has two different coordination modes to a metal center depending on how many atoms of the ligand are bound to the metal: η^3 and η^1

(Figure 1.8a and 1.8b),[32,33] which is referred to as hapticity. In the case of □[3]-coordination, the molecular orbitals of the π system can overlap with the metal d-orbitals having the correct symmetry (1.8d). The lowest-energy MO forms a σ bond to d_z^2 (Ψ_1). The HOMO level behaves as a π-donor to the d_{xz} metal orbital ($\Psi 1_2$) while the LUMO is a π-acceptor interacting with the d_{yz} level of the metal ($\Psi 12_3$).

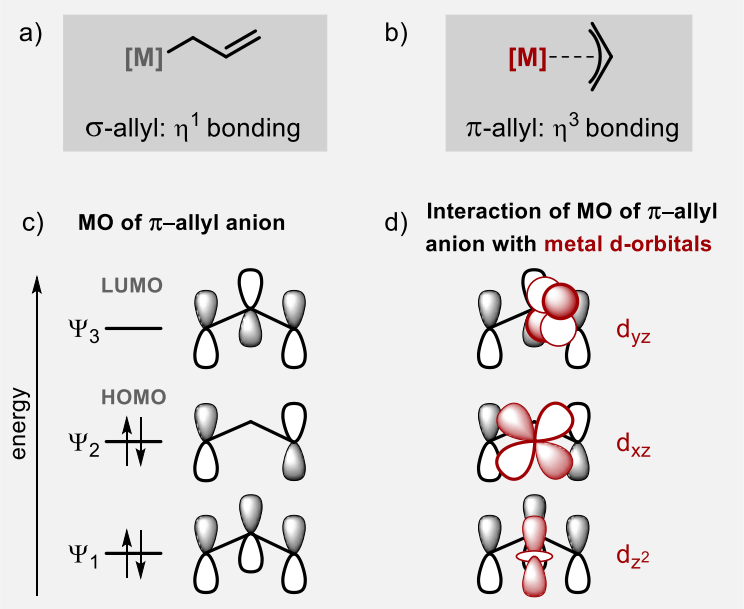

Figure 1.8: Allyl anion binding to a metal center as a □-allyl [□[1] hapticity, (a)], and as a □-allyl [□[3] hapticity, (b)]. Molecular orbitals of a □-allyl anion system (c) showing interactions with metal d-orbitals represented in red (d).

The propargyl anion, on the other hand, has only a □-coordination mode (□[1] hapticity) compared with the allyl anion.[34] Analysis of the molecular orbitals of the acetylide anion interact with the d-orbitals of a metal (Figure 1.9b) shows that the d_{xz} and d_{yz} orbitals offer a correct π-type symmetry to interact with the acetylide π-orbitals ($\Psi 1_2$). This provides an extended, π-conjugated and thus stabilized electronic structure. Localization of an unpaired electron (represented in the $\Psi 12_3$ SOMO level)

[32] University of Liverpool, *π Molecular Orbitals of the Allyl Anion.* https://www.chemtube3d.com/orbitalsallylanion/.
[33] University of Liverpool, *Interactions between Allyl Molecular Orbitals and Metal d Orbitals.* https://www.chemtube3d.com/orbitalsm-allyl/.
[34] University of Liverpool, *Bonding orbitals in Acetylene (Ethyne) sp.* https://www.chemtube3d.com/orbitalsacetylene/.

enables a direct interaction with the d_{z^2} orbital, which is responsible of the σ bond formation between the metal and the acetylide ligand.[35,36]

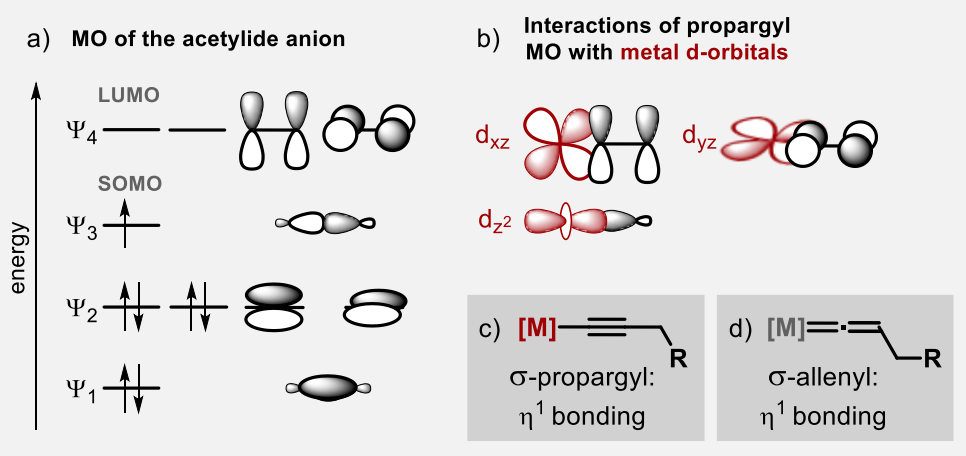

Figure 1.9: a) Molecular orbitals of the acetylide anion and their interaction (b) with the d-orbitals of the metal (in red). c) □□bonding of the propargyl unit, and d) allenyl ligands (d).

1.2.3 Allyl and propargyl moieties utilization

The allyl and the propargyl anions can bind in various ways to transition metal centers as coordinating ligands. Here some examples are presented where these fragments are used as part of the reagents and are converted into products.

In general, olefinic and allylic metal complexes have been widely used in the last half century. These type of complexes have been employed as pre-catalysts for several reactions. For instance, the $[Pd_2(allyl)_2Cl_2]$ dimer is a well-known pre-catalyst, which is able to initiate many organic transformations including cross-coupling reactions, nucleophilic additions to dienes and decomposition of diazo compounds towards reactive carbenes, and also, it is has been proven as a resourceful precursor for other Palladium active catalysts. Nonetheless, in general allylic complexes are mainly classified as reactive intermediates found in TM-catalyzed organic transformations. An example that has been explored during the last decades is the oxidative C–H functionalization of unactivated allylic substrates. This transformation requires the stoichiometric addition of oxidants to regenerate the active catalytic species. However,

[35] Lichtenberger, D. L.; Renshaw, S. K.; Bullock, R. M. *J. Am. Chem. Soc.* 1993, 115, 3276.
[36] Milan, D. C.; Vezzoli, A.; Planje, I. J.; Low, P. J. *Dalton Trans.* 2018, 47, 14125.

the most known and exploited transformation involving allyl fragments are **allylic substitutions**.

In propargylic chemistry, transition-metal propargyl (Figure 1.9c) and allenyl (1.9d) type complexes both participate in common reactions that characterize TM-alkyl compounds: (i) insertion into the -CH_2- bond terminal gamma position, (ii) electrophilic addition to the triple bond, and (iii) addition of organometallic reagents to build up complexes of higher nuclearity. Moreover, these metal-propargyl based complexes also have the capacity to engage in reactions analogous to those known for organic acetylenes and allenes, undergoing propargyl to allenyl rearrangement and *vice versa*). In the next sections, further details are provided discussing the intricacies of allylic and propargylic substitutions for new bond formations through the coupling of both nucleophiles and electrophiles.[37]

[37] Wojcicki, A.; Shuchart, C. E. *Coord. Chem. Rev.* 1990, 105, 35.

1.3 Metal-catalyzed allylic substitutions

Substitution reactions of allylic electrophiles are classical processes catalyzed by transition metals that achieve the formation of new C–C and C–heteroatom bonds using external nucleophiles. Generally, the allylic surrogates are activated substrates, which means that they have an activated leaving group (LG) at one of the allylic termini. These LGs can be protected allylic alcohols (acetates, carbonates, carbamates) but may also be allylic halide derivatives, epoxides or phosphates.[31]

1.3.1 Origins of the allylic substitution

The first reported allylic substitution was developed by Tsuji and co-workers 50 years ago as a stoichiometric reaction.[38] Years later, this classic transformation was converted into a catalytic process by Hata, Atkins and coworkers within Toray and Union Carbide Industries achieving good regio-selectivities and higher reactivities using a Pd-based metal catalyst. After these discoveries, and seeking to achieve better selectivities, Trost and co-workers reported the first asymmetric allylic substitution reaction, which reached 24% *ee*.[39] Since then, the field has evolved by the design of new, more effective catalysts and chiral ligands that nowadays can promote similar reactions with >99% *ee*.

Figure 1.10 shows a clear schematic picture of the generally accepted mechanism for the Tsuji-Trost reaction, an optimized catalytic process of a Pd-catalyzed allylic substitution. The transformation starts with the complexation of a [Pd^0] precursor and the ligand, generating an active species [Pd^0L]. This low-valent complex undergoes oxidative addition by an (activated) alkene (note: these can be both *linear* or *branched*) forming a [Pd^{II}(allyl)] species. Importantly, the allylic moiety is typically geometrically labile and can undergo facile isomerization, and therefore the initial nature of the allylic substrate is not relevant towards the reaction outcome. An active (pro)nucleophile can attack the electrophilic [Pd^{II}(allyl)] species through pathway **a** or **b**, which eventually controls the regio-selectivity of the process.

[38] Tsuji, J; Takahashi, H.; Morikawa, M. *Tetrahedron Lett.* 1965, 6, 4387.
[39] Trost, B. M. *Tetrahedron* 2015, 71, 5708.

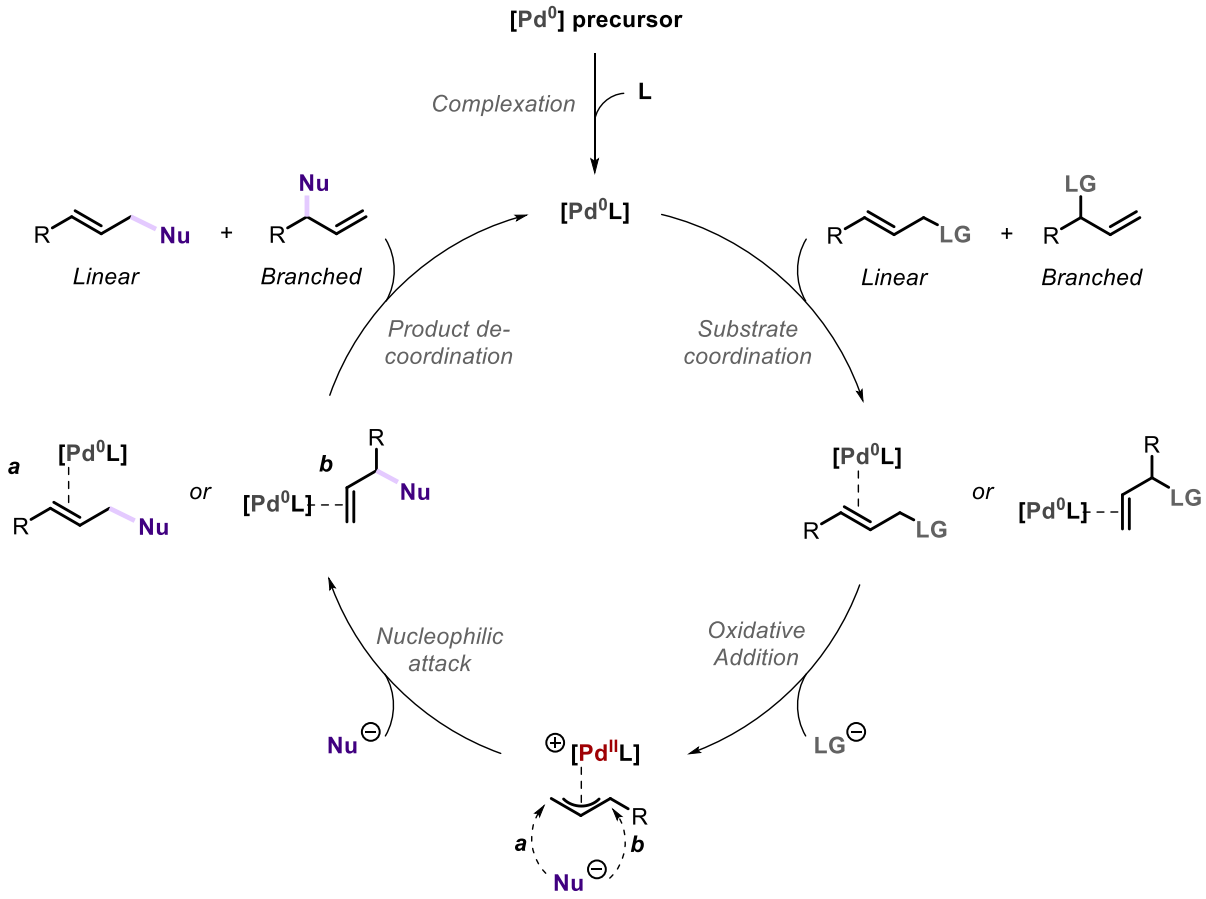

Figure 1.10: Proposed mechanism of a Pd-catalyzed allylic substitution: the Tsuji-Trost reaction.

1.3.2 The nucleophilic attack: inner vs. outer sphere mechanisms

The nucleophilic attack involves the formation of a new C–C or C–heteroatom bond. Thus, it is important to consider the two plausible mechanisms that accommodate this bond formation process. In the literature, two possibilities have been classified according to the presence or absence of a coordination of the nucleophile to the metal center. In the first case, when the nucleophilic fragment coordinates to the the metal prior to attacking the electrophilic allyl group, the type of mechanism is considered an "inner sphere" attack (Figure 1.11a). This pathway involves a ligand exchange of the LG anion by the incoming nucleophile. Conversely, if the nucleophile attacks the allyl fragment without prior coordination to the metal center, the process is considered "outer sphere" (Figure 1.11b).[31]

Initially, the key variable that was used to classify the different nucleophiles and predict which type of mechanism these would induce was their acidity of the pro-nucleophilic

species (pK_a). If the pK_a is lower than 25, it is considered a *soft* nucleophile, while pK_a higher than 25 are classified as *hard* nucleophiles. After several years of exploring allylic chemistry, there have been many exceptions observed, and nowadays, more variables are taken into consideration before a reaction is classified as *inner-* or *outer-*sphere. For example, the nature of the metal itself, the ligand (anchoring points and nature of the donor atoms), the solvent used in the reaction and even the use of external additives are all relevant features.[40, 41, 42, 43]

After discussing these basic principles of the allylic substitution reaction, next the dynamic processes and equilibria that can be observed in these transformations are outlined. The control over these phenomena helps to rationalize how high selectivity in allylic substitution can be achieved (Figure 1.2, Section 1.0.1) as to maximize the synthetic output.

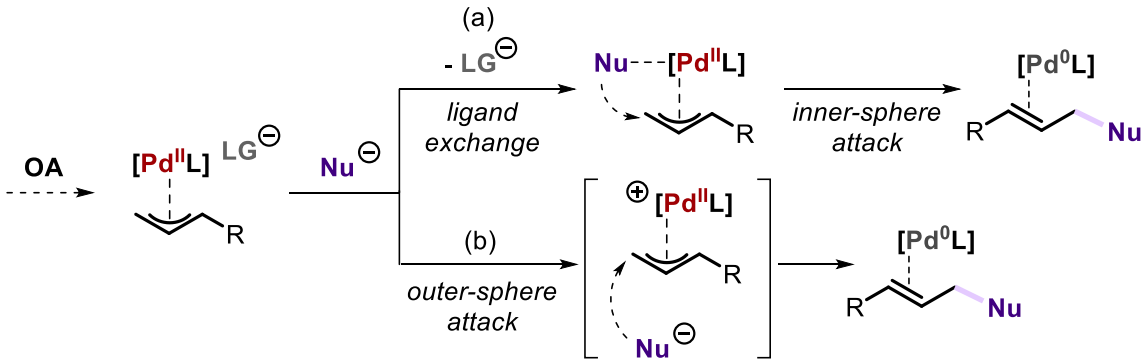

Figure 1.11: Inner (a) and outer (b) attack mechanisms at the less hindered position.

[40] Trost, B. M; Thaisrivongs, D. A. *J. Am. Chem. Soc.* 2009, 131, 12056.
[41] Trost, B. M; Thaisrivongs, D. A.; Hartwig, J. *J. Am. Chem. Soc.* 2011, 133, 12439.
[42] Zhang, J.; Stanciu, C.; Wang, B; Hussain, M. M.; Da C.S.; Carroll, P. J.; Dreher, S. D.; Walsh, P. J. *J. Am. Chem. Soc.* 2011, 133, 20552.
[43] Sha, S.-C.; Zhang, J.; Carroll. P. J. *J. Am. Chem. Soc.* 2013, 135, 17602.

1.3.3 Dynamic processes of the allylic moiety as ligand

An important feature of allyl ligands is that they exhibit dynamic behavior. These phenomena can be observed throughout the catalytic cycle through a number of different equilibria, for example dimerization, allyl plane rotations and π-σ-π isomerization.[31]

Dimerization processes start when two molecules of [Pd^{II}(allyl)]X interact and bind to each other (Figure 1.12a). Depending on the bulkiness of the ligand and on the substituents of the alkene, this process occurs with or without de-coordination of ligand L. The resulting complex is a bimetallic bis-allylic species with the counter ion bridging both metal centers. This is usually the case when X is a Cl, Br, OAc or CF_3COO anion. These dimeric species are sometimes unreactive and considered as *off-cycle* species.

Another phenomenon is the interconversion of *exo* and *endo* isomers. This is particularly observed with C_1-symmetry ligands, and the allyl fragment can have two different conformations depending on how the allyl substituents are positioned compared to the metal center. When the allyl fragment points “inwards” it is categorized as the *endo* isomer, and when the fragment points “outwards” it is considered the *exo* form (Figure 1.12b).[44]

There have been different computational studies trying to understand whether this exchange happens through a formal □[3] flip (as depicted in Figure 1.12b) or going through a formal □□□□□ isomerization (□[3]-□[1]-□[3]). Depending on the system, different studies point out different conclusions.[45] This isomerization is important to foresee the site-preference of the nucleophilic attack.[46]

[44] Sherden, N., H., Dissertation (Ph.D.), California Institute of Technology. 2011, doi:10.7907/QEAX-9N40.
[45] Ariafard, A.; Bi, S.; Lin, Z. *Organometallics* 2005, 24, 2241.
[46] Kocovsky, P.; Backvall, J. E. *Chem. Eur. J.* 2015, 21, 36.

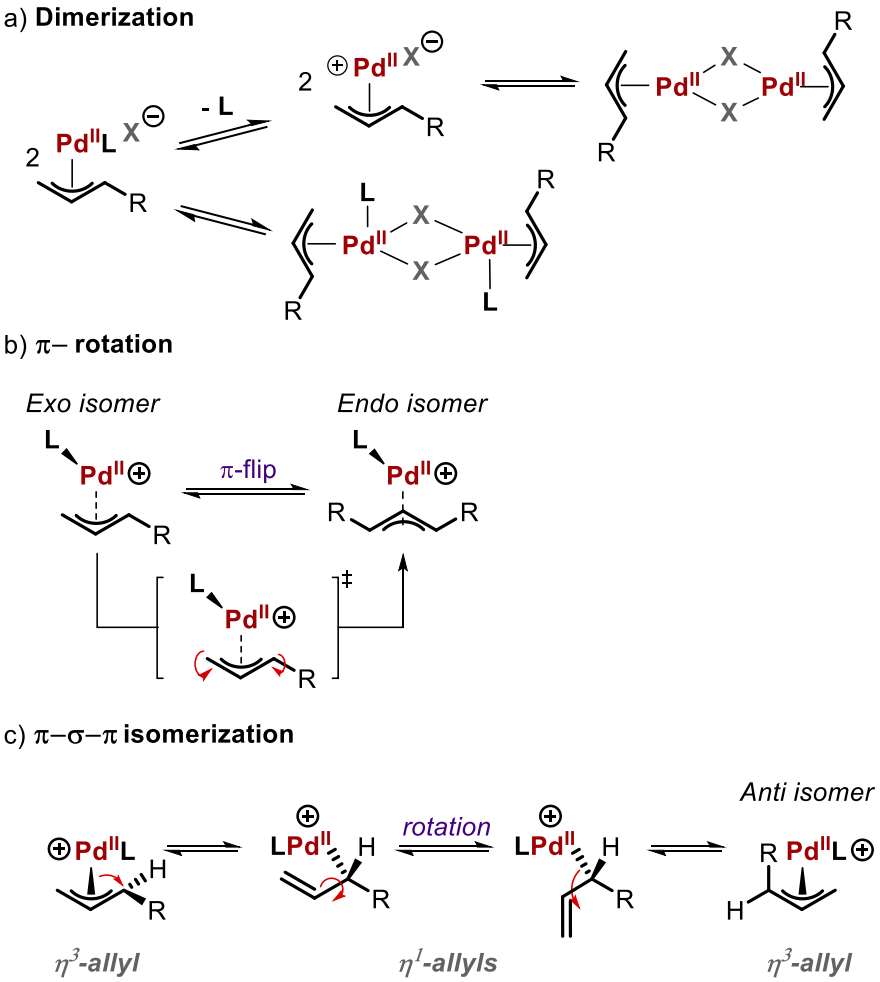

Figure 1.12: Dynamic processes of the allyl group; dimerization (a), □-rotation (b) and □□□□□ isomerization (c). Counter anions X are omitted for clarity in equations (b) and (c).

Finally, one of the most relevant equilibria observed in allylic chemistry is the interconversion of *syn* to *anti* isomers via □□□□□ isomerization of the allyl group (Figure 1.12c).[47,48] This occurs through a change of coordination from □^{3} to □^{1} in the Pd^{II}(allyl) species with a consecutive 180 degrees rotation of the allyl moiety, thereby positioning the double bond and the R substituent in *anti*-positions. The subsequent back-equilibration to a □-hapticity (□^{3}) delivers the *anti*-isomer. This pair of intermediate □^{3}-Pd-isomers are considered diastereo-isomers as long as the allyl group has a substituent (-R). It is also important to note that this kind of isomerization process has an equilibrium constant 10^1-to-10^3 higher than the actual substitution process. Thus, the population of each □^{3}-Pd-isomer can lead to different outcomes

[47] Fagnou, K.; Lautens, M. *Angew. Chem. Int. Ed.* 2002, 41, 26.
[48] Ogasawara, M.; Takizawara, K.-I; Hayashi, T. *Organometallics* 2002, 21, 4853.

regarding the regio/stereo-selectivity of the product. As shown in Figure 1.13, the ratio between *syn*- and *anti*-isomers can play a role in the outcome of the stereo-selectivity of the reaction. In situation (1) when the system is under a *Curtin-Hammett* regime, the ratio of *E*- and *Z*-product depends on the concentration of each Pd isomer [*syn*/*anti*], which directly depends on the equilibrating □□□□□ process between them (k_{iso}). It also depends to some extent on the rate of the reduction elimination (RE) process (k_E vs. k_Z). On the other hand, situation (2) shows another possibility, where there is no competitive interconversion between *syn*- and *anti*-isomers, and therefore, the *E*/*Z*-ratio in the product depends on the rate of the RE process (k_E vs. k_Z) and also possibly on the stereospecificity of the oxidative addition (OA) step to populate both s*yn*- and *anti*-isomers.

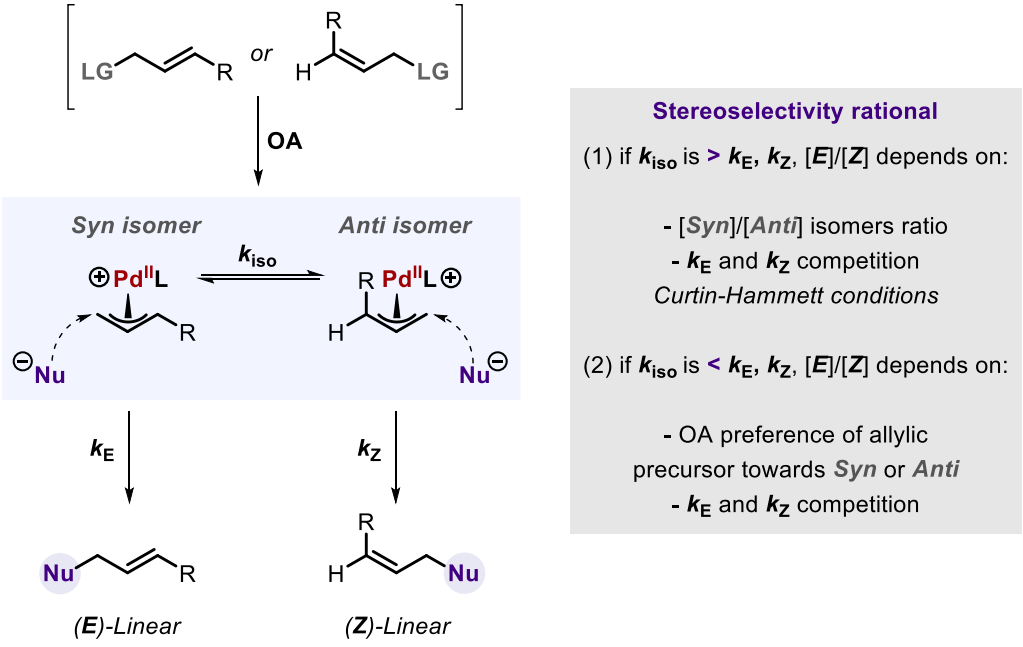

Figure 1.13: Outcome of the regio/diastereo-selectivity depending on the rate of *syn*/*anti* isomerization process and/or their initial population.

1.3.4 Reactivity behavior of allylic species

Before discussing relevant and selected literature examples of allylic substitutions, it is important to highlight the different reactivity behavior that allylic species can have. As seen in the previous section, the allyl ligand can equilibrate changing hapticity (Figure 1.14a), and each coordination mode has a different reactivity. While the □-allyl species act as a nucleophile akin of the reactivity behavior of alkenes, □-allyls act as

electrophiles undergoing attack of (external) nucleophilic species (Figure 1.14b). The explanation for this difference in reactivity is the distinct electron density distributed among the □-system of the activated double bond: in a □^{3} arrangement, the electrons are delocalized through the entire (formal cationic) metal-□-allyl system leaving the allyl fragment with an electrophilic character. In a □^{1} coordination, the □-electrons do not interact with the metal center and the double bond retains a nucleophilic character (Figure 1.14c and 1.14d).

This dichotomy provides versatility of the allylic fragment in organic synthesis, where the moiety can act as an electrophile or as a nucleophile giving multiple synthetic options.[49,50,51,52,53]

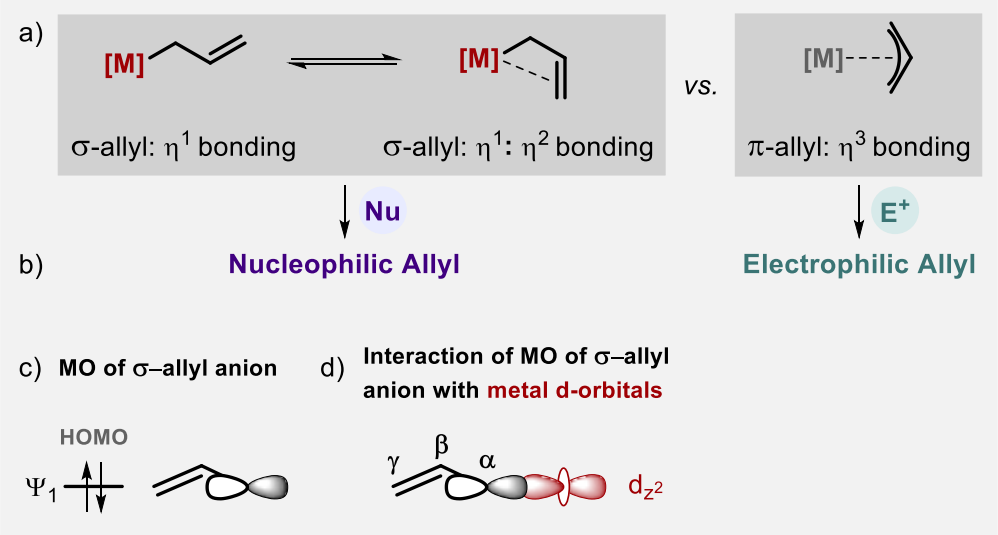

Figure 1.14: a) Modes of hapticity of the allyl group and (b) its comparison with the type of reactivity. c) Molecular orbitals of the allyl anion at the terminal position of the –CH_2-CH=CH_2.

[49] Mayr, H.; Bug, T.; Gotta, M. F.; Hering, N.; Irrgang, B.; Janker, B.; Kempf, B.; Loos, R.; Ofial, A. R.; Remennikov, G.; Schimmel, H. *J. Am. Chem. Soc.* 2001, 123, 9500.
[50] Mayr, H.; Kempf, B.; Ofial, A. R. *Acc. Chem. Res.* 2003, 36, 66.
[51] Dulich, F.; Muller, K.-H.; Ofial, A. R.; Mayr, H. *Helv. Chim. Acta* 2005, 88, 1754.
[52] Ammer, J.; Nolte, C.; Mayr, H. *J. Am. Chem. Soc.* 2012, 134, 13902.
[53] Garcia-Ruiz, C.; Chen, J. L. Y.; Sandford, C.; Feeney, K.; Lorenzo, P.; Berionni, G.; Mayr, H.; Aggarwal, V. K. *J. Am. Chem. Soc.* 2017, 139, 15324.

1.3.5 Enantioselective allylic substitutions with nucleophiles and electrophiles

Most of the recent advances in the field of allylic substitution have been achieved by exhaustive ligand engineering and design. As it can be imagined, amidst other various selectivities, enantio-induction is promoted by different parameters of a given system (chiral ligand, substrate, choice of metal and employed additives), with the chiral ligand being one of the most crucial factors that controls this selectivity. In this section, a selection of examples will be discussed and classified according to the chiral ligand employed, and the intricacies of the enantio-induction process.[54]

Coupling of allyl fragments with nucleophiles

In Pd-catalyzed enantioselective allylic substitutions, the most early and seminal examples were introduced by the Trost group. They developed ligands comprising of two diphenylphosphino benzoic acids linked to a chiral diamine (designated as DPPBA, also known as the Trost ligand), which are C_2-symmetric and whose Pd-complexes display excellent regio- and enantio-selectivity for a wide range of allylic substitution reactions featuring either cyclic or acyclic substrates and numerous nucleophilic (C-, N-, O- or S-based) coupling partners. The success of the Trost ligand finds its origin in the confined chiral environment created by the phenyl substituents of the phosphine groups, which are perpendicular to the plane of the allyl moiety (see Figure 1.15). This way, there are two quadrants of the accessible space blocked by a wall created by the phenyl groups.[55] It is important noting that the strained environment created by these systems is ineffective when bulkier substrates are used, limiting the scope of the transformations mediated by Pd(DPPBA) complexes to primary and secondary substituted alkenes.

[54] van Leeuwen, P. W. N. M.; Kamer, P. C. J.; Reek, J. N. H.; Dierkes, P. *Chem. Rev.* 2000, 100, 2741.
[55] Trost, B. M.; Machacek, M. R.; Aponick, A. *Acc. Chem. Res.* 2006, 39, 747.

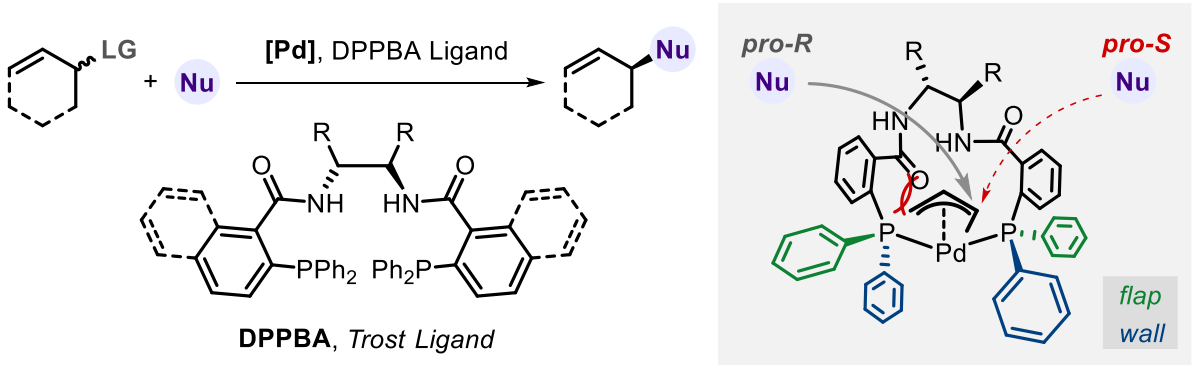

Figure 1.15: Enantio-induction and regio-selectivity optimized in Pd-catalyzed allylic substitutions with chiral Trost ligands.

Another family of chiral ligands that has been widely explored for allylic substitution reactions are the so called Phox ligands. These are chiral phosphine-oxazolines, and were initially developed by Helmchen, Pfaltz and Williams. With this new scaffold, a wide range of bulky 1,3-disubstituted allylic substrates were functionalized with high degrees of asymmetric induction.[56] The key aspect of Phox ligands that controls the enantio-selectivity is the electronic differentiation between the phosphine and the oxazoline groups. The nucleophilic addition normally occurs at the carbon center opposite to the P-atom, which is known as the *trans* effect. Apart from the atomistic electronic effects, there is also an influence of the dynamics of the *exo* and *endo* isomers formed after OA. Figure 1.16 depicts the different effects that lead to the nucleophilic attack on the *endo* isomer. First of all, the *trans* effect directs the attack to the most accessible C_1 that is more accessible in the *endo* isomer, as in the *exo* one the allylic backbone itself is sterically blocking the approach of the nucleophile.[57,58] Secondly, the steric repulsion of the phenyl ring (in **red**) blocks the attack at the opposite C-terminus in both isomers. Finally, the steric effects defining this system also influence the *exo*/*endo* isomer ratio, populating the *endo* isomer at the expense of the *exo* isomer. Therefore, the thermodynamic speciation also contributes to a more likely attack of a nucleophile on the *endo* intermediate.[59]

[56] Helmchen, G.; Pfatz, A. *Acc. Chem. Res.* 2000, 33, 336.
[57] Sprinz, J.; Kiefer, M.; Helmchen, G.; Reggelin, M.; Huttner, G.; Walter, O.; Zsolnai, L. *Tetrahedron Lett.* 1994, 35, 1523.
[58] Schaffner, S.; Muller, J. F. K.; Neuburger, M.; Zehnder, M. *Helv. Chim. Acta* 1998, 81, 1223.
[59] Armstrong, P. B.; Dembicer, E. A.; DesBois, A. J.; Fitzgerald, J. T.; Gehrmann, J. K.; Nelson, N. C.; Noble, A. L.; Bunt, R. C. *Organometallics* 2012, 31, 6933.

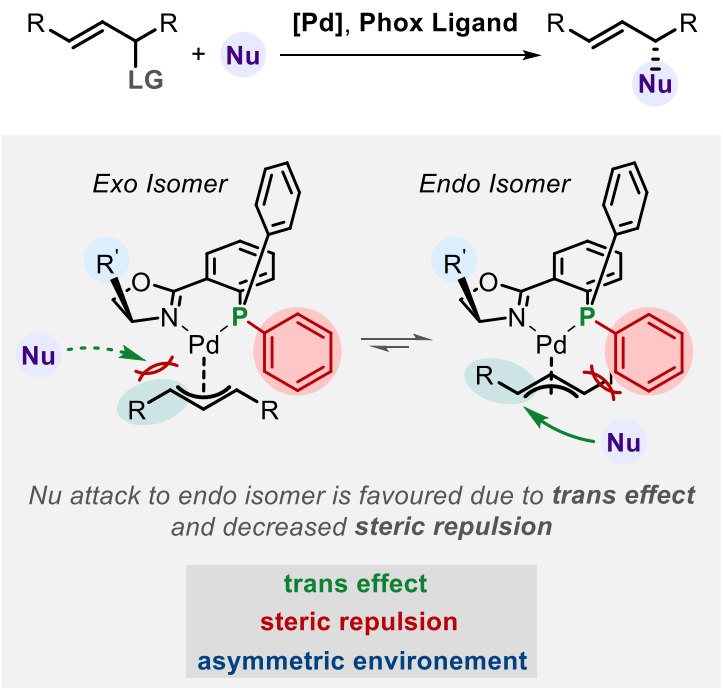

Figure 1.16: Stereo-selective model of Pd-Phox ligands for allylic substitution reactions.

To complete this section, it is worth citing another family of sophisticated chiral ligands (known as phosphoramidites) that have been used to develop highly enantio-selective transformations. These so called Feringa ligands have been used in numerous transformations.[60] One of the most explored reactions is the asymmetric version of the Pd-catalyzed trimethylenemethane cycloaddition reactions to forge five-membered rings, which was designed by Trost and co-workers. Few years later in 2003, the Hartwig group reported a landmark contribution exploring allylic aminations. They discovered that complexation of an Ir pre-catalyst with a chiral phosphoramidite involves a base-assisted cyclometallation through C(sp^3)–H bond activation.[61] This first step generates the active species to which the allylic precursor oxidative adds. In this catalytic system, they discovered that the enantio-discrimination is induced by repulsive steric interactions between the chiral binaphthol moiety and the 1,5-cyclooctadiene (COD ligand) surrounding the allyl fragment (see Figure 1.17). This type of cationic Ir complex shows excellent reactivity and enantio-induction, tolerating a variety of stabilized nucleophiles. However, one of the limitations of these catalysts is the required use of linear allylic instead of branched substrates, as the latter ones

[60] Rossler, S. L.; Petrone, D. A.; Carreira, E. M. *Acc. Chem. Res.* 2019, 52, 2657.
[61] Madrahimov, S. T.; Li, Q.; Sharma, A.; Hartwig, J. F. *J. Am. Chem. Soc.* 2015, 137, 14968.

decrease the enantio-selectivity. Hartwig and co-workers explained this observation by a stereo-determining OA step.

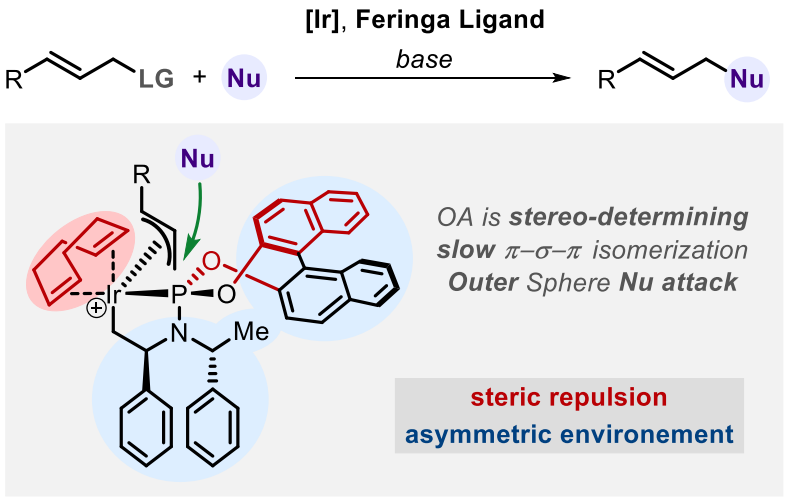

Figure 1.17: Enantio-selective Ir-catalyzed allylic substitutions using cyclometallated Iridium complexes derived from phosphoramidite ligands.

To conclude this section, three different examples of chiral ligands able to induce high asymmetric induction in Pd- and Ir-catalyzed allylic substitutions are discussed here, setting a contextual background for the research reported in Chapter 3.

Coupling of allyl fragments with electrophiles

The last disclosed example in section 1.3 is a transformation in which the allyl fragment acts as a nucleophile and treated with (electrophilic) primary alcohols. This reactivity pattern was developed by Krische and co-workers in 2008, achieving primarily branched selectivity of the resulting homoallylic alcohol products with high enantio-control. Additionally, these products featuring tertiary carbons are obtained in excellent *anti*-diastereo-selectivity. They propose that the cyclometalated Ir^{III}(allyl) pre-catalyst can *in situ* oxidize the primary alcohols to aldehydes (before allylation), and as such, the methodology can be defined as a redox-triggered C=O coupling (Figure 1.18).

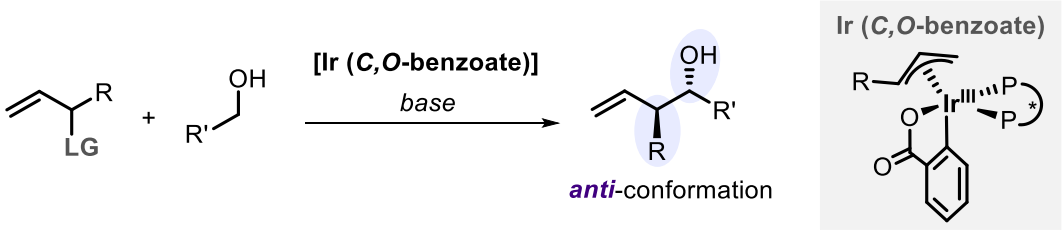

Figure 1.18: Enantio-selective Ir-catalyzed allylation of aldehydes.

1.4 Metal-catalyzed propargylic substitution reactions

Metal-promoted propargylic substitution reactions of propargylic alcohols (or *O*-protected alcohols and similar derivatives) are important and versatile transformations in organic synthesis. They allow the formation of new C–C and C–heteroatom bonds vicinal to the α-position of the propargyl moiety typically under mild reaction conditions while featuring wide tolerance for functional groups present in the substrates.

1.4.1 Early propargylic substitutions

Initially, propargylic substitutions were developed using metals such as Au, Pt, Pd, Ru and Rh. However, more sustainable methodologies have been reported in the last decade using first row metals such as Cu and Ni. [62,63,80,83,84,] In the past 30 years, metal and ligand exploration studies have culminated into optimal catalyst design for the tuning of the regio-selectivity in this type of reactions providing either allene or alkyne products (Figure 1.19).

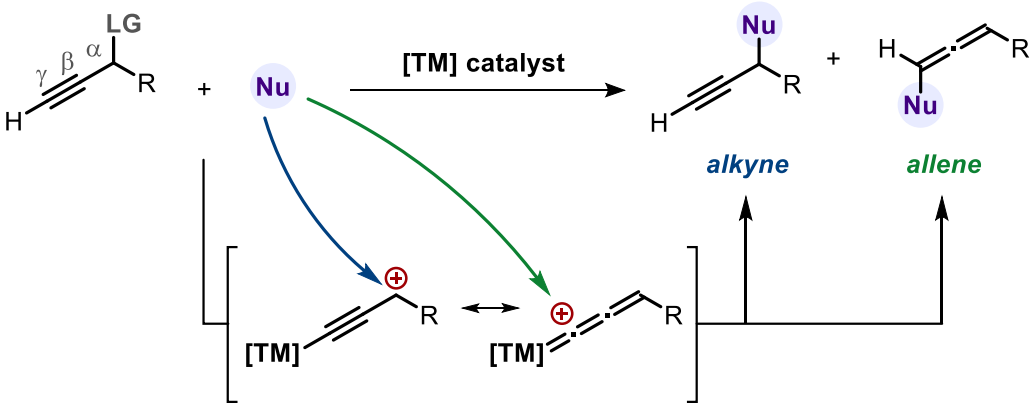

Figure 1.19: Regio-selectivity in metal-catalyzed propargylic substitution reactions: alkyne vs. allene product formation.

In Cu-catalyzed propargylic substitutions, most of the methodologies developed have focused on the achievement of the alkyne product, however, there have been some reports in the last years where this route could be biased towards axially chiral allenes.[64,65] Focusing on the propargylic substitution of terminal alkynes with earth

[62] Ding, C.-H; Hou, X.-L. *Chem. Rev.* 2011, 111, 1914.
[63] Bauer, E. B. *Synthesis* 2012, 44, 1131.
[64] Roy, R.; Saha, S. *RSC Adv.* 2018, 8, 31129.
[65] Yokobori, U.; Ohmiya, H.; Sawamura, M. *Organometallics* 2012, 31, 7909.

abundant metals, the first racemic example was pioneered by Murahashi and coworkers in 1994 when the amination of propargylic esters was accomplished using a Cu catalyst.[66] Its enantio-selective variation will be outlined and discussed in the introduction section of Chapter 2 of this thesis.

[66] Imada, Y.; Yuasa, M.; Nakamura, I.; Murahashi, S.-I. *J. Org. Chem.* 1994, 59, 2282.

1.5 Non-linear effects in asymmetric chemistry

Before discussing the objectives of this experimental thesis, there is one concept that needs to be introduced. In asymmetric chemistry, when racemic mixtures of the auxiliary ligand are used, a phenomenon known as a **Non-Linear Effect (NLE)** can be observed. It can be determined by plotting the $ee_{product}$ vs. ee_{ligand}. Changing the enantiomer ratio of the ligand, different *ee* of the chiral product are obtained generating the graph depicted in Figure 1.20 where three different tendencies can be observed: an asymmetric amplification (a) asymmetric attenuation (b), and a linear relationship (c).[67]

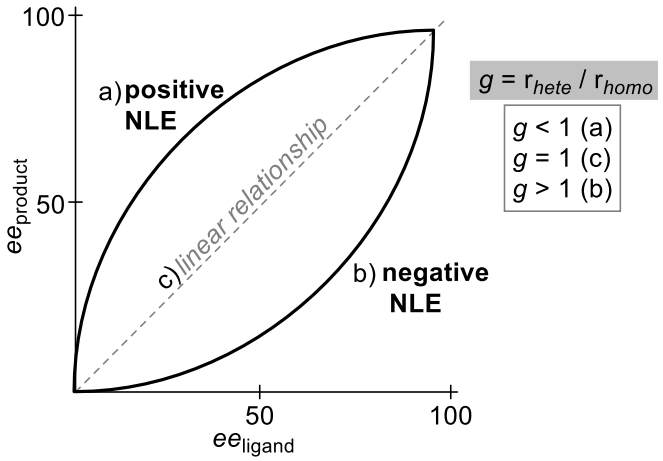

Figure 1.20: a) Positive NLE, b) Negative NLE and c) linear relationship between $ee_{product}$ and ee_{ligand}.

1.5.1 Kagan's ML_2 model

Evidence of a NLE was first reported by Wynberg and Feringa back in 1976.[68] At that time, the purity of the ligands that were being developed for asymmetric chemistry was not very high, and it allowed to observe non-linear correlation between the enantiomeric ratio (*er*) of the ligand used and the *er* of the product obtained. Later in the 1990s, Kagan and coworkers revised this phenomenon trying to understand its origin by applying mathematical models.[69] They started by considering the simplest

[67] Blackmond, D. G. *Acc. Chem. Res*. 2000, 33, 402.
[68] Wynberg H.; Feringa, B. *Tetrahedron* 1976, 32, 2831.
[69] Puchot C.; Samuel O.; Dunach E.; Zhao S.; Agami C.; Kagan, H. B. *J. Am. Chem. Soc.* 1986, 108, 2353.

model (ML_2) to explain the enhancement of the $ee_{product}$ by studying the complexation of catalytically active species in solution. After optimizing the mathematical models and forging equations, they managed to understand that during the catalytic transformation *homo*- and *hetero*-dimers had to be forming in solution.[70]

The following example reflects the ML_2 model, where 2 ligands can bind in a single metal center, generating three possible chiral complexes: M(L_S)$_2$ (**Homo-1**), M(L_R)$_2$ (Homo-2) and M(L_S)(L_R) (Hetero), pictured in Figure 1.21.

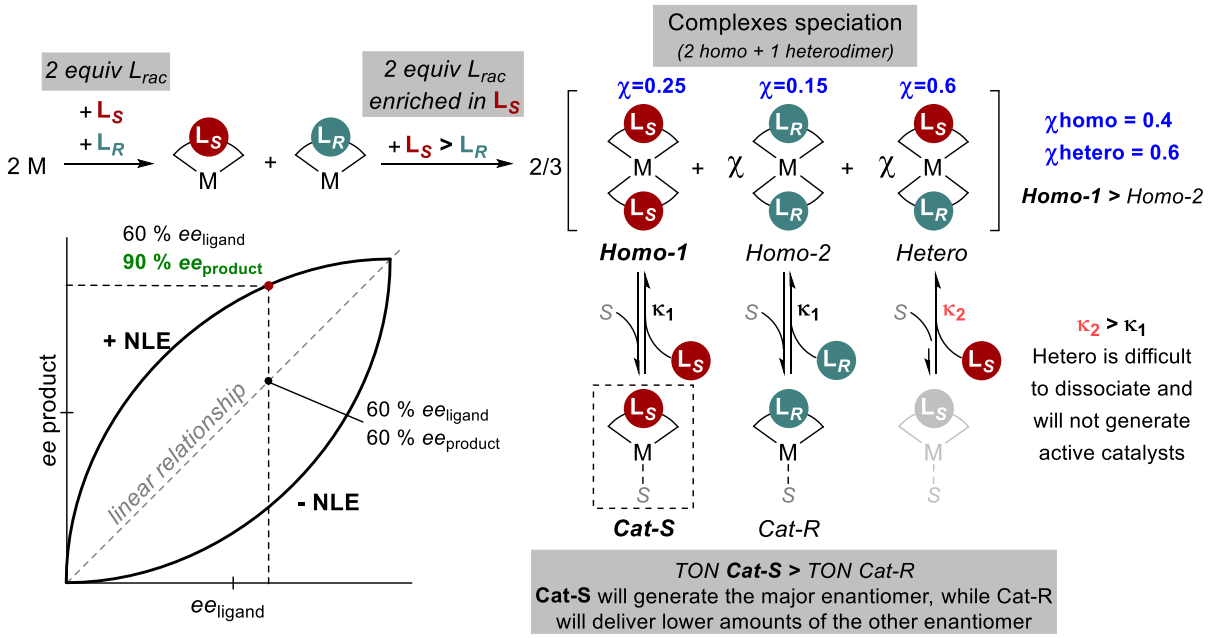

Figure 1.21: ML_2 model adapted for an asymmetric amplification of *S*- vs. *R*-catalyst. In this example, the *g* parameter (κ_2/κ_1) is >1.

In the case of a (+) NLE, heterodimers are thermodynamically more stable than the homodimers resulting into a higher concentration in solution (χ_{hetero} = 0.6 vs. χ_{homo} = 0.4), and being also more stable in solution (K_2>K_1). In terms of activity, this translates into the homochiral species being more active towards catalytic pathways by dissociation of one ligand (L_S) and coordination of the substrate (*S*). The heterochiral complex is relatively stable and binds a significant fraction of ligand in its coordination sphere, and it thereby generates an inactive racemic species. This phenomenon is also referred to as *reservoir effect*. The two enantio-pure homochiral complexes compete for the coordination of substrate forming two active catalyst species (***Cat-S***

[70] Guillaneux D.; Zhao S.; Samuel O.; Rainford, D.; Kagan, H. B. *J. Am. Chem. Soc.* 1986, 108, 2353.

vs. *Cat-R*). Even though the rate of both chiral catalysts is the same, ***Cat-S*** will be responsible for asymmetric amplification as its concentration in solution is significantly higher than that of *Cat-R* (□Cat-S = 0.25 vs. □Cat-R = 0.15).

In the case of asymmetric attenuation (□1>□2), the thermodynamic stability of the homodimer complex is higher, therefore the homodimer acts as an inactive reservoir species, and the heterodimer complex is the more active one generating a racemic catalyst. This results into a curvature opposite to the asymmetric amplification and thus a less efficient asymmetric induction. Analogously, when the dissociation rates of both homo- and hetero-chiral complexes are similar (□□□~□□□□, the corresponding graph should be a linear one (Figure 1.20c).

1.5.2 Higher order systems

In this thesis, two examples of positive NLE are presented, and in both cases, we studied its origin and the possibility of having ML_2 species in solution. In both examples, the model applied was based on a ML_2 species since no higher order slopes were observed in the $ee_{product}$ and ee_{ligand} graph (see Chapters 2 and 3).

However, it is important to emphasize that higher order NLE have been reported in the literature when metal complexes form with ML_3, M_2L_3 and even ML_4 complexation stoichiometries.[71],[72],[73]

To select the easiest example different from the ML_2 model, ML_3 systems give higher order curvatures such as the one shown in Figure 1.22. In this case, four different ML_3 species can be formed: two homochiral ones being $M(L_S)_3$ and $M(L_R)_3$, and two heterochiral complexes designated as $M(L_S)(L_R)_2$ and $M(L_S)_2(L_R)$. To understand the ML_3 model, it is important to consider that the heterochiral complexes can have dual behavior: they can either lead to racemic product or they deliver enantiomerically enriched product.

[71] Bryliakov, K. P. *ACS Catal.* 2019, 9, 5418.
[72] Geiger, Y.; Achard, T.; Maisse-François, A.; Bellemin-Laponnaz, S. *Nat. Catal.* 2020, 3, 422.
[73] Thierry, T.; Geiger, Y.; Bellemin-Laponnaz, S. *Molecules* 2022, 27.

$g = r_{hete}/r_{homo}$

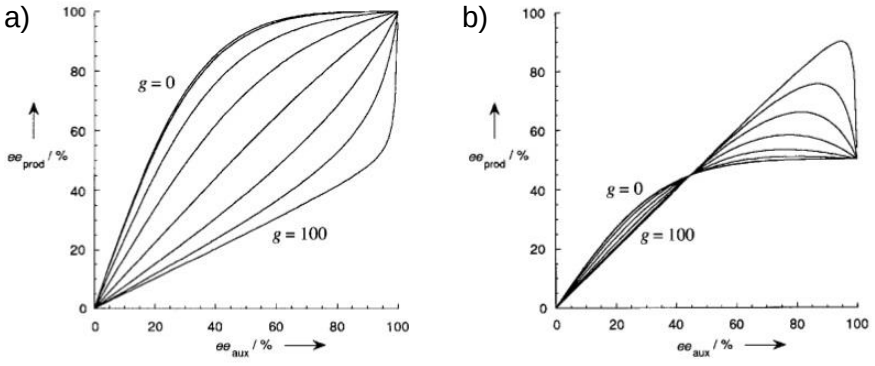

Figure 1.22: ML_3 model theoretical graphs. When homochiral (a) or heterochiral (b) complexes are more selective towards product formation. *g* value refers to the rate constant relation between heterochiral and homochiral complexes.[74]

Although in the ML_3 model the *g* value can be calculated in a similar way as done within a ML_2 model, the mathematical equation to calculate the enantio-selectivity, and thus predicting a positive or negative NLE, is much more complex.

[74] Non-linear effects: https://en.wikipedia.org/wiki/Non-linear_effects.

1.6 Objectives and outline of this thesis

The previous sections have shown the importance of the use of transition metal catalysis to achieve high selectivities in organic synthesis, and more precisely in the field of allylic and propargylic substitution reactions. Considering the long-standing interest of our group to develop new methodologies for the formation of highly congested stereocenters in an enantio-selective way, the **Main Objective** of this thesis was to get a deep understanding of the intricacies involved in some challenging allylic/propargylic transformations by an exhaustive analysis and exploration of their reaction mechanism. Such knowledge would not only help to rationalize the reactivity and selectivity patterns previously observed, but prospectively also provide a blueprint for the development of novel types of asymmetric transformations. This thesis, apart from the initial introduction (**Chapter 1**), consists of the following sections:

Chapter 2 reports a detailed study on the origin of the enantio-selection in a Cu-catalyzed propargylic substitution reaction using sulfinate nucleophiles leading to propargylic sulfones featuring tertiary, tetrasubstituted carbon stereogenic centers. In this project, the traditionally accepted mechanism was revisited, and the combined results suggest that the enantio-induction occurs in a proto-demetalation step taking place after the nucleophilic attack. Moreover, the pre-activation of the Cu precursor and the productive cycle have been experimentally and computationally scrutinized, while the origin of the experimentally observed NLE in this transformation could be ascribed with help of a $Cu^{I}(L)_2$ model.

In **Chapter 3**, we describe the mechanistic analysis of a Pd-catalyzed allylic substitution reaction involving aliphatic amines as nucleophiles utilizing a combined experimental and computational approach. In this project, the detection of catalytic intermediates under turnover conditions was crucial to assign the rate-limiting step(s) of the productive cycle, and combined with DFT studies a rationalization of the high chemo-, regio- and enantio-selectivity of the process could be provided. The role of the co-solvent, the temperature, excess of ligand and the experimentally observed NLE were also evaluated and validated.

In the last project (**Chapter 4**), we address the mechanistic evaluation of a recently discovered methodology in our group that centers on a Ni-catalyzed cross-allylic homo-coupling delivering 1,5-dienes comprising of quaternary carbon stereocenters

under high chemo-, regio-, diastereo- and enantio-control. In this chapter, we present detailed information on the activation of the Ni pre-catalyst before it enters the productive catalytic cycle using EPR, NMR and UV-Vis spectroscopies, and X-ray analysis of Ni-based reaction intermediates. Moreover, the use of kinetics, control experiments and other stoichiometric studies helped us to draw a general picture of this complex system.

Finally, **Chapter 5** provides a short summary of the thesis together with the main overall conclusion of the thesis work including an outlook on how these PhD results may be of value to future synthetic protocols in the field. In particular, the value that the mechanistic findings have to streamline efforts that focus on the realization of synthetic targets with sterically dense stereogenic carbon centers that are forged through allylic or propargylic substitution chemistry.

Chapter 2.

A Comprehensive Mechanistic Scenario for the Cu-Mediated Asymmetric Propargylic Sulfonylation forging Tertiary Carbon Stereocenters

This project was developed in collaboration with the group of Prof. Feliu Maseras (ICIQ). The computational work was performed by ***Dr. Raúl Pérez Soto****.*

The results described in this chapter have been published in:

Garcia-Roca A.,‡ Pérez-Soto R.,‡ Stoica G., Benet-Buchholz J., Maseras F. Kleij A. W., *J. Am. Chem. Soc*. **2023**, 145, 6442–6452. https://doi.org/10.1021/jacs.3c00188

2.1 Introduction

Asymmetric propargylic substitution reactions (APS) are of high interest in synthetic chemistry providing access to functionalize pro-chiral precursors with a family of diverse nucleophiles in an enantioselective manner.[75,76,77] As stated in section **1.3.1** in the introduction, less abundant metals such as rhodium, ruthenium, palladium and gold have been widely used to achieve this strategy, however, copper-catalyzed APS transformations have emerged as a useful alternative to earlier methodologies using noble-metals.[78,79] The two first examples of APS reactions catalyzed by copper were reported in the early 2000's. The groups of Nishibayashi[80] and van Maarseveen[81] independently presented a copper-catalyzed enantioselective propargylic amination using different ligands although under similar reaction conditions employing phosphorus bidentate and nitrogen-based bisoxazoline (BOX) ligands, respectively (see Figure 2.1a). Since then, copper has been used in APS reactions with different ligand systems and a wide variety of nucleophiles has been explored.[64] In 2019, our group achieved the first enantioselective propargylic sulfonation accomplishing C-S bond formation while creating tertiary stereocenters by using alkynyl cyclic carbonates (ACC) as propargylic surrogates (Figure 2.1b).[82] Here, ACCs proved to be beneficial towards high enantiomeric ratios (*er*) compared with other propargylic surrogates (Figure 2.1c). Intrigued by these favourably outcomes, we evaluated the mechanism of this new methodology and compared the outcome with the previously reported experimental and computational studies from Nishibayashi. The latter group extensively described the formation and reactivity of chiral allenylidene intermediates.[83,84]

[75] Miyake, Y.; Uemura, S.; Nishibayashi, Y. *ChemCatChem* 2009, 1, 342.
[76] Detz, R. J.; Hiemstra, H.; van Maarseveen, J. H. *Eur. J. Org. Chem.* 2009, 6263.
[77] Tsuji, H.; Kawatsura, M. *Asian J. Org. Chem*. 2020, 9, 1924.
[78] Zhang D.-Y.; Hu X.-P. *Tetrahedron Lett.* 2015, 56, 283.
[79] Nishibayashi, Y. *Chem. Lett.* 2021, 50, 1282.
[80] Hattori, G.; Matsuzawa, H.; Miyake, Y.; Nishibayashi, Y. *Angew. Chem. Int. Ed.* 2008, 47, 3781.
[81] Detz, R. J.; Delville, M. M. E.; Hiemstra, H.; van Maarseveen, J. H. *Angew. Chem. Int. Ed*. 2008, 47, 3777.
[82] Gomez, J. E.; Cristòfol, À.; Kleij, A. W. *Angew. Chem. Int. Ed.* 2019, *58*, 3903.
[83] Hattori, G.; Sakata, K.; Matsuzawa, H.; Tanabe, Y.; Miyake, Y.; Nishibayashi, Y. *J. Am. Chem. Soc.* 2010, 132, 10592.
[84] Sakata, K.; Nishibayashi, Y. *Catal. Sci. Technol*. 2018, 8, 12.

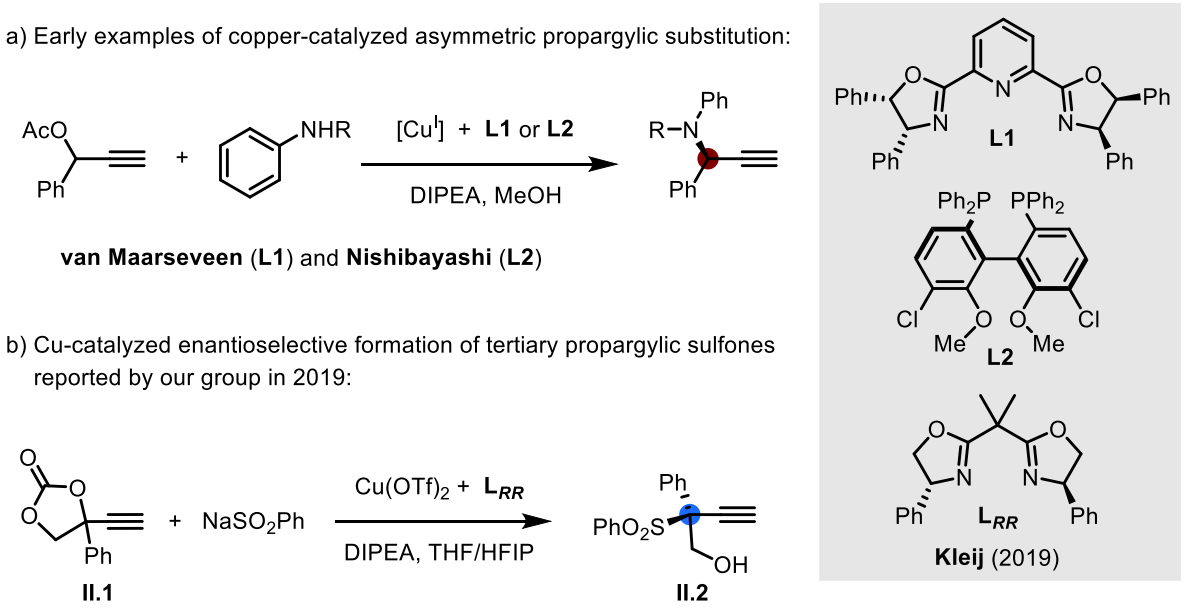

c) Effect on yield and enantioselectivity of propargylic surrogates in propargylic sulfonation:

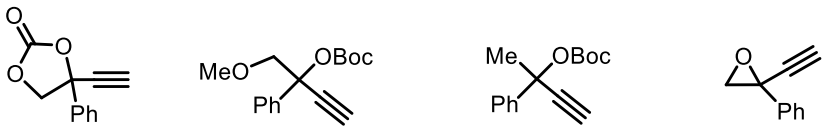

93 %, **97:3** — **II.1**
90 %, **85:15** — **II.3**
90 %, **75:25** — **II.4**
0 % [1] — **II.5**

Figure 2.1: a) First examples of enantio-selective APS reactions under Cu-catalysis, b) benchmark reaction of our mechanistic study and c) *ee* dependence of the product of the propargylic precursor in our reported methodology from 2019.[82] Note that the alkynil epoxide reacted through different chemo-selectivity with hexafluoro-isopropanol (HFIP) and a different chemo-selectivity was observed.

2.2 Aims and objectives

One of our questions to address in this study was the understanding of the pre-activation of the Cu precursor activation towards an active chiral catalyst. Back in 1998, Evans et al. reported the synthesis and characterization of Cu(BOX) complexes for their use in Aldol reactions.[85] Our second objective was to find an explanation for the high enantio-selectivity obtained with the combination of our Cu-bisoxazoline pre-catalyst and the PCC. The generally accepted mechanism considers the nucleophilic attack to be the enantio-determining step, and a subsequent proto-demetalation as an innocent (Scheme 2a).[83] Another intriguing aspect to tackle in our study was a better understanding of the positive non-linear effect (NLE) observed in this process.[82] During our studies, the work from Franz and co-workers on the determination of an NLE in Cu-catalysed *spiro*-annulation reactions with bidentate bis-oxazolines ligands (Figure 2.2) was insightful.[86] They proposed an ML_2 NLE model during the pre-activation stage of the Cu precursor based on Kagan´s seminal contributions.[87,88]

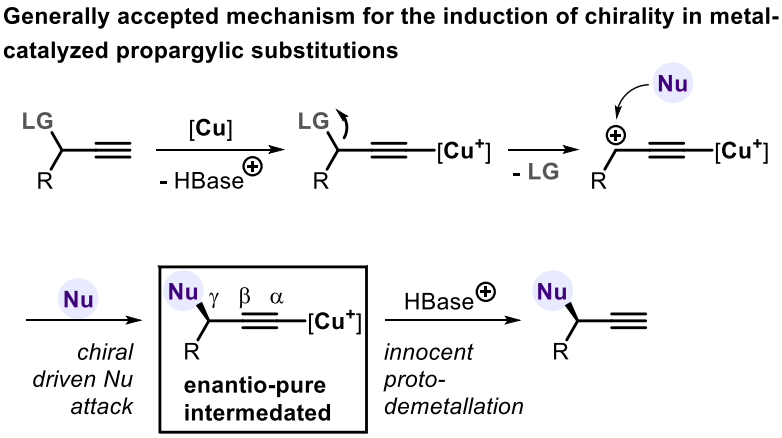

Figure 2.2: a) Generally accepted mechanism of the enantio-selective metal-catalyzed APS reaction.

[85] Evans, D. A.; Tregay, S. W.; Burgey, C. S.; Paras, N. A.; Vojkovsky, T. *J. Am. Chem. Soc.* 2000, 122, 7936.
[86] Armstrong, B. M.; Sayler, R. I.; Shupe, B. H.; Stich, T. A.; Britt, R. D.; Franz, A. K. *ACS Catal.* 2019, 9, 1224.
[87] Girard, C.; Kagan, H. B. *Angew. Chem. Int. Ed*. 1998, 37, 2922.
[88] Satyanarayana, T.; Abraham, S.; Kagan, H. B. *Angew. Chem. Int. Ed*. 2009, 48, 456.

2.3 Results and discussion

2.3.1 Catalyst order and determination of oxidation states

As mentioned above, the first objective of our study was to gather information on how the Cu-precursor is activated. Thereto, the order in the Cu reagent and the oxidation state of the active species were determined. We decided to perform kinetic studies to examine the order in [Cu]. Taking advantage of the carbonate functionality present in the propargylic precursor, *in situ* IR spectroscopy was chosen to monitor the disappearance of the substrate (Figure 2.3a). Applying visual time normalization analysis (VTNA),[89,90] we could determine an approximate order of 1 in [Cu] during the rate determining step (2.3b). This result suggests that a monometallic Cu complex is the active species in the productive cycle. Also, while performing these IR measurements, we could detect and monitor the band of the released CO_2, providing further evidence for the catalytic conversion (see experimental section 2.6.4).

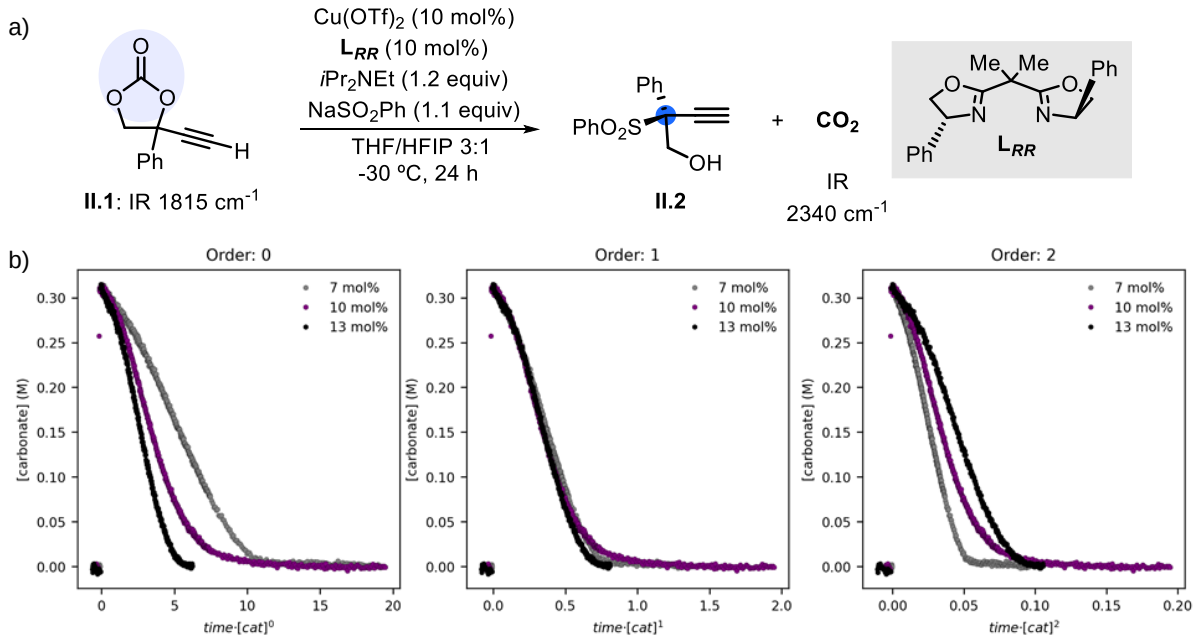

Figure 2.3: a) Benchmark reaction, b) Order of catalyst by VTNA plots. HFIP stands for hexafluoro-isopropanol.

The next target was to determine the oxidation state of the active Cu species. Due to the paramagnetism found in Cu(II) species, Electron Paramagnetic Resonance (EPR)

[89] Nielsen, C. D. T.; Burés, J. *Chem. Sci.* 2019, *10*, 348.
[90] Burés, J. *Angew. Chem. Int. Ed.* 2016, *55*, 16084.

was used to monitor the reaction progress over several hours. The first results showed the clear reduction of a characteristic Cu(II) band during the first 30 minutes of reaction (Figure 2.4a). Hereafter, the reaction mixture remained nearly EPR-silent throughout the rest of the time frame (1-24 h), which indicaties that a Cu(I) species plays a crucial role.

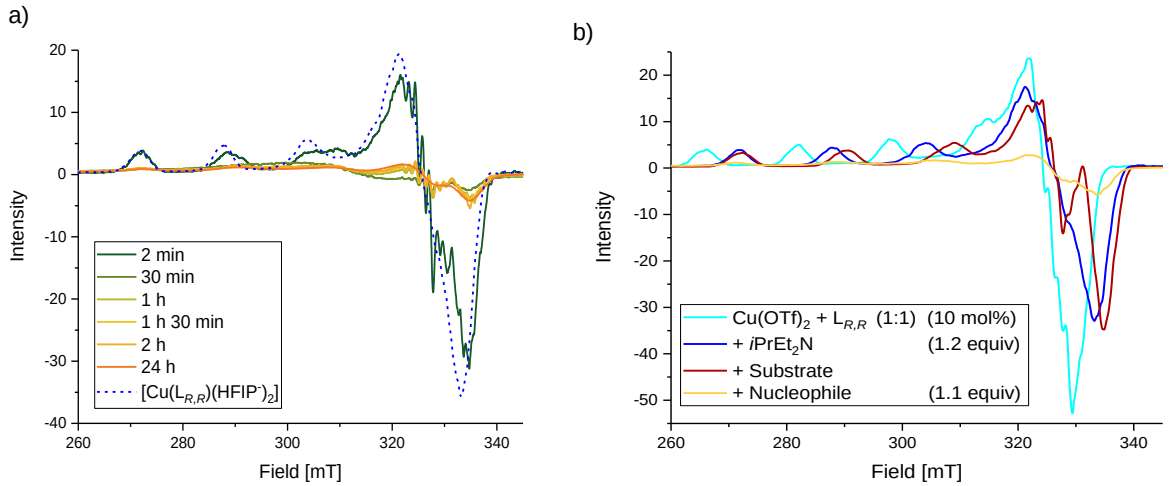

Figure 2.4: a) EPR monitoring of a catalytic mixture, and b) EPR analysis of of activation of the Cu(II) precursor and its evolution in time upon addition of reagents.

We then considered evaluating the evolution of the Cu species through the stepwise addition of the reagents used in the transformation of $Cu(OTf)_2$ precursor. The complexation between this copper salt and the Box ligand (**L*RR***) showed the formation of a turquoise Cu(II) complex with a characteristic EPR pattern, which was not identified in the previous experiment (Figure 2.4b first entry in the box vs 2.4a). Upon addition of DIPEA, a dark blue complex was formed with a shifted EPR signal (second entry in the box). This EPR signal reasonably matches the EPR obtained after 2 min of the catalytic mixture monitoring and suggests that the base is important to allow for catalyst activation (Figure 2.4a, first *vs* seventh line in the box). Intrigued to know whether the substrate could react with the complex formed after DIPEA addition we continued with the addition of PCC under catalytic conditions. At this third stage of addition, we observed a slight right shift of the EPR band corresponding to a red colour change in solution, (Figure 2.4b, third line in the box). This slight change of the EPR signal hints to a change in the coordination sphere of the Cu compared to the previous stage (second *vs* third line in the box). Finally, upon addition of $NaSO_2Ph$ (nucleophile),

after 2h of stirring the EPR signal becomes virtually silent, which is similar to the previous EPR monitoring under standard catalytic conditions (fourth line in the box).

Overall, the EPR bands initially observed after the complexation of $Cu(OTf)_2$ and $\mathbf{L}_{\boldsymbol{RR}}$ significantly change upon the addition of reagents indicating different stages during pre-catalyst activation and thus the isolation and characterization of these species could shed further light on the course of this process.

2.3.2 Isolation and characterization of pre-activation complexes

To potentially identify the structure of each detected Cu(II) species, stoichiometric synthesis was used to isolate and characterize the pre-catalysts. We started examining the complexation between the $Cu(OTf)_2$ precursor and the chiral ligand $\mathbf{L}_{\boldsymbol{RR}}$ in a THF/HFIP solvent mixture. The product obtained was crystallized in a 62 % yield and characterized by X-ray crystallography, unveiling an octahedral complex with a pair of water molecules coordinated in the equatorial positions (Figure 2.5a, complex **II.6**). The presence of coordinating water molecules is coherent with the experimental conditions, which do not strictly require dry solvents for productive catalysis.[91,92] To endorse this view, we also carried out the same complexation reaction between $Cu(OTf)_2$ and $\mathbf{L}_{\boldsymbol{RR}}$ under anhydrous conditions. In this case, a green-coloured Cu(II) complex is formed. The isolation, crystallization and X-ray analysis of this compound revealed a Cu(II) complex with a 1:2 Cu:$\mathbf{L}_{\boldsymbol{RR}}$ ratio (complex **II.10**). After revelation of this stoichiometry, we optimized the synthesis by independently preparing it from a 1:2 mixture of $Cu(OTf)_2$ and $\mathbf{L}_{\boldsymbol{RR}}$, achieving the same product with a markedly improved isolated yield of 95% (72% yield of crystalline material).[93]

Following the reagent order of addition used to initiate catalysis, we evaluated the role of the base when exposed to the octahedral complex **II.6**. When DIPEA was added to a THF/HFIP mixture of $[Cu^{II}(\mathbf{L}_{\boldsymbol{RR}})(H_2O)](OTf)_2$, a new dark blue Cu(II) complex could

[91] Note that Evans and coworkers reported on the use of Cu(Box) complexes in Lewis acid mediated enantioselective catalysis, including complex **II.6** and its X-ray structure, see (a) Evans, D. A.; Burgey, C. S.; Paras, N. A.; Vojkovsky, T.; Tregay, S. W. *J. Am. Chem. Soc.* 1998, *120*, 5824. (b) Evans, D. A.; Tregay, S. W.; Burgey, C. S.; Paras, N. A.; Vojkovsky, T. *J. Am. Chem. Soc.* 2000, *122*, 7936.

[92] Feng, F.-F.; Wang, X.-Q.; Sun, L.; Cheung, C. W.; Nie, J.; Ma, J.-U. *Org. Lett.* 2021, *23*, 4379.

[93] Both Franz and Murphy independently reported the EPR analysis of homochiral complex **II.10**, see: Owen, M. E.; Carter, E.; Hutchings, G. J.; Ward, B. D.; Murphy, D. M. *Dalton Trans.* 2012, *41*, 11085 and ref. 86.

be isolated (**II.7**, 86% yield) and characterized by X-ray analysis as a distorted square-planar complex with two deprotonated molecules of HFIP coordinating to the metal centre. The drastic change in the EPR bands between these two complexes (**II.6** and **II.7**) is explained by the geometric change from octahedral to square planar (a_{II} values can be found in experimental section).[94] In the same reaction, the salt DIPEA·HOTf was identified as a predictable by-product. Having identified the two first Cu(II) intermediates, we attempted to study the next pre-catalytic complex. Complex **II.6** was mixed with 1.5 equiv of substrate **II.1** (PCC) and 2.5 equiv of DIPEA in a 3:1 (v/v) solvent mixture of THF and HFIP.

Unfortunately, we could neither isolate nor further characterize this latter Cu(II) complex due to its instability in solution. Although this last reaction was also conducted at lower temperatures, we were not able to obtain further data that could clarify the identity of this intermediate.

With the intention to understand the observed reduction of Cu(II), the isolation of an envisioned Cu(I)-acetylide intermediate was attempted by reacting complex **II.6** with substrate **II.1** in presence of DIPEA. To our surprise, yellow-colored crystals could be isolated (72 % yield) and its X-ray diffraction revealed an unexpected dimer $[Cu^{I}_2(\mathbf{L}_{\boldsymbol{RR}})_3](OTf)_2$ stoichiometry (**II.9**)] with one of the Box ligands bridging between the two Cu(I) centers having an unusual T-shaped coordination geometry. [95] Interestingly, when the homo-dimer **II.10** (Cu^{II}) was treated with the deprotonated version of our substrate **II.1**, the homologous homo-chiral structure was isolated as a Cu(I) species (complex **II.11**) in 48 % yield.[96]

[94] There have been few examples in which the HFIP acidic solvent could directly coordinate to other types of catalysts.

[95] For limited examples of Cu(I) complexes with a T-shaped coordination geometry: (a) van der Vlugt, J. I.; Pidko, E. A.; Vogt, D.; Lutz, M.; Spek, A. L.; Meetsma, A. *Inorg. Chem.* 2008, *47*, 4442. (b) Tano, T.; Mieda, K.; Sugimoto, H.; Ogura, T.; Itoh, S. *Dalton Trans.* 2014, *43*, 4871. (c) Bezuidenhout, D. I.; Kleinhans, G.; Guisado-Barrios, G.; Liles, D. C.; Ung, G.; Bertrand, G. *Chem. Commun.* 2014, *50*, 2431. (d) Kleinhans, G.; Chan, A. K.-W.; Leung, M.-Y.; Liles, D. C.; Fernandes, M. A.; Yam, V. W.-W.; Fernandez, I.; Bezuidenhout, D. I. *Chem. Eur. J.* 2020, *26*, 6993.

[96] When Cu(II) complex **II.7** was treated in similar way with the same reagent combination though in the presence of O_2, no formation of the target Cu(I)acetylide or complex **II.11** could be observed as evidenced by EPR studies.

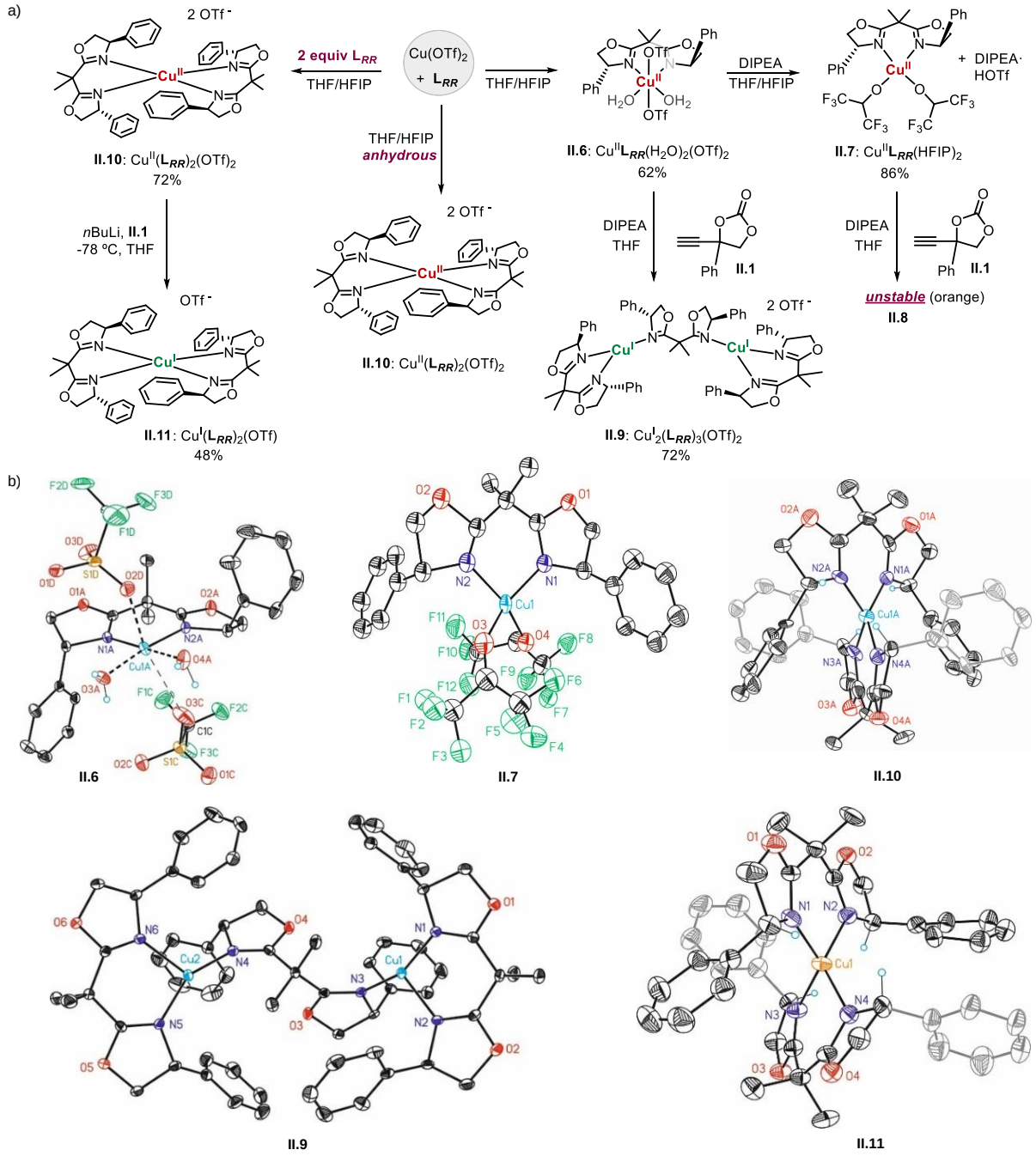

Figure 2.5: a) Synthesis and characterization of Cu(II) and Cu(I) complexes **II.6** to **II.11**, and b) X-ray analysis of complexes **II.6** to **II.11** (note: anions omitted for clarity) with displacement ellipsoids at the 50% probability level.

With most of the Cu(II) and Cu(I) structures characterized, these complexes were then evaluated as pre-catalysts in the benchmark transformation. As can be deduced from Table II.I, both Cu(II) complexes **II.6** and **II.7** reproduced the catalysis results under standard conditions, while Cu(II)-homo-chiral complex **II.10** displayed no observable

activity. Dinuclear Cu(I) complex **II.9** was not active, but homo-chiral Cu(I) **II.11** achieved a 30% product yield of the chiral sulfone **II.2** with a similar level of chiral induction as noted under standard conditions (entry 7 *vs* 1).

Table **II.I**: Activity of Cu(II) and Cu(I) complexes studied under catalytic conditions.

Entry	Cu complex	Oxidation state	Yield (%)	*ee*
1	*Benchmark reaction*	-	97	96.5 : 3.5
2	**II.6** $[Cu^{II}(L_{RR})(H_2O)](OTf^-)_2$	Cu(II)	*result of entry 1 reproduced*	
3	**II.7** $[Cu^{II}(L_{RR})(HFIP^-)]$	Cu(II)	*result of entry 1 reproduced*	
4	**II.10** $[Cu^{II}(L_{RR})_2](OTf^-)_2$	Cu(II)	0	-
5	**II.12** $[Cu^{II}(L_{RR})(L_{SS})](OTf^-)_2$	Cu(II)	0	-
6	**II.9** $[Cu^{I}_2(L_{RR})_3](OTf^-)_2$	Cu(I)	0	-
7	**II.11** $[Cu^{I}(L_{RR})_2](OTf^-)_2$	Cu(I)	30	97 : 3

The isolation of the two Cu(I) complexes (**II.9** and **II.11**) aligns well with the reductive potential of the catalytic reaction mixture, and this data combined with the first-order dependence on [Cu] and the information gathered from the EPR studies, we propose that a mononuclear Cu(I) species is the active species entering the productive cycle.

2.3.3 Disclosure of NLE in propargylic sulfonylation subtitution

As mentioned in the introduction, our original catalytic propargylic sulfonylation process displays a positive NLE as observed from an ee_{ligand} *vs* $ee_{product}$ plot (Figure 2.9a, *vide infra*). Taking the ML_2 model presented by Kagan in 1998 as a reference,[87] we hypothesized the possibility of the formation of stable Cu(**L**)$_2$ complexes in solution. Franz and co-workers previously determined the origin of a NLE during the pre-activation stage in *spiro*-annulation reactions with similar Box ligands. They explained the positive NLE as a result of stable Cu(II)-based, heterochiral ML_2 species that acts as a catalytically inactive complex.[86]

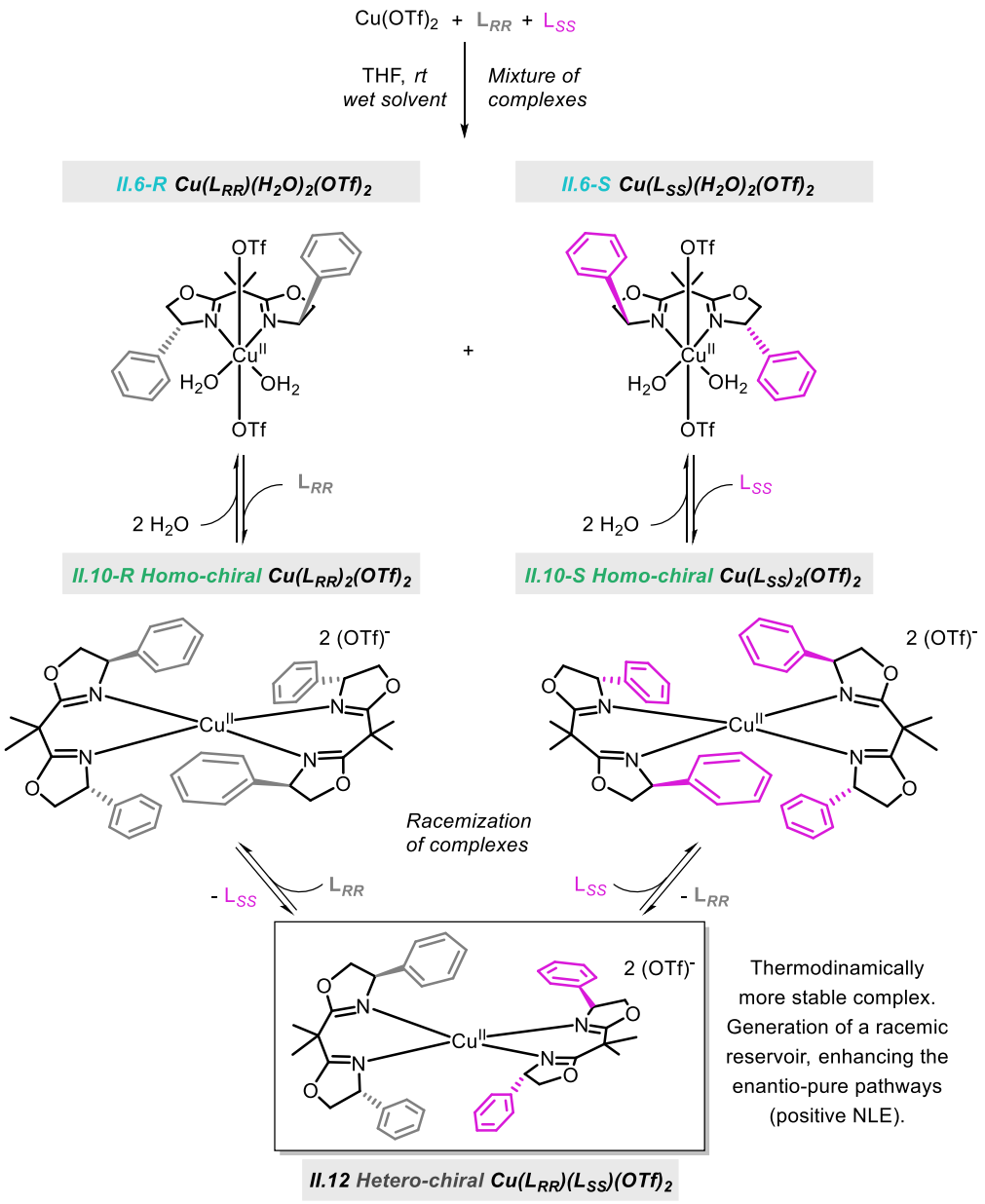

Figure 2.6: Initially proposed equilibria between homo- and hetero-chiral Cu(II) complexes and generation of the hetero-chiral complex **II.12**, being the focal point of the reservoir effect that was initially hypothesized to lead to the observation of a positive NLE.

In our case, after isolating Cu(II) complex **II.10** and Cu(I) complex **II.11**, we considered the possibility of having similar stable ML_2 systems in solution. It is important to mention that when this methodology was developed back in 2018 in our group, the conditions were optimized using a slight excess of $\mathbf{L_{RR}}$ (11 mol%) compared to the precursor $Cu(OTf)_2$ (10 mol%). We thus wondered at which stage of our reaction a ML_2 reservoir species could be formed: (*i*) during the pre-activation at a Cu(II) oxidation

state, or (*ii*) at the Cu(I) state during the productive catalytic cycle, with a heterochiral $Cu^{I}(\mathbf{L}_{RR})_2$ being relatively stable in solution.

With a well-defined structure of complex **II.10** in hand, we first attempted the synthesis of hetero-chiral complex **II.12** $[Cu^{II}(\mathbf{L}_{RR})(L_{SS})](OTf)_2$ by mixing a 1:1:1 composition of $Cu(OTf)_2$, $\mathbf{L}_{RR}$ and $\mathbf{L}_{SS}$. This reaction set up allowed the isolation of a green crystalline solid in 64% yield. The crystallographic analysis of this sample was challenging because three different types of single crystals diffracted at the same time. Fortunately, the combined data set could be deconvoluted and three different complexes structurally characterized: homo-chiral complex **II.10** $[Cu^{II}(\mathbf{L}_{RR})_2](OTf)_2$ (42.5 %), the other enantiomeric homo-chiral complex $[Cu^{II}(\mathbf{L}_{SS})_2](OTf)_2$ (42.5 %), and the hetero-dimer complex **II.12** $[Cu^{II}(\mathbf{L}_{RR})(\mathbf{L}_{SS})](OTf)_2$ (15 %). The structures are rather similar, although the phenyl groups bearing the chirality in hetero-complex **II.12** perfectly fit in a confined cage (see Figure 2.9b for a visual). Entry 5 of Table II.I demonstrates that this hetero-chiral complex is catalytically incompetent.

Initially, the experimentally observed NLE was proposed to occur at a Cu(II) oxidation level during the pre-activation stage (Figure 2.6 in previous page depicts the equilibriums proposed).

However, later on we questioned whether the proposed NLE indeed takes place at the Cu(II) oxidation state. The first set of experiments that fueled this doubt were related to the evaluation of the relative stabilities of Cu(II) and Cu(I) complexes by using EPR spectroscopy and UV-Vis analysis. The behavior of these complexes was examined by adding DIPEA in the presence of HFIP as a co-solvent. In the case of complexes **II.10** and **II.12,** we observed that both structures convert into $[Cu^{II}(\mathbf{L}_{RR})(HFIP^{-})]$ **II.7** being either homochiral (Figure 2.7a) or racemic (Figure 2.7b) in nature. These experiments confirmed that both homo-chiral **II.10** and hetero-chiral **II.12** in the presence of DIPEA/HFIP can be further activated towards the productive catalytic cycle.

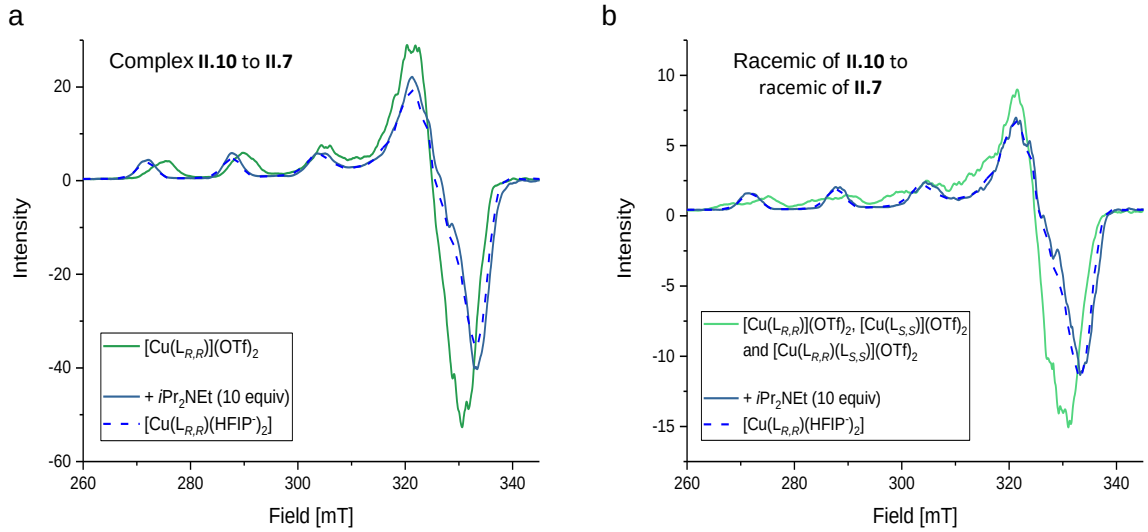

Figure 2.7: a) Stability analysis of complexes **II.10** and b) racemic of **II.10** (a) in front of DIPEA analyzed by EPR spectroscopy at 77K in THF/HFIP 3:1 mixture.

Next, we analyzed how stable Cu(I) complexes are when exposed to DIPEA. This experiment was carried using UV-Vis spectroscopy following the characteristic bands of complexes **II.9** and **II.11**. As can be observed in Figure 2.8, both spectroscopic traces of Cu(I) structures remained unchanged, suggesting that these Cu(Box) complexes are more stable in the Cu(I) than Cu(II) oxidation state.

To gain a more detailed thermodynamic picture and relationship between the Cu(I) and Cu(II) complexes, we calculated the relative free energies by DFT of all possible Cu(II) and Cu(I) ML_2 type complexes and three Cu(I) M_2L_3 type assemblies. As can be seen in Figure 2.9c, the relative free energies of the homo- and hetero-chiral Cu(II) based ML_2 complexes have very similar energies compared to the aquo-complex **II.6**, which agrees with the fact that mixtures of these compounds equilibrate in solution when $\mathbf{L}_{RR}$ and $\mathbf{L}_{SS}$ are used for complexation with $Cu(OTf)_2$ (see data in section 2.6.9). Also, the small difference of only 0.2 kcal/mol between homochiral **II.10** and heterochiral **II.12** is not supportive that these Cu(II) complexes are responsible for the occurrence of a NLE. In addition, the >11 kcal/mol difference in free energy between HFIP-complex **II.7** and **II.10**/**II.12** (in favor of the former) explains why the Cu(II) homo- and hetero-chiral complexes have the tendency to reform **II.7** in solution (see Figure 2.9).

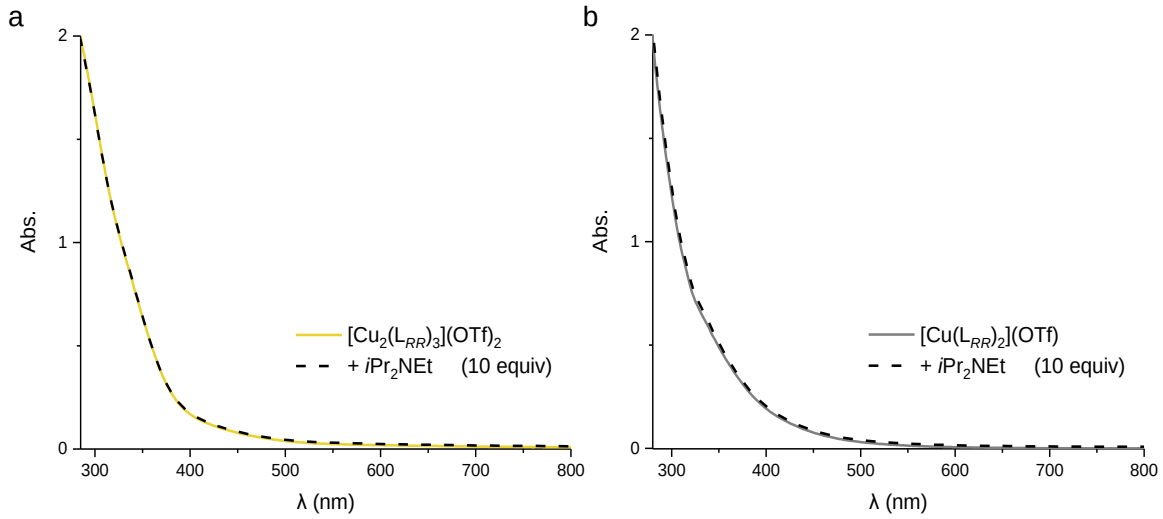

Figure 2.8: a) Stability analysis of complexes **II.9** and b) racemic of **II.11** in the presence of DIPEA analyzed by UV-Vis spectroscopy at 293 K in THF/HFIP (3:1 v/v).

Next, we turned our focus on the comparison of free energies of the Cu(I) complexes. Here, all energies are referenced to [Cu(I)(**L*RR***)(HFIP)], which contrary to the Cu(II) series, is >16 kcal/mol higher than homo-chiral complex **II.10** thus rationalizing why Cu(I) complexes do not react in a basic solution containing HFIP. Within the series of Cu(I) complexes, the 4.3 kcal/mol difference between homo-chiral **II.11** (at -16.6 kcal/mol) and hetero-chiral **II.12** (at -20.9 kcal/mol) illustrates the different stabilities of these Cu(I)M**L**$_2$ complexes. These latter calculations are in line with the positive NLE observed in catalysis (Figure 2.9a). Further to this, although a large excess of ligand is not used during this catalytic transformation, the evaluation of M$_2$**L**$_3$ complexes to explain the NLE was considered as well (dinuclear complex **II.9** in Figure 2.5). The computed relative free energies show that dinuclear Cu(I) complexes of type M$_2$**L**$_3$ could co-exist in a competitive equilibrium with the Cu(I)**L**$_2$ species. However, this M$_2$**L**$_3$ stoichiometry cannot correctly predict the positive NLE as the three structures computed in Figure 2.9 have too similar energies, which does not lead to a reservoir effect. Altogether, our system behaves differently to the one reported by Franz et al. The NLE during the pre-activation stage in our catalytic reaction occurs at the Cu(I) oxidation stage while in the Franz system it is arises within Cu(II) activation.

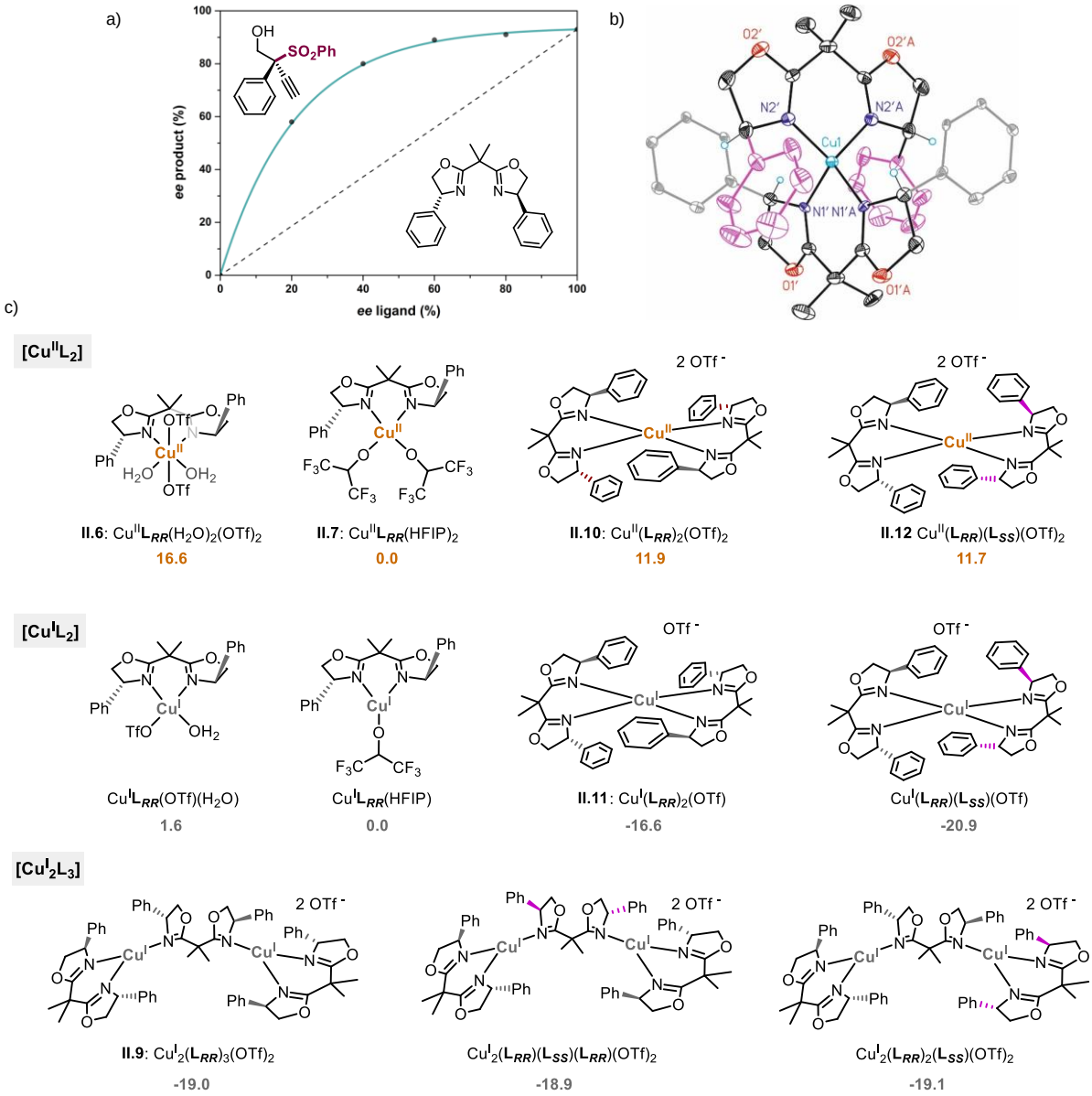

Figure 2.9: a) Previously reported NLE effect in propargylic sulfonylation of substrate **II.1** with $NaSO_2Ph$ giving sulfone product **II.1**, b) Cationic part of the X-ray structure of hetero-chiral Cu(II) complex **II.12**, and c) Relative free energies in kcal/mol computed for the cationic part of the homo- and hetero-chiral Cu(II)L, Cu(I)L and $Cu(I)_2L_3$ complexes.

2.4 DFT studies

After a detailed experimental investigation of the pre-activation stage of the Cu-mediated propargylic sulfonylation reaction including the determination of the order in [Cu], reaction intermediates and the origin of the NLE, we wanted to decipher the

source of enantio-control in the formation of **II.2**. Therefore, we first studied various substrates **II.*x*** to understand the role of the propargylic precursor as we previously observed that the nature of the substrate is important for the chemo- and the enantio-selectivity of the reaction (see Figure 2.10). Notably, the use of the alkynyl epoxide **II.5** led to high yield of the undesired ring-opened by-product **II.5-P**.

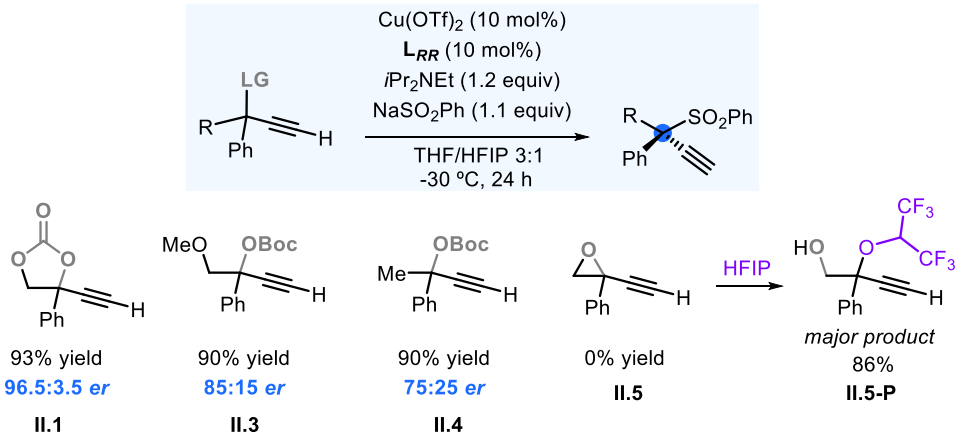

Figure 2.10: Effect of the propargylic precursor **II.*x*** on the reaction efficiency.

2.4.1 Productive cycle

Following the generally accepted steps for propargylic substitution mediated by Cu as reported by Nishibayashi, [79] we calculated the catalytic cycle (Figure 2.11), considering that the active species is a monometallic Cu(I) complex.[97]

In the first step, alkynyl carbonate **II.1** is coordinating to the Cu(I) precursor via □-bonding (**I0**) with the nucleophile interacting reversibly (**I0Nu**). In the next step, DIPEA assists in the deprotometalation of the substrate forming Cu-acetylide intermediate **I3**, which may be directly attacked by the sulfonate anion, but we disregarded this pathway because the associated barrier with an S_N2 attack on a quaternary carbon is typically high. However, this type of attack can be expected when epoxides are used as substrates, leading to different products (see Figure 2.10, **II.5**-to-**II.5-P**). The reaction continues with the generation of a carbocation in the □-position of the propargylic moiety (**I8**), that in the case of **II.1** involves two steps: the ring opening of the cyclic carbonate and subsequent decarboxylation.

[97] Calculations used the B3LYP-D3 functional and included optimizations in solvent. Full computational details are given in the experimental section 2.6.1.

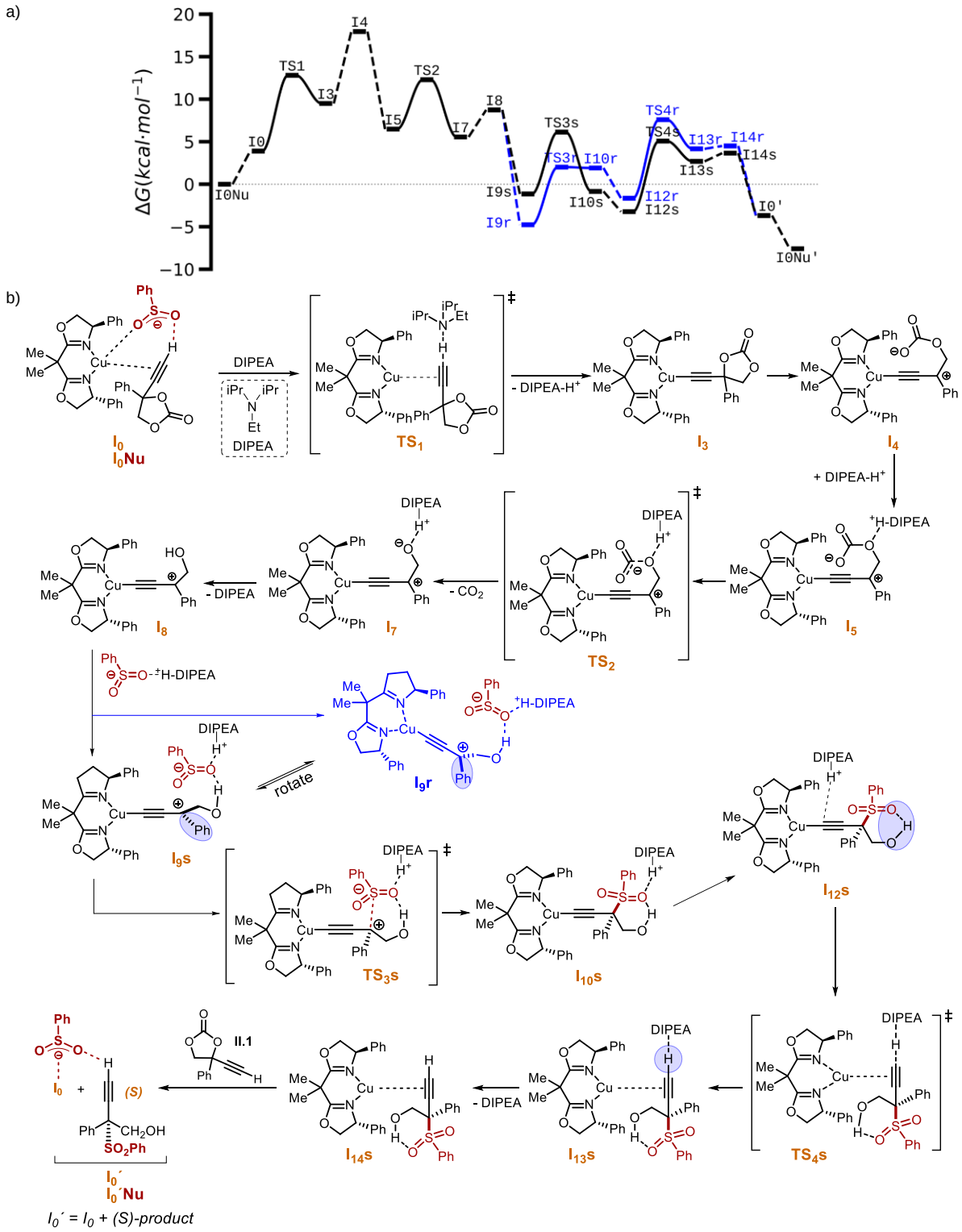

Figure 2.11: (a) Gibbs free-energy profile and (b) mechanistic proposal for the Cu-mediated conversion of alkynyl carbonate **II.1** into propargylic sulfone (*S*)−**II.2**. The energy values correspond to relative free energies at −30 °C, 1 M concentration in kcal/mol. The blue profile corresponds to the pathway leading to product (*R*)−**II.2**.

The ring opening step of the carbonate moiety leads to intermediate **I4**. The transition state (TS) of this step could not be located, but the barrier might be low as indicated by single-point scans (see section 2.6.14). The process entails the rotation around the single bond of the carbonate fragment that is linked to the tertiary carbocation. Next, the decarboxylation step is assisted by DIPEA-H^+ transferring a proton to the propargylic alcohol leading to **I8** and the conversion of **I5** to **I7** proceeding *via* **TS2**. Intermediate **I8** can also be represented as a Cu-allenylidene being a different resonance form opposed to the acetylide-Cu structure depicted in Figure 2.11 providing thus electronic stabilization.[84] After the formation of adducts **I9r** and **I9s**, which can be interconverted without the need for full dissociation, the next step is the C–S bond formation through nucleophilic attack of the sulfinate anion on the □-position of the carbocation (**I9** to **I10** *via* **TS3**). Consecutively, the proto-demetallation of the chiral sulfone is assisted again by an equivalent of protonated base (DIPEA-H^+) forming **I13** from **I12** *via* **TS4**, followed by the regeneration of base and the coordination of the next molecule of substrate to initiate to next turnover (**I13** to **I14** generating **I0'**).

The activation barrier of this entire manifold (18 kcal/mol) is compatible with a slow reaction optimized at -30 ºC delivering chiral product **II.2**. The highest energy level presented in the free-energy profile is the zwitterionic product **I4** generated after the ring-opening step. Thus, we propose that this is the rate-determining step of the transformation.

2.4.2 Origin of enantio-selectivity

As stated in the introduction of this chapter (Section 2.1), traditionally the formation of stereogenic centers during a propargylic substitution process are thought to occur during the nucleophilic attack on the carbocation formed after LG activation, with asymmetric induction being controlled through the chiral environment around the metal center. Therefore, we initially thought that the enantio-induction takes place during C–S bond formation (**I9** to **I10** *via* **TS3**). The computational calculation of this step is not trivial, due to its bimolecular nature and because of the highly exergonic nature of the step when only considering the nucleophilic anion (see data section 2.6.14). We initially assessed this problem by performing relaxed scans of the C–S bond

dissociation. The two lowest conformations of each diastereo-isomer with their respective dissociations were calculated obtaining a rather barrierless potential energy profile. Luckily, when the formation of an adduct between **I8** and an ion pair comprising of the sulfinate anion and DIPEA-H^+, we were able to find the transition states **TS3r** and **TS4s**. These transition states showed small imaginary frequencies that coupled with the non-covalent nature of the intermediates **I9r** and **I9s** lead to difficult to converge conformations. As a consequence, we can only state that those transition states provide an estimate of the upper limit of the barriers of the nucleophilic attack. A kinetic competition between transition states **TS4r** and **TS4s** seems reasonable, which would lead to the experimentally observed (*S*)-sulfone product. Thus, the proto-demetallation (**TS4**) plays a key role to achieve high enantiomeric control over the product. These findings are an unexpected rational for the chirality induction observed in this propargylic substitution process.

2.4.3 Previously reported chiral proto-demetallations

Proto-demetallation in catalytic reactions is rarely proposed as the enantio-determining step. In 2017, Ackermann and co-workers reported a CoCp*-promoted C−H alkylation that features an asymmetric proto-demetallation step (Figure 2.12a), and their proposal was supported by DFT analysis.[98] One year later, Matsunaga et al. hypothesized the induction of enantio-selectivity by proto-demetalation in a Rh-mediated C−H functionalization alkylation (Figure 2.12b).[99]

In line with these previous examples, the stereo-determining pathway shown in Figure 2.11, has a key differentiation between the ways to obtain (*S*) and (*R*) manifold taking place when the protonated base (DIPEAH$^+$) is in the coordination sphere of the Cu-acetylide complex (intermediates **I8** to **I9**)[100]. Therefore, the role of the protonated base during the proto-demetalation step is crucial for the enantio-control promoted during the reaction.

[98] (a) Zell, D.; Bursch, M.; Müller, V.; Grimme, S.; Ackermann, L. *Angew. Chem. Int. Ed*. 2017, 56, 10378; (b) Pesciaioli, F.; Dhawa, U.; Oliveira, J. C. A.; Yin, R.; John, M.; Ackermann, L. *Angew. Chem. Int. Ed*. 2018, 57, 15425.

[99] Satake, S.; Kurihara, T.; Nishikawa, K.; Mochizuki, T.; Hatano, M.; Ishihara, K.; Yoshino, T.; Matsunaga, S. *Nat. Catal.* 2018**,** 1, 585.

[100] The *Si*-attack leads to (*S*)-**II.2** sulfone product, whereas a *Re*-attack provides (*R*)- **II.2**.

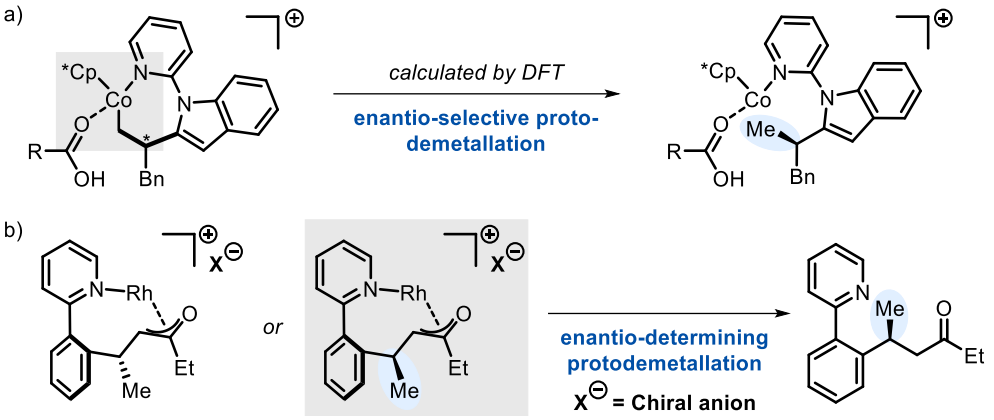

Figure 2.12: a) Enantio-selective proto-demetallation step via CoCp*-catalyzed C–H alkylation of pyridyl indoles by Ackermann and co-workers and b) enantio-selective C–H functionalization of phenyl-pyridines by a Rh catalyst in which chirality is induced by the counter-anion.

2.4.4 Distortion-interaction model to assess the key TS4

To find an explanation why in this overall manifold **TS4s** is more stable than **TS4r**, we carried out an energy decomposition of these transition states following a distortion/interaction model[101] as presented in Table II.II. Importantly, the potential energies do not exactly fit with the free energies listed in Figure 2.11, but regardless, the obtained date predicts the (*S*)-diastereoisomer of **TS4** as the most stable one. The potential energy difference between the (*S*) and (*R*) configured diastereomer is 5.4 kcal/mol with the (*S*) isomer being more stable. Of this energy difference, 5.3 kcal/mol correspond to the difference in distortion energy of the complex, meaning that the (*R*)-diastereoisomer undergoes a higher distortion when the complex-base adduct is formed compared to the (*S*)-diastereoisomer. Note that the difference in distortion of the base is negligible. Finally, the remaining 0.1 kcal/mol of energy difference comes from the interaction of the protonated base with the Cu-complex.

To gain further understanding of what causes the differences in distortion forces during the transition step related to proto-demetallation, we partitioned the TS into two fragments: the Cu-$\mathbf{L}_{RR}$ platform and the [Nu−DIPEA-H$^+$] as a second fragment.

[101] Bickelhaupt, F. M.; Houk, K. N. *Angew. Chem. Int. Ed.* 2017, 56, 10070.

Table **II.II**: Distortion/interaction analysis of the (*R*)- and (*S*)-diastereo-isomers of transition states **TS4**. All energies (values in kcal/mol) presented are potential energies in vacuum. The sub-index $_1$ refers to the original geometries of **TS4s** and **TS4r**. The sub-index $_0$ stands for the relaxed geometries of each fragment without the presence of the other fragment. Base stands for DIPEA.

Entry	Energy type	Fragment	(*R*)	(*S*)	Δ(*R*-*S*)
1	E_1-E_0	base + complex	-8.6	14.0	5.4
2	*distortion*	base	1.3	1.3	0.0
3		complex	29.8	24.5	5.3
4		total	31.1	25.8	5.3
5	*interaction*	base complex	-39.7	39.8	0.1

We looked into the non-covalent interactions of the two fragments using the reduced density gradient with the NCIPLOT 4.0 program[102] (Figure 2.13). In both cases, abundant interactions between DIPEA-H^+ and both diastereo-isomers can be observed. More precisely, the attractive forces feature π−π interactions between the phenyl groups of the sulfone and of the chiral ligand. However, none of these interactions seem to cause the different stabilities of the TSs, but, with a closer look into the bottom views of Figure 2.13, it can be observed that the (*S*)-diastereoisomer exhibits Cu−O interactions between the sulfinate (-SO_2-) group and the metal center that are virtually non-existent in the (*R*)-diastereoisomer.

In order to validate our computational model, we decided to challenge our system by calculating the expected enantiomeric ratio (**ΔΔG**) with other bases. The enantio-induction levels computed in this propargylic sulfonylation reaction were calculated by DFT and compared against the previously attained experimental data (Table II.III).[82] The agreement of the computed behavior of TEA, DABCO, and NMM with the experimental results is not perfect, a result that is associated to the low energy differences involved. This could be related to different speciation of the catalytic intermediates formed while interacting with potentially coordinating bases.

[102] (a) Contreras-Garcia, J.; Johnson, E. R.; Keinan, S.; Chaudret, R.; Piquemal, J.-P.; Beratan, D. N.; Yang, W. *J. Chem. Theory Comput.* 2011, *7*, 625. (b) Johnson, E. R.; Keinan, S.; Mori- Sanchez, P.; Contreras-Garcia, J.; Cohen, A. J.; Yang, W. *J. Am. Chem. Soc.* 2010, *132*, 6498. (c) Boto, R. A.; Peccati, F.; Laplaza, R.; Quan, C.; Carbone, A.; Piquemal, J.-P.; Maday, Y.; Contreras-Garcia, J. *J. Chem. Theory Comput.* 2020, *16*, 4150.

Nonetheless, the trend that lower enantio-induction is attained compared to DIPEA under similar conditions is reproduced. These results suggest that the computational model used to describe the conversion of substrate **II.1** into propargylic sulfone **II.2** (Figure 2.1b) is reasonable and helps us to highlight a key relation between the base and the enantiomeric ratio.

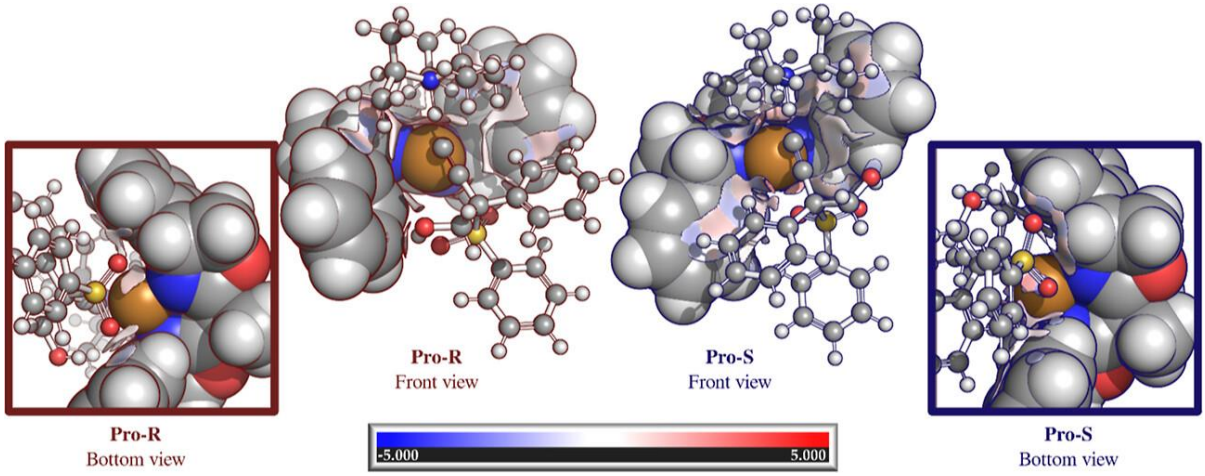

Figure 2.13: Reduced density gradient iso-surfaces, value of 0.35, between the [**CuL*RR***] (van der Waals spheres) and the product+DIPEA-H^+ (ball and stick) obtained with NCIPLOT for the **TS4r** (pro-*R*) and **TS4s** (pro-*S*). *Iso*-surfaces are colored by the signed density, sign(λ_2)ρ; blue represent strong favorable interactions while red regions correspond to repulsive forces.

Table **II.III**: Comparison of computationally and experimentally obtained enantiomeric ratios in the synthesis of propargylic sulfone **II.2** at −30 °C. Computed energies are given in kcal/mol. TEA = triethyl amine, DABCO = 1,4-diazabicyclo[2.2.2]octane, and NMM = *N*-methylmorpholine.

		Computational			*Experimental*
Entry	base	**ΔΔG**	ee (%)	S/R	S/R
1	DIPEA	2.5	98.9	99.5:0.5	96.5:3.5
2	TEA	0.3	28.4	64.2:35.8	95:5
3	DABCO	0.3	28.2	64.1:35.9	85:15
4	NMM	0.5	48.9	74.5:25.5	87:13

2.5 Conclusions

In this chapter, we present a study that allowed us to achieve a detailed insight into the mechanism of a previously reported enantio-selective Cu-catalyzed propargylic sulfonylation using a combination of experimental and computational techniques. Different from the generally accepted mechanism, we propose the proto-demetallation as the enantio-determining step, whereas during the step that involves nucleophilic attack of the sulfinate we were not able to observe to distinct enough diastereomeric adducts. Moreover, we have been able to assign non-covalent interactions responsible for the enantio-selectivity during the protonation of the Cu-acetylide intermediate, and a key role for the base has been uncovered. Apart from this main conclusion, we have also unravelled the activation pathway of the precursor $Cu(OTf)_2$ that evolves in various steps into a monometallic Cu(I) active catalyst. The previously experimentally observed NLE can be rationalized by formation of a reservoir complex based on Cu(I). Overall, our study sheds new light on enantio-selective propargylic substitution chemistry, considering proto-demetallation as an unusual step for chirality transfer.

2.6 Experimental section

2.6.1 General methods

All standard reactions were set up under air. Where needed, reactions were prepared under an argon atmosphere in oven-dried glassware using standard Schlenk techniques or in a nitrogen-filled glovebox (mBraun UnilabPro) with concentrations of O_2 and H_2O < 0.1 ppm.

Commercially available reagents [$Cu(OTf)_2$, ***L*$_{RR}$** and ***L*$_{SS}$** chiral Box ligands, *i*Pr_2NEt, $NaSO_2Ph$) were used without further purification and used as received from their commercial suppliers, and stored under inert gas, and at low temperature where needed. Previously reported compounds were prepared as described in the literature.[82] Synthesis grade solvents including tetrahydrofuran (THF), 1,2-dichloromethane (DCM) and 1,1,1,3,3,3-hexafluoroisopropanol (HFIP) were used as purchased without drying before use. When necessary, the solvents (THF, DCM and hexane) were used from a solvent purification system pure-solv (SPS-400, Innovative Technology) and after degassing they were stored under N_2 over activated 4 Å molecular sieves. Where required, HFIP, benzene, diethyl ether and pentane (acquired from commercial suppliers) were degassed, dried over molecular sieves and stored under inert gas. CD_2Cl_2 and THF-d_8 were stored under N_2 over activated molecular sieves. Glassware was washed with a base bath (KOH in water/isopropyl alcohol) after every use. Magnetic stirring bars were cleaned using an acid mixture of 20% HNO_3 + 10% HCl in water.

***Electron Paramagnetic Resonance (EPR)*:** Continuous wave (CW) EPR spectra were acquired on a Bruker EMX X-band EPR spectrometer with an ER 4116 HS cavity (9.86 GHz at room temperature). A 150 mL Suprasil offset liquid nitrogen Dewar flask (Wilmad Lab Glass) was used for low-temperature measurements (77 K). The spectral data was collected under ambient conditions with the following spectrometer settings: microwave power = 0.5506 mW; center field = 3000 G, sweep width = 1200 G, sweep time = 20 s, modulation frequency = 100 KHz, modulation amplitude = 4 G, power attenuation = 25 dB, time constant = 0.01 ms. Individual EPR tubes were filled with the sample and were placed at the same position of the resonant cavity for EPR spectral acquisition.

Ultraviolet-Visible Spectroscopy (UV-Vis): UV-Vis measurements were carried out on a Shimadzu UV-2401PC spectrophotometer equipped with a photomultiplier detector, double beam optics and D2 and W light sources. All the spectra were recorded in a 1 mm Hellma Quartz SUPRASIL® cuvette. Due to the high concentration of the solutions, short path cuvettes were employed in order to avoid signal saturation.

***X-ray Analysis*:** The crystals used for structure determination were selected using a Zeiss stereomicroscope using polarized light and prepared under inert conditions immersed in perfluoropolyether as protecting oil for manipulation. Crystal structure determination was carried out using an Apex DUO Kappa 4-axis goniometer equipped with an APPEX 2 4K CCD area detector, a Microfocus Source E025 IuS using MoK_α radiation, Quazar MX multilayer Optics as monochromator and an Oxford Cryosystems low temperature device Cryostream 700 plus (T = -173 °C). Crystal structure determination for samples Full-sphere data collection was used with ω and φ scans. Data was collected with program APEX-2,[103] data reduction Bruker Saint[104] V/.60A and absorption correction SADABS.[105] Other X-ray equipment was also used: a Rigaku diffractometer equipped with a Pilatus 200K area detector, a Rigaku MicroMax007HF microfocus rotating anode with MoK_α radiation, Confocal Max Flux optics and an Oxford Cryosystems low temperature device Cryostream 700 plus (T = –173 ° C). Full-sphere data collection was used with ω and φ scans. Programs used: Data collection and reduction with CrysAlisPro[106] V/.60A and absorption correction with Scale3 Abspack scaling algorithm.[107] Crystal structure solution was achieved using the computer program SHELXT.[108] Visualization was performed with the program ShelXIe.[109] Missing atoms were subsequently located from difference Fourier synthesis and added to the atom list. Least-squares refinement on F^2 using all measured intensities was carried out using the program SHELXL 2015.[110] All non-hydrogen atoms were refined including anisotropic displacement parameters.

[103] Data collection with APEX II version v2013.4-1, Bruker AXS Inc., Madison, Wisconsin, USA 2007.
[104] Data reduction with Bruker SAINT version V8.30c, Bruker AXS Inc., Madison, Wisconsin, USA 2007.
[105] (a) SADABS, V2012/1, Bruker AXS Inc., Madison, Wisconsin, USA 2001. (b) Blessing, R. H. *Acta Cryst*. 1995, A51, 33.
[106] Data collection and reduction with CrysAlisPro, 1.171.39.12b, Rigaku OD, 2015.
[107] Empirical absorption correction using spherical harmonics implemented in Scale3 Abspack scaling algorithm, CrysAlisPro 1.171.39.12b, Rigaku OD, 2015.
[108] SHELXT, V2014/4, Sheldrick 2014: Sheldrick, G. M. *Acta Cryst*. 2015, A71, 3.
[109] Huebschle, C. B; Sheldrick, G. M.; Dittrich, B. *J. Appl. Cryst*. 2011, 44, 1281.
[110] Sheldrick, G. M. *Acta Cryst*. 2015, C71, 3-8.

Nuclear magnetic resonance (NMR): NMR spectra were obtained on a Bruker 400, 500 MHz or a 500 MHz with cryoprobe spectrometers equipped with probe-heads capable of producing gradients in the *z* direction with a maximum strength of 53.5 G/cm. ^{1}H, ^{13}C and ^{19}F NMR chemical shifts are reported in parts per million (ppm), relative to tetramethylsilane (TMS) for ^{1}H and ^{13}C with the residual solvent peak used as an internal reference, and $CFCl_3$ (Freon) for ^{19}F measurements. Multiplicities are reported as follows: singlet (s), broad band (br), d (doublet), dd (doublet of doublets), triplet (t) and multiplet (m).

IR-Spectroscopy – Kinetics (REACT-IR): In situ IR monitoring of catalytic reactions were carried out on a Mettler Toledo FTIR ReactIR 15 spectrometer. The equipment was coupled to a MTC detector and a diamond AgX Fiber Probe. The glass reactor that was used had 3 inlets: the upper one was used to insert the probe and the two lateral entries were closed with septa. The temperature of the reactor was cooled down and controlled with an external chiller using an isopropanol bath. The Burés method[111] was applied for the data treatment.

High Resolution Mass Spectrometry (HR-MS): High Resolution Mass Spectrometry (HRMS) data was recorded using two different methodologies depending on the complex to be analyzed. ESI-MS analyses were performed in a MicroTOF Focus mass spectrometer (Bruker Daltonics) by direct injection. Cold-spray ionization-MS (CSI-MS) analyses were performed in a MicroTOF Focus mass spectrometer (Bruker Daltonics) equipped with a cold-spray ionization source by direct injection and using nitrogen as sprayer and dry gas.

Computational calculations (DFT): All the DFT calculations were carried out with Gaussian09[112] (Revision D.01) with a grid of 99 radial shells and 590 angular points

[111] Burés, J. A. *Angew. Chem. Int. Ed.* 2016, *55*, 2028-2031.

[112] Frisch, M. J.; Trucks, G. W.; Schlegel, H. B.; Scuseria, G. E.; Robb, M. A.; Cheeseman, J. R.; Scalmani, G.; Barone, V.; Mennucci, B.; Petersson, G. A.; Nakatsuji, H.; Caricato, M.; Li, X.; Hratchian, H. P.; Izmaylov, A. F.; Bloino, J.; Zheng, G.; Sonnenberg, J. L.; Hada, M.; Ehara, M.; Toyota, K.; Fukuda, R.; Hasegawa, J.; Ishida, M.; Nakajima, T.; Honda, Y.; Kitao, O.; Nakai, H.; Vreven, T.; Montgomery, J. A. Jr.; Peralta, J. E.; Ogliaro, F.; Bearpark, M.; Heyd, J. J.; Brothers, E.; Kudin, K. N.; Staroverov, V. N.; Keith, T.; Kobayashi, R.; Normand, J.; Raghavachari, K.; Rendell, A.; Burant, J. C.; Iyengar, S. S.; Tomasi, J.; Cossi, M.; Rega, N.; Millam, J. M.; Klene, M.; Knox, J. E.; Cross, J. B.; Bakken, V.; Adamo, C.; Jaramillo, J.; Gomperts, R.; Stratmann, R. E.; Yazyev, O.; Austin, A. J.; Cammi, R.; Pomelli, C.; Ochterski, J. W.; Martin, R. L.; Morokuma, K.; Zakrzewski, V. G.; Voth, G. A.; Salvador, P.; Dannenberg, J. J.; Dapprich, S.; Daniels, A. D.; Farkas, O.; Foresman, J. B.; Ortiz, J. V.; Cioslowski, J.; Fox, D. J. Gaussian 09, Revision D.01, Gaussian, Inc., Wallingford CT, 2013.

per shell ("Ultrafine" in Gaussian). All calculations were carried out using B3LYP-D3[113] (where D3 stands for GD3[114] empirical dispersion) with RRHO approximations for the free energy corrections and implicit SMD[115] solvation for tetrahydrofuran (THF). Free energies were recalculated at -30ºC using the Goodvibes[116] program and reference state corrections[117] for liquid phase at 1M and -30ºC were added as well as Grimme-style quasi-harmonic corrections with a threshold of 100cm^{-1}.[118] All geometries were optimized using a lower basis set, BS1, and then their energies refined with single point (SP) calculations with a larger basis set, BS2. Per each optimized structure a frequency calculation was performed to ensure its minima/transition state nature. The relaxed scans were carried out using the BS1.

The lower basis set, BS1, used was LANL2DZ with its corresponding electron core potential (ECP) for Cu[119] and 6-31g(d)[120] for the rest of the atoms. The larger basis set used, BS2, was the LANL2TZ with f polarization and the corresponding ECP for Cu,[119,121] aug-cc-pVTZ for all N, O and S atoms and cc-pVTZ for C, H and F atoms.[122]

[113] (a) Stephens, P. J.; Devlin, F. J.; Chabalowski, C. F.; Frisch, M. J. *J. Phys. Chem.* 1994, 98, 11623. (b) Lee, C.; Yang, W.; Parr, R. G. *Phys. Rev. B* 1988, 37, 785. Becke, A. D. *J. Chem. Phys.* 1993, 98, 5648.

[114] Grimme, S. *J. Comput. Chem.* 2006, 27, 1787.

[115] Marenich, A. V.; Cramer, C. J.; Truhlar, D. G. *J. Phys. Chem. B* 2009, 113, 6378.

[116] (a) Luchini, G.; Alegre-Requena, J.; Funes-Ardoiz, I.; Rodríguez-Guerra, J.; Chen, J. R. 2019. GoodVibes v3.0.0. Zenodo. https://doi.org/10.5281/zenodo.3346166. (b) Luchini, G.; Alegre-Requena, J. V.; Funes-Ardoiz, I.; Paton R. S. *F1000Research* 2020, 9, 291. https://doi.org/10.12688/f1000research.22758.1.

[117] Ribeiro, R. F.; Marenich, A. V.; Cramer, C. J.; Truhlar, D. G. *J. Phys. Chem. B* 2011, 115, 14556.

[118] Grimme, S. *Chem. Eur. J.* 2012, 18, 9955.

[119] Hay, P. J.; Wadt, W. R. *J. Chem. Phys.*, 1985, 82, 299.

[120] (a) Ditchfield, R.; Hehre, W. J.; People, J. A. *J. Chem. Phys.* 1971, 54, 724;(b) Hehre, W. J.; Ditchfield, R.; Pople. J. A. *J. Chem. Phys.* 1972, 56, 2257; (c) Hariharan, P. C.;People, J. A. *Theor. Chim. Acta* 1973, 28, 213.

[121] Roy, L. E., Hay, P. J.; Martin, R. L. *J. Chem. Theory Comput.* 2008, 4, 1029.

[122] (a) Dunning, T. H. Jr. *J. Chem. Phys.* 1989, 90, 1007. (b) Kendall, R. A.; Dunning Jr., T. H.; Harrison, R. J. *J. Chem. Phys.* 1992, 96, 6796. (c) Woon, D. E.; Dunning T. H. Jr. *J. Chem. Phys.* 1993, 98, 1358. (d) Davidson, E. R. *Chem. Phys. Lett.* 1996, 260, 514.

2.6.2 Synthesis and characterization of complexes

Synthetic procedure for complex II.6 [123]

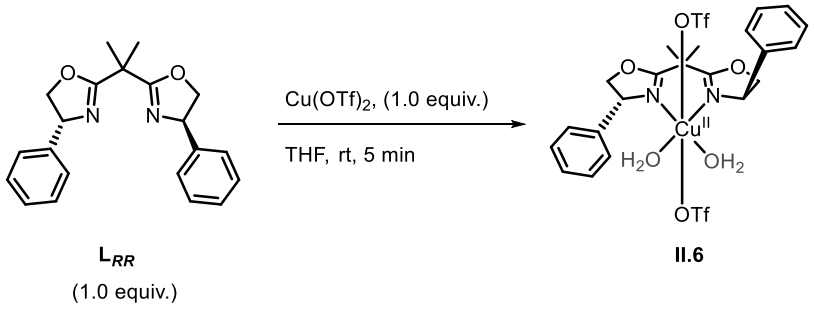

Figure 2.14: Reaction scheme for complex **II.6**.

To a round-bottomed flask equipped with a magnetic stirring bar ***L*$_{RR}$** (0.15 mmol, 50.2 mg) and $Cu(OTf)_2$ (0.15 mmol, 54.3 mg) were dissolved in THF (10 mL). The reaction mixture was stirred at room temperature for 5 min. Hereafter, the turquoise solution was filtered through Celite and the solvent was removed under vacuum to obtain a turquoise-colored, viscous oil. The oil was dissolved in THF and it was prepared for crystallization via vapor diffusion using pentane. A turquoise, crystalline solid (**II.6**, 68.1 mg) was isolated in 62%.

EPR in THF [13 mM]: $A_{||}$ = 404.80 MHz, $g_{||}$ = 2.39

UV-Vis (THF) [16 mM]: λ (nm), Abs: (740, 0.046)

[123] Evans, D. A.; Tregay, S. W.; Burgey, C. S.; Paras, N. A.; Vojkovsky, T. *J. Am. Chem. Soc*. 1998, 120, 5824.

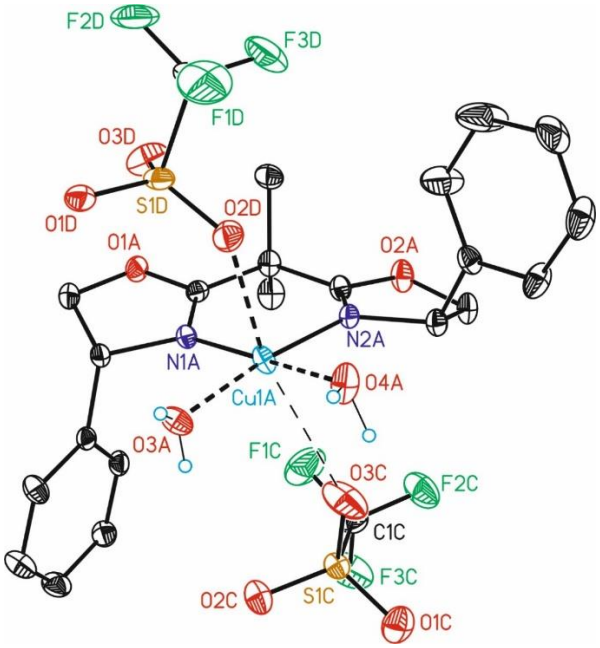

Figure 2.15: ORTEP representation of **II.6** with 50 % probability ellipsoids (H atoms are omitted for clarity).

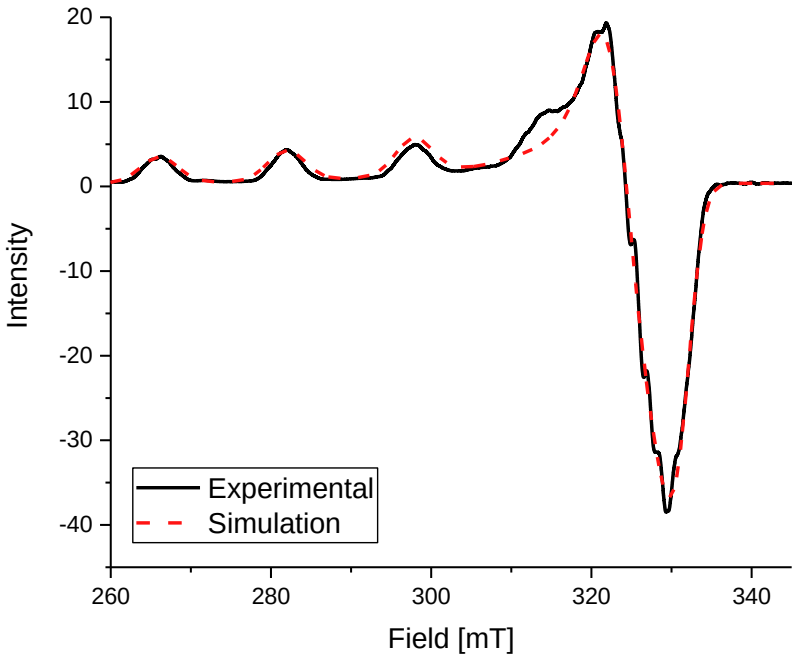

Figure 2.16: Experimental and simulated EPR spectrum of **II.6** in THF/HFIP at 77 K.

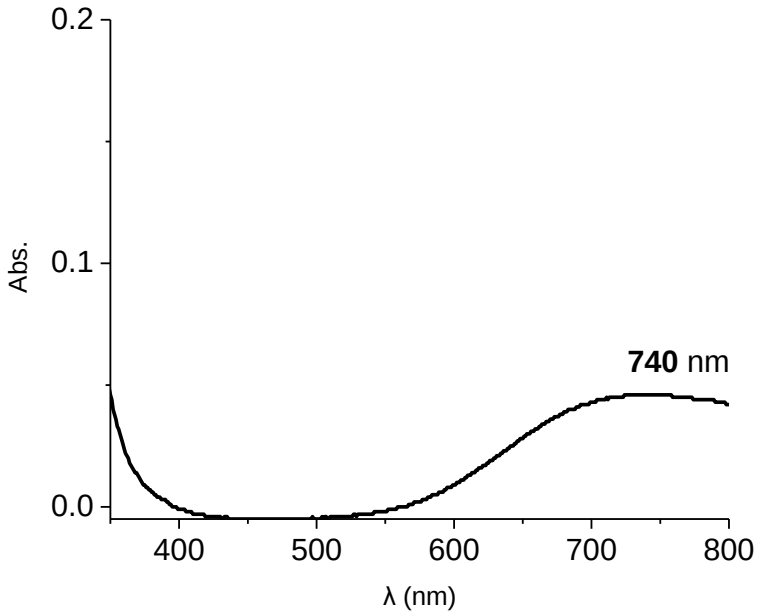

Figure 2.17: UV-Vis spectrum of **II.6** in THF/HFIP at 298 K.

Synthetic procedure for complex II.7 in THF/HFIP (3:1)

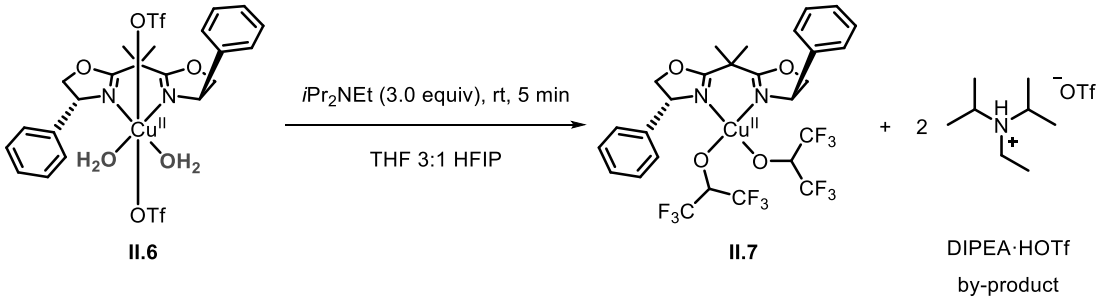

II.6 **II.7**

Figure 2.18: Reaction scheme for complex **II.7**.

Inside a glovebox,[124] complex **II.6** (0.132 mmol, 94.7 mg) was charged into an oven-dried Schlenk flask equipped with a magnetic stirring bar and it was dissolved in dry and degassed THF/HFIP (3:1 v/v, 6 mL in total). Furthermore, *i*Pr$_2$NEt (0.396 mmol, 69. 0 µL, 3.0 equiv) was added with a Hamilton micro-syringe and the mixture was stirred for 5 minutes converting **II.6** to **II.7** with a visual color change from turquoise to dark blue. At this point, the solvent was removed *in vacuo* and the complex was extracted with dry benzene allowing the precipitation of a white salt, identified as by-

[124] Complex **II.7** decomposes after several days when stored under air.

product DIPEA·HOTf.[125] The solution was filtered into an empty Schlenk flask and the benzene was removed under vacuum to obtain a dark blue-colored powder. The powder was dissolved in THF and it was set for slow vapor diffusion crystallization using pentane at –30 ºC producing single crystals of complex **II.7** (83.6 mg, 86%).

EPR in THF/HFIP 3:1 [13 mM]: $A_{||}$ = 424.70 MHz, $g_{||}$ = 2.35

UV-Vis (THF) [16 mM]: λ (nm), Abs: (620, 0.161)

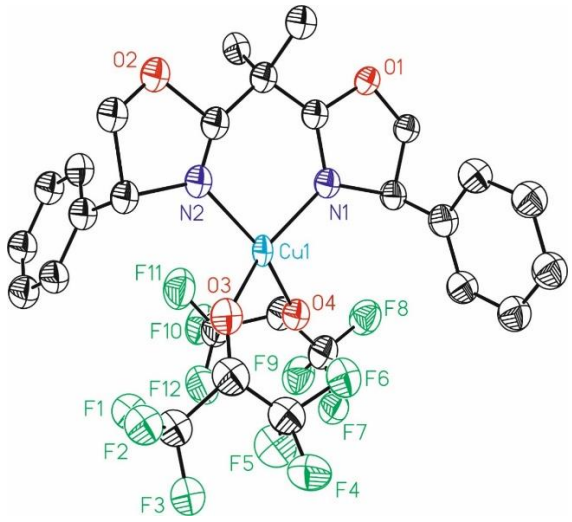

Figure 2.19: ORTEP representation of **II.7** with 50 % probability ellipsoids (H atoms omitted for clarity).

[125] The by-product DIPEA·HOTf co-crystallized in a THF/pentane solvent system via slow vapor diffusion.

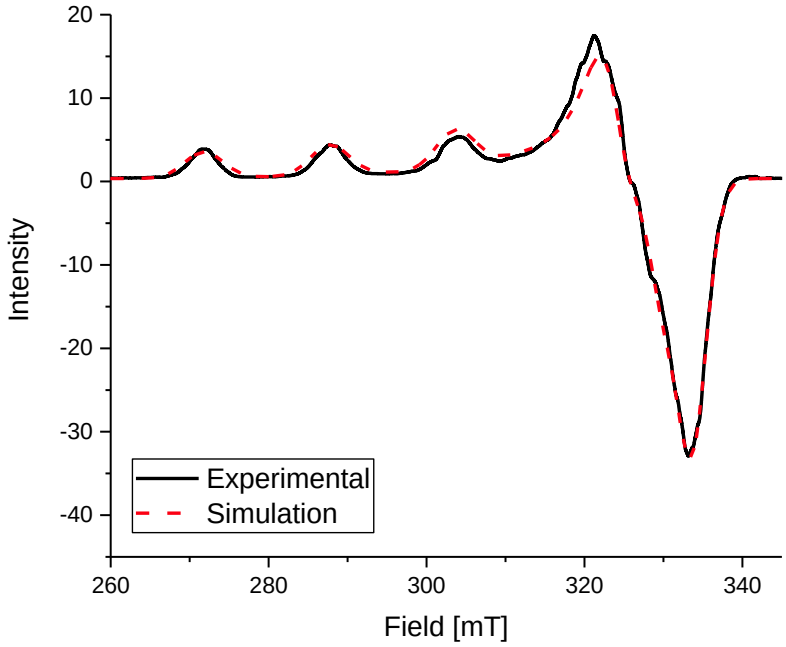

Figure 2.20: Experimental and simulated EPR spectrum of **II.7** in THF at 77 K.

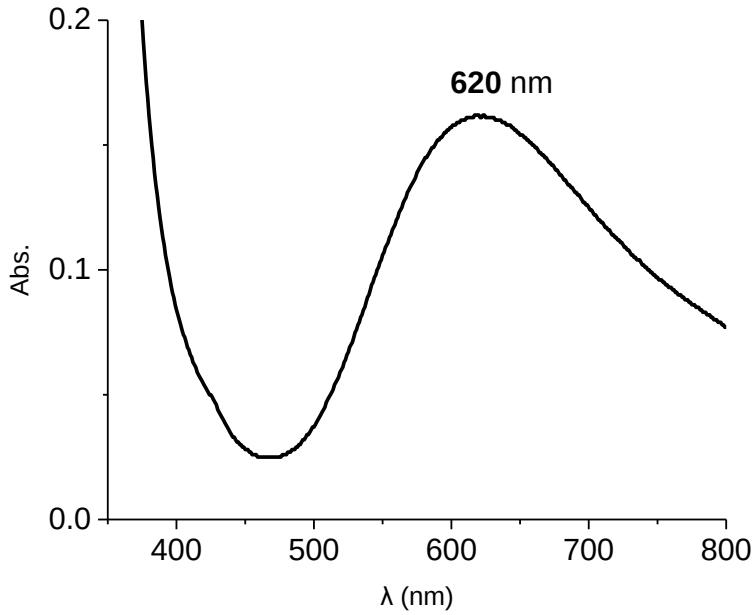

Figure 2.21: UV-Vis spectrum of **II.7** in THF/HFIP at 298 K.

Characterization of the by-product DIPEA·HOTf:

^{1}H NMR (400 MHz, $CDCl_3$ at 298 K) δ: 8.30 (br, 1H, N**H**$_1$), 3.70-3.62 (m, 2H, -C**H**-$_{isopropyl}$), 3.14-3.08 (m, 2H, -C**H**$_2$-$_{ethyl}$), 1.51-1.46 (m, 9H, overlapping of –C**H**$_3$ $_{isopropyl}$ and –C**H**$_3$ $_{ethyl}$), 1.42 (d, 6H, $^{3}J_{H,H}$ = 6.6 Hz, –C**H**$_3$ $_{isopropyl}$).

^{13}C{^{1}H} NMR (101 MHz, $CDCl_3$ at 298 K) δ: 54.95 (-**C**H-$_{isopropyl}$), 43.18 (-**C**H$_2$-$_{ethyl}$), 18.73 (–**C**H$_3$ $_{isopropyl}$), 17.36 (–**C**H$_3$ $_{isopropyl}$), 12.55 (–**C**H$_3$ $_{ethyl}$).

^{19}F NMR (376 MHz, $CDCl_3$ at 298 K) δ: -78.45 (SO_3C**F**$_3$).

ESI(+)-HRMS (DCM); *m/z* found (calc.): 130.1592 (130.1596), $C_8H_{20}N^+$, [DIPEA-H]$^+$

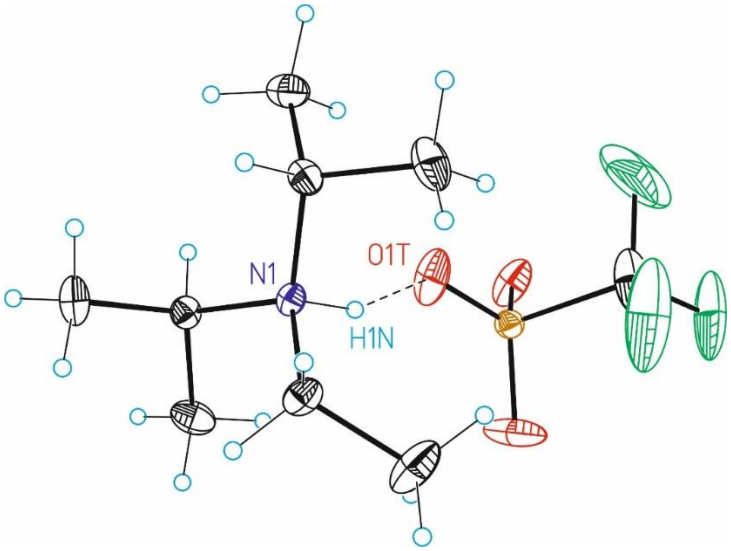

Figure 2.22: ORTEP representation of DIPEA·HOTf with 50 % probability ellipsoids.

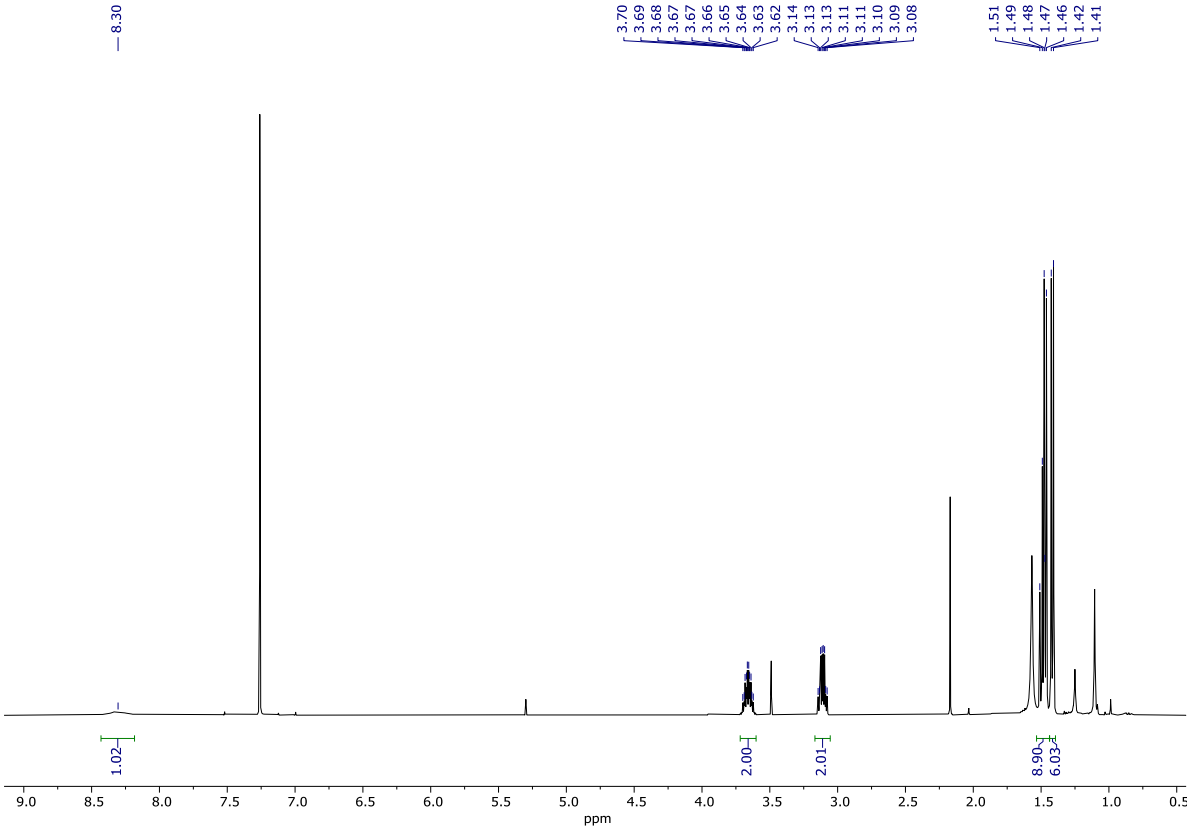

Figure 2.23: ^{1}H NMR (400 MHz) spectrum of DIPEA·HOTf in $CDCl_3$ at 298 K.

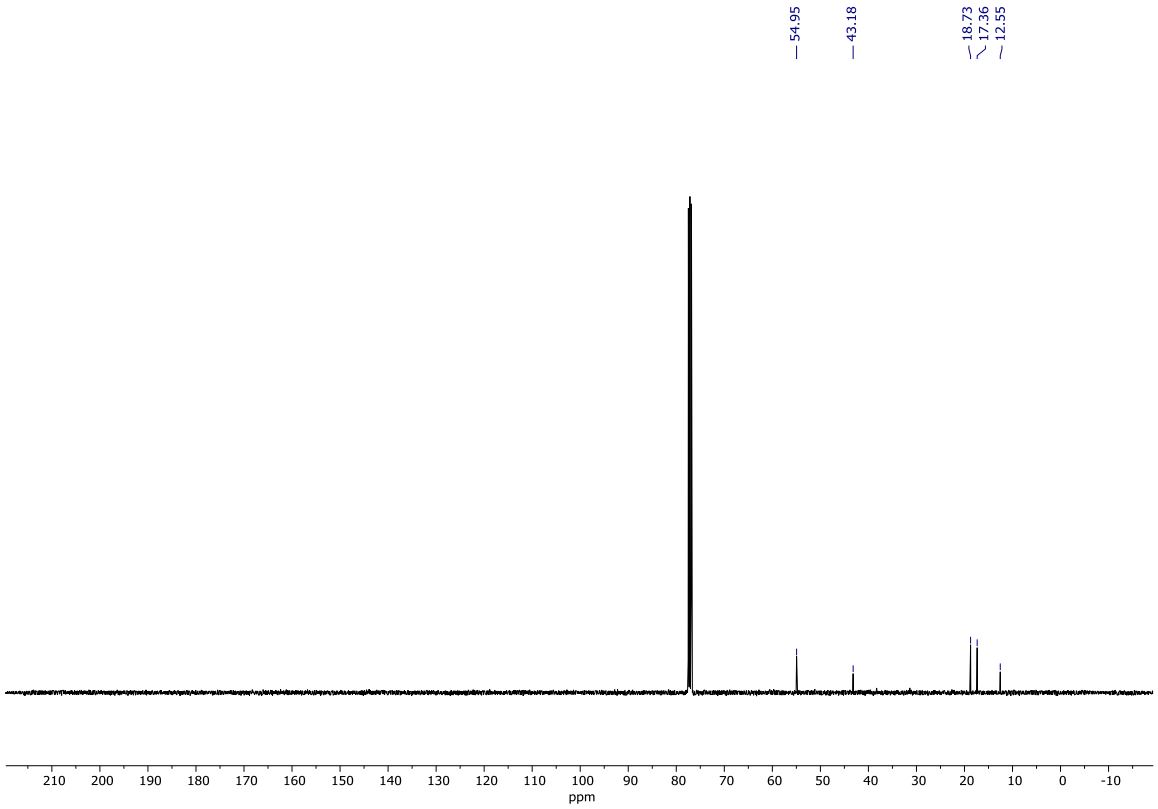

Figure 2.24: $^{13}C\{^{1}H\}$ NMR (101 MHz) spectrum of DIPEA·HOTf in $CDCl_3$ at 298 K.

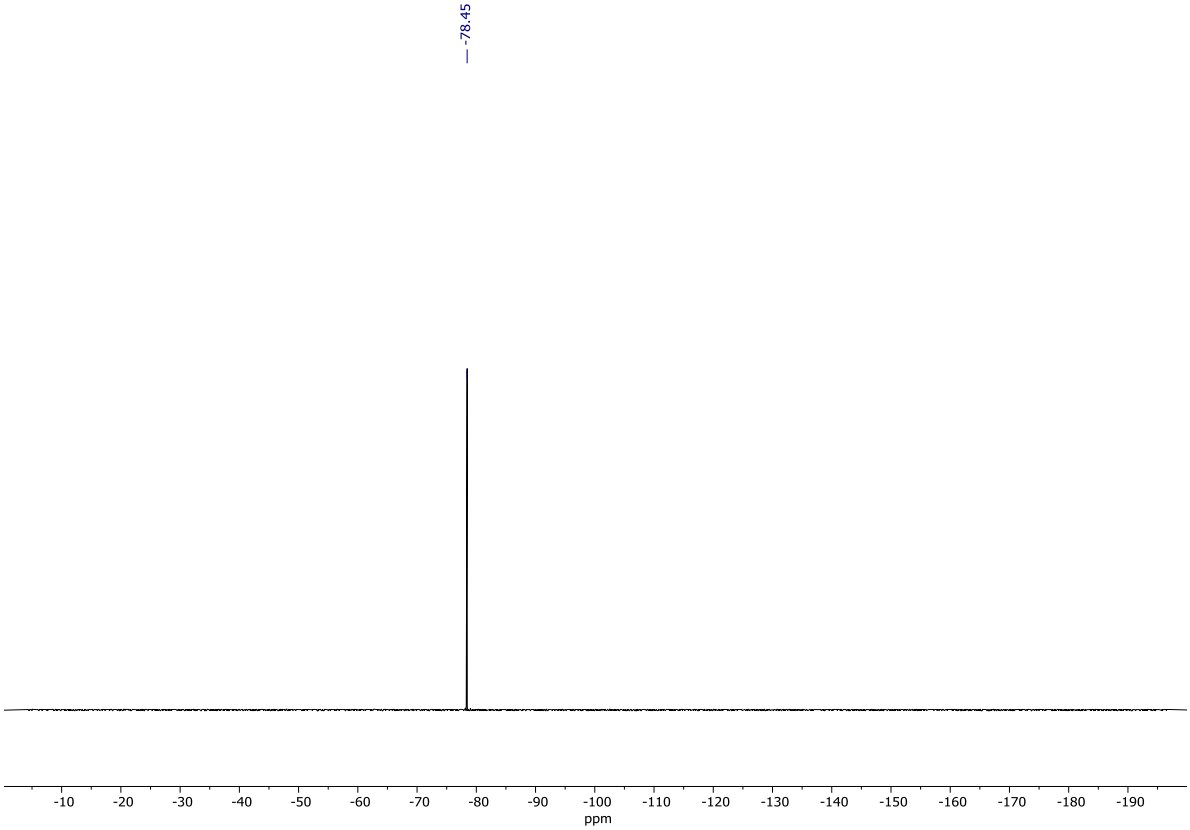

Figure 2.25: ^{19}F NMR (376 MHz) spectrum of DIPEA·HOTf in $CDCl_3$ at 298 K.

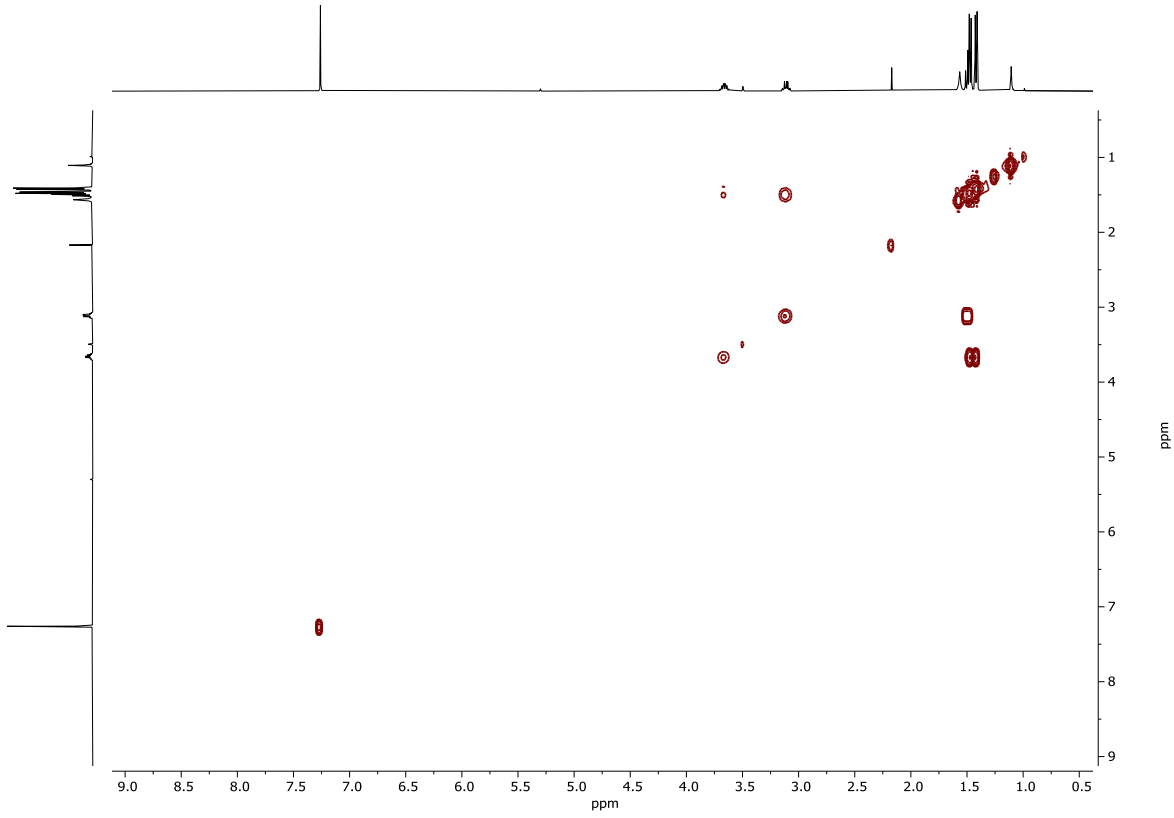

Figure 2.26: COSY NMR spectrum of DIPEA·HOTf in $CDCl_3$ at 298 K.

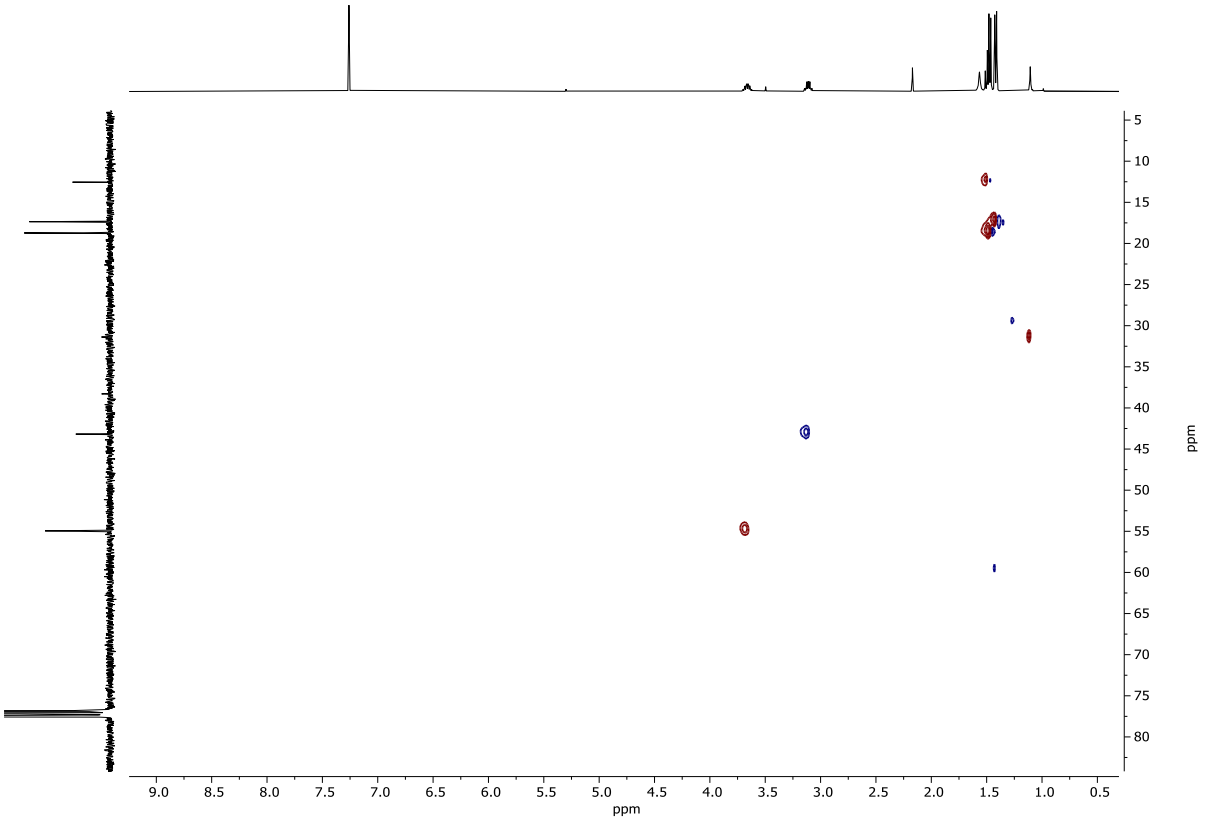

Figure 2.27: HSQC NMR spectrum of DIPEA·HOTf in $CDCl_3$ at 298 K.

2.6.3 EPR and UV-Vis study of Complex II.6 reaction to Complex II.7

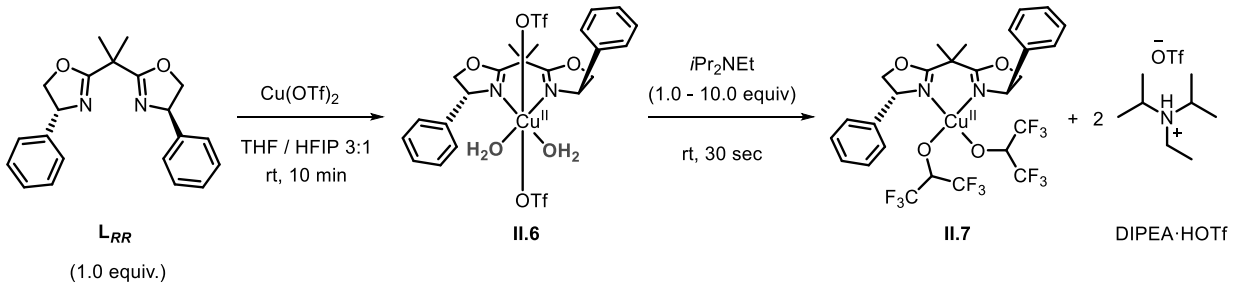

Figure 2.28: Reaction scheme for the titration of **II.6** with base towards the formation of complex **II.7**.

EPR procedure:

In a 2 mL vial, $Cu(OTf)_2$ (5.2 µmol, 1.9 mg, 1.0 equiv) and ligand $\mathbf{L}_{\boldsymbol{RR}}$ (5.1 µmol, 1.7 mg, 1.0 equiv) were dissolved in 0.4 mL of THF/HFIP (3:1 v/v). The solution was stirred for 10 min and then transferred to an EPR tube, and the sample was measured identifying complex **II.6**. Then, *i*Pr_2NEt (5.2 µmol, 0.9 µL, 1.0 equiv) was added to the mixture with a Hamilton syringe. After 30 seconds, the sample was measured again by EPR. To the same EPR tube, portions of 1.0 equiv of *i*Pr_2NEt were added until a total of 10 equiv were reached. After each addition, the sample was measured. Full conversion of complex **II.6** into **II.7** was observed when 3.0 equiv of *i*Pr_2NEt were present in solution.

UV-Vis procedure:

In a 2 mL vial, $Cu(OTf)_2$ (4.7 µmol, 1.7 mg, 1.0 equiv) and ligand $\mathbf{L}_{\boldsymbol{R,R}}$ (4.7 µmol, 1.6 mg, 1.0 equiv) were dissolved in 0.3 mL of THF/HFIP (3:1 v/v). The solution was stirred for 10 min and then transferred to a 1 mm quartz cuvette. First, complex **II.6** was measured by UV-Vis. Then, *i*Pr_2NEt (4.7 µmol, 0.8 µL, 1.0 equiv) was added with a Hamilton syringe. After 30 seconds, the sample was measured again. Into the same cuvette, further portions of 1.0 equiv of *i*Pr_2NEt were added and the sample measured after each consecutive addition until a total of 10 equiv of *i*Pr_2NEt was added. Isosbestic point for small peak transition: THF/HFIP (3:1 v/v); λ (nm), Abs. [0.22 mM]: (768, 0.046).

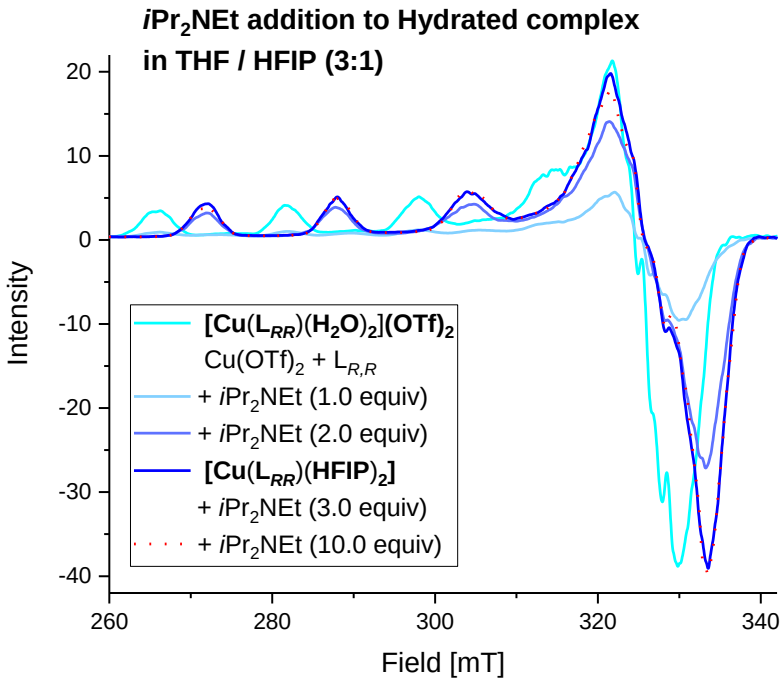

Figure 2.29: EPR spectra for the titration of complex **II.6** with *i*Pr$_2$NEt from 260-340 mT in 3:1 v/v THF/HFIP [13 mM] at 77 K.

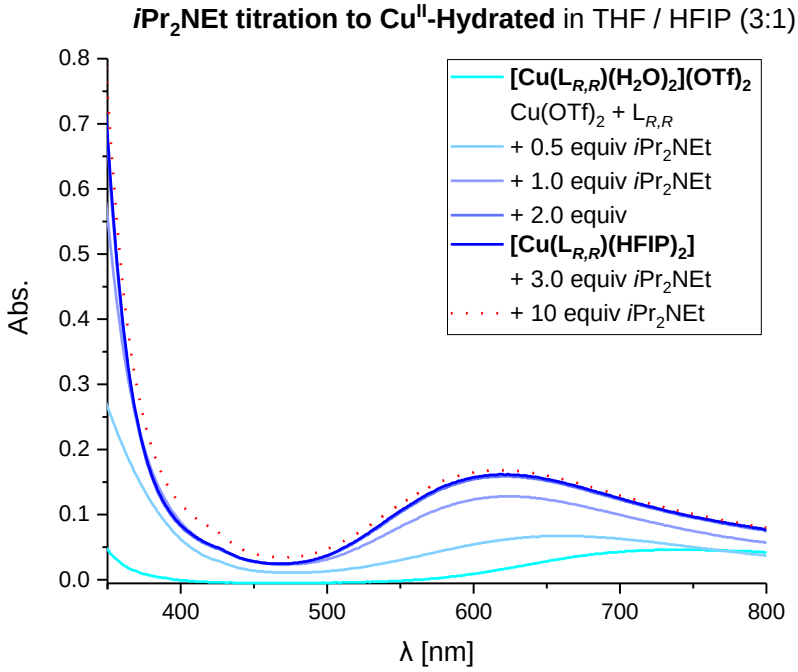

Figure 2.30: UV-Vis titration of complex **II.6** with *i*Pr$_2$NEt from 350 to 800 nm in 3:1 THF/HFIP [16 mM] at 298 K – region visualized from 350 to 800 nm.

2.6.4 Kinetics data – Order of catalyst

Order in [Cu]:

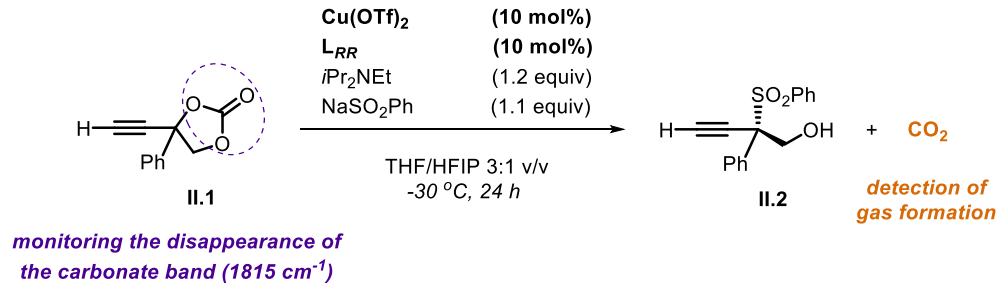

Figure 2.31: Reaction scheme for the catalytic monitoring of the conversion of **II.1** into **II.2**.

Procedure: In a 2 mL vial, $Cu(OTf)_2$ (28.8 mg, 0.08 mmol, 10 mol%) and $\mathbf{L_{RR}}$ (26.8 mg, 0.08 mmol, 10 mol%) were dissolved in 2.0 mL of THF/HFIP (3:1 v/v). The mixture was left stirring for 5 min. Then, *i*Pr_2NEt (167 µL, 0.96 mmol, 1.2 equiv) was added and the solution was stirred for 2 more minutes before it was transferred to a glass reactor. $NaSO_2Ph$ (144.0 mg, 0.88 mmol, 1.1 equiv) was added to the mixture and the reactor was closed with a septum and coupled to the IR equipment. The mixture was cooled down to –30 °C and the measurements was started. Meanwhile, in a 1 mL vial, cyclic carbonate **II.1** (150 mg, 0.80 mmol, 1.0 equiv) was dissolved in 0.4 mL of solvent (THF/HFIP, 3:1 v/v). After ensuring that the temperature was stable, the substrate was injected inside the reactor with a syringe through the septum. While the catalytic reaction was monitored by IR at –30 °C, spectra were recorded every minute during a period of 24 h.

Other quantities of the precursors:

$Cu(OTf)_2$ (mg): 20.2 (7 mol%) and 37.4 (13 mol%)

$\mathbf{L_{RR}}$ (mg): 18.8 (7 mol%) and 34.8 (13 mol%)

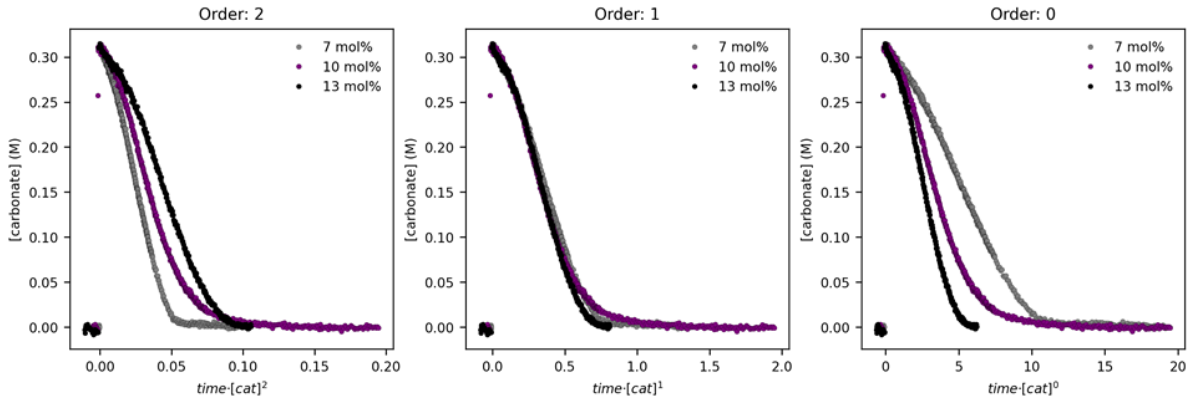

Figure 2.32: Determination of the order in [Cu] by the normalized time scale method.

Note that the alignment of the kinetic profiles at α = 1 examining three different concentrations of catalyst indicates that a monometallic species is involved in the rate-limiting step of the process.

Monitoring of CO_2 evolution

During the kinetic measurements followed by in situ IR monitoring, a peak assigned to free CO_2 could be detected. As can be observed in Figures 2.33, 2.34 and 2.35, the formation of CO_2 is directly correlated to the disappearance of the substrate.

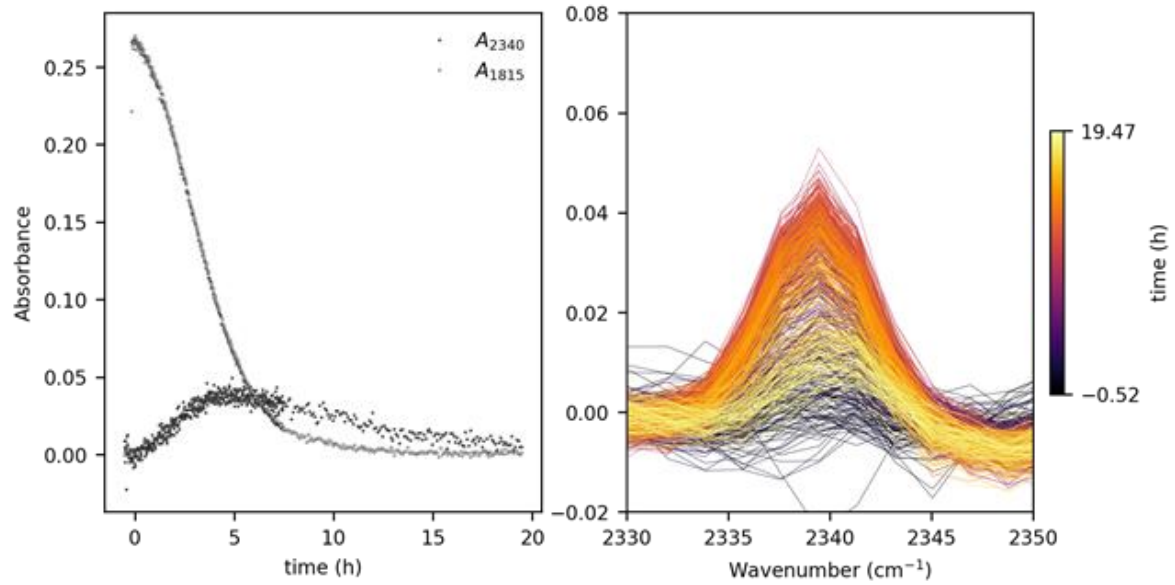

Figure 2.33: Appearance of a CO_2 peak during the course of the catalytic reaction ([Cu] loading at 13 mol%).

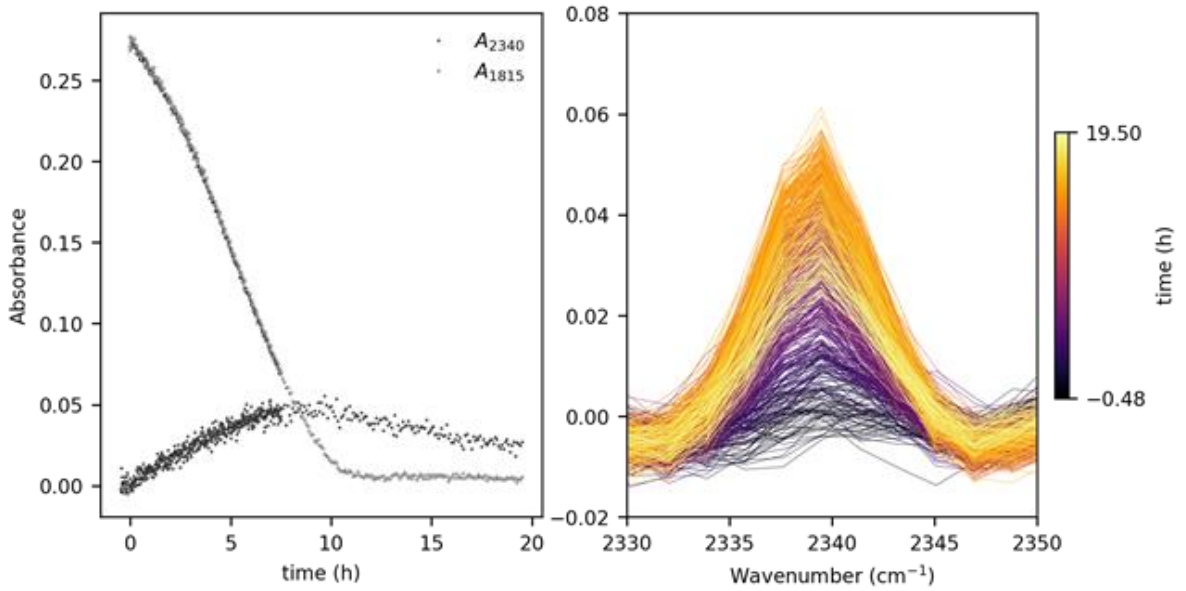

Figure 2.34: Appearance of a CO_2 peak during the course of the catalytic reaction ([Cu] loading at 10 mol%).

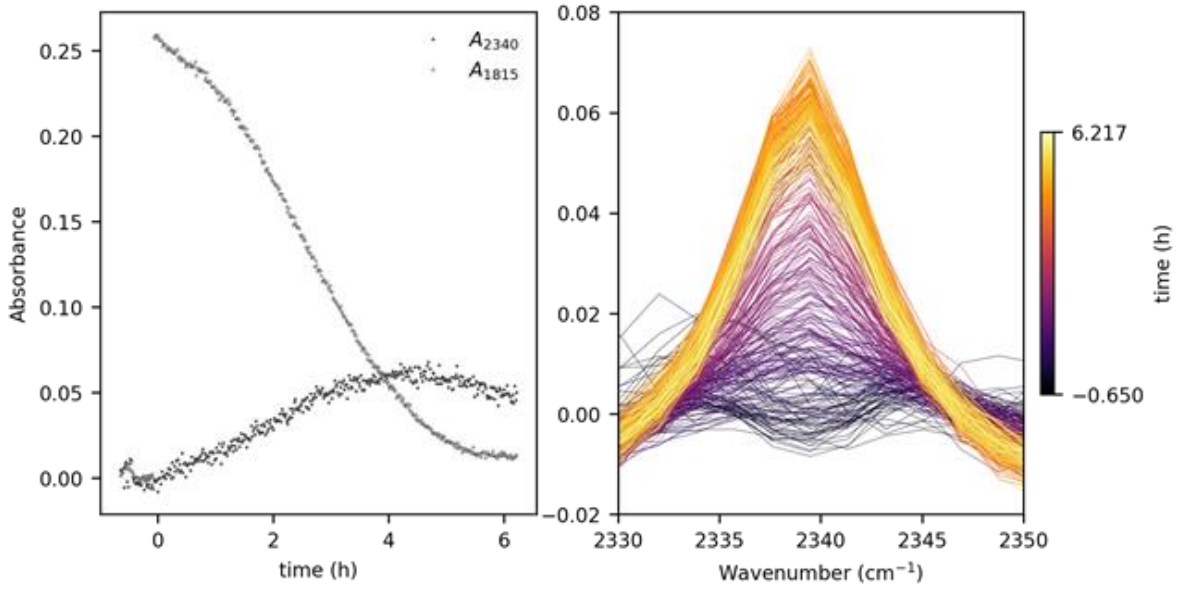

Figure 2.35: Appearance of a CO_2 peak during the course of the catalytic reaction ([Cu] loading at 7 mol%).

2.6.5 EPR studies: influence of reagents and catalysis monitoring

Stepwise addition

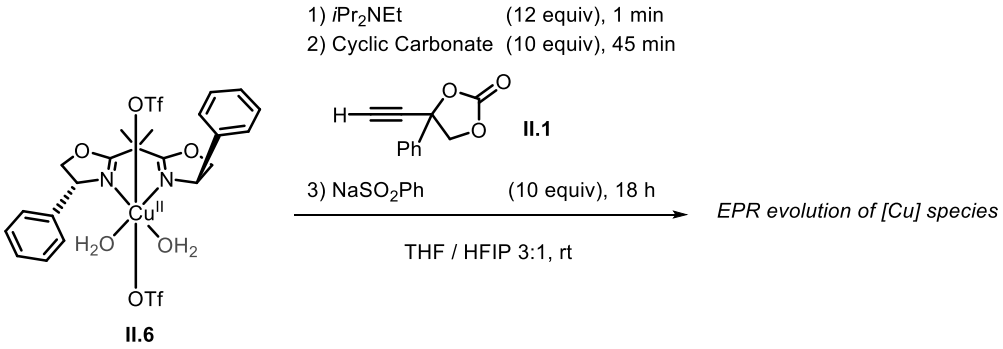

Figure 2.36: Reaction scheme for the evolution of complex **II.6** under catalytic conditions.

Preparation under air: This reaction sample was prepared following the original experimental order of addition: In a 2 mL vial equipped with a magnetic stirring bar, complex **II.6** (5.2 µmol, 3.8 mg) was dissolved in 0.4 mL of THF/HFIP (3:1 v/v). The solution was stirred for 1 min after which it was transferred to an EPR tube. After measuring the EPR signal of complex **II.6**, *i*Pr$_2$NEt (64 µmol, 11 µL, 12.0 equiv) was added to the solution and it was left for 1 min. At this point, the sample was measured again and in the second step, cyclic carbonate **II.1** (53 µmol,10.0 mg, 10.0 equiv) was added. The mixture was left for 45 min and it was measured again. In the last step, NaSO$_2$Ph (53 µmol, 8.7 mg, 10.0 equiv) was added to the mixture and after 18 h the EPR sample was re-measured.

Preparation under inert conditions: Following the same procedure as described above, the sample was prepared inside a glovebox, and every reagent was also added under an inert atmosphere.

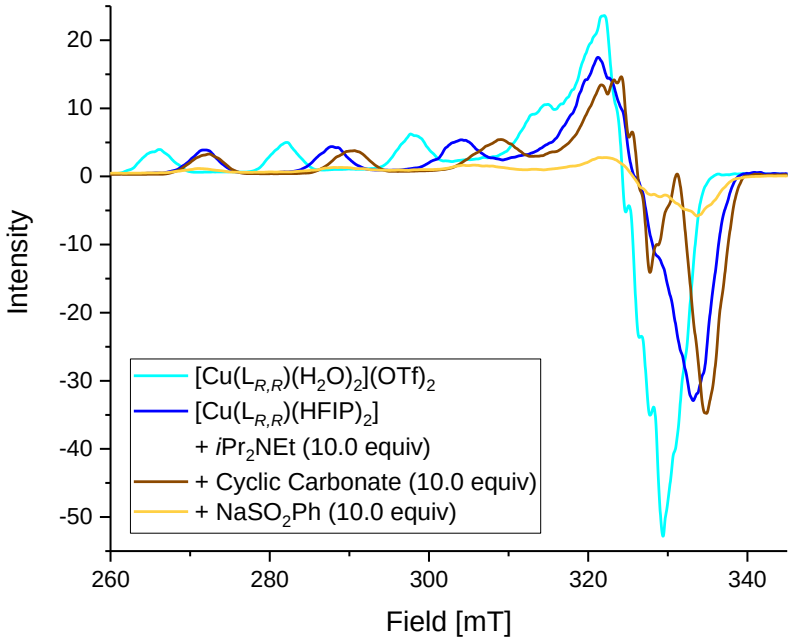

Figure 2.37: EPR spectra of complex **II.6** in 3:1 v/v THF/HFIP upon sequential addition of the catalytic components performed **under air** and measured at 77 K.

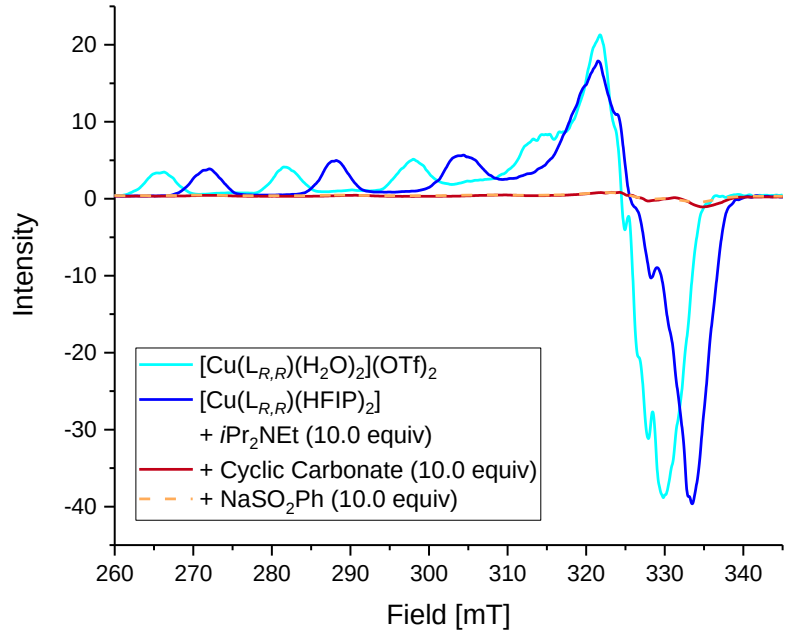

Figure 2.38: EPR spectra of complex **II.6** in 3:1 v/v THF/HFIP upon sequential addition of the catalytic components performed **under N_2** and measured at 77 K.

Catalysis monitoring

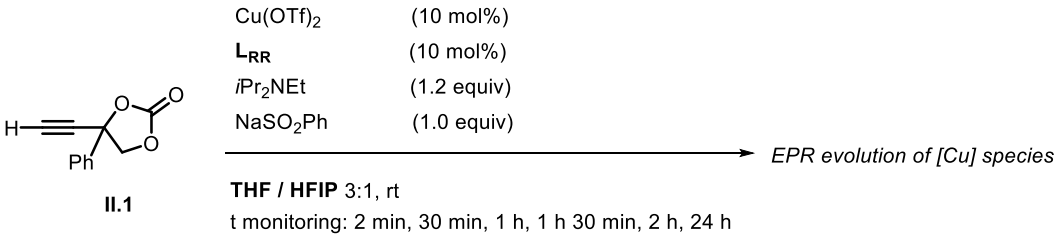

Figure 2.39: Reaction scheme for the EPR study of complex **II.6** under catalytic conditions.

Preparation: In a 2 mL vial equipped with a magnetic stirring bar, complex **II.6** (5.2 µmol, 3.8 mg) was dissolved in 0.4 mL of THF/HFIP (3:1). The solution was stirred for 1 min. Then, *i*Pr$_2$NEt (64 µmol, 11 µL, 12.0 equiv), NaSO$_2$Ph (53 µmol, 8.7 mg, 10.0 equiv) and cyclic carbonate **II.1** (47 µmol,10.0 mg, 10.0 equiv) were added to the vial. The reaction mixture was stirred for 2 min before it was transferred to an EPR tube and frozen for the measurement. Once the sample was measured, the EPR tube was kept stirring in a spinning wheel for 30 min before it was frozen again for the next measurement. The latter part of the procedure was repeated for a total of reaction time of 2 h, and the sample was then stirred for 24 h and measured one last time.

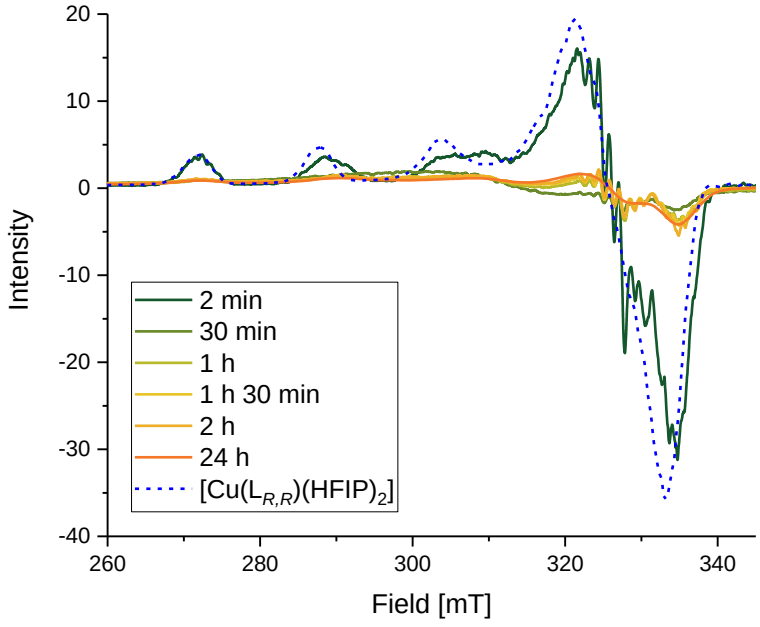

Figure 2.40: EPR spectra of a catalytic mixture in 3:1 v/v THF/HFIP monitored **under air** and measured at 77 K.

2.6.6 Synthetic procedure and characterization data of copper(I) complexes

Synthetic procedure for complex II.9

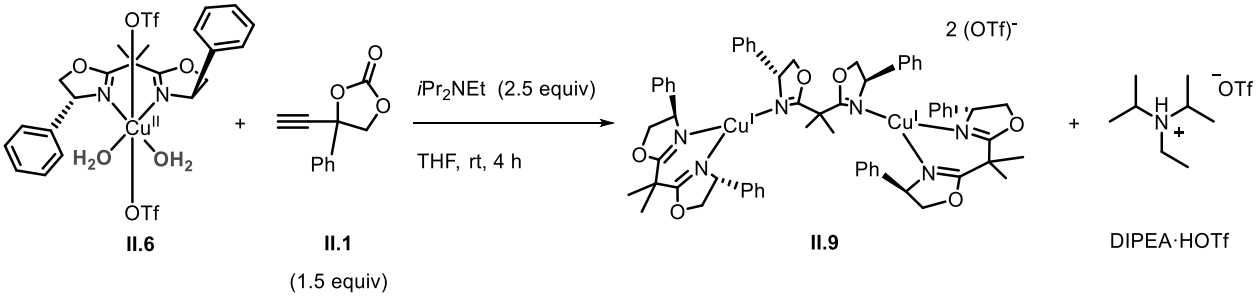

Figure 2.41: Reaction scheme for the synthesis of complex **II.9**.

Procedure: Inside a glovebox, complex **II.6** (0.054 mmol, 39.5 mg) was charged into an oven-dried Schlenk flask equipped with a magnetic stirring bar and it was dissolved in dry and degassed THF (4 mL). Then, *i*Pr$_2$NEt (0.135 mmol, 23. 5 µL, 2.5 equiv) was added with a Hamilton micro-syringe and the mixture was stirred for 5 minutes. Hereafter, cyclic carbonate **II.1** (0.081 mmol, 15.2 mg, 1.5 equiv) was added to the solution and the mixture was stirred for 4 h, accompanied by a visual color change from turquoise to pale brown. After the reaction had finished, THF was removed under vacuum and the product was extracted with benzene while a white precipitate formed. The benzene solution was filtered into an empty Schlenk flask and it was concentrated under reduced pressure to obtain a brown powder. Single crystals of yellow-colored complex **II.9** were obtained by slow diffusion of pentane into a THF solution of the product at −30 ºC. Yield 72% (18.4 mg).

^{1}H NMR (500 MHz, THF-d$_8$ at 193 K): 7.24-7.17 (m, 30H, -Ph-**H**), 5.66 (m, 6H, -C**H**-), 4.94 (t, 6H, $^3J_{H,H}$ = 9.6 Hz, -C**H**$_2$), 4.09 (t, 6H, $^3J_{H,H}$ = 7.7 Hz,-C**H**$_2$), 1.09 (s, 18H, -C**H**$_3$).

DEPTQ-135{^{1}H} NMR (126 MHz, THF-d$_8$ at 193 K): 171.48 (-**C**$_q$=N-), 142.80 (-Ph-**C**$_q$), 129.26 (-Ph-**C**$_m$), 128.38 (-Ph-**C**$_p$), 127.08 (-Ph-**C**$_o$), 76.78 (-**C**H$_2$), 69.91 (-**C**H-), 40.84 (-**C**$_q$-(CH$_3$)$_2$), 26.28 (-**C**H$_3$).

^{19}F NMR (376 MHz, THF-d$_8$ at 193 K): -81.09 (OTf).

ESI(+)-HRMS cryospray (DCM) (DCM): *m/z*. Found (Calc.): 397.0967 (397.0977) $C_{21}H_{22}CuN_4O_2^+$, [Cu + **L**$_{RR}$]$^+$. Found (Calc.): 731.2628 (731.2659) $C_{42}H_{44}CuN_4O_4^+$, [Cu + 2 **L**$_{RR}$]$^+$.

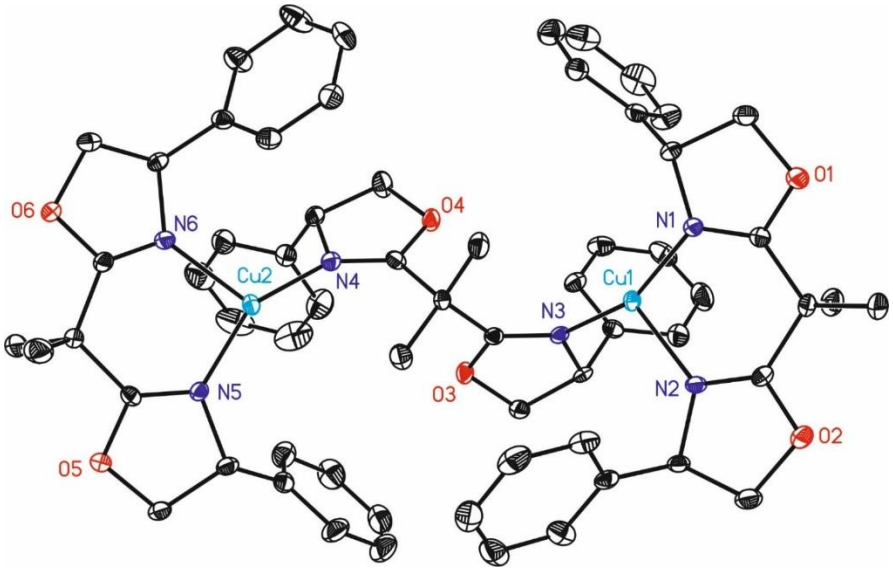

Figure 2.42: ORTEP representation of **II.9** with 50% probability ellipsoids (H-atoms and the two OTf anions are omitted for clarity).

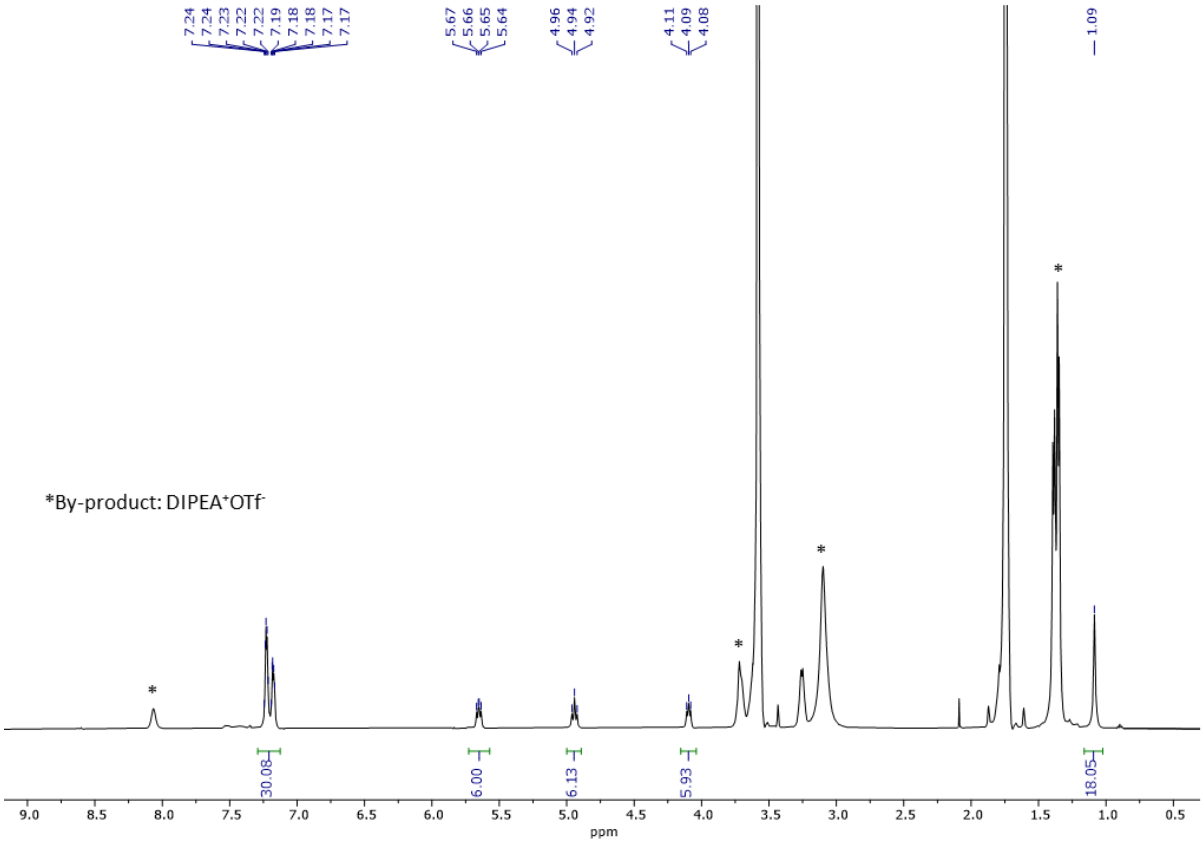

Figure 2.43: ^{1}H NMR (500 MHz) spectrum of **II.9** in THF-d_8 at 193 K. The asterisks denote the byproduct DIPEA·HOTf.

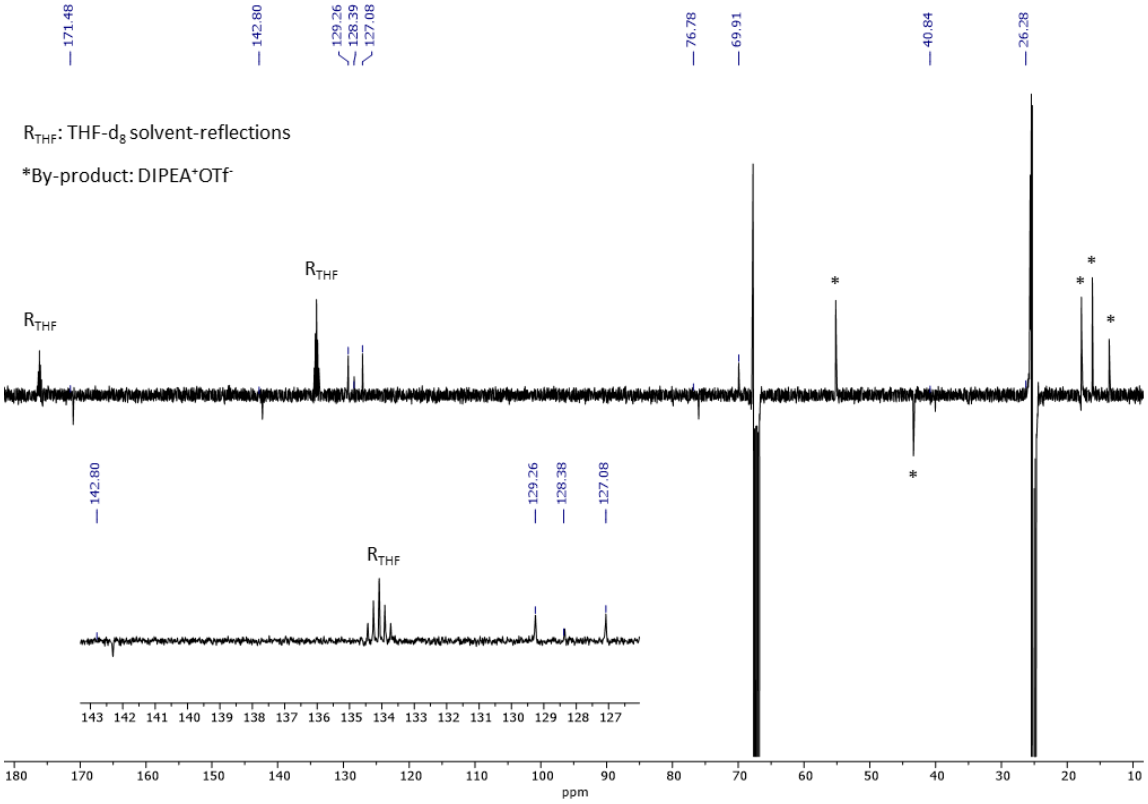

Figure 2.44: DEPTQ-135{^{1}H} NMR (126 MHz) spectra of **II.9** in THF-d_8 at 193 K.

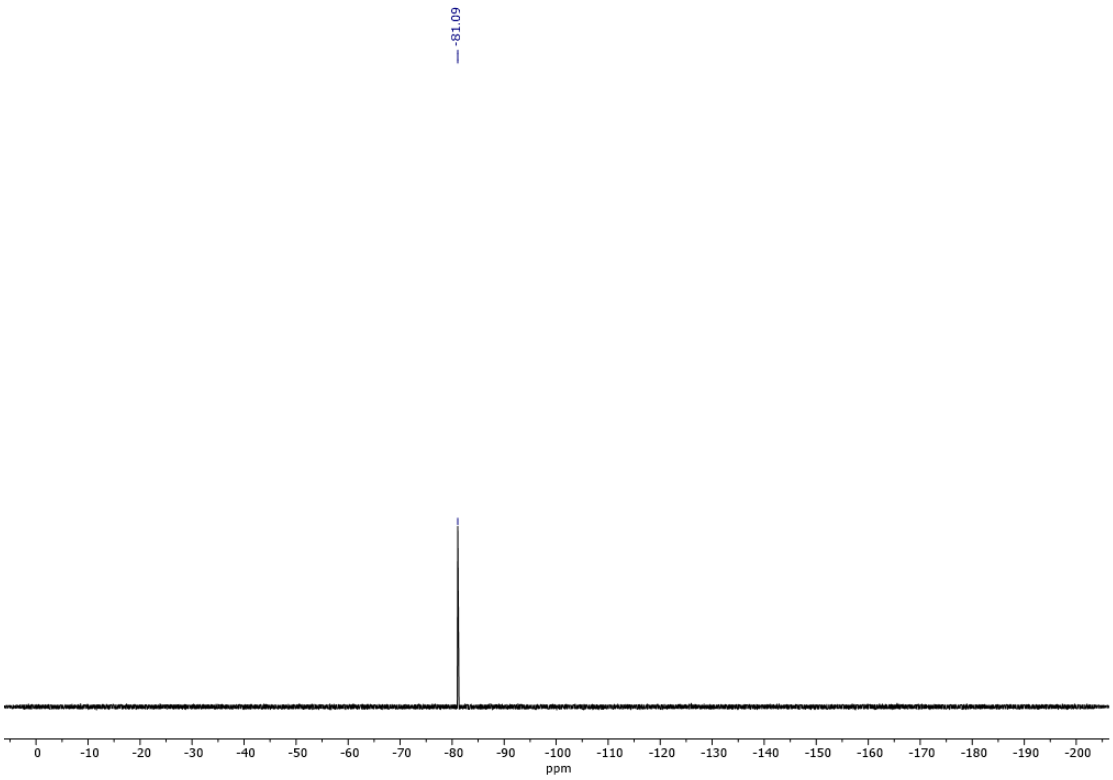

Figure 2.45: ^{19}F NMR (376 MHz) spectrum of **II.9** in THF-d_8 at 193 K.

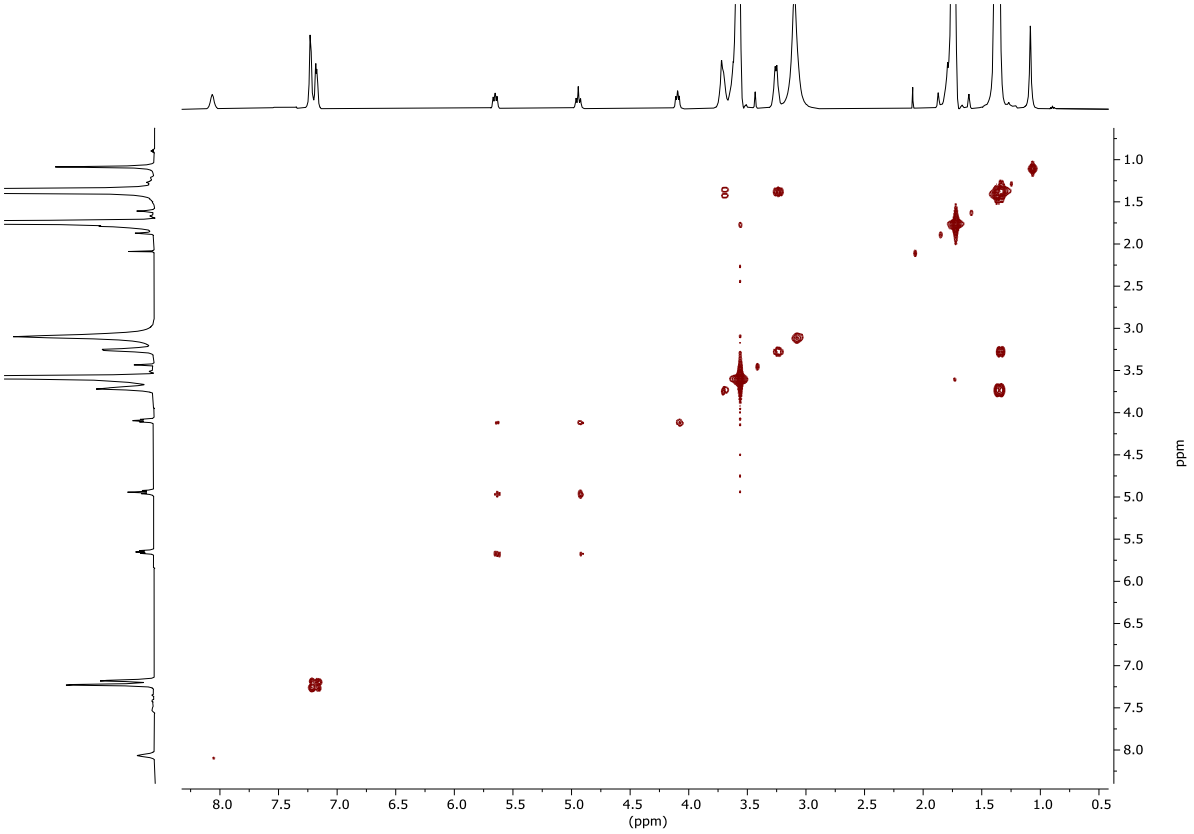

Figure 2.46: COSY NMR spectrum of **II.9** in THF-d_8 at 193 K.

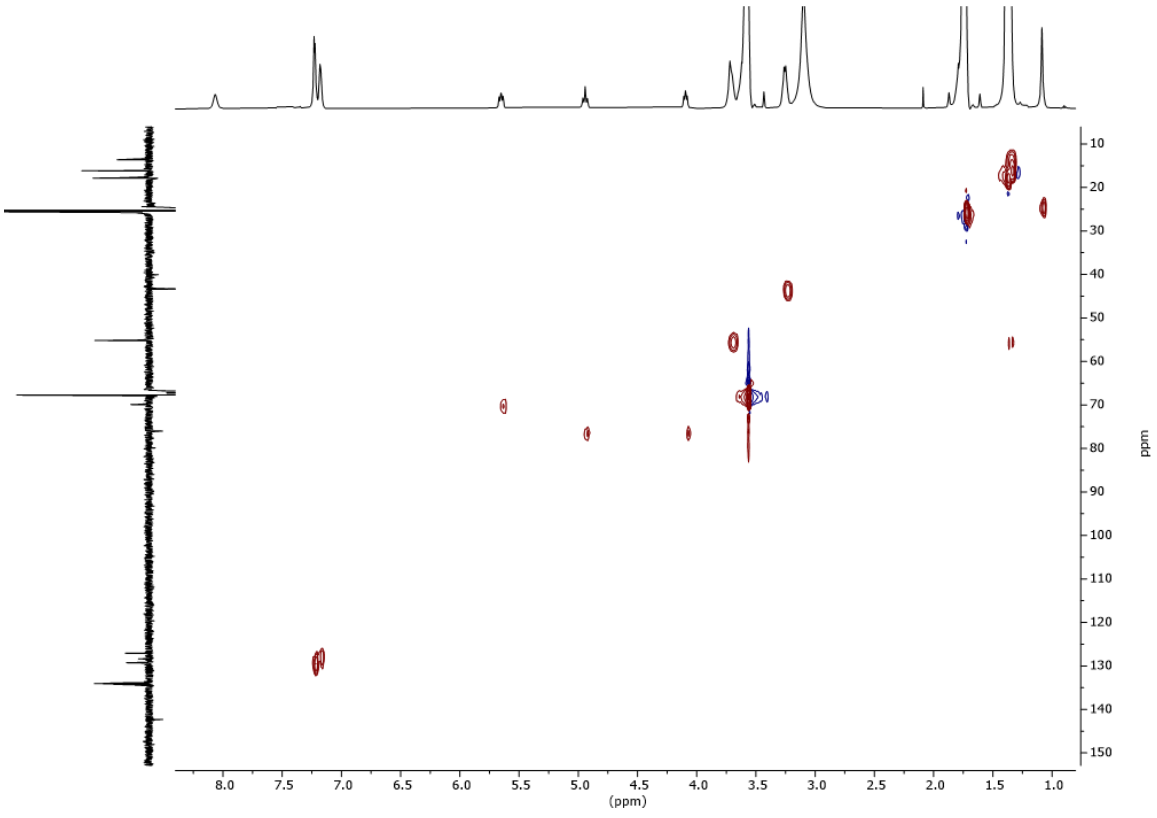

Figure 2.47: HSQC NMR spectrum of **II.9** in THF-d_8 at 193 K.

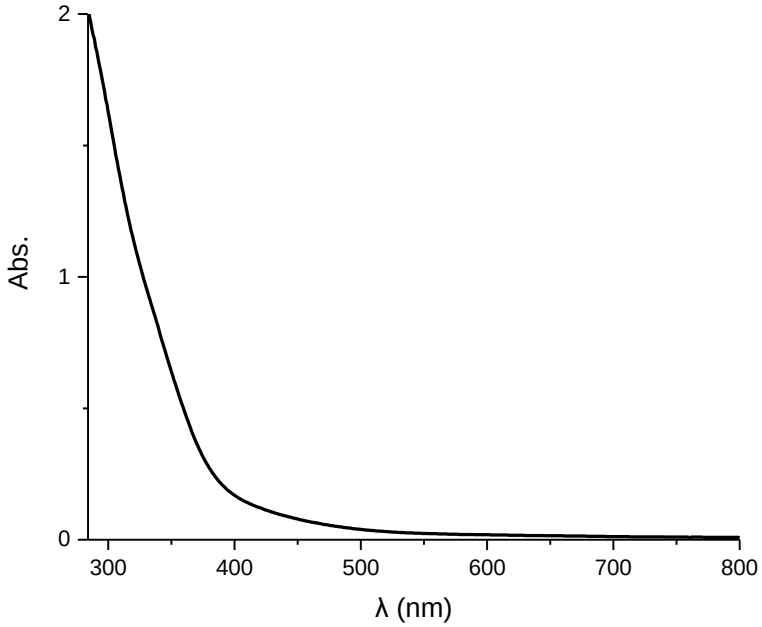

Figure 2.48: UV-Vis spectrum of **II.9** in THF/HFIP at 298 K.

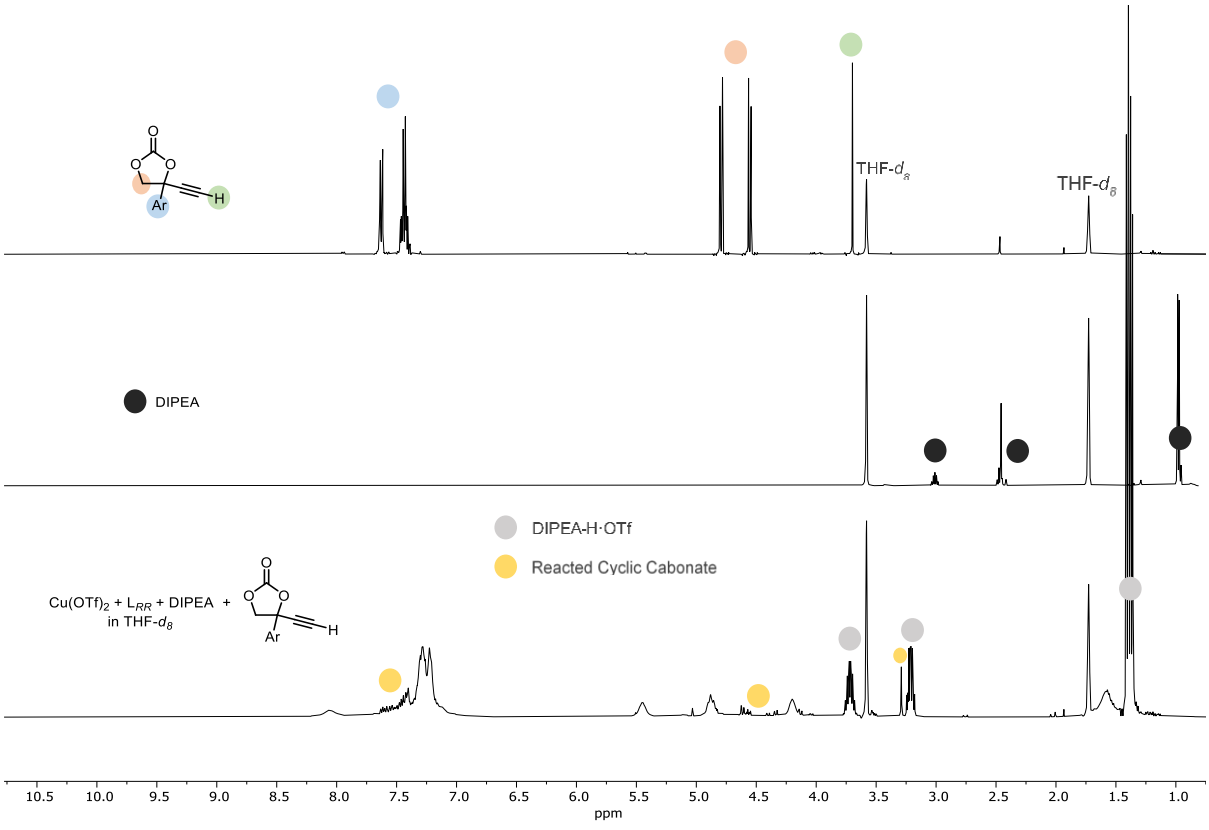

Figure 2.49: ^{1}H NMR (500 MHz) stacked spectra of **II.1** (top), DIPEA (middle) and reaction mixture (bottom) in THF-d$_8$ at 298 K.

Synthetic procedure for complex II.11:

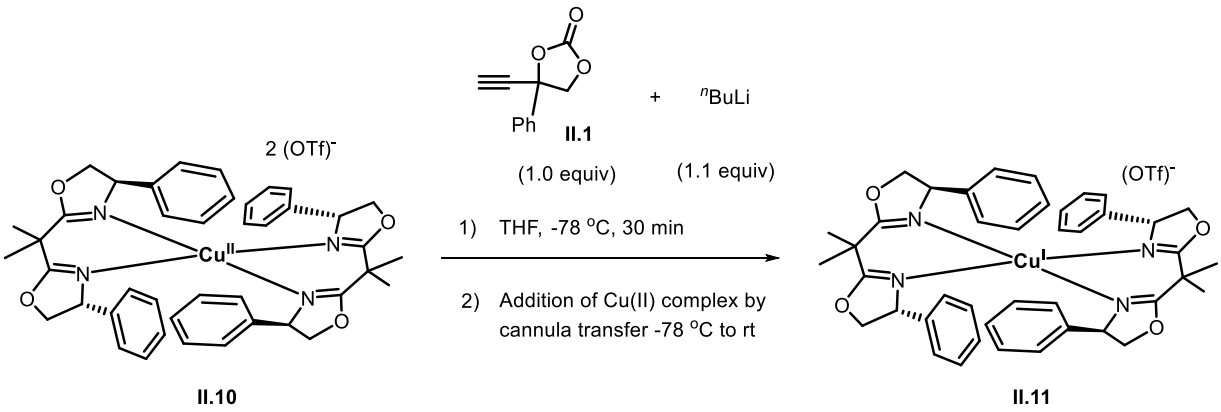

Figure 2.50: Reaction scheme for the synthesis of complex **II.11**.

Inside a glovebox, cyclic carbonate **II.1** (0.10 mmol, 18.9 mg) was dissolved inside an oven-dried Schlenk flask in THF (4 mL). In another Schlenk, complex **II.10** (0.10 mmol, 73 mg, 1.0 equiv) was charged and dissolved in THF (8 mL). Both Schlenk flasks were taken out of the glovebox and the solutions cooled down using two cool baths set at −78 °C. Then *n*BuLi (0.11 mmol, 4 mL, 1.1 equiv) was added to the solution containing **II.1** and the mixture was left stirring for 30 min. Then, the solution containing complex **II.10** was transferred through a cannula to the cyclic carbonate solution in a dropwise fashion while stirring. A visual color change from green to brown was observed during the course of the reaction from −78 °C to room temperature. The solvent was removed *in vacuo* and the content of the Schlenk vessel was transferred back inside the glovebox. The crude was washed with dry benzene and complex **II.11** was re-dissolved in THF. After filtration through Celite, slow vapor diffusion crystallization was performed using pentane at −30 °C. Single crystals of pale-brown **II.11** were obtained. Yield: 43% (31.5 mg).

^{1}H NMR (500 MHz, THF-d_8 at 298 K): 7.34-7.28 (m, 20H, -Ph-**H**), 5.45 (m, 4H, -C**H**-), 4.91 (t, 4H, $^{3}J_{H,H}$ = 9.7 Hz, -C**H**$_2$), 4.25 (t, 4H, $^{3}J_{H,H}$ = 7.6 Hz,-C**H**$_2$), 1.62 (s, 16H, -C**H**$_3$).

^{13}C {^{1}H} NMR (126 MHz, THF-d_8 at 298 K): 173.01 (-**C**$_q$=N-), 141.27 (-Ph-**C**$_q$), 129.47 (-Ph-**C**$_m$), 128.75 (-Ph-**C**$_p$), 127.97 (-Ph-**C**$_o$), 76.21 (-**C**H$_2$), 70.54 (-**C**H-), 40.39 (-**C**$_q$-(CH$_3$)$_2$), 25.62 (-**C**H$_3$).

^{19}F NMR (376 MHz, THF-d_8 at 298 K): -80.82 (OTf).

ESI(+)-HRMS cryospray (DCM): *m/z* Found (Calc.): 731.2620 (731.2659) $C_{42}H_{44}CuN_4O_4^+$, [Cu + 2 **L*RR***]$^+$

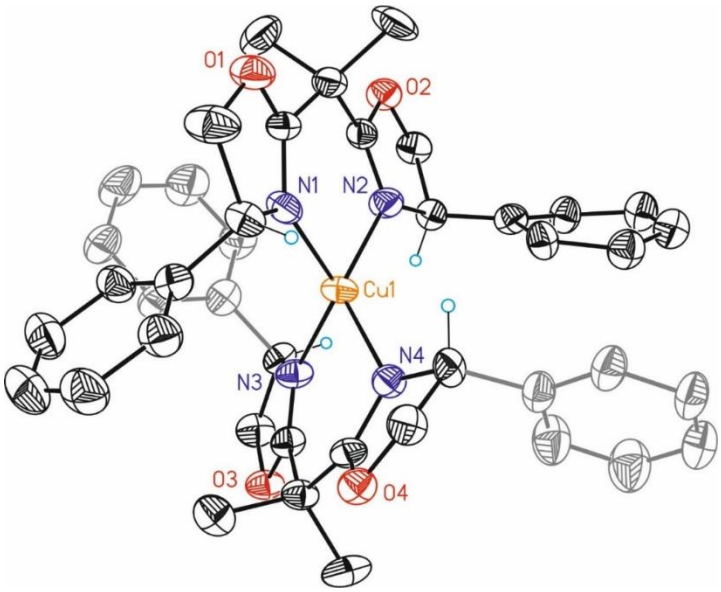

Figure 2.51: ORTEP representation of **II.11** with 50% probability ellipsoids (H-atoms are omitted for clarity).

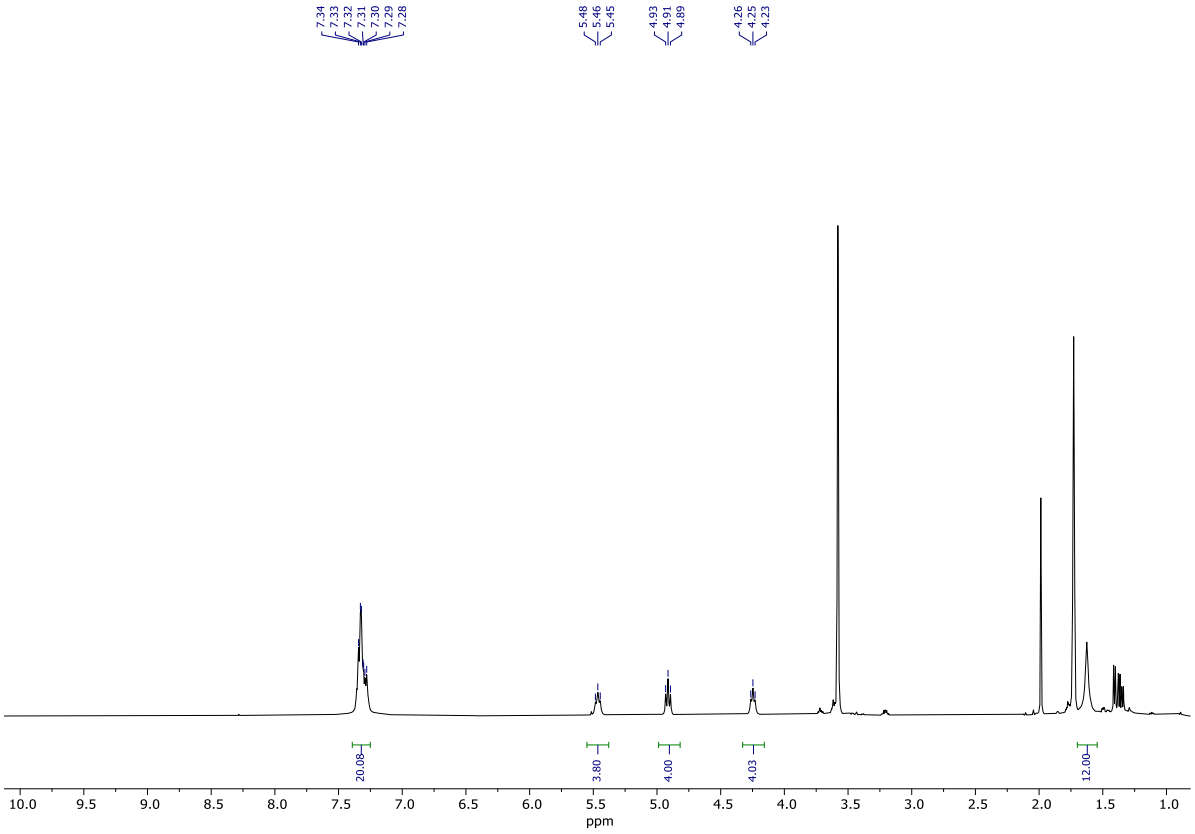

Figure 2.52: ^{1}H NMR (500 MHz) spectrum of **II.11** in THF-d_8 at 298 K.

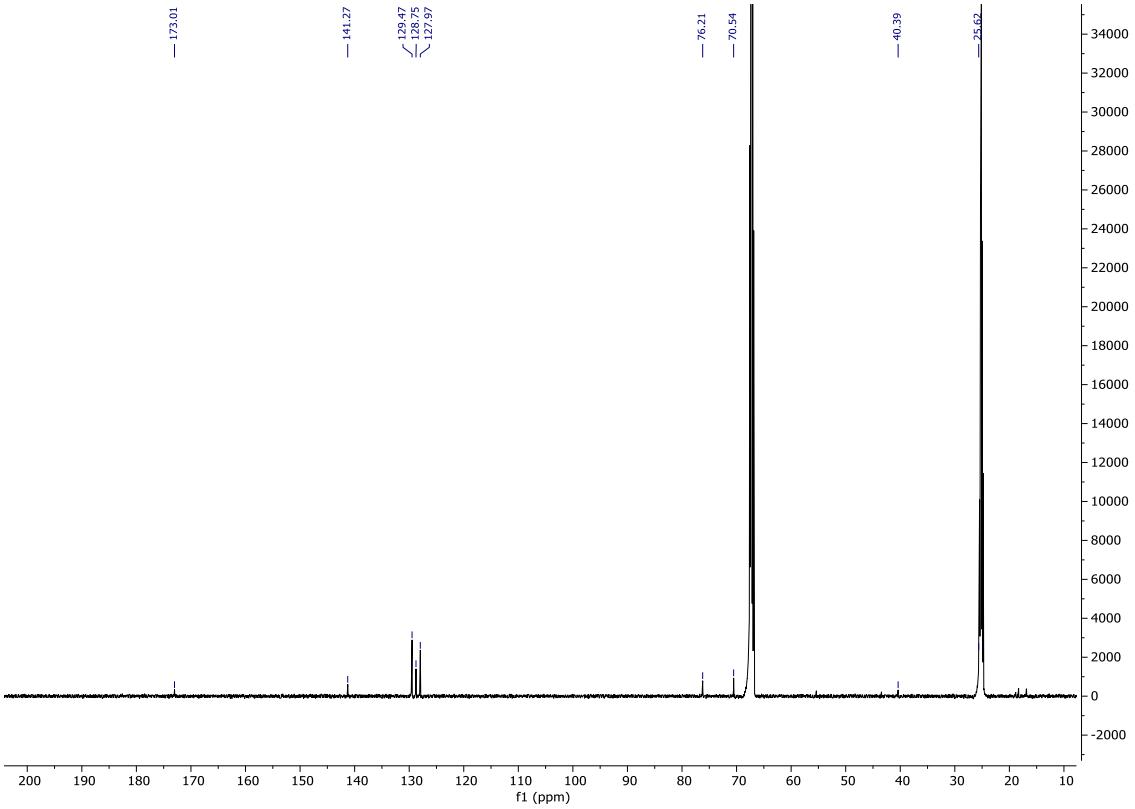

Figure 2.53: ^{13}C NMR (126 MHz) spectrum of **II.11** in THF-d_8 at 298 K.

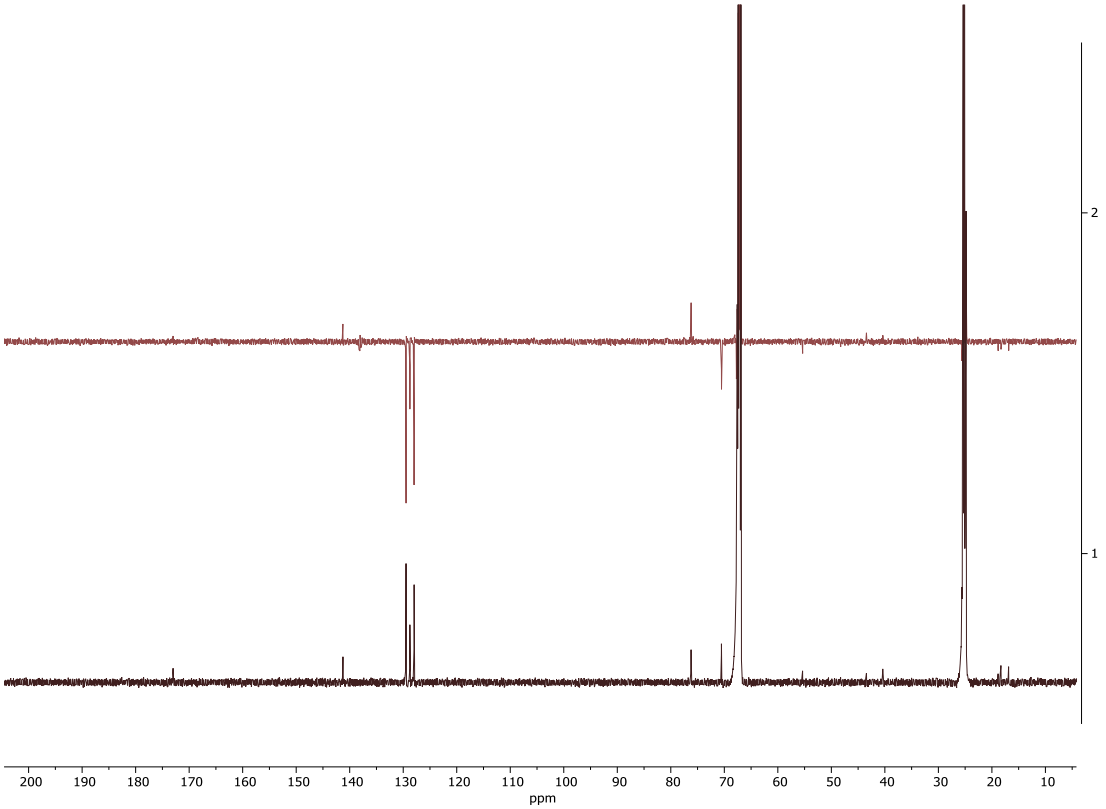

Figure 2.54: ^{13}C NMR (126 MHz) and DEPTQ-135{^{1}H} NMR (126 MHz) spectral comparison for **II.11** in THF-d_8 at 298 K.

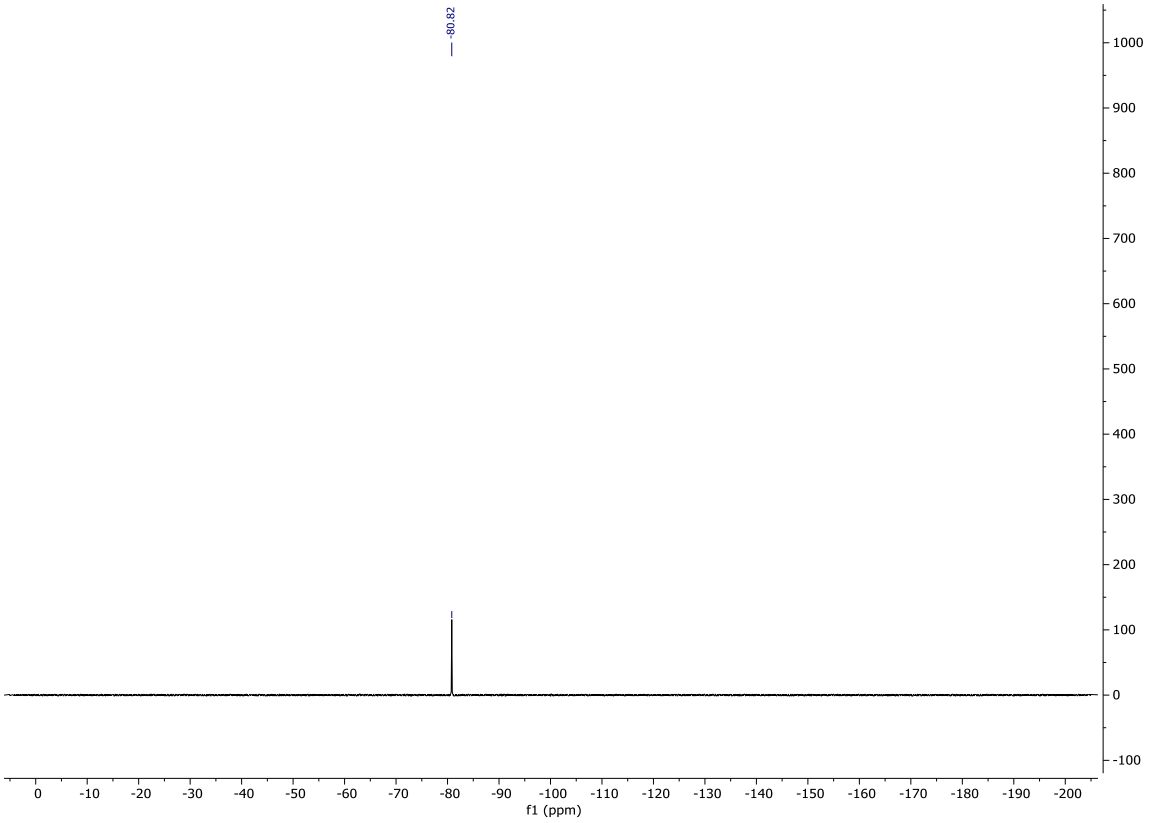

Figure 2.55: ^{19}F NMR (376 MHz) spectrum of **II.11** in THF-d_8 at 298 K.

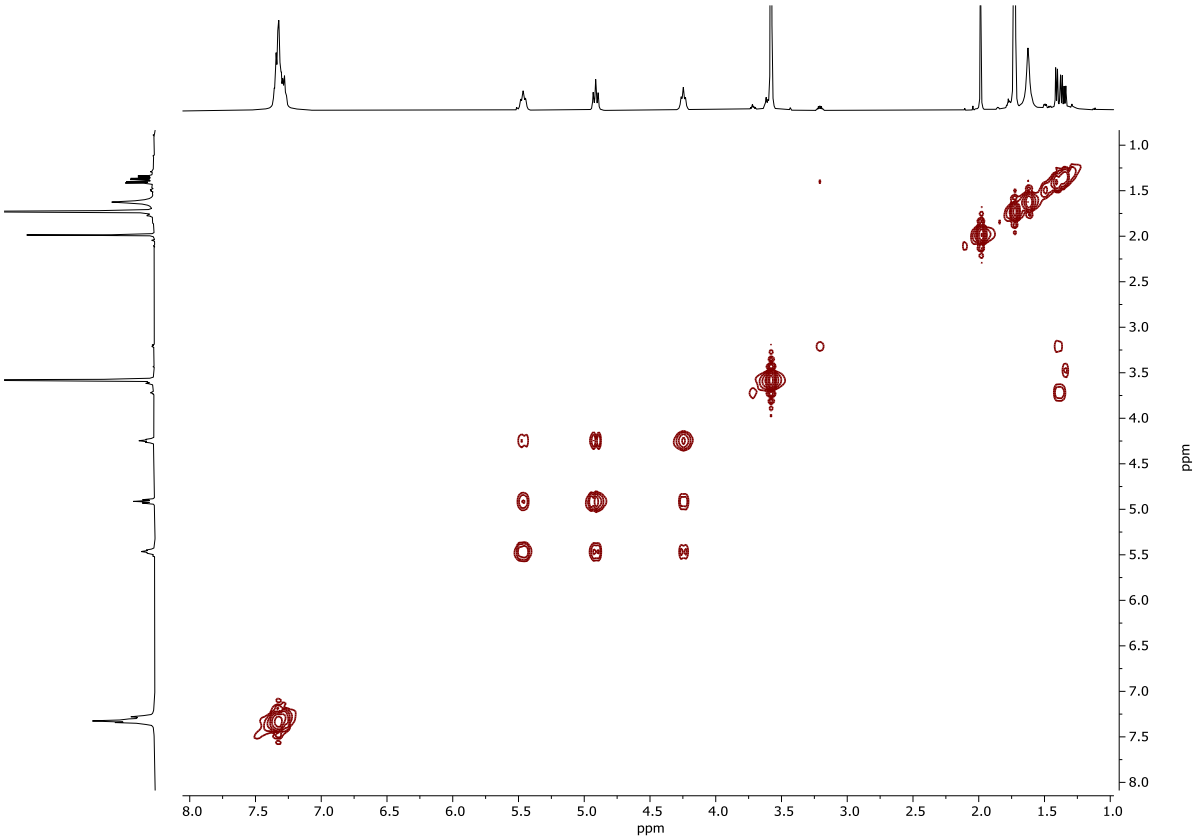

Figure 2.56: COSY NMR spectrum of **II.11** in THF-d_8 at 298 K.

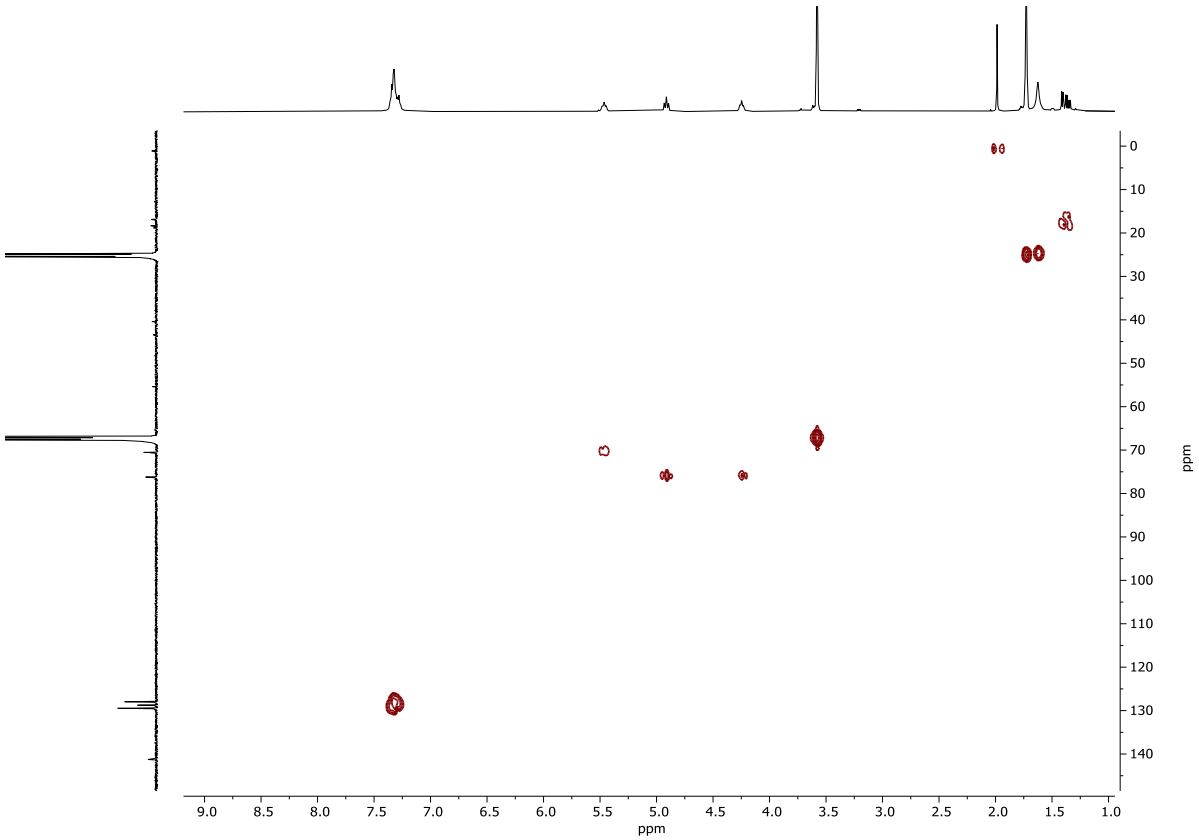

Figure 2.57: HMQC NMR spectrum of **II.11** in THF-d_8 at 298 K.

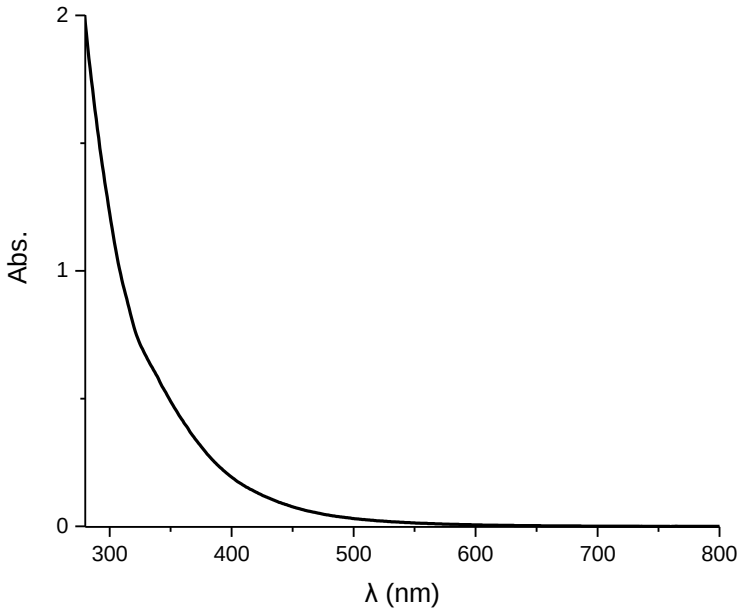

Figure 2.58: UV-Vis spectrum of **II.11** in THF/HFIP at 298 K.

2.6.7 UV-Vis study on the effect of HFIP to copper(I) complexes in presence of base

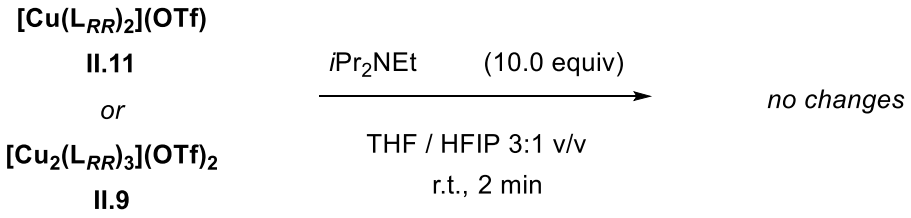

Figure 2.59: Effect of *i*Pr$_2$NEt addition to Cu^{I} complexes **II.9** and **II.11** in the presence of HFIP.

Procedure: Inside a glovebox, complex **II.11** (3 µmol, 2.6 mg, 1.0 equiv) was dissolved in 1 mL of THF/HFIP (3:1 v/v) in a 2 mL vial. The solution was transferred to a quartz cuvette (*l* = 1 cm) and solvent (THF/HFIP) added until a final volume of 3.0 mL. The cuvette was closed with a septum and it was taken outside the glovebox. Then, *i*Pr$_2$NEt (4.7 µmol, 0.8 µL, 1.0 equiv) was added to the solution with a Hamilton syringe. After 2 minutes, the sample was measured again. The amount of complex **II.9** used was 3 µmol (4.3 mg, 1.0 equiv).

As can be noted in **Figures 2.7a** and **2.7b (Results section 2.3.2)**, the addition of *i*Pr$_2$NEt to Cu(I) in the presence of HFIP does not seem to affect the integrity/structure of these complexes. We conclude here that HFIP does not coordinate to the metal center under these conditions.

2.6.8 Catalytic experiments with copper(I) complexes tested as precatalysts

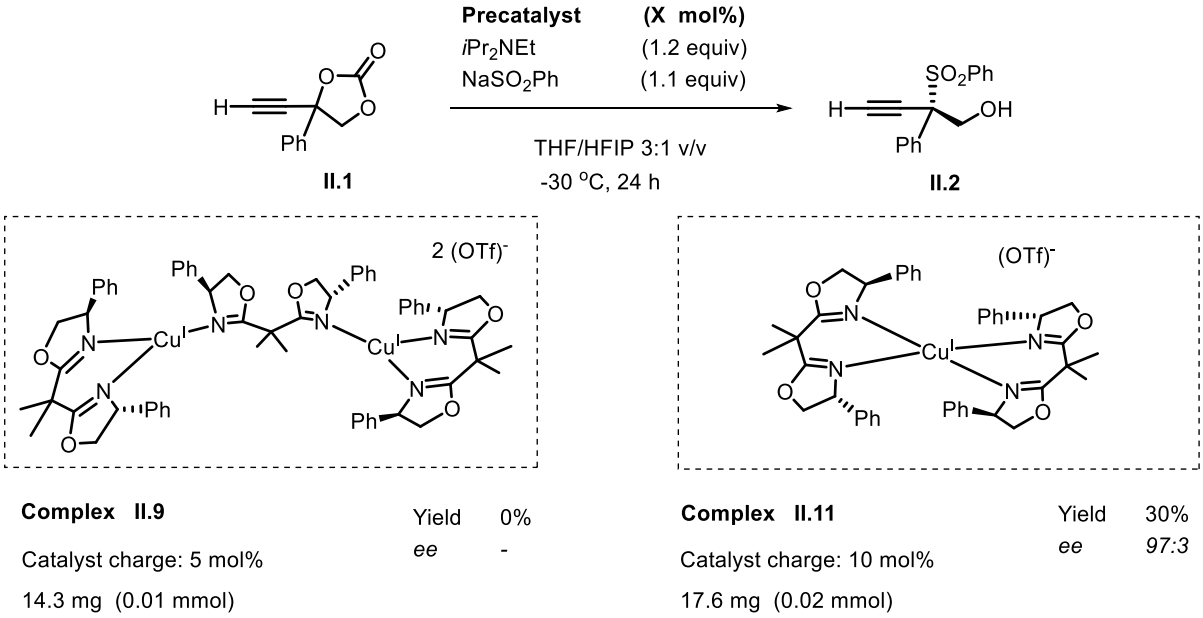

Figure 2.60: Cu(I) complexes as potential pre-catalysts for the transformation of cyclic carbonate **II.1** into chiral propargylic sulfone **II.2**.

Procedure: Inside a glovebox, a vial was charged with precatalyst **II.9** or **II.11** and it was dissolved in 0.6 mL of THF/HFIP (3:1 v/v). The other reagents were added in the following order: *i*Pr$_2$NEt (41.8 µL, 0.24 mmol, 1.2 equiv), NaSO$_2$Ph (36.0 mg, 0.22 mmol, 1.1 equiv) and cyclic carbonate **II.1** (37.6 mg, 0.20 mmol, 1.0 equiv). The mixture was stirred at –30 °C. After 24 h, the catalytic mixture was quenched with NH$_4$Cl, extracted with EtOAc and dried over anhydrous Na$_2$SO$_4$. The yield was calculated by ^{1}H NMR using mesitylene as internal standard. The *ee* of the product was analyzed by UPC2.

2.6.9 Synthesis of dimeric copper(II) complexes for the study of non-linear effects

Synthetic procedure for complex II.10:

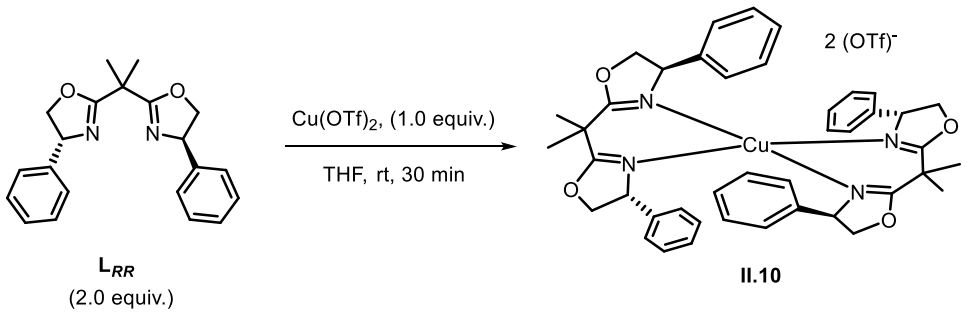

Figure 2.61: Reaction scheme for the formation of complex **II.10**.

Procedure: Inside a glovebox, $\mathbf{L}_{RR}$ (0.30 mmol, 100 mg, 2.0 equiv) and $Cu(OTf)_2$ (0.15 mmol, 61.5 mg) were charged into an oven-dried Schlenk flask equipped with a magnetic stirring bar. Dry and degassed THF (15 mL) was added and the mixture was stirred for 30 min at room temperature outside the glovebox. At this point, the solution was filtered through a cannula under argon into another Schlenk flask and the solution was concentrated *in vacuo* to obtain a green colored, viscous oil. The Schlenk flask was transferred back inside the glovebox and the oil was dissolved in THF, and the product crystallized by slow vapor diffusion of pentane into the THF layer. Single crystals of complex **II.10** were obtained with a 72% yield (111 mg).

EPR in THF [13 mM]: $A_{||}$ = 397.74 MHz, $g_{||}$ = 2.33

ESI(+)-HRMS (DCM): *m/z* found (calc.): 731.2689 (731.2659) $C_{42}H_{44}CuN_4O_4^+$, [Cu + 2 $\mathbf{L}_{RR}$]$^+$

UV-Vis (THF) [13.7 µM]: (λ in nm, Abs): (664, 0.125)

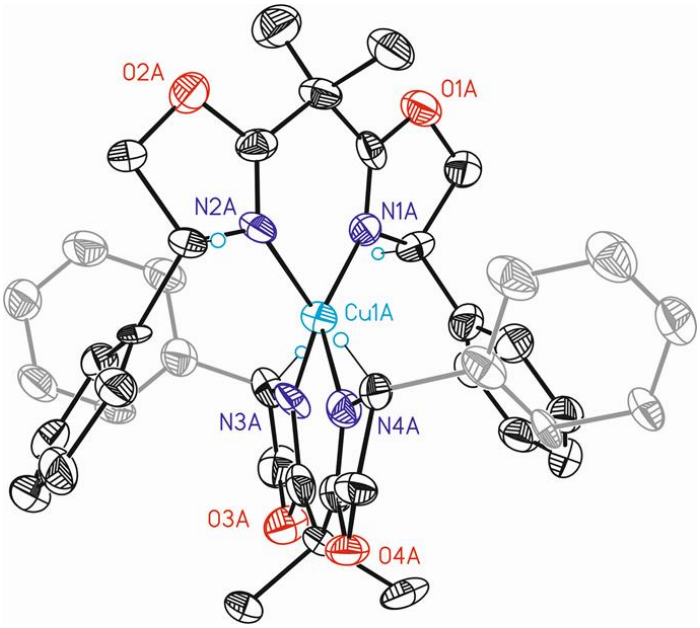

Figure 2.62: ORTEP representation of **II.10** with 50 % probability ellipsoids (H-atoms and counter-anions are omitted for clarity).

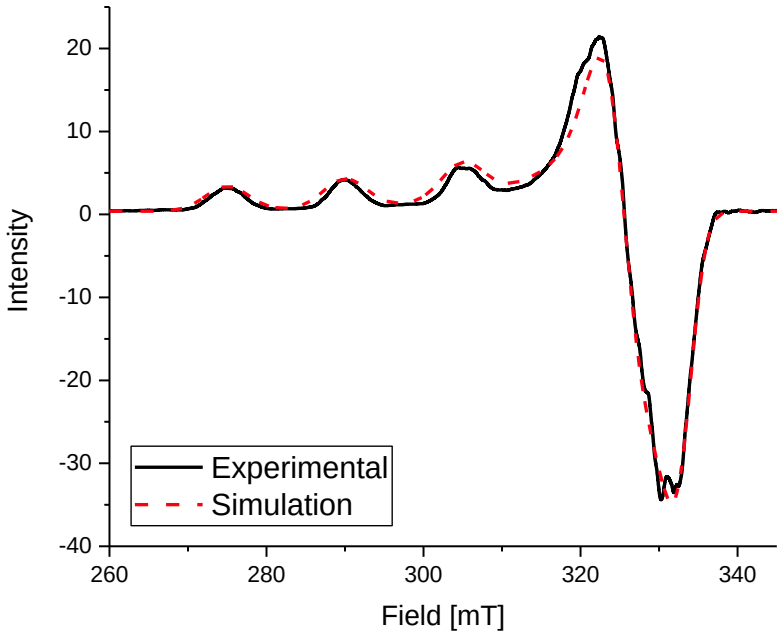

Figure 2.63: Experimental and simulated EPR spectrum of **II.10** in THF at 77 K.

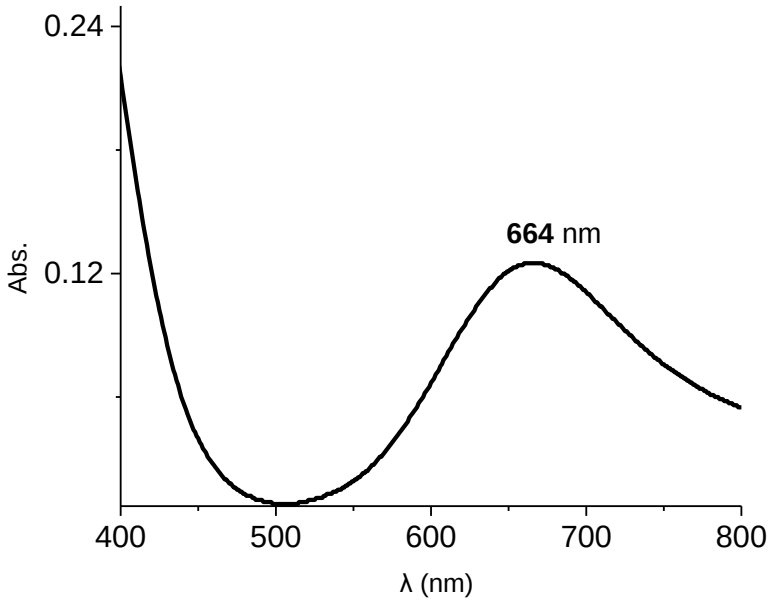

Figure 2.64: UV-Vis spectrum of **II.10** in THF at 298 K.

Synthetic procedure for complex Cu(L_{RR})(L_{SS})$(OTf)_2$

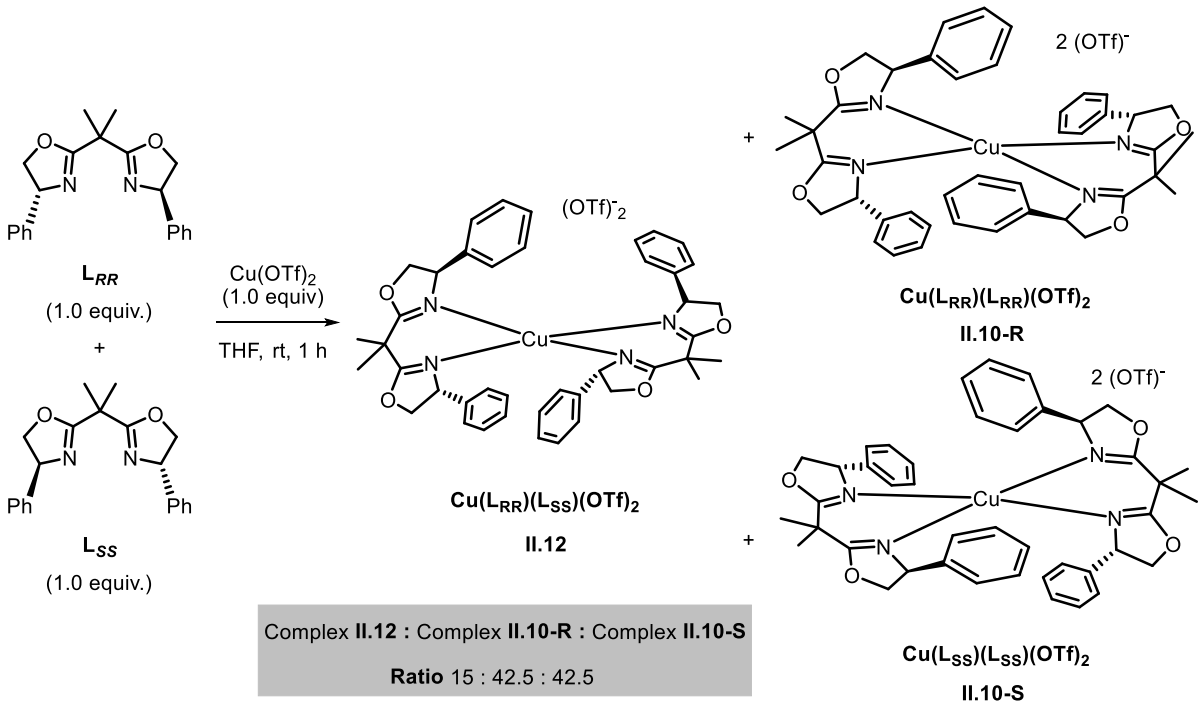

Figure 2.65: Reaction scheme for the preparation of a mixture of complexes **II.10-R, II.10-S** and **II.12**.

Procedure: Inside a glovebox, **L*RR*** (0.15 mmol, 50.1 mg, 1.0 equiv), **L*ss*** (0.15 mmol, 50.1 mg, 1.0 equiv) and $Cu(OTf)_2$ (0.15 mmol, 61.5 mg) were charged into an oven-dried Schlenk flask equipped with a magnetic stirring bar. Dry and degassed THF (15 mL) was added and the mixture was left stirring for 1 h at room temperature outside de glovebox. At this point, the solution was filtered through a cannula under argon into another Schlenk flask and the solution was concentrated *in vacuo* to obtain a green-colored, viscous oil. This Schlenk flask was transferred back inside the glovebox and the oil was dissolved in THF and the product crystallized by slow vapor diffusion of pentane into the product solution. Single crystals of a mixture of complexes **II.12** (15%), **II.10-R** (42.5%) and **II.10-S** (42.5%) were obtained in a 64% yield (99.0 mg).

EPR in THF [13 mM]: $A_{||}$ = 378.40 MHz, $g_{||}$ = 2.35

ESI(+)-HRMS (DCM): *m/z* found (calc.): 731.2679 (731.2659) $C_{42}H_{44}CuN_4O_4^+$, [Cu + 2 **L*RR***]$^+$

UV-Vis (THF) [13.7 µM]: (*λ* in nm, Abs): (687, 0.106)

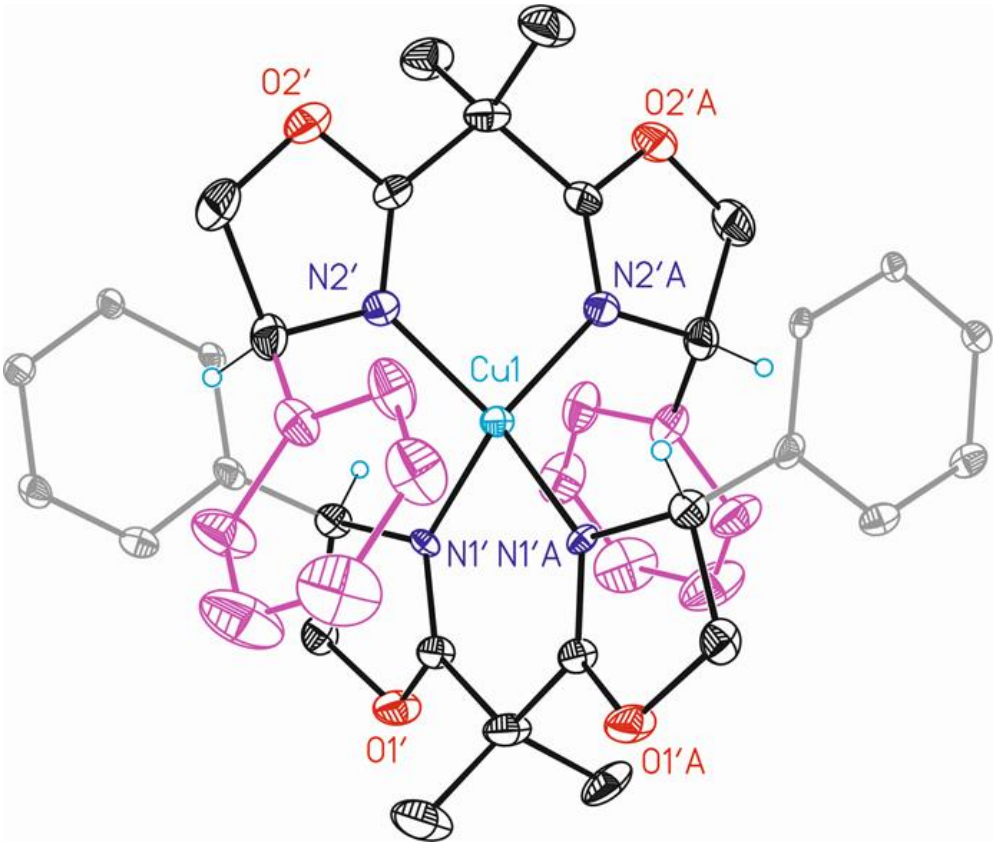

Figure 2.66: ORTEP representation of **II.12** with 50 % probability ellipsoids (H-atoms and anions are omitted for clarity).

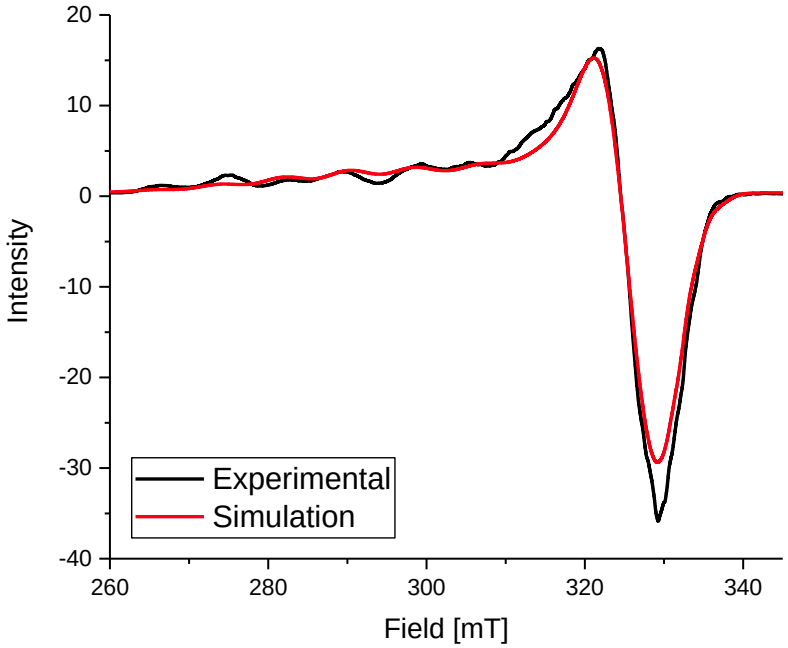

Figure 2.67: Experimental and simulated EPR spectrum of a mixture of complexes **II.12**, **II.10-R** and **II.10-S** in THF at 77 K.

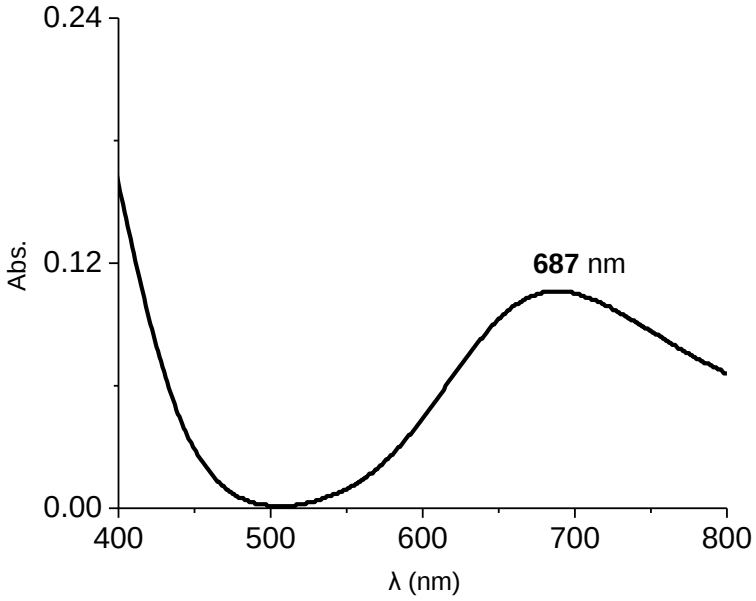

Figure 2.68: UV-Vis spectrum of a mixture of complexes **II.12**, **II.10-R** and **II.10-S** in THF at 298 K.

2.6.10 EPR study on the effect of HFIP to dimeric copper(II) complexes in the presence of base

Cu(**L*RR***)$_2$(OTf)$_2$

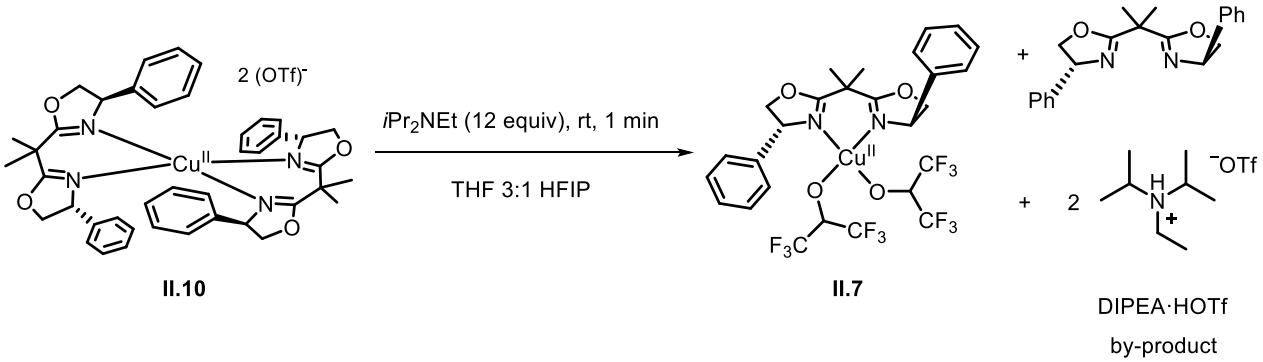

Figure 2.69: Reaction scheme of the conversion of **II.10** into **II.7** by addition of *i*Pr$_2$NEt.

Procedure: In a 2 mL vial, Cu(OTf)$_2$ (5.2 µmol, 1.9 mg, 1.0 equiv) and ligand **L*RR*** (5.1 µmol, 1.7 mg, 2.0 equiv) were dissolved in 0.4 mL of THF/HFIP (3:1 v/v). The solution was stirred for 10 min and then transferred to an EPR tube, and the sample was measured identifying complex **II.10**. Then, *i*Pr$_2$NEt (10.8 µL, 62.4 µmol, 12.0 equiv) was added to the mixture with a Hamilton syringe. After 1 min of reaction, the sample was re-measured by EPR. Note: the addition of base to complex **II.10** in the presence of HFIP leads to the formation of complex **II.7**.

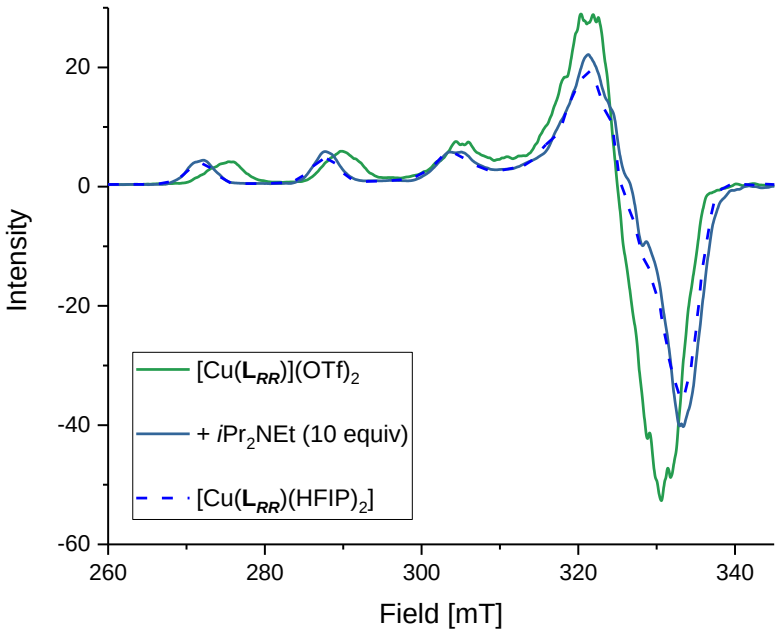

Figure 2.70: EPR spectra related to the transformation of complex **II.10** into complex **II.7** in the presence of base.

<u>Cu(**L*RR***)$_2$(OTf)$_2$, Cu(**L*ss***)$_2$(OTf)$_2$ and Cu(**L*RR***)(**L*ss***)(OTf)$_2$ mixture</u>

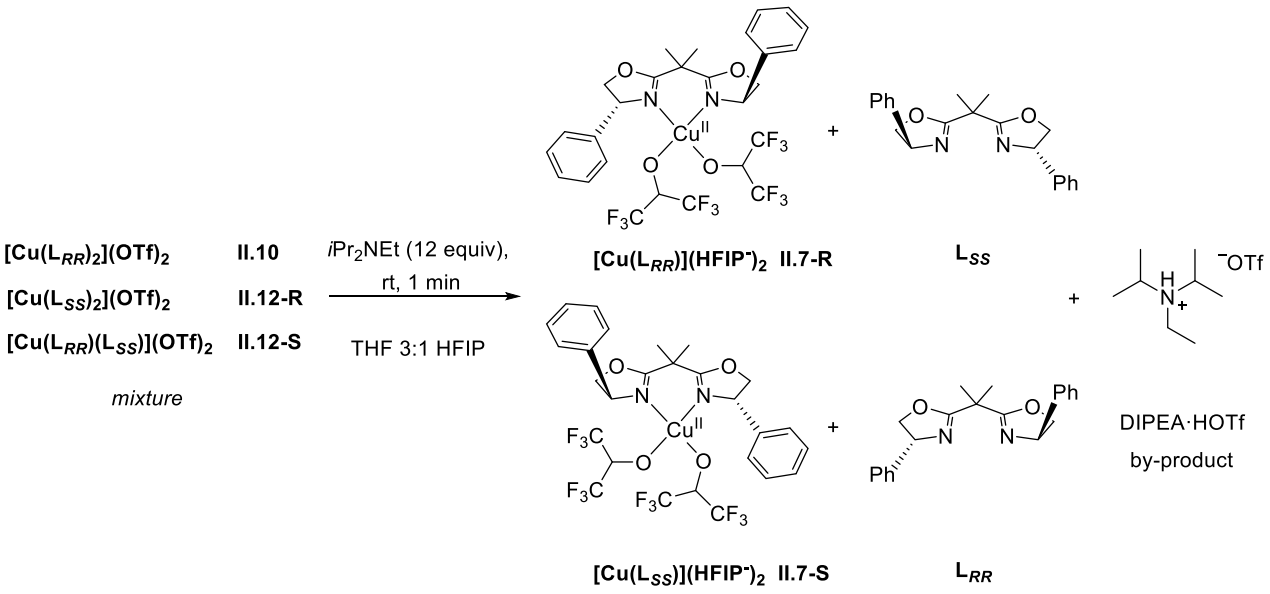

Figure 2.71: Reaction scheme for the transformation of a mixture of Cu(II) complexes into a racemic mixture of **II.12-R** and **II.12-S** by addition of *i*Pr$_2$NEt.

Procedure: In a 2 mL vial, $Cu(OTf)_2$ (5.2 µmol, 1.9 mg, 1.0 equiv), ligand $\mathbf{L}_{RR}$ (2.6 µmol, 0.9 mg, 1.0 equiv) and ligand $\mathbf{L}_{SS}$ (2.6 µmol, 0.9 mg, 1.0 equiv) were dissolved in 0.4 mL of THF/HFIP (3:1 v/v). The solution was stirred for 10 min and then transferred to an EPR tube, and the sample was measured identifying a mixture of complexes **II.10**, **II.12-R** and **II.12-S**. Then, *i*Pr_2NEt (10.8 µL, 62.4 µmol, 12.0 equiv) was added to this mixture with a Hamilton syringe. After 1 min, the sample was re-measured by EPR. Note: The addition of base to a mixture of Cu(II) complexes in the presence of HFIP leads to the formation of complexes **II.7-R** and **II.7-S**.

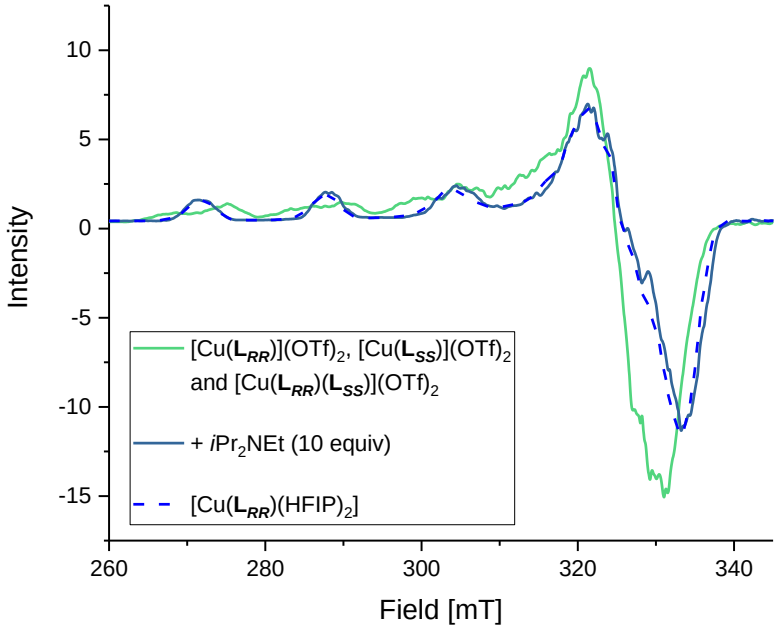

Figure 2.72: EPR spectra for the transformation of Cu(II) complexes **II.10**, **II.12-R** and **II.12-R** into a mixture of **II.7-R** and **II.7-R** by the addition of base.

2.6.11 Catalytic experiments with dimeric copper(II) complexes tested as pre-catalysts

Cu(**L*RR***)$_2$(OTf)$_2$ as pre-catalyst

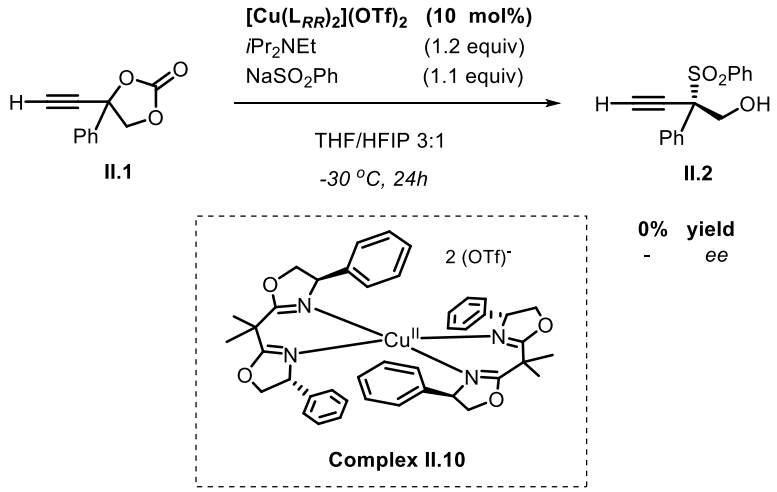

Figure 2.73: Homochiral Cu(II) complex **II.10** as a potential pre-catalyst for the transformation of cyclic carbonate **II.1** into chiral propargylic sulfone **II.2**.

Procedure: Inside a glovebox, a vial was charged with pre-catalyst **II.10** (20.6 mg, 0.02 mmol, 10 mol%) and it was dissolved in 0.6 mL of THF/HFIP (3:1 v/v). The other reagents were added with in the following order: *i*Pr$_2$NEt (41.8 µL, 0.24 mmol, 1.2 equiv), NaSO$_2$Ph (36.0 mg, 0.22 mmol, 1.1 equiv) and cyclic carbonate **II.1** (37.6 mg, 0.20 mmol, 1.0 equiv). The mixture was stirred at –30 °C. After 24 h, the catalytic reaction was quenched with NH$_4$Cl, extracted with EtOAc and dried over anhydrous Na$_2$SO$_4$. The yield was determined by ^{1}H NMR using mesitylene as internal standard.

Mixture of Cu(**L*RR***)$_2$(OTf)$_2$, Cu(**L*SS***)$_2$(OTf)$_2$ and Cu(**L*RR***)(**L*SS***)(OTf)$_2$ mixture as pre-catalyst

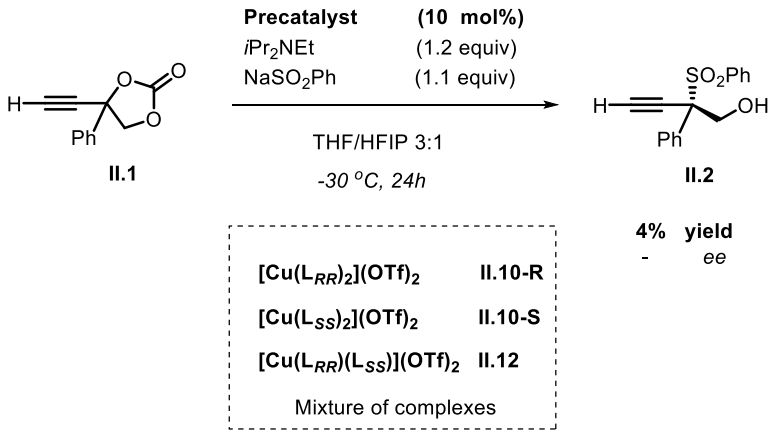

Figure 2.74: Mixture of Cu(II) complexes **II.10-R**, **II.10-S** and **II.12** used as a pre-catalyst for the transformation of cyclic carbonate **II.I** into chiral propargylic sulfone **II.2**.

Procedure: Inside a glovebox, a vial was charged with Cu(OTf)$_2$ (7.2 mg, 0.02 mmol, 10 mol%), **L*RR*** (6.7 mg, 0.02 mmol, 10 mol%) and **L*SS*** (6.7 mg, 0.02 mmol, 10 mol%) and these were dissolved in 0.6 mL of THF/HFIP (3:1 v/v). The other reagents were added in the following order: *i*Pr$_2$NEt (41.8 µL, 0.24 mmol, 1.2 equiv), NaSO$_2$Ph (36.0 mg, 0.22 mmol, 1.1 equiv) and cyclic carbonate **II.1** (37.6 mg, 0.20 mmol, 1.0 equiv). The mixture was stirred at −30 °C. After 24 h, the catalytic reaction was quenched with NH$_4$Cl, extracted with EtOAc and dried over anhydrous Na$_2$SO$_4$. The yield was determined by ^{1}H NMR using mesitylene as internal standard.

2.6.12 EPR spectroscopy to study the equilibrium between dimeric copper(II) complexes

Transformation of Cu-aquo complex **II.6** to homochiral Cu(II) complex **II.10**

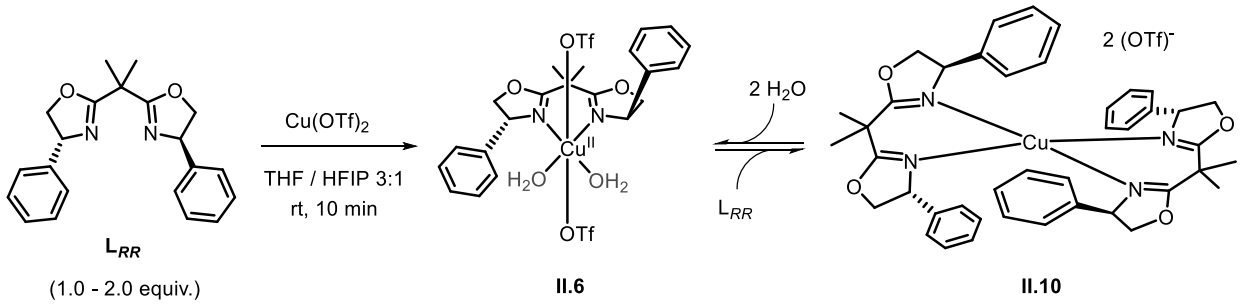

Figure 2.75: Reaction scheme for the transformation study of complex **II.6** to **II.10**.

Procedure: In a 2 mL vial, $Cu(OTf)_2$ (5.2 µmol, 1.9 mg, 1.0 equiv) and ligand $\mathbf{L}_{\boldsymbol{RR}}$ (1.0 – 2.0 equiv) were dissolved in 0.4 mL of THF/HFIP (3:1 v/v). The reaction mixture was stirred for 10 min and then transferred to an EPR tube. To study the transformation of **II.6** into **II.10**, five EPR samples with different ratios between $Cu(OTf)_2$ and ligand $\mathbf{L}_{\boldsymbol{RR}}$ were prepared (see Table **II.IV**).

Table II.IV: Amount of $\mathbf{L}_{\boldsymbol{RR}}$ used for each sample.

$Cu(OTf)_2$ (equiv)	$\mathbf{L}_{\boldsymbol{RR}}$ (equiv)	$\mathbf{L}_{\boldsymbol{RR}}$ (µmol)	$\mathbf{L}_{\boldsymbol{RR}}$ (mg)
1.0	1.0	5.1	1.7
1.0	1.3	7.1	2.4
1.0	1.5	7.6	2.6
1.0	1.7	8.1	2.7
1.0	2.0	10.2	3.4

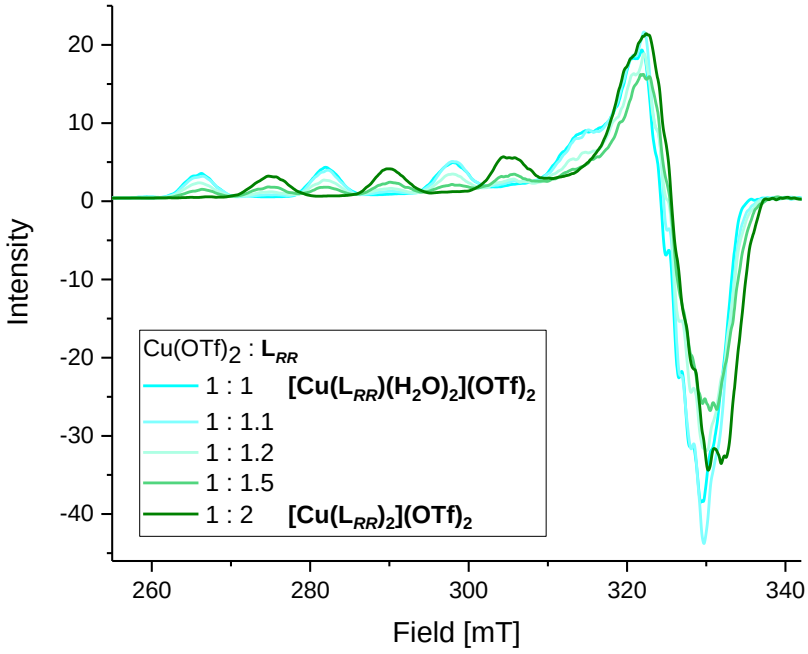

Figure 2.76: Equilibrium study between complexes **II.6** and **II.10** by EPR at 77 K.

Reversibility experiment for homodimer cleavage in the presence of excess of water

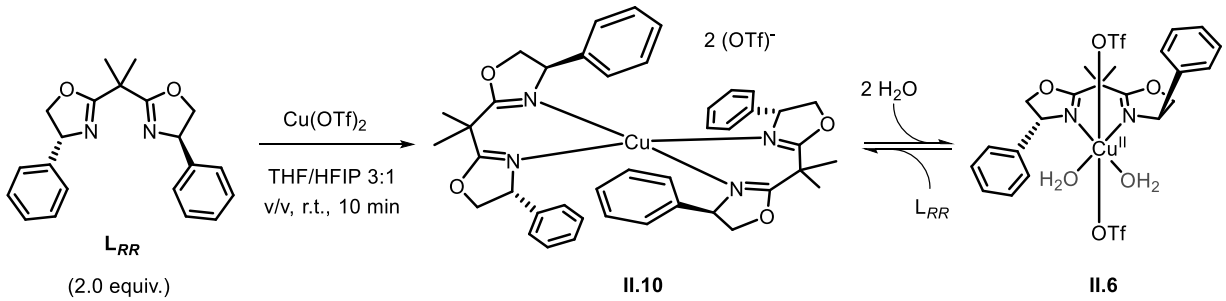

Figure 2.77: Reaction scheme for the equilibrium study between complex **II.10** and **II.6**.

Procedure: In a 2 mL vial, $Cu(OTf)_2$ (5.2 µmol, 1.9 mg, 1.0 equiv) and ligand **L*RR*** (5.2 µmol, 1.7 mg, 2.0 equiv) were dissolved in 0.4 mL of THF/HFIP (3:1 v/v). The reaction mixture was stirred for 10 min and then transferred to an EPR tube. After a first measurement, 10 equiv (1 µL) of water were added to the mixture and its EPR spectrum was measured again. This procedure was repeated for the addition of 50 and 100 equiv of water to similar sample solutions of **II.10** (see Table **II.IV**). At an addition of 50 equiv of water, the equilibrium shifted to an approximate distribution of 50:50 of complexes **II.10** and **II.6**.

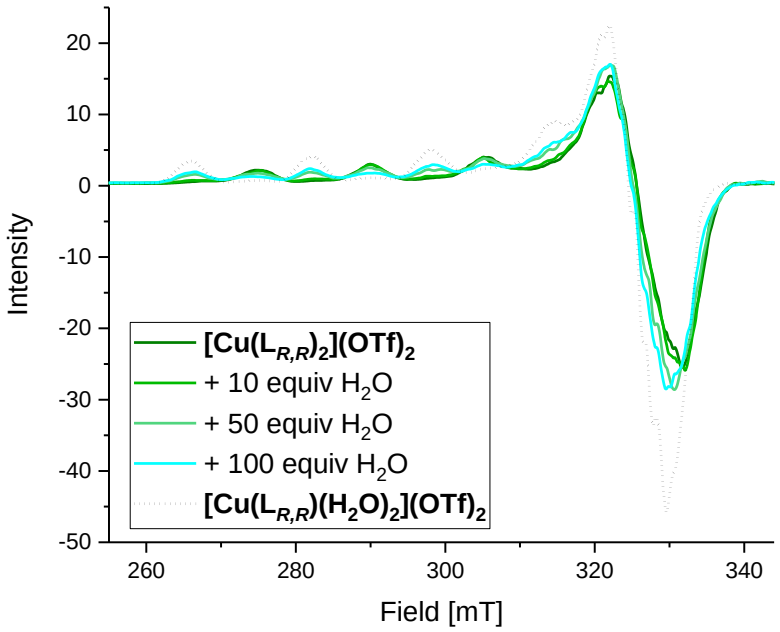

Figure 2.78: Studied equilibrium between complexes **II.10** and **II.6** by EPR at 77 K.

Distribution study of hetero- and homochiral CuL_2 complexes

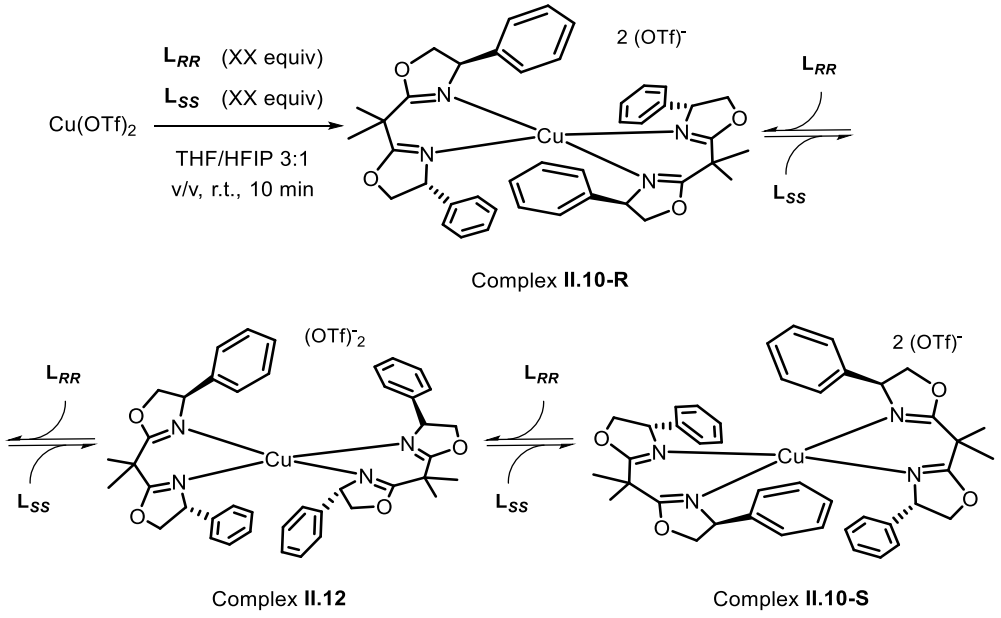

Error! Not a valid link.

Figure 2.79: Reaction scheme for the formation of a mixture of complexes **II.10-R**, **II.12** and **II.10-R**.

Procedure: $Cu(OTf)_2$ (5.2 µmol, 1.9 mg, 1.0 equiv), ligand $\mathbf{L}_{RR}$ (2.0 – 1.0 equiv) and ligand $\mathbf{L}_{SS}$ (0 – 1.0 equiv) were dissolved in 0.4 mL of THF/HFIP (3:1 v/v). The mixture was stirred for 10 min and then transferred to an EPR tube. Five EPR samples with different ratios between $Cu(OTf)_2$ ligand $\mathbf{L}_{RR}$ and ligand $\mathbf{L}_{SS}$ were prepared (see Table **II.V**). Stock solutions of chiral ligand were prepared by dissolving 10 mg of chiral ligand in 1 mL of THF.

Table **II.V**: Ligands $\mathbf{L}_{RR}$ and $\mathbf{L}_{SS}$ and their used amounts for each sample.

$Cu(OTf)_2$ (equiv)	$\mathbf{L}_{RR}$ (equiv)	$\mathbf{L}_{SS}$ (equiv)	$\mathbf{L}_{RR}$ (µmol)	$\mathbf{L}_{SS}$ (µmol)
1.0	2.0	0	10.2	0
1.0	1.7	0.3	8.1	2.0
1.0	1.5	0.5	7.6	2.6
1.0	1.3	0.7	7.1	3.1
1.0	1.0	1.0	5.1	5.1

Note: For the last entry of Table **II.V**, when $Cu(OTf)_2$, $\mathbf{L}_{RR}$ and $\mathbf{L}_{SS}$ were present in a 1:1:1 ratio, a maximum level of scrambling between the Cu(II) complexes was observed.

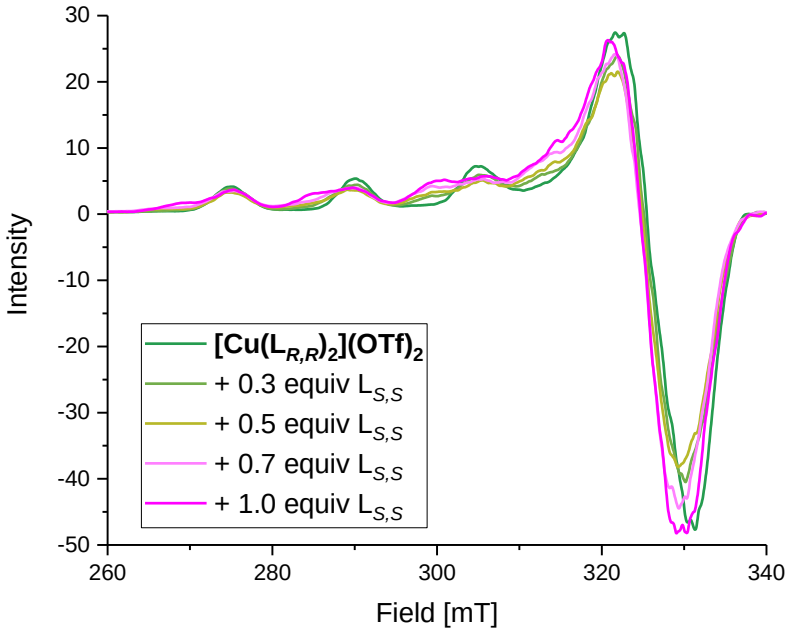

Figure 2.80: Equilibrium study between complexes **II.10-R**, **II.12** and **II.10-S** by EPR at 77 K.

Transformation of Cu-aquo complex **II.6** to hetero-chiral Cu(II) complex **II.10** studied by EPR Spectroscopy

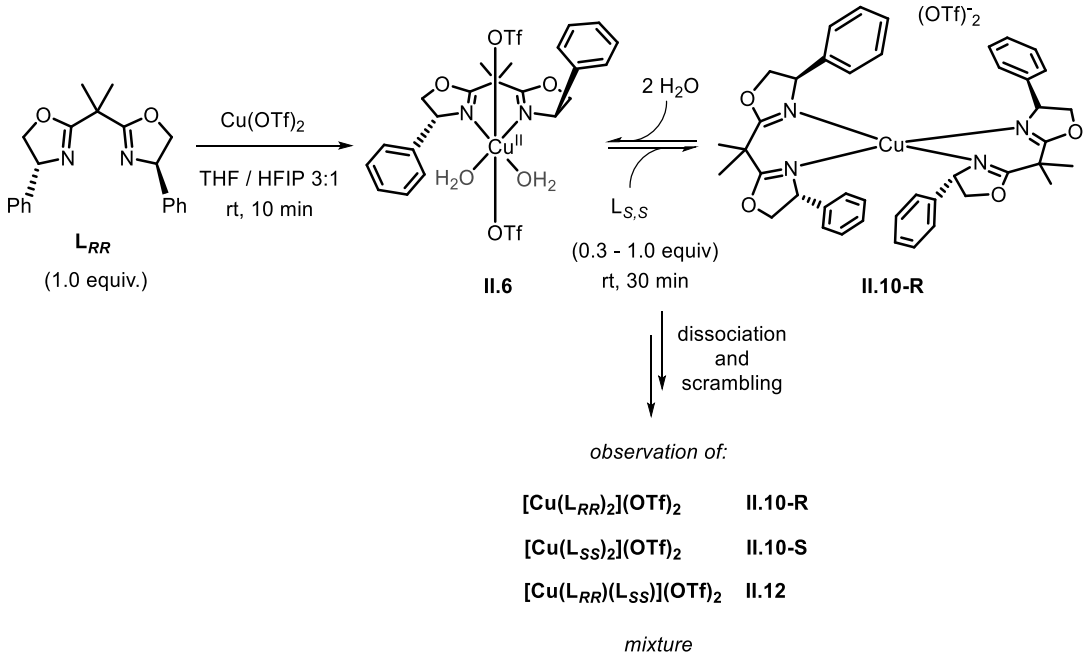

Figure 2.81: Reaction scheme for the equilibrium study between complexes **II.6** and **II.10-R** in the presence of **L*ss*** leading to a scrambling of ligand entities to form a mixture of **II.10** and **II.12**.

Procedure: In a 2 mL vial, $Cu(OTf)_2$ (5.2 µmol, 1.9 mg, 1.0 equiv) and ligand **L*RR*** (5.1 µmol, 1.7 mg, 1.0 equiv) were dissolved in 0.4 mL of THF/HFIP (3:1 v/v). The mixture was stirred for 10 min allowing the formation of complex **II.6**. Then, ligand **L*ss*** (0.2 – 1.0 equiv) was added and the solution was stirred for 30 min before transferring it to an EPR tube. To study the equilibrium between complexes **II.6** and **II.10-R**, five EPR samples with different ratios between $Cu(OTf)_2$ and ligand **L*R,R*** were prepared (see Table **II.VI**). Stock solutions of **L*ss*** were prepared dissolving 10 mg of the ligand in 1 mL of THF.

Table **II.VI**: Amounts of **L*ss*** used for each sample.

$Cu(OTf)_2$ (equiv)	**L*RR*** (equiv)	**L*ss*** (equiv)	**L*ss*** (µmol)	**L*ss*** (µL)
1.0	1.0	0	0	0
1.0	1.0	0.3	1.5	50
1.0	1.0	0.5	2.5	84
1.0	1.0	0.7	3.6	120
1.0	1.0	1.0	5.1	170

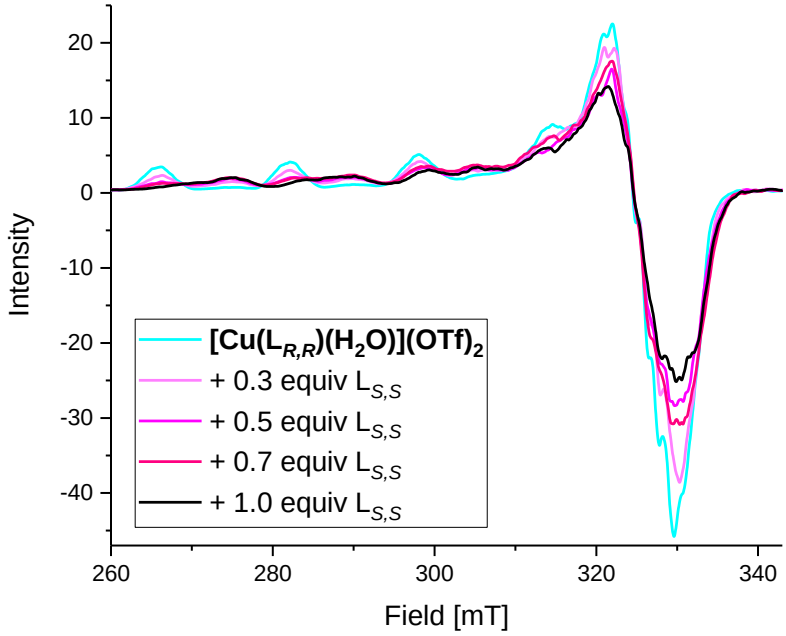

Figure 2.82: Equilibrium study of complexes **II.10-R**, **II.12** and **II.10-R** upon the addition of **L*ss*** to complex **II.6** followed by EPR at 77 K.

Reversibility experiment for the cleavage of the hetero- and homo-chiral complexes in the presence of excess water

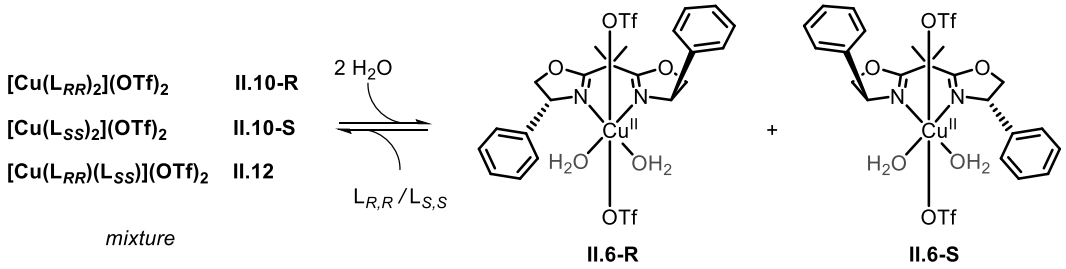

Figure 2.83: Reaction scheme for the equilibrium study between complexes **II.10-R**, **II.10-S** and **II.12** transforming into complexes **1-R** and **1-S** upon addition of H_2O.

Procedure: To the same samples prepared in Table **II.VI** (entry 5), 10.0 equiv of water (1 µL) were added. The mixture was left for 5 min and was then measured again by EPR. Consecutive additions were done (50 and 100 equiv of H_2O) to study the conversion of the initial mixture of complexes **II.10-R**, **II.10-S** and **II.12** into a racemic mixture of **II.6** (Cu(**L*RR***)$(H_2O)_2(OTf)_2$ and Cu(**L*ss***)$(H_2O)_2(OTf)_2$).

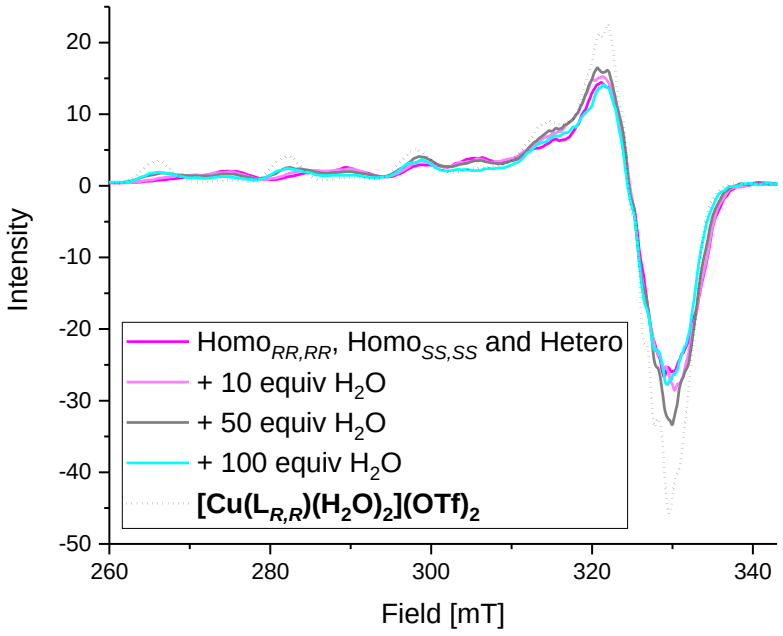

Figure 2.84: Equilibrium investigation between complexes **II.10-R**, **II.10-S** and **II.12** and complexes **II.6-R** and **II.6-S** by EPR at 77 K.

2.6.13 Crystallographic data

The measured crystals were air and moisture sensitive. The samples were treated under inert conditions immersed in perfluoro-polyether as protecting oil for manipulation. Data collection was made following the procedure stated in section 2.6.1.

Crystal data for **II.6**:

$C_{23}H_{29.25}CuF_6N_2O_{11.62}S_2$, *M*r = 761.39, monoclinic, $P2_1$, *a* = 9.6821(4) Å, *b* = 15.3077(6) Å, *c* = 20.8622(9) Å, α = 90°, β = 94.0990(1)°, γ = 90°, *V* = 3084.1(2) Å^3, *Z* = 4, ρ = 1.640 mg·M^{-3}, μ = 0.941 mm^{-1}, λ = 0.71073 Å, *T* = 100(2) K, *F(000)* = 1557, θ(min) = 1.651°, θ(max) = 34.353°, 70568 reflections collected, 20750 reflections unique (R_{int} = 0.0404), GoF = 1.019, R_1 = 0.0382, wR_2 = 0.0839 [$I>2\sigma(I)$], R_1 = 0.0461, wR_2 = 0.0869 (all indices), min/max residual density = −0.601/0.720 [e·Å^{-3}], Completeness to θ(31.711°) = 98.4 %. This structure has previously been reported in the literature [cite].

Crystal data for **II.7**:

$C_{23}H_{24}CuF_6N_2O_9S_2$, *M*r = 714.10, trigonal, *P*2(1), *a* = 10.3933(13) Å, *b* = 19.997(2) Å, *c* = 14.2470(18) Å, α = 90°, β = 105.113(4)°, γ = 90°, *V* = 2858.7(6) Å^3, *Z* = 4, ρ = 1.659 mg·M^{-3}, μ = 1.002 mm^{-1}, λ = 0.71073 Å, *T* = 100(2) K, *F(000)* = 1452, θ(min) = 1.797°, θ(max) = 27.700°, 6795 reflections collected, 6795 reflections unique, GoF = 1.550, R_1 = 0.1041, wR_2 = 0.2350 [$I>2\sigma(I)$], R_1 = 0.1222, wR_2 = 0.2417 (all indices), min/max residual density = −0.789/4.298 [e·Å^{-3}], Completeness to θ(27.700°) = 98.6 %.

Crystal data for **DIPEA·HOTf**:

$C_9H_{20}F_3NO_3S$, *M*r = 279.32, monoclinic, $P2_1/n$, *a* = 10.3788(7) Å, *b* = 9.0444(6) Å, *c* = 14.3815(11) Å, α = 90°, β = 91.228(4)°, γ = 90°, *V* = 1349.48(16) Å^3, *Z* = 4, ρ = 1.375 mg·M^{-3}, μ = 0.273 mm^{-1}, λ = 0.71073 Å, *T* = 100(2)K, *F(000)* = 592, θ(min) = 2.396°, θ(max) = 30.571°, 19438 reflections collected, 4122 reflections unique (R_{int} = 0.0289), GoF = 1.062, R_1 = 0.0342, wR_2 = 0.0899 [$I>2\sigma(I)$], R_1 = 0.0397, wR_2 = 0.0942 (all indices), min/max residual density = -0.394/0.401 [e·Å^{-3}], Completeness to θ(30.571°) = 99.4 %. This structure has previously been reported in the literature [cite].

Crystal data for **II.9**:

$C_{31.5}H_{37}CuF_3N_3O_{6.5}S$, *M*r = 750.27, monoclinic, $P2_1$, *a* = 11.6093(5) Å, *b* = 18.4311(9) Å, *c* = 16.6223(7) Å, α = 90°, β = 103.1546(14)°, γ = 90°, *V* = 3463.4(3) Å^3, *Z* = 4, ρ = 1.439 mg·M^{-3},

μ = 0.757 mm^{-1}, λ = 0.71073 Å, *T* = 100(2) K, *F(000)* = 1556, θ(min) = 1.674°, θ(max) = 31.605°, 39543 reflections collected, 18233 reflections unique (R_{int} = 0.0350), GoF = 1.015, R_1 = 0.0424, wR_2 = 0.0833 [I>2σ(I)], R_1 = 0.0599, wR_2 = 0.0895 (all indices), min/max residual density = -0.490/0.585 [e·Å^{-3}], Completeness to θ(54.978°) = 94.1 %.

Crystal data for **II.10**:

$C_{43.5}H_{43.5}CuF_6N_{4.5}O_{10}S_2$, *M*r = 1030.99.52, triclinic, *P*1, *a* = 11.3978(10) Å, *b* = 11.64230(10) Å, *c* = 18.9872(16) Å, α = 98.755(2)°, β = 92.385(3)°, γ = 117.680(2)°, *V* = 2298.8(3) Å^3, *Z* = 2, ρ = 1.489 mg·M^{-3}, μ = 0.652 mm^{-1}, λ = 0.71073 Å, *T* = 100(2) K, *F(000)* = 1062, θ(min) = 1.916°, θ(max) = 25.291°, 46611 reflections collected, 46611 reflections unique, GoF = 1.047, R_1 = 0.0948, wR_2 = 0.2356 [I>2σ(I)], R_1 = 0.1177, wR_2 = 0.2542 (all indices), min/max residual density = -0.952/1.359 [e·Å^{-3}], Completeness to θ(25.291°) = 99.23 %.

Crystal data for **II.11**:

$C_{47}H_{52}CuF_3N_4O_8S$, *M*r = 953.52, trigonal, $P3_1$, *a* = 11.64230(10) Å, *b* = 11.64230(10) Å, *c* = 29.2631(3) Å, α = 90°, β = 90°, γ = 120°, *V* = 3435.01(7) Å^3, *Z* = 3, ρ = 1.383 mg·M^{-3}, μ = 0.592 mm^{-1}, λ = 0.71073 Å, *T* = 100(2) K, *F(000)* = 1494, θ(min) = 2.136°, θ(max) = 31.711°, 127112 reflections collected, 15029 reflections unique (R_{int} = 0.0279), GoF = 1.043, R_1 = 0.0383, wR_2 = 0.1055 [I>2σ(I)], R_1 = 0.0414, wR_2 = 0.1079 (all indices), min/max residual density = -0.341/0.664 [e·Å^{-3}], Completeness to θ(31.711°) = 97.9 %.

Crystal data for **II.12**:

$C_{46}H_{48}Cl_4CuF_6N_4O_{10}S_2$, *M*r = 1200.34, monoclinic, *I*2/a, *a* = 20.2564(2) Å, *b* = 12.56790(10)Å, *c* = 20.3894(2) Å, α = 90°, β = 98.1620(10)°, γ = 90°, *V* = 5138.16(8) Å^3, *Z* = 4, ρ = 1.308 mg·M^{-3}, μ = 0.796 mm^{-1}, λ = 0.71073 Å, *T* = 293(2) K, *F(000)* = 608, θ(min) = 1.909°, θ(max) = 54.978°, 295536 reflections collected, 32316 reflections unique (R_{int} = 0.0502), GoF = 1.049, R_1 = 0.0504, wR_2 = 0.1305 [I>2σ(I)], R_1 = 0.0731, wR_2 = 0.1416 (all indices), min/max residual density = -1.711/1.263 [e·Å^{-3}], Completeness to θ(54.978°) = 98.2 %.

2.6.14 Quantum mechanical calculations (DFT)

For further information regarding DFT calculations, single step scan analysis, and for Cartesian coordinates, please, refer to the supplementary information document provided at https://doi.org/10.1021/jacs.3c00188.

Additional free energy profile

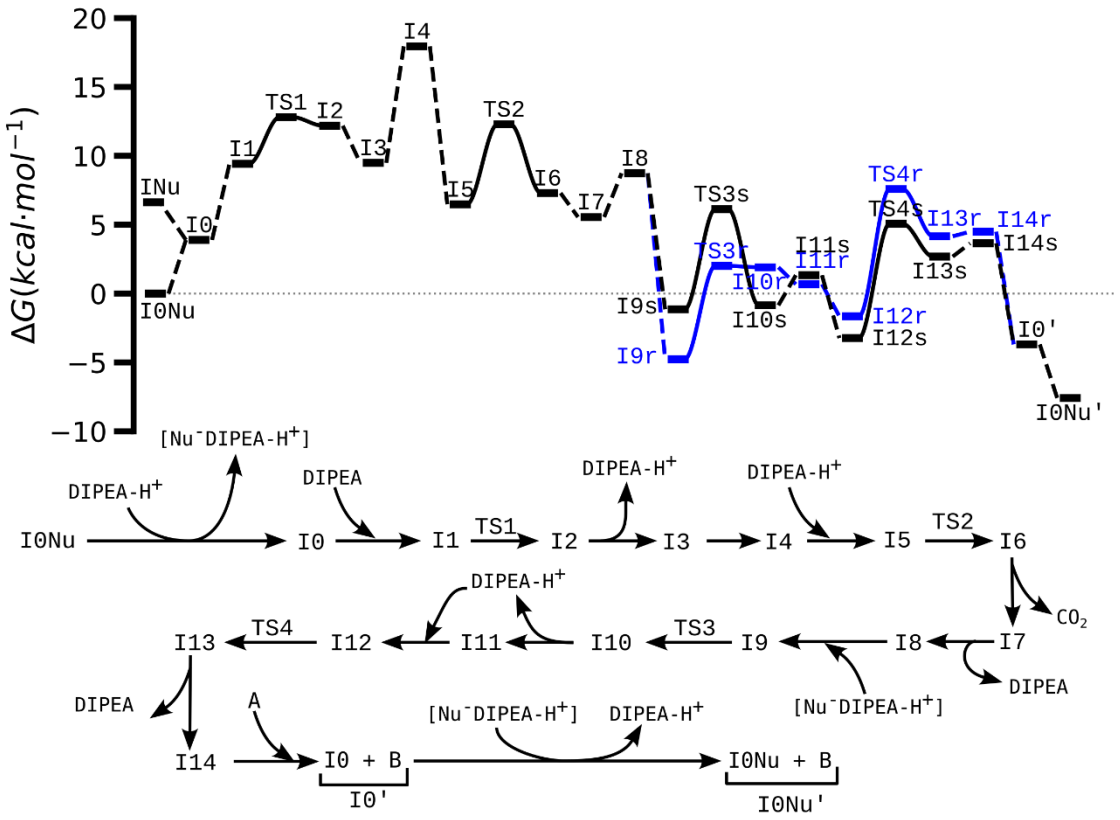

Figure 2.85: (a) Full Gibbs free energy diagram and (b) mechanistic proposal for the Cu-mediated conversion of substrate **II.1** into the propargylic sulfone *(S)*-**II.2**. Energy values correspond to relative free energies at -30ºC at 1 M concentration with quasi-harmonic (100 cm^{-1}) corrections. All values are reported in kcal/mol. The blue profile under (a) corresponds to the pathway leading to product *(R)*-**II.2**.

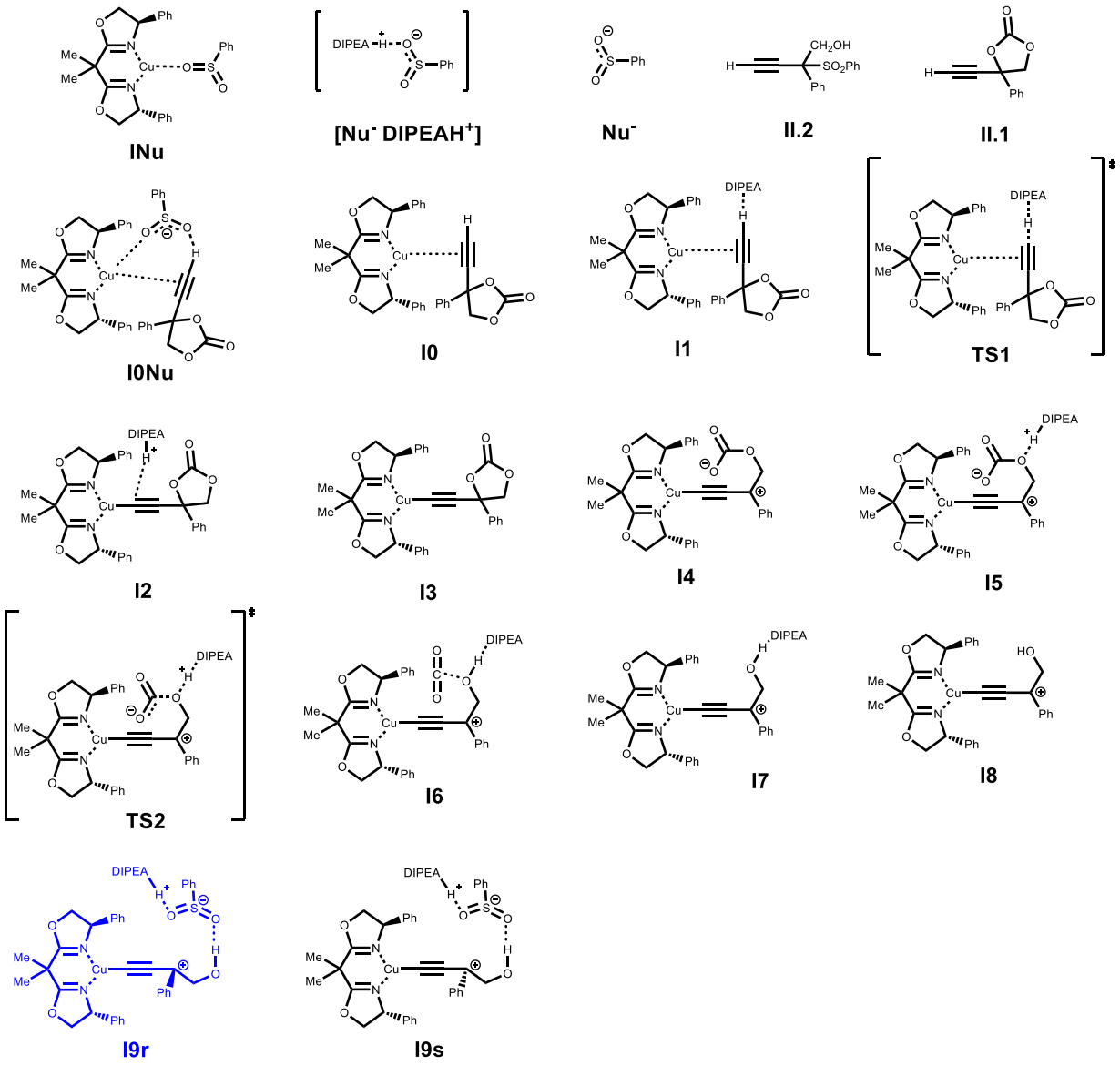

Figure 2.86: Full set of structures and their labels as used in the proposed mechanism for reagents and Intermediates **I0** to **I9r** and **I9s**.

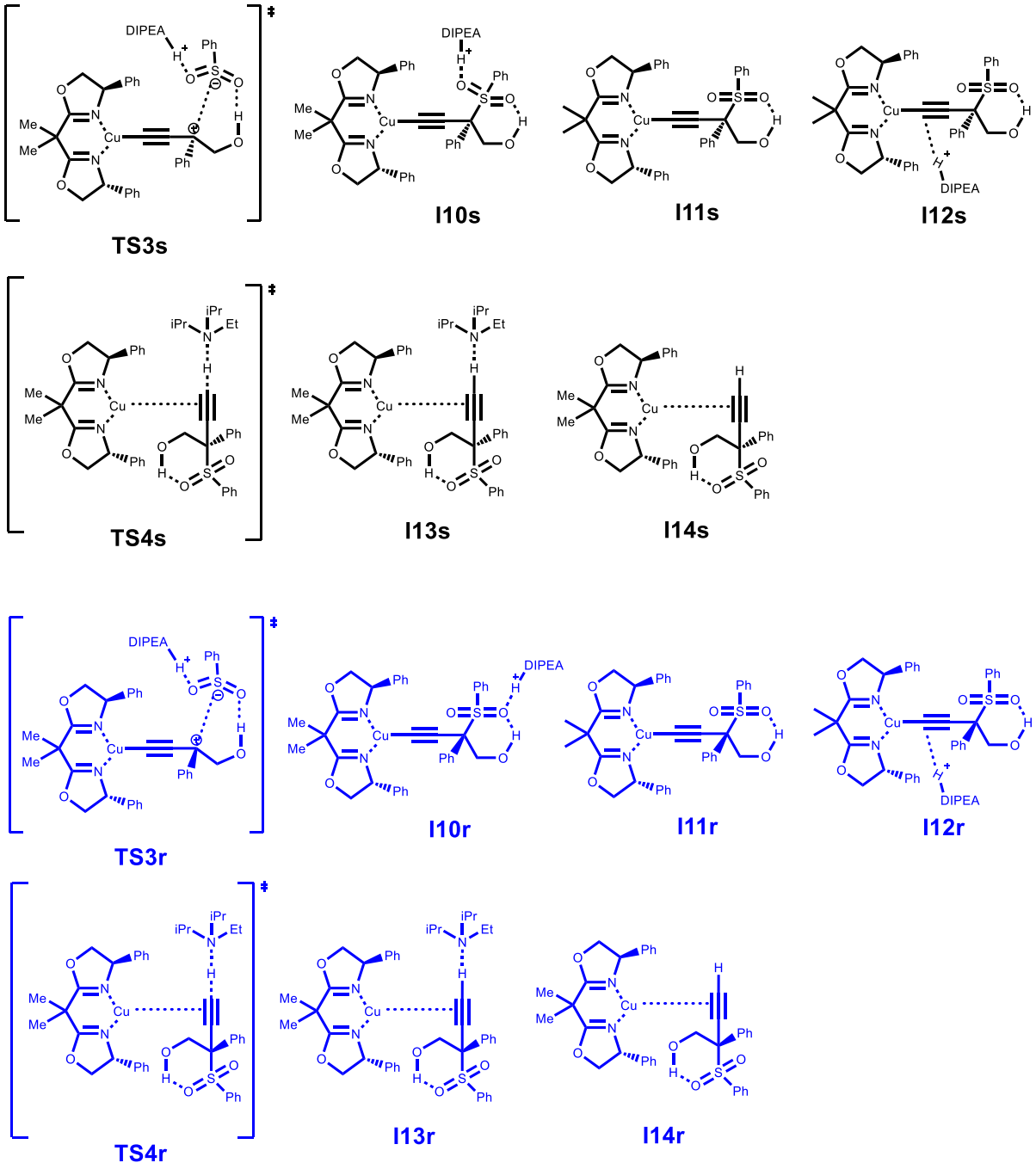

Figure 2.87: Full set of structures and their labels as used in the proposed part of the mechanism from **TS3r** and **TS3s** to **I14s** and **I14r**.

Chapter 3.

Inner-Sphere Pd-Catalyzed Allylic Amination: A Comprehensive Computational and Experimental Mechanistic Study

This project was developed in collaboration with the group of Prof. Genping Huang (Tianjin University, China). The computational work was done by ***Dr. Hongli Wu*** *and* ***Deng Pan****.*

The results described in this chapter have been submitted:

Garcia-Roca A.‡ Wu H.,‡ Pan D., Pérez-Temprano M. H., Huang G., Kleij A. W., *J. Am. Chem. Soc*. **2023**, *submitted - under review* (ja-2023-039833)

3.1 Introduction

The construction of sterically congested stereocenters through allylic substitution reactions is of high interest to the synthetic chemistry community[126] as it allows to create chiral synthons useful for natural product synthesis and for the development of pharma-active precursors.[127] The privileged and user-friendly nature of the allylation process enables the cross-coupling of versatile allylic precursors with a wide variety of pro-nucleophiles[128] and pro-electrophiles[129] (in the latter case if proper umpolung of the transient metal-allyl species can be achieved). Allylic amination represents a well-established process in this area allowing to create functionalized amine scaffolds reminiscent of amine modules present in bioactive compounds.[130] The synthesis of allylic amines has therefore been subject of intense studies,[131] with a special focus on asymmetric methodologies.[132] The catalytic, asymmetric preparation of sterically challenging allylic amines featuring tertiary, tetra-substituted carbon stereocenters has limited scope with only a handful of successful methodologies being available.[133] Pd-

[126] a) Süsse, L.; Stoltz, B. M. *Chem. Rev*. 2021, 121, 4084, b) Wu, G.; Wu, J.-R.; Huang, Y.; Yang, Y.-W. *Chem. Asian J*. 2021, 16, 1864, c) Sawano, T.; Takeuchi, R. *Catal. Sci. Technol*. 2022, *12*, 4100.

[127] a) Enquist, J. A., Jr.; Stoltz, B. M. *Nature* 2008, 453, 1228. b) Ling, T.; Rivas, F. *Tetrahedron* 2016, 43, 6729. c) Quasdorf, K. W.; Overman, L. E. *Nature* 2014, 516, 181. d) Li, C.; Ragab, S. S.; Liu, G.; Tang, W. *Nat. Prod. Rep*. 2020, 37, 276. e) Müller, J. M.; Stark, C. B. W. *Angew. Chem. Int. Ed*. 2016, 55, 4798.

[128] a) Sandmeier, T.; Goetzke, F. W.; Krautwald, S.; Carreira, E. M. *J. Am. Chem. Soc*. 2019, 141, 12212. b) Madrahimov, S. T.; Li, Q.; Sharma, A.; Hartwig, J. F. *J. Am. Chem. Soc*. 2015, 137, 14968. c) Turnbull, B. W. H.; Evans, P. A. *J. Am. Chem. Soc*. 2015, 137, 6156. d) Khan, A.; Khan, S.; Khan, I.; Zhao, C.; Mao, Y.; Chen, Y.; Zhang, Y. J. *J. Am. Chem. Soc*. 2017, 139, 10733. e) Xie, J.; Xue, S.; Escudero-Adán, E. C.; Kleij, A. W. *Angew. Chem. Int. Ed*. 2018, 57, 16727.

[129] a) Guo, W.; Kuniyil, R.; Gómez, J. E.; Maseras, F.; Kleij, A. W. *J. Am. Chem. Soc*. 2018, 140, 3981. b) Wang, H.; Qiu, S.; Wang, S.; Zhai, H. *ACS Catal*. 2018, 8, 11960. c) Huang, S.; Zhang, G.-P.; Jiang, Y.-J.; Yu, F.-L.; Ding, C.-H.; Hou, X.-L. *Chem. Commun*. 2022, 58, 3513; d) Liu, J.; Cao, C.–G.; Sun, H.-B.; Zhang, X.; Niu, D. Catalytic *J. Am. Chem. Soc.* 2016, 138, 13103.

[130] a) Trost, B. M.; Crawley, M. L. *Chem. Rev*. 2003, 103, 2921. b) Trost, B. M.; Zhang, T.; Sieber, J. D. *Chem. Sci*. 2010, 1, 427. c) Johannsen, M.; Jørgensen, K. A. *Chem. Rev*. 1998, 98, 1689.

[131] a) Mizuno, S.; Terasaki, S.; Shinozawa, T.; Kawatsura, M. *Org. Lett*. 2017, 19, 3, 504. b) Pattillo, C. P.; Strambeanu, I. I.; Calleja, P.; Vermeulen, N. A.; Mizuno, T.; White, M. C. *J. Am. Chem. Soc.* 2016, 138, 1265. c) Mellegaard-Waetzig, S. R.; Rayabarapu, D. K.; Tunge, J. A. *Synlett* 2005, 2759. d) Dočekal, V.; Šimek, M.; Dračínský, M.; Veselý, J. *Chem. Eur. J.* 2018, 24, 13441. e) Xie, J.; Qiao, C.; Martínez Belmonte, M.; Escudero-Adán, E. C.; Kleij, A. W. *ChemSusChem* 2019, 12, 3152.

[132] a) Kawatsura, M.; Uchida, K.; Terasaki, S.; Tsuji, H.; Minakawa, M.; Itoh, T. *Org. Lett.* 2014, 16, 1470. b) Ghorai, S.; Chirke, S. S.; Xu, W.-B.; Chen, J.-F.; Li, C. *J. Am. Chem. Soc*. 2019, 141, 11430. c) You, S.-L.; Zhu, X.-Z.; Luo, Y.-M.; Hou, X.-L.; Dai, L.-X. *J. Am. Chem. Soc.* 2001, 123, 7471. d) Weihofen, R.; Tverskoy, O.; Helmchen, G. *Angew. Chem. Int. Ed*. 2006, *45*, 5546. e) Leitner, A.; Shekhar, S.; Pouy, M. J.; Hartwig, J. F. *J. Am. Chem. Soc.* 2005, 127, 15506. f) Kim, S. W.; Schwartz, L. A.; Zbieg, J. R.; Stivala, C. E.; Krische, M. J. *J. Am. Chem. Soc*. 2019, 141, 671.

[133] a) Fischer, D. F.; Xin, Z.; Peters, R. *Angew. Chem. Int. Ed.* 2007, 46, 7704. b) Trost, B. M.; Bunt, R. C.; Lemoine, R. C.; Calkins, T. L. *J. Am. Chem. Soc*. 2000, 122, 5968. c) Arnold, J. S.; Nguyen, H. M. *J. Am. Chem. Soc*. 2012, 134, 8380. d) Arnold, J. S.; Cizio, G. T.; Nguyen, H. M. *Org. Lett*. 2011, 13, 5576.

promoted asymmetric synthesis of such targets remained without significant progress until recently the use of substituted allylic precursors with either cyclic[134] or linear[135] carbonate leaving groups offered a significant step forward providing generic protocols. As a result of these findings, other types of pro-nucleophiles have been fruitfully utilized in the context of forging sterically hindered acyclic[136] and cyclic[137] carbon stereocenters.

While Pd-promoted allylic alkylation processes typically prefer outer-sphere attack of the nucleophilic species onto a Pd(allyl) intermediate, various examples of C–C and C–X (X = O or N) bond formations that operate via an inner-sphere regime have been reported but still remain rare. Most of these efforts focused on the utilization of computational methods to study the intricacies of the respective manifolds and key interactions that drive an inner-sphere attack of the nucleophilic species.[138] Some further experimental evidence was reported by Morken et al. (Figure 3.1a),[139] who used a combination of calorimetric measurements, substrate labelling and a detailed DFT analysis to unravel the mechanistic scenario involved in formal allyl-allyl couplings. A second example utilizing C-based nucleophiles is the decarboxylative allylation of *in situ* formed enolates, which was closely examined by Goddard and Stoltz (Scheme 3.1a).[140] In a similar way, Hu and coworkers studied the coupling between ketones and allylic reagents and concluded that an inner-sphere attack of an

[134] Cai, A.; Guo, W.; Martínez-Rodríguez, L.; Kleij, A. W. *J. Am. Chem. Soc*. 2016, 138, 14194.

[135] Guo, W.; Cai, A.; Xie, J.; Kleij, A. W. *Angew. Chem. Int. Ed.* 2017, 56, 11797.

[136] a) Xie, J.; Guo, W.; Cai, A.; Escudero-Adán, E. C.; Kleij, A. W. *Org. Lett*. 2017, 19, 6388. b) Cai, A.; Kleij, A. W. *Angew. Chem. Int. Ed*. 2019, 58, 14944. c) Guo, W.; Zuo, L.; Cui, M.; Yan, B.; Ni, S. *J. Am. Chem. Soc.* 2021, 143, 7629.

[137] You, Y.; Li, Q.; Zhang, Y.-P.; Zhao, J.-Q.; Wang, Z.-H.; Yuan, W. C. *ChemCatChem* 2022, 14, e202101887. b) Khan, A.; Zheng, R.; Kan, Y.; Ye, J.; Xing, J.; Zhang, Y. J. *Angew. Chem. Int. Ed.* 2014, 53, 6439. c) Khan, I.; Zhao, C.; Zhang, Y. J. *Chem. Commun*. 2018, 54, 4708. d) Rong, Z.-Q.; Yang, L.-C.; Liu, S.; Yu, Z.; Wang, Y.-N.; Tan, Z. Y.; Huang, R.-Z.; Lan, Y.; Zhao, Y. *J. Am. Chem. Soc*. 2017, 139, 15304.

[138] a) Cárdenas, D. J.; Echavarren, A. M. *New. J. Chem*. 2004, 28, 338. b) Chen, J.-P.; Peng, Q.; Lei, B.-L.; Hou, X.-L.; Wu, Y.-D. *J. Am. Chem. Soc*. 2011, 133, 14180. c) Keith, J. A.; Behenna, D. C.; Sherden, N.; Mohr, J. T.; Ma, S.; Marinescu, S. C.; Nielsen, R. J.; Oxgaard, J.; Stoltz, B. M.; Goddard, W. A. *J. Am. Chem. Soc*. 2012, 134, 19050. d) Hu, L.; Cai, A.; Wu, Z.; Kleij, A. W.; Huang, G. A *Angew. Chem. Int. Ed*. 2019, 58, 14694. e) Cusumano, A. Q.; Stoltz, B. M.; Goddard III, W. A. *J. Am. Chem. Soc*. 2020, 142, 13917. f) Wang, K.; Wang, B.; Liu, X.; Fan, H.; Liu, Y.; Li, C. *Chin. J. Catal.* 2021, 42, 1227. g) Wu, H.; Hu, L.; Shi, Y.; Shen, Z.; Huang, G. *ACS Catal*. 2022, 12, 2722. h) Keith, J. A.; Behenna, D. C.; Mohr, J. T.; Ma, S.; Marinescu, S. C.; Oxgaard, J.; Stoltz, B. M.; Goddard, W. A. *J. Am. Chem. Soc*. 2007, 129, 11876. i) Nagae, H.; Xia, J.; Kirillov, E.; Higashida, K.; Shoji, K.; Boiteau, V.; Zhang, W.; Carpentier, J.-F.; Mashima, K. *ACS Catal*. 2020, 10, 5828.

[139] Ardolino, M. J.; Morken, J. P. *J. Am. Chem. Soc*. 2014, 136, 7092.

[140] See references 138c and 138e.

enolate nucleophile occurs on the basis of control (labelling) experiments and *in silico* calculations.[141]

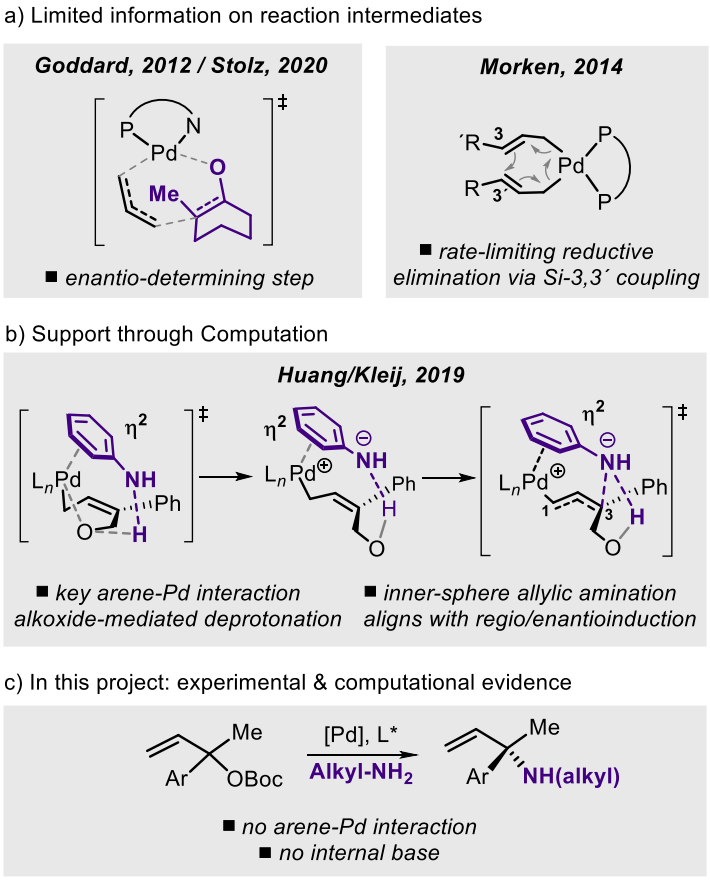

Figure 3.1: Previously proposed key intermediates for inner-sphere allylation of C-centered nucleophiles, b) recently disclosed allylic amination via an inner-sphere mechanism by Huang and Kleij, and c) detailed analysis of an allylic amination involving alkyl amines and linear carbonates.

Recently, our group reported a coordination-assisted Pd-catalyzed allylic amination using vinyl cyclic carbonates and aromatic amines yielding products with congested carbon stereocenters (Figure 3.1b).[142] In this scenario, there is a key role for the O-atom that remains part of the substrate after initial decarboxylation, and guides the incoming amine thereby controlling the regio-selectivity of the allylic substitution process. Later on we reported the use of linear carbonates and alkyl amines that under Pd-catalysis also afforded chiral □□□-disubstituted branched allylic amine products.

[141] Bai, D.-C.; Yu, F.-L.; Wang, W.-Y.; Chen, D.; Li, H.; Liu, Q.-R.; Ding, C.-H.; Chen, B.; Hou, X.-L. *Nat. Commun*. 2015, 7, 11806.
[142] See reference 138d.

However, in these latter cases, the Pd(allyl) intermediates were devoid of any potentially coordinating motif (Figure 3.1c).[143]

3.2 Aims and objectives

Intrigued by the high level of control in this last procedure (Figure 3.1c), we started a detailed mechanistic analysis of the involved Pd intermediates. Our efforts were directed to try to determine whether the C–N bond coupling occurs through an intermediate where the nucleophile is directly coordinated to the Pd center (Figure 3.2a: inner-sphere attack) or if the reaction possibly proceeds via an outer sphere attack (Figure 3.2b). A more profound understanding of the mechanism should enable to explain the regio-preference and asymmetric induction observed in this process. Previous work in the literature did not focus much on the involved Pd-species under turnover conditions, and in this chapter several spectroscopic and computational efforts will be discussed that helped to detect and assign key Pd-intermediates. The combined experimental/theoretical approach allowed us to create a comprehensive picture of this complex allylic amination manifold. It is crucial to understand in detail the mechanistic implications of these latter transformations to advance new protocols that built on the use of reactive nucleophiles, electrophiles or even radical based reactants leading to such bulky stereogenic carbons.

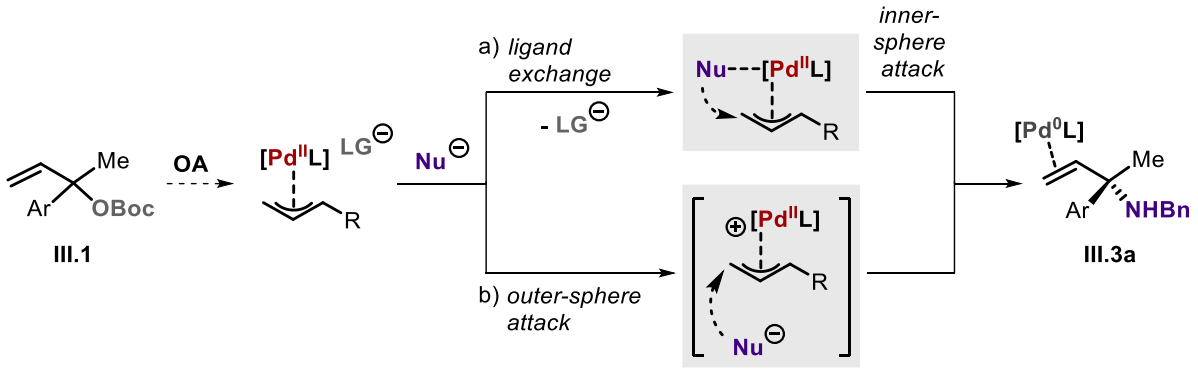

Figure 3.2: Hypothetical pathways of our previously reported enantio-selective allylic amination process; a) inner-sphere nucleophilic attack with previous ligand exchange, and b) outer-sphere mechanism.

[143] See reference 136b.

3.3 Results and discussion

3.3.1 Kinetic experiments

We started our investigations revisiting the previously reported benchmark reaction between allylic carbonate **III.1** and benzyl amine **III.2** in the presence of $Pd_2dba_3 \cdot CHCl_3$/phosphoramidite $\mathbf{L}_{PN}$ in THF/MeCN (3:1 v/v) at 0 ºC (Figure 3.3a). The reaction was monitored by ^1H NMR spectroscopy (Figure 3.3c) which helped to identify and quantify three different products: the desired branched allylic amine (product **III.3a**), the corresponding linear regio-isomer as an *E*/*Z* mixture (products **III.3b**), and a diene product (**III.3c**) resulting from a hydride-elimination pathway. After the identification of all the main products formed in our catalysis, we scrutinized various conditions (temperature, solvent medium, amount of amine nucleophile) that influences the regio-selectivity (branched/linear, (B:L), ratio) and the chemo-selectivity of the reaction (Figure 3.3b). The use of a solvent mixture (THF/MeCN, 3:1 v/v) increases the selectivity towards the branched product (entry 1 vs 3). We also noticed that lower temperatures favor the formation of the branched allylic amine (entry 1 vs 2). Interestingly, the reaction in THF as a medium at 0 ºC is significantly more sluggish and requires a longer (72 h) reaction time (entry 4). The addition of higher relative amounts of the pro-nucleophile increases the yield towards the branched product, although it compromises the B:L ratio (entry 1 vs. entries 5 and 6), but somehow these conditions supress the formation of the 1,3-diene **III.3c** and thus favors the chemo-control. The data highlighted in entry 2 those obtained using the typically used catalytic protocol, which were previously selected on the basis of the high regio-selectivity for chiral **III.3a**. Note that these are also the conditions we used for the spectroscopic analyses that are described in the following sections. With all this information, we wondered how the Pd catalyst could favor the formation of α,α-disubstituted allylic amines with such high regio- and enantio-selectivities.

a)

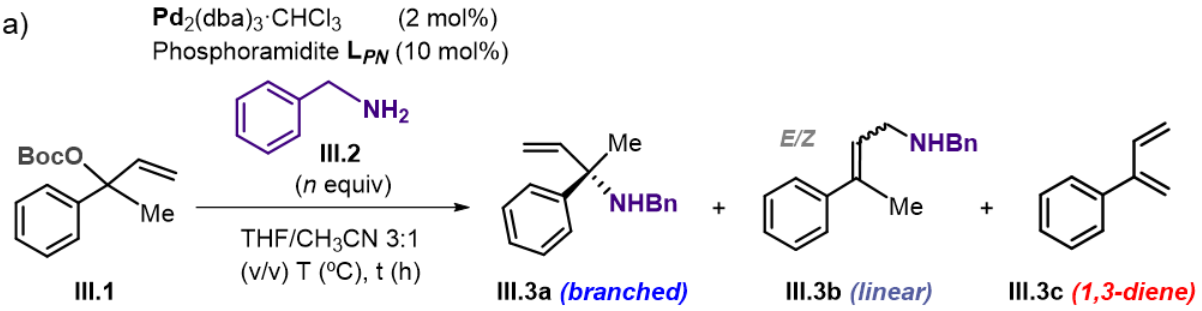

b)

Entry	T (º C)	Solvent[a]	$BnNH_2$ (equiv)	**3a** (%)[b]	**3b** (%)[b]	**3c** (%)[b]	**3a**:**3b**
1	20	THF/CH_3CN	1.1	58	7	35	8:1
2	**0**	**THF/CH_3CN**	**1.1**	**70**	**4**	**26**	**18:1**
3	20	THF	1.1	47	36	17	1.3:1
4[c]	0	THF	1.1	58	21	21	3:1
5	20	THF/CH_3CN	1.5	73	18	8	4:1
6	20	THF/CH_3CN	2.0	77	14	9	6:1

[a] For the mixtures, the v/v ratio was 3:1 (V = 0.35 mL). [b] Yield determined by ^1H NMR ($CDCl_3$) using mesitylene as internal standard. [c] Reaction time was 72 h.

c)

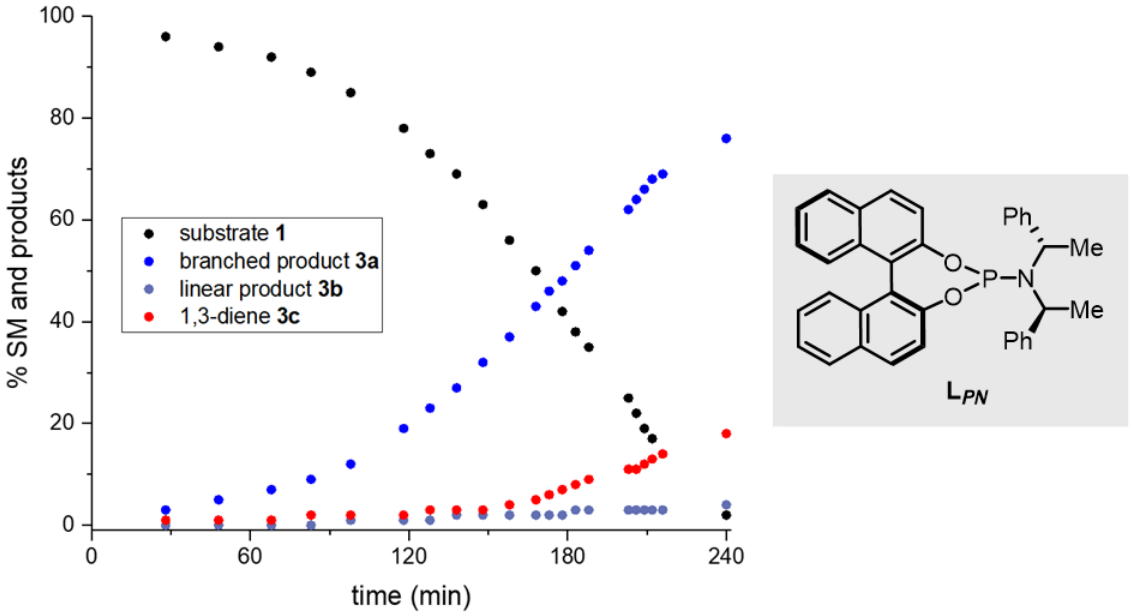

Figure 3.3: a) Reaction scheme of the Pd-catalyzed allylic amination reaction between carbonate **III.3** and benzyl amine **IIII.2** with all the identified products, b) **Table III.I**: Variation of reaction conditions (temperature, solvent mixture and equiv. of amine) and their effect on the chemo/regio-control and c) kinetic profile for the formation of **III.3a**, **III.3b** and **III.3c** under the reaction conditions at Entry 6 in the table under b).

In order to gather more kinetic data for our transformation, the orders in [Pd], [$\mathbf{L}_{PN}$], [substrate] and [nucleophile] were determined by variable time normalization analysis (VTNA) using experimental React-IR data (Figure 3.4).[89,90,144] This method allows for a reliable analysis of raw spectroscopic data and extracting the reaction orders of the whole kinetic profile (contrary to initial rates method, for instance) under synthetically relevant conditions. As may be expected, the order in [Pd] is close to 1 suggesting that the active catalyst in the rate-limiting step of the process is a monometallic species. Intriguingly, the order in phosphoramidite ligand $\mathbf{L}_{PN}$ was 1.5, whereas a virtually zero order dependence of the reaction rate were obtained for both substrate **III.1** and $BnNH_2$ (**III.2**). For the complete kinetic data set, please refer to section 3.6.2.

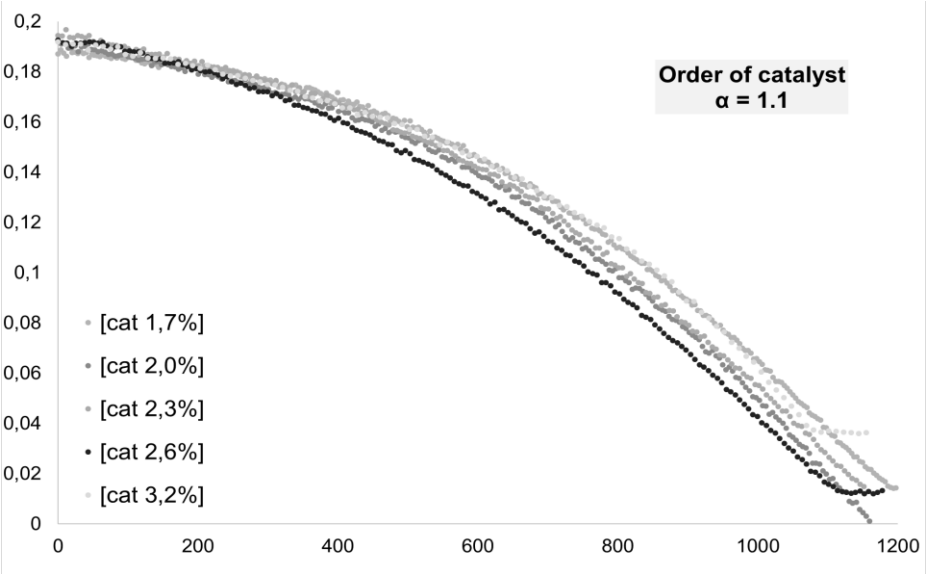

Figure 3.4 Selected data obtained from variable time normalization analysis (VTNA) of the kinetic data, and determined orders for [Pd].

3.3.2 Identification of Pd(0) species: Pre-catalysts characterization

To understand how the catalysis is initiated, the benchmark reaction was inspected spectroscopically. Taking advantage of the chiral P-ligand employed in this transformation, the catalysis reaction was monitored by $^{31}P\{^{1}H\}$ NMR at 20 ºC in a THF/MeCN mixture. With an initial 4 mol% catalyst loading we could already observe the formation of multiple species in the reaction mixture. At the initial stage of the catalysis, a first broad resonance was observed at 140 ppm. Consecutively, while the

[144] Nielsen, D.-T. C.; Burés, J. *Chem. Sci.* 2019, 10, 348.

reaction progresses, after ~60 min a second less intense resonance is observed upfield around 110 ppm (Figure 3.5). After 150 min, the resonances at 140 ppm have mostly disappeared while the one at 110 ppm is still observed. During the whole course of these measurements, the presence of free ligand **L*PN*** is observed at 151 ppm as a consequence of the 2.5-fold excess vs. the 1.0 equiv of Pd employed.

Interestingly, at the end of the reaction various Pd species are noted downfield (165-175 ppm), which are similar to the ones we observed by mixing Pd_2dba_3 and **L*PN*** in a 1:2.5 stoichiometry. We therefore ascribed these species to Pd(0) type resting states once the transformation has been completed. One of these Pd(0) is characterized by a singlet resonance around 170 ppm and a second major species is represented by a double doublet (~ 164.5 ppm).

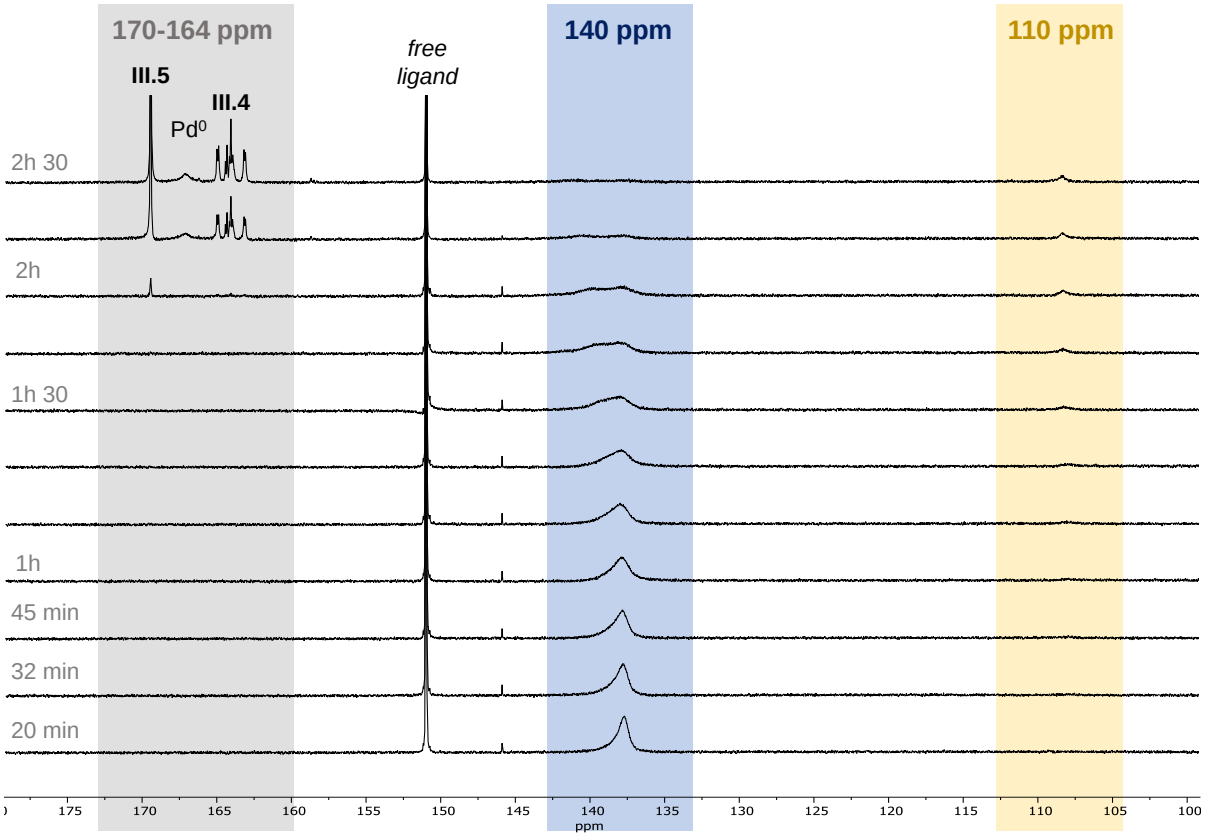

Figure 3.5: $^{31}P\{^{1}H\}$ NMR kinetic profile at 20 ºC (293 K) in a THF/MeCN (3:1, v/v) using $Pd_2(dba)_3{\cdot}CHCl_3$ (2 mol%), **L*PN*** (10 mol%), allylic carbonate **III.1** (1.0 equiv) and $BnNH_2$ **III.2** (1.1 equiv).

We then examined the influence of the Pd:**L*PN*** stoichiometry on the speciation of these Pd(0) complexes (Figure 3.6a). A higher amount of **L*PN*** results into a relatively higher amount of the species located at 170 ppm, reducing the amount of the species at 164.5 ppm. Another observation is that at a Pd:**L*PN*** ratio of 1:1 only the complex at 164 ppm is observed and no free **L*PN*** is noted. With these first indications, we already imagined that the ***dba*** ligand introduced by the $Pd_2(dba)_3$ precursor may play an important role in the complexation of Pd(0) with the chiral ligand **L*PN***. For this reason, further to the influence of **L*PN*** on the speciation, we added excess of dba (3 equiv) to NMR mixtures containing a Pd:**L*PN*** ratio of 2.5 and 1:5 (Figure 3.6b). In both cases, a clear decrease is observed in the relative amount of the species appearing at 170 ppm, indicating that the presence of additional ***dba*** has an opposite effect on the speciation compared to **L*PN***. Finally, a DOSY NMR evaluation of both Pd(0) species (see Figure 3.40 in section 3.6.3) suggested that (*i*) their molecular size is significantly larger than the free ligand **L*PN***, and that (*ii*) the doublet-based species (165 ppm) likely has a higher molecular weight than the species observed at 170 ppm.

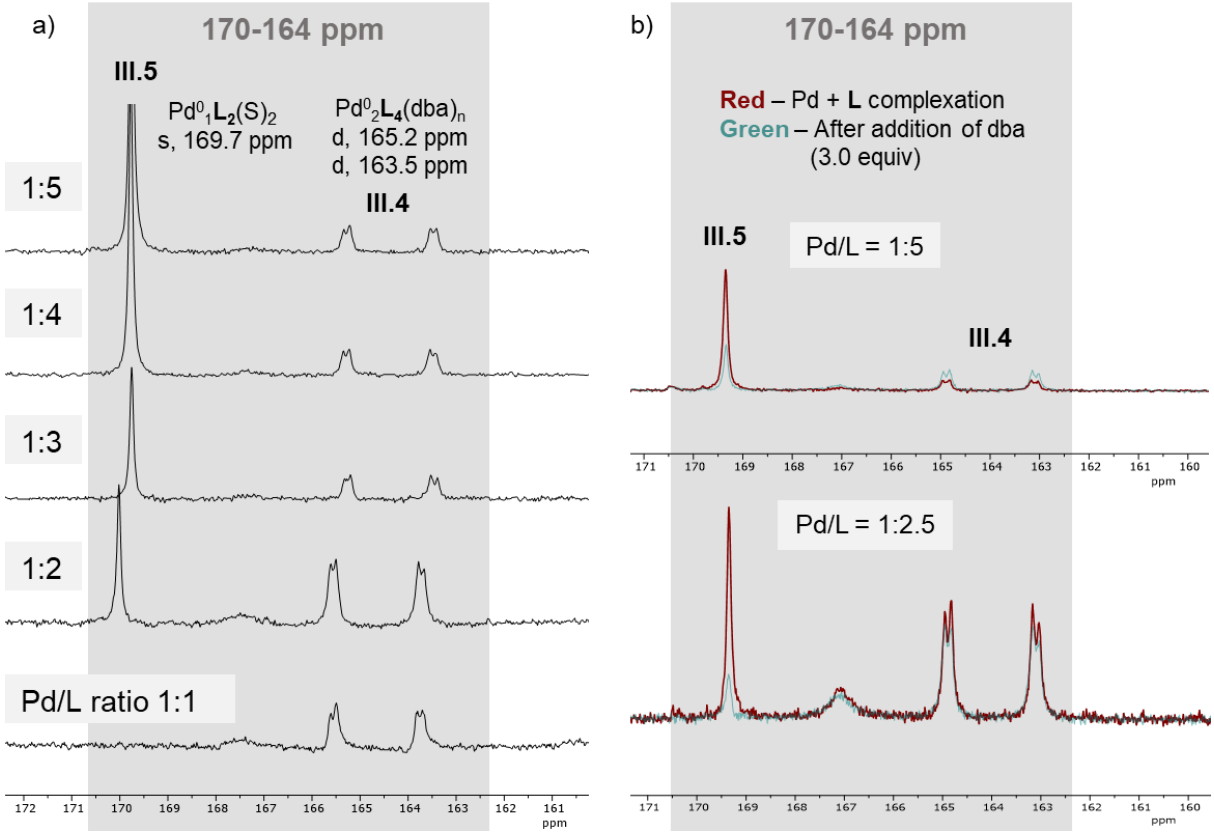

Figure 3.6: a) Influence of the Pd:**L*PN*** ratio on the Pd(0) speciation and b) Influence of ***dba*** on the Pd(0) speciation at two different Pd:**L*PN*** ratios.

In order to get further insights into the stoichiometry and the structure of the Pd(0) species, quantitative analysis of various ^{31}P NMR spectra at different Pd:**L*PN*** ratios was performed considering both the total concentration of Pd and **L*PN***, and their molar fractions (*X*). From these studies we extracted two major conclusions: (*i*) both Pd(0) species have a relative Pd:**L*PN*** ratio of 2, and (*ii*) the species at ~165 ppm is likely dinuclear (Pd_2) whereas the one appearing at ~170 ppm is a mononuclear complex (detailed calculations in section 3.6.7).

As mentioned above, the changes in the relative abundance of **III.4** and **III.5** (Figure 3.7) in the presence of larger excess of either **L*PN*** or *dba* suggests that **L*PN*** is competing for coordination to Pd with dba in a similar way as described previously by McIndoe[145] for the activation and aggregation of $Pd_2(dba)_3$ with phosphine ligands.[146] From our control experiments, calculations and prior observations we assigned the dinuclear **III.4** species to a $Pd_2(\mathbf{L_{PN}})_4(dba)_n$ complex (with n = 1 or 2) and mononuclear species **III.5** to $Pd(\mathbf{L_{PN}})_2S_2$ (with S being a solvent molecule) with equation 1 representing the relationship between $Pd_2(dba)_3$ and the other Pd(0) species.

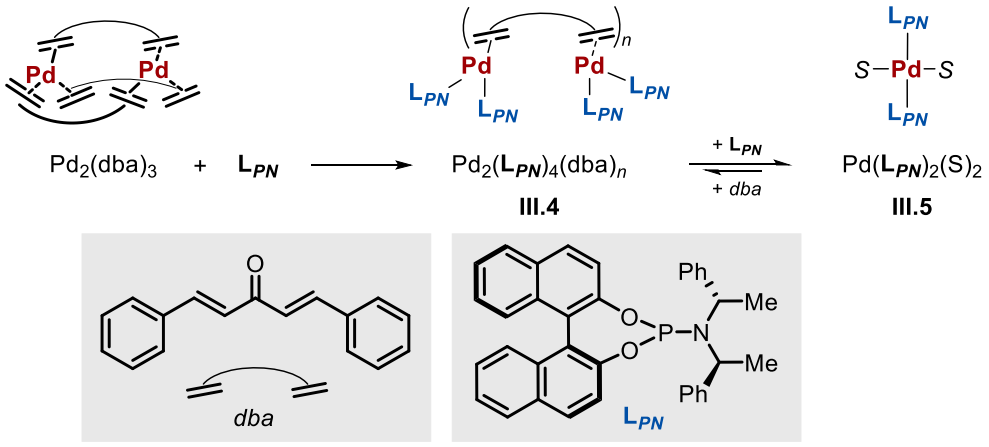

Figure 3.7: Proposed equilibrium of the Pd(0) complexes **III.4** and **III.5** upon complexation of $Pd_2(dba)_3$ with **L*PN***.

When $Pd_2(dba)_3$ and **L*PN*** are mixed in a 1:2 ratio, all the ligand **L*PN*** is consumed (Figure 3.35, section 3.6.3) and under these conditions almost exclusive formation of dinuclear $Pd_2(\mathbf{L_{PN}})_4(dba)_n$ **III.4** is noted. These conditions allowed to independently study the

[145] Janusson, E.; Zijlstra, H. S.; Nguyen, P. P. T.; MacGillivray, L.; Martelino, J.; McIndoe, J. S. *Chem. Commun*. 2017, 53, 854.
[146] A DOSY NMR evaluation of both Pd(0) species (see Figure 3.40 in Section 3.6.2) suggested that their molecular size is significantly larger than the free ligand **L*PN***.

activity of this dinuclear pre-catalyst. In addition, dba-free mononuclear Pd**L**$_2$S$_2$ **III.5** could be independently prepared (see Figure 3.41).

Both Pd(0) complexes were evaluated as pre-catalysts in the formation of products **III.3** from **III.1** and **III.2**, and their activity and efficiency was compared to the *in situ* prepared catalyst system previously reported by us (Table **III.II**). The first two entries of Table **III.II** show the catalytic performance of the original catalyst at 20 ºC (entry 1) and 0 ºC (entry 2). The pre-catalyst Pd$_2$(**L*PN***)$_4$(dba)$_n$ **III.4** appears to be slower and less selective compared to the original process performed at 20 ºC (entries 1 vs 3), especially when taking into account that it coexists with 50% unreacted Pd$_2$dba$_3$ under these conditions. Contrarily, dba-free, mononuclear complex Pd**L**$_2$S$_2$ **III.5** shows good activity with an enantiomeric ratio (*er*) similar to the benchmark conditions performed at 20 ºC (entries 1 vs 4). Furthermore, in this latter case we observed a singlet peak at 170 ppm at the end of the catalytic reaction, corresponding to Pd^0(**L*PN***)$_2$(S)$_2$ (**III.5**). The absence of Pd$_2$(**L*PN***)$_4$(dba)$_n$ (**III.4**) in the spectra confirms that the Pd(0) species at 170 ppm does not contain dba as a ligand (Figure 3.46 in section 3.6.3). The combined spectroscopic findings and the results listed in Table **III.II** points at a decelerating role of dba liberated *in situ* when an appropriate excess of **L*PN*** is added to Pd$_2$(dba)$_3$ forming Pd^0(**L*PN***)$_2$(S)$_2$ (**III.5**) as the dominant pre-catalytic species at the Pd(0) oxidation level.

Table **III.II**: Catalytic activity of various Pd(0) pre-catalysts derived from Pd$_2$(dba)$_3$ and **L*PN*** ratios. [a]Measured by ^{1}H NMR analysis. [b]The *er* values were determined by UPC2. [c]Original in situ prepared pre-catalyst at 20 ºC, see ref. *136b*. [d]T was set at 0 ºC. [e]In situ prepared dinuclear pre-catalyst **III.4** from a 1:1 Pd$_2$(dba)$_3$/**L*PN*** ratio. [f]*Dba*-free mononuclear **III.5** pre-catalyst Pd**L**$_2$S$_2$ synthesized independently. [g]Same amount of [Pd] present as in the other reactions.

Entry	t (h)	Pre-catalyst	Conv. (%)[a]	**III.3 a**:**b**:**c** (%)[a]	*er*[b]
1	8.5	*In situ* **Pd:**L*PN* (1/2.5)[c]	>99	79 : 9 : 12	91:9
2	12	*In situ* **Pd:**L*PN* (1/2.5)[d]	>99	70 : 4 : 26	95.5:4.5
3	8.5	**III.4**[e]	94	49 : 22 : 23	77:23
4	8.5	**III.5**[f]	>99	82 : 5 : 13	87:13
5	8.5	Pd$_2$dba$_3$[g]	>99	80 : 8 : 12	–

3.3.3 Identification of Pd(II) reaction intermediates

Once two potential reaction intermediates were identified, we examined the ^{31}P NMR region 105-145 ppm to understand how the mononuclear $Pd^0(\mathbf{L}_{\boldsymbol{PN}})_2(S)_2$ (**III.5**) species evolves upon addition of the reagents. We lowered the temperature of the NMR measurements to see if we could associate the initially observed broad signal to potentially equilibrating species.[147]

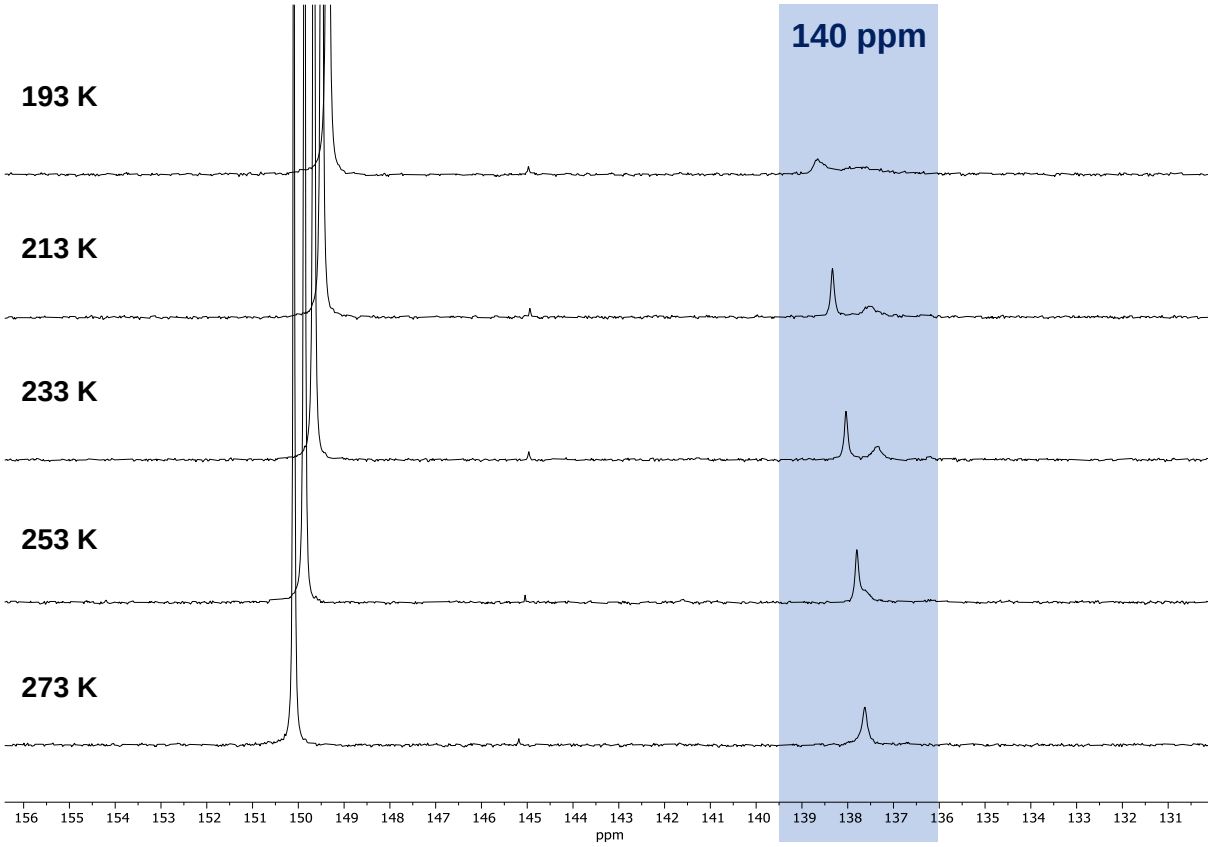

Figure 3.8: $^{31}P\{^1H\}$ NMR stacked spectra of low temperature measurements of the catalytic intermediate near 140 ppm in THF.

To facilitate the low temperature analysis, we used THF as the reaction solvent avoiding thus mixtures with MeCN. Decreasing the temperature from 293 to 213 K indeed allowed us to observe the splitting of the initially broad signal at 140 ppm into several peaks (Figure 3.8), which suggests the presence of equilibrating species. The presence of cross-peaks in the 2D EXSY $^{31}P\{^1H\}$ NMR confirmed this hypothesis (Figure 3.56, Section 3.6.3). With this data in hand, we assigned the two resonances to two mono-ligated interconverting Pd(II)(allyl) species, in accordance to previous

[147] DiRenzo, G. M.; White, P. S.; Brookhart, M. *J. Am. Chem. Soc*. 1996, 118, 6225.

NMR assignments by Pregosin, Albinati and co-workers on related Pd(allyl) phosphoramidite-coordinated species.[148]

After collecting these initial results, we wondered whether we could assign the intermediates at 140 and 110 ppm to particular species proposed in generally accepted mechanisms (Figure 1.10 Section 1.3.1). Hence, we envisioned that the displacement of the chemical shifts in these two intermediates would depend on the nature of the allylic substrate, the leaving group (LG) and the pro-nucleophile (amine) while performing the $^{31}P\{^{1}H\}$ NMR measurements at low temperature. As such, we would be able to determine which reagents are involved in the formation of both intermediates. We first focused the attention on the species appearing at 140 ppm as it is the first intermediate formed at the early stage of the catalysis.

[148] Filipuzzi, S.; Pregosin, P. S.; Albinati, A.; Rizzato, S. *Organometallics* 2006, 25, 5955.

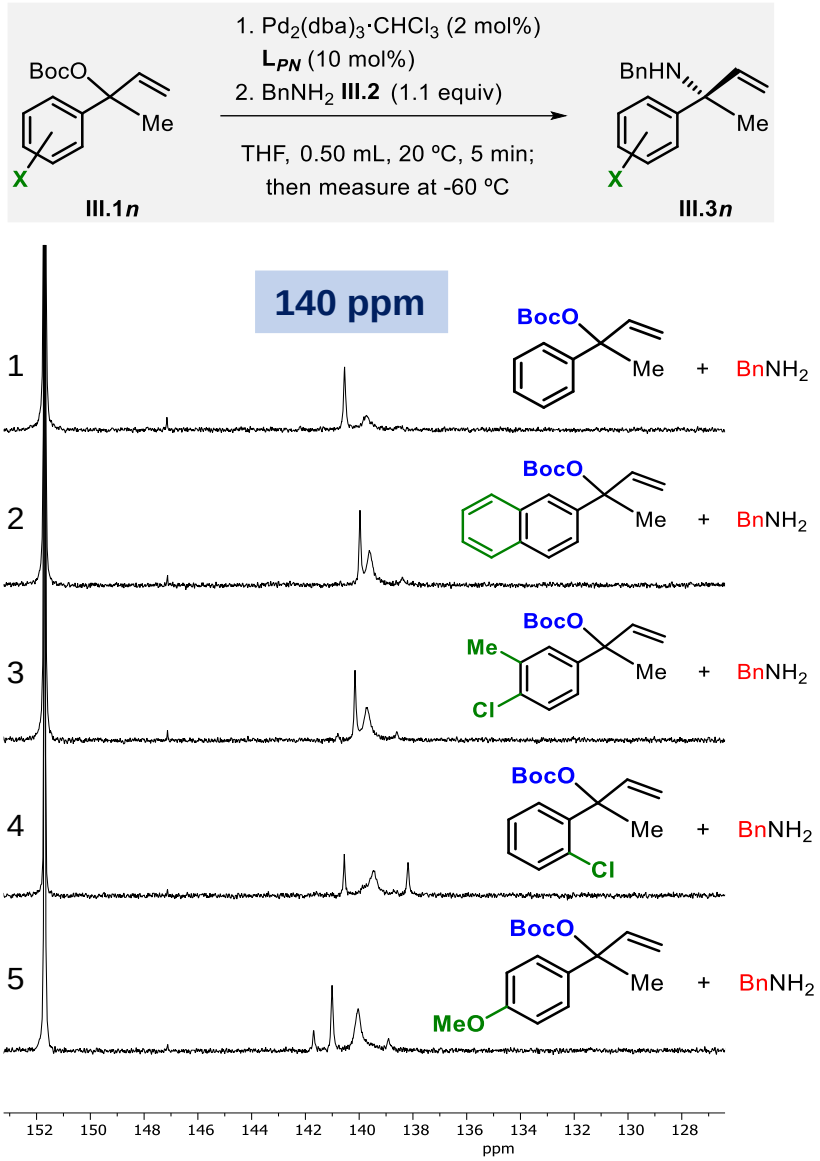

Figure 3.9: $^{31}P\{^{1}H\}$ NMR spectra at 213 K in THF of the catalytic intermediates around 140 ppm produced from ***differently substituted allylic substrate***.

We detected a clear relationship between the NMR features for the intermediate around 140 ppm and both the allylic substrate (Figure 3.9) and the nature of the LG (Figure 3.10, entry 4). Upon variation of the allylic species, different NMR populations were noted depending on the aryl substituents of the allylic substrate (entries 1-5). The nature of the LG (Figure 3.10, entry 4 vs entry 1) also affected, to some extent, the spectroscopic signature of the reaction mixture.

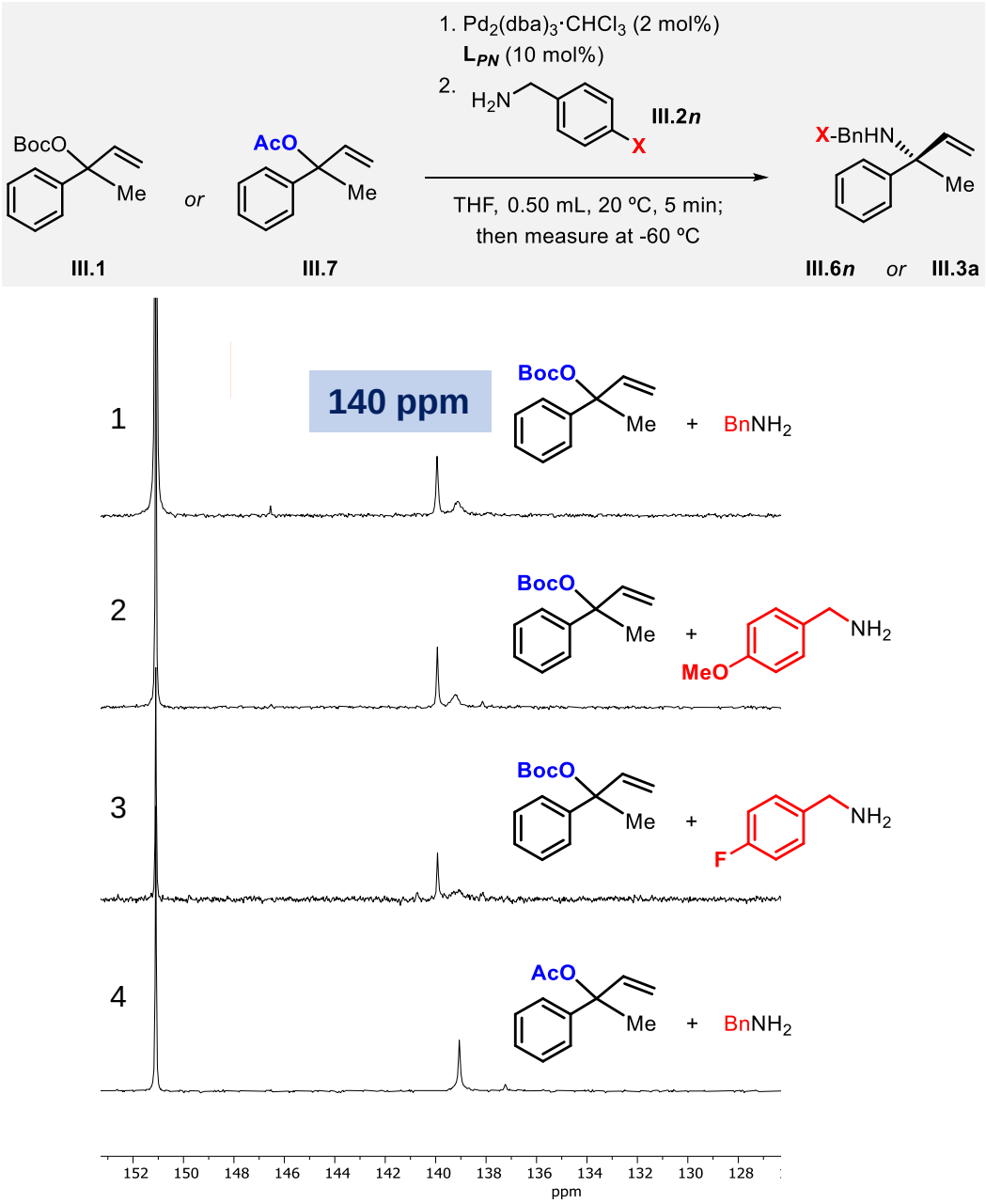

Figure 3.10: $^{31}P\{^{1}H\}$ NMR spectra at 213 K of the catalytic intermediate at 140 ppm varying **benzyl amine nucleophile** and the **leaving group** (LG) of the protected alcohol analysed in THF solvent.

These data suggest that the first intermediate observed in this catalytic transformation comprises an allyl unit and the leaving group as a counter anion. Importantly, no implication of the amine reagent is detected at this stage of the reaction.

At this stage, a molar quantification through ^{31}P NMR analysis was performed similarly to the one used for the Pd(0) species to deduce the equivalents of **L_{PN}** found in each of the Pd(II) species. Unexpectedly, these calculations revealed that both Pd(II)

species observed at 140 and 110 ppm are ligated by a single chiral ligand **L*PN*** (see *Quantification of coordinated ligand in Pd^0 precatalysts and Pd^{II} intermediates* in section 3.6.3 for details).

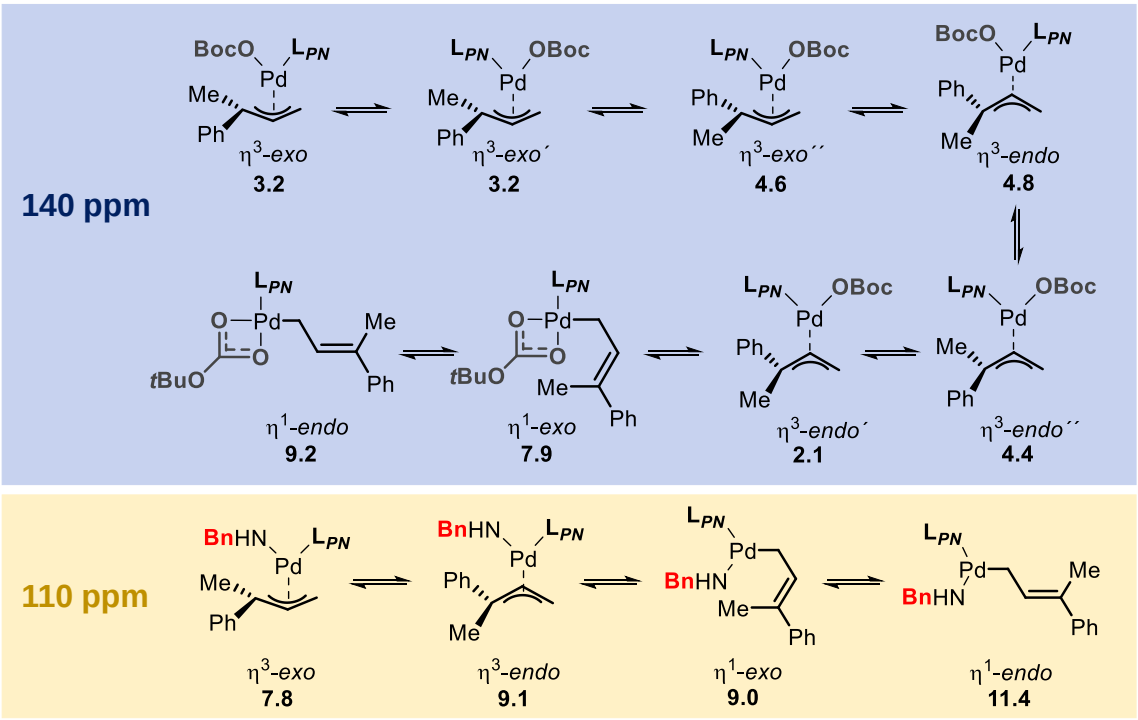

Figure 3.11: Calculated energies (in kcal/mol) of various *endo*/*exo* mono-ligated Pd species with either a □^{3}- or □^{1}-allyl coordination mode connected to the intermediate observed around 140 ppm (**blue**) and the one noted at around 110 ppm (**yellow**).

DFT calculations allowed us to gain further knowledge on which Pd(allyl)**L*PN*** species would be most stable, and both *endo*- and *exo*-isomers with a □^{3}-coordinating allyl group should be energetically most favored within a small range of energetic states between 2.1 to 4.8 kcal/mol (Figure 3.11). Altogether, these data are in line with the Pd(II) intermediate found around 140 ppm being the result of an oxidative addition of the allylic substrate to Pd(0) forming a Pd(II)allyl(**L*PN***) complex.[149] This conclusion is also in line with previous work reported by Pregosin on Pd-allylic complexes featuring phosphoramidite ligands.[150]

[149] We performed a stoichiometric reaction between Pd_2dba_3/**L*PN*** (1:2.5) and the substrate **III.1** in the absence of benzyl amine **III.2** to study the oxidative addition in more detail. The major product found under these conditions is the β-H elimination compound **III.3c**. Though we were unable to isolate Pd(allyl)(OBoc)**L*PN***, the outcome is in line with an oxidative addition step.

[150] a) Filipuzzi, S.; Pregosin, P. S.; Albinati, A.; Rizzato, S., *Organometallics* 2006, 25, 5955. b) Filipuzzi, S.; Pregosin, P. S.; Calhorda, M. J.; Costa, P. J. *Organometallics* 2008, 27, 2949.

Next, the intermediate observed at 110 ppm was studied following a similar strategy. It is worth noting that this second intermediate follows an opposite trend when the nature of the allylic substrate is varied (Figure 3.12) with no apparent influence on the chemical shifts of the species noted in this region.

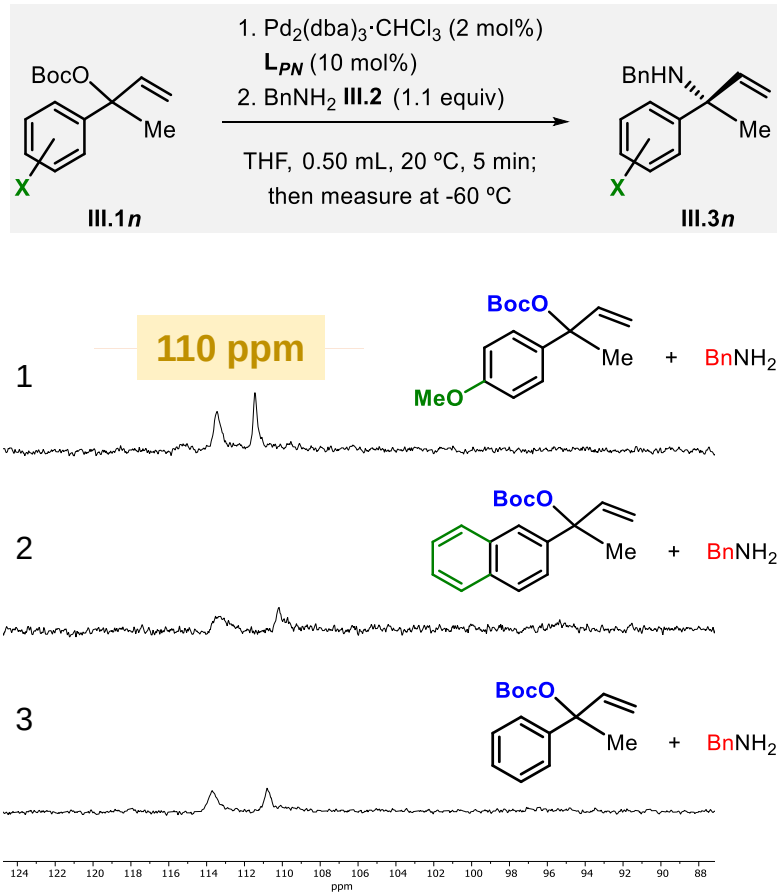

Figure 3.12: $^{31}P\{^{1}H\}$ NMR spectra at 213 K in THF of the catalytic intermediates around 110 ppm changing the **aryl substituent** in the allylic substrate.

However, in sharp contrast to the intermediate at 140 ppm, the nature of the pro-nucleophile does affect the chemical shifts of the equilibrating species at 110 ppm (Figure 3.13). This change is most pronounced in the case of *para*-methoxy-benzyl amine causing a □□ of about –16 ppm (only one peak observed, entry 2) compared to the reaction mixture containing benzyl amine.

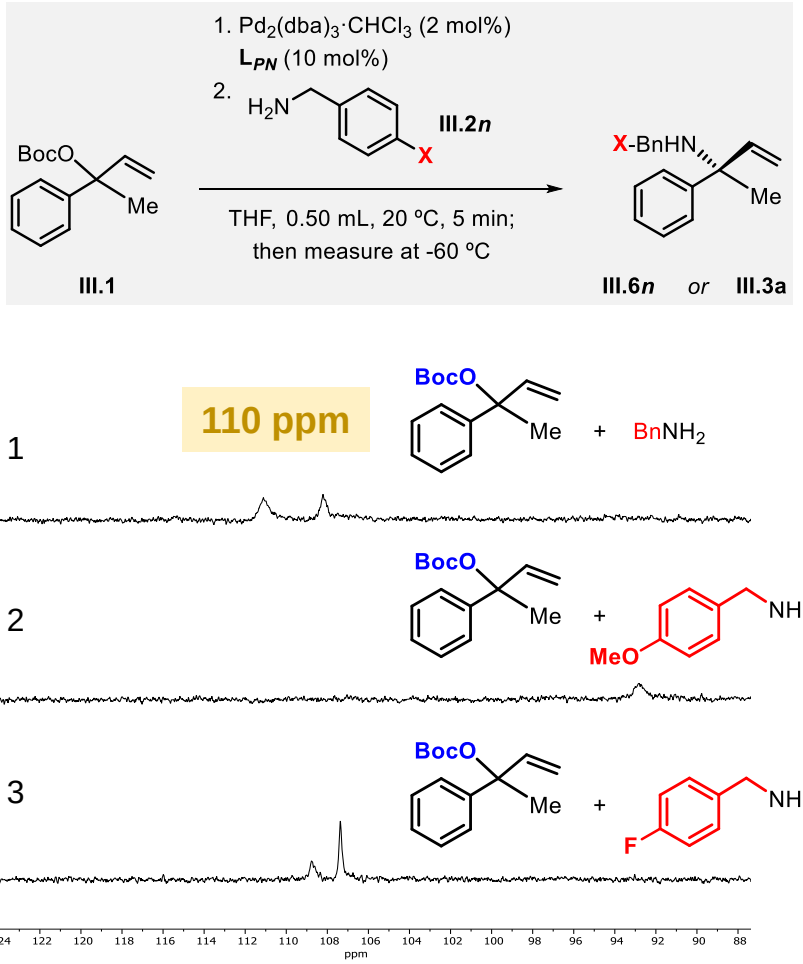

Figure 3.13: $^{31}P\{^{1}H\}$ NMR spectra at 213 K of the catalytic intermediate at 110 ppm monitoring the shift of intermediate located in the range 110-115 ppm in the presence of **different benzyl amines** in THF.

These latter results suggest the coordination of the nucleophile to Pd for the species around 110 ppm, as the substituent of the amine would directly perturb the ^{31}P NMR chemical shift of the phosphorous (a **BnHN**-Pd-L_{PN} species is implied). This experimental observation is a clear and unique piece of evidence that points towards an inner sphere mechanism prior to C–N bond formation via reductive elimination and product release from the Pd complex.

Another aspect that is worth mentioning is that during IR-monitoring of the catalytic reaction, the CO_2 band at 2340 cm^{-1} was not observed when the LG of the allylic substrate was acetate (substrate **III.7**), confirming that decarboxylation is not crucial towards the formation of the first intermediate around 140 ppm. This illustrates that the

first intermediate is part of an initial regime that is followed by decarboxylation as calculated in Figure 3.14, and a second regime relates to C–N bond formation.

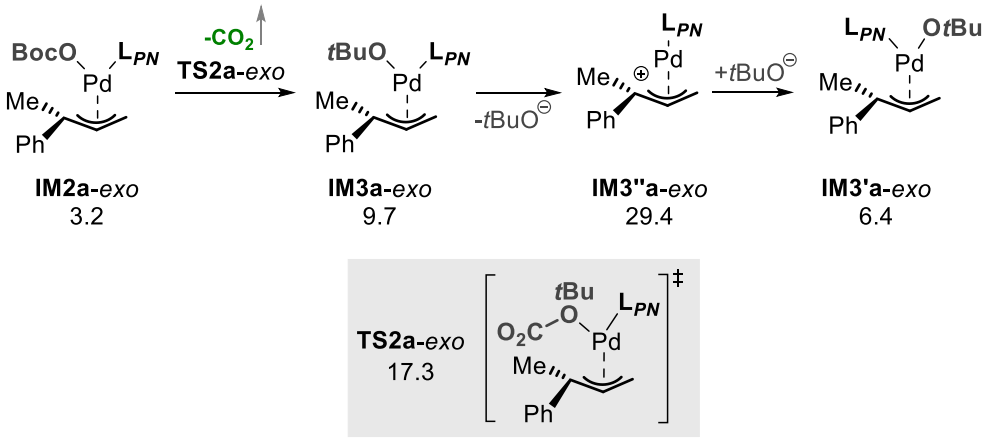

Figure 3.14: Computed decarboxylation of a selected η^3-allyl-Pd(OBoc) species delivering a *t*BuO-ligated complex. All reported energies are in kcal/mol.

Further experimental evidence for the presence of Pd**L*PN***(allyl) species could be obtained using high resolution ESI(+)-HRMS analysis of a catalytic reaction mixture (Figure 3.15). Apart from the identification of a cationic Pd**L*PN***(allyl) species with *m/z* = 776.1878 (calcd. 776.1909; after loss of the OBoc group), also an amine-coordinated Pd(allyl)(BnNH) complex with an *m/z* of 882.0968 (calcd. 882.2566) was observed.[151] The latter can be regarded as an intermediate prior to deprotonation of the amine by *tert*-butoxide, and subsequent formation of the amide complex Pd^{II}(allyl)(NHBn)**L*PN***.

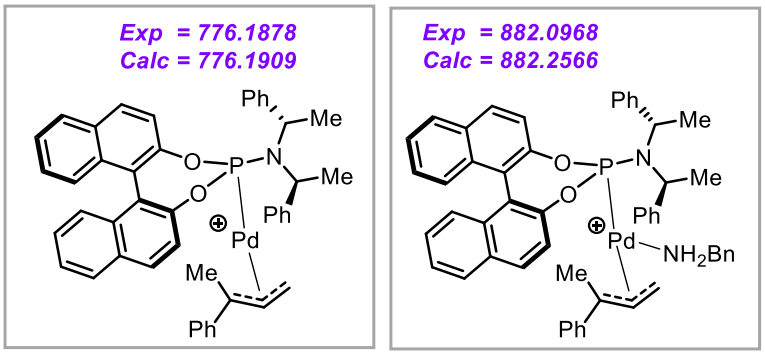

Figure 3.15: Proposed Pd-intermediates detected by ESI(+)-HRMS reminiscent of intermediate 140 ppm (left) and intermediate 110 ppm (right).

[151] These two observed Pd(allyl) species should relate to the first intermediate after loss of the OBoc group and prior to amine deprotonation/activation by O*t*Bu (the ligand exchange).

After collection of the results from the spectroscopic studies, we make the following notions:

(i) The two different intermediates spotted by $^{31}P\{^{1}H\}$ NMR are believed to be equilibrating allylic species.

(ii) The one at 140 ppm ought to be the result of an OA of allylic substrate **III.1** to Pd(0)**L*PN*** generating an intermediate that follows a ligand exchange.

(iii) This ligand exchange is relatively easy as it involves an irreversible decarboxylation step.

(iv) The second intermediate around 110 ppm in the $^{31}P\{^{1}H\}$ NMR should relate to a species existing before the C–N bond formation through an inner-sphere attack.

(v) According to the ^{31}P NMR studies, there are two distinct stages for this catalytic event. A first one, during which we can observe a build-up of a Pd(allyl) species around 140 ppm, and second stage in which the intermediate at 140 ppm is gradually consumed while a second Pd(allyl) complex emerges around 110 ppm and more rapid product formation occurs.

At this point, we checked if this latter observation (*v*) could be explained due to a product-enhancement of the catalytic process, as the kinetic profile suggests an induction period (Figure 3.3c and Figure 3.16 left). Contrarily, when we added enantio-pure branched product **III.3a** as an additive in the reaction, the catalysis rate was slightly lower. The occurrence of an induction period during which a Pd(II)(allyl)(OBoc) species is formed made us consider the possibility that autocatalytic species could enhancing the substrate conversion rate. Envisioning that the next step would be related to the decarboxylation of the OBoc anion, we tried to use additives to see if the initial rate could be enhanced. However, using 10 mol% of *t*BuOK or adding 10 mol% of *t*BuOH did not improve the initial rate. When 1.5 equiv of benzyl amine were used, the curve flattened but the overall rate of the reaction did not increase (Figure 3.16, right). This aligns well with the observed nearly zero-order dependence of the rate on the concentration of benzyl amine **III.2**. Interestingly, in the presence of this larger excess of **III.2**, the chemo-selectivity of the process improves (Figure 3.3b, entry 5) minimizing undesired hydride-elimination.

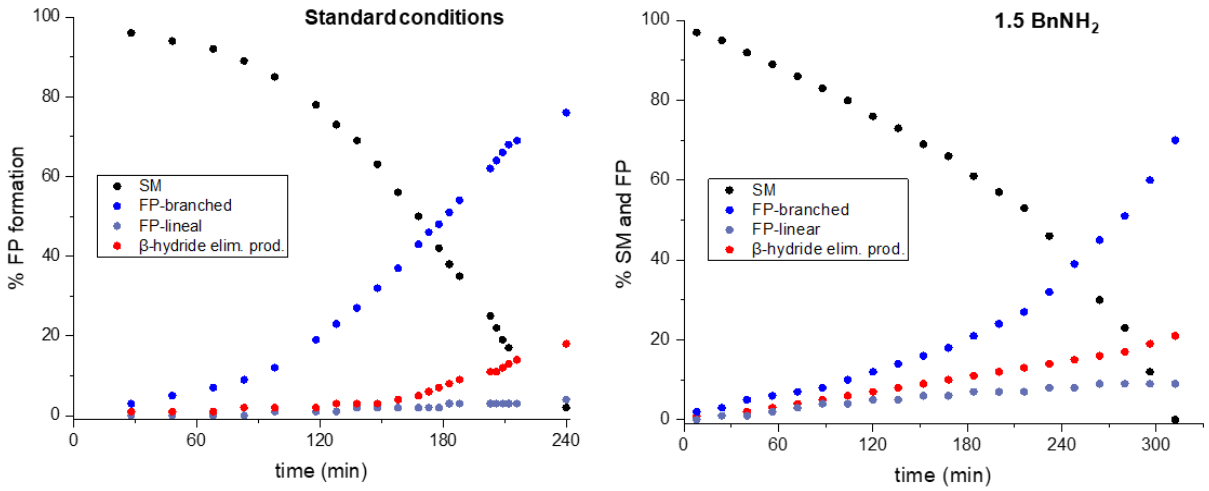

Figure 3.16: ^{1}H NMR kinetic profiles of standard conditions at 20 ºC vs. the addition of 1.5 equiv. of benzyl amine.

3.3.4 Role of MeCN co-solvent in Pd(II)(allyl)(OBoc) speciation

After the identification of key Pd(II)(allyl) catalytic intermediates, our efforts were directed to understanding the role of MeCN and specifically towards control over (*i*) the regio-selectivity between branched **III.3a** and linear **III.3b** allylic amine products, and (*ii*) the overall rate of the catalysis and how the speciation of the identified resting states might be affected by the solvent medium. Important in this context are the following observations:

(i) In Figure 3.3b, entries 3 and 4 illustrate the loss of regio-selectivity in the absence of MeCN.

(ii) If we compare Figure 3.5 with Figures 3.60 and 3.61 in section 3.6.3, it can be observed that the presence of MeCN drastically increases the rate of the reaction.

First, the intermediate at 140 ppm was analyzed at 233 K by ^{31}P{^{1}H} NMR using different ratios of a THF/MeCN solvent mixture (Figure 3.17).[152] The distribution of the Pd^{II}(allyl)(OBoc) species clearly varies according to the solvent mixture used. As observed in the section above, the intermediate around 140 ppm features two broad peaks in THF, with the left one (139.5 ppm) being more populated than the minor peak

[152] Low-temperature experiments were re-optimized to 233 K for ^{31}P{^{1}H} NMR measurements with a 3:1 (v/v) THF/MeCN solvent mixture.

at the right (138.9 ppm, Figure 3.17 entry 5).To our surprise, the use of THF/MeCN solvent combinations with an increased amount of MeCN inverting the population of these species. A low relative amount of this co-solvent (40 mol% of MeCN with respect to the Pd catalyst) does not change the distribution (entries 4 vs 5), but higher amounts of acetonitrile influence the equilibration between Pd^{II}(allyl)(OBoc) species (entries 1-3). These first results show how the polarity of the solvent can influence the population of these allylic species likely through solvation effects. The direct coordination of MeCN to Pd is discarded as no observable effect is noted between entries 1 and 2 in Figure 3.17, retaining a rather similar distribution of the two species in the region around 140 ppm.

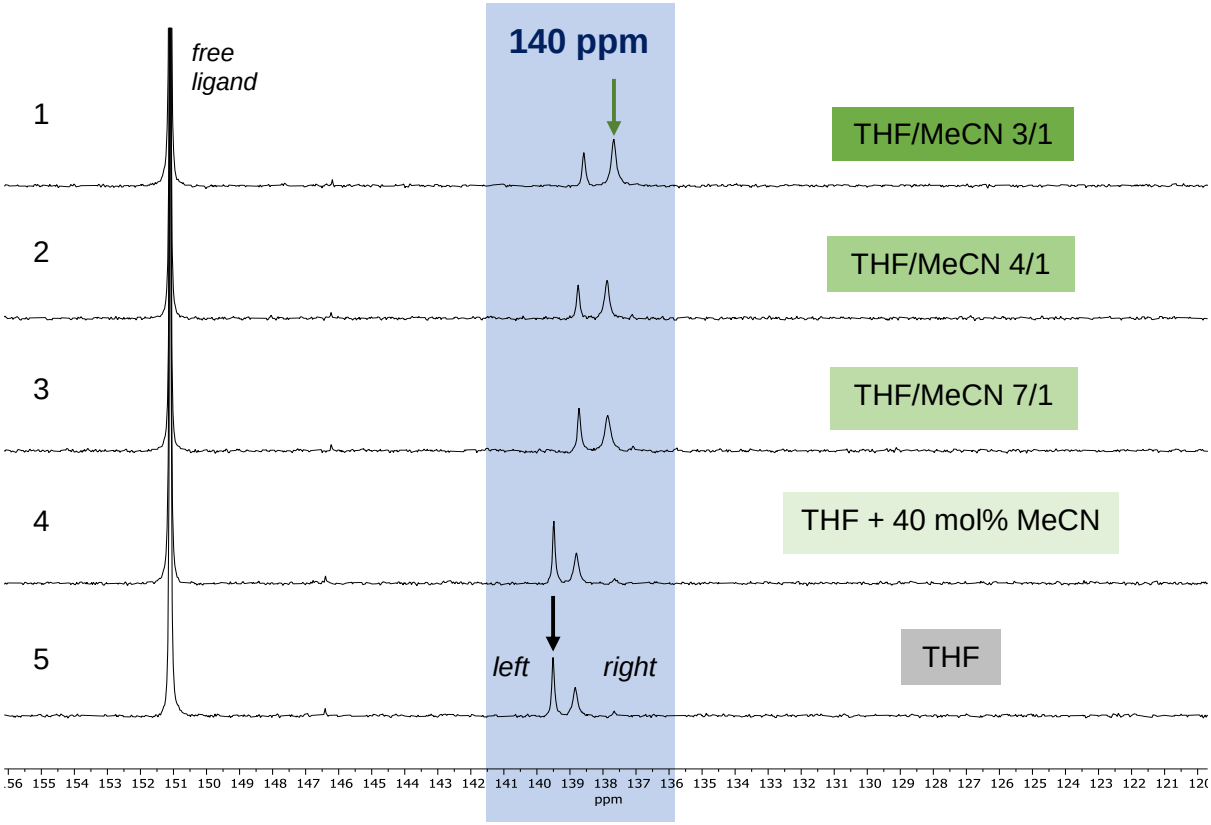

Figure 3.17: $^{31}P\{^{1}H\}$ NMR spectra of the intermediates at 140 ppm measured at 233 K at different ratios (v/v) of THF/MeCN. In all cases, the Pd/**L*PN*** ratio =1/2.5.

Next, the consumption of these intermediates around 140 ppm was measured by ^{31}P NMR preparing two different catalytic samples in different media: THF vs. THF/MeCN (3:1 v/v). The NMR measurements were done at 233 K every 30-60 min, while the reaction mixtures were allowed the react at 293 K (20ºC) in-between measurements. Curiously, both experiments show that the peak that is consumed at a higher rate is

the peak at the right (Figure 3.18 and 3.19, **red arrow**). In the first case, using THF, the minor peak is consumed at a higher rate while the second Pd(allyl) intermediate at 110 ppm appears as the reaction advances (Figure 3.18 entries 1-4, **red arrow**). Similarly, in a THF/MeCN mixture, the major species at the right disappears faster compared to the peak at the left (Figure 3.19 entries 1-4, **red arrow**).

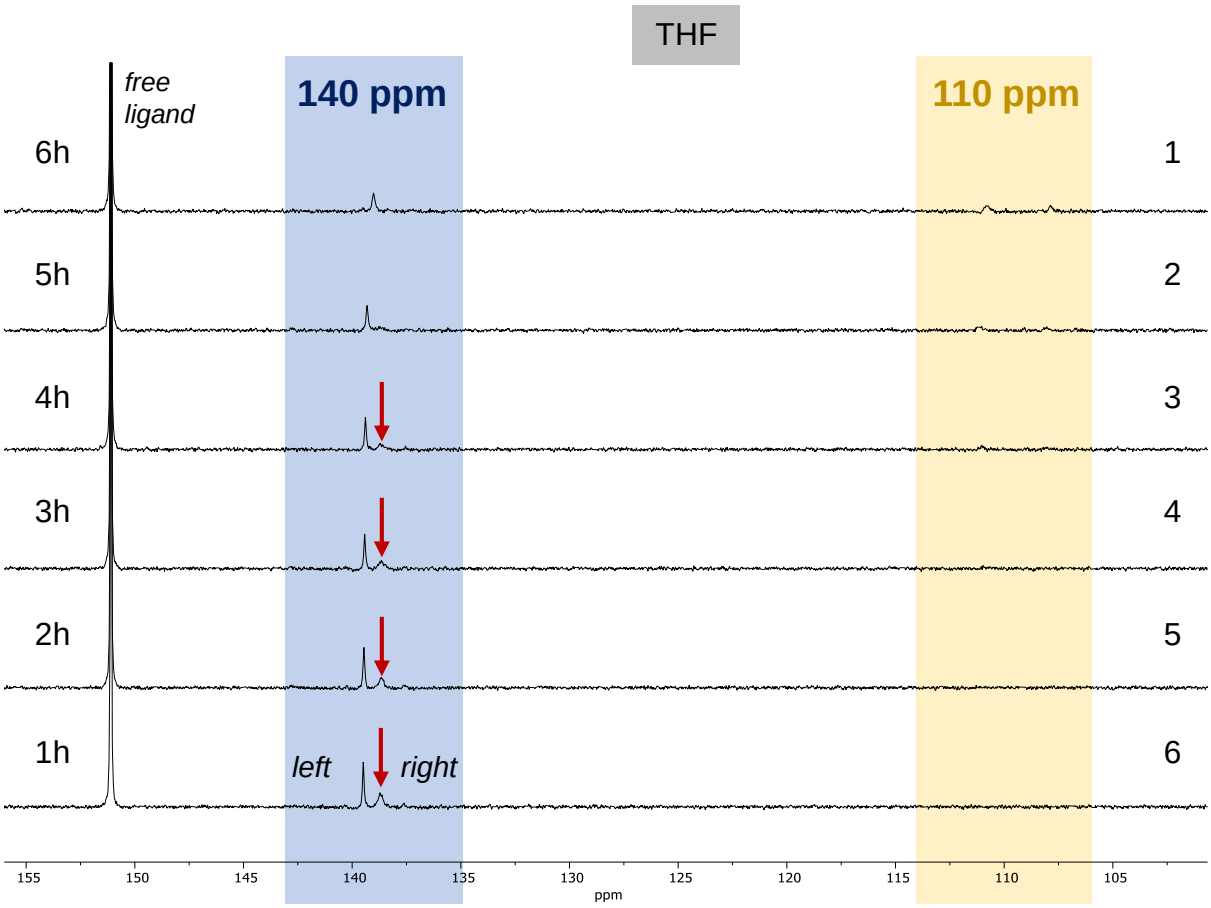

Figure 3.18: $^{31}P\{^{1}H\}$ NMR spectral monitoring at 213 K of the evolution of intermediates around 140 ppm in THF. In all cases, the Pd/**L*PN*** ratio =1/2.5.

We therefore note here that MeCN solvation effects offer an advantage for the overall catalytic process by favouring the presence of a more reactive Pd^{II}(allyl)(OBoc) intermediate (140 ppm) allowing faster decarboxylation and thus accelerates the initial rate of the transformation.

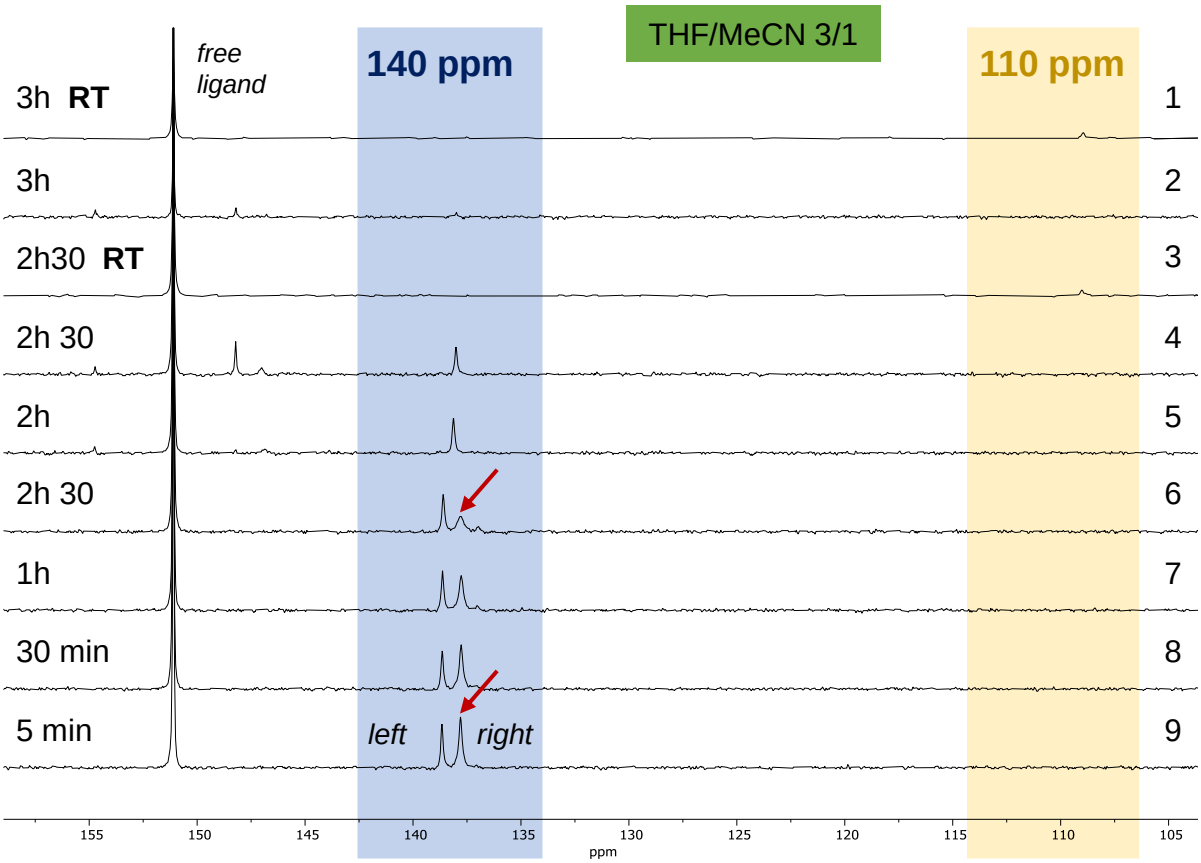

Figure 3.19: $^{31}P\{^{1}H\}$ NMR analysis at 233 K monitoring the evolution of the intermediates around 140 ppm using THF/MeCN (3:1, v/v). **RT** here means 293 K. In all experiments, the Pd:**L*PN*** ratio was 1:5. Entries 1 and 3 were NMR experiments measured at RT.

This section demonstrates that the polarity of the solvent can influence the population of the different allylic intermediates that are in equilibrium during the first stage of the catalytic process (intermediates around 140 ppm). Although MeCN has apparently a key role by reducing the induction period of the reaction, this co-solvent is not thought to exert this influence by coordination to Pd. This clarification is important, as the use of implicit solvent was initially considered as an input for our computational model (*vide infra*). Several computational trials were conducted using MeCN as a coordinating solvent in key steps, but the direct coordination of acetonitrile was discarded as it actually destabilized the involved species increasing their free energy. In the following sections, various DFT computations are presented using a solvent mixture of THF/MeCN (3:1, v/v) as an explicit solvent medium.

3.3.5 Origin of non-linear effects

Knowing that the complexity of our catalytic system is fairly high judging from the first part of this experimental chapter, we were determined to gather more experimental evidence for the enantio-determining step before setting up a DFT model. More precisely, we wanted to ensure the number of ligands (**L*PN***) present in our catalytic species during the enantio-selective step of the process.

We started to investigate the Pd**L*PN***(II) species formed during the C–N bond formation and initially explored a possible non-linear effect (NLE) in our catalytic system. By variation of the *ee* of the ligand **L*PN*** and monitoring the *ee* of the product **III.3a**, we determined a clear and strong positive NLE for this transformation (Figure 3.20a, red trace).[153] As we observed an unexpected order in [**L*PN***] of 1.5 during the kinetic studies (Figure 3.27 in section 3.6.2), we wondered whether this dependency could be connected to the experimentally observed NLE. Increasing the relative amount of **L*PN*** (Pd:**L** increased from 1:2.5 to 1:5, blue trace in Figure 3.20a) did not provoke any substantial change in the observed NLE.

The overall rate of the reaction proved to be dependent on whether enantio-enriched **L*PN*** or (*rac*)-**L*PN*** was present (Figure 3.20b), with a much faster rate observed in the presence of either enantiomer of the chiral ligand. At the same time, we noted that ^{31}P NMR comparison between mixtures containing either chiral **L*PN*** (**L*SSS***) or (*rac*)-**L*PN*** (Figure 3.20c; **L*RRR***:**L*SSS*** = 1) displayed different speciation behavior for the Pd(0) complexes. In the case of the chiral ligand, a clear preference exists for mononuclear Pd**L**$_2$S$_2$ isomer (singlet resonance) whereas the presence of (*rac*)-**L*PN*** causes the mononuclear versus dinuclear ratio to shift in favor of hetero-chiral Pd$_2$(**L*PN***)$_4$(dba)$_n$. The observed higher preference for more stable racemic dinuclear complex converges well with the lower catalytic activity (Figure 3.20b) and the lower efficiency noted in Table **III.I** entry 3 (Figure 3.3b). We thus explain the positive NLE in the formation of branched allylic amine product **III.3a** by the formation of more stable and thus less

[153] In our previous work, we used vinyl cyclic carbonates as allylic precursors giving rise to Pd(allyl) intermediates with a potentially *N,O*-chelating framework which could facilitate a more easy oxidative addition step from mononuclear Pd(0) to Pd(II). This may explain the much weaker NLE observed in these cases being competitive with respect to the ligation of dba originating from the Pd$_2$(dba)$_3$ precursor. See reference.138d

active hetero-chiral Pd^0_2 species (see Figure 3.20b) enriching the solution with the more active, homo-chiral mononuclear Pd^0 species.

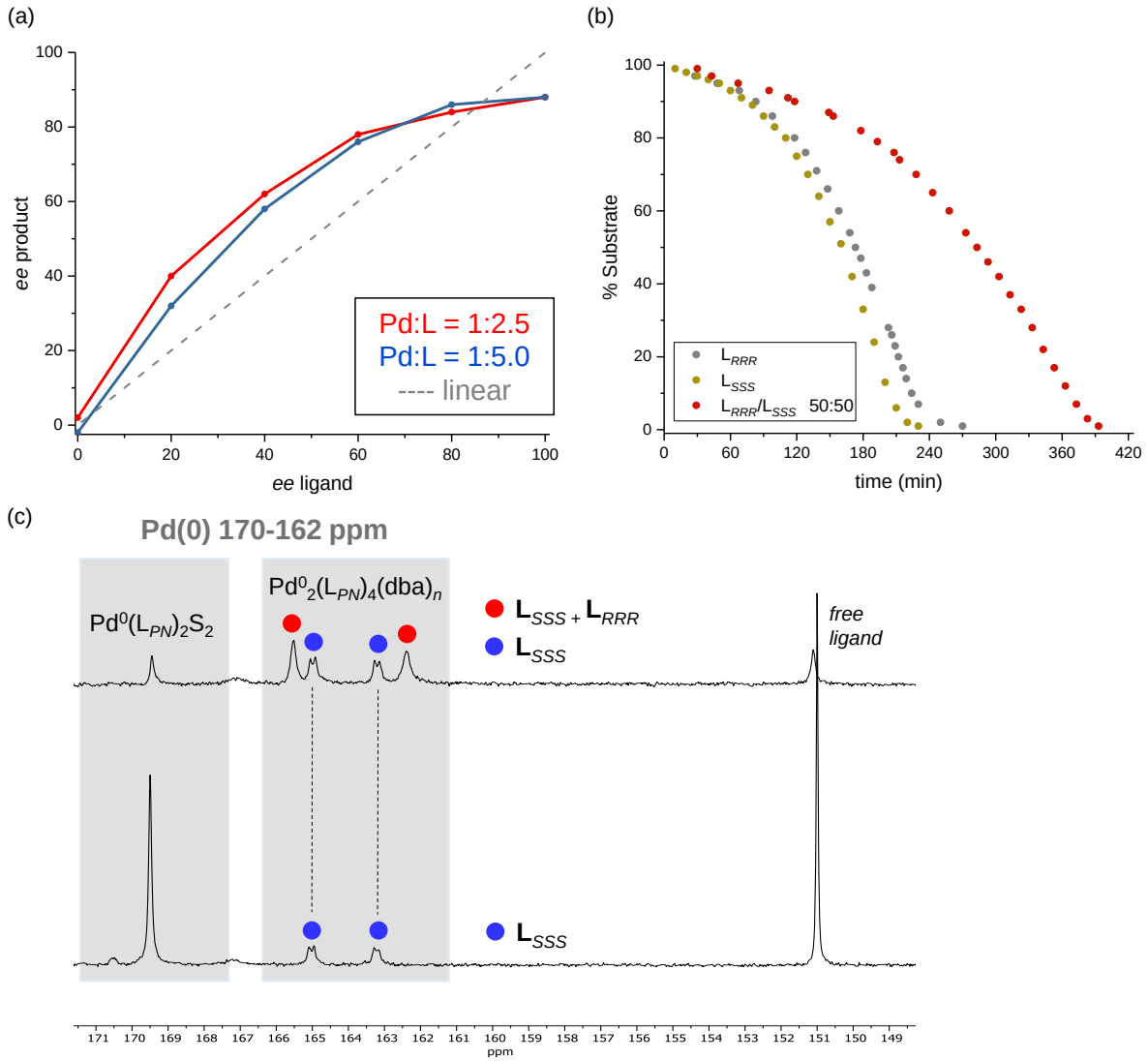

Figure 3.20. a) Observed NLE in the conversion of **III.1** into allylic amine **III.3a** at two different Pd:**L*PN*** ratios, b) rate enhancement while comparing (*rac*) and both enantiomers of chiral **L*PN*** and c) speciation of stereoisomers of dinuclear Pd_2(**L*PN***)$_4$(dba)$_n$ depending on the presence of (*rac*) or chiral **L*PN*** in THF/MeCN (3:1) at 20 ºC using a Pd:**L*PN*** ratio of 1:2.5.

We then scrutinized the effect of adding a larger excess of **L*PN*** by following in time the evolution of both Pd(allyl) species around 140 and 110 ppm through ^{31}P NMR (THF, 20 ºC; see Figures 3.60 and 3.61 in section 3.6.3). The rate of the reaction in the presence of a larger excess of **L*PN*** (Pd:**L*PN*** = 1:5) is significantly higher with faster

consumption of the first Pd(allyl) intermediate ~140 ppm and more pronounced population of the second one around 110 ppm.[154]

Knowing that the excess of chiral ligand does not influence the enantio-selectivity of our reaction and that only an initial saturation of **L*PN*** is needed for the pre-activation of Pd(0) species, we continued our mechanistic study with a DFT approximation of our catalytic cycle where Pd(0) species generally bear 2 equivalents of **L*PN*** while activated Pd(II) species coordinate a single molecule of phosphoramidite **L*PN***.

[154] After 9 h, we could observe both mononuclear (major) and dinuclear (traces) Pd(0) resting states suggesting that most of the allylic carbonate substrate had been consumed. At the end of the reaction, these Pd(0) complexes should be competing with substrate binding at Pd(0) after reductive elimination and prior to the next turnover starting with oxidative addition.

3.4 Computational analysis of the catalytic cycle

3.3.4 Productive cycle

The computed manifold begins with the coordination of substrate **III.1** to Pd(0) giving **IM1a**-*endo* located at -3.2 kcal/mol and follows with the oxidative addition step through **TS1a**-*endo* (+7.7 kcal/mol) delivering **IM2a**-*endo* at 5.8 kcal/mol as pictured in Figure 3.21, which summarizes the lowest calculated energy pathway (more details are provided in section 3.6.7). The OBoc anion can switch position within *endo*- and *exo*-Pd(allyl)(OBoc)**L*PN***, with the latter being most competitive (**IM2a**-*exo*, 3.2 kcal/mol). In this computationally-based mechanistic proposal, decarboxylation occurs (**RDS1**, +20.5 kcal/mol) delivering the *t*BuO-ligated intermediate **IM3a**-*exo* (9.7 kcal/mol), which in the absence of a suitable nucleophile can undergo hydride-elimination towards formation of 1,3-diene **III.3c**. The extrusion of CO_2 (**TS2a**-*exo*, +17.3 kcal/mol; as observed by time-dependent React-IR analysis) disables the whole manifold from reversibility. The separation of the two regimes into a pre- and post-CO_2 extrusion phase can now explain the experimental detection of two resting states at the same time. In the pre-CO_2 extrusion phase, **IM2a** clearly represents the first observed Pd(allyl) intermediate observed at ~140 ppm by ^{31}P NMR monitoring of the catalytic mixture. The manifold continues (post-CO_2 extrusion phase) by activation of the amine **III.2** via **TS3a**-*exo* being 8.4 kcal/mol above **IM3a**-*exo* and produces the amide-based Pd(allyl)(NHBn)**L*PN*** complex **IM4a**-*exo* (+7.8 kcal/mol) while delivering *t*BuOH as an observed by-product as identified by time-dependent NMR analysis (see Figure 3.31 in section 3.6.3). The η^3-to-η^1 isomerization of the Pd(allyl) intermediate **IM4a**-*exo* (considered as the second observable intermediate by ^{31}P NMR at around 110 ppm) results into **IM5a**-*exo* setting the system up for C–N bond formation through (*S*)-**TS4** (+24.0 kcal/mol). This latter step has a barrier of 16.2 kcal/mol being the RDS of the second independent kinetic regime (**RDS2**). To finalize the turnover, substrate **III.1** and **L*PN*** replace the coordinated product **III.3a** (**IM6**) in the coordination sphere and this regenerates **IM1a**-*endo*.

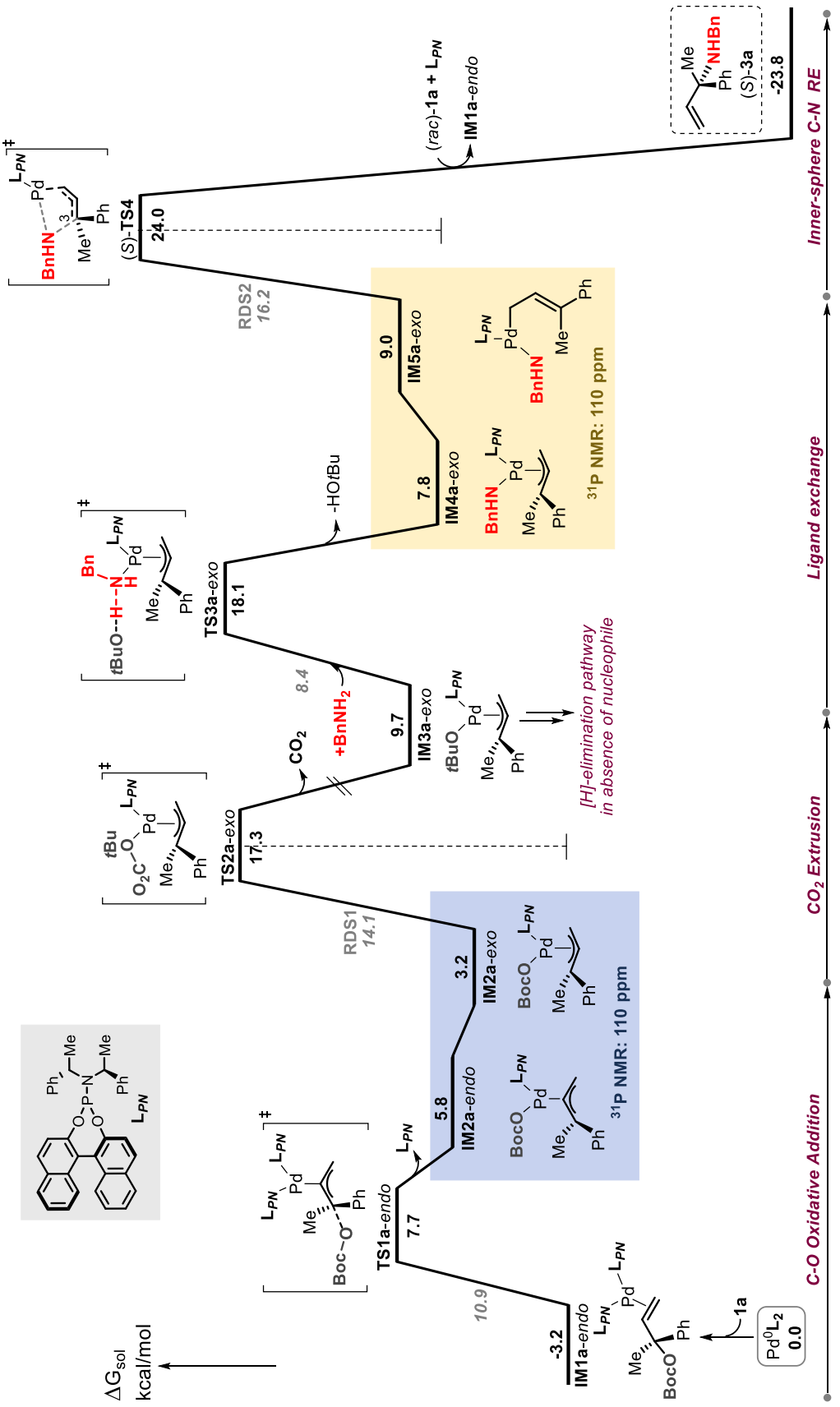

Figure 3.21: DFT computed profile for the catalytic formation of (*S*)-**III.3a** through an inner-sphere mechanism. All energies are given in kcal/mol. Note that the energy

barrier of the C–N reductive elimination was calculated relative to the lowest energy intermediate **IM4a**-*exo* instead of **IM1a**-*endo*, since the CO_2 extrusion is irreversible. Highlighted in the rectangles are the proposed intermediates to be linked with the ones observed by ^{31}P NMR.

A rationalization for the observed experimental regio-isomeric preference for the formation of (*S*)-**III.3a** could be provided by comparing the energetic spans for linear and branched allylic amine formation departing from **IM4a**-*endo* or **IM4a**-*exo* (Figure 3.22) and describing essentially the last phase of the inner sphere C–N formation process. Under the original experimental conditions (0 ºC, 12-36 h) equilibration between the initial states of the Pd(allyl)(NHBn)**L*PN*** complexes (*endo*/*exo* forms, barrier for their interconversion being 11.8 kcal/mol) should be considerably feasible and therefore a total of 4 pathways were completed. Starting from **IM4a**-*exo*, it can be seen that formation of branched allylic amine product (*S*)-**III.3a** is more favored compared to linear product *E*-**III.3b** judging from the barriers involved (16.2 versus 23.4 kcal/mol). This seems predictable considering the requirement for a sterically disfavored intermediate having the metal center connected at the internal carbon center (*E*-**TS5a**) leading to C_1-amination. For **IM4a**-*endo*, a similar relationship is found for the pathways leading to either *E*-**III.3b** and *R*-**III.3a**, with barriers of 20.3 and 18.0 kcal/mol, respectively. From all these data we can infer that the pathway leading to (*S*)-**III.3a** is indeed the energetically most favored one, being this finding in line with the experimental data.

The optimized geometries of the selectivity-determining transition states (*S*)-**TS4** and (*R*)-**TS4** (at the reductive elimination stage) were scrutinized in detail (Figure 3.24a, *vide infra*). The enantio- and regio-selectivity obtained through (*S*)-**TS4** can be attributed to the combination of both lone pair-π repulsive interaction between the N-atom of the nucleophile and the C–C double bond on the phenyl ring of ligand **L*PN***, and dispersion interactions between the ligand **L*PN*** and substrate **III.1** (Figure 3.24b). The computed □□G‡ between the two pathways (both relative to the lowest energy intermediate **IM4a**-*exo*) leading to branched product **III.3a** is 1.8 kcal/mol in favor of the (*S*) enantiomer, which corresponds to a calculated *er* of 96:4 at 273.15 K, being in excellent agreement with the experimental value of 95.5:4.5.[8e]

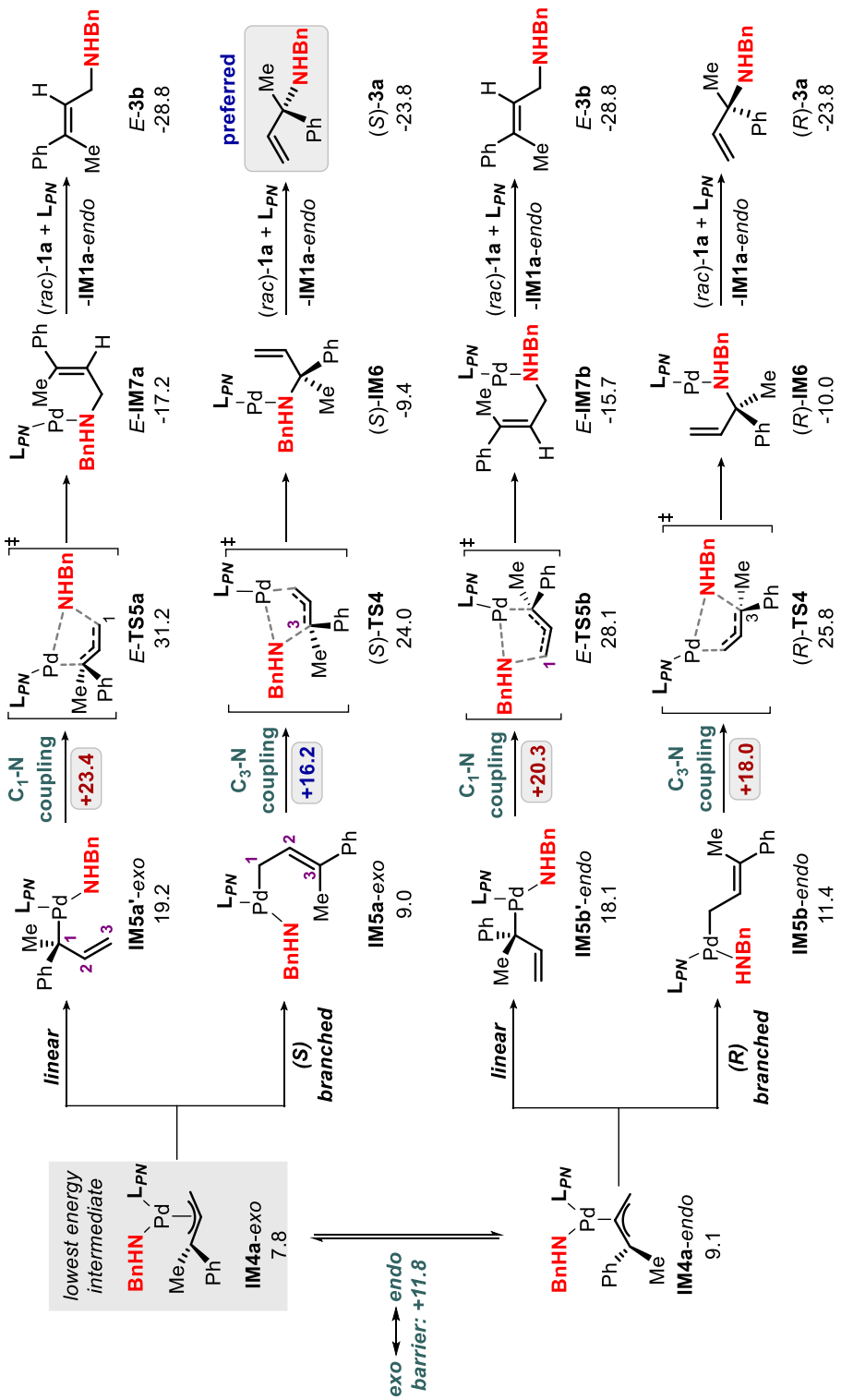

Figure 3.22: Rationalization of enantio- and regio-selectivity in the conversion of **III.1** into **III.3a** mediated by Pd/**L*PN*** departing from the intermediate **IM4a**-*exo* or **IM4a**-*endo*. All energies are provided in kcal/mol. Numbers in red/blue are all relative to **IM4a**-*exo*.

Figure 3.22 suggests that trace formation of the linear regio-isomeric product may be possible and indeed its formation was observed in minimal amounts (see Figure 3.3b, Table entry 2; 4%). The model used to predict its formation indicates that this linear product should have an *E*-configuration, and this is indeed what we observed experimentally.

3.4.2 Other explored routes towards the formation of branched III.3a

Apart from the inner-sphere pathway discussed above, an alternative route to product formation initiated from **IM2a**-*endo* can be considered (Figure 3.23). While the inner-sphere mechanism in Figure 3.21 starts from a consecutive decarboxylation and ligand exchange sequence, an alternative manifold could be a concerted C–N bond formation process with the -OBoc anion acting as a chelate. The energetic requirement of this *pseudo*-inner-sphere type process is 25.6 kcal/mol (**RDS1´**) leading to transition state (*S*)-**TS6** (+22.4 kcal/mol) where the C–N bond is formed. Competitive and irreversible decarboxylation through **TS2a**-*exo* in the inner-sphere pathway takes place with an energetic span of only 20.5 kcal/mol relative to **IM1a**-*endo*, and therefore on the basis of the significant difference in energy requirements between both pathways (5.1 kcal/mol), we can discard this concerted C–N bond formation as competitive.

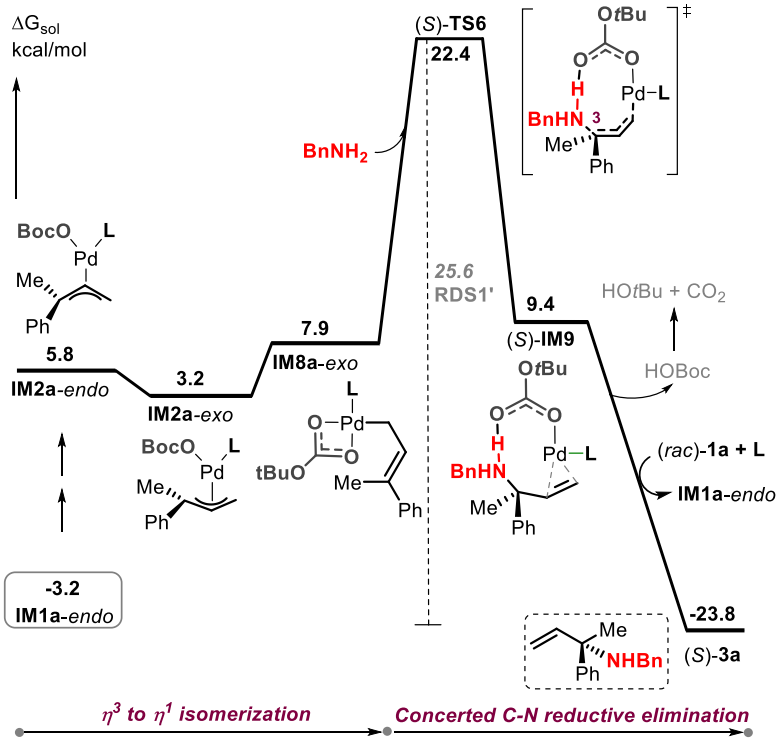

Figure 3.23 Concerted C–N bond formation starting from intermediate **INT2a**.

The possibility of an outer-sphere pathway that starts from Pd(allyl)(O*t*Bu)**L*PN*** (**IM3a**-*exo*, Figure 3.21) was also considered. The outer-sphere attack of $BnNH_2$ **III.2** on this intermediate and thus not involving a O*t*Bu-*for*-BnNH ligand exchange requires >20 kcal/mol and is not competitive with the inner-sphere manifold (**RDS2** = 16.2 kcal/mol) depicted in Figure 3.21.

3.4.3 Origin of the regio- and enantio-selectivities

Figure 3.24a shows the optimized geometries of the selectivity-determining, reductive-elimination based transition states (*S*)-**TS4**, (*R*)-**TS4**, *E*-**TS5a** and *E*-**TS5b**. From these transition states it can be inferred that the ones leading to the linear allylic amine product (*E*-**TS5a** and *E*-**TS5b**) have the Pd ion bound to a tertiary carbon center. In contrast, transition states (*S*)-**TS4** and (*R*)-**TS4** leading to a branched allylic amine have the Pd ion connected to a primary carbon atom. The steric repulsion involved in breaking the Pd-C^3 bond in *E*-**TS5a** and *E*-**TS5b** should be larger and therefore favor the formation of the branched product. The origin of the enantio-selectivity can be attributed to the combination of both lone pair/π repulsive interactions between the *N*-atom of the nucleophile and a C=C double bond of a phenyl group of **L*PN***, and dispersive interactions between the ligand **L*PN*** and the allylic fragment (Figure 3.24b). To extend the validation of our theoretical model, the predicted enantiomeric ratios (*er´*s) of two other substrate combinations (see Table **III.III**) were calculated and compared against the experimentally obtained data,[8e] showing a reasonable similarity between theory and experiment.

Table III.III: Predicted enantio-selectivities for three distinct substrate combinations. The same computational method was applied here as reported in Figures 3.21 and 3.22. The experimental *er* values were extracted from ref. 136b.

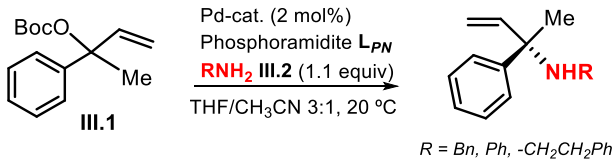

Entry	R	*er*Calc	*er*Exp
1	Bn	96:4	95.5:4.5
2	Ph	91.8:8.2	88:12
3	CH_2CH_2Ph	81:19	70:30

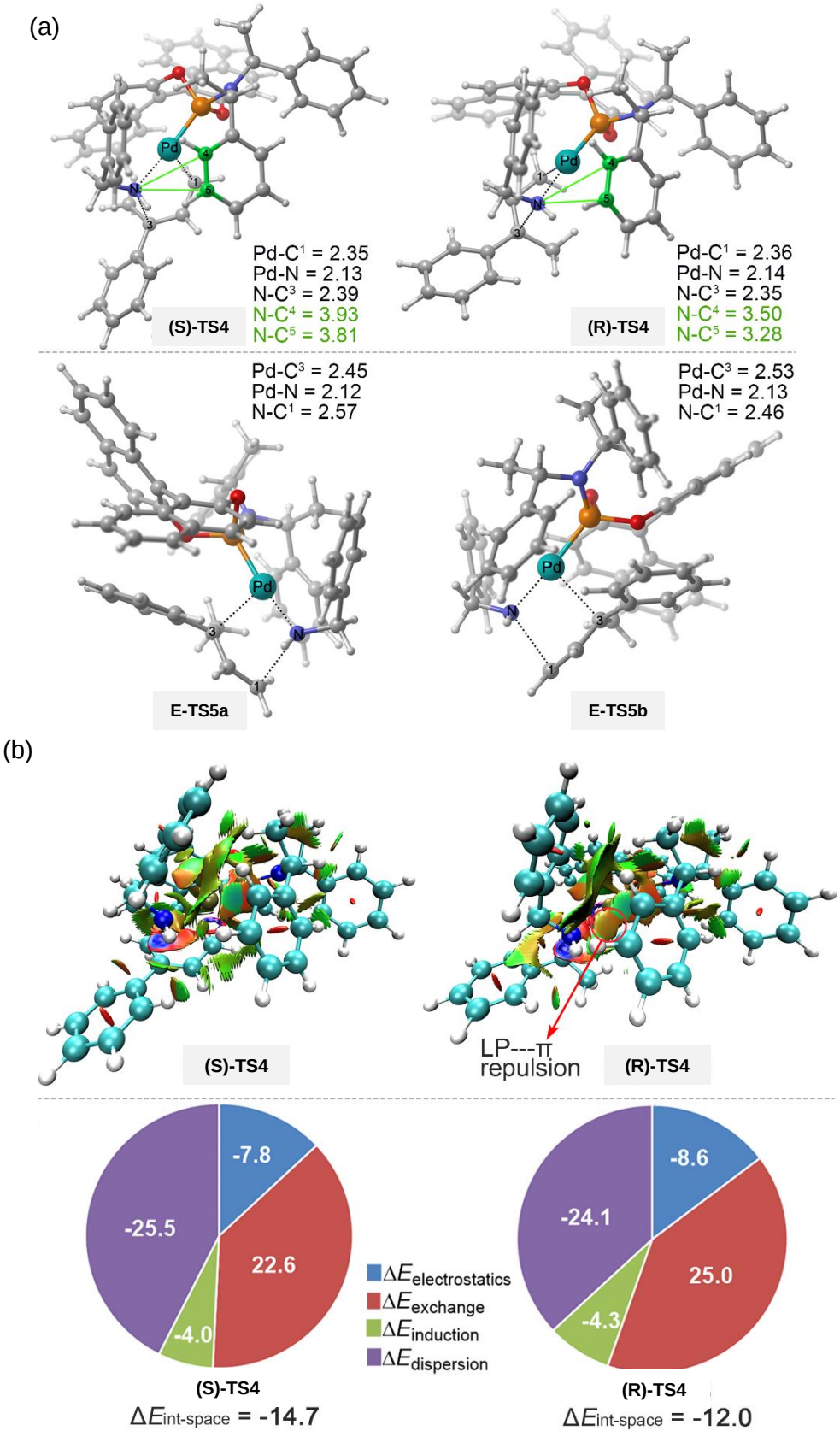

Figure 3.24: a) Computed transition state structures leading to linear or branched allylic amine, and b) key interactions involved in (*S*)-**TS4** and (*R*)-**TS4.**

3.5 Conclusions

In this chapter, we present a full mechanistic analysis of a Pd-catalyzed allylic amination reaction. After determination of the key variables enhancing the formation of the desired branched product **III.3a**, two key Pd(II) intermediates were detected and assigned by $^{31}P\{^{1}H\}$ NMR. The first intermediate is a post-oxidative addition complex being a mixture of Pd^{II}(allyl)(OBoc) isomers, and a second intermediate is proposed to be a Pd^{II}(allyl)(NHBn) species prior to the C–N bond formation step. This last intermediate is considered as a unique species supporting the inner-sphere mechanism of this allylic amination process. DFT calculations have been used to construct a predictive PdL_1 model aligning with this experimental evidence for an inner-sphere attack based mechanism. The proposed DFT model correctly predicts the (*S*)-enantiomeric product and the experimentally observed level of enantio-induction, while it also foresees linear (*E*)-configured allylic amines as minor by-products. Another non-competitive cycle has been computed in which the nucleophilic attack is assisted by the OBoc anion in a concerted mechanism. This second pathway has a higher activation barrier, though it does predicts the (*S*)-configured branched allylic amine as the major product.

Intrigued by how MeCN boosts the regio-selectivity of the reaction, we found that the decarboxylation is apparently affected by the medium. In the presence of MeCN as a co-solvent, the isomeric ratio of the Pd^{II}(allyl)(OBoc) intermediate can be positively influenced with a larger population of the more reactive isomer more prone to undergo decarboxylation and thus favouring overall kinetics.

Altogether, this combined experimental and computational effort highlights the importance of a deep understanding of catalytic processes that accommodate the formation of sterically stereocenters, and their value towards the design of efficient and selective protocols that widen the scope of accessible small molecules featuring tetra-substituted tertiary and even quaternary stereogenic carbons.

3.6 Experimental section

3.6.1 General methods

All reactions were set up in a nitrogen-filled glovebox (mBraun UnilabPro) with concentrations of O_2 and H_2O < 0.1 ppm or under a nitrogen atmosphere in oven-dried glassware using standard Schlenk techniques. Commercially available reagents ($Pd_2(dba)_3 \cdot CHCl_3$, chiral phosphoramidite ligands $\mathbf{L}_{PN\text{-}SSS}$ and $\mathbf{L}_{PN\text{-}RRR}$, NH_2Bn **III.2** and other benzyl amines*)* were used as received without further purification from the respective commercial suppliers and stored under inert gas and/or low temperature where required. Previously reported vinyl linear carbonates **III.1** was prepared as described in the literature.[155] Synthesis grade solvents such as tetrahydrofuran (THF), acetonitrile (MeCN), 2-MeTHF and deuterated tetrahydrofuran (THF-d_8) were dried over 4 Å molecular sieves and degassed by bubbling N_2 through it prior to their use. Glassware was washed in a base bath (KOH in water/isopropyl alcohol) after each use. Magnetic stirring bars were cleaned using an acid mixture of 20% HNO_3 +10% HCl in water.

Nuclear magnetic resonance (NMR): NMR spectra were obtained on a Bruker 400 MHz, a 500 MHz or a 500 MHz (equipped with a cryoprobe) spectrometers and with probe heads capable of producing gradients in the *z* direction with a maximum strength of 53.5 G/cm. ^{31}P NMR chemical shifts are reported in parts per million (ppm) relative to 85% H_3PO_4 for ^{31}P with the free ligand peak of **L** as an internal reference. In the ^{31}P NMR spectra measured in non-deuterated solvents, a coaxial tube containing acetone-d_6 was used to maintain the lock ^2H signal. Multiplicities are reported as follows: singlet (s), broad band (br), d (doublet) and multiplet (m). All the $^{31}P\{^1H\}$ NMR spectra have been referenced to the free ligand (**L**) signal at 151.1 ppm.

IR-spectroscopy - kinetics (REACT-IR): In situ IR monitoring of the catalytic reactions was carried out on a Mettler Toledo FTIR ReactIR 15 spectrometer. The equipment was coupled to a MTC detector and a diamond AgX Fiber Probe. The glass reactor used had 3 inlets: the upper one was used to insert the probe and the two lateral entries were closed by septums. The temperature of the reactor was cooled

[155] Guo, W.; Cai, A.; Xie, J.; Kleij, A. W. *Angew. Chem. Int. Ed.* 2017, 56, 11797.

down and controlled with an external chiller in an isopropanol bath. The Burés method was applied for the data treatment.[90]

High resolution mass spectrometry (HR-MS): HRMS data was recorded using two different methodologies: ESI-MS analyses were performed on a MicroTOF Focus mass spectrometer (Bruker Daltonics) by direct injection. Cold-spray ionization-MS (CSI-MS) analyses were performed on a MicroTOF Focus mass spectrometer (Bruker Daltonics) equipped with a cold-spray ionization source by direct injection and using nitrogen as sprayer and dry gas.

Computational analysis (DFT): Optimization: B97D-SMD(THF-ACN)/6-31G(*d*) (LANL2TZ(*f*) for Pd). Single point energy: M06-SMD(THF-ACN)/6-311+G(*d*,*p*) (LANL2TZ(*f*) for Pd). ΔG_{sol} = single point energies corrected by the Gibbs free energy corrections.

3.6.2 Kinetic experiments quantified by IR

General procedure: First, a 3-inlet glass jacketed-reactor was equipped with a stirring bar and an IR diamond probe. After the 2 other inlets had been closed by septums, the reactor was purged with nitrogen gas for 20 min. Hereafter, the cooling system integrated in the reactor was set at 0 ºC. Meanwhile, in a glovebox, a 2 mL via was filled with $Pd_2(dba)_3 \cdot CHCl_3$ (6 mg, 2 mol%) and ligand **L*PN*** (16 mg, 10 mol%) dissolved in 1.0 mL of a THF/MeCN (3:1 v/v) solvent mixture. The reaction mixture was stirred for 5 min before benzyl amine **III.2** (37 µL, 0.34 mmol, 1.1 equiv) was added through a Hamilton syringe. After reaching a homogeneous state, the reaction mixture was transferred into a syringe. Substrate **III.1** (74 mg, 0.30 mmol, 1.0 equiv) was dissolved in another vial in 0.40 mL of the same solvent mixture. This latter solution was transferred into another syringe. Both syringes were taken out of the glovebox after capping the needles with septums. In the React-IR set up, the purging system was closed and the system configured following the IR software indications. When the equipment was ready to use, the solution containing the catalyst and benzyl amine **III.2** was transferred inside the glass jacketed-reactor using one of the inlets closed by a septum. The magnetic stirring was set and the solution left stirring for few minutes until the temperature had stabilized. A blank spectrum of this solution was measured and the experiment then started with a rate of 1 scan/min. After 3 scans, the substrate solution was injected inside the stirred solution and the measurements maintained for 18 h. The disappearance of the substrate was monitored by following the carbonate signal of the leaving group at □ = 1741 cm^{-1}.

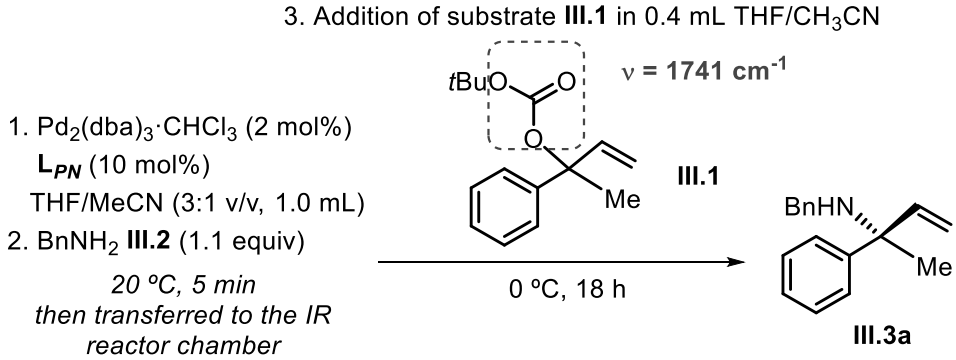

Figure: 3.25: Catalytic reaction conditions of the optimized procedure for IR-monitoring measurements.

Determination of the order in the reaction components

Order of [Pd]:

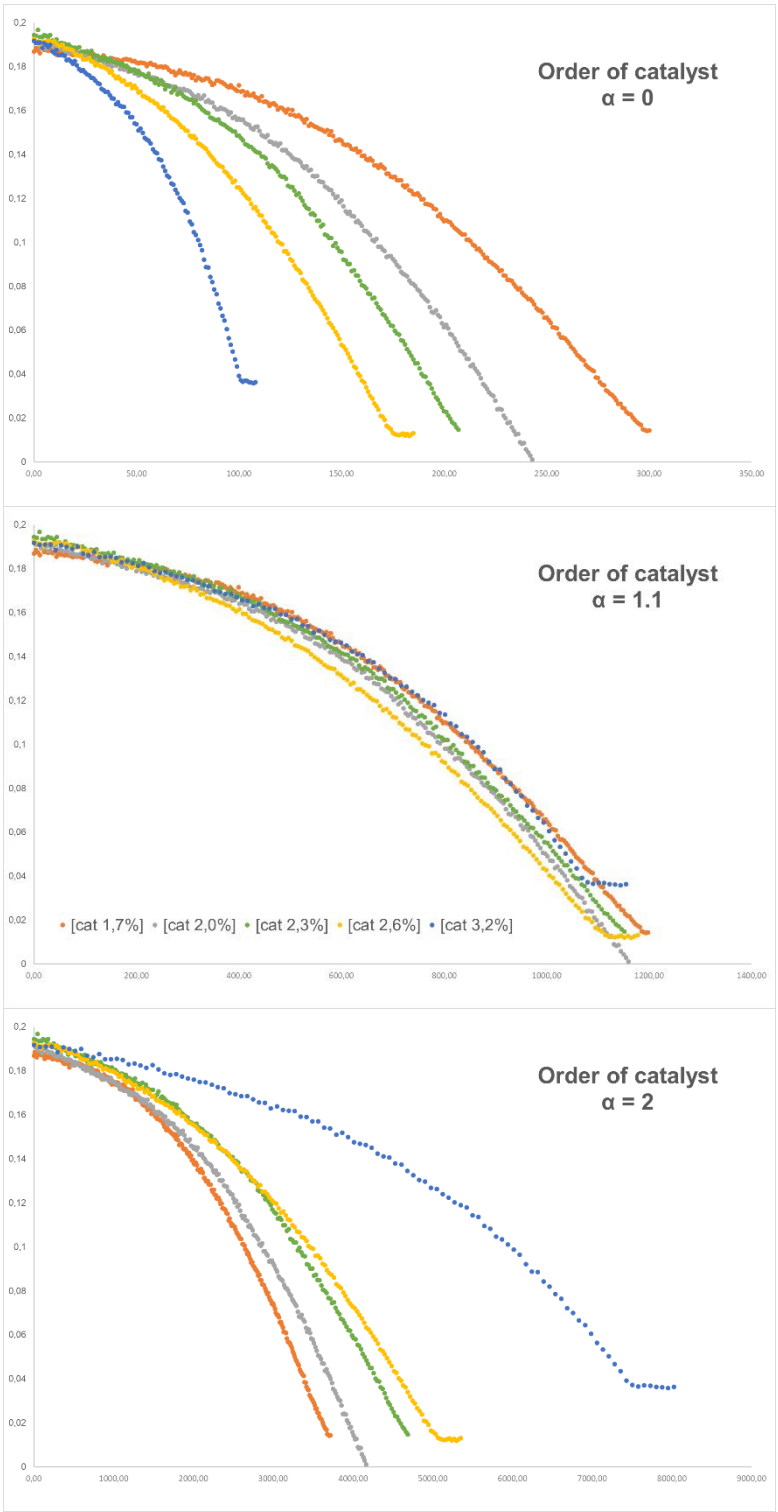

Figure 3.26: VTNA graphic of [substrate] vs. $t \cdot [cat]_T^{\alpha}$ for the determination of order in [Pd] (in this case α = 1.1) using 5 different concentrations of Pd.

Order in ligand **L**:

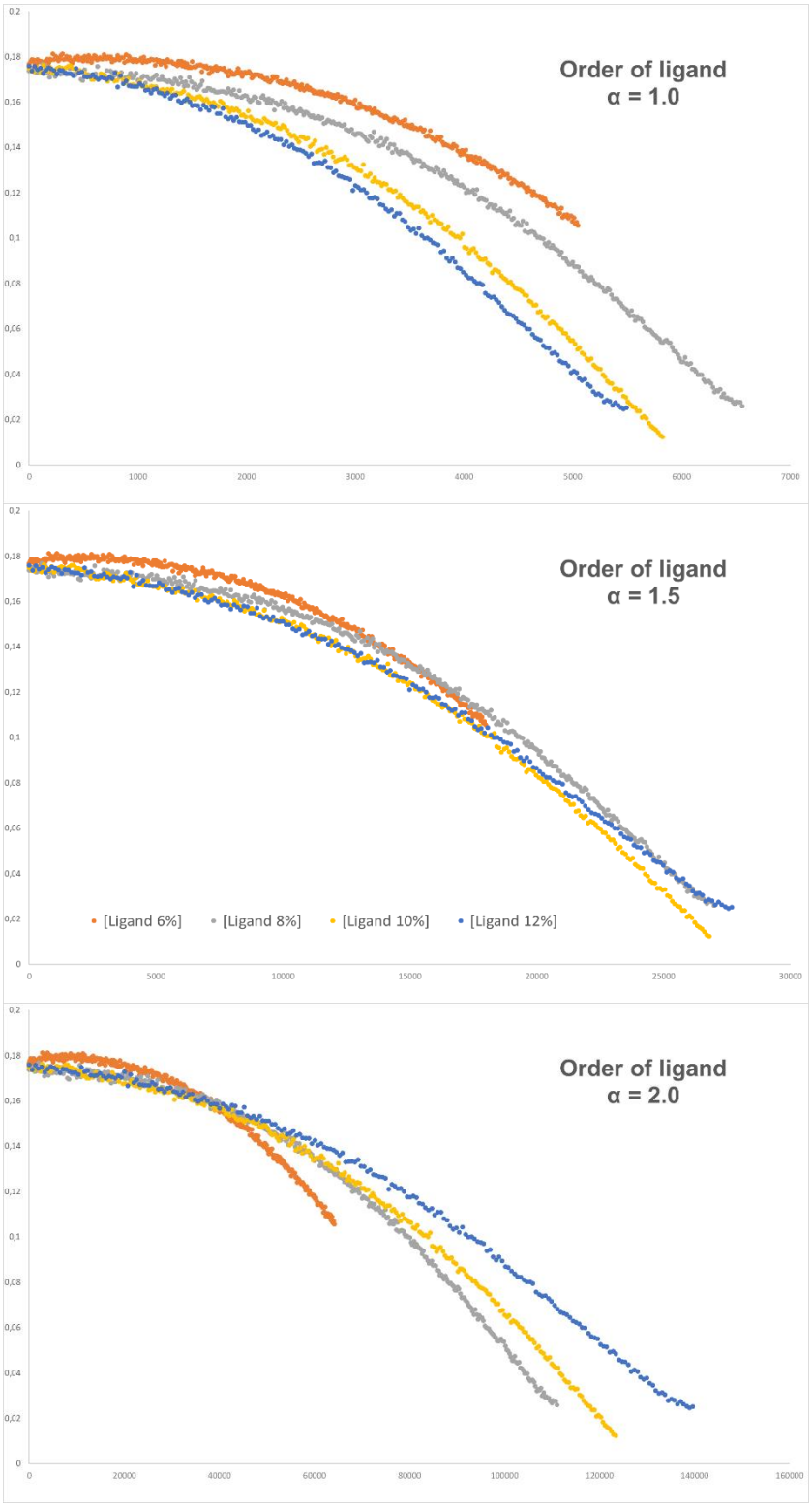

Figure 3.27: VTNA graphic of [substrate] vs. $t \cdot [cat]_T^{\alpha}$ for the determination of the order in $\mathbf{L}_{PN}$ (in this case α = 1.5) with 4 different concentrations of ligand.

Order in carbonate substrate **III.1**:

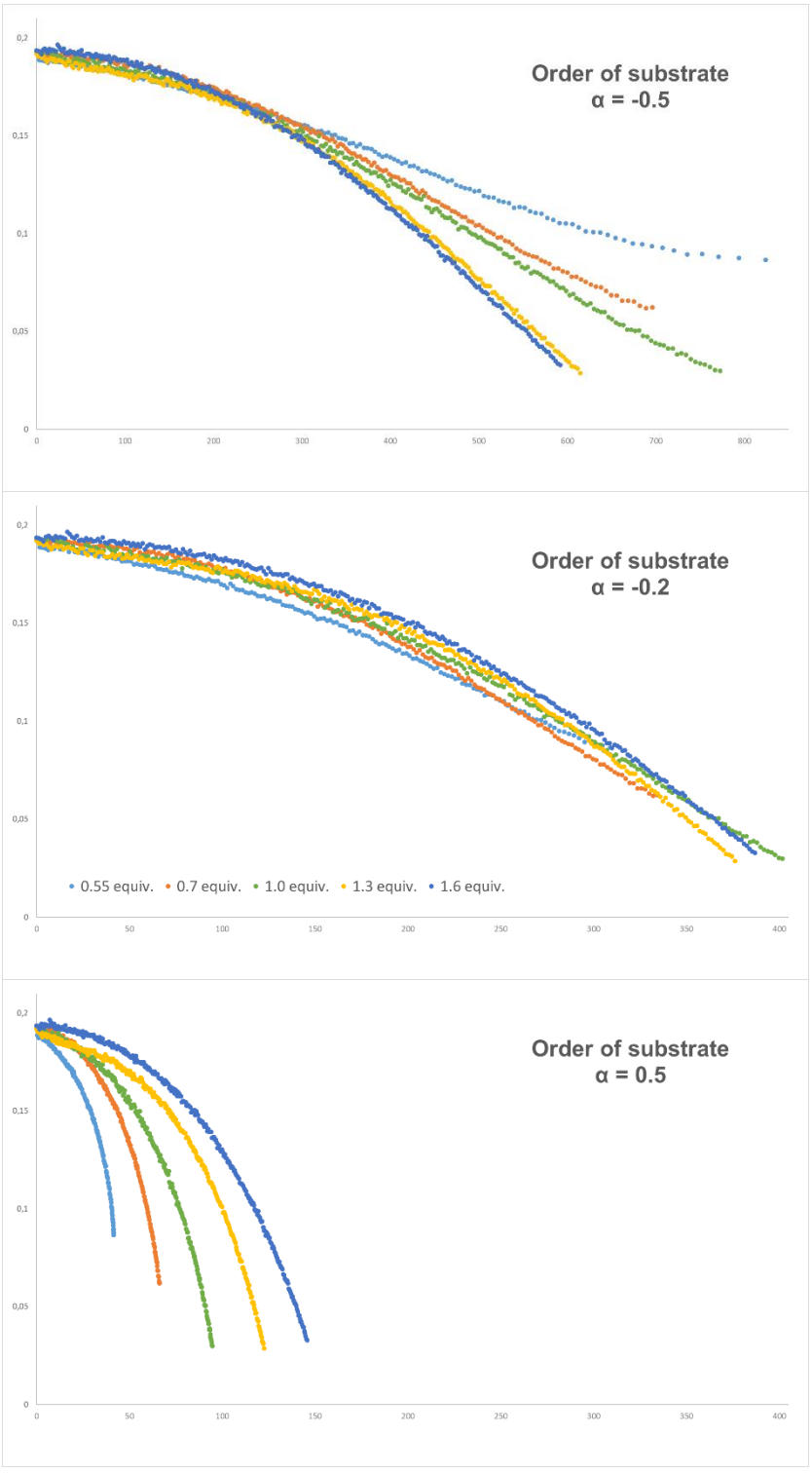

Figure 3.28: VTNA graphic of [substrate] vs. $\Sigma[substrate]^{\alpha}\cdot\Delta t$ for the determination of order in carbonate substrate **III.1** (in this case α = -0.2) using 5 different concentrations of substrate (0.55, 0.70, 1.0, 1.3 and 1.6 equiv).

Order in benzyl amine **III.2**:

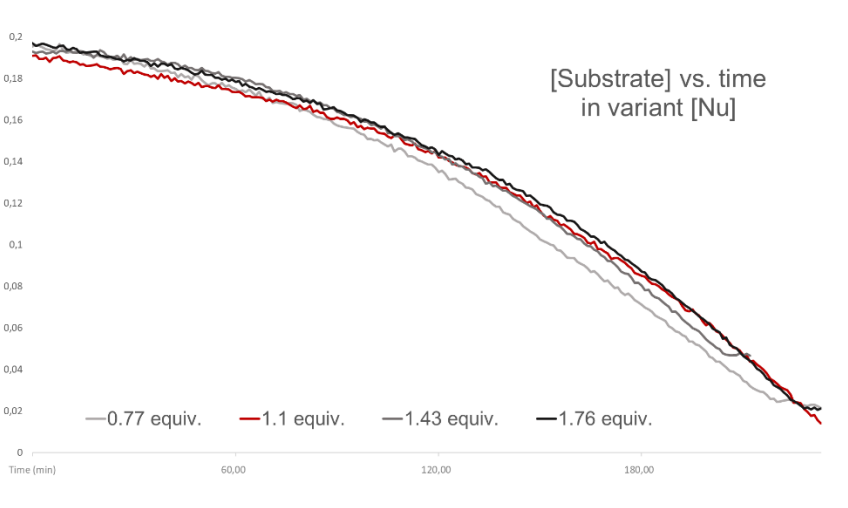

Figure 3.29: Concentration vs. time graphic of [nucleophile] vs. time for the determination of the order in benzyl amine **III.2** using 4 different concentrations (0.77, 1.1, 1.43 and 1.76 equiv). In this case the orders appears to be zero, as changing the concentration of the nucleophile does not change the rate of the catalysis.

Table III.IV: Catalytic amounts of Pd and chiral ligand $\mathbf{L_{PN}}$ for the determination of the order in Pd.

Pd precursor [$Pd_2(dba)_3 \cdot CHCl_3$]	**Chiral ligand L_{PN}**
1.7 mol%	8.5 mol%
2.0 mol%	10 mol%
2.3 mol%	11.5 mol%
2.6 mol%	13 mol%
3.2 mol%	16 mol%

Table III.V: Catalytic amounts of Pd and chiral ligand $\mathbf{L_{PN}}$ for the determination of the order in $\mathbf{L_{PN}}$.

Pd precursor [$Pd_2(dba)_3 \cdot CHCl_3$]	**Chiral ligand L_{PN}**
2.0 mol%	6 mol%
2.0 mol%	8 mol%
2.0 mol%	10 mol%
2.0 mol%	12 mol%

3.6.3 Nuclear Magnetic Resonance studies

Kinetic experiments quantified by 1H NMR

Procedure for the preparation of catalytic experiments for ^{1}H NMR kinetic measurements: In a 2 mL vial, $Pd_2(dba)_3{\cdot}CHCl_3$ (3 mg, 2mol%) and ligand **L_{PN}** (8 mg, 10 mol%) were dissolved in 0.40 mL of THF-d_8 and 0.10 mL of MeCN. The reaction mixture was stirred for 5 min before adding benzyl amine **III.2** (18.5 µL, 0.17 mmol, 1.1 equiv) using a Hamilton syringe. Then, mesitylene was added (6.9 µL, 0.05 mmol, 0.33 equiv) with another Hamilton syringe. After reaching a homogeneous state, the substrate **III.1** (37 mg, 0.15 mmol, 1.0 equiv) was added and the catalysis mixture was transferred to an NMR tube. See also Figure 3.3c for kinetic graphs.

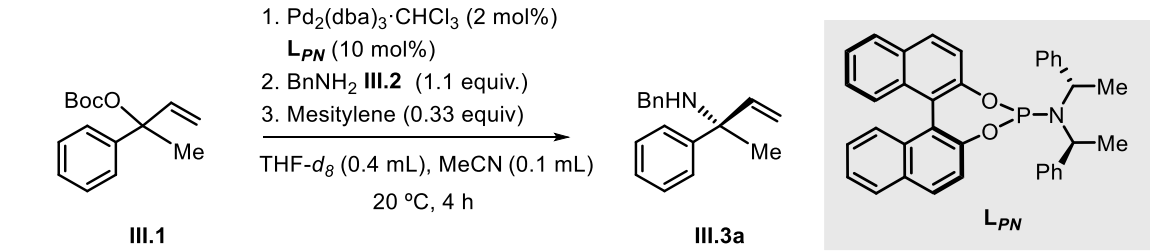

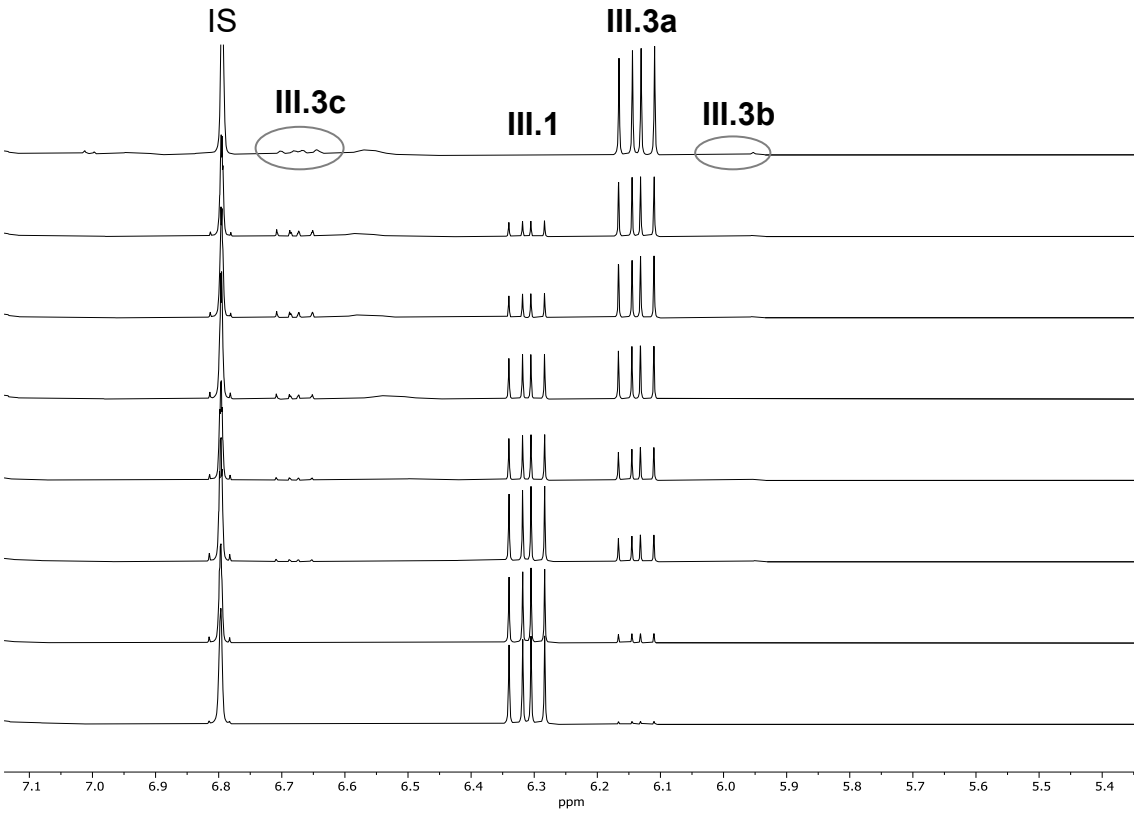

Figure 3.30: ^{1}H NMR kinetic spectra at 20 ºC in a THF-d_8/MeCN mixture (4:1).

Screening of conditions for chemo- and regio-selectivity

Table III.VI: Catalytic experiments varying solvent, equiv of Nu ($BnNH_2$), the Pd/**L** ratio and the reaction temperature. Volume = 0.35 mL, 24 h.

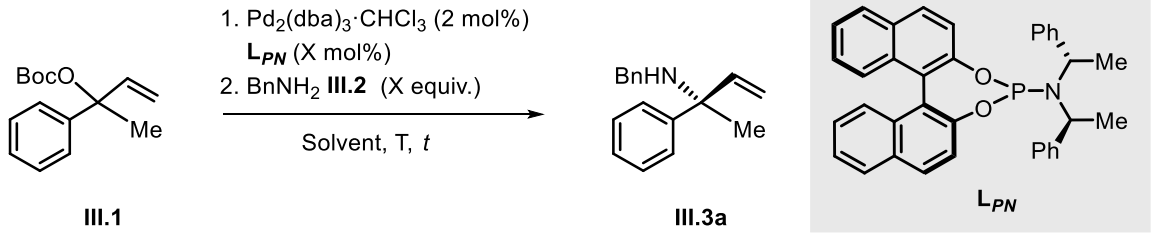

III.1 **III.3a**

En-try	T (ºC)	Solvent	Eq. Nu	Pd/L ratio	SM (III.1)	Branched (III.3a)	B/L ratio	Linear (III.3b)	*Z/E* ratio	hydride (III.3c)
1	20	THF/MeCN	1.1	1/2.5	0	0.58	8/1	0.07	1/1.5	0.35
2	20	THF/MeCN	1.1	1/4	0	0.61	7/1	0.08	1/1.5	0.31
3	20	THF/MeCN	1.1	1/6	0	0.60	6/1	0.09	1/1.5	0.31
4	0	THF/MeCN	1.1	1/2.5	0	0.70	18/1	0.04	1/4	0.26
5	0	THF/MeCN	1.1	1/6	0	0.71	18/1	0.04	0/1	0.25
6	20	THF	1.1	1/2.5	0	0.47	1/1	0.36	0/1	0.17
7	20	THF	1.1	1/6	0	0.55	2/1	0.30	0/1	0.15
8[a]	0	THF	1.1	1/2.5	0	0.58	3/1	0.21	1/3.5	0.21
9[b]	0	THF	1.1	1/6	0	0.68	5/1	0.15	1/3.5	0.17
10	20	THF/MeCN	1.5	1/2.5	0	0.73	4/1	0.18	1/2.6	0.08
11	20	THF/MeCN	2	1/2.5	0	0.77	6/1	0.14	1/3.5	0.09
12	0	THF/MeCN	2	1/2.5	0	0.40	4/1	0.09	1/9	0.51
13	0	THF	2	1/2.5	0.08	0.10	1/1	0.08	0/1	0.74
14	20	THF/MeCN	3	1/2.5	0.80	0.06	1/1	0.09	1/2.1	0.05
15	20	THF	3	1/2.5	0	0.65	2/1	0.28	0/1	0.06
16	20	THF/MeCN	5	1/2.5	0.82	0.05	1/1	0.07	1/8	0.06
17	20	THF	5	1/2.5	0	0.76	4/1	0.18	0/1	0.05

[a]48 h, [b]72 h. Yield determined with an internal standard (mesitylene).

Table III.VII: Use of different nitrile solvents. THF/nitrile (3:1), Volume = 0.35 mL, 24 h, 20 ºC.

En-try	Nitrile	Pd/L ratio	SM (III.1)	Branched (III.3a)	B/L ratio	Linear (III.3b)	*Z/E* ratio	hydride (III.3c)
1	CH_3-	1/2.5	0	0.58	8/1	0.07	1/1.5	0.35
2	CH_3-CH_2-	1/2.5	0	0.69	4/1	0.16	1/1.5	0.15
3	CH_3-CH_2- CH_2-	1/2.5	0	0.67	4/1	0.15	1/2.2	0.18

Detection of *t*BuOH formation

During the catalytic experiments we could detect the formation of *t*BuOH (□ = 1.16 ppm, CH_3 groups). Note that the relaxation time of the ^1H measurements were not adapted for the integration of aliphatic protons, therefore the quantification of *t*BuOH reaches >100%.

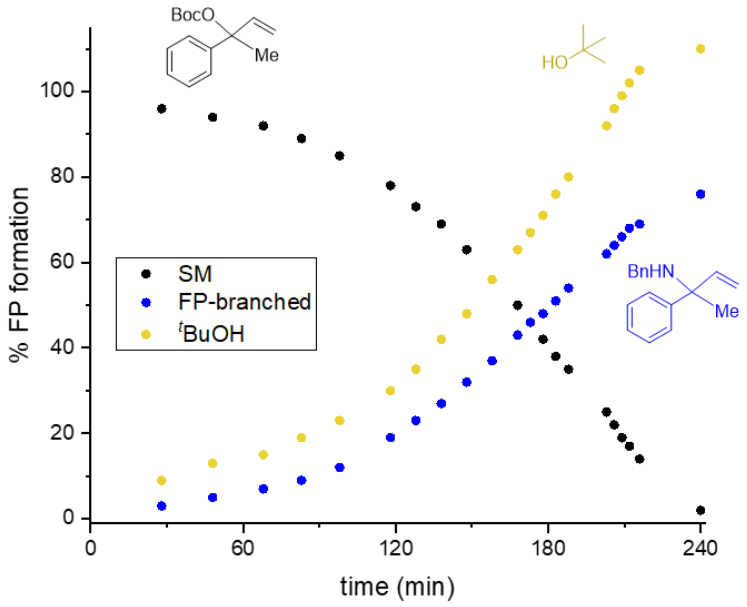

Figure 3.31: Quantification of *t*BuOH by ^1H NMR at 20 ºC in a THF-d_8/MeCN mixture (4:1). Yields were determined using mesitylene as internal standard.

Complexation of Pd(0) + L_{PN} using different equivalents of L_{PN} by ^{31}P NMR

Procedure for the preparation of complexation reactions for ^{31}P NMR measurements: In a 2.0 mL vial, $Pd_2(dba)_3 \cdot CHCl_3$ (3 mg, 3 µmol, 2 mol%) and ligand **L_{PN}** (3.2 – 16 mg, 6 – 30 µmol, 4 - 20 mol%) were dissolved in 0.50 mL of a THF/MeCN (3:1, v/v) solvent mixture. The reaction mixture was stirred for 10 min before it was transferred to an NMR tube equipped with an acetone-d_6 capillary. Five solutions were prepared this way with different Pd-to-**L_{PN}** ratios ranging from 1:1 to 1:5.

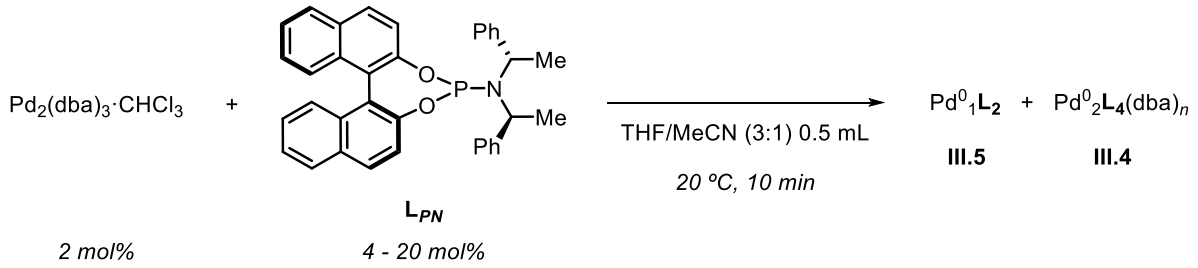

Figure 3.32: Reaction scheme for the complexation reaction of $Pd_2(dba)_3 \cdot CHCl_3$ and ligand **L_{PN}** using different ratios of Pd precursor and ligand.

Observations: At ratios >1:1 the signal of free ligand is observed. The singlet signal at 169.7 ppm and two doublet signals at 165.2 and 163.5 ppm are observed by $^{31}P\{^1H\}$ NMR. In order to confirm that the two doublets signals correspond to the same species, a 2D $^{31}P\{^1H\}$ COSY NMR experiment was measured (see Figure 3.48). The cross peaks confirm this hypothesis. The observed signals were assigned to two different complexes: $Pd^0{}_1\mathbf{L_2}$ **III.5** and $Pd^0{}_2\mathbf{L_4}(dba)_n$ **III.4**, see Figure 3.33. Also, it is worth mentioning that in the absence of MeCN, the same complexes are formed with the same dependency on the Pd-to-**L_{PN}** ratio (Figure 3.35 and 3.37).

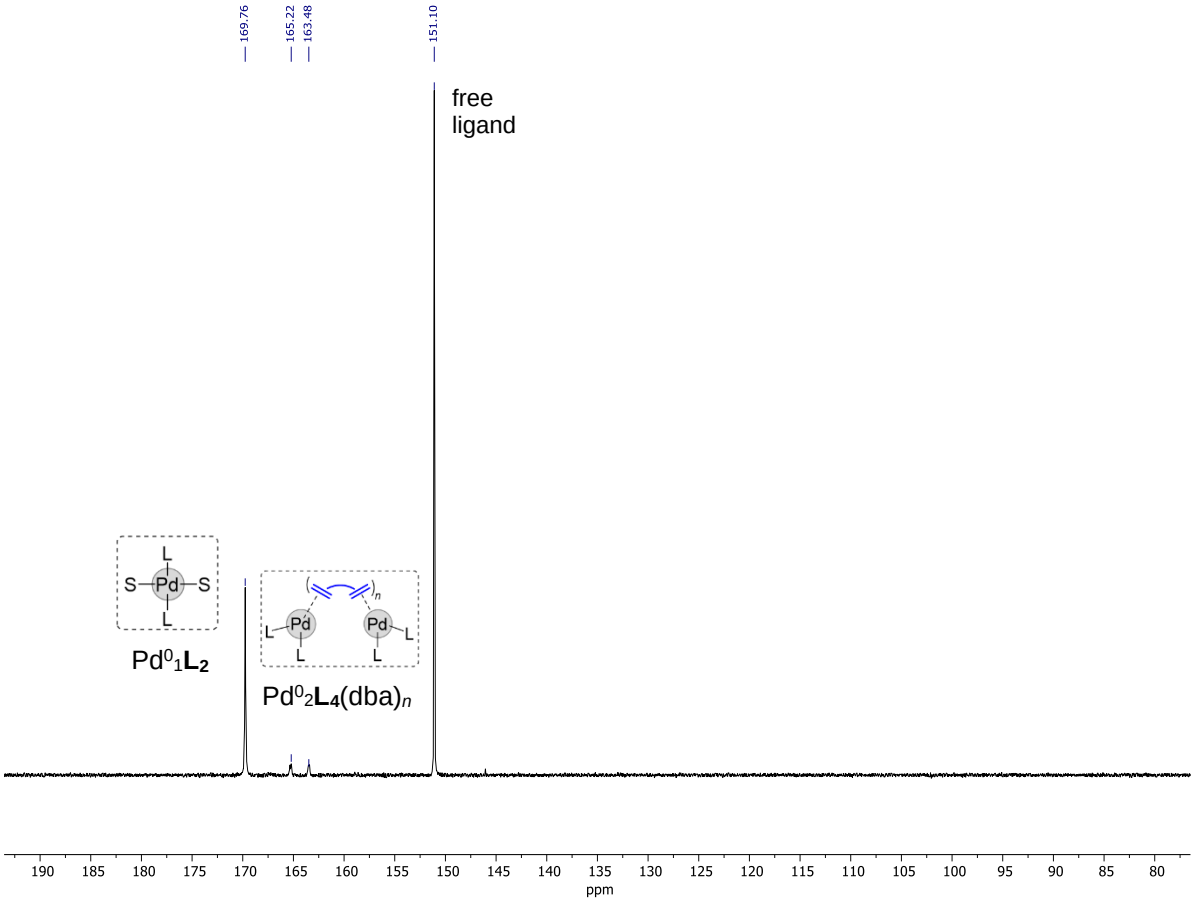

Figure 3.33: $^{31}P\{^{1}H\}$ NMR spectrum after complexation of Pd_2dba_3 and **L*PN*** (Pd:**L*PN*** = 1:5) at 20 ºC in a THF/MeCN mixture (3:1, v/v).

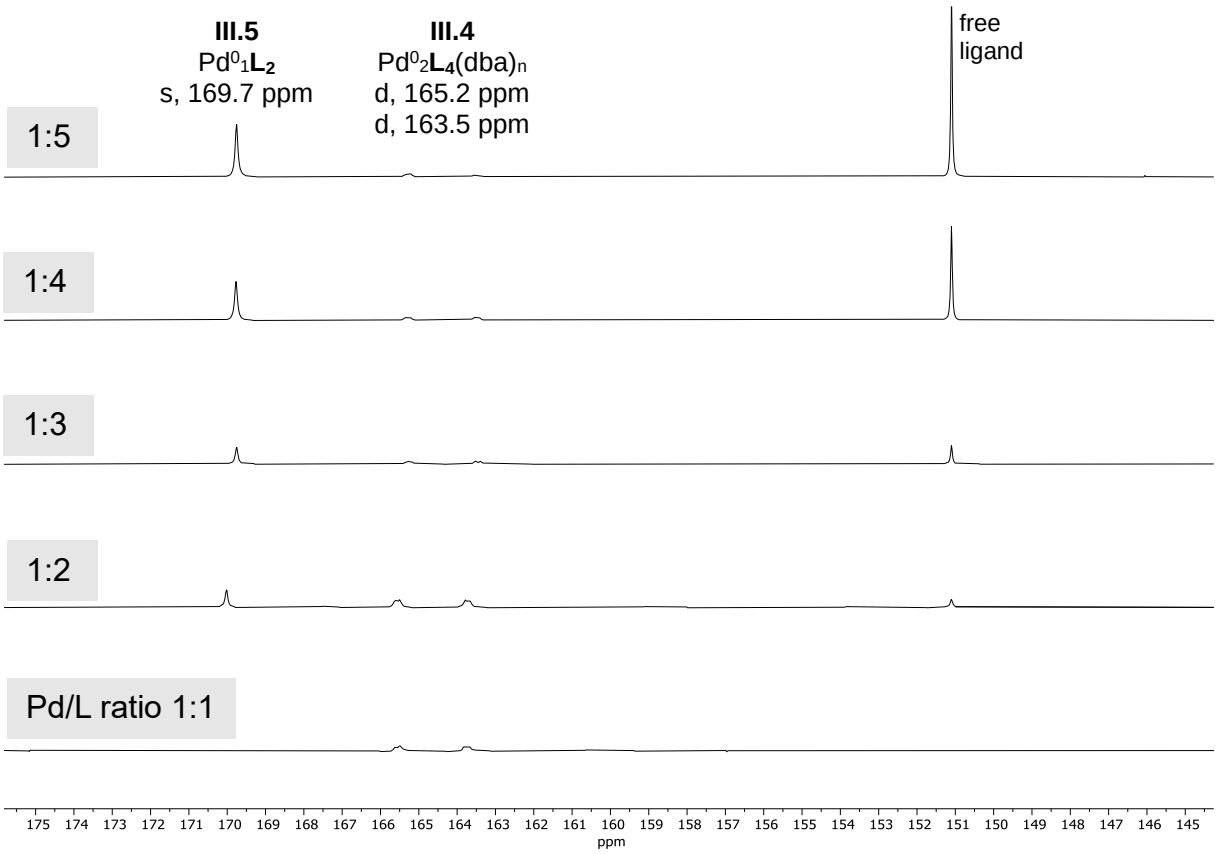

Figure 3.34: $^{31}P\{^1H\}$ NMR stacked spectra of five samples with different Pd:$\mathbf{L}_{PN}$ ratios at 293 K in a THF/MeCN mixture (3:1, v/v).

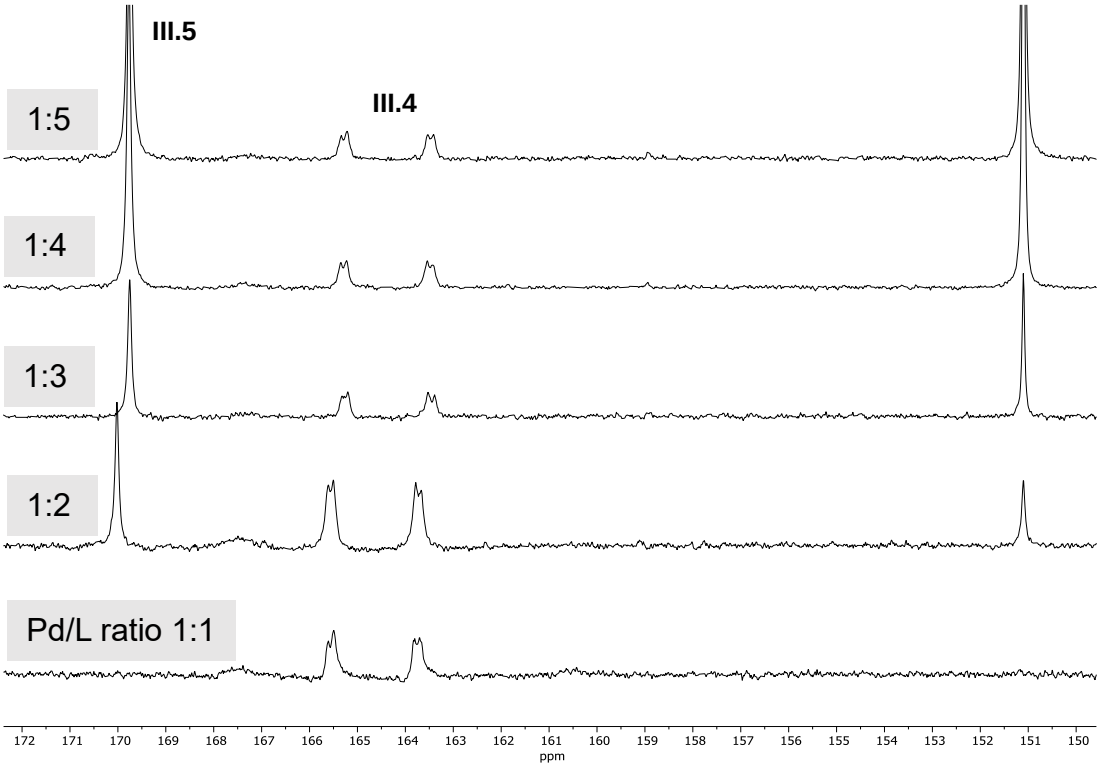

Figure 3.35: Selected zoom of the previous Figure 3.34.

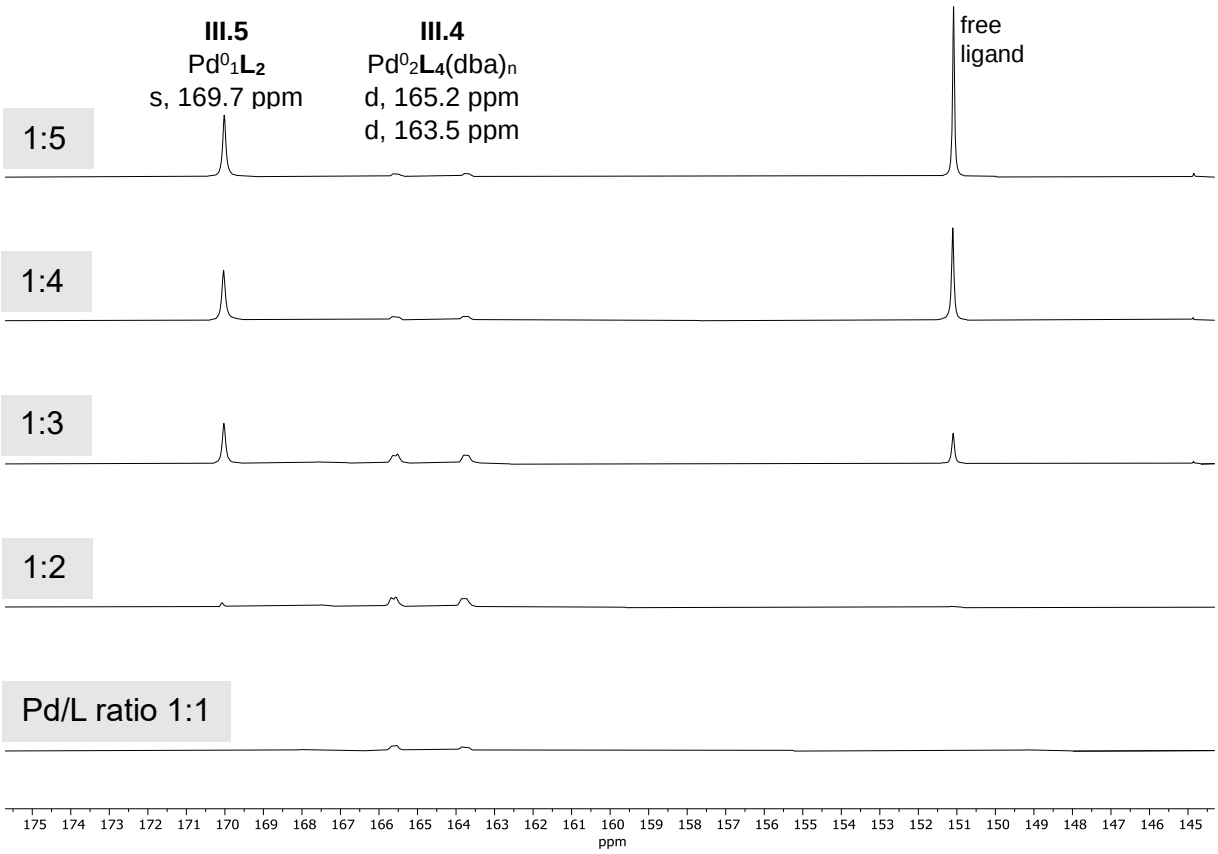

Figure 3.36: $^{31}P\{^{1}H\}$ NMR stacked spectra of five samples with different Pd:**L*PN*** ratios at 293 K in THF.

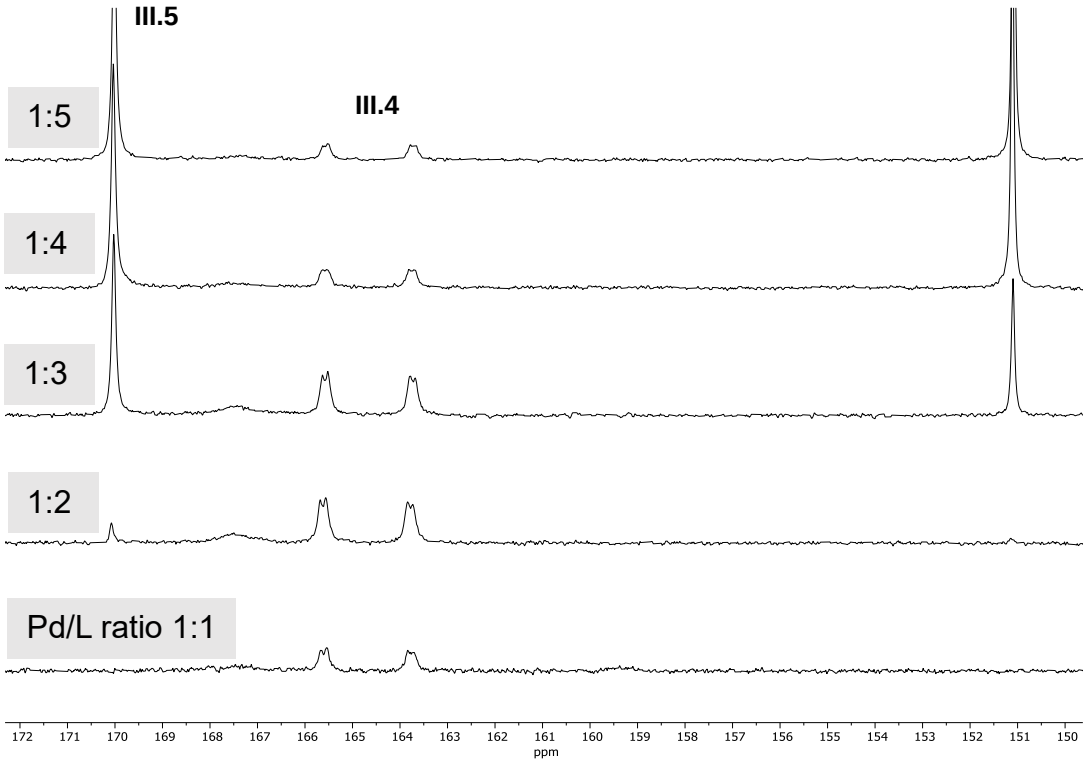

Figure 3.37: Selected zoom of the previous Figure 3.36.

Quantification of coordinated L_{PN} in Pd^0 precatalysts and Pd^{II} intermediates

X = molar fraction *(Value obtained from $^{31}P\{^1H\}$ NMR integrations. No internal standard used).*

[Pd] = total conc. of Pd *(a full complexation of Pd is considered under catalytic conditions).*

[**L**] = total conc. of phosphoramidite $\mathbf{L_{PN}}$

$[Pd_{int}]_m$ = conc. of Pd in an specific intermediate

$[\mathbf{L}_{int}]_m$ = conc. of phosphoramidite $\mathbf{L_{PN}}$ in an specific intermediate

m = intermediate name

Initial considerations:

If the intermediate is Pd$\mathbf{L}_1$, then $[\mathbf{L}_{int}] = [Pd]$

If the intermediate is Pd$\mathbf{L}_2$, then $[\mathbf{L}_{int}]/2 = [Pd]$

n = number of **L** (Pd$\mathbf{L}_1$ or Pd$\mathbf{L}_2$)

$[Pd] = \Sigma\ [Pd_{int}]_m$

General equation: $[\mathbf{L}_{int}]_m = X \bullet [\mathbf{L}]/n$

On the next page, we will evaluate and calculate the following scenarios (**a** and **b**). With these two different conditions, we observed the same Pd**L** quantification in each species, validating the stoichiometry that we propose. We will give different values to *n* (number of ligands). Values in green match the employed concentrations of the Pd precursor (Pd_2dba_3), while values in red mark an error of the Pd/**L** stoichiometry used.

(a) Catalytic experiment with Pd/L = 1:2 in THF/MeCN (3:1, v/v) – *relates to Figure 3.5*

(b) Catalytic experiment Pd/L = 1:5 in THF – *relates to Figure 3.61*

(a) Pd/L = 1:2 in THF/MeCN (3:1 v/v):

[Pd] = 0.0116 M; [**L**] = 0.0237 M

t = 8 min $X_{140ppm} = 0.44$

n = 1 $[\mathbf{L}_{int}]_m = X \cdot [\mathbf{L}]$ $[\mathbf{L}_{int}]_{140ppm} = 0.44 \cdot 0.0237 = 0.0104$ M

n = 2 $[\mathbf{L}_{int}]_m = X \cdot [\mathbf{L}]$ $[\mathbf{L}_{int}]_{140ppm} = 0.44 \cdot 0.0237 / 2 = 0.005214$ M

$[Pd_{int}]_{140ppm} = 0.0116$ M

t = 1h 30 $X_{140ppm} = 0.38$; $X_{110ppm} = 0.04$

n = 1 $[\mathbf{L}_{int}]_m = X \cdot [\mathbf{L}]$ $[\mathbf{L}_{int}]_{140ppm} = 0.38 \cdot 0.0237 = 9 \cdot 10^{-3}$ M

$[\mathbf{L}_{int}]_{110ppm} = 0.04 \cdot 0.0237 = 9.5 \cdot 10^{-4}$ M

$\Sigma [\mathbf{L}_{int}] = 9 \cdot 10^{-3} + 9.5 \cdot 10^{-4} = 0.00995$ M

n = 2 $[\mathbf{L}_{int}]_m = X \cdot [\mathbf{L}]$ $[\mathbf{L}_{int}]_{140ppm} = 0.38 \cdot 0.0237 / 2 = 4.5 \cdot 10^{-3}$ M

$[\mathbf{L}_{int}]_{110ppm} = 0.04 \cdot 0.0237 / 2 = 4.75 \cdot 10^{-4}$ M

$\Sigma [\mathbf{L}_{int}] = 4.5 \cdot 10^{-3} + 4.75 \cdot 10^{-4} = 0.00498$ M

$[Pd_{int}]_{tot} = 0.0116$ M

The data demonstrates that both species around 140 ppm and 110 ppm are intermediates of type Pd$\mathbf{L}_1$.

Analysis of a more complicated situation where almost all species coexist:

t = 2h 30 $X_{140ppm} = 0.05$; $X_{110ppm} = 0.05$; $X_{trans} = 0.28$; $X_{cis} = 0.38$; $X_{unk} = 0.09$

$n_{140ppm} = 1$; $n_{110ppm} = 1$; $n_{trans} = 2$; $n_{cis} = 2$; $n_{unk} = x$

$[\mathbf{L}_{int}]_m = X \cdot [\mathbf{L}]$ $[\mathbf{L}_{int}]_{140ppm} = 0.05 \cdot 0.0237 = 1.19 \cdot 10^{-3}$ M

$[\mathbf{L}_{int}]_{110ppm} = 0.05 \cdot 0.0237 = 1.19 \cdot 10^{-3}$ M

$[\mathbf{L}_{int}]_{trans} = 0.28 \cdot 0.0237 / 2 = 3.3 \cdot 10^{-3}$ M

$[\mathbf{L}_{int}]_{cis} = 0.38 \cdot 0.0237 / 2 = 4.5 \cdot 10^{-3}$ M

$[\mathbf{L}_{int}]_{unknown}$ =0.38•0.0237 /x = $2.13 \cdot 10^{-3}$ /x M

Σ $[\mathbf{L}_{int}]$ (*x* = *1*) = 0.0112 M

Σ $[\mathbf{L}_{int}]$ (*x* = *2*) = 0.0123 M

$[Pd_{int}]_{tot}$ = 0.0116 M

Residual (small) broad signal between species $Pd^0{}_1\mathbf{L_2}$ and $Pd^0{}_2\mathbf{L_4}(dba)_n$ (see Figure 3.35 at 160 ppm) is a species of type $Pd\mathbf{L_2}$.

(b) Pd/L = 1:5 in THF:

[Pd] = 0.0116 M; [**L**] = 0.0712 M

t = 1h X_{140ppm} = 0.14; X_{110ppm} = 0.01

n = 1 $[\mathbf{L}_{int}]_m$ = X • [**L**] $[\mathbf{L}_{int}]_{140ppm}$ = 0.14•0.0237 = $9.97 \cdot 10^{-3}$ M

$[\mathbf{L}_{int}]_{110ppm}$ = 0.01•0.0237 = $7.12 \cdot 10^{-4}$ M

Σ $[\mathbf{L}_{int}]$ = $9.97 \cdot 10^{-3}$ + $7.12 \cdot 10^{-4}$ = 0.01068 M

n = 1.5 $[\mathbf{L}_{int}]_m$ = X • [**L**] $[\mathbf{L}_{int}]_{110ppm}$ = 0.01•0.0237 /1.5 = $4.14 \cdot 10^{-4}$ M

Σ $[\mathbf{L}_{int}]$ = $9.97 \cdot 10^{-3}$ + $4.74 \cdot 10^{-4}$ = 0.01044 M

n = 2 $[\mathbf{L}_{int}]_m$ = X • [**L**] $[\mathbf{L}_{int}]_{110ppm}$ = 0.01•0.0237 /2 = $3.56 \cdot 10^{-4}$ M

Σ $[\mathbf{L}_{int}]$ = $9.97 \cdot 10^{-3}$ + $3.56 \cdot 10^{-4}$ = 0.01032 M

$[Pd_{int}]_{tot}$ = 0.0116 M

These data demonstrate that both species around 140 ppm and 110 ppm are intermediates of type $Pd\mathbf{L_1}$.

Analysis of a more complicated situation where almost all species coexist:

t = 9 h X_{110ppm} = 0.11; X_{trans} = 0.11; X_{unk} = 0.01

n_{110ppm} = x; n_{trans} = 2; n_{unk} = 2

$[\mathbf{L}_{int}]_m$ = X • [**L**] $[\mathbf{L}_{int}]_{110ppm}$ = 0.05•0.0237 /x=

$[\mathbf{L}_{int}]_{trans}$ = 0.28•0.0237 /2 = $3.916 \cdot 10^{-3}$ M

$[\mathbf{L}_{int}]_{unknown}$ =0.38•0.0237 /2 = $3.56 \cdot 10^{-4}$ /x M

Σ [**L**$_{int}$] (x = *1*) = 0.0121 M

Σ [**L**$_{int}$] (x = *1.5*) = 0.0082 M

Σ [**L**$_{int}$] (x = *2*) = 0.0095 M

[Pd$_{int}$]$_{tot}$ = 0.0116 M

Again, intermediate at 110 ppm should be a species of type PdL_1.

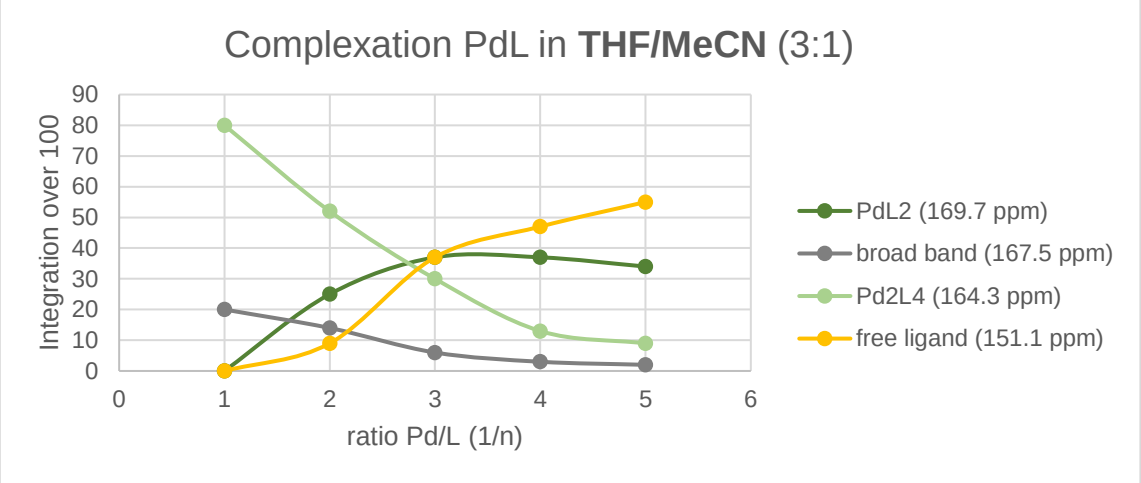

Figure 3.38: Integration of $^{31}P\{^1H\}$ NMR spectra of Pd/**L**$_{PN}$ based complexes at different Pd:**L**$_{PN}$ ratios at 20 ºC in a THF/MeCN mixture (3:1, v/v).

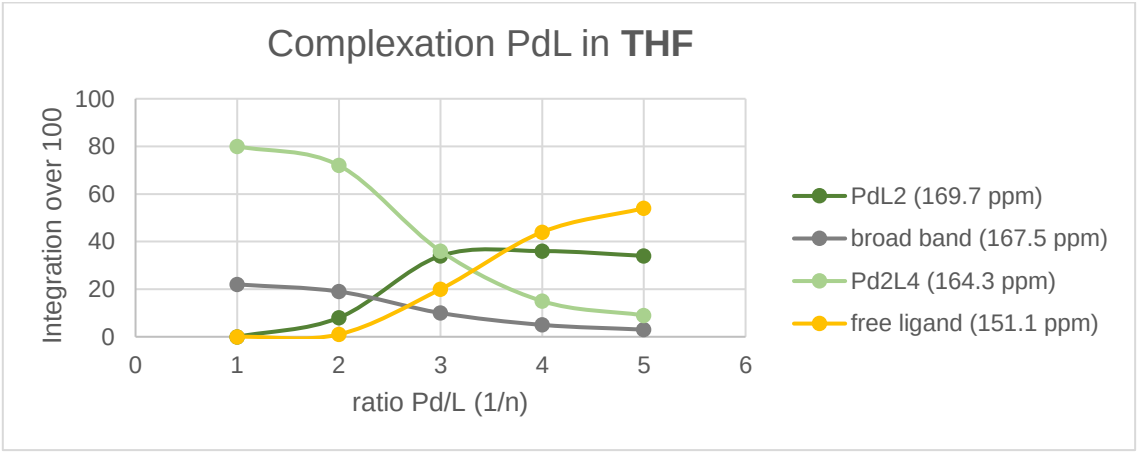

Figure 3.39: Integration of $^{31}P\{^1H\}$ NMR spectra of Pd/**L**$_{PN}$ based complexes at different Pd:**L**$_{PN}$ ratios at 293 K in THF.

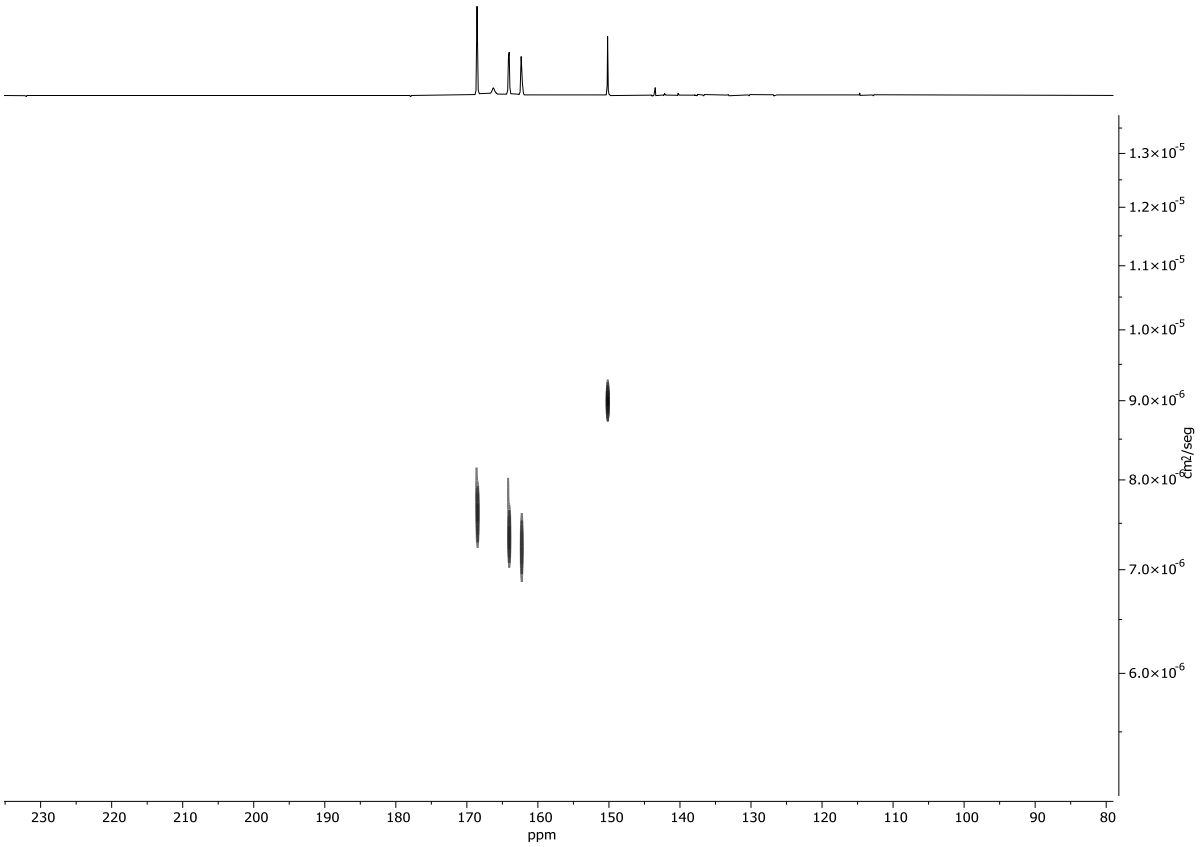

Figure 3.40: $^{31}P\{^{1}H\}$ DOSY NMR spectrum of Pd^{0} species with Pd:**L*PN*** = 1/2.5 at 293 K in THF/MeCN (3:1, v/v).

Synthesis, analysis and catalytic use of $Pd^0{}_1L_2$ complex

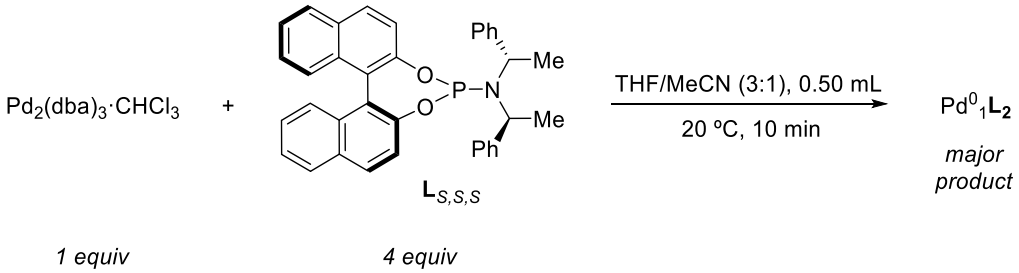

Figure 3.41: Reaction scheme for the synthesis of $Pd^0{}_1L_2$.

Procedure: In a 5 mL vial, $Pd_2(dba)_3{\cdot}CHCl_3$ (7 mg, 0.0135 mmol) and ligand $\mathbf{L_{PN}}$ (29.9 mg, 0.055 mmol, 4.0 equiv) were dissolved in 1.5 mL of a THF/MeCN (3:1 v/v) solvent mixture. The reaction mixture was stirred for 5 min and the solution was then filtered through Celite into an empty Schlenk flask. The solvent was removed in *vacuo* and the product introduced inside a glovebox. The crude product was washed with 15 mL of Et_2O resulting in a yellow solution (i.e., removing the dba) and a white solid (the Pd^0 complex). The latter was washed a second time with 10 mL of Et_2O and then dried under vacuum. An apparent crystalline product was obtained by dissolving the colorless solid by a minimum amount of THF/Et_2O and kept at -30 ºC (yield: 10.1 mg). Two different crops of product of this compound were measured by X-ray analysis but both samples were classified as amorphous under an optic microscope.

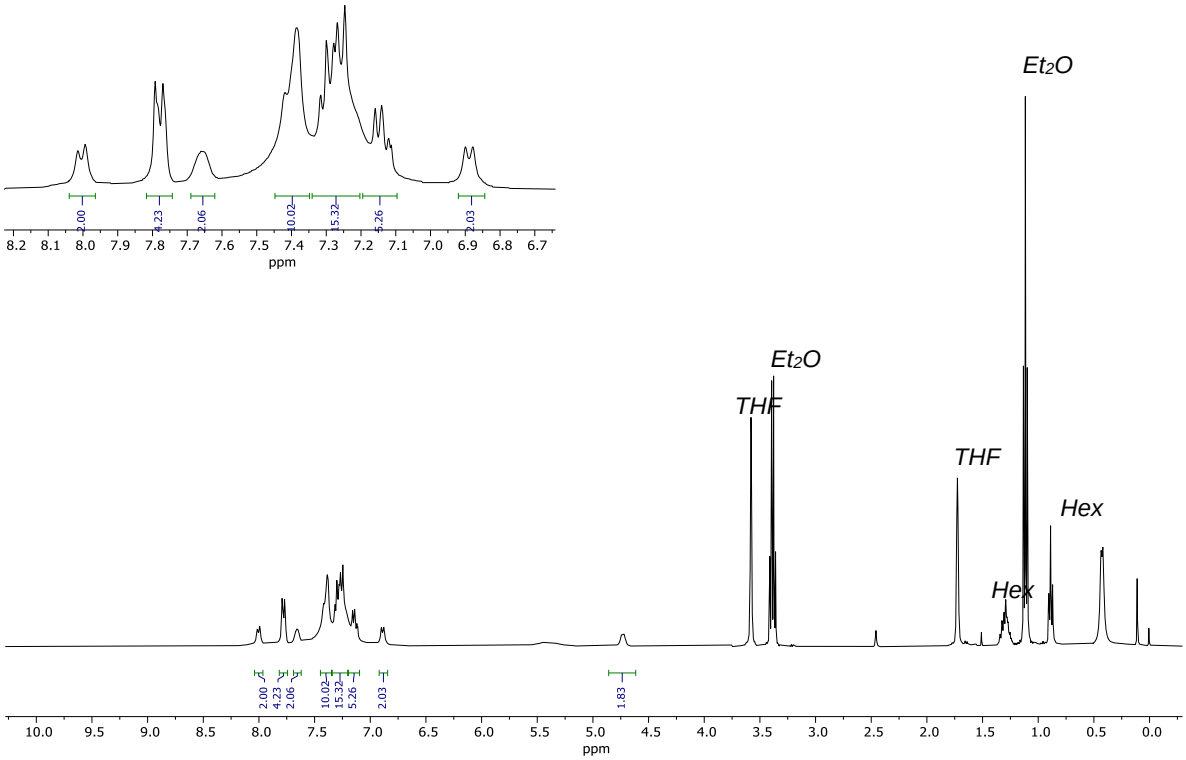

Figure 3.42: ^{1}H NMR spectrum of $Pd^{0}_{1}\mathbf{L_2}$ complex at 293 K in THF-d_8.

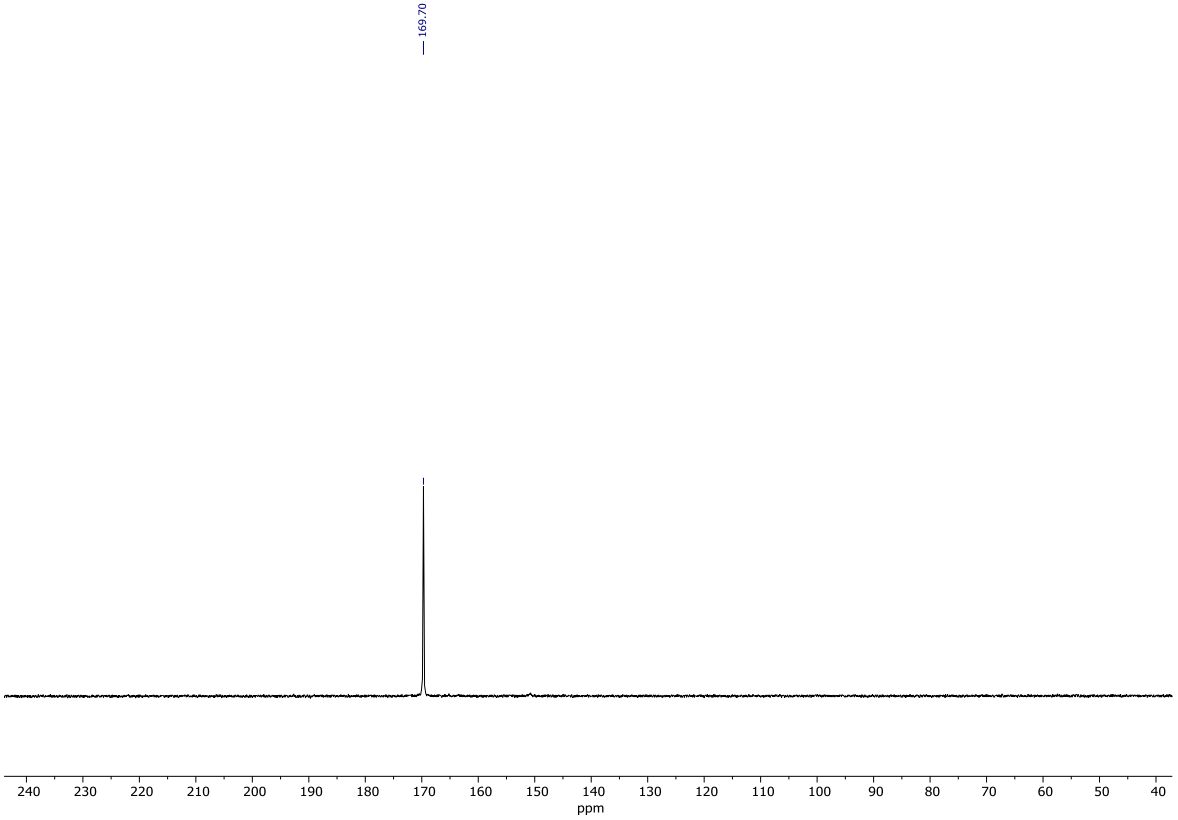

Figure 3.43: ^{31}P{^{1}H} NMR spectrum of $Pd^{0}_{1}\mathbf{L_2}$ complex at 293 K in THF-d_8 externally referenced to the free ligand $\mathbf{L_{PN}}$.

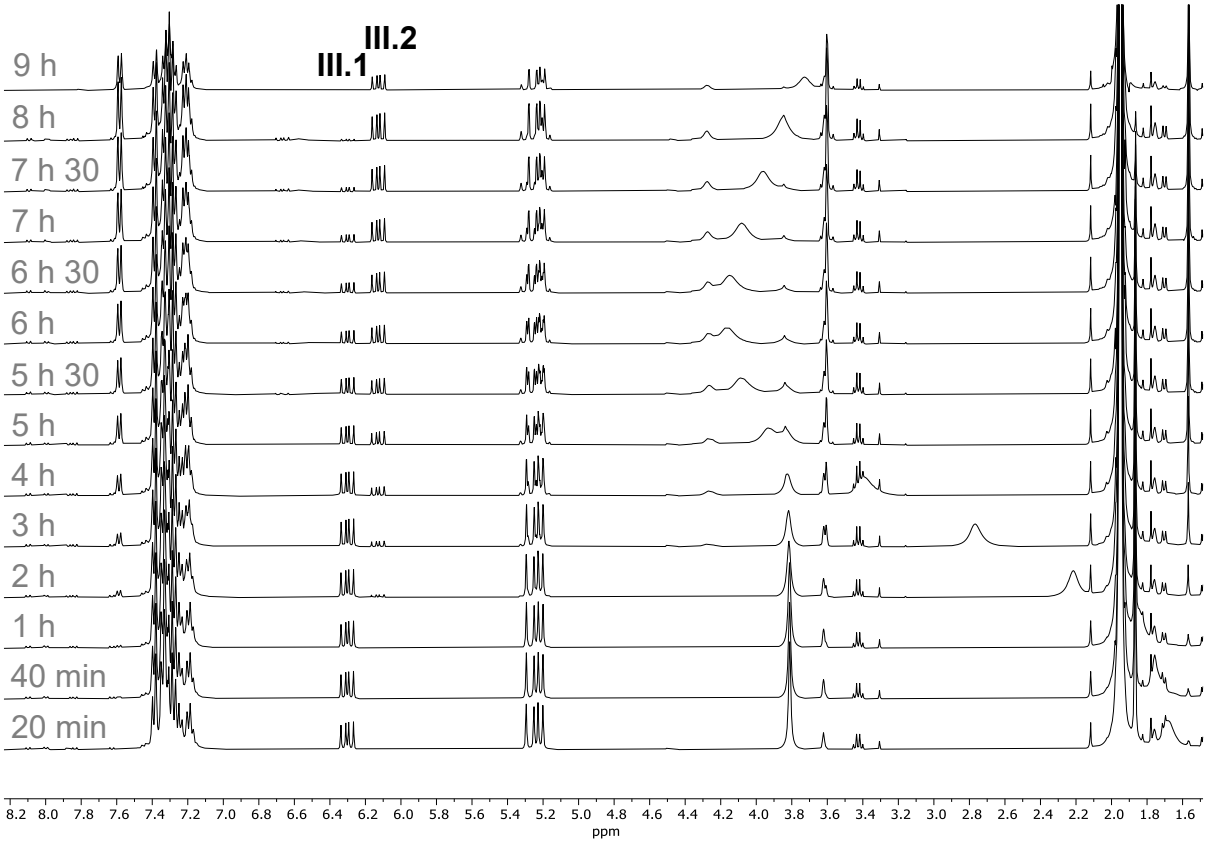

Figure 3.44: ^{1}H NMR spectra of a kinetic experiment using $Pd^0_1\mathbf{L_2}$ as pre-catalyst at a Pd/$\mathbf{L_{PN}}$ ratio of 1:2.5 at 293 K in THF/MeCN (3:1, v/v). Conversion of **III.1** to **III.2** as major product.

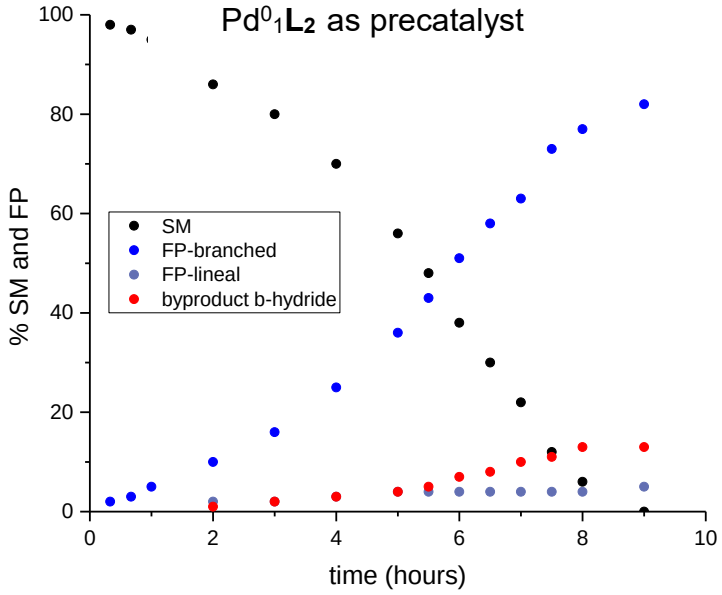

Figure 3.45: ^{1}H NMR kinetic plot of the catalytic allylic amination of substrate **III.1 (SM)** with $Pd^0_1\mathbf{L_2}$ **III.5** as pre-catalyst at 20 ºC in THF-d_8/MeCN (3:1, v/v).

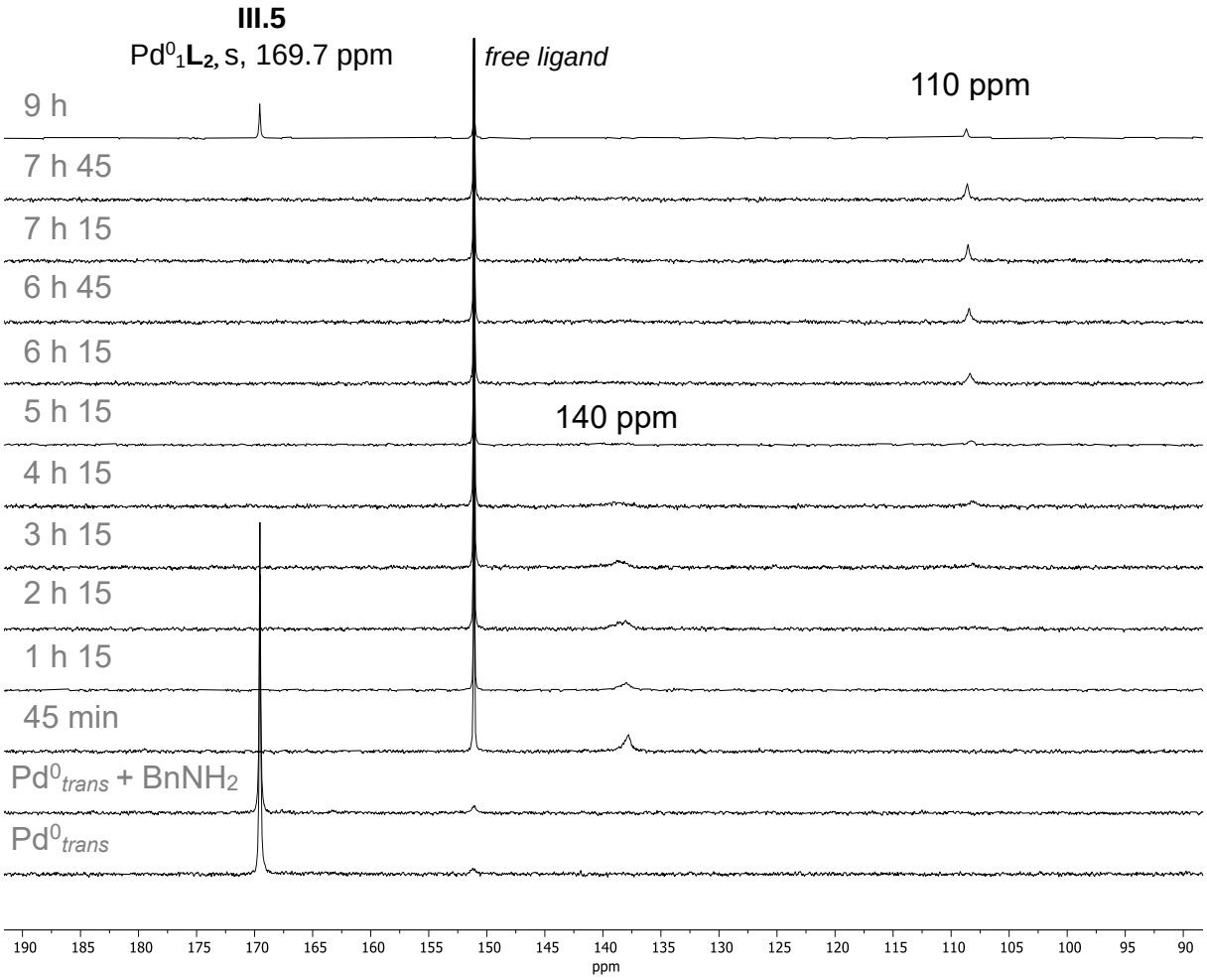

Figure 3.46: $^{31}P\{^{1}H\}$ NMR spectra of a kinetic catalytic experiment with Pd^0_1**L₂ III.5** as precatalyst; Pd/**L*PN*** = 1/2.5 at 293 K in THF/MeCN (3:1).

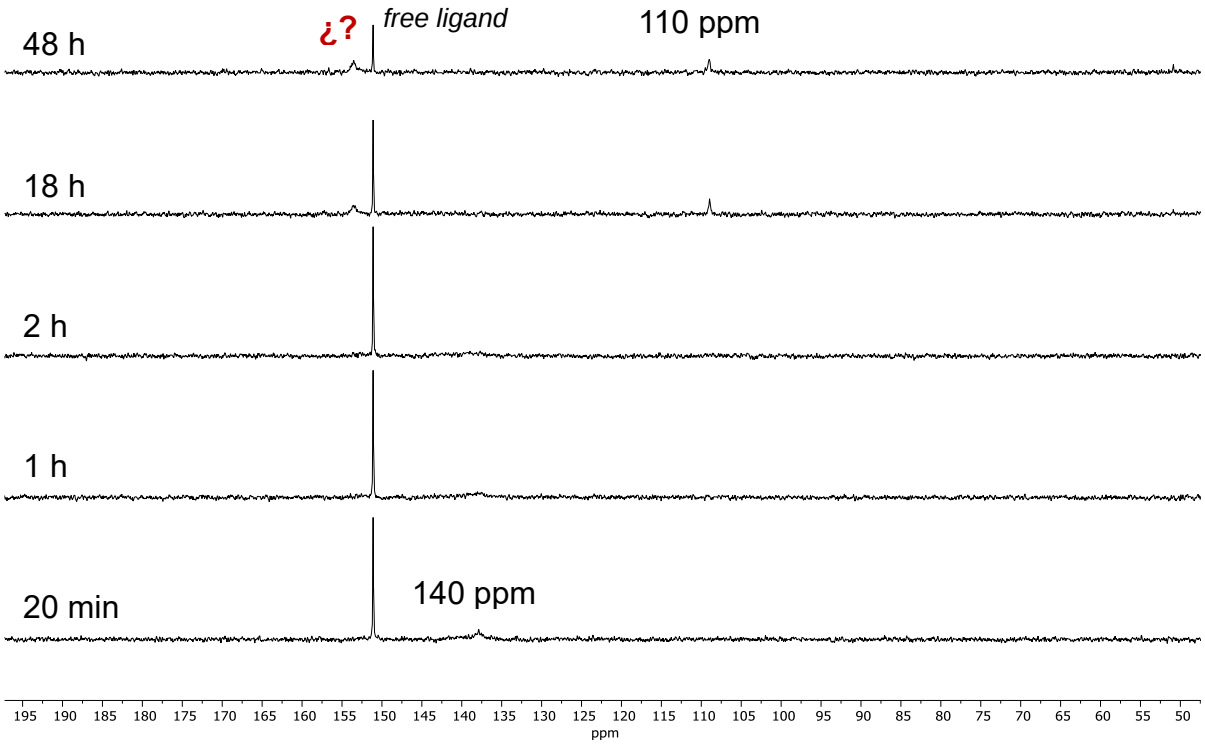

Figure 3.47: $^{31}P\{^{1}H\}$ NMR spectra of a catalytic experiment using $Pd^0_2\mathbf{L}_4(dba)_n$. Pd/$\mathbf{L}_{PN}$ = 1/1 at 293 K in THF/MeCN (3:1, v/v).

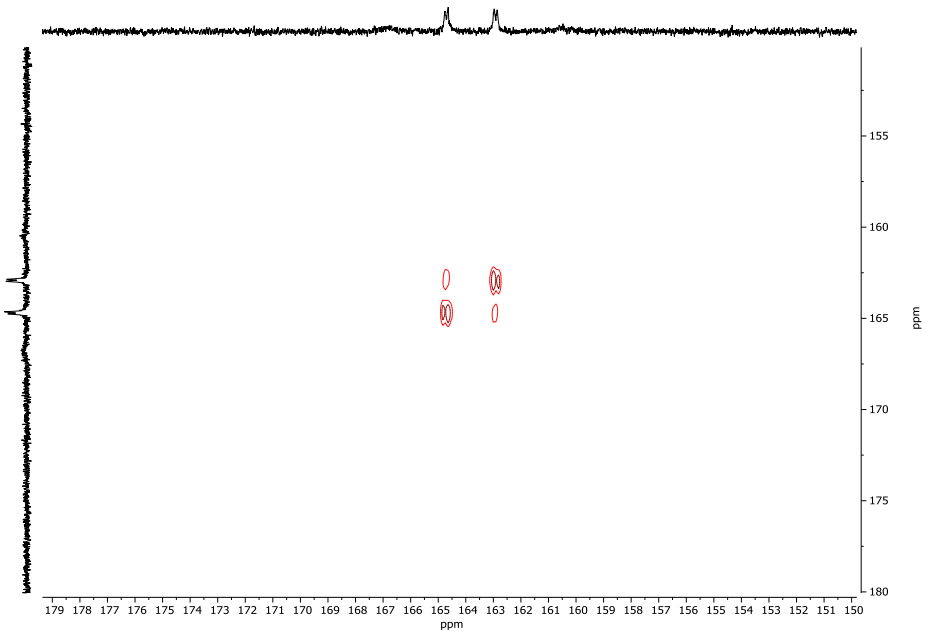

Figure 3.48: 2D $^{31}P\{^{1}H\}$ COSY NMR spectrum of $Pd^0_2\mathbf{L}_4(dba)_n$ **III.4** at a Pd/$\mathbf{L}_{PN}$ ratio of 1:1 at 20 ºC in a THF/MeCN mixture (3:1, v/v).

Complexation studies of Pd and L_{PN}, and influence of an excess of *dba*

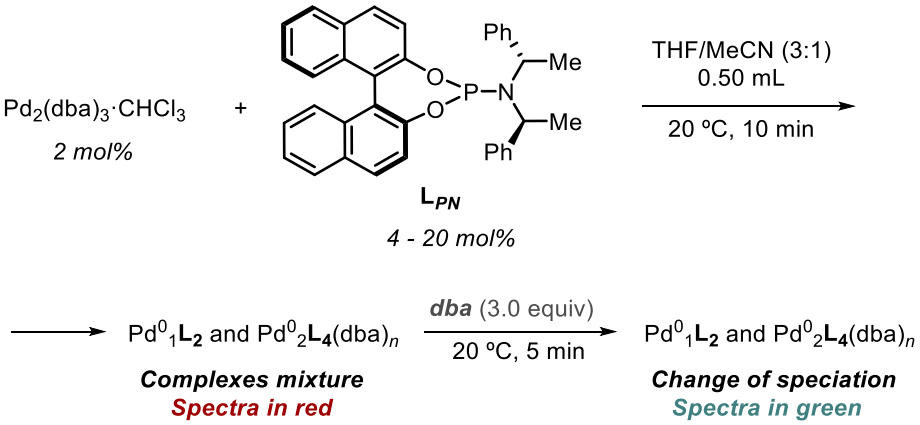

Figure 3.49: Reaction scheme for the complexation reaction of Pd_2dba_3 and L_{PN} and further addition of an excess of ***dba***.

Procedure for the preparation of pre-catalyst mixture with an excess of dba: In a 2 mL vial, $Pd_2(dba)_3{\cdot}CHCl_3$ (3 mg, 3 µmol , 1.0 equiv) and ligand L_{PN} (8 or 16 mg, 15 or 30 µmol, 2.5 or 5.0 equiv) were dissolved in 0.50 mL of a THF/MeCN (3:1, v/v) solvent mixture. The reaction mixture was stirred for 10 min before it was transferred to an NMR tube equipped with an acetone-d_6 capillary. The $^{31}P\{^1H\}$ NMR was measured and the tube was introduced back into the glovebox. There, dba (6 mg, 9 µmol 3.0 equiv) was added to the tube. Two solutions were prepared with different amounts of Pd-to-L_{PN}, the first one being 1:2.5 ratio and the second 1:5.

Observations: The addition of an excess of dba to a mixture of complexes $Pd^0{}_1L_2$ **III.5** and $Pd^0{}_2L_4(dba)_n$ **III.4** reduces the signal at 169.7 ppm ($Pd^0{}_1L_2$) and increases the free ligand signal at 151.1 ppm. This implies that dba favors back-equilibrium towards $Pd_2L_4(dba)_n$ **III.4** and free L_{PN}. At lower ratios of Pd-to-L_{PN} this effect is more pronounced compared to the case where a Pd-to-L_{PN} ratio of 1:5 was used.

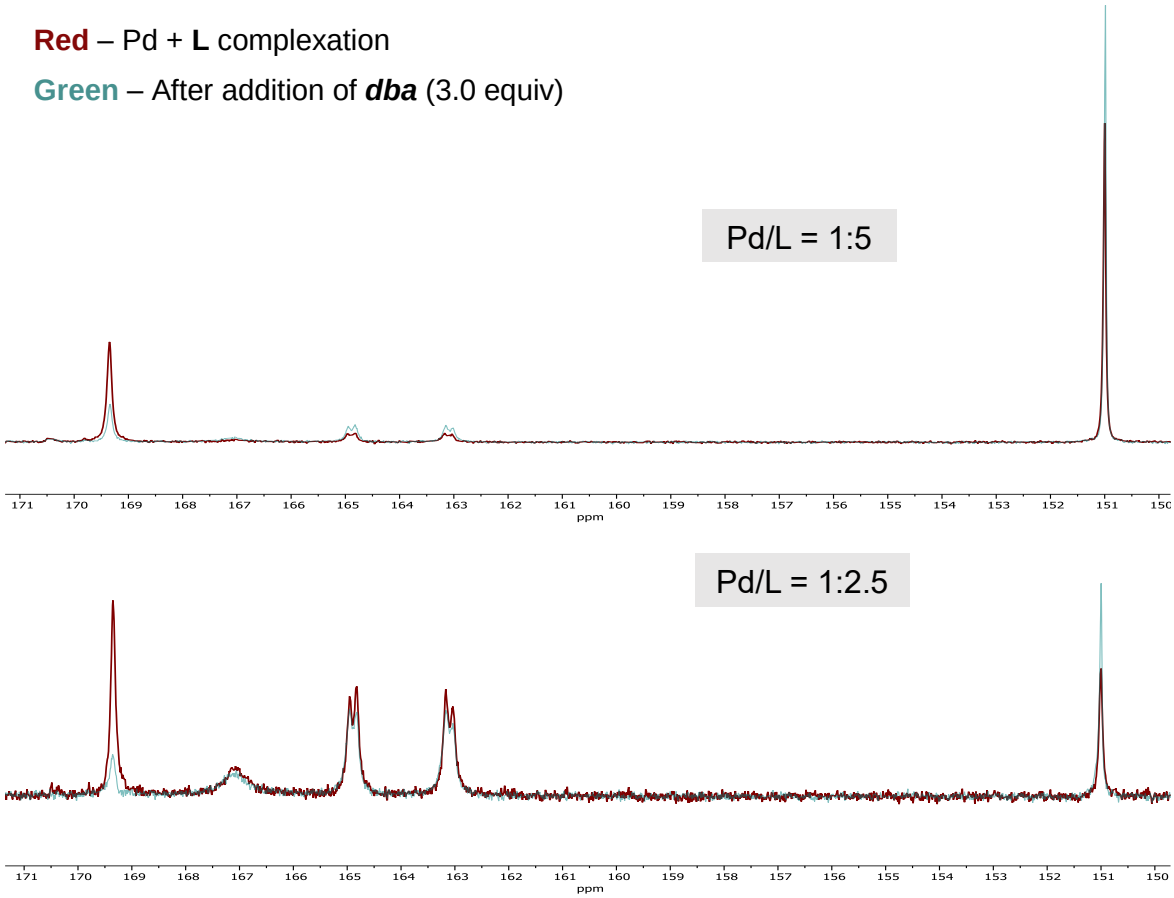

Figure 3.50: Comparison of overlaid $^{31}P\{^{1}H\}$ NMR spectra of complexes Pd^{0}_{1}**L₂ III.5** and Pd^{0}_{2}**L₄**$(dba)_n$ **III.4** after the addition of ***dba*** at 20 ºC in THF/MeCN mixture (3:1, v/v) at two different ratios of Pd-to-**L*PN*** (1:5, top; and 1:2.5 below).

$^{31}P\{^{1}H\}$ NMR experiments for the Detection of intermediates (140 ppm and 110 ppm)

Room-temperature experiments

Procedure: In a 2 mL vial, $Pd_2(dba)_3{\cdot}CHCl_3$ (3 mg, 2 mol%) and ligand **L*PN*** (8 mg, 10 mol% or 16 mg, 20 mol%) were dissolved in 0.50 mL of a THF/MeCN (3:1, v/v) solvent mixture. The reaction mixture was stirred for 5 min before adding benzyl amine **III.2** (18.5 µL, 0.17 mmol, 1.1 equiv) with a Hamilton syringe. After reaching a homogeneous solution, substrate **III.1** (37 mg, 0.15 mmol, 1.0 equiv) was added and the catalytic solution was transferred to an NMR tube equipped with an acetone-d_6 capillary. Two experiments were conducted with two different Pd-to-**L*PN*** ratios being 1:2.5 (Figure 3.52) and 1:5 (Figure 3.53).

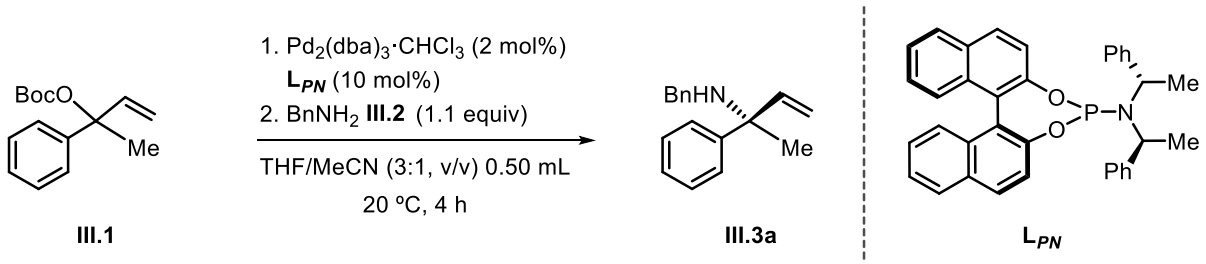

III.1 **III.3a** **L*PN***

Figure 3.51: Catalytic conditions for $^{31}P\{^{1}H\}$ NMR kinetic experiments for the detection of reaction intermediates.

Observations: When the catalytic mixture was followed by $^{31}P\{^{1}H\}$ NMR, we could detect more than one intermediate species. Initially, one broad peak is observed around 140 ppm. While this signal slowly disappears, another broad peak is spotted around 110 ppm. The reaction appears to be complete when the signal at 140 ppm is completely consumed and the starting Pd^0 species reappear between 160-170 ppm. Another observation is the presence of free ligand **L*PN*** throughout the course of the catalysis. At a higher Pd:**L*PN*** ratio (Figure 3.53), the observations are quite similar with the only difference being that the catalysis is faster.

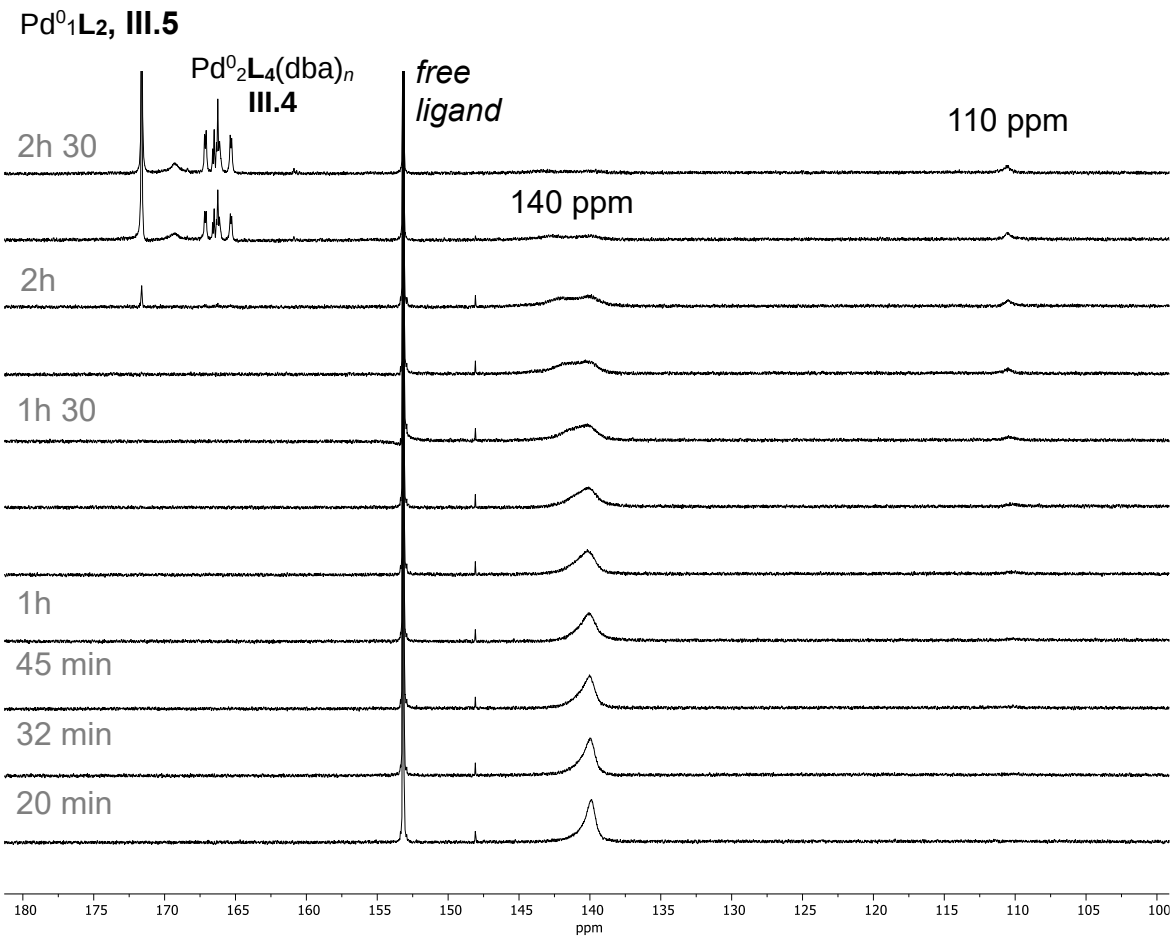

Figure 3.52: $^{31}P\{^{1}H\}$ NMR spectra of a catalytic experiment with a Pd:$\mathbf{L}_{PN}$ ratio of 1:2.5 in THF/MeCN (3:1, v/v) at 20 °C.

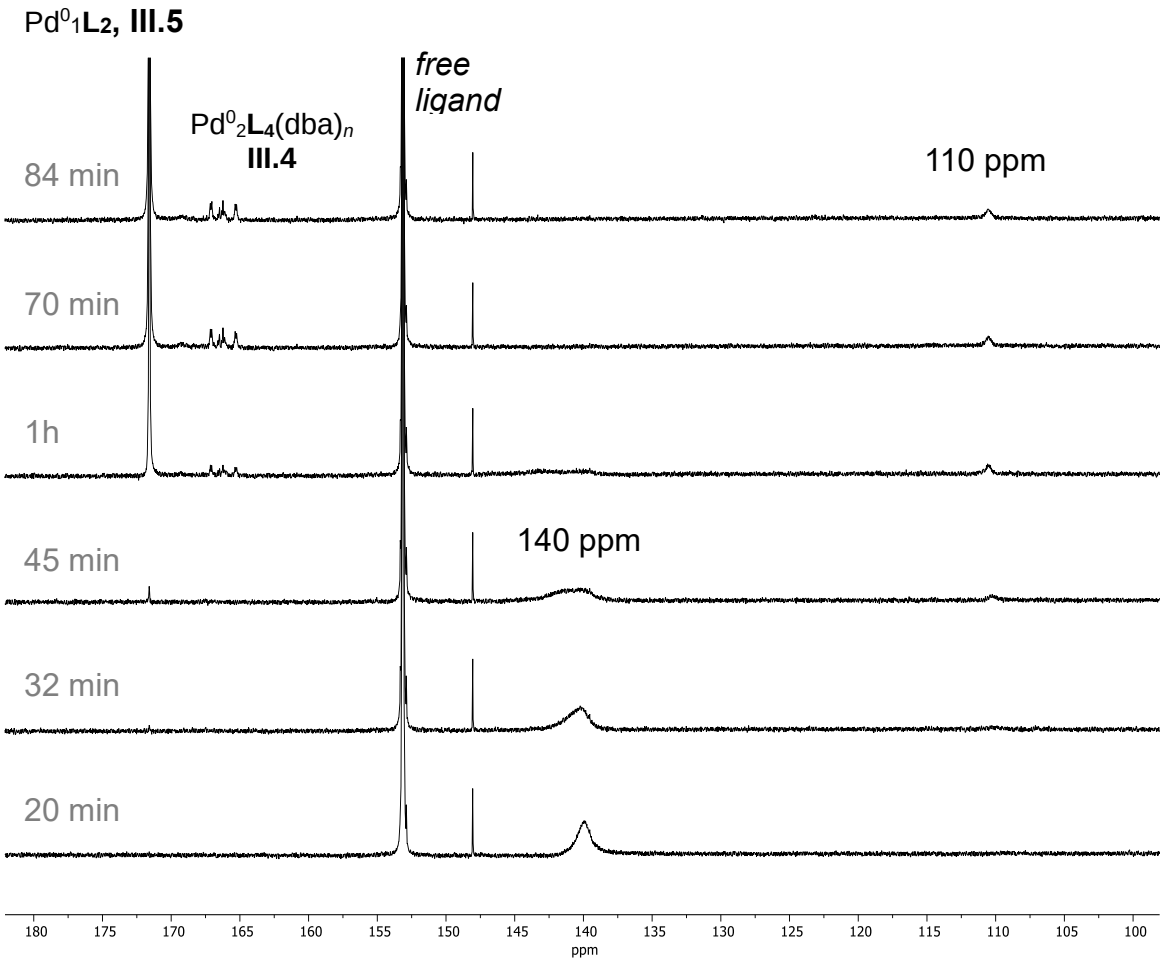

Figure 3.53: $^{31}P\{^{1}H\}$ NMR spectra of a catalytic experiment with a Pd:**L*PN*** ratio of 1:5 in THF/MeCN (3:1, v/v) at 20 °C.

Low temperature $^{31}P\{^{1}H\}$ NMR measurements

The optimization of low temperature measurements was prepared as described in Figure 3.51. The spectra can be observed in Figure 3.8 (Section 3.3.3).

Observations from Figure 3.8 in Section 3.3.3: This experiment was conducted following the conditions reported in Figure 3.51 with two differences: THF was used as the only solvent and the sample was measured at different temperature intervals. The broad band observed at 140 ppm at 293 K splits into two major peaks at lower temperatures (≤ 233 K). We assigned the splitting of signals to equilibrating Pd species as mentioned in Figure 3.11 where we provide the calculated energies of the possible Pd(allyl) species involved at this stage.

Intermediate at 140 ppm: Dependence on the amount of ligand L_{PN} at 213 K

Procedure: In a 2 mL vial, $Pd_2(dba)_3{\cdot}CHCl_3$ (3 mg, 2 mol%) and ligand **L_{PN}** (8 mg, 10 mol% or 16 mg, 20 mol%) were dissolved in 0.50 mL of THF. The reaction mixture was stirred for 5 min before adding benzyl amine **III.2** (18.5 µL, 0.17 mmol, 1.1 equiv) with a Hamilton syringe. After reaching a homogeneous state, substrate **III.1** (37 mg, 0.15 mmol, 1.0 equiv) was added and the catalysis mixture transferred to an NMR tube equipped with an acetone-d_6 capillary. The mixture was left for 5 min before measuring the $^{31}P\{^{1}H\}$ NMR at 213 K. Two mixtures were prepared with different Pd-to-**L_{PN}** ratios being 1:2.5 and 1:5. The example in the scheme below refers to Pd:**L_{PN}** = 1:5.

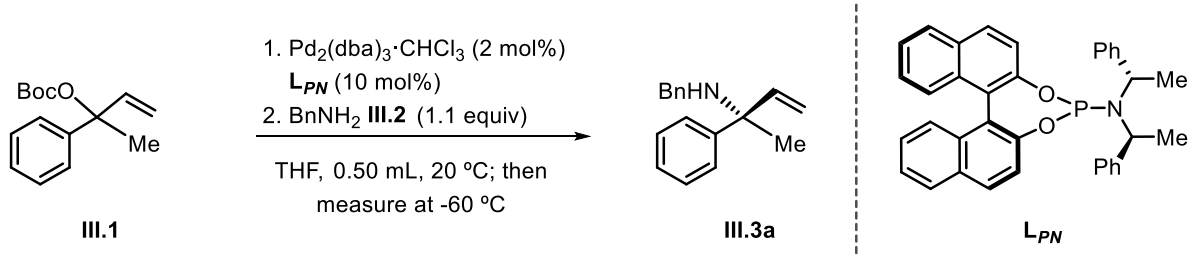

III.1 **III.3a** **L_{PN}**

Figure 3.54: Catalytic reaction conditions for $^{31}P\{^{1}H\}$ NMR experiments for the detection of 140 ppm intermediate at different Pd:**L** ratios.

Observation: The intensity of each species at 140.0 ppm and 139.2 ppm does not noticeably vary depending in the presence of more free **L_{PN}**.

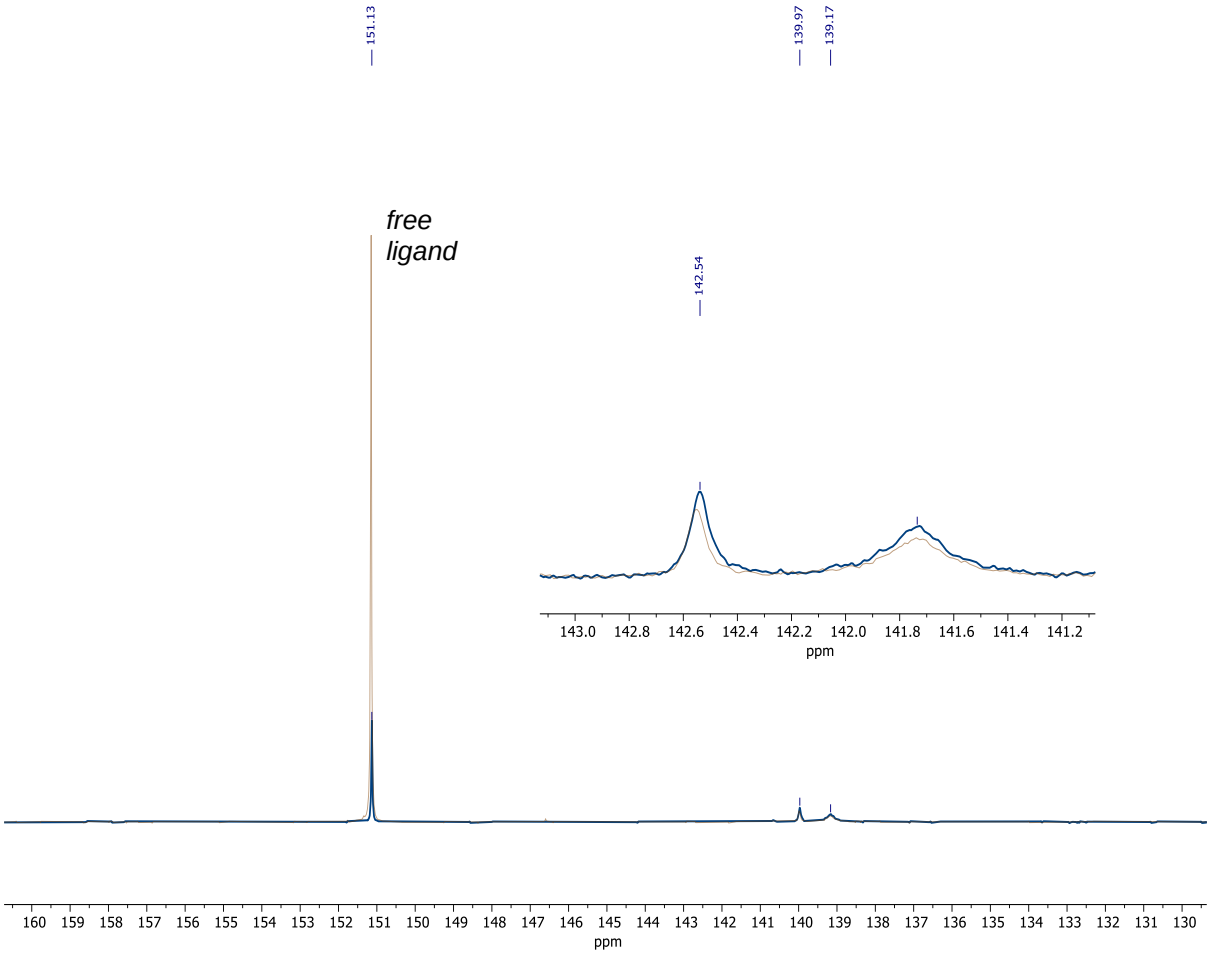

Figure 3.55: $^{31}P\{^{1}H\}$ NMR overlaid spectra of the intermediates around 140 ppm at different Pd:$\mathbf{L}_{PN}$ ratios. In **blue**, Pd:$\mathbf{L}_{PN}$ = 1:2.5 and in **red** Pd:$\mathbf{L}_{PN}$ = 1:5, both at 213 K in THF.

Intermediate at 140 ppm: Equilibrium exchange study by EXSY NMR at 233 K

The sample used for the ^{31}P NMR EXSY low temperature measurement was prepared as described in Figure 3.51 with a difference in the solvent mixture used. In this case: THF/MeCN 3/1.

Observation: There is indeed exchange between signals around 140 ppm (cross peaks observed), therefore equilibrating species are present.

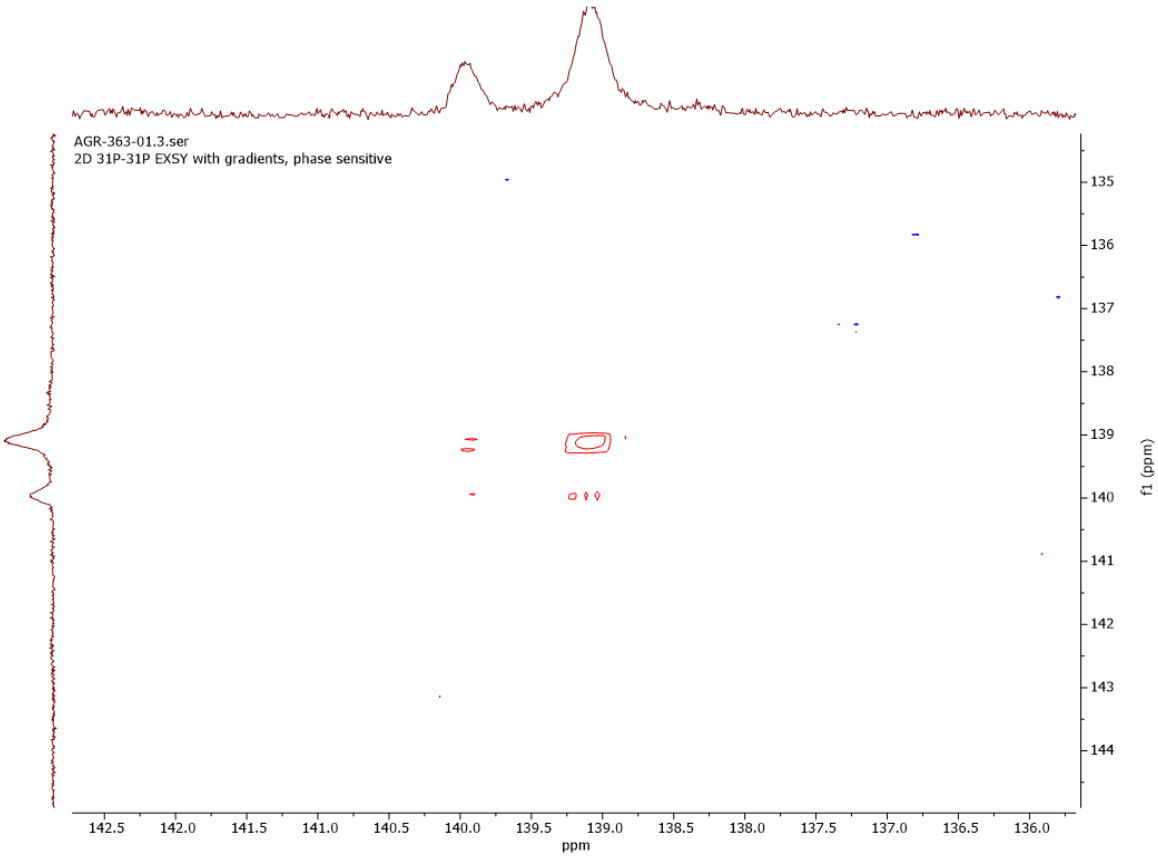

Figure 3.56: ^{31}P NMR EXSY NMR for the intermediates found around 140 ppm at 233 K in a 3:1 (v/v) THF/MeCN mixture.

Intermediate 140 ppm and 110 ppm: Dependence on the benzyl amine and the leaving group

Procedure: In a 2 mL vial, $Pd_2(dba)_3 \cdot CHCl_3$ (3 mg, 2 mol%) and ligand $\mathbf{L}_{PN}$ (8 mg, 10 mol%) were dissolved in 0.50 mL of THF. The reaction mixture was stirred for 5 min before adding the respective benzyl amine (18.5 µL, 0.17 mmol, 1.1 equiv) through a Hamilton syringe. After reaching a homogeneous state, substrate **III.1** (37 mg, 0.15 mmol, 1.0 equiv) was added and the catalysis mixture was transferred to an NMR tube equipped with an acetone-d_6 capillary. Several experiments were prepared with different substrates (cf., leaving groups) and benzyl amines.

Intermediate 140 ppm: The mixture was first stirred for 5 min at r.t. before the $^{31}P\{^1H\}$ NMR was measured at 213 K.

Intermediate 110 ppm: The mixture was followed by $^{31}P\{^1H\}$ NMR and when the second intermediate at 110 ppm was observed, it was cooled to 213 K.

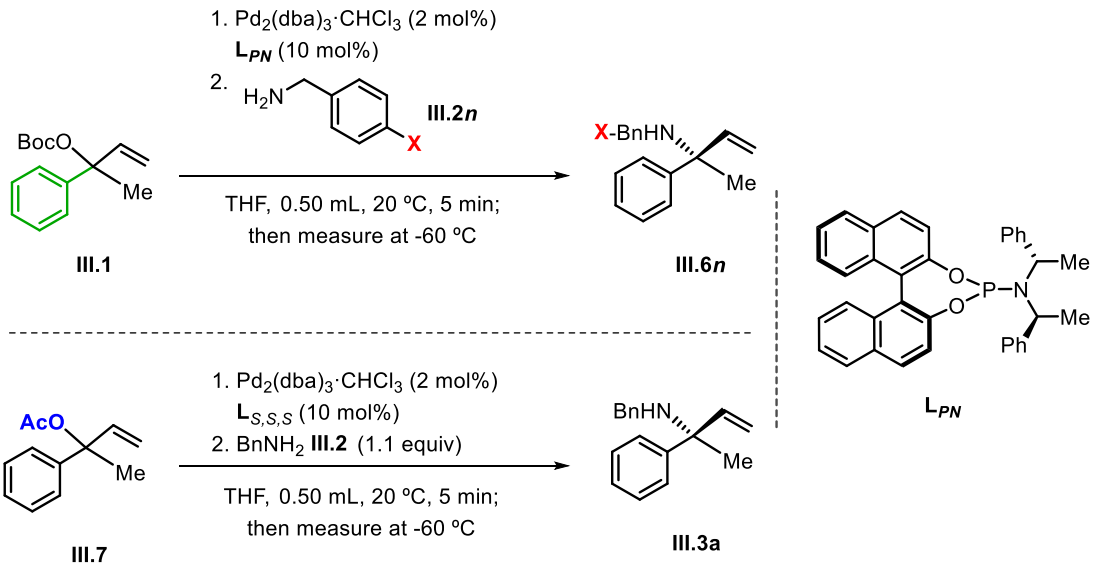

Figure 3.57: Catalytic conditions for the study of the intermediates resonating around140 and 110 ppm using different **allylic substrate**, **benzyl amines** and **leaving groups** at 213 K.

Observations in Figures 3.9, 3.10, 3.12 and 3.13.: The intermediate(s) observed around 140 ppm only depend on the substrate and on the leaving group. When the amine was changed, no significant displacement of the chemical shift was observed by $^{31}P\{^{1}H\}$ NMR. On the other hand, the position of the intermediate at 110 ppm depends on both the substrate and on the nucleophile. While studying the effect of the leaving group by switching from OBoc to OAc, we were not able to detect the second intermediate at 110 ppm. In the case of carbonate substrates decorated with substituted aryl groups (*ortho*-Cl, *para*-Cl, *meta*-Me), we were also not able to detect an intermediate in the region around 110 ppm. A list of peaks reported for each substrate combination is provided below (**Table III.VIII**).

Table III.VIII: Reported peaks for Pd-intermediates observed at 140 ppm and 110 ppm for carbonate substrates having different substituents **III.1*n*** and benzyl amine **III.2*n***, and for a substrate having a different leaving group (OAc). The ^{31}P NMR peaks are referenced to free $\mathbf{L}_{PN}$ (δ = 151.1 ppm).

	First intermediate(s), in ppm	*Second intermediate(s), in ppm*
Benchmark	140.0, 139.2	111.1, 108.2
Leaving group		
OAc	139.0; 137.2	*not observed*
Benzyl amine		
para-F	140.0; 139.2	108.7; 107.3
para-OMe	140.0; 139.2	92.8
Substrate		
naphthyl	139.5; 139.1; 138.0	110.7; 107.5
para-Cl; *meta*-Me	139.4; 139.0; 137.8	*not observed*
ortho-Cl	139.9; 138.9; 137.6	*not observed*
para-OMe	141.1; 140.4; 139.4; 138.3	108.0; 105.2

Effect of MeCN for regio-selectivity: Kinetic study of the disappearance of intermediate 140 ppm

Procedure: In a 2 mL vial, $Pd_2(dba)_3{\cdot}CHCl_3$ (3 mg, 2 mol%) and ligand **L*PN*** (8 mg, 10 mol%) were dissolved in 0.50 mL of solvent (see different conditions below). The reaction mixture was stirred for 5 min before adding benzyl amine (18.5 µL, 0.17 mmol, 1.1 equiv) through a Hamilton syringe. After reaching a homogeneous state, substrate **III.1** (37 mg, 0.15 mmol, 1.0 equiv) was added and the catalysis mixture was transferred to an NMR tube equipped with an acetone-d_6 capillary.

THF: The reaction mixture was stirred for 5 min at r.t. before recording a $^{31}P\{^1H\}$ NMR analysis at 213 K. The reaction mixture was measured every h at 213 K. During the time intervals, the reaction mixture was kept reacting at 293 K.

THF/MeCN (3:1): The reaction mixture was stirred for 5 min at r.t. before the $^{31}P\{^1H\}$ NMR was measured at 233 K. The mixture was measured every 30 min at 233 K. During the time intervals, the reaction was kept reacting at 293 K. In this experiment, the Pd:**L*PN*** ratio was 1:5, using 3 mg of Pd_2dba_3 and 16 mg of ligand **L*PN***.

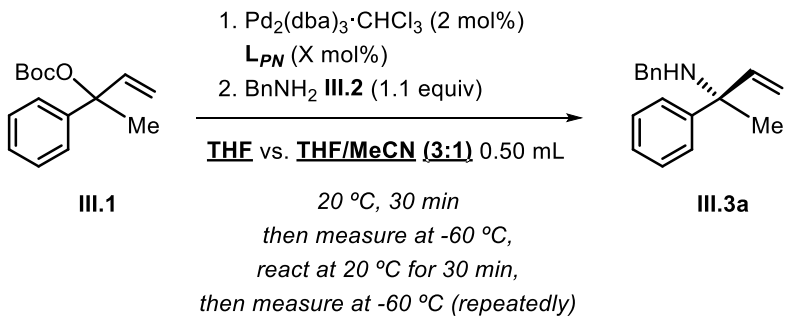

Figure 3.58: Catalytic conditions to the study the intermediates around 140 and 110 ppm with differently substituted substrates at 213 K.

Observations: In Figure 3.17, a change in the solvent ratio (THF:MeCN) changes the population of the different allylic species in equilibrium. In Figure 3.18 we can observe that in THF the minor species (right-hand side at around 140 ppm) is the peak disappearing faster. Similarly, in THF/MeCN (Figure 3.19), the major peak at the right is the species reacting faster.

Presence of Nucleophile required for the Oxidative Addition step

This series of experiments was carried out to examine whether the substrate could undergo oxidative addition in the absence of benzyl amine **III.2**.

Procedure: Two different tubes were prepared following these steps. In two different 2 mL vials, $Pd_2(dba)_3{\cdot}CHCl_3$ (3 mg, 2 mol%) and ligand $\mathbf{L}_{S,S,S}$ (8 mg, 10 mol%) were dissolved in 0.50 mL of a THF/MeCN (3:1, v/v) solvent mixture. The reaction mixtures were stirred for 5 min and the solutions were then transferred to two NMR tubes equipped with acetone-d_6 capillaries. After measuring the $^{31}P\{^1H\}$ NMR spectra of both samples, the next additions were prepared. In one case, the substrate **III.1** (37 mg, 0.15 mmol, 1.0 equiv) was added. In the second case, benzyl amine **III.2** (18.5 µL, 0.17 mmol, 1.1 equiv) was introduced via a Hamilton syringe. The homogeneous solutions were kept for 20 min before the $^{31}P\{^1H\}$ NMR was measured.

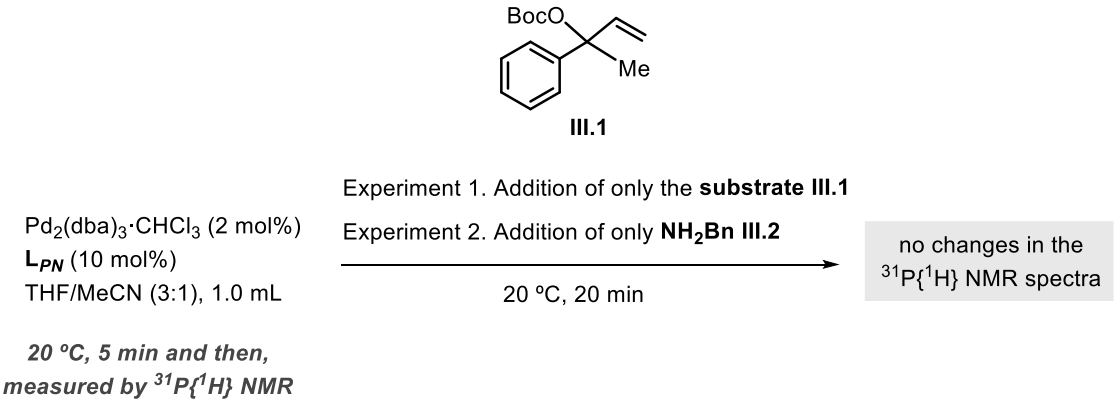

Figure 3.59: Reaction conditions for the study of the influence of both reaction partners by $^{31}P\{^1H\}$ NMR.

Observations: We do not observe the formation of the first intermediate(s) around 140 ppm intermediate unless all reaction components are present in solution. The co-presence of benzyl amine **III.2** is required in order to see the formation of this first intermediate, but its sole addition to a mixture of Pd^0 complexes $Pd^0{}_1\mathbf{L_2}$ **III.5** and $Pd^0{}_2\mathbf{L_4}(dba)_n$ **III.4** does not affect the NMR spectrum.

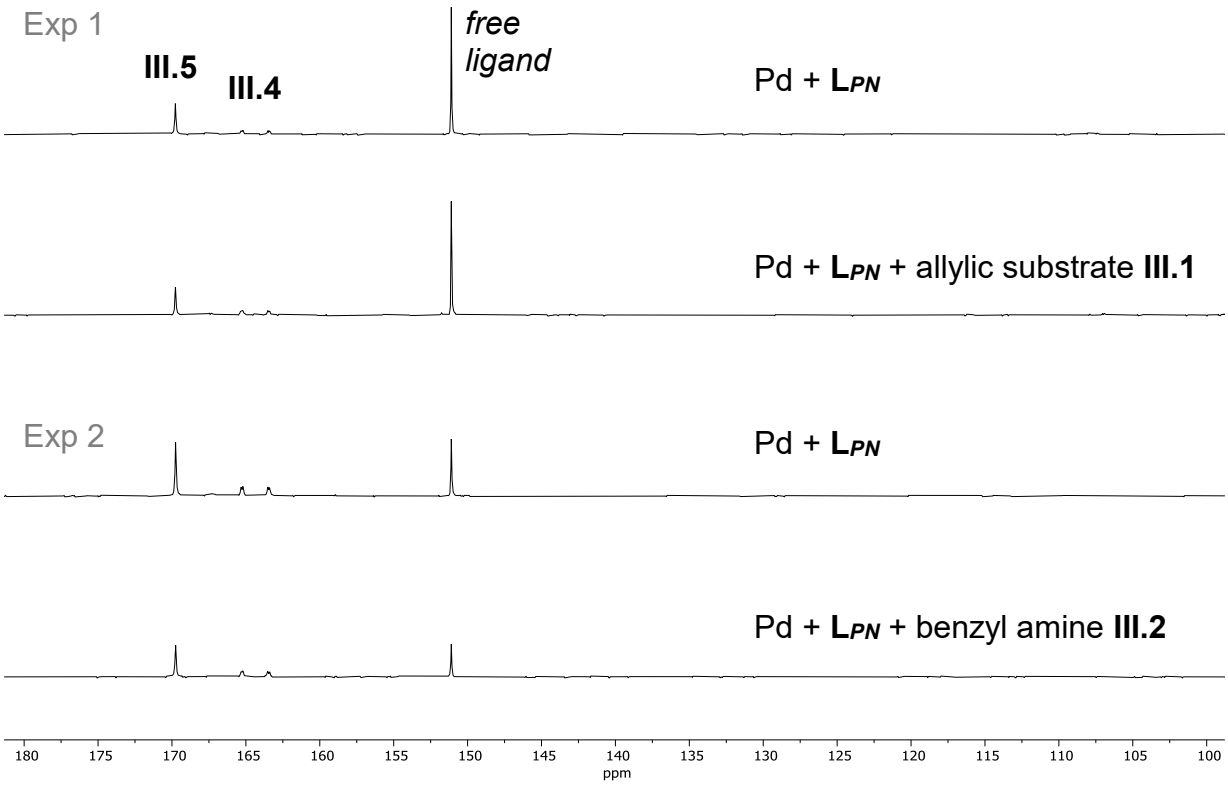

Figure 3.60: $^{31}P\{^{1}H\}$ NMR stacked spectra of the experiments studying the influence of the substrates.

Rate of the reaction, absence of MeCN and excess of *dba* ligand

This series of experiments was performed to see how the rate of the reaction is affected by the co-solvent and excess of dba ligand.

Procedure to study the influence of MeCN: In a 2 mL vial, $Pd_2(dba)_3 \cdot CHCl_3$ (3 mg, 2 mol%) and ligand **L*PN*** (8 mg, 10 mol% or 16 mg, 20 mol%) were dissolved in 0.50 mL of a THF. The reaction mixture was stirred for 5 min before adding benzyl amine **III.2** (18.5 µL, 0.17 mmol, 1.1 equiv) via a Hamilton syringe. After reaching a homogeneous state, substrate **III.1** (37 mg, 0.15 mmol, 1.0 equiv) was added and the catalysis mixture was transferred to an NMR tube equipped with an acetone-d_6 capillary. Two experiments were done with different Pd:**L*PN*** ratios being 1:2.5 (Figure 3.61) and 1:5 (Figure 3.62).

Observations: Following the catalytic mixtures by $^{31}P\{^1H\}$ NMR, we observed both broad peaks at around 140 and 110 ppm. When the reaction is completed, the initial Pd^0 species were spotted between 160-170 ppm. At a higher amounts of ligand **L*PN*** (Figure 3.61), the catalysis is faster.

Procedure to examine the influence of an excess of dba: The procedure for this experiment is the same as above, but after the addition of the substrate, also extra dba is added into the reaction mixture (6.3 mg, 0.027 mmol, 18 mol%). This reaction mixture was prepared with a mixture of solvents THF/MeCN (3:1, v/v) and a Pd-to-**L*PN*** ratio of 1:4.

Observations: The catalysis appears to be slower (Figure 3.61) compared to the benchmark reaction (Figure 3.5 in section 3.3.1).

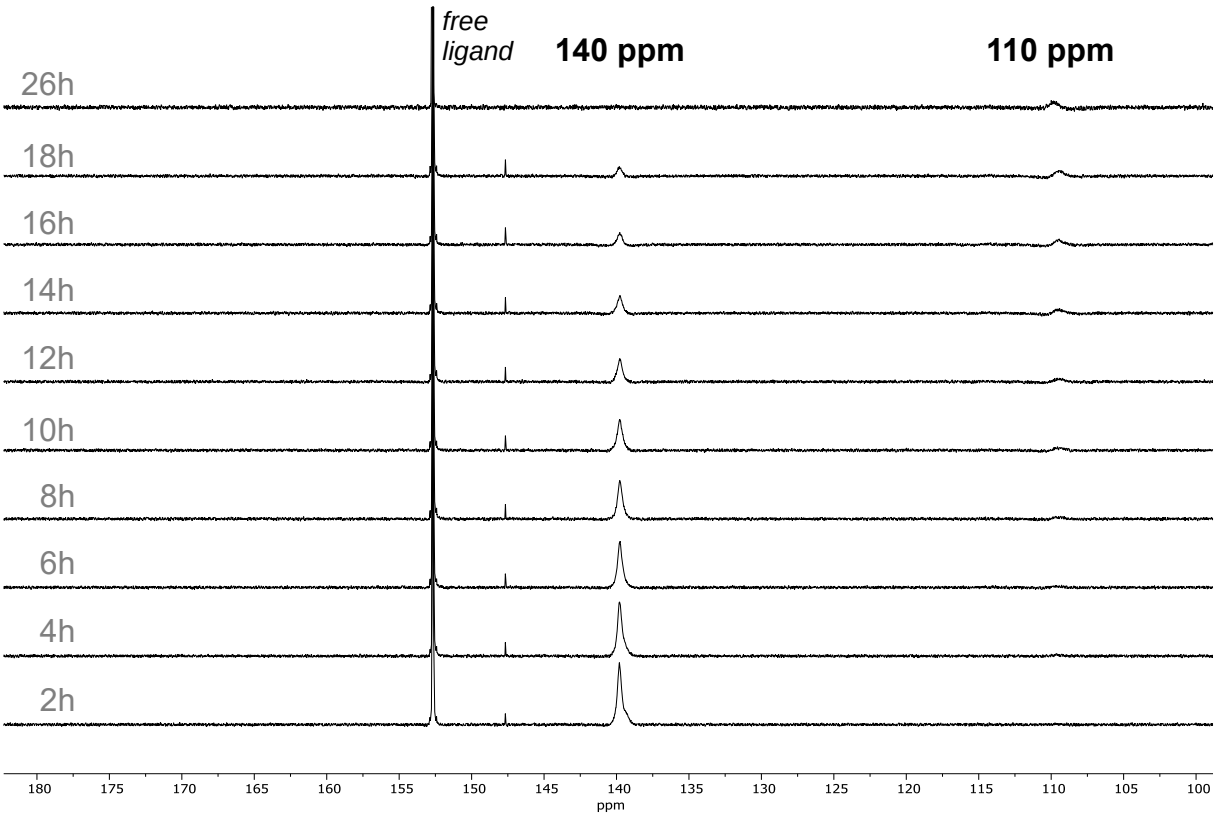

Figure 3.60: $^{31}P\{^{1}H\}$ NMR spectra of a catalytic experiment with a Pd/**L*PN*** ratio of 1:2.5 in THF at 20 °C.

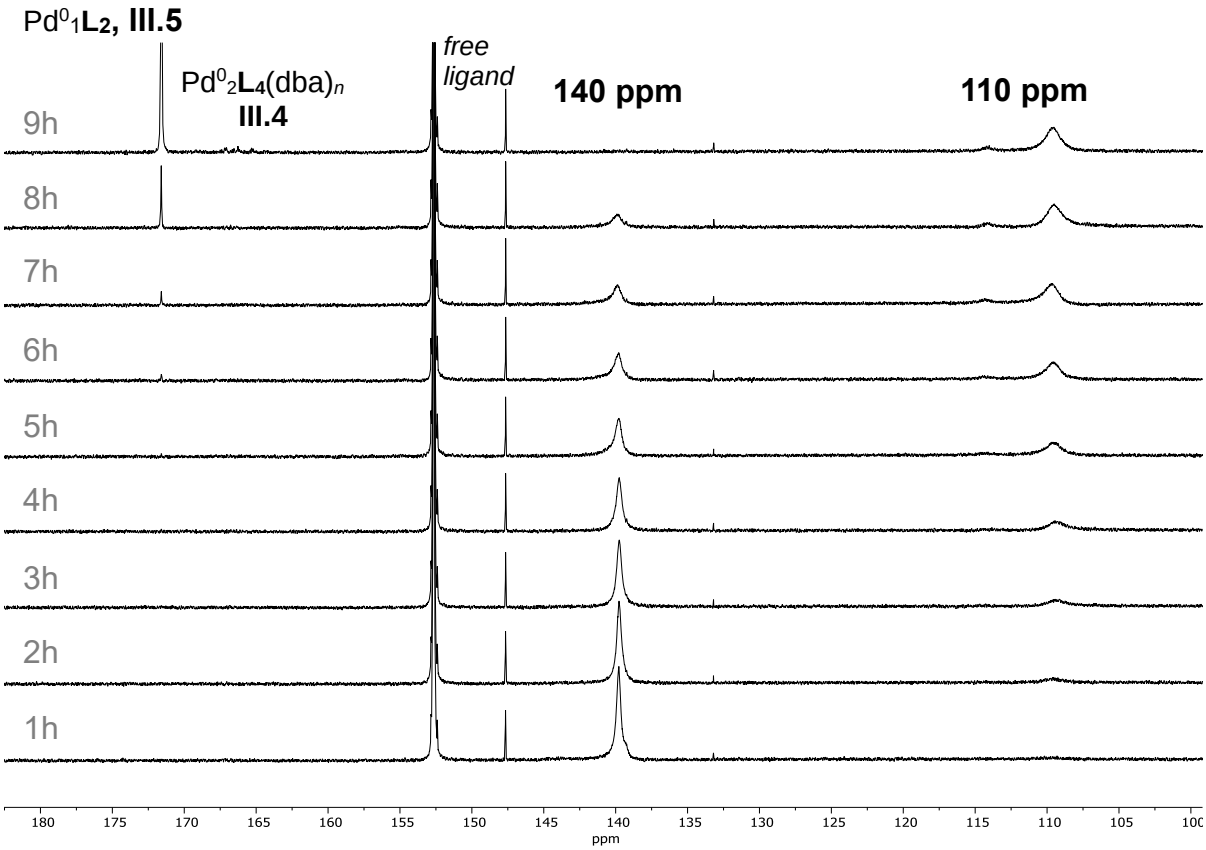

Figure 3.61: $^{31}P\{^{1}H\}$ NMR spectra of a catalytic experiment with a Pd/**L*PN*** ratio of 1:5 in THF at 20 °C.

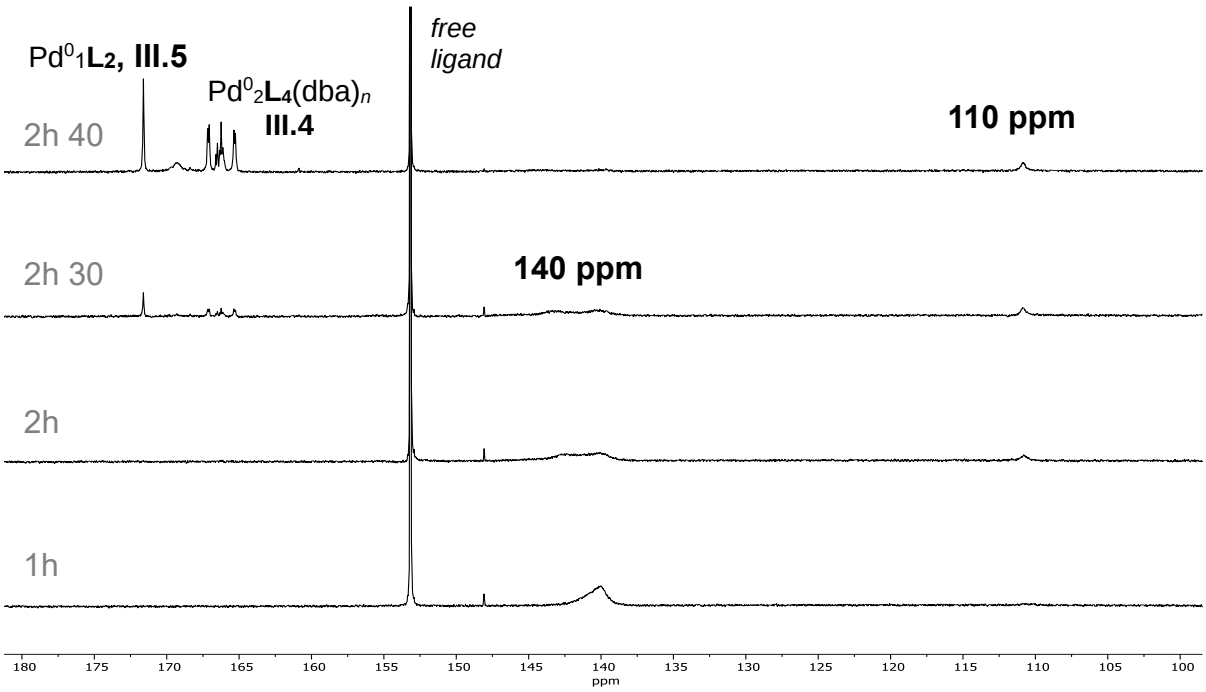

Figure 3.62: $^{31}P\{^{1}H\}$ NMR spectra in the presence of an excess of ***dba*** ligand and a Pd/**L*PN*** ratio 1:2.5 in THF/MeCN (3:1, v/v) at 20 °C.

3.6.4 Non-linear effect studies

Procedure: In a 2 mL vial, $Pd_2(dba)_3 \cdot CHCl_3$ (3 mg, 2 mol%) and ligand **L_{PN}-*(S)*** (X mol%) and **L_{PN}-*(R)*** (X mol%) was dissolved in 0.50 mL of a THF/MeCN (3:1, v/v) solvent mixture. The reaction mixture was stirred for 5 min before adding benzyl amine **III.2** (18.5 µL, 0.17 mmol, 1.1 equiv) via a Hamilton syringe. After reaching a homogeneous state, substrate **III.1** (37 mg, 0.15 mmol, 1.0 equiv) was added and the catalysis mixture was transferred outside the glovebox and stirred in a chiller-cooled isopropanol bath.

Two sets of 6 experiments each were prepared to complete the study at Pd-to-**L_{PN}** ratios of 1:2.5 and 1:5.

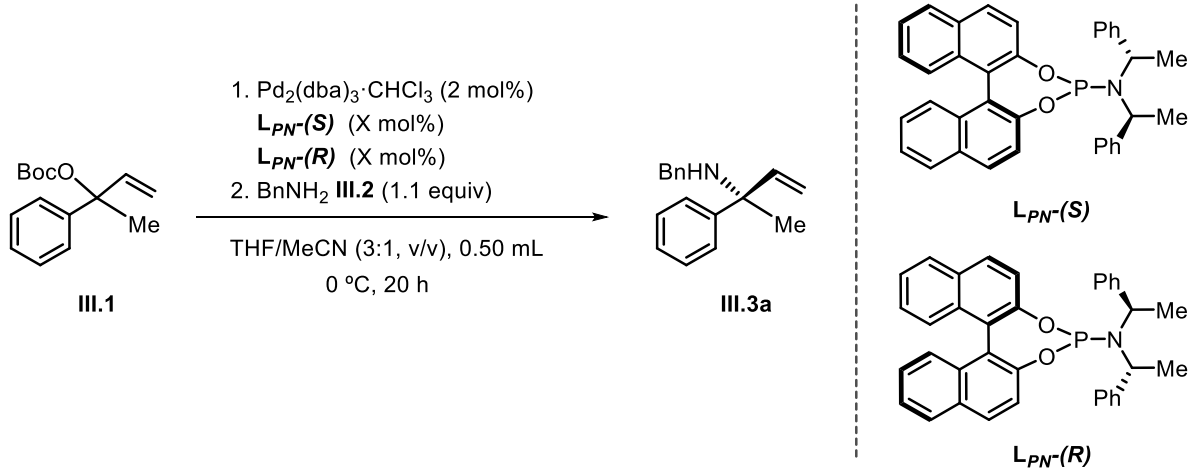

Figure 3.63: Catalytic reaction conditions for the NLE experiments.

Observations for Figure 3.17: A positive NLE was observed when using different mixtures of **L_{PN}-*(S)*** and **L_{PN}-*(R)***. At higher Pd-to-**L_{PN}** ratios, a similar positive NLE is attained.

Kinetic plots of enantio-pure vs. racemic ligand

Procedure: In a 2 mL vial, $Pd_2(dba)_3{\cdot}CHCl_3$ (3 mg, 2 mol%) and ligand **L_{PN}-*(S)*** (8 mg, 10 mol%) **or** ligand **L_{PN}-*(R)*** (8 mg, 10 mol%) were dissolved in 0.50 mL of a THF/MeCN (3:1, v/v) solvent mixture. The reaction mixture was stirred for 5 min before adding benzyl amine **III.2** (18.5 µL, 0.17 mmol, 1.1 equiv) through a Hamilton syringe. After reaching a homogeneous state, substrate **III.1** (37 mg, 0.15 mmol, 1.0 equiv) was added and the solution was transferred to an NMR tube. Note that for the "racemic" experiment, a mixture of ligands **L_{PN}-*(S)*** (4 mg, 5 mol%) and **L_{PN}-*(R)*** (4 mg, 5 mol%) was used.

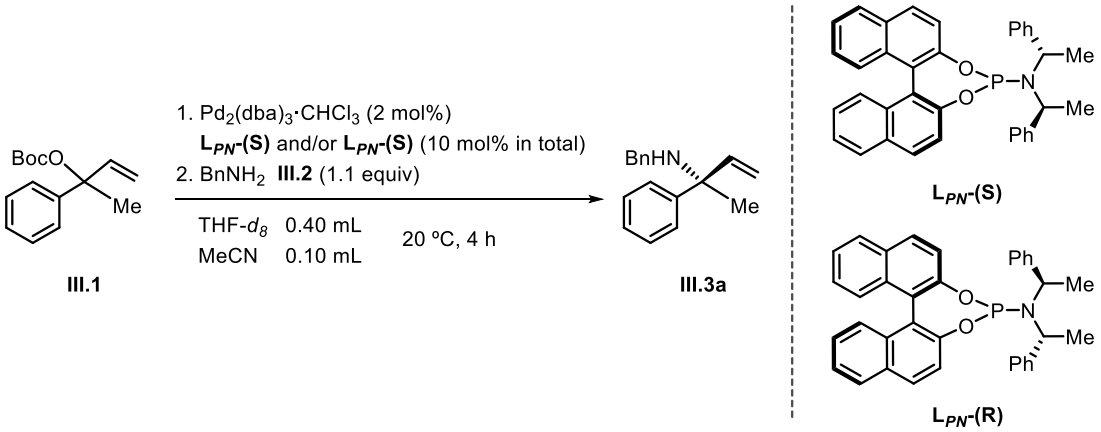

Figure 3.64: Catalytic conditions for the kinetic experiments using a racemic mixture or pure chiral ligand **L_{PN}**.

Observations: In the discussion section 3.3.5 we state that "*Pd(**L_{PN}-(S)**)$_2$ and Pd(**L_{PN}-(R)**)$_2$ should be more active than heterochiral Pd(**L_{PN}-(S)**)(**L_{PN}-(R)**) species*." We confirmed this measuring the rate of consumption of **III.1** using pure **L_{PN}-*(S)*** or **L_{PN}-*(S)*** and compared these with the rate of the reaction promoted by the racemic catalyst, which is almost 2 times slower. Thus, homo-chiral Pd(**L_{PN}-*(S)***)$_2$ and Pd(**L_{PN}-*(R)***)$_2$ should be more prone to provide an active catalyst than Pd(**L_{PN}-*(S)***)(**L_{PN}-*(R)***).

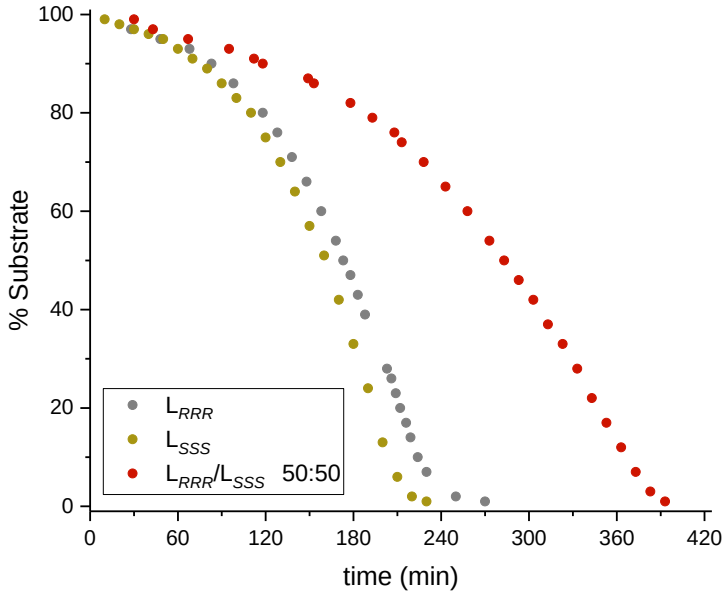

Figure 3.65: Disappearance of substrate **III.1** in time for pure chiral ligands (**L_{PN}-*(S)* <u>or</u> L_{PN}-*(R)***) vs. racemic ligand **L_{PN}** at 20 ºC in a THF-d_8/MeCN mixture (4:1).

Identification of dimeric homochiral [Pd(L_{PN}-*S*)2]^0 and heterochiral [Pd(L_{PN}-*S*)(L_{PN}-*R*)]^0 species by $^{31}P\{^1H\}$ NMR

Procedure: In a 2 mL vial, $Pd_2(dba)_3{\cdot}CHCl_3$ (3 mg, 2 mol%) and ligand **L_{PN}-*(S)*** (8 mg, 10 mol%) or ligand **L_{PN}-*(R)*** (8 mg, 10 mol%) were dissolved in 0.50 mL of a THF/MeCN (3:1, v/v) solvent mixture. The reaction mixture was stirred for 10 min., and after homogenizing the solution it was transferred to an NMR tube. For the "racemic" experiment, a 1:1 mixture (8 mg in total, 10 mol% in total) of both ligand enantiomers was prepared instead.

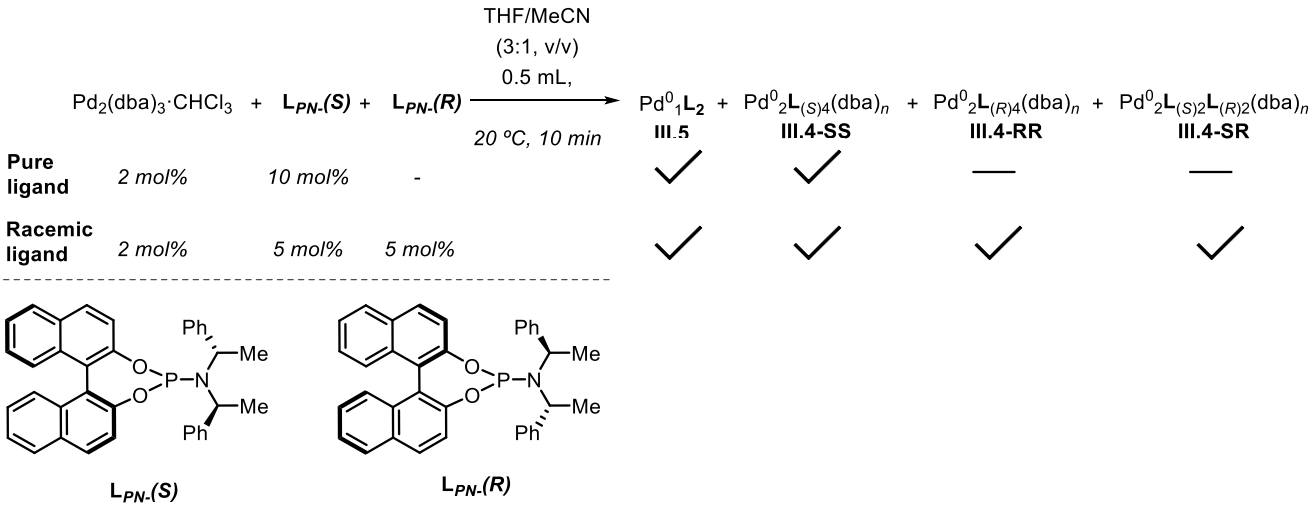

Figure 3.66: Complexation conditions for the kinetic experiments using racemic vs. chiral **L_{PN}**.

Observations: A mixture of homo- and hetero-chiral Pd_2 complexes are observed when a racemic mixture of ligand **L_{PN}** is used (top spectrum in Figure 3.67). Comparing with the use of a chiral **L_{PN}** (lower part in Figure 3.67), it looks indeed that the ***racemic*** dinuclear $Pd_2(0)$ complex is more favored and with the mononuclear Pd_1 complex significantly less populated, in line with our NLE discussion in the main text.

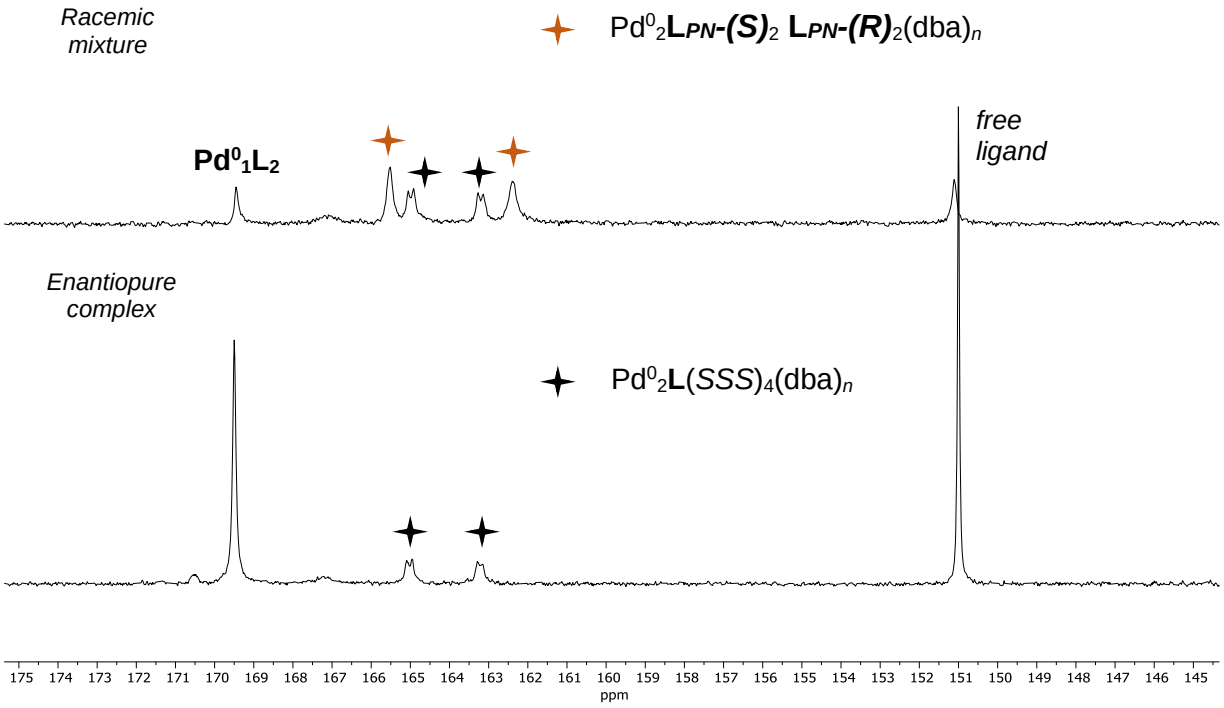

Figure 3.67: $^{31}P\{^{1}H\}$ NMR stacked spectra of enantio-pure Pd^0 species (below) and those observed using (*rac*)-**L*PN*** (above) at 20 ºC in THF/MeCN (3:1, v/v).

3.6.5 IR-monitored experiments

CO_2 detection and absence of CO_2 when –OAc is the leaving group

During the IR-monitoring during these kinetic experiments, the CO_2 band (= 2341 cm^{-1}) through OBoc degradation (tBuO$^-$ + CO_2) was indeed detected. When an OAc-based allylic substrate was employed (= 1743 cm^{-1}), this CO_2 band was not detected.

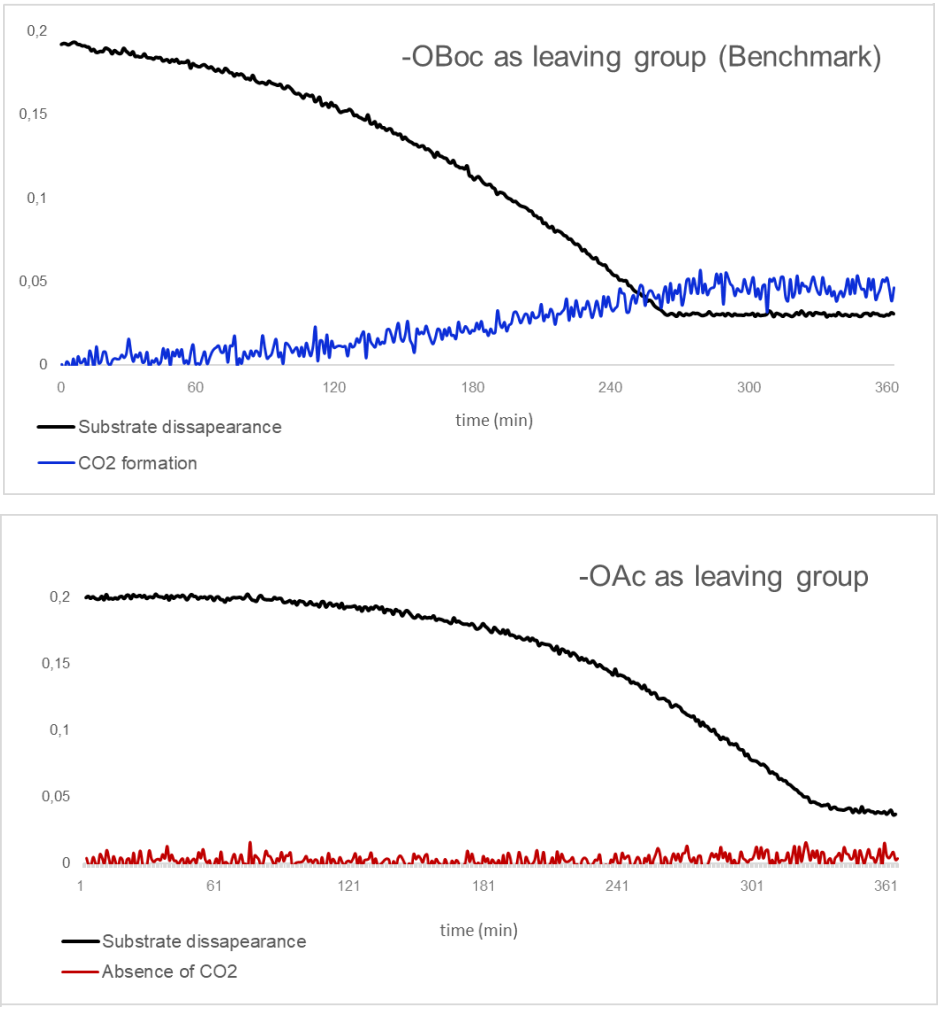

Figure 3.68: Comparison between allylic substrates having an -OBoc (left) or -OAc (right) leaving group, and CO_2 detection in the case of allylic substrate **III.1** that features an -OBoc group.

3.6.6 High Resolution Mass Experiments

Detection of Pd^{II}(allyl) intermediates

Procedure: In a 2 mL vial, $Pd_2(dba)_3 \cdot CHCl_3$ (3 mg, 2 mol%) and ligand **L_{PN}** (8 mg, 10 mol%) were dissolved in 0.35 mL of a THF/MeCN (3:1, v/v) solvent mixture. The reaction mixture was stirred for 5 min before adding benzyl amine **III.2** (18.5 µL, 0.17 mmol, 1.1 equiv) via a Hamilton syringe. After homogenizing, substrate **III.1** (37 mg, 0.15 mmol, 1.0 equiv) was added and the mixture transferred to an NMR tube equipped with an acetone-d_6 capillary. The catalysis was monitored by $^{31}P\{^1H\}$ NMR. When both intermediates (140 and 110 ppm) were detected, the NMR tube was transferred back to a glovebox. It was then filtered through Celite and the filtrate dissolved in 1 mL of MeCN. The sample was injected (direct inlet) in the ESI mass spectrometer (positive mode). The following two species were proposed from the observations done in the HRMS spectra:

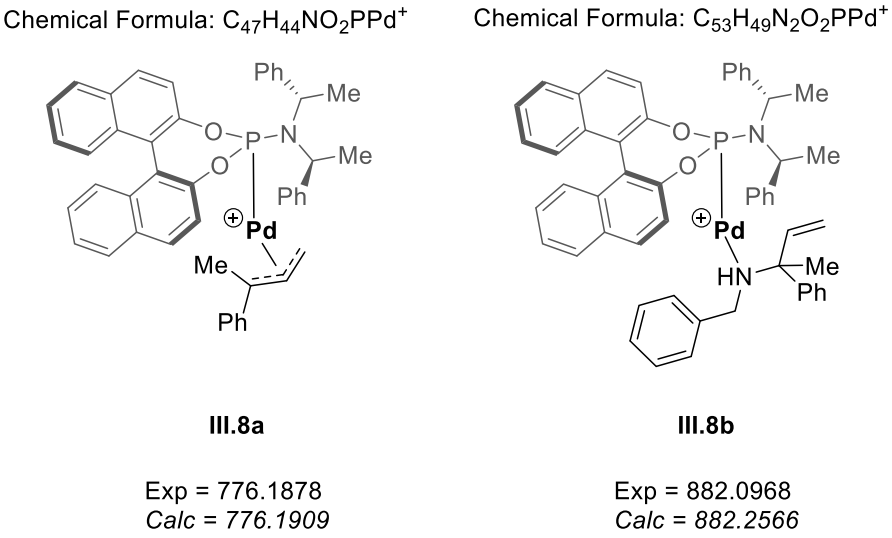

III.8a

Exp = 776.1878
Calc = 776.1909

III.8b

Exp = 882.0968
Calc = 882.2566

Figure 3.69: Proposed structures for Pd^{II}(allyl) intermediates detected by HRMS.

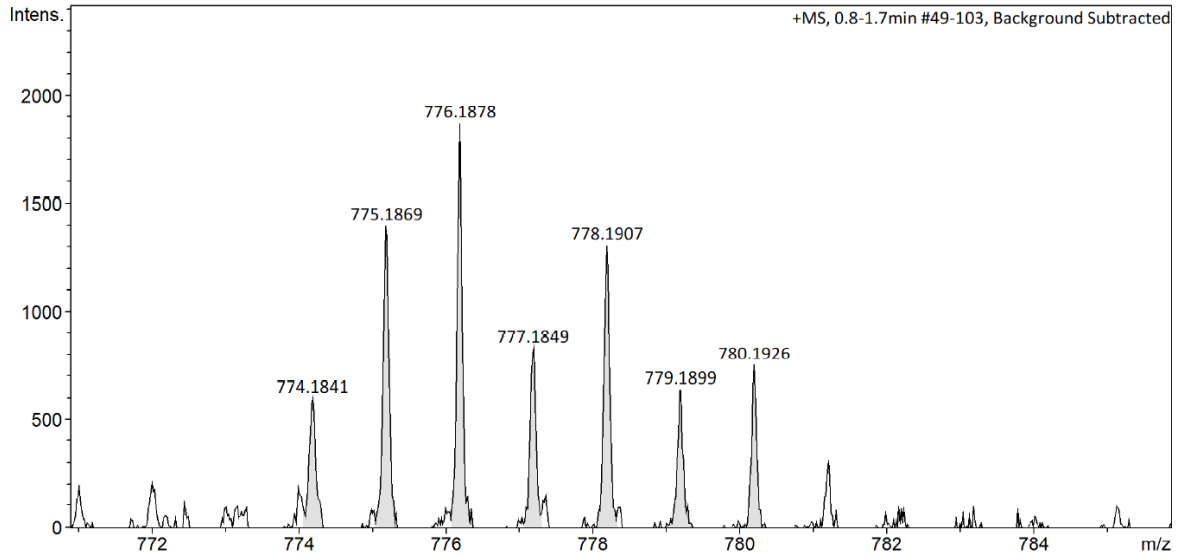

Figure 3.70: Isotopic pattern observed for **8a**.

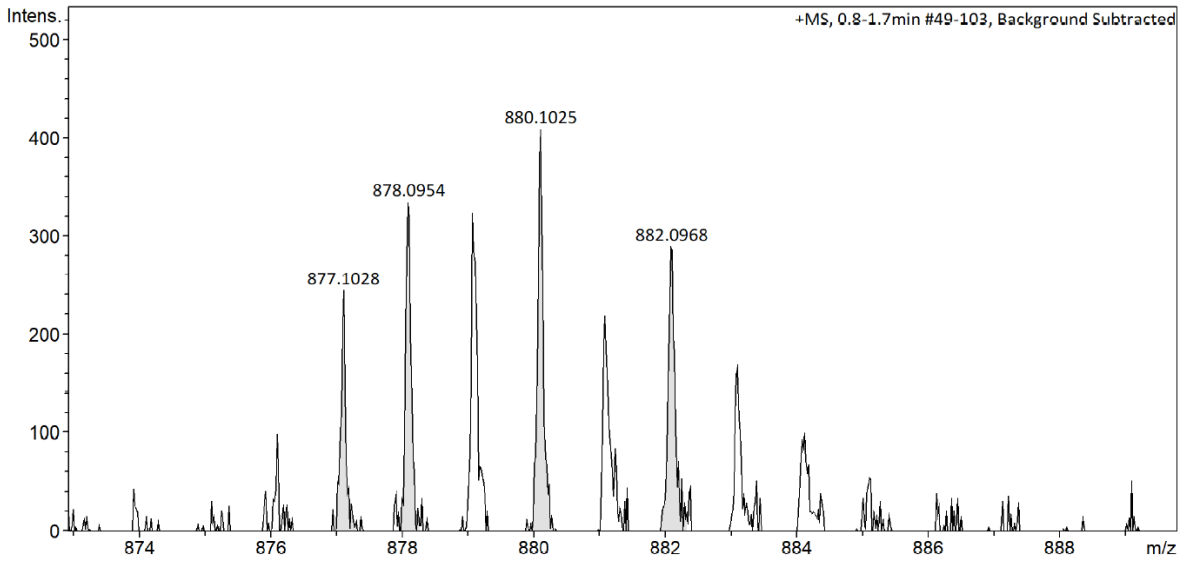

Figure 3.71: Isotopic pattern observed for **8b**.

3.6.7 Computational analysis

All the calculations were performed using the Gaussian 09 package.[156] The geometry optimizations were carried out in a mixed solvent system consisting of tetrahydrofuran and acetonitrile (THF/MeCN = 3:1, ε = 14.49) using the SMD[157] model at the B97D[158] level of theory with a mixed basis set of LANL2TZ(*f*)[159] for Pd and 6-31G(*d*) for all other atoms. Frequencies were computed analytically at the same level of theory to confirm whether the structures are minima (no imaginary frequencies) or transition states (only one imaginary frequency). Key transition-state structures were confirmed to connect the correct reactants and products by intrinsic reaction coordinate (IRC) calculations.[160] To obtain better accuracy, energies for the optimized geometries were recalculated using M06[161] single-point calculations with a larger basis set, which is LANL2TZ(*f*) for Pd and 6-311+G(*d*,*p*) for all other atoms. The final free energies reported in the article (ΔG_{sol}) are the large basis set single-point energies with Gibbs free energy correction (at 298.15 K). All 3D structures of the optimized geometries were generated using CYLview.[162] Non-covalent interactions was performed with Multiwfn[163] to investigate the weak interaction between the substrate and catalyst, and it was visualized with visual molecular dynamics (VMD).[164] The energy decomposition

[156] Frisch, M. J.; Trucks, G. W.; Schlegel, H. B.; Scuseria, G. E.; Robb, M. A.; Cheeseman, J. R.; Scalmani, G.; Barone, V.; Men-nucci, B.; Petersson, G. A.; Nakatsuji, H.; Caricato, M.; Li, X.; Hratchian, H. P.; Izmaylov, A. F.; Bloino, J.; Zheng, G.; Son-nenberg, J. L.; Hada, M.; Ehara, M.; Toyota, K.; Fukuda, R.; Hasegawa, J.; Ishida, M.; Nakajima, T.; Honda, Y.; Kitao, O.; Nakai, H.; Vreven, T.; Mont-gomery, J. A., Jr.; Peralta, J. E.; Ogliaro, F.; Bearpark, M.; Heyd, J. J.; Brothers, E.; Kudin, K. N.; Staroverov, V. N.; Kobayashi, R.; Nor-mand, J.; Raghavachari, K.; Rendell, A.; Burant, J. C.; Iyengar, S. S.; Tomasi, J.; Cossi, M.; Rega, N.; Millam, N. J.; Klene, M.; Knox, J. E.; Cross, J. B.; Bakken, V.; Adamo, C.; Jaramillo, J.; Gomperts, R.; Stratmann, R. E.; Yazyev, O.; Austin, A. J.; Cammi, R.; Pomelli, C.; Ochter-ski, J. W.; Martin, R. L.; Morokuma, K.; Zakrzewski, V. G.; Voth, G. A.; Salvador, P.; Dannenberg, J. J.; Dapprich, S.; Dan-iels, A. D.; Farkas, Ö.; Foresman, J. B.; Ortiz, J. V.; Cioslowski, J.; Fox, D. J. Gaussian 09, Revision E.01; Gaussian, Inc.: Wall-ingford, CT, 2013.

[157] Marenich, A. V.; Cramer, C. J.; Truhlar, D. G. *J. Phys. Chem. B* 2009, 113, 6378.

[158] a) Grimme, S. *J. Comput. Chem*. 2006, 27, 1787; Becke, A. D. *J. Chem. Phys*. 1997, 107, 8554.

[159] Pritchard, B. P.; Altarawy, D.; Didier, B.; Gibson, T. D.; Windus, T. L. *J. Chem. Inf. Model.* 2019, 59, 4814.

[160] a) Fukui, K. *J. Phys. Chem*. 1970, 74, 4161; b) Fukui, K. *Acc. Chem. Res*. 1981, 14, 363.

[161] a) Zhao, Y.; Truhlar, D. G., *Theor. Chem. Acc.* 2008, 120, 215; b) Zhao, Y.; Truhlar, D. G. *Acc. Chem. Res.* 2008**,** 41, 157; c) He, X.; Zhu, L.; Heng, D.; Liu, F.; Liu, S.; Zhong, K.; Shan, C.; Bai, R.; Lan, Y. *Org. Chem. Front.* 2021**,** 8, 1739; d) Zhang, M.; Wu, H.; Yang, J.; Huang, G. *ACS Catal* 2021, 11, 4833.

[162] Legault, C. Y. *CYLview, ver. 1.0b*; Université de Sherbrooke: 2009; http://www.cylview.org.

[163] a) Lu, T.; Chen, F. Multiwfn: *J. Comput. Chem*. 2012, 33, 580; b) Lu, T.; Chen, F. *J. Mol. Graphics Modell*. 2012, 38, 314.

[164] Humphrey, W.; Dalke, A.; Schulten, K. VMD: Visual molecular dynamics. *J. Mol. Graphics* 1996, 14, 33. VMD Official Web site: http://www.ks.uiuc.edu/Research/vmd/.

analysis was performed using SAPT[165] module with density-fitted sSAPT0 and the jun-cc-pVDZ[166] basis set in the PSI4[167] package. In the following ChemDraw pictures, **L** is referred to as $\mathbf{L}_{PN}$.

[165] a) Hohenstein, E. G.; Sherrill, C. D. *J. Chem. Phys*. 2010, 132, 184111; b) Hohenstein, E. G.; Parrish, R. M.; Sherrill, C. D.; Turney, J. M.; Schaefer III, H. F. *J. Chem. Phys*. 2011, 135, 174107.

[166] Kendall, R. A.; Dunning, T. H.; Harrison, R. J. *J. Chem. Phys*. 1992, 96, 6796.

[167] Turney, J. M.; Simmonett, A. C.; Parrish, R. M.; Hohenstein, E. G.; Evangelista, F. A.; Fermann, J. T.; Mintz, B. J.; Burns, L. A.; Wilke, J. J.; Abrams, M. L.; Russ, N. J.; Leininger, M. L.; Janssen, C. L.; Seidl, E. T.; Allen, W. D.; Schaefer, H. F.; King, R. A.; Valeev, E. F.; Sherrill, C. D.; Crawford, T. D. *WIREs Comp. Mol. Sci*. 2012, 2, 556.

The *endo*/*exo* and OBoc/L interconversion pathways

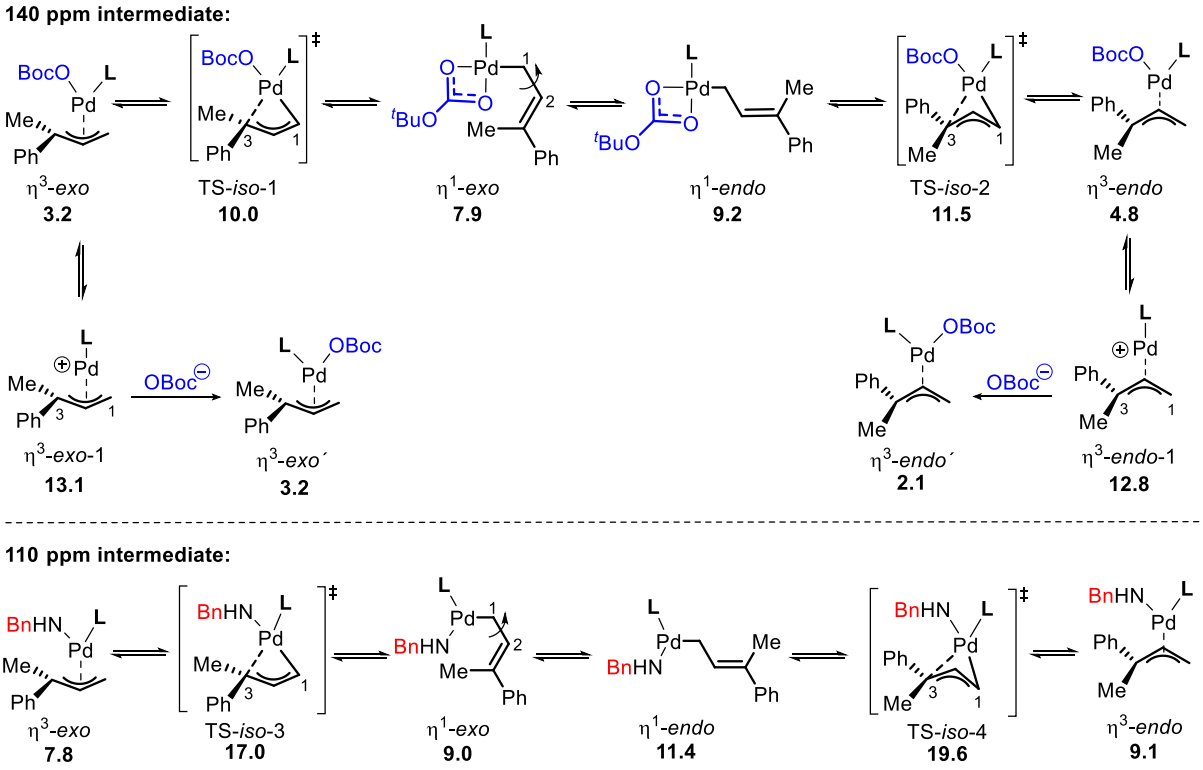

Figure 3.72: Computed ***endo/exo*** and ***OBoc/L*** interconversion pathways of η^3-allyl-Pd(OBoc) (140 ppm intermediate) and η^3-allyl-Pd(NHBn) (110 ppm intermediate) species to different η^3- and η^1-allyl-Pd equilibrating compounds. All reported energies are in kcal/mol.

Decarboxylation of the other η³-allyl-Pd(OBoc) species

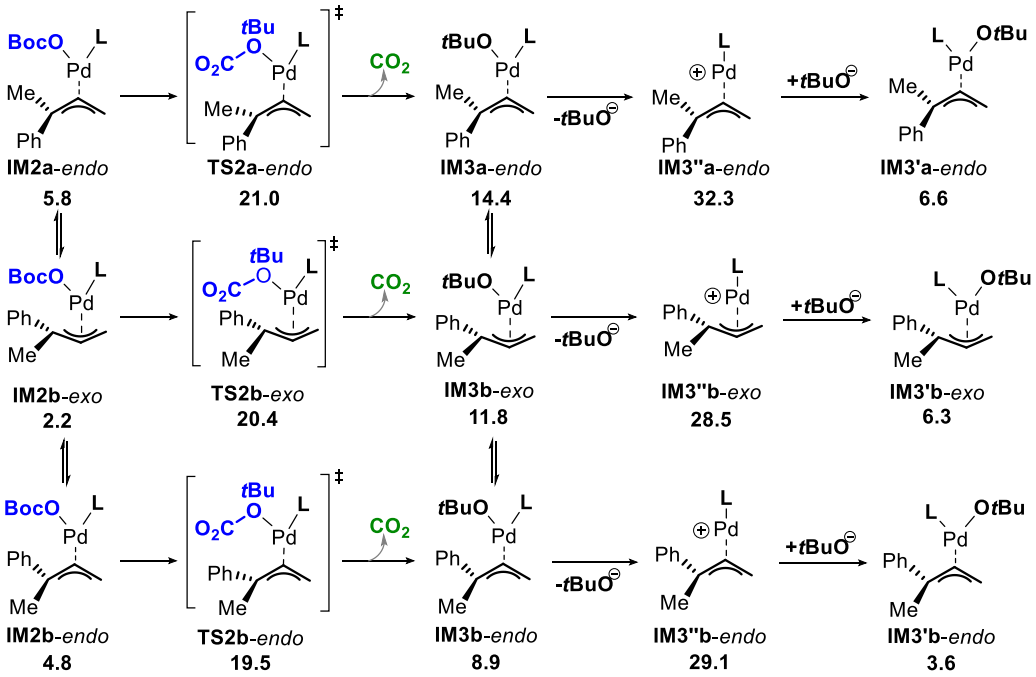

Figure 3.73: Computed decarboxylation pathways of different □³-allyl-Pd(OBoc) intermediates. All reported energies are in kcal/mol.

The interconversion of η³-allyl-Pd(O*t*Bu) species via □□□□□ isomerization

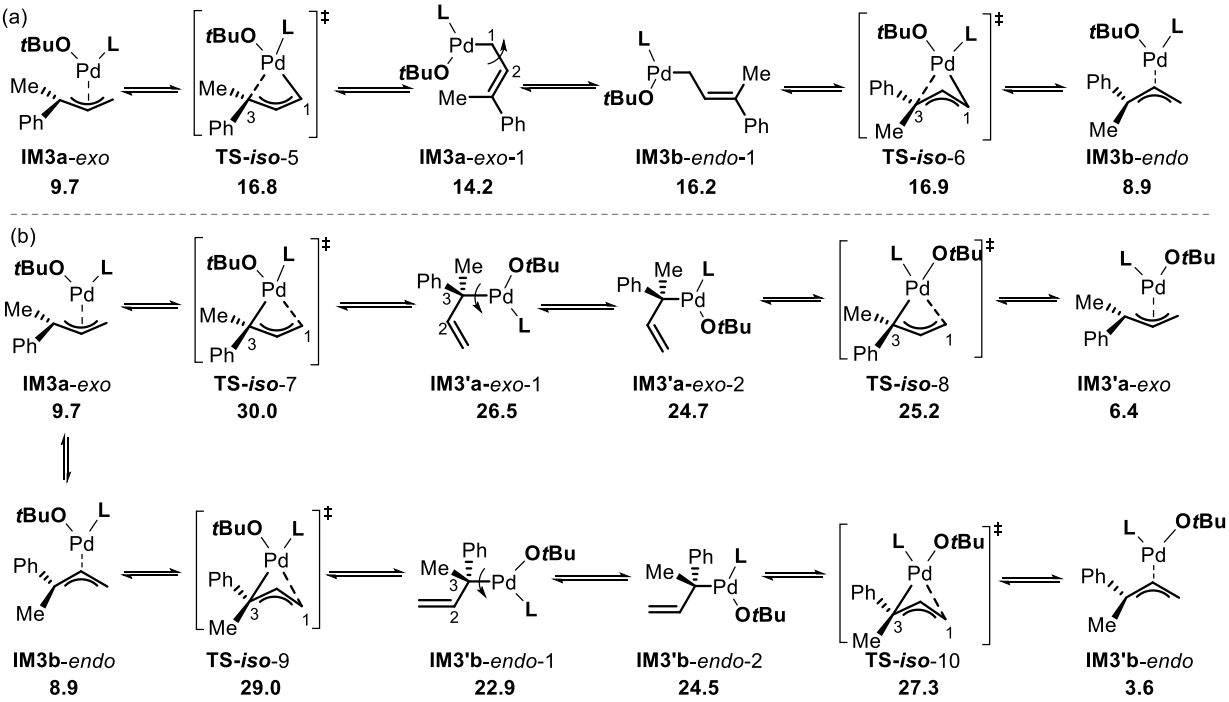

Figure 3.74: Computed interconversion pathways of η³-allyl-Pd(O*t*Bu) species via □□□□□ isomerization through η¹-coordination at the a) C_1 carbon and the b) C_3 carbon. All reported energies are in kcal/mol.

DFT computed full pathways for the catalytic formation of (*S*)-3a and (*R*)-3a

C–O oxidative addition and CO_2 extrusion

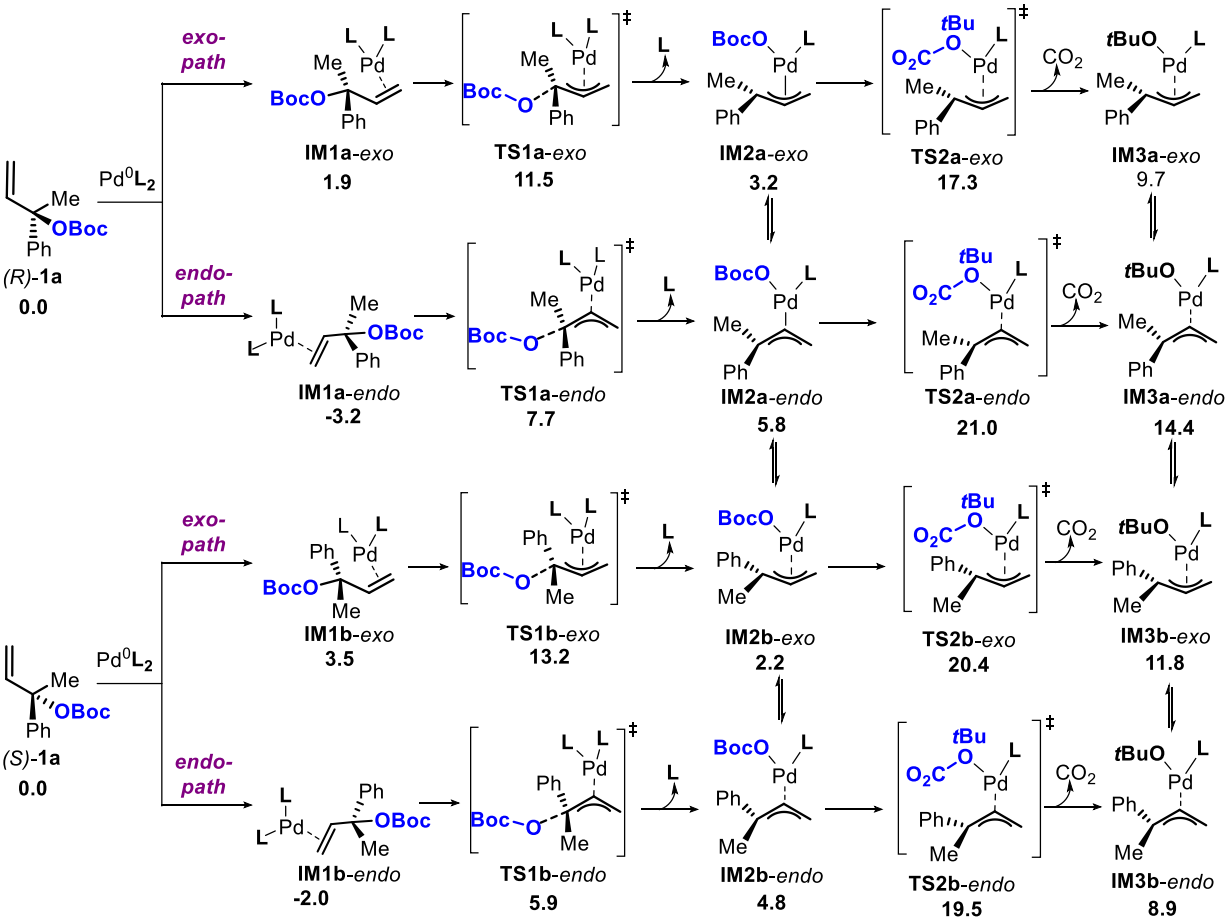

Figure 3.75: Computed pathways for the OA (with 2**L**) and decarboxylation steps of (*S*)-**1a** and (*R*)-**1a** allylic carbonates. All reported energies are in kcal/mol.

Ligand exchange and inner-sphere C-N reductive elimination

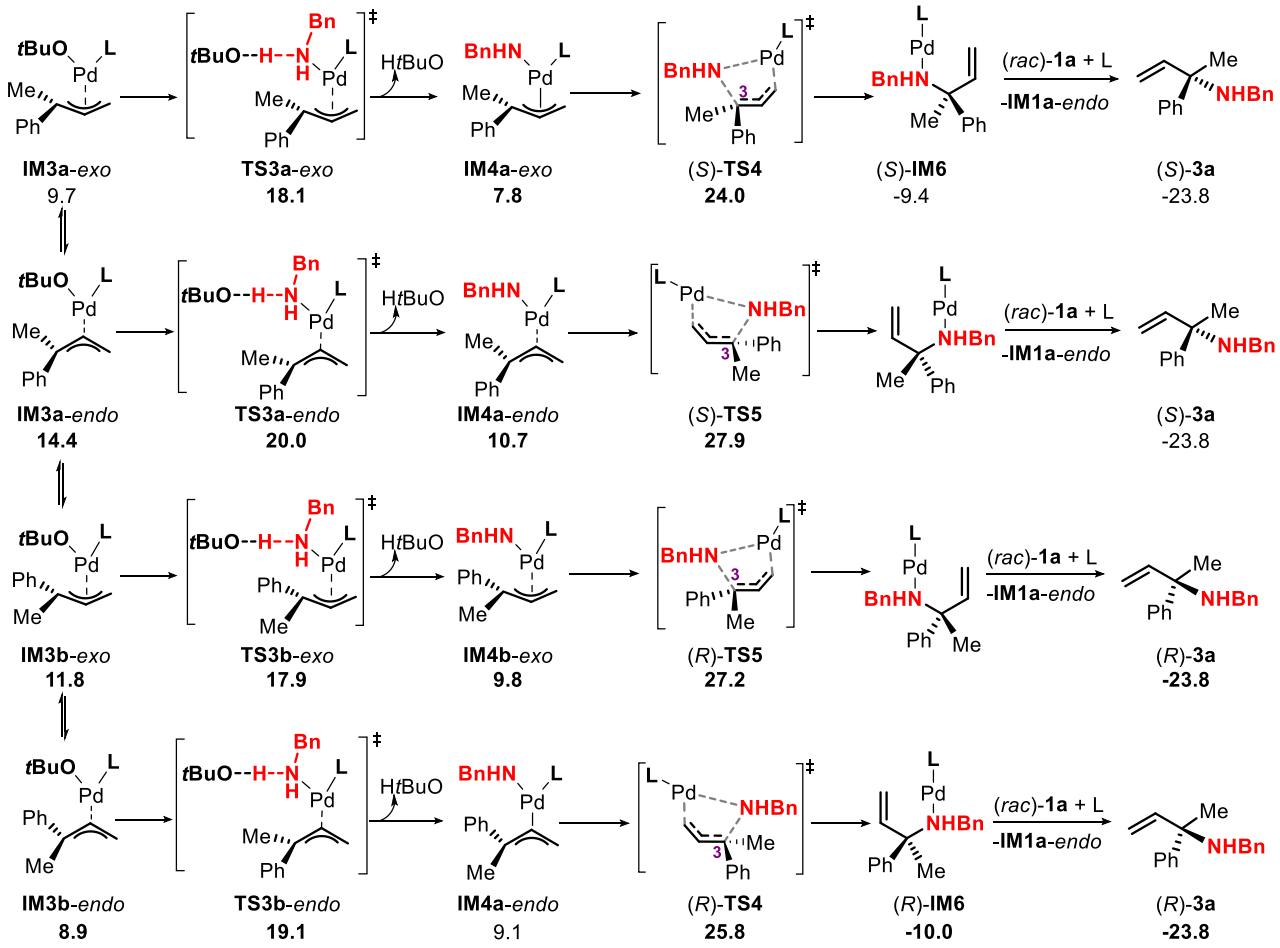

Figure 3.76: Computed pathways for the ligand exchange and the inner-sphere C-N reductive elimination steps from **IM3a**-*exo*, **IM3a**-*endo*, **IM3b**-*exo* and **IM3b**-*endo* to form (*S*)-**1a** and (*R*)-**1a** allylic amines. All reported energies are in kcal/mol.

C–O oxidative addition with one ligand

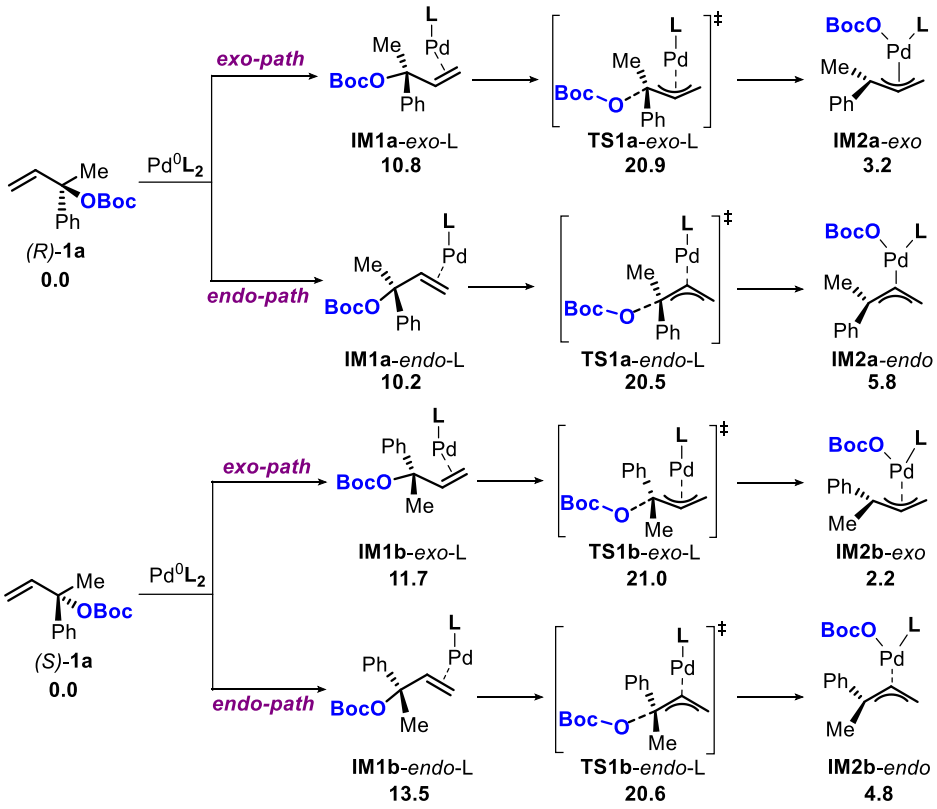

Figure 3.77: Computed pathways for the OA (with 1**L**) step of (*S*)-**1a** and (*R*)-**1a** allylic carbonates. All reported energies are in kcal/mol.

Outer-sphere pathway from Pd(allyl)(O*t*Bu)**L**

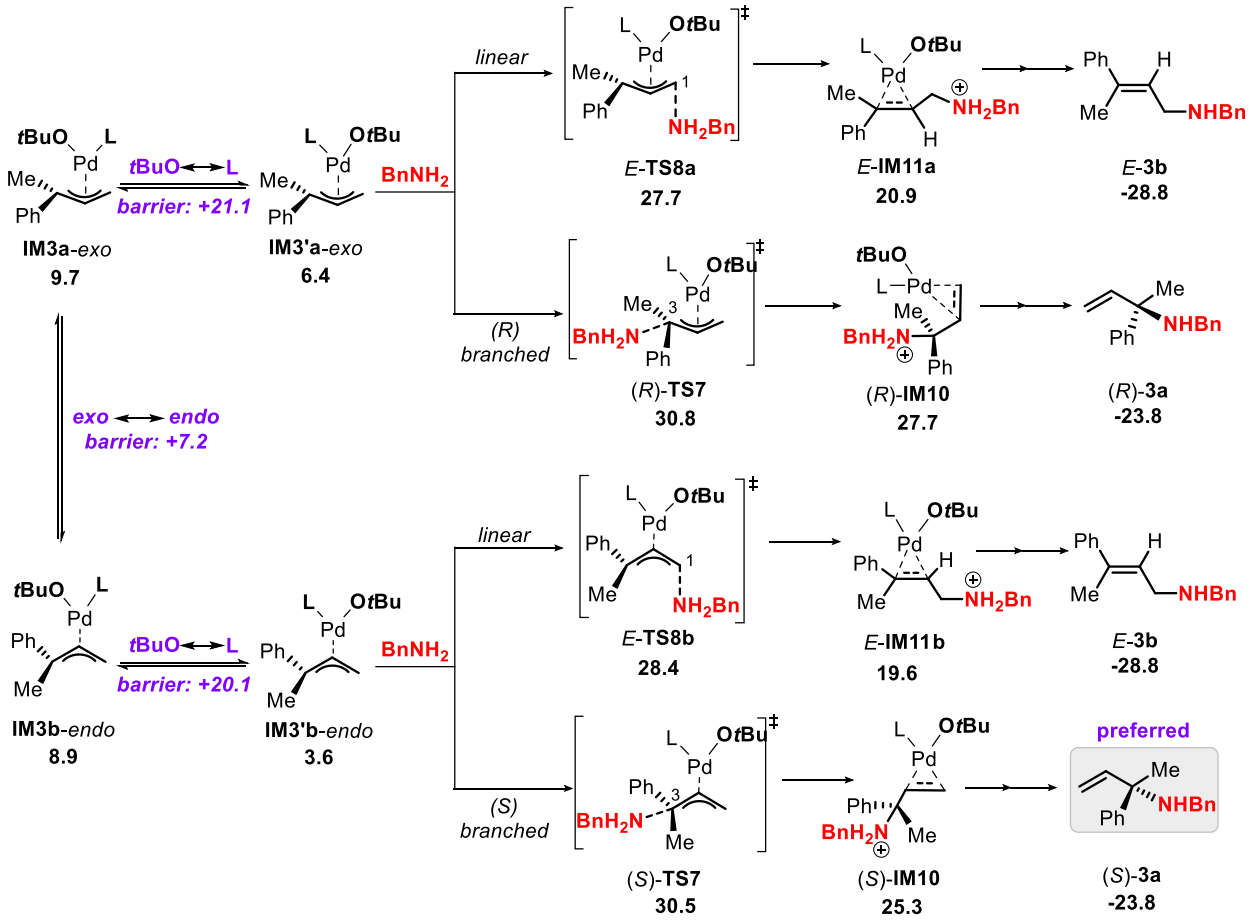

Figure 3.78: Computed pathways for the outer-sphere C-N reductive elimination step from **IM3a**-*exo* and **IM3b**-*endo* species. All reported energies are in kcal/mol.

Predicted enantiomeric ratios (*er*) of two other substrate combinations

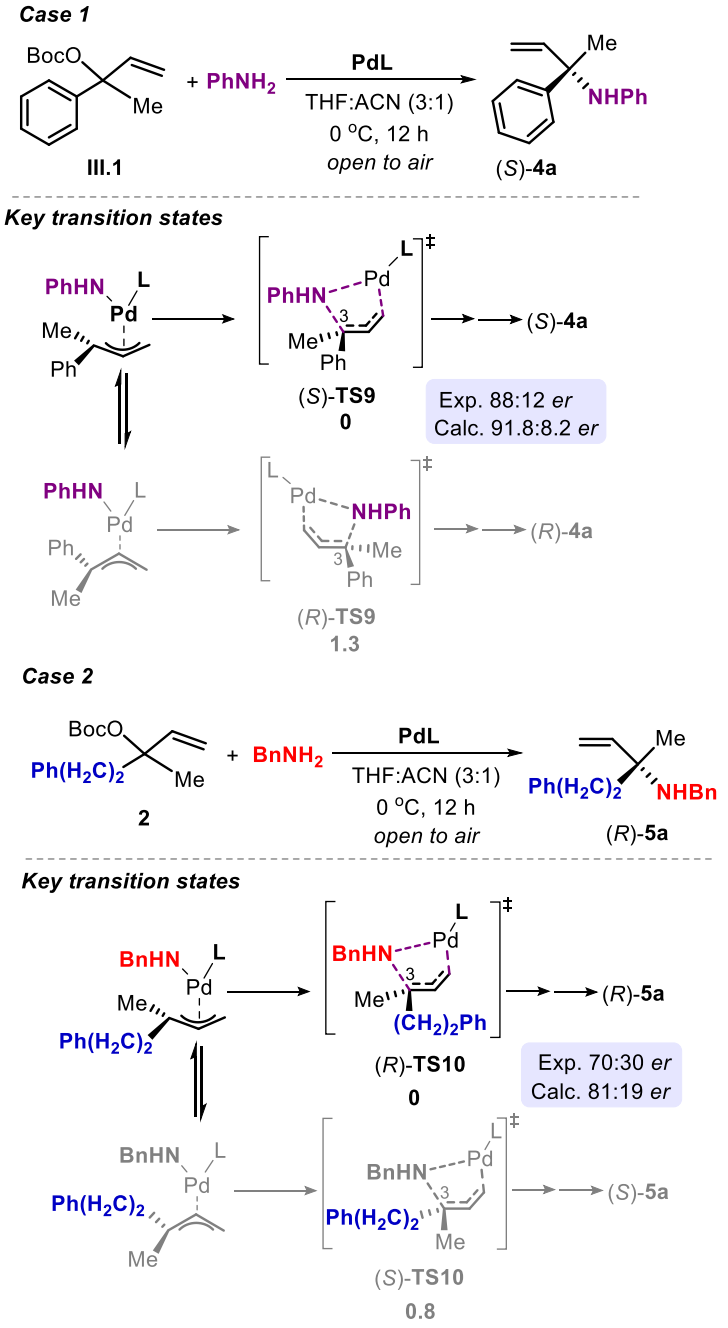

Figure 3.79: Predicted *er´*s for two other reagent combinations. Case 1: benzyl amine was replaced by phenyl amine. Case 2: Phenyl substituent of substrate **III.1** was replaced for a longer aliphatic chain (-CH_2CH_2Ph).

Chapter 3

Chapter 4.

Mechanistic Analysis of a Nickel-Catalyzed Asymmetric Formal Cross-Electrophile Reaction: Preparation of Branched 1,5-Dienes featuring a Quaternary Stereogenic Center

The methodology development presented in the introduction section of this chapter was developed by ***Dr. Debasish Ghorai****.*

The results described in this chapter have been communicated:

Ghorai D.,‡ **Garcia-Roca A.**‡, Benet-Buchholz, J., Kleij A. W., *submitted*

Chapter 4

4.1 Introduction

The enantio-selective construction of quaternary and tetra-substituted tertiary carbon centers has attracted substantial attention because of their presence in a wide variety of natural products, drugs and biologically active molecules.[168] The challenge associated with their construction is the steric repulsion around the carbon center upon formation. Even more challenging in this realm is the development of asymmetric protocols, which may require various synthetic steps and substrate pre-functionalization. Often, these protocols are characterized by low productivity, selectivity and/or the releasing of undesired (metal) waste. Despite these requirements and limitations, expanding on methodologies for the asymmetric construction of impeded stereogenic carbon centers remains appealing especially in the context of further optimizing process sustainability, cost-effectiveness, functional group diversity and operational simplicity.[169]

Among the many transition metal (TM) catalyzed asymmetric C−C bond formation reactions, metal-catalyzed allyl−allyl coupling reactions between allyl-metal species and allylic electrophiles is attractive because it has the potential to generate a new stereogenic center when forming a branched 1,5-diene product (Figure 4.1a).[170] Chiral 1,5-dienes are valuable building blocks in organic synthesis and represent substructures of many biologically active substances and naturally occurring terpenes.[171] However, There are only a limited number of reports on regio- and enantioselective synthesis of branched 1,5-dienes that feature quaternary carbon stereocenters. For example, Morken and co-workers disclosed an elegant Pd-catalyzed regio- and enantioselective cross-coupling of tertiary allylic carbonates and allyl boronates to produce products that comprise a quaternary carbon stereocenter

[168] a) Li, C.; Ragab, S. S.; Liu, G.; Tang, W. *Nat. Prod. Rep.* 2020, 37, 276. b) Zeng, X.-P.; Cao, Z.-Y.; Wang, Y.-H.; Zhou, F.; Zhou, J. *Chem. Rev.* 2016, 116, 7330. c) Liu, Y.; Han, S.-J.; Liu, W.-B.; Stoltz, B. M. *Acc. Chem. Res.* 2015, 48, 740. d) Quasdorf, K. W.; Overman, L. E. *Nature* 2014, 516, 181. e) Das, J. P.; Marek, I. *Chem. Commun.* 2011, 47, 4593. f) Trost, B. M.; Jiang, C. *Synthesis* 2006, 369.

[169] a) Marek, I.; Minko, Y.; Pasco, M.; Mejuch, T.; Gilboa, N.; Chechik, H.; Das, J. P. *J. Am. Chem. Soc.* 2014, 136, 2682. b) Feng, J.; Holmes, M.; Krische, M. J. *Chem. Rev.* 2017, 117, 12564.

[170] a) Yuan, Q.; Yao, K.; Liu, D.; Zhang, W. *Chem. Commun*. 2015, 51, 11834. b) Flegeau, E. F.; Schneider, U.; Kobayashi, S. *Chem. Eur. J.* 2009, 15, 12247. c) Porcel, S.; López-Carrillo, V.; García-Yebra, C.; Echavarren, A. M. *Angew. Chem. Int. Ed.* 2008, 47, 1883. d) Nakamura, H.; Bao, M.; Yamamoto, Y. *Angew. Chem. Int. Ed.* 2001, 40, 3208.

[171] a) Breitmaier, E. *Terpenes, Flavors, Fragrances, Pharmaca, Pheromones*. Wiley-VCH, Weinheim, 2006. b) Dewick, P. M. *Medicinal Natural Products: A Biosynthetic Approach*, Wiley, Chichester, 2002.

forged through an inner-sphere 3,3´-reductive elimination mechanism.[172] Additionally, both Carreira and Yang individually reported a highly regio- and enantio-selective Ir-catalyzed cross-coupling process between either allyl silanes or allyl boronates and allylic electrophiles.[173] However, these processes require air- and moisture-sensitive allyl–metal reagents, a relatively expensive transition metal catalyst and generate tertiary rather than quaternary carbon stereocenters. More recently, the Yu group developed a Pd/photoredox-catalyzed enantio-selective reductive homo-coupling of allylic acetates to give enantio-enriched C_2-symmetrical chiral 1,5-dienes that incorporate two contiguous tertiary carbon stereocenters (Figure 4.1c).[174]

Cheap and abundant nickel is an attractive alternative within the family of 3d transition metals because it has unique features such as the potential to form σ- and π-allyl complexes and known to successfully promote various allylic substitution reactions.[175] An illustrative example is the work from Kobayashi, who demonstrated the potential of Ni-catalysis to mediate allyl-allyl coupling reactions between allylic alcohols and allyl boronates forming predominantly linear 1,5-diene products.[176] Liu and coworkers further expanded the potential of Ni-catalysis towards the homo- and cross-coupling of allylic alcohols providing linear 1,5-dienes through in situ generation of an allyl boronate species (Figure 4.1b).[177]

A somewhat related contribution from Jamison focused on the cross-coupling of vinyl bromides and allylic electrophiles under stereo-selective Ni-catalysis delivering skipped dienes.[178] As far as we know the synthesis of unsymmetrical chiral 1,5-dienes that possess a quaternary stereocenter under Ni-catalysis remains elusive. Below a summary is given of the experimentally determined scope of our Ni-based

[172] a) Zhang, P.; Brozek, L. A.; Morken, J. P. *J. Am. Chem. Soc.* 2010, 132, 10686. b) Zhang, P.; Le, H.; Kyne, R. E.; Morken, J. P. E *J. Am. Chem. Soc.* 2011, 133, 9716. c) Ardolino, M. J.; Morken, J. P. *J. Am. Chem. Soc.* 2014, 136, 7092.

[173] a) Zheng, Y.; Yue, B.-B.; Wei, K.; Yang, Y.-R. *Org. Lett.* 2018, 20, 8035. b) Hamilton, J. Y.; Hauser, N.; Sarlah, D.; Carreira, E. M. *Angew. Chem. Int. Ed.* 2014, 53, 10759.

[174] Zhang, H.-H.; Tang, M.; Zhao, J.-J.; Song, C.; Yu, S. *J. Am. Chem. Soc.* 2021, 143, 12836.

[175] a) Süsse, L.; Stoltz, B. M. *Chem. Rev*. 2021, 121, 4084. b) Ravichandiran, V.; Jana, A. *Org. Chem. Front*. 2023, 10, 267. c) Ghorai, D.; Cristofol, A.; Kleij, A. W. *Eur. J. Inorg. Chem.* 2022, e202100820. d) Knappke, C. E. I.; Grupe, S.; Gärtner, D.; Corpet, M.; Gosmini, C.; von Wangelin, A. J. *Chem. Eur. J*. 2014, 20, 6828.

[176] Jimenez-Aquino, A.; Ferrer Flegeau, E.; Schneider, U.; Kobayashi, S. *Chem. Commun.* 2011, 47, 9456.

[177] Gan, Y.; Hu, H.; Liu, Y. *Org. Lett.* 2020, 22, 4418.

[178] McGeough, C. P.; Strom, A. E.; Jamison, T. F. *Org. Lett*. 2019, 21, 3606.

methodology (executed by Dr. Debasish Ghorai) functioning as a prelude to the mechanistic studies that form the basis of this thesis chapter.

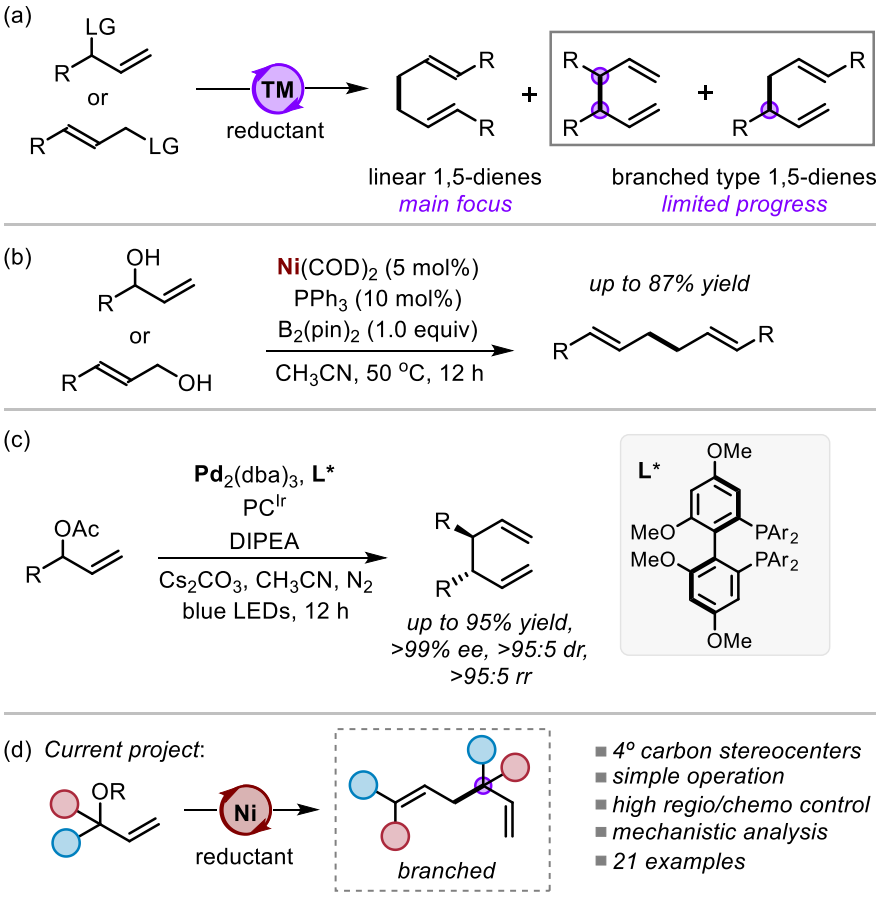

Figure 4.1: a) TM-catalyzed reductive homoallylic coupling reactions, b) Ni- and c) Pd-catalyzed homoallylic coupling, and d) current approach towards branched chiral 1,5-dienes.

4.1.1 Methodology development

Screening phase. We began designing our strategy by applying an adapted Ni-catalyzed reductive coupling protocol in the presence of various chiral ligands using tertiary allylic precursors to induce the formation of a branched 1,5-diene product (Figure 4.1d and Table **IV.I**). The reaction of **IV.1a** in the presence of a catalytic amount of $NiBr_2 \cdot 3H_2O$, *dppf* as ligand and Zn as a reducing agent in DMA as solvent (entry 1) resulted in the formation of a combined yield of 91% (85% isolated) of a homo-coupled diene product as an approximate 2:1 mixture of regio-isomers **IV.2a** and **IV.3a**.[179] This outcome was encouraging in terms of the mild operating conditions, the avoidance of stoichiometric organometallic reagents and the potential to deliver the desired branched 1,5-diene product **IV.2a** with appreciable regio-control. We subsequently screened various Ni precursors, chiral ligands, reductants, solvents and other reaction parameters to examine this homo-allylic coupling process (Note: only a selection is presented in Table **IV.I**, entries 2-21). After identifying $NiBr_2$(DME) as the Ni precursor, DMA as preferred solvent and 3 equiv of Zn reductant (entry 12), a variety of other chiral diphosphine ligands (**L1-L7**) were scrutinized to favor both high branched selectivity and asymmetric induction towards 1,5-diene **IV.2a** using first the unprotected allylic alcohol **IV.1a´** (R = H).

The presence of phosphaoxazoline ligand **L1** gave a high substrate conversion (entry 12: 85%), a good b:l ratio of 5:1 and a decent level of enantio-control (87:13 *er*). The other three examined phosphaoxazoline **L2**-**L4** (entries 13-15) led to lower substrate conversions under comparable conditions. The presence of **L2** further boosted enantio-selection (93:7 *er*) though only a low yield (~10%) and a modest b:l ratio of 3.7:1 (entry 13) was attained for **IV.2a**. We then used JosiPhos type ligands **L5**-**L7** which proved to be beneficial towards both the regio- and enantio-selectivity of the process (entries 16-22).

[179] For examples of non-innocent behavior of divalent Zn species in Ni-catalyzed cross-couplings see: a) Day, C. S.; Somerville, R. J.; Martin, R. *Nat. Catal*. 2021, 4, 124. b) Anderson, T. J.; Vicic, D. A. *Organometallics* 2004, 23, 623.

Table IV.I: Selected screening data towards the synthesis of branched 1,5-diene **IV.2a**[a]

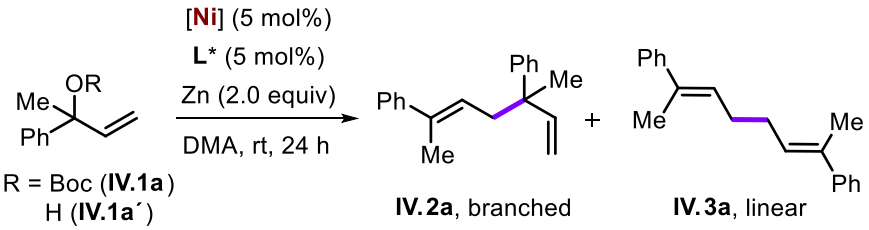

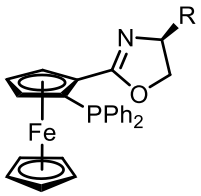

L1: R = *i*Pr; **L2**: R = *t*Bu

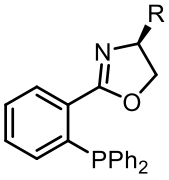

L3: R = *i*Pr; **L4**: R = Ph

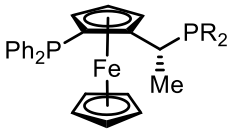

L5: R = Cy; **L$_{JP}$**: R = *t*Bu
L7: R = 3,5-$(Me)_2C_6H_3$

Entry	[Ni]	L*	Conv. (%)[b]	b/l[b]	*er*[b]
1	$NiBr_2 \cdot 3H_2O$	dppf	91 (85)[c]	2.2:1	–
2[d]	$NiBr_2 \cdot 3H_2O$	dppf	44	3:1	–
3[e]	$NiBr_2 \cdot 3H_2O$	dppf	<1	–	–
4	$Ni(acac)_2$	dppf	<1	–	–
5	$Ni(cod)_2$	dppf	35	1:2.4	–
6	$NiCl_2(dme)$	dppf	87	2:1	–
7[f]	$NiBr_2 \cdot 3H_2O$	dppf	84	3:1	–
8[g]	$NiBr_2 \cdot 3H_2O$	dppf	<1		–
9	$NiBr_2 \cdot 3H_2O$	dtbpy	10	1:1.5	–
10	$NiBr_2 \cdot 3H_2O$	dppe	<1	–	–
11	$NiBr_2 \cdot 3H_2O$	binap	<10	9:1	–
12[h]	$NiBr_2(dme)$	**L1**	85	5:1	87:13
13[h]	$NiBr_2(dme)$	**L2**	<10	3.7:1	93:7
14[h]	$NiBr_2(dme)$	**L3**	57	1.4:1	69:31
15[h]	$NiBr_2(dme)$	**L4**	55	1.2:1	61:39
16[h]	$NiBr_2(dme)$	**L5**	60	>20:1	70:30
17[h]	$NiBr_2(dme)$	**L$_{JP}$**	55	20:1	94:6
18[h]	$NiBr_2(dme)$	**L7**	91	8.5:1	51:49
19[j]	$NiBr_2(dme)$	**L$_{JP}$**	85	20:1	94:6
20[i]	$NiBr_2(dme)$	**L$_{JP}$**	95 (90)[c]	>20:1	94:6
21[i]	–	**L$_{JP}$**	<1	–	–
22[i]	$NiBr_2(dme)$	–	<1	–	–

[a] **IV.1a** (0.10 mmol), [Ni] (5 mol%), **L*** (5 mol%), Zn (0.20 mmol) were combined in DMA (0.10 mL) at 25 °C, 48 h, under an Ar atmosphere. [b]Conversion and b/l ratios were determined by ^{1}H NMR analysis using 1,3,5-trimethoxybenzene as an internal standard. Enantiomeric ratios (*er*) were determined by UPC2. [c]Yield of isolated product in parenthesis. [d]After 1 h. [e]At 0°C. [f]In the presence of Mn as reductant. [g]In the presence of $B_2(pin)_2$. [h]**IV.1a´** (0.10 mmol), $NiBr_2$(DME) (10 mol%), **L*** (10 mol%), Zn (0.30 mmol) were combined in DMA (0.10 mL), 25 °C, 48 h, under Ar. [i]**IV.1a** (0.10 mmol), $NiBr_2$(dme) (10 mol%), $\mathbf{L_{JP}}$ (20 mol%), Zn (0.30 mmol) were combined in DMA (0.10 mL), 25 °C, 48, under Ar. [j]Conditions as in entry 17, but using 20 mol% $\mathbf{L_{JP}}$.

While the free allylic alcohol **IV.1a´** was conveniently transformed into **IV.2a** (entry 19: 85% conversion) with high enantio-induction (94:6 *er*), the use of the OBoc derivative **IV.1a** under similar conditions was more productive promoting the formation of branched 1,5-diene **IV.2a** with a higher overall efficiency (entry 20: 95% conversion, 90% isolated yield, b:l ratio = 20:1, 94:6 *er*). In the absence of either $NiBr_2$(DME) or JosiPhos ligand (entries 21 and 22), no observable formation of 1,5-diene product could be detected. Based on all screening results, we continued the investigation of the scope of this transformation using $\mathbf{L_{JP}}$ as chiral ligand, OBoc protected allylic substrates and the conditions reported in entry 20.[180]

Scope of Products. After having optimized the benchmark process, the generality of the reaction was examined by exposing differently substituted allylic precursors to the conditions of Table **IV.I** (entry 19), see Figure IV.2. Variation of the *para* substituents on the aryl ring of **IV.1** provided excellent yields of chiral 1,5-diene products IV.2 of up to 92% (**IV.2a**-**2f**) with typically high to very high regio-control (b:l up to >20:1) and high *er* values of up to 94:6 (for **IV.2a**, **IV.2b** and **IV.2f**). We were able to analyze **IV.2e** by X-ray diffraction (top in Figure IV.2) revealing that the quaternary center has an (*R*) and the trisubstituted double bond an *E* configurations.[181]

[180] We were not able to separate regio-isomers **IV.2** and **IV.3** from each other by normal silica gel chromatography. In order to isolate pure **IV.2**, it was necessary to use Ag-impregnated silica as reported previously: Aponte, J. C.; Dillon, J. T.; Tarozo, R.; Huang, Y. *J. Chromatogr. A*. 2012, 1240, 83.

[181] The same assignments were done for the other products.

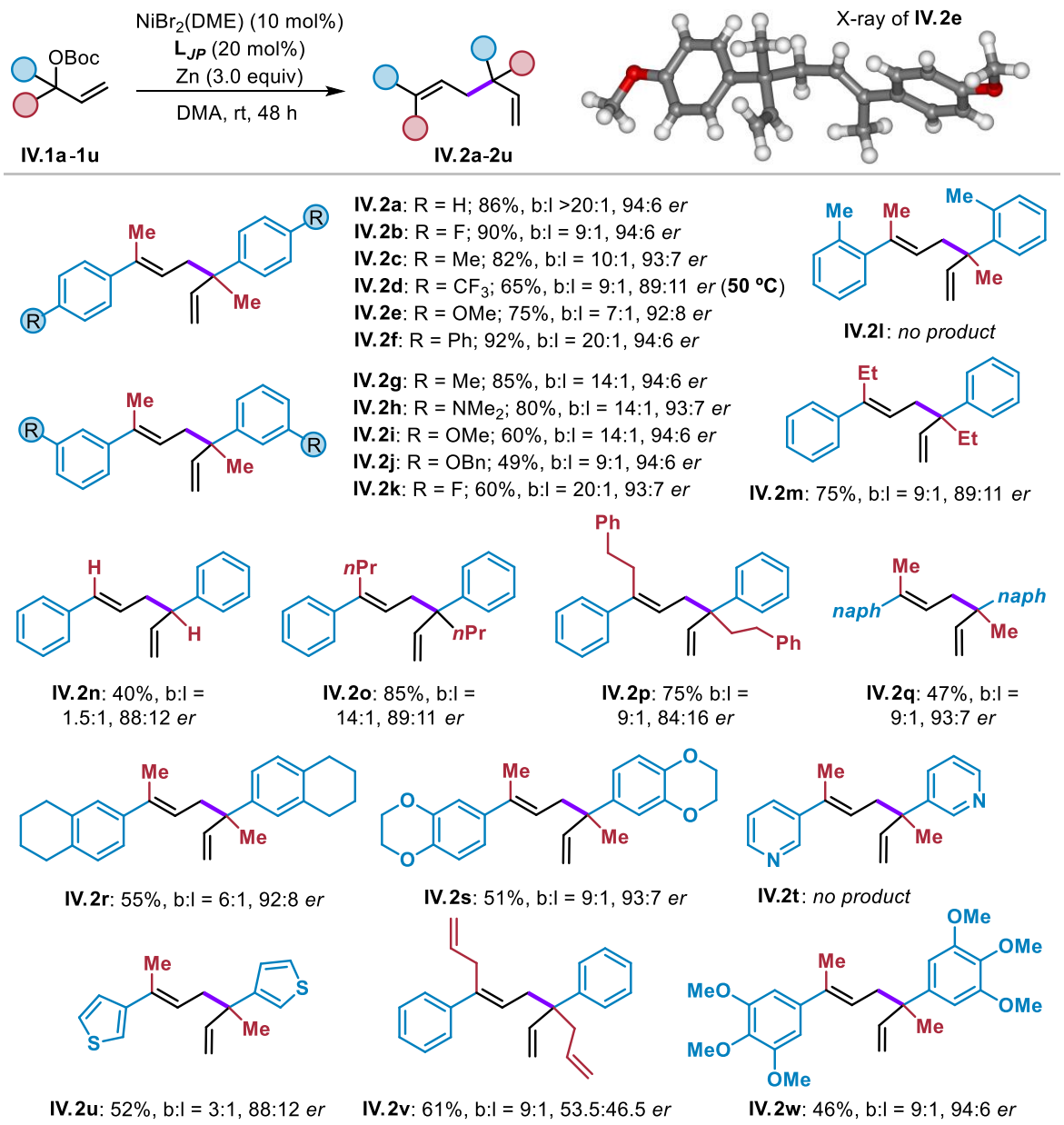

Figure 4.2. Scope of branched 1,5-diene products featuring quaternary carbon stereocenters[a]

Substitution in the *meta* position of the aryl ring in substrates **IV.1** was productive and allowed to produce 1,5-dienes **IV.2g-2k** in appreciable to high yield and high b:l ratios (9:1 to 20:1) and enantio-induction levels similar to the ones observed for products **IV.2a**, **IV.2b** and **IV.2f**. Unfortunately, *ortho* substituted aryl-functionalized substrate **IV.1l** could not be converted into to any observable product **IV.2l** under the optimized reaction conditions indicating a certain degree of steric modulation in this transformation. Other variations were also probed including the introduction of ethyl, propyl and 2-phenyl-ethyl substituents in the allylic precursor (cf., **IV.2m**, **IV.2o** and

IV.2p), which did not significantly alter the outcome of the allylic cross-coupling process (75-85% yield, b:l = 9:1-14:1) with only slightly eroded *er* values of up to 89:11. We also tested a secondary allylic substrate (**IV.1n**) whose conversion proved to less selective (b:l = 1.5:1; 40% yield) though with appreciable enantio-control (88:12 *er*). Other aromatic/functional groups in the allylic precursors were also tolerated in this procedure (cf., synthesis of **IV.2q**-**2w**). The naphthyl-substituted allylic electrophile **IV.1q** was converted into **IV.2q** with moderate yield (47%) but high regio- (b:l = 9:1) and enantio-control (93:7 *er*). Tetrahydronaphthalene- and benzo-1,4-dioxane-substituted allylic substrates **IV.1r** and **IV.1s** were transformed with a similar degree of efficiency furnishing their respective 1,5-dienes **IV.2r** (55%) and **IV.2s** (51%). Whereas pyridyl-based tertiary allylic compound **IV.1t** was not a productive substrate, the use of a thiophene-based allylic carbonate (**IV.1u**) did lead to a 1,5-diene product (**IV.2u**: 52%) with moderate regio-selectivity and appreciable asymmetric induction. The presence of an allyl substituent in the substrate (**IV.1v**) gave access to tetraene **IV.2v** in 61% yield and high regio-control (b:l = 9:1) though virtually a racemic product was isolated. The reasons for lack of enantio-control in this case are unknown, but we speculate that the additional double bonds present in the substrate may unfavorable interact with the intermediate Ni-species. Finally, poly-substituted aryl groups such as present in **IV.1w** are endorsed as well leading in this particular case to the 1,5-diene target **IV.2w** in 46% yield with high regio- and enantio-selection.

Synthetic manipulations. The cross-coupling of tertiary allylic carbonates by Ni-catalysis can be scaled up 10-fold to 1 mmol quantities with a lower Ni/**L*JP*** loading (5 and 10 mol%, respectively) affording 78% yield of the benchmark product **IV.2a** with a similar level of regio/enantio-induction (Figure 3a). We further examined tertiary allylic precursors with other leaving groups (Figure 3b) and found that acetate, pivalate and unprotected OH substituted substrates gave rather similar results (though with lower substrate conversions) in terms of overall selectivity under the optimized conditions. In general, the use of unprotected allylic alcohols can be attractive as it makes the protocol more user-friendly given the easy accessibility of these specific precursors,[182] despite the somewhat lower substrate conversion compared to the use of OBoc

[182] Lumbroso, A.; Cooke, M. L.; Breit, B. *Angew. Chem. Int. Ed*. 2013, 52, 1890.

derivative **IV.1a**. 1,5-Diene **IV.2a** was then modified to illustrate its synthetic potential (Figure 3c). Sequential hydroboration/oxidation of **IV.2a** provided hept-5-en-1-ol **IV.3a** in 60% yield. Biocatalytic epoxidation of **IV.2a** promoted by Novozyme/H_2O_2 gave access to epoxy-ene **IV.4a** (80%). In both cases, no noticeable loss of chirality was observed attesting the stable character of the quaternary stereocenter. In order to examine the possible presence of radical intermediates, various radical trapping agents were used (Figure 3d).

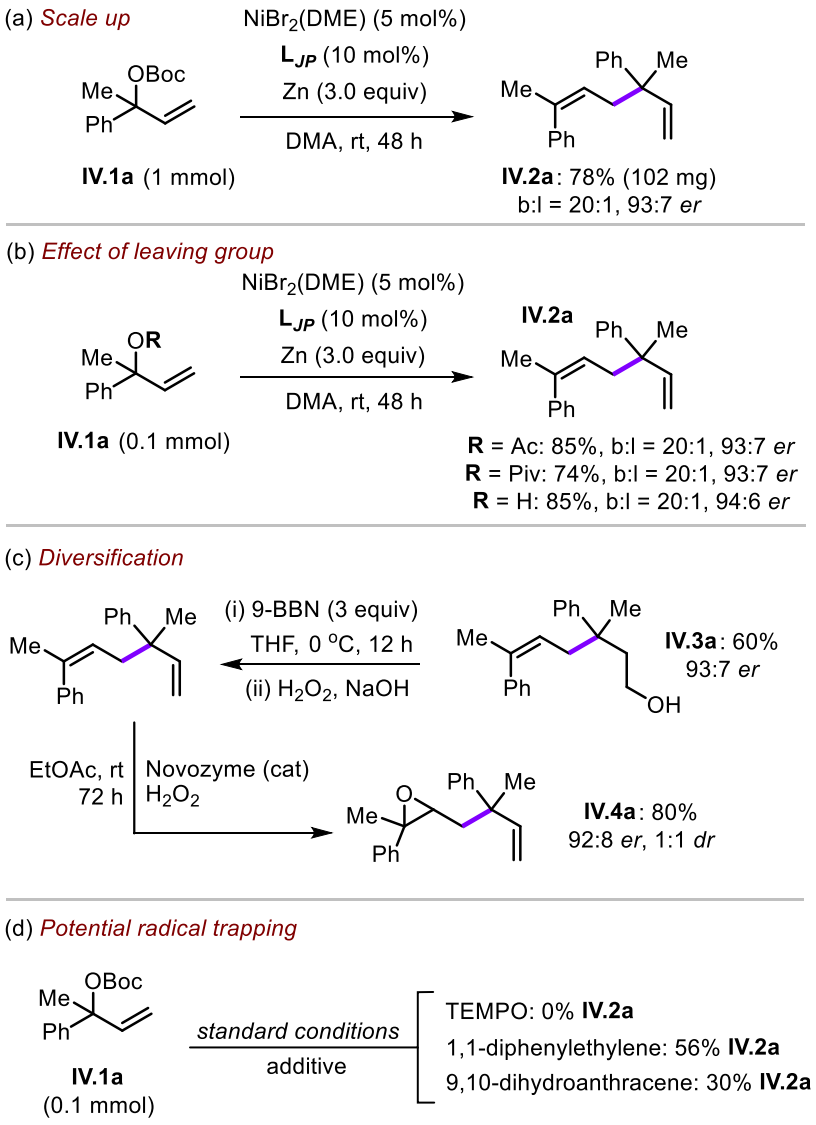

Figure 4.3. a) Scale-up, b) effect of leaving group, c) post-synthetic modification and d) radical scavenging experiments.

Though the addition of TEMPO shut down the formation of product, it may very well be a consequence of catalyst deactivation. The results from the other scavenging

experiments seems to suggest that no free organic radicals are present during the course of the reaction.

4.2 Aims and objectives

The main purpose of this part of the thesis work was to investigate how the high branched-to-linear regio-selectivity to form 1,5-dienes **IV.2a** is achieved against the more typical formation of the linear-to-linear product **IV.3a**. Our initial hypothesis was that the hapticity of the allylic fragment coordinated to the nickel center had to play an important role. Moreover, we also wanted to understand how the $NiBr_2$(DME) pre-catalyst generates a low-valent nickel species that subsequently activates the carbonate-based allylic precursor to form a Ni^n(allyl) species. Ni(0) formation from the Ni(II)Br_2 salt is often reported in the literature as a first step of the catalytic cycle, but knowing that Zn can act as a one-electron reductant, we were curious to determine if our system could alternatively follow a two-electron reduction of the nickel precursor.

Cross-electrophile coupling reactions (CEC) have been widely studied in the last decade, and several mechanistic pathways have been proposed differing in substrate activation, coupling manifold and the contribution from additives. Altogether, four mechanisms are generally known and are depicted in Figure 4.4.[183]

Overall, we were interested to determine if our transformation followed one of these proposed pathways or whether a new characteristic feature could be identified for this type of highly enantio- and regio-selective process.

[183] a) Biswas, S.; Weix, D. J. *J. Am. Chem. Soc*. 2013, 135, 16192. b) Weix, D. J. *Acc. Chem. Res*. 2015, 48, 1767. c) Lucas, E., Jarvo, E. *Nat. Rev. Chem*. 2017, 1, 10065. d) Poremba, K. E.; Dibrell, S. E.; Reisman, S. E. *ACS Catal*. 2020, 10, 8237. See also ref. 179a.

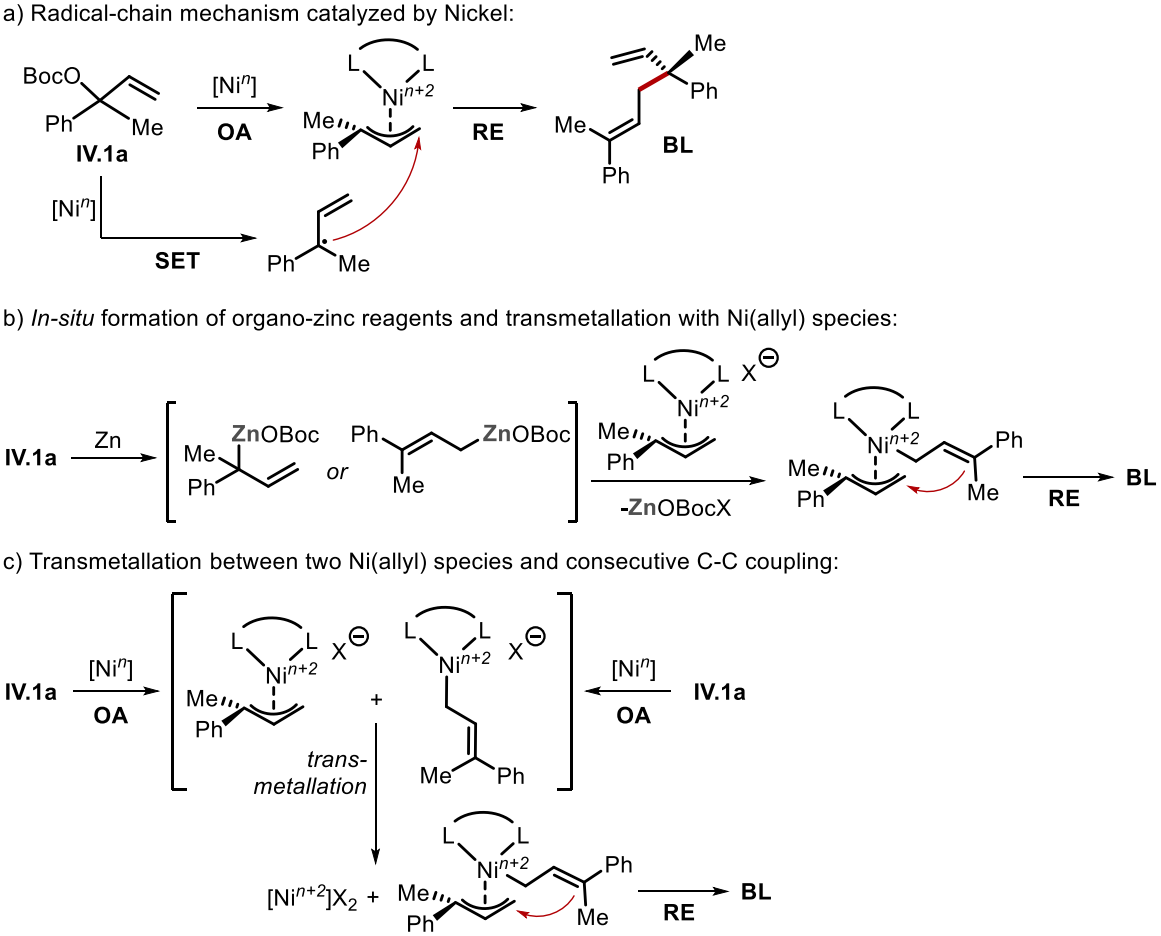

Figure 4.4: Hypothetical pathways for the nickel-catalyzed regio- and enantio-selective cross-electrophile coupling of allylic alcohols to from 1,5-branched dienes. These four different proposals were generated from generally accepted mechanisms of CEC reductive reactions as described in the literature.[183]

4.3 Results and discussion

4.3.1 Initial control screening

To initially discard any of the possible mechanistic pathways presented in section 4.2, we performed a small series of control experiments. A radical-chain mechanism (Figure 4.4a) may be operative where single-electron transfer (SET) of a Ni species activates the substrate generating an organic radical that can be trapped by a Ni(allyl) species generated through oxidative addition (OA). This option seems unlikely in our case considering the results gathered in Figure 4.3d. A second possibility is the in situ formation of organo-zinc reagents that consecutively undergo a cross-coupling step with the Ni(allyl) intermediate (Figure 4.4b). A third pathway would involve a transmetalation between two allyl-Ni species independently formed through OA with the allylic precursor following reductive elimination from a bis-allyl-Ni complex (Figure 4.4c). As a final option, two sequential oxidative addition steps could occur at a single Ni species (with an intermediate reduction step promoted by a proper reductant) following allyl cross-coupling. Intrigued by the high regio- and enantio-preference found for many of the allyl cross-couplings in Figure 4.2, we decided to experimentally examine the benchmark transformation.

Upon substituting the metallic reductant (Zn) by an organic one (TDAE, tetrakis(dimethylamino)ethylene (Figure 4.5a), no productive catalysis was noted. Considering that the zinc reductant is important for our transformation, we checked whether the formation of organozinc species would be feasible under the catalytic conditions but substrate **IV.1a** did not react in the presence of Zn in DMA or THF as medium (Figure 4.5b). This observation seems to suggest that our allyl cross-coupling reaction do not proceed via in situ formation of allyl-Zn species and subsequent transmetalation of an allyl-Ni intermediate.

To be able to discern between a possible transmetalation pathway involving two Ni(allyl) species and a sequential OA pathway, we envisioned that kinetic experiments to determine the order in [Ni] could be helpful as both pathways have a different dependency at the carbon-carbon formation stage (assumed to be rate-limiting) of the reaction. We recently reported the use of React-IR as a versatile tool for following the

consumption of carbonate substrates[184] and determination of reaction orders (also reported in Chapter 3). However, in the present case the heterogeneity of the reaction mixture does not allow for accurate IR-measurements and therefore, we determined a kinetic profile of the benchmark reaction in a classical way by performing a series of catalysis experiments. For each time interval, an average substrate conversion (duplicate experiments) was determined by ^{1}H NMR (Figure 4.5c) and a kinetic profile was extracted for two different Ni-to-**L*JP*** ratios (1:1 and 1:2).

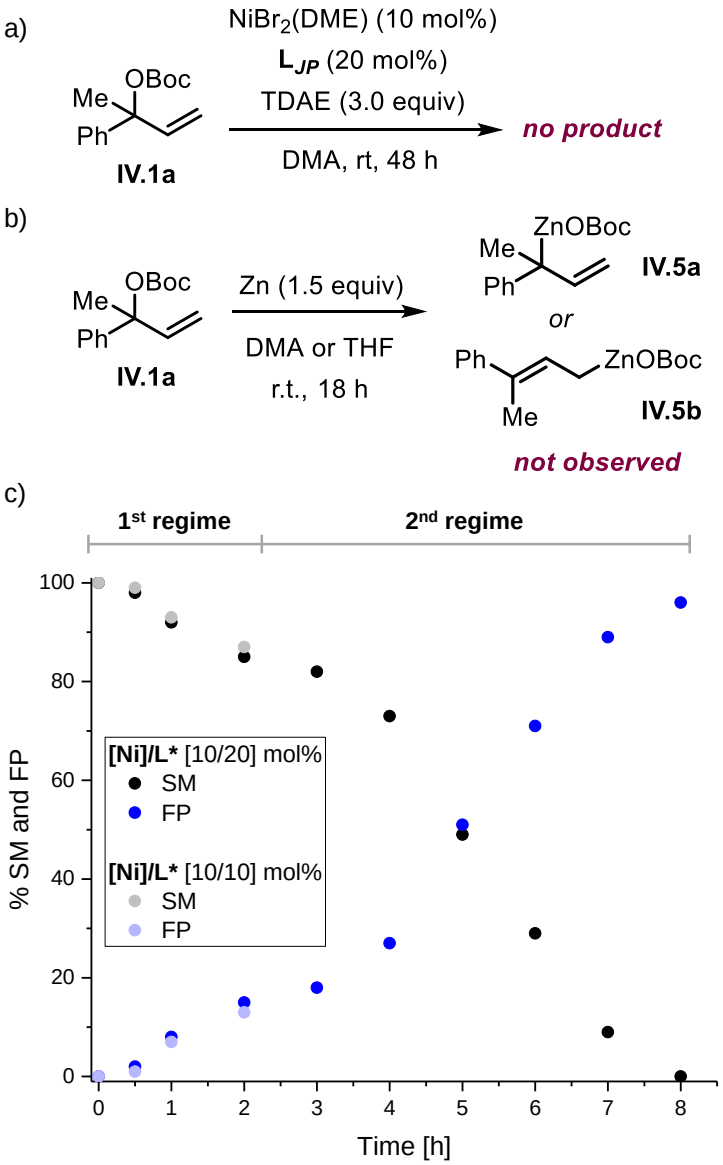

Figure 4.5. Initial control experiments and kinetic profile for the benchmark conversion.

[184] Garcia-Roca, A.; Pérez-Soto, R.; Stoica, G.; Benet-Buchholz, J.; Maseras, F.; Kleij, A. W. *J. Am. Chem. Soc*. 2023, 145, 6442.

At both ratios, a rather similar profile is obtained, and remarkably there seem to exist two different catalytic regimes. In the first hours of the reaction, the catalysis is comparatively slow, and in due course the rate steadily increases suggesting some kind of incubation time. The complexity of the kinetic slope prevented us from collecting convincing evidence for either of the two above-mentioned possible manifolds, and we therefore decided to focus on a detailed spectroscopic and structural analysis of the involved Ni-species in this process.

4.3.2 Spectroscopic monitoring: Nickel activation and detection of intermediates

We started with the X-ray analysis of the Ni(II) complex derived from **L*JP*** and $NiBr_2$(dme), which confirmed the formation of the tetrahedral complex $NiBr_2$**L*JP*** (Figure 4.6a: **IV.A**, left). Addition of Zn to complex **IV.A** caused an abrupt color change from dark green to dark yellow. After a detailed study of this first step by EPR spectroscopy, we established that only 1.0 equiv of Zn was required to observe the corresponding signal for the Ni^{I} complex **IV.B** (see Figure 4.6b, bright yellow trace). Unambiguous confirmation of the formation of **IV.B** was obtained by X-ray crystallographic analysis (Figure 4.6a: right) revealing a Y-shaped coordination geometry around the Ni(I) center. When both Ni(II) and Ni(I) complexes **IV.A** and **IV.B** were treated with (excess) Zn we could not observe any formation of a Ni(0) species. This is important to emphasize, as generally the oxidative addition (OA) of an electrophilic precursor is thought to occur via a requisite Ni(0) intermediate.[15b]

We then monitored the influence of the addition of 10 equiv of substrate **IV.1a** to the initial mixture of $NiBr_2$(DME), **L*JP*** and Zn in DMA by EPR spectroscopy (Figure 4.6b). Over time, the EPR signal for paramagnetic Ni(I) complex **IV.B** disappeared, and notably the shape of the signal changed from isotropic to rhombic-anisotropic and became silent after roughly 3 h. These observations led us to conclude that at this point full consumption of the Ni(I) complex **IV.B** had occurred. The loss of paramagnetic species at the early stage of the reaction inspired us to monitor the same catalytic experiment by $^{31}P\{^{1}H\}$ NMR spectroscopy revealing the start of a diamagnetic domain displaying the presence of multiple species (Figure 4.6c).

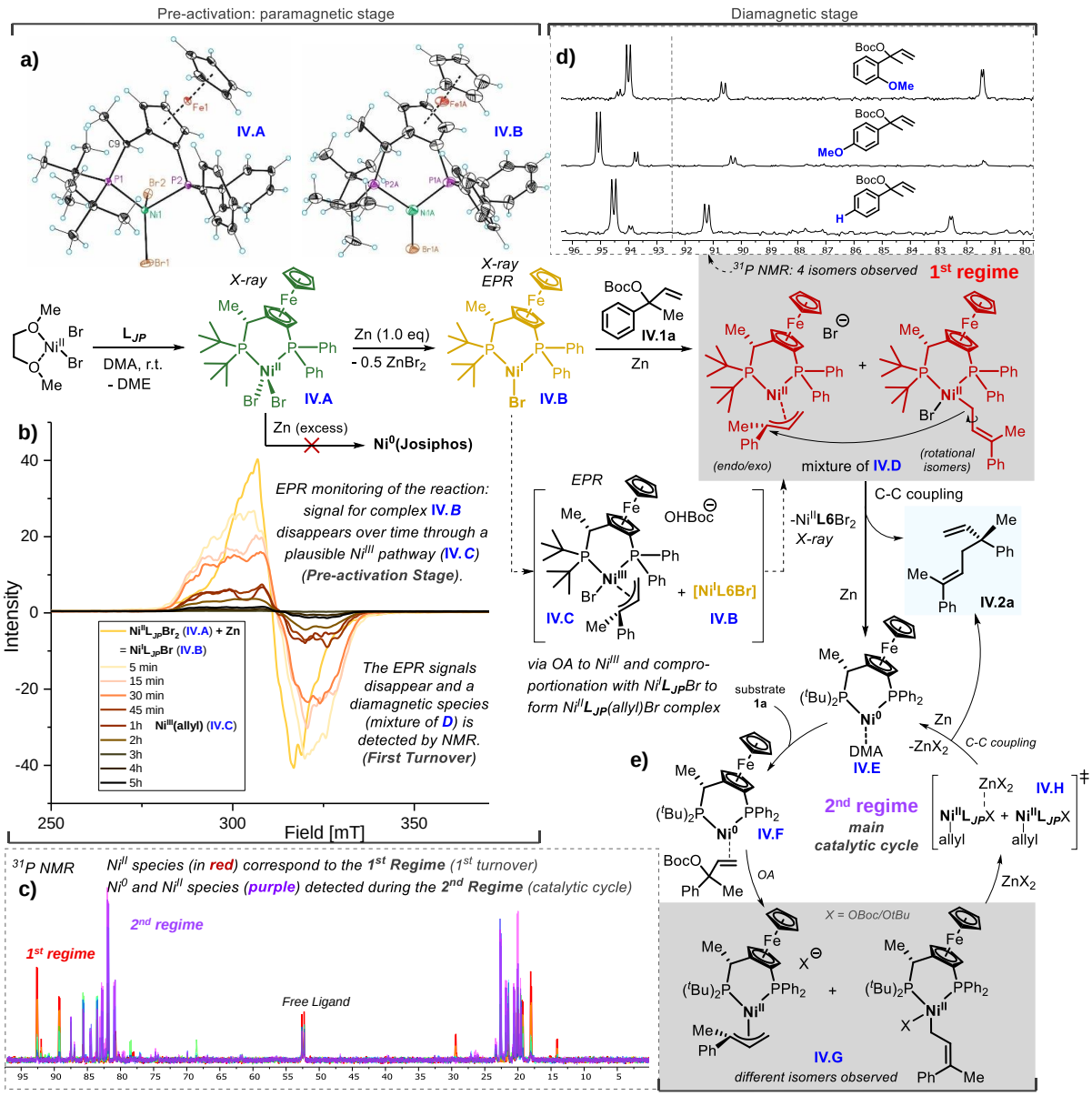

Figure 4.6: a) Pre-activation stage: synthesis and isolation of complexes **IV.A** and **IV.B**, b) monitoring of the catalysis by EPR spectroscopy, c) ^{31}P NMR spectroscopic fingerprint of the reaction mixture during the second regime, d) proposed initial turnover of the catalytic transformation via a Ni(III) Intermediate **IV.C** forming a mixture of allylic isomers **IV.D**, and e) Ni^0/Ni^{II} based redox couple in the productive cycle of the second regime.

Interestingly, their spectral features showed a clear time-dependency. In the first regime (1-2 h reaction time, Figure 4.5c), a set of resonances appeared in the region

91-95 ppm (red-colored signals) while Ni^{I}**L**$_{JP}$Br **IV.B** was being consumed.[185] The second regime started after approximately 2 h, when a new set of signals appeared between 82-88 ppm (purple signals) matching the time frame for the species in red to disappear, and the timeframe where both kinetic regimes are overlapping.

After collecting this spectroscopic information, we then focused on gathering further evidence for the conversion of complex **IV.B** into a presumable Ni(II)allyl species in the presence of allylic substrate **IV.1a**. We tested complex **IV.B** as a potential pre-catalyst, but under the optimized conditions (**Table IV.I**, entry 19) no conversion of **IV.1a** could be detected. ^{31}P NMR analysis was used to examine whether the formation of the presumed Ni(II) intermediates **IV.D** was dependent on the presence of $ZnBr_2$, which is the by-product formed when complex **IV.A** is converted to complex **IV.B** at the beginning of the reaction (Figure 4.6a). Treatment of complex **IV.B** with 1.5 equiv of both Zn and **IV.1a** resulted after 30 min in a color change with the NMR spectrum showing the envisioned Ni(II)allyl species **IV.D** as a mixture of complexes. Importantly, when performing the same reaction in the absence of Zn, the ^{31}P NMR spectrum remained silent. These control experiments demonstrate the crucial role of $ZnBr_2$ to activate the Ni^{I}**L**$_{JP}$ species **IV.B** in the presence of the allylic substrate **IV.1a**. Onwards, we studied the nature of the mixture of species **IV.D** by changing the substituents of the tertiary carbonate substrate. As illustrated in Scheme 5d, the position and relative population of the ^{31}P resonances are a clear function of the nature of the aryl substituent (*para*-H, *para*-OMe and *ortho*-OMe) in **IV.1**. The effect of the leaving group (LG) in **IV.1** was also scrutinized by changing the OBoc for other groups such as OAc and OPiv. This structural change did not affect the chemical shifts for complexes **IV.D** in the ^{31}P NMR spectrum, suggesting similar behavior of these substrates during catalysis (see results in Figure 4.3b). Combining these spectroscopic findings, we conclude that the species observed during the first regime of the diamagnetic stage represent a mixture of allylic isomers with different ligand hapticity (η^3 vs η^1) and/or

[185] Note that the mass balance between the red (1st regime) and the purple (2nd regime) NMR peaks does not make a perfect fit. While the red species are being formed, these NMR measurements do not visualize the disappearance of the Ni(I) complex **IV.A** in the same timeframe. Although we cannot quantify a full mass balance including all paramagnetic and diamagnetic species, the overall process balance should likely be [Ni^{I}**L**$_{JP}$Br] + [Ni^{II}**L**$_{JP}^{1st\ regime}$] = [Ni^{II}**L**$_{JP}^{2nd\ regime}$].

rotational η^1-isomers as proposed in Figure 4.6a (Ni^{II} structures in red) with a key role for non-innocent $ZnBr_2$.[186]

Based on the information presented above, we propose that the formation of **IV.D** occurs through an oxidative addition step (OA) of **IV.1a** to **IV.B** producing Ni^{III}**L**$_{JP}$(allyl)Br complex **IV.C** (Figure 4.6) that rapidly undergoes comproportionation with unreacted Ni^{I}**L**$_{JP}$Br **IV.B**.[187] The resulting allylic isomers **IV.D** with the allyl moiety coordinating η^1 (nucleophilic) or η^3 (electrophilic) have different reactivity, providing a pathway towards C–C coupling through a bimetallic mechanism [188] enabling a reductive elimination of the chiral 1,5-diene product **IV.2a**. Bimetallic C–C formations catalyzed by Ni^{II} complexes have precedent and two plausible mechanisms have been proposed including "closed-shell" transmetallation [189] and "open-shell" group transfer.[190] In our cross-coupling process, the formation of the C–C bond leading to product **IV.2a** occurs in a diamagnetic regime, where the resting state is represented by a mixture of allylic isomers **IV.D**. We propose here that a closed-shell transmetalation step occurs between isomers of **IV.D** re-forming Ni(II)**L**$_{JP}$$Br_2$ **IV.A** and Ni(0)**L**$_{JP}$(DMA) complex **IV.E** (Figure 4.6e). The latter will then be part of a catalytic cycle creating additional substrate turnover as will be discussed below.

The main catalytic cycle is discussed in Figure 4.6e, with complex **IV.E** as starting point. We were able to detect various Ni(0) species apart from the Ni(II) ones by ^{31}P NMR spectroscopy (see Figure 4.43 in Section 4.6.5). Coordination of substrate **IV.1a** furnishes Ni^0 intermediate **IV.F** that undergoes OA generating a new set of Ni^{II}(allyl) complexes **IV.G**, which aligns well with the ^{31}P NMR observations in Scheme 4c displaying two diamagnetic catalysis regimes. Complex **IV.G**[191] likely exist as a mixture of η^1 and η^3 isomers (with an OBoc and/or O*t*Bu anion after loss of CO_2) that participates in an envisioned bimetallic coupling (**IV.H**) to deliver the 1,5-diene product **IV.2a**. Subsequent turnovers are based on a Ni^0/Ni^{II} redox couple being part of the

[186] a) Zhang, T.; Zhong, K.; Lin, Z.-K.; Niu, L.; Li, Z.-Q.; Bai, R.; Engle, K. M.; Lan, Y. *J. Am. Chem. Soc*. 2023, 145, 4, 2207. See also reference 179b.

[187] a) Kerackian, T.; Bouyssi, D.; Pilet, G.; Médebielle, M.; Monteiro, N.; Vantourout, J. C.; Amgoune, A. *ACS Catal.* 2022, 12, 12315. b) Ting, S. I.; Williams, W. L.; Doyle, A. G. *J. Am. Chem. Soc.* 2022, 144, 5575.

[188] a) Pye, D. R.; Mankad, N. P. *Chem. Sci*. 2017, 8, 1705. b) Xu, H.; Diccianni, J. B.; Katigbak, J.; Hu, C.; Zhang, Y.; Diao, T. *J. Am. Chem. Soc*. 2016, 138, 4779.

[189] Yamamoto, T.; Abla, M.; Murakami, Y. *Bull. Chem. Soc. Jpn.* 2002, 75, 1997.

[190] Tsou, T. T.; Kochi, J. K. *J. Am. Chem. Soc.* 1979, 101, 6319.

[191] Further evidence for the intermediacy of Ni(II)allyl complexes **IV.G** was obtained by HRMS analysis, see section 4.5.7.

second regime (Figure 4.6c), and we exclude the re-formation of Ni(I) during the second stage of the process.

Although a plausible overall picture of the different stages of this allyl cross-coupling process has been presented, we sought to collect more evidence for the last stage of the mechanistic proposal given under Figure 4.6e. Thus, we continued to perform additional control experiments (Figure 4.7). The preceding data already hinted towards a positive role of divalent Zn species on the reactivity of the Ni-catalyst.

Whereas 1,5-diene formation (**IV.2a**: 18% after 3 h; Figure 4.5c) is initially slow, addition of 1 equiv of $ZnBr_2$ significantly accelerates the overall kinetics producing in the same time-frame 55% of **IV.2a** albeit with a somewhat reduced preference for the branched product (b:l = 6:1), see Figure 4.7a. To illustrate the positive effect of Zn, we also performed the same experiment with LiBr showing a rather similar yield/regioselectivity of **IV.2a** (20%, b:l >20:1) compared to the standard reaction. Remarkably, when the reaction was carried out in the presence of an excess of an external (competitive) electrophile (benzaldehyde), a racemic allylation product was isolated in 63% yield (2:1 *dr*, Figure 4.7b). This supports the idea that the intermediate Ni(II)allyl species here preferentially reacts as a nucleophilic (η^1) species superseding allyl cross-coupling. In this aldehyde allylation event, there is likely only one Ni-complex involved, with racemic **IV.5** being formed too far away from the chiral environment of the Ni(II) complex.

Ni(II) complex **IV.J** (Figure 4.7c) can be quantitatively prepared *in situ* by combining $Ni(COD)_2$ and allyl bromide (giving **IV.I** in situ) as judged from ^1H and ^{31}P NMR analysis. A crystallographic analysis of the oxidative addition product **IV.J** revealed a η^3-allyl Ni species with an non-coordinating bromide anion. We assume that this coordination mode may also be accessible in solution and that there exists an equilibrium between η^1 and η^3 coordination modes at the Ni(II)allyl stage in the catalytic process, with the allyl substituents obviously influencing the population of both types of allyl complexes.

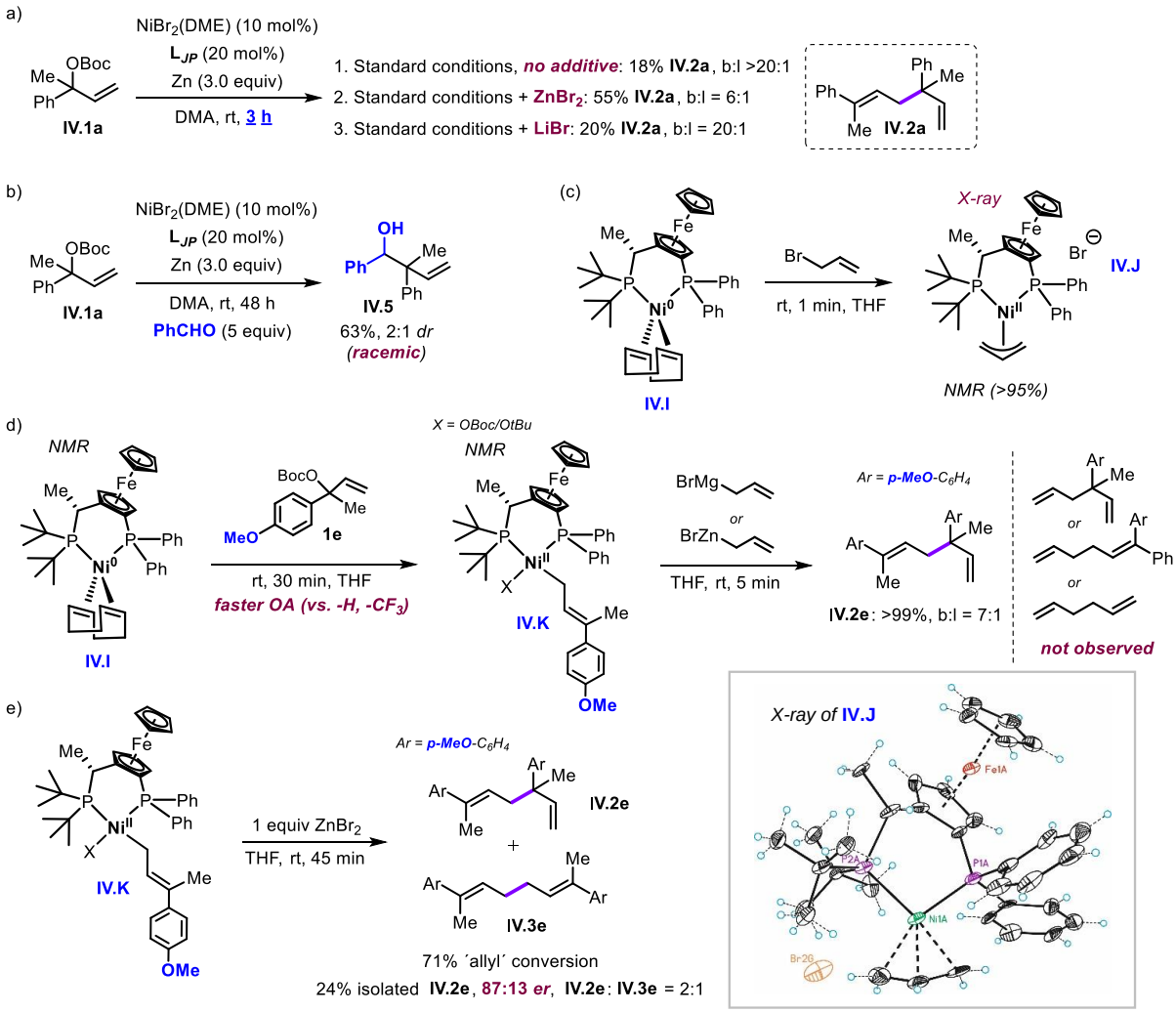

Figure 4.7: a) Effect of metal additives on substrate conversion, b) intermediacy of a nucleophilic Ni(II)allyl complex, c) model η^3-Ni(II)allyl complex **IV.J** characterized by NMR and X-ray analysis, d) evidence for the requirement of a bimetallic pathway towards product **IV.2e**, and e) chiral 1,5-diene formation from complex **IV.K** in the presence of $ZnBr_2$.

To avoid comproportionation observed when **IV.1a** is mixed with *in situ* prepared Ni(0) complex **IV.I**, we decided to use a more electron-rich carbonate substrate (**IV.1e**, Figure 4.7d) leading to faster OA.[192] Utilizing **IV.1e**, we could quantitatively access well-defined Ni^{II}(allyl)(OBoc) complex **IV.K** as confirmed by NMR. Subsequently **IV.K** was treated with nucleophilic allyl species. In these latter trials, we could only observe the homo-allyl coupled product **IV.2e** (>99%, b:l = 7:1) with a very similar regio-control

[192] a) Bajo, S.; Laidlaw, G.; Kennedy, A. R.; Sproules, S.; Nelson, D. J. *Organometallics* 2017, 36, 1662. b) Pérez−García, P. M.; Darù, A.; Scheerder, A. R.; Lutz, M.; Harvey, J. N.; Moret, M.-E. *Organometallics* 2020, 39, 1139.

as observed for **IV.2e** under the optimized catalytic conditions reported in Figure 4.2 (**IV.2e**, 75% yield, b:l = 7:1). The absence of any hetero-allyl cross-coupled product not only indicates that Ni(II) complex **IV.K** most likely prefers a η^1 coordination mode for the allyl ligand but also demonstrates the beneficial presence of Lewis acidic Zn given the very short reaction time ($\leq$ 5 min). This hypothesis could be further supported by preparing **IV.K** separately and leaving this solution (without additives) for 24 h. After this time, we found that only about 65% of **IV.2e** was selectively formed (see Figure 4.41 in Section 4.6.4 for details).

The non-innocent behavior of divalent Zn was then further examined by treating **IV.K** with 1 equiv of $ZnBr_2$ (Figure 4.7e). These latter conditions provided around 71% conversion of **IV.K,** and 24% of 1,5-diene **IV.2e** was isolated having an *er* value (87:13) close to the one observed under the optimized conditions (Figure 4.2: 92:8 *er*).[193] From the results depicted in Scheme 6 we conclude that Lewis acidic ZnX_2 species indeed play an active role in this cross-coupling likely inducing a bimetallic event during C–C bond formation through an –ate species as previously proposed by Vicic.[179b]

[193] Note that the addition of $ZnBr_2$ does not ideally reflect divalent Zn speciation throughout the reaction. With the concentrations of $Zn(OBoc)_2$ and/or $Zn(O\textit{t}Bu)_2$ increasing over time, the lower regio/chemo-selectivity in the presence of $ZnBr_2$ as additive is likely not completely representative compared to the standard catalytic process.

4.4 Conclusions

In this chapter, we describe a Ni-promoted homo-allylic coupling process that enables the asymmetric synthesis of rarely reported chiral unsymmetrical 1,5-dienes featuring a quaternary carbon stereocenter. This new methodology fills a gap in this area and combining easily accessible and modular allylic carbonates as precursors, and Zn as a reducing agent. The developed protocol combines a preferential formation of a branched regio-isomer with high *E*-selectivity and enantio-control, and highlights the use of a cheap and abundant metal in a formal enantio-selective cross-electrophile coupling process.

Our mechanistic studies presented in this chapter reveal that this catalysis process features two distinct kinetic regimes, with the first turnovers deviating from the subsequent productive cycle. Various Ni-complexes and intermediates could be identified by X-ray analysis, EPR, ^{31}P NMR, MS and these spectroscopic/structural findings were complemented by a series of control experiments. We are able to conclude that a main cycle exists in the course of the catalysis that depends on a Ni(0)/Ni(II) redox couple. Allyl-allyl coupling is promoted by the presence of divalent Zn that helps to equilibrate the allyl fragment between η^1 and η^3 coordination modes in a Ni(II)allyl intermediate enabling a bimetallic pathway towards the formation of the chiral 1,5-diene product. Our findings are useful in the context of developing new types of mechanism-driven cross-coupling reactions forging quaternary carbon stereocenters.

4.5 Experimental section

4.5.1 General methods

All reactions were set up in a nitrogen-filled glovebox (mBraun UnilabPro) with concentrations of O_2 and H_2O < 0.1 ppm or under a nitrogen atmosphere in oven-dried glassware using standard Schlenk techniques. Commercially available reagents $Ni(DME)Br_2$, $Ni(COD)_2$, chiral JosiPhos ligand **L*JP*** and Zn were used as received without further purification from the respective commercial suppliers and stored under inert gas and/or low temperature where required. Previously reported vinyl linear carbonates **IV.1a** were prepared as described in the literature.[155] Synthesis grade solvents such as tetrahydrofuran (THF), dimethylacetamide (DMA) and deuterated tetrahydrofuran (THF-d_8) were dried over 4 Å molecular sieves and degassed by bubbling N_2 through it prior to their use. Glassware was washed in a base bath (KOH in water/isopropyl alcohol) after each use. Magnetic stirring bars were cleaned using an acid mixture of 20% HNO_3 +10% HCl in water.

Nuclear magnetic resonance (NMR): NMR spectra were obtained on a Bruker 400 MHz, a 500 MHz or a 500 MHz (equipped with a cryoprobe) spectrometers and with probe heads capable of producing gradients in the *z* direction with a maximum strength of 53.5 G/cm. ^{31}P NMR chemical shifts are reported in parts per million (ppm) relative to 85% H_3PO_4. In the ^{31}P NMR spectra measured in non-deuterated solvents, a coaxial tube containing acetone-d_6 was used to maintain the ^{2}H lock signal. Multiplicities are reported as follows: singlet (s), broad band (br), d (doublet) and multiplet (m). All the $^{31}P\{^{1}H\}$ NMR spectra have been referenced to the free ligand (**L*JP***) signal at -22.9 ppm.

Electron paramagnetic resonance (EPR): Continuous wave (CW) EPR spectra were acquired on a Bruker EMX X-band EPR spectrometer with an ER 4116 HS cavity (9.86 GHz at room temperature). A 150 mL Suprasil offset liquid nitrogen Dewar flask (Wilmad-LabGlass) was used for low-temperature measurements (77 K). The spectral data was collected at ambient conditions with the following spectrometer settings: microwave power = 0.5506 mW; center field = 3000 G, sweep width = 1200 G, sweep time = 20 s, modulation frequency = 100 KHz, modulation amplitude = 4 G, power attenuation = 25 dB, time constant = 0.01 ms. Individual EPR tubes were filled with the sample and were placed at the same position of the resonant cavity for EPR spectral acquisition.

Ultraviolet-Visible spectroscopy (UV-Vis): UV-Vis measurements were carried out on a Shimadzu UV-2401PC spectrophotometer equipped with a photomultiplier detector, double beam optics and D2 and W light sources.

All the spectra were recorded in a 1 mm Hellma Quartz SUPRASIL® cuvette. Due to the high concentration of the solutions, short path cuvettes were employed in order to avoid signal saturation.

X-ray crystallography: The crystals used for structure determination were selected using a Zeiss stereomicroscope using polarized light and prepared under inert conditions immersed in perfluoropolyether as protecting oil for manipulation. Crystal structure determination was carried out using a Apex DUO Kappa 4- axis goniometer equipped with an APPEX 2 4K CCD area detector, a Microfocus Source E025 IuS using MoK_α radiation, Quazar MX multilayer Optics as monochromator and an Oxford Cryosystems low temperature device Cryostream 700 plus (T = -173 °C). Crystal structure determination for samples Full-sphere data collection was used with ω and φ scans. Data was collected with program APEX-2, data reduction Bruker Saint V/.60A and absorption correction SADABS. A second equipement was also used: Rigaku diffractometer is equipped with a Pilatus 200K area detector, a Rigaku MicroMax007HF microfocus rotating anode with MoK_α radiation, Confocal Max Flux optics and an Oxford Cryosystems low temperature device Cryostream 700 plus (T = –173 ° C). Fullsphere data collection was used with ω and φ scans. Programs used: Data collection and reduction with CrysAlisPro V/.60A and absorption correction with Scale3 Abspack scaling algorithm. Crystal structure solution was achieved using the computer program SHELXT. Visualization was performed with the program ShelXIe. Missing atoms were subsequently located from difference Fourier synthesis and added to the atom list. All non-hydrogen atoms were refined including anisotropic displacement parameters.

High resolution mass spectrometry (HR-MS): HRMS data was recorded using two different methodologies: ESI-MS analyses were performed on a MicroTOF Focus mass spectrometer (Bruker Daltonics) by direct injection. Cold-spray ionization-MS (CSI-MS) analyses were performed on a MicroTOF Focus mass spectrometer (Bruker Daltonics) equipped with a cold-spray ionization source by direct injection and using nitrogen as sprayer and dry gas.

4.5.2 EPR, UV-Vis and NMR monitoring of the catalysis

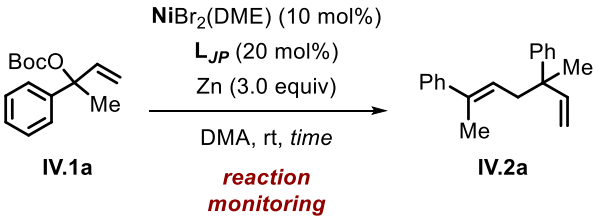

Figure 4.8: Reaction scheme for the catalytic transformation.

EPR monitoring of the catalysis (Figure 4.9)

Procedure: A catalysis sample was prepared for each EPR measurement. In this case, the plot consists of 9 stacked EPR spectra. A total of 9 samples were prepared and they were measured at different reaction times: 5, 15, 30 and 45 min; and then every 1 hour until 5 h.

In a 2 mL vial, $Ni(DME)Br_2$ (7.0 mg, 0.023 mmol), **L*JP*** (25.6 mg, 0.046 mmol) and zinc powder (44.8 mg, 0.69 mmol) were dissolved in 0.4 mL of DMA. The allylic substrate **IV.1a** (57 mg, 0.23 mmol) was added and the reaction mixture was left stirring for the required time. The reaction crude was transferred to an EPR tube without filtration and the sample was frozen at 77 K before the measurement.

UV-Vis monitoring of the catalysis (Figure 4.10)

Procedure: Contrary to the EPR monitoring set up, a single catalysis sample was prepared for monitoring the catalytic reaction by UV-Vis. In this case, the reaction mixture was continuously stirred and a 20 µL volume was sampled out for each measurement. 5 samples were prepared (5 min, 30 min, 1 h, 1h 30 min and 2 h) by diluting the aliquot sampled from the reaction crude with a dilution factor of 1/100 in DMA.

In a 2 mL vial, $Ni(DME)Br_2$ (7.0 mg, 0.023 mmol), **L*JP*** (25.6 mg, 0.046 mmol) and zinc powder (44.8 mg, 0.69 mmol) were dissolved in 0.5 mL of DMA. The allylic substrate **IV.1a** (57 mg, 0.23 mmol, 1.0 equiv) was added and the reaction mixture was left stirring. At each scheduled time, 20 µL were sampled from the reaction mixture, and the aliquot was transferred without filtration to a septum-capped UV-Vis cuvette (*l* = 1cm) and 2 mL of DMA were used for dilution.

NMR monitoring of the catalysis (Figure 4.11, 4.12 and 4.14)

Procedure: Several samples were prepared with different catalyst loadings and equiv of Zn. The solvent used was DMA and all samples were measured by ^{1}H and ^{31}P NMR every 30 min for 7 h.

In a 2 mL vial, $Ni(DME)Br_2$ (7.0 mg, 0.023 mmol), **L*JP*** (25.6 mg, 0.046 mmol) and zinc powder (44.8 mg, 0.69 mmol) were dissolved in 0.5 mL of DMA. The allylic substrate **IV.1a** (57 mg, 0.23 mmol, 1.0 equiv) was added and the reaction mixture was transferred to an NMR tube with an acetone-d_6 capillary to monitor the catalysis by ^{31}P NMR. The sample was stirred using an NMR tube spinner during the interval times.

In Figure 4.11: Catalyst loading of 10 mol% and 3.0 equiv Zn. ^{1}H paramagnetic NMR shows the loss of [Ni^{I}] paramagnetic signal during the first 2 h.

In Figure 4.12: Catalyst loading of 20 mol% with an excess of 6.0 equiv of Zn. ^{31}P NMR allows detection of catalytically relevant species.

In Figure 4.14: [Ni/L] loading of 20/40 mol% (excess of JosiPhos ligand **L*JP***) and 3.0 equiv of Zn. Ni species detection depends on the Zn concentration.

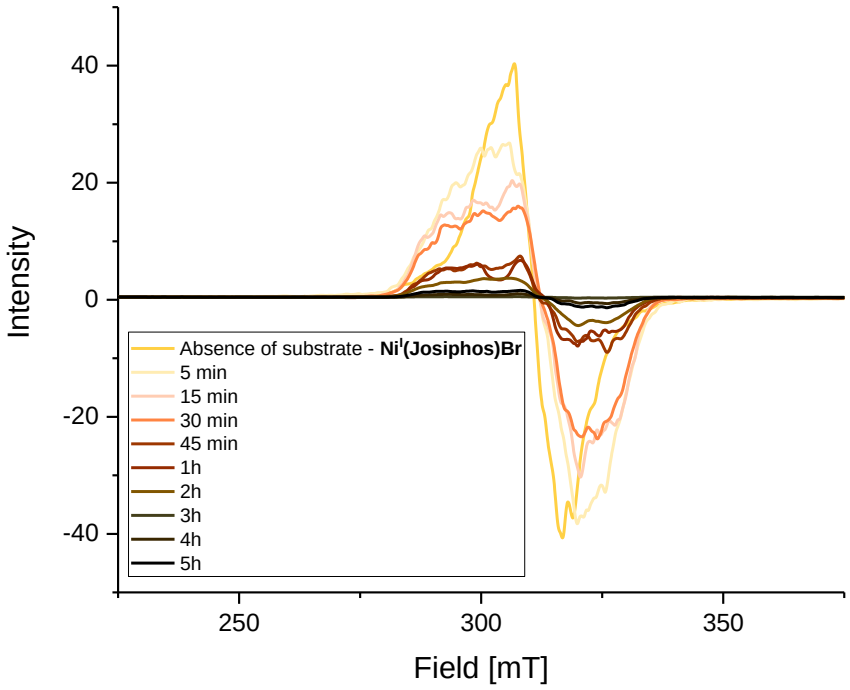

Figure 4.9: EPR monitoring of catalytic experiments at 10 mol% Ni and 20 mol% **L*JP*** and 3.0 equiv of Zn in DMA. Reaction temperature: 298 K. Measurement temperature: 77 K.

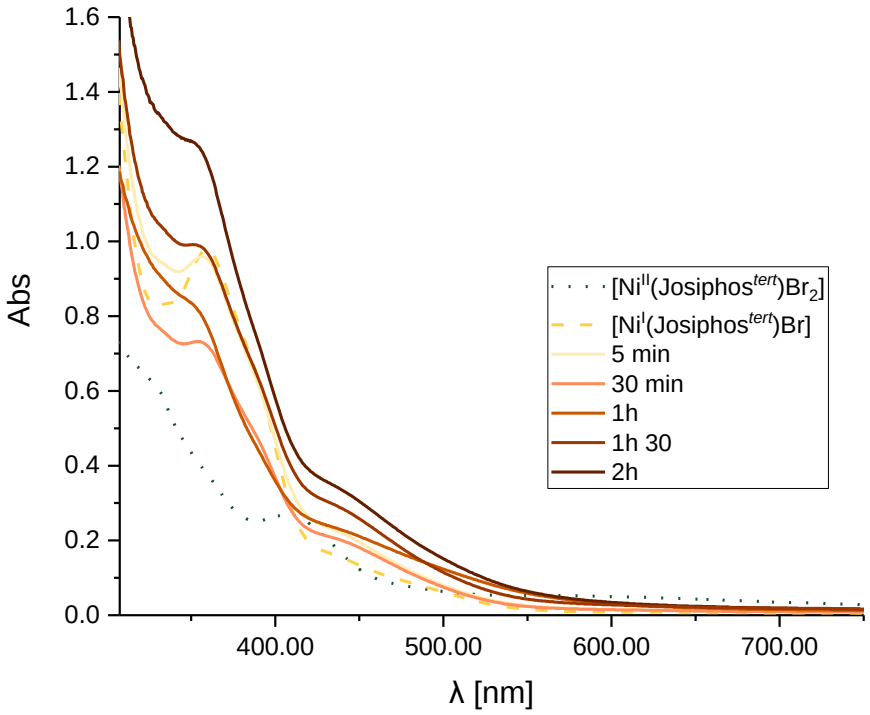

Figure 4.10: UV-Vis monitoring of a catalytic experiment at 10 mol% Ni and 20 mol% **L*JP*** and 3.0 equiv of Zn in DMA. Reaction temperature: 298 K. Measurement temperature: 298 K.

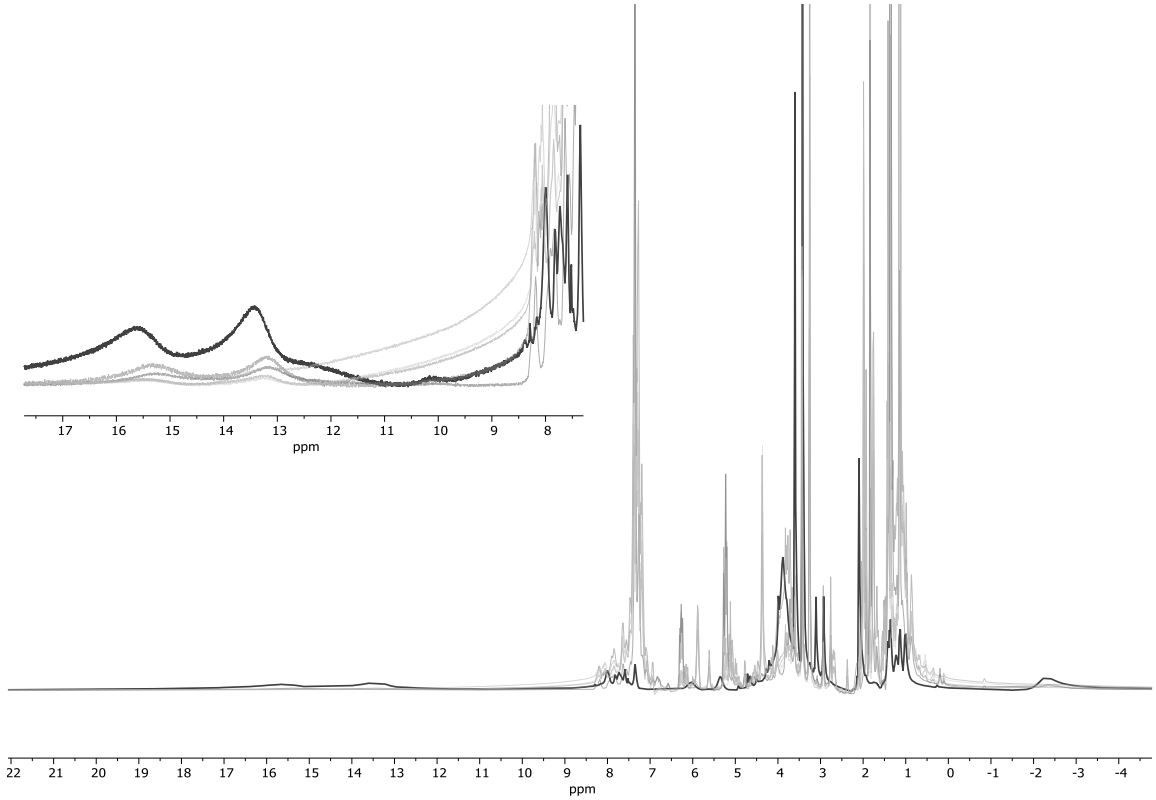

Figure 4.11: ^{1}H NMR paramagnetic NMR stacked spectra of catalysis monitoring at 298 K in DMA-d_9. [Ni/**L**$_{JP}$] = 10/10 mol%, 3.0 equiv of Zn.

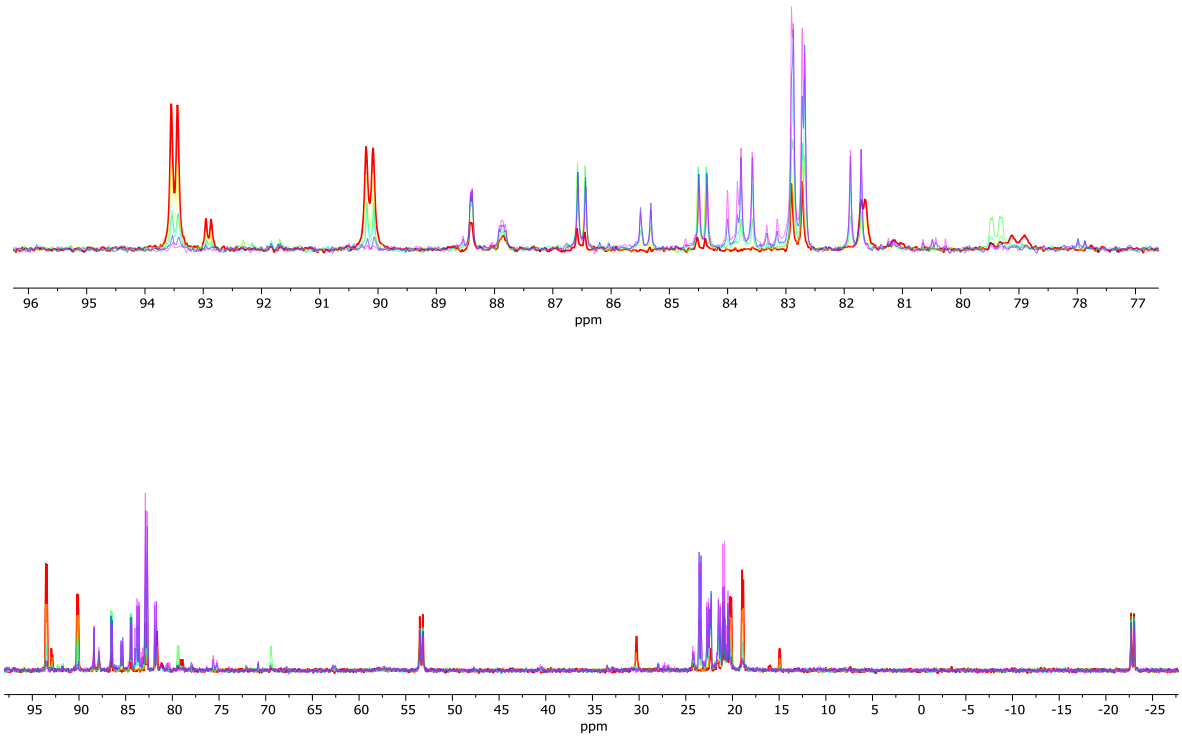

Figure 4.12: Stacked ^{31}P NMR spectra of a catalysis mixture monitored at 298 K in DMA-d_9. Catalyst charge [Ni/**L**$_{JP}$] = 20/20 mol% using 6.0 equiv of Zn.

Signal	*J (Hz)*	*δ (ppm)*
Ni-1	17.8	93.5
Ni-2	19.0	90.2
Ni-3 **Ni-3'**	29.9 30.1	82.8
Ni-4	21.7	86.5
Ni-5	29.0	85.4
Ni-6	22.7	84.4
Ni-7	31.4	83.7
Ni-8	30.0	81.9
Ni-9 (dd)	26.0 // 6.4	79.4
Ni-10 (dt)	20.9 // 6.2	69.4

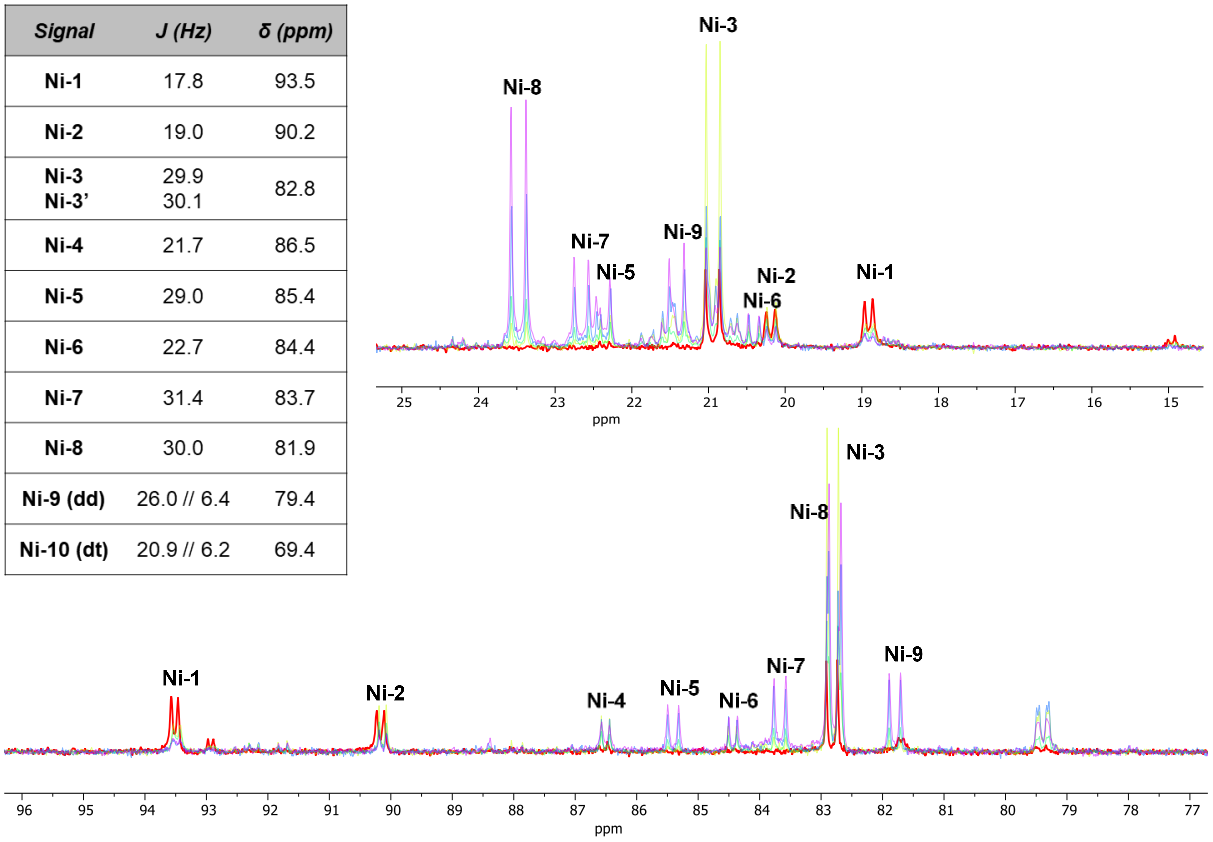

Figure 4.13: Analysis data of the species observed in Figure 4.12 (zoomed spectra are provided in Figure 4.12). All spectra are referenced to free ligand **L*JP***.

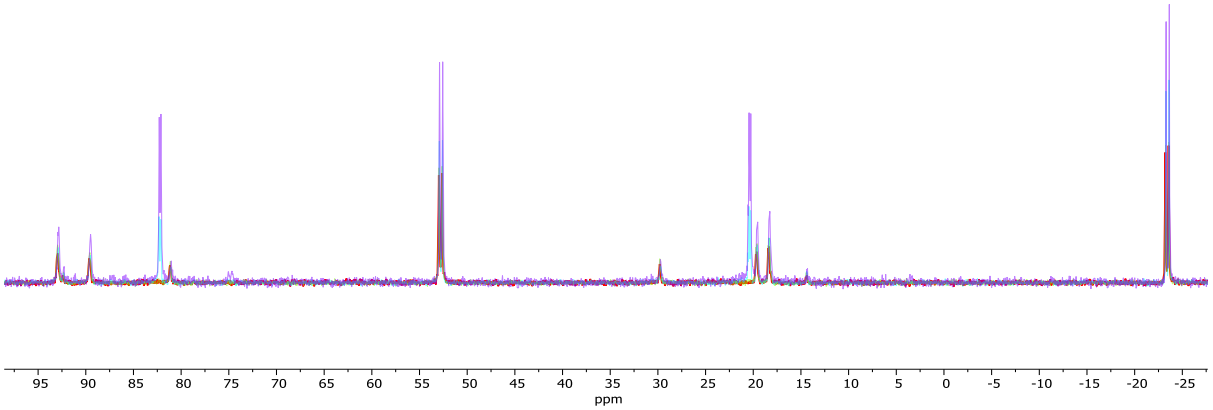

Figure 4.14: Stacked ^{31}P NMR spectra of a catalytic mixture monitored at 298 K. in DMA. Catalyst charge [Ni/**L*JP***] = 20/40 mol%, 3.0 equiv of Zn.

4.5.3 Kinetic analysis by ^{1}H NMR

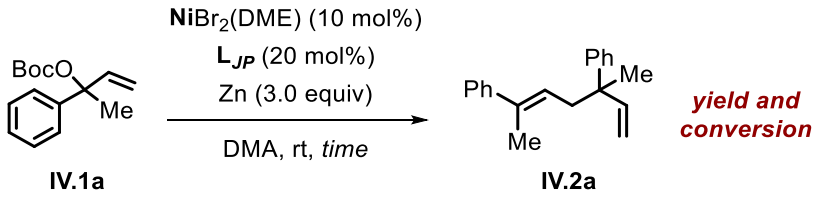

Figure 4.15: Reaction scheme for the catalytic transformation of **IV.1a** into **IV-2a**. Yield and conversion were calculated by ^{1}H NMR.

Initially, we tried to gather a kinetic profile by *in situ* IR monitoring of the catalysis but the heterogeneity of the reaction mixture did not allow for good data acquisition. Similarly, sampling of aliquots of single experiments also did not help, as reproducibility problems were observed. As a last option, the kinetic profile of our transformation was obtained by analyzing the reaction crude of different catalytic experiments stopped at different reaction times. The crude was analyzed by ^{1}H NMR and the yields reported were determined with mesitylene as an internal standard.

Procedure: A catalytic sample was prepared for each kinetic point. In this case, the plot consists of 9 points. A total of 9 samples were thus prepared and they were measured at different reaction times: at 30 min and then every 1 hour until 8 h. In a 2 mL vial, Ni(DME)Br$_2$ (6.2 mg, 0.020 mmol), **L$_{JP}$** (22.3 mg, 0.040 mmol) and zinc powder (39.2 mg, 0.60 mmol) were dissolved in 0.5 mL of DMA. The allylic substrate (49.6 mg, 0.20 mmol) was added and the reaction mixture was left stirring for the required time. The reaction solvent was evaporated *in vacuo* and the reaction crude was extracted by CDCl$_3$ and filtered through Celite before measuring by ^{1}H NMR.

Observations: As can be observed in Figure 4.15, the kinetic profile is rather complex, showing two different kinetic regimes (**black** and **blue** points). The first one from initial time to 2h and the second one from 2h until the benchmark reaction is finished at 8h of reaction time.

In parallel, another set of experiments was prepared using a different Ni/**L$_{JP}$** ratio: [10/10] mol% (**grey** and **light blue** points in Figure 4.15). In this case, only 3 points were collected: 30 min, 1 h and 2 h of reaction time. By comparing Ni/**L$_{JP}$** ratios (20/10 vs 10/10 mol%) we can observe that (*i*) the curvature of the kinetic profile can be

reproduced during the first regime, and that (*ii*) an excess of **L*JP*** does not influence the rate of the reaction during the first regime.

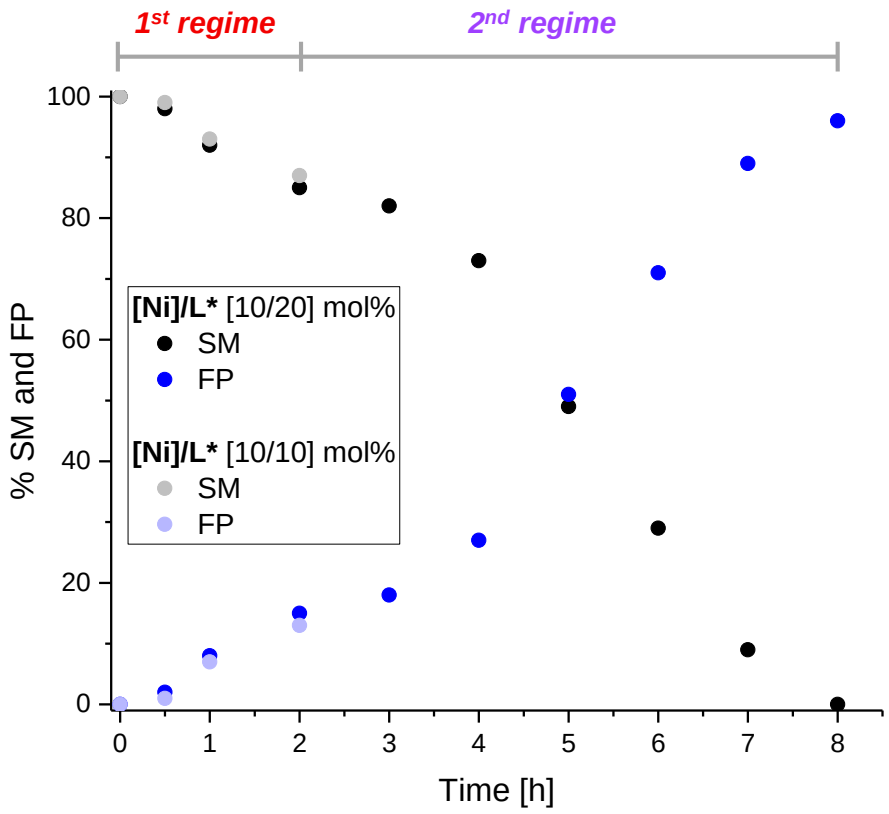

Figure 4.16: Kinetic profile of the catalytic transformation using ^{1}H NMR analysis of different reaction crudes.

4.5.4 Synthetic procedure and characterization data of nickel complexes

Synthetic procedure of complex IV.A

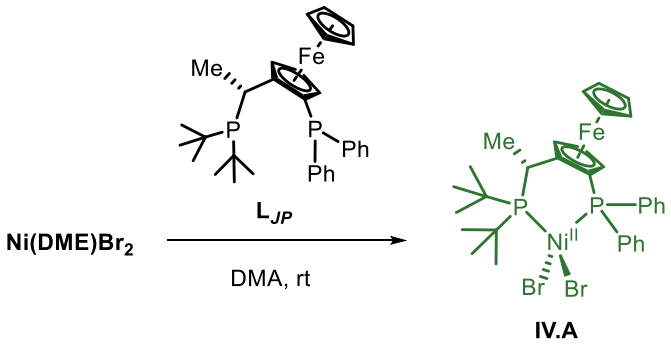

Figure 4.17: Reaction scheme for the synthesis of complex **IV.A**.

In a 5 mL screwed vial, $Ni(DME)Br_2$ (7.0 mg, 0.023 mmol) and $\mathbf{L_{JP}}$ (12.8 mg, 0.023 mmol) were dissolved in 2 mL of DMA. The reaction mixture was stirred at room temperature for 1 h. After this, the dark green solution was filtered through Celite and the solvent was removed under vacuum to obtain a dark solid. The solid was dissolved in THF and it was set for crystallization via vapor diffusion method with pentane at 20 ºC. 15.1 mg of single crystals were isolated corresponding to 86% of dark green complex **IV.A**.

EPR in DMA: *Silent*

^{1}H NMR (400 MHz, $CDCl_3$ at 298 K): Paramagnetic setup, see Figure 4.19 for Spectral data.

UV-Vis (DMA) [42 mM]: λ (nm), Abs: (408, 0.266)

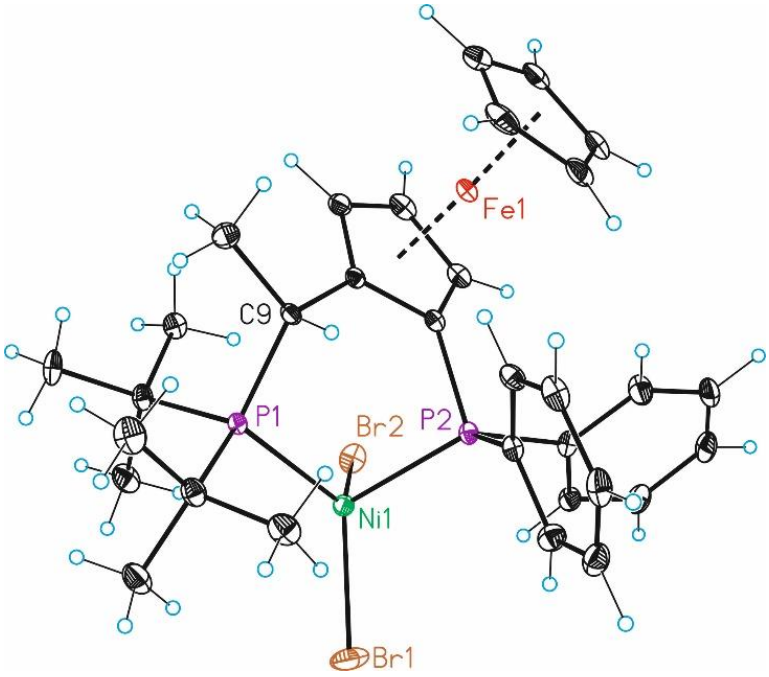

Figure 4.18: ORTEP representation of **IV.A** with 50 % probability ellipsoids.

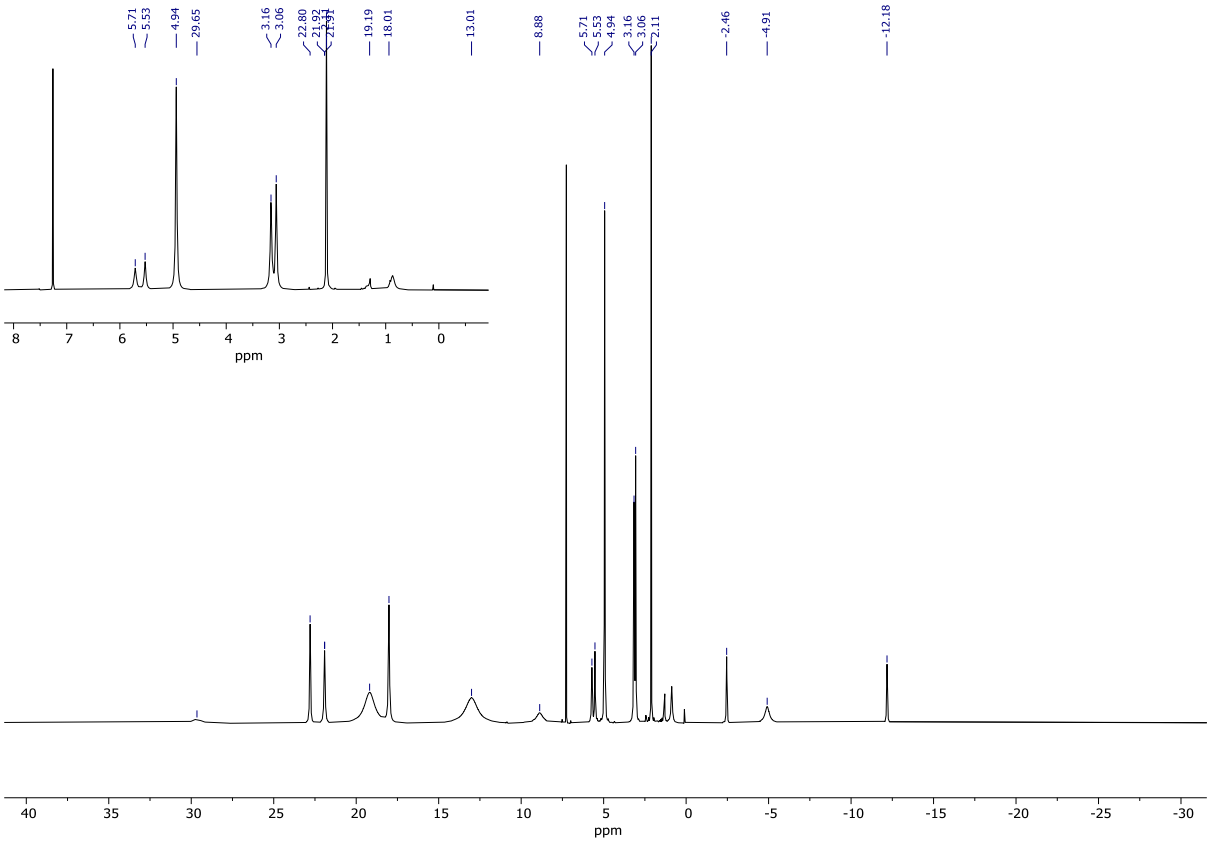

Figure 4.19: ^{1}H paramagnetic NMR spectra of complex **IV.A** in $CDCl_3$ at 293 K.

Synthetic procedure of complex IV.B

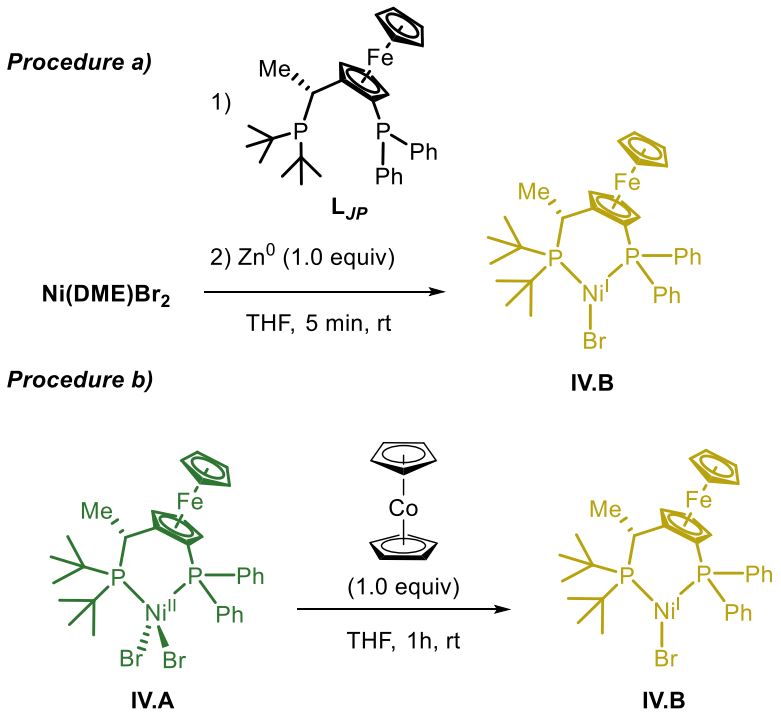

Figure 4.20: Reaction scheme for the synthesis of complex **IV.B**.

Procedure a) In a 5 mL screwed vial, Ni(DME)Br_2 (7.0 mg, 0.023 mmol), **L_{JP}** (12.8 mg, 0.023 mmol) and Zn powder (1.5 mg, 0.023 mmol, 1.0 equiv) were dissolved in 2 mL of DMA. The reaction mixture was stirred at room temperature for 5 min. After this, the orange solution was filtered through Celite and the solvent was removed under vacuum to obtain 11.8 mg of a light brown solid (75% yield) of complex **IV.B**. *This synthesis did not give a sample that could be successfully crystallized. An alternative chemical reductant was used (see procedure b).*

Procedure b) A 10 mL screwed vial was charged with complex **IV.A** (20 mg, 0.026 mmol) and it was dissolved in 3 mL of THF forming a dark green colored suspension. At that point, cobaltocene (5.0 mg, 0.026 mmol, 1.0 equiv) was added and the mixture was left stirring for 1 hour with the color of the solution changing from dark green to a dark purple. After the reaction was complete, the color had changed to a slightly brown solution and grey solid was observed. The mixture was filtered through Celite and the solvent was evaporated. The solid reaction crude was washed with hexane (to remove any possible unreacted cobaltocene) and the brown solid was extracted with benzene (removing any possible unreacted complex **IV.A**). The resulting dark orange solution

was set for crystallization via vapor diffusion using cyclohexane at 20 ºC. Pale orange crystals were obtained (9.4 mg, 53% yield) suitable for X-ray diffraction.

EPR in DMA [13 mM]: $g_{||} = 2.15$

UV-Vis (DMA) [46 mM]: λ (nm), Abs: (368, 0.976)

^{1}H NMR (400 MHz, C_7D_8 at 298 K): Paramagnetic setup acquisition, see Figure 4.21 for spectral data.

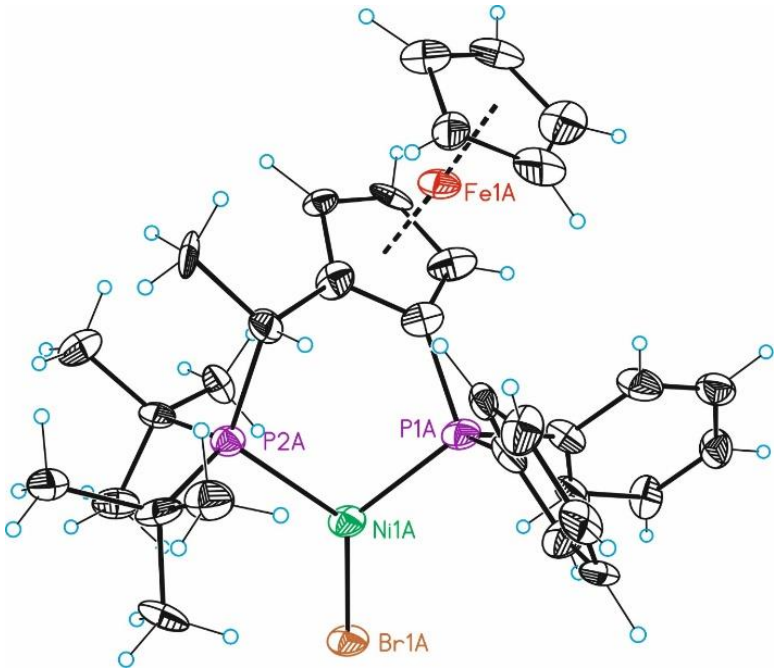

Figure 4.21: ORTEP representation of **IV.B** with 50 % probability ellipsoids.

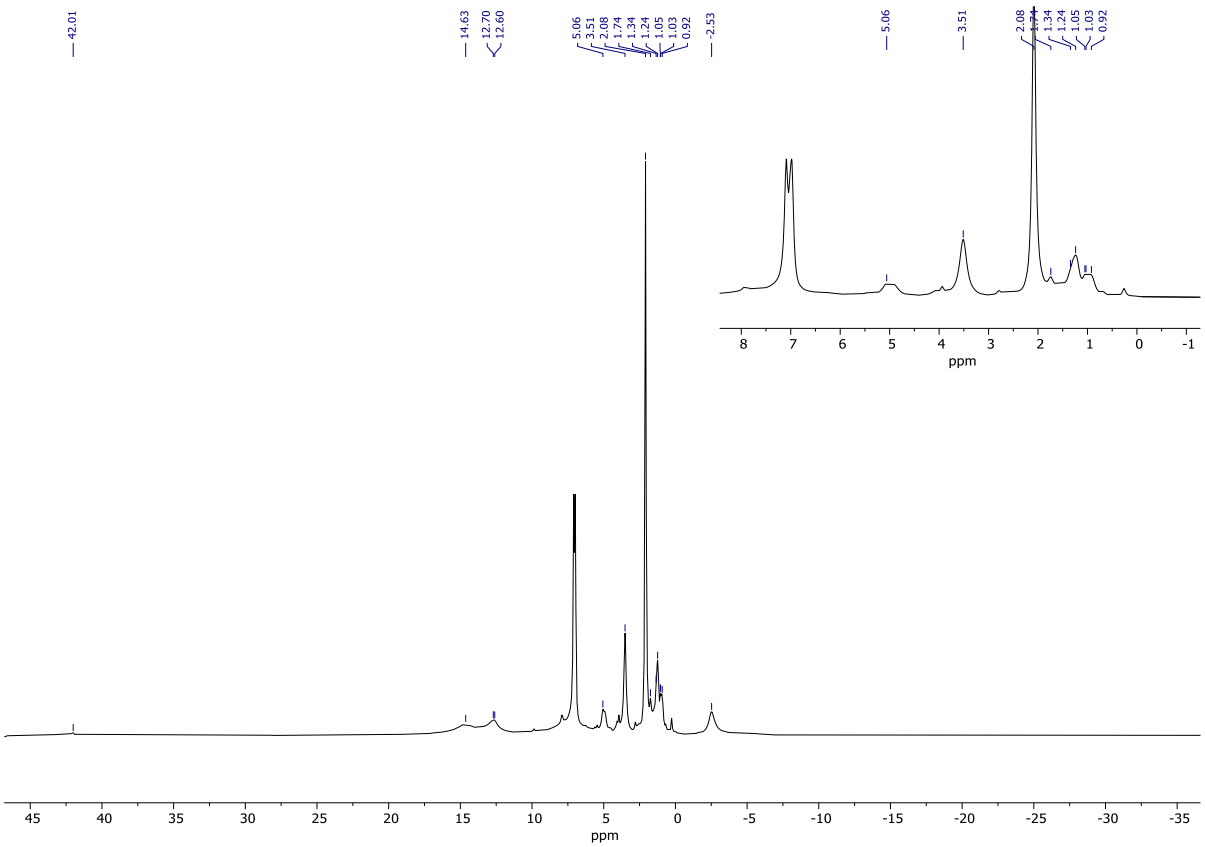

Figure 4.21: ^{1}H paramagnetic NMR spectra of complex **IV.B** in C_7D_8 at 293 K.

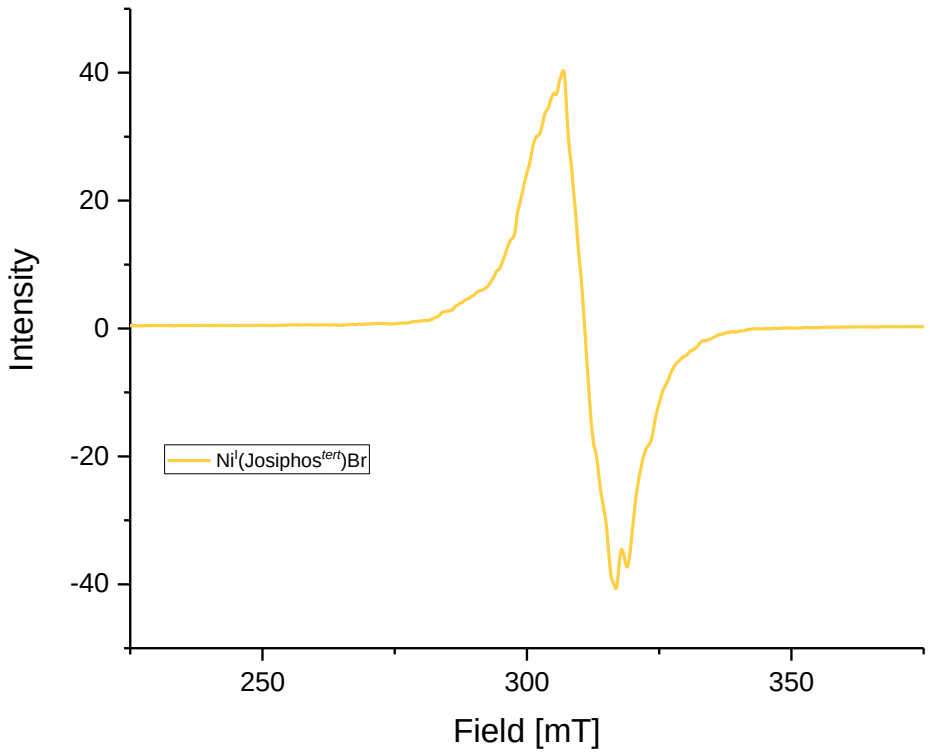

Figure 4.22: EPR spectrum of complex **IV.B** in DMA at 77 K.

UV-Vis Characterization of complexes IV.A and IV.B

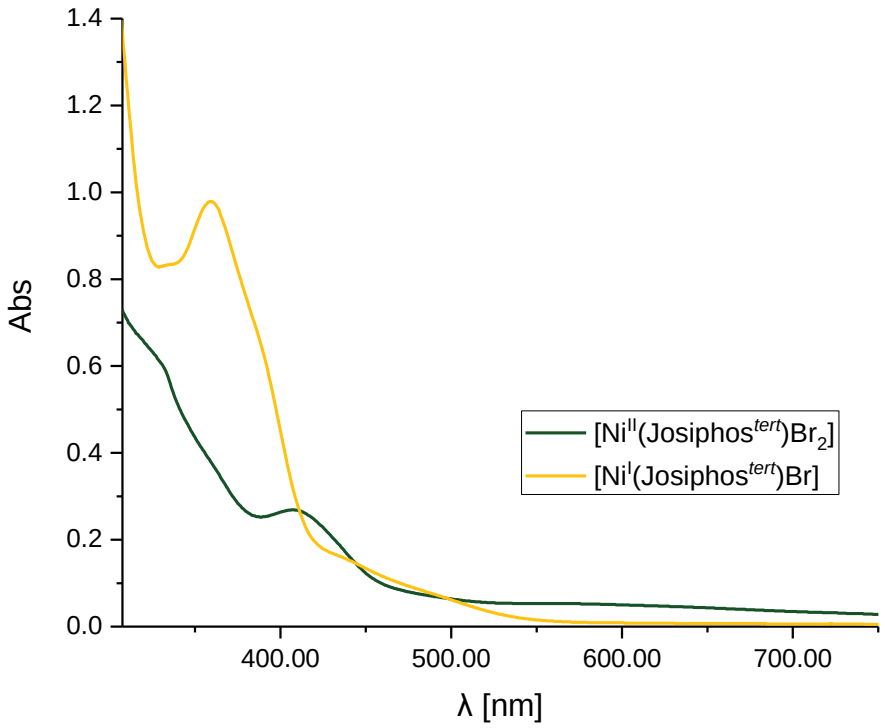

Figure 4.23: UV-Vis spectra for complexes **IV.A** (Ni^{II}) and **IV.B** (Ni^{I}) in DMA at 298 K.

Synthetic procedure of complex IV.I

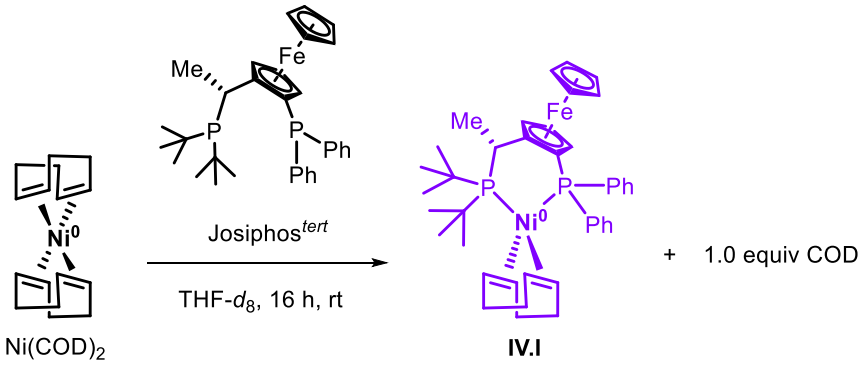

Figure 4.24: Reaction scheme for the synthesis of complex **IV.I**.

Procedure: In a 2 mL screwed vial, $Ni(COD)_2$ (5.5 mg, 0.02 mmol) and $\mathbf{L}_{\boldsymbol{JP}}$ (10.8 mg, 0.02 mmol) were dissolved in 0.5 mL of THF-d_8. The reaction mixture was stirred at room temperature for a total amount of 16h. The complexation is fairly slow as could be observed by $^{31}P\{^{1}H\}$ NMR monitoring. The $Ni^0(\mathbf{L}_{\boldsymbol{JP}})(COD)$ bright red colored complex **IV.I** was characterized by NMR Spectroscopy. Please, refer to previous literature for the synthesis of Ni^0(JosiPhos) complexes.[194]

^{1}H NMR (400 MHz, DMA-d_9 at 298 K): 8.05 (m, 1H, Ph^b), 7.43 (m, 5H, Ph^a), 7.21 (m, 4H, Ph^b), 4.49 (s, 1H, Cp_{bottom}), 4.21 (s, 1H, Cp_{bottom}), 4.15 (s, 2H, Cp_{top}), 4.03 (s, 1H, Cp_{top}), 3.67 (s, 2H, Cp_{top}), 3.21 (s, 1H, Cp_{bottom}), 2.95 (s, 8H, Cod ligand), 2.82 (s, 8H, Cod ligand), 2.03 (s, 3H, -C**H**$_3$*), 1.94 (s, 4H, Cod ligand), 2.03 (s, 3H, -C**H**-CH_3*), 1.53 (d, 9H, -(^{t}Bu)$_3^a$), 1.10 (d, 9H, -(^{t}Bu)$_3^b$).

^{31}P $\{^{1}H\}$ NMR (162 MHz, THF-d_8 at 298 K): 84.2 (d, $^3J_{P,P}$ = 22.1 Hz, 1P, -PPh_2-), 25.0 (d, $^3J_{P,P}$ = 22.1 Hz, 1P, -P(^{t}Bu)$_2$-).

[194] Derhamine, S. A.; Krachko, T.; Monteiro, N.; Pilet, G.; Schranck, J.; Tlili, A.; Amgoune, A. *Angew. Chem. Int. Ed.* 2020**,** 59, 18948.

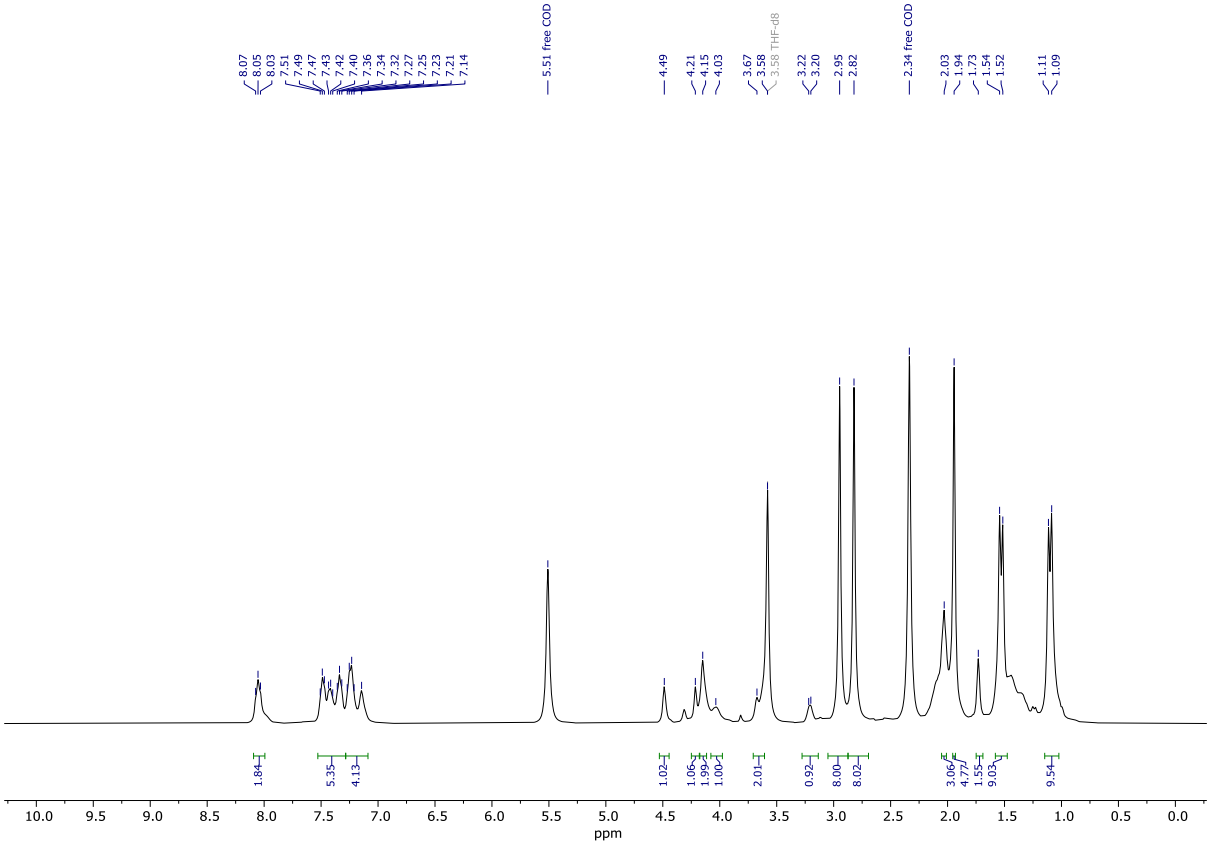

Figure 4.25: ^{1}H NMR of *in situ*-generated **IV.I** in THF-d_8 at 293 K.

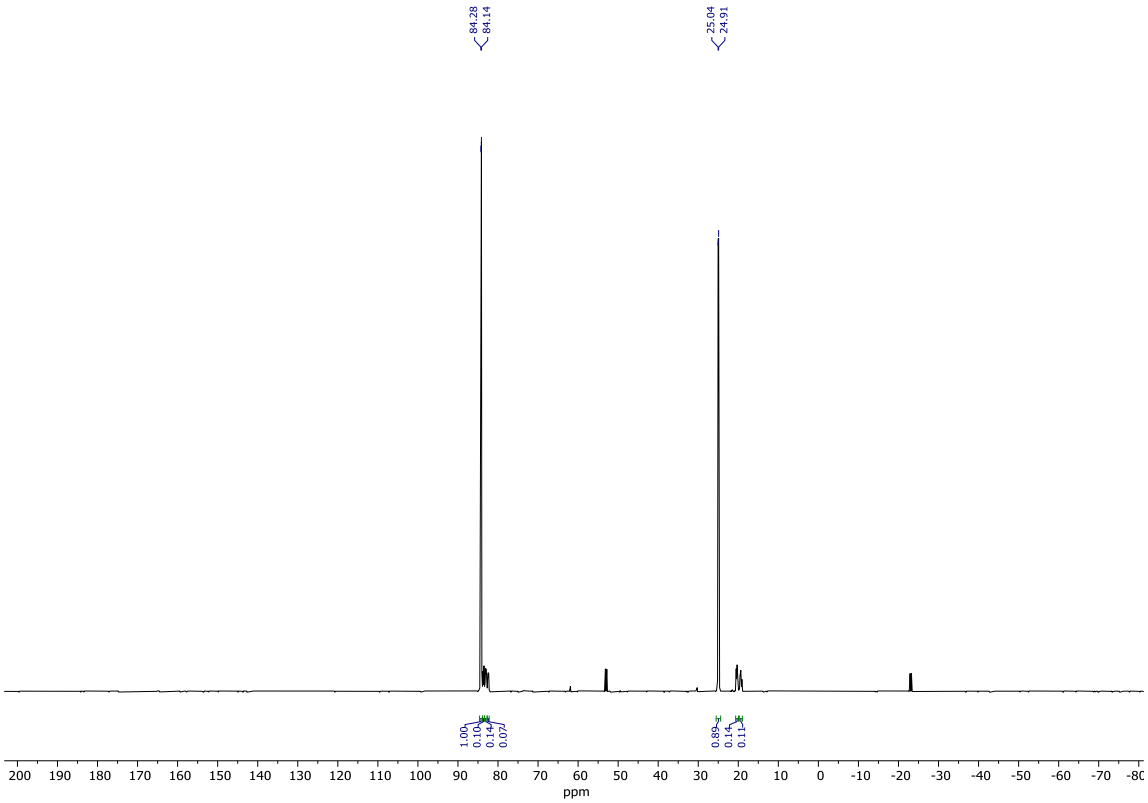

Figure 4.26: ^{31}P NMR of *in situ*-generated **IV.I** in THF-d_8 at 293 K.

Synthetic procedure of complex IV.J

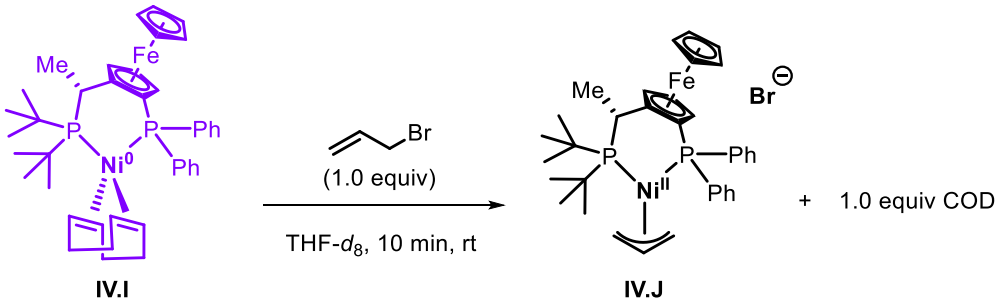

Figure 4.27: Reaction scheme for the synthesis of complex **IV.J**.

Procedure: In a 2 mL screwed vial, $Ni(COD)_2$ (5.5 mg, 0.02 mmol) and $\mathbf{L}_{\boldsymbol{JP}}$ (10.8 mg, 0.02 mmol) were dissolved in 0.5 mL of THF-d_8. The reaction mixture was stirred at room temperature for a total amount of 16 h and it was then transferred to an NMR tube equipped with an acetone-d_6 capillary. When the complexation to obtain $Ni^0(\mathbf{L}_{\boldsymbol{JP}})(COD)$ complex **IV.I** was confirmed by $^{31}P\{^1H\}$ NMR, 1.0 equiv of allyl bromide (2.4 mg, 0.02 mmol) were added to the NMR tube with a Hamilton syringe. As observed by $^{31}P\{^1H\}$ NMR, the reaction showed full conversion to complex **IV.J**. The crystals obtained for an X-ray characterization measurement where obtained by oversaturation of the NMR sample at low temperature (-30 ºC).

^1H NMR (400 MHz, THF-d_8 at 298 K): 8.54 (dt, 2H, Ph^b), 7.81 (dd, 2H, Ph^a), 7.55 (dt, 2H, Ph^b), 7.48 (m, 1H, Ph^b), 7.34 (m, 3H, Ph^a), 4.98 (m, 1H, Cp_{bottom}), 4.69 (s, 1H, allyl), 4.33 (s, 1H, allyl), 4.02 (s, 5H, Cp_{top}), 3.98 (m, 2H, Cp_{bottom}), 3.82 (s, 1H, allyl), 3.16 (m, 1H, allyl), 2.11(m, 3H, -C**H**$_3$*), 1.33 (d, $^4J_{H,P}$ = 2.5 Hz, 9H, -(^{t}Bu)$_2^a$), 1.30 (d, $^4J_{H,P}$ = 2.5 Hz, 9H, -(^{t}Bu)$_3^b$).

$^{31}P\{^1H\}$ NMR (162 MHz, THF-d_8 at 298 K): 84.3 (d, $^3J_{P,P}$ = 17 Hz, -PPh_2-), 18.1 (d, $^3J_{P,P}$ = 17 Hz, -P(^{t}Bu)$_2$-).

DEPTQ-135 $\{^1H\}$ NMR (126 MHz THF-d_8 at 298 K): 136.1 (d, $^1J_{C,P}$ = 12.5 Hz, Ph^b), 135.3 (d, $^1J_{C,P}$ = 9.5 Hz, Ph^a), 130.9 (s, Ph^b_q), 130.4 (s, Ph^a_q), 129.3 (d, $^1J_{C,P}$ = 12.5 Hz, Ph^b), 128.5 (d, $^1J_{C,p}$ = 9.5 Hz, Ph^a), 107.4 (s, allyl), 75.8 (s, Cp_{bottom}), 73.3 (s, allyl), 71.9 (d, $^1J_{C,p}$ = 8.1 Hz, Cp_{bottom}), 71.1 (s, Cp_{top}), 69.2 (d, $^1J_{C,P}$ = 7.2 Hz, Cp_{bottom}), 33.1 (s, allyl), 32.5 (d, $^1J_{C,P}$ = 3.7 Hz, -(^{t}Bu)$_2^a$), 32.1 (d, $^1J_{C,P}$ = 4.1 Hz, -(^{t}Bu)$_3^b$), 18.73 (s, -C**H**$_3$*).

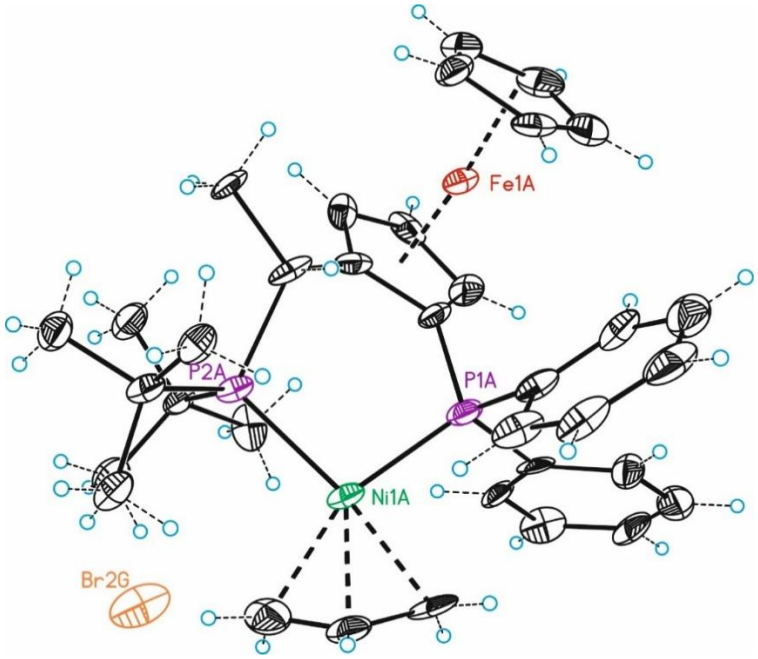

Figure 4.28: ORTEP representation of **IV.J** with 50 % probability ellipsoids.

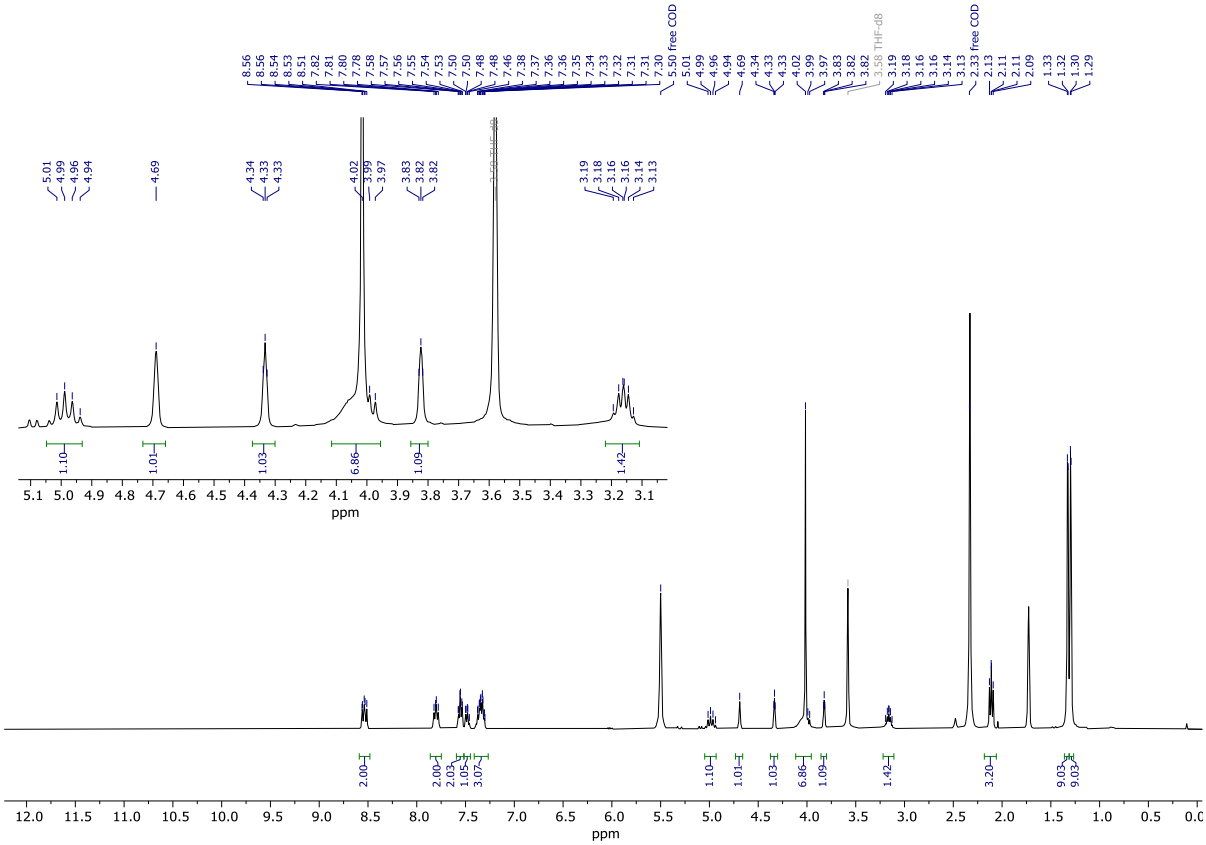

Figure 4.29: ^{1}H NMR of **IV.J** in THF-d_8 at 293 K.

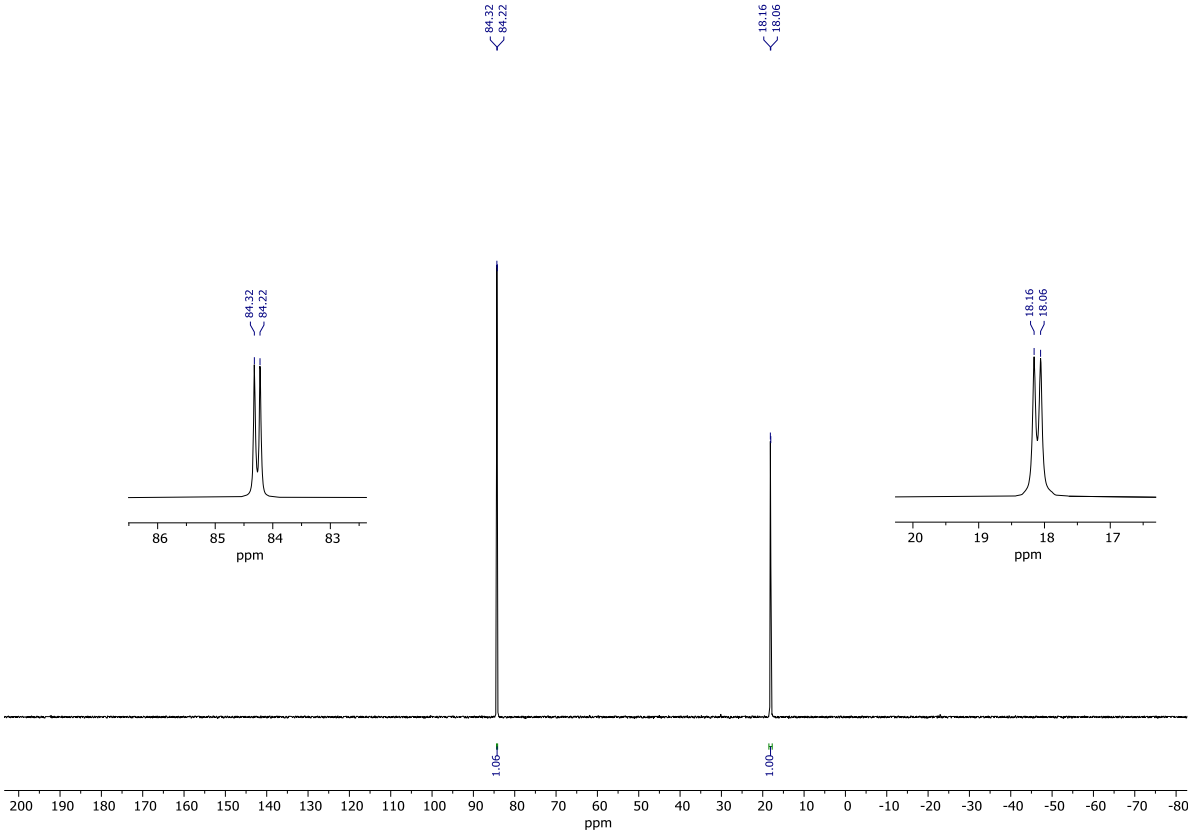

Figure 4.30: ^{31}P NMR of **IV.J** in THF-d_8 at 293 K.

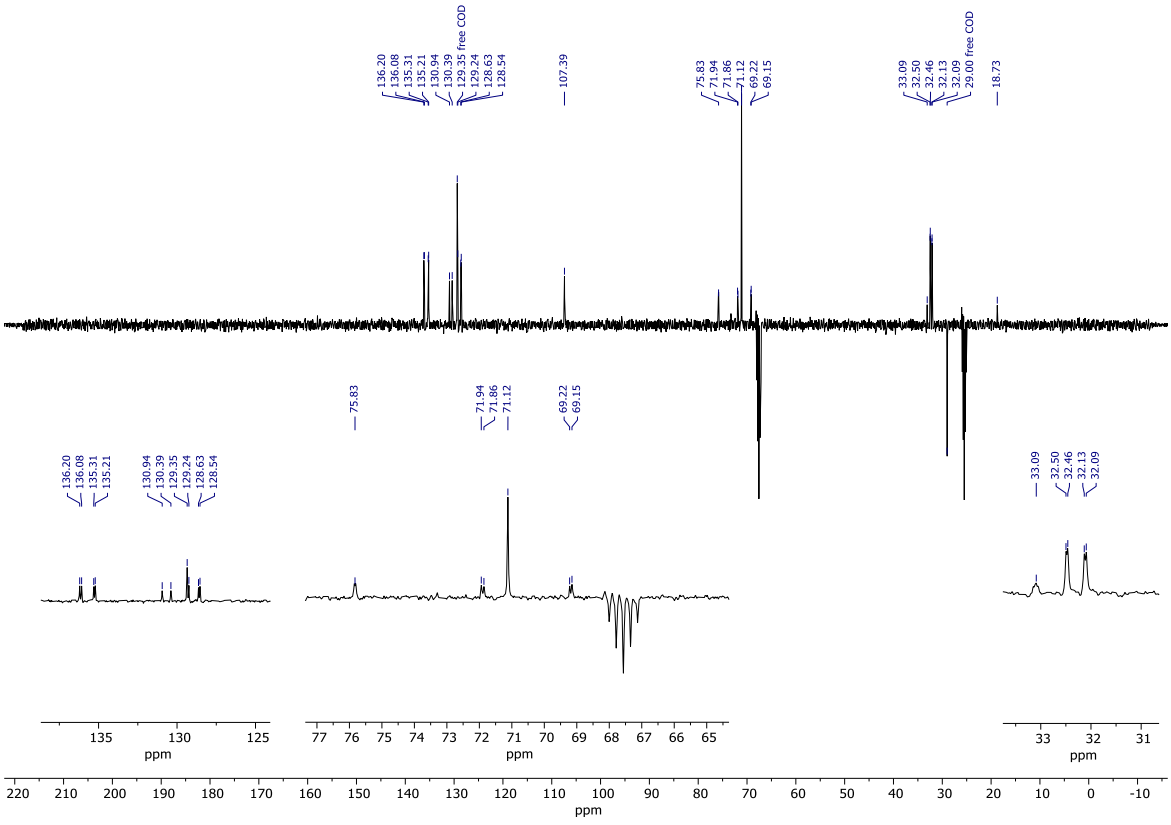

Figure 4.31: DEPTQ-135{^{1}H} NMR of **IV.J** in THF-d_8 at 293 K.

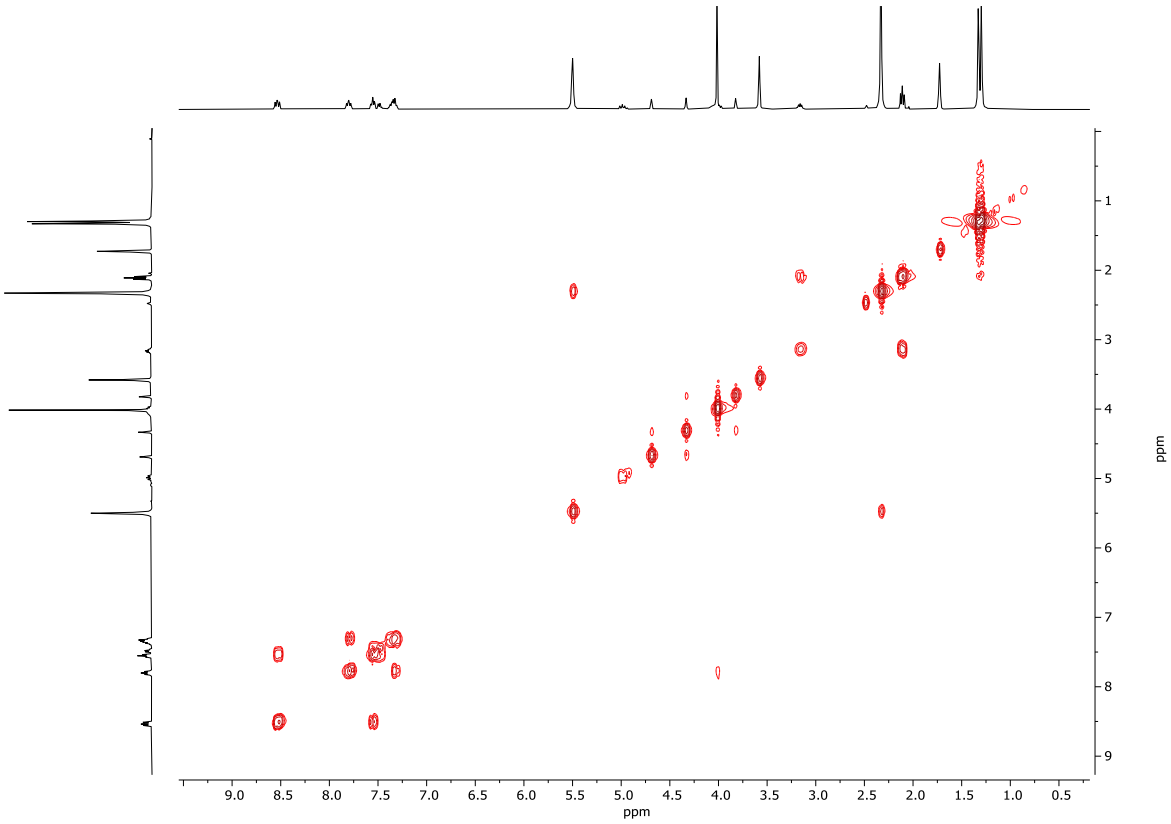

Figure 4.32: COSY ^{1}H NMR of **IV.J** in THF-d_8 at 293 K.

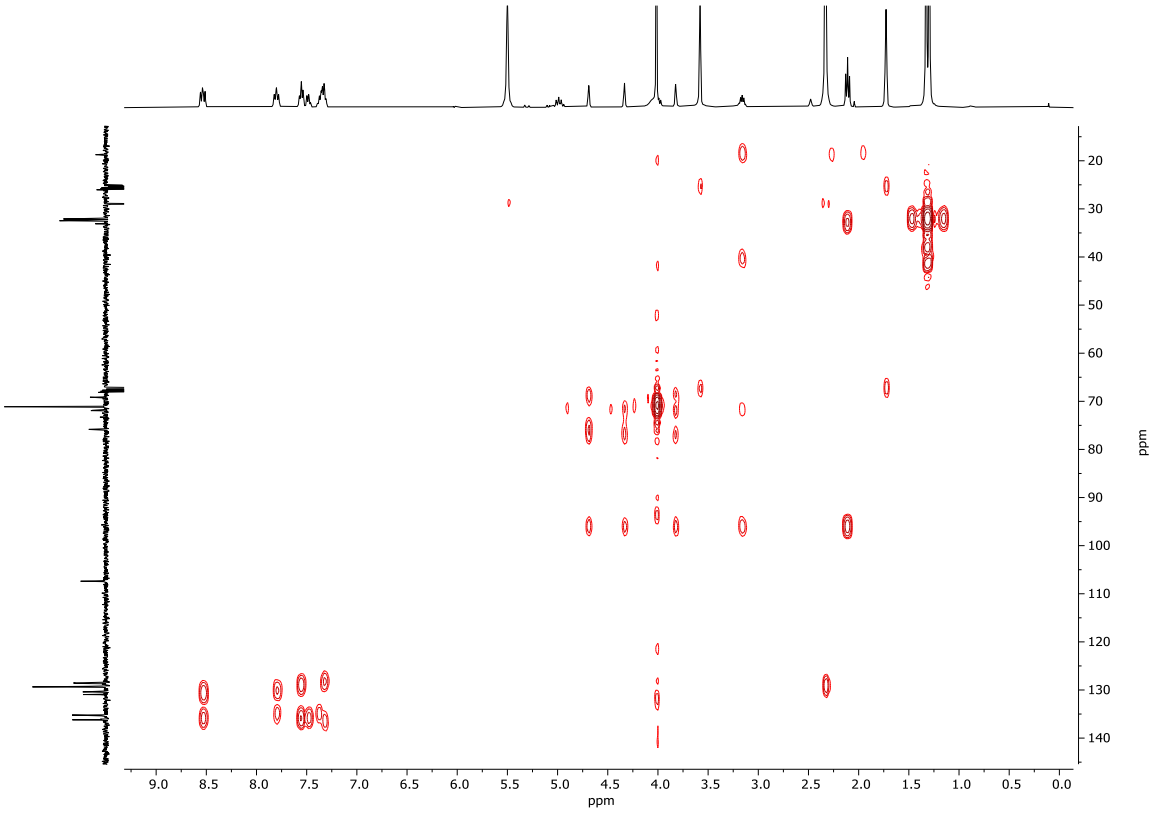

Figure 4.33: HMBC NMR of **IV.J** in THF-d_8 at 293 K.

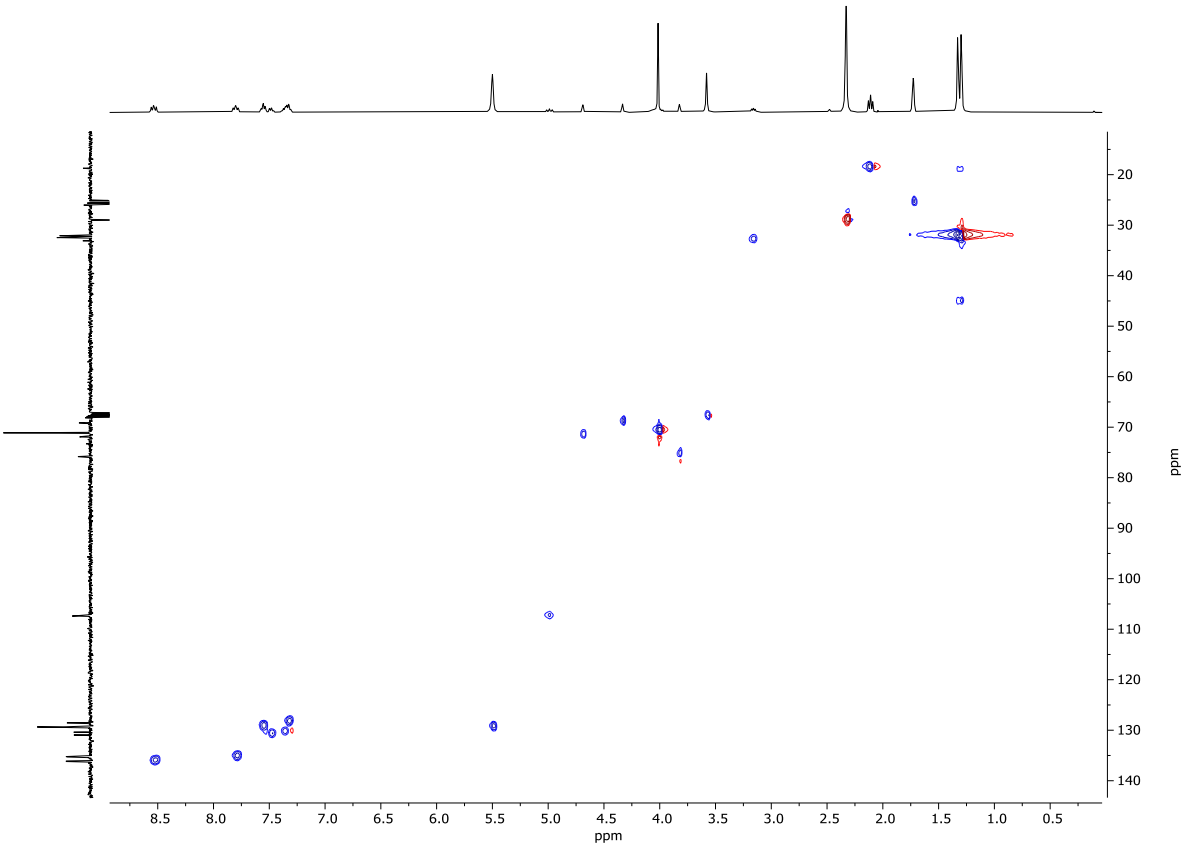

Figure 4.34: HSQC NMR of **IV.J** in THF-d_8 at 293 K.

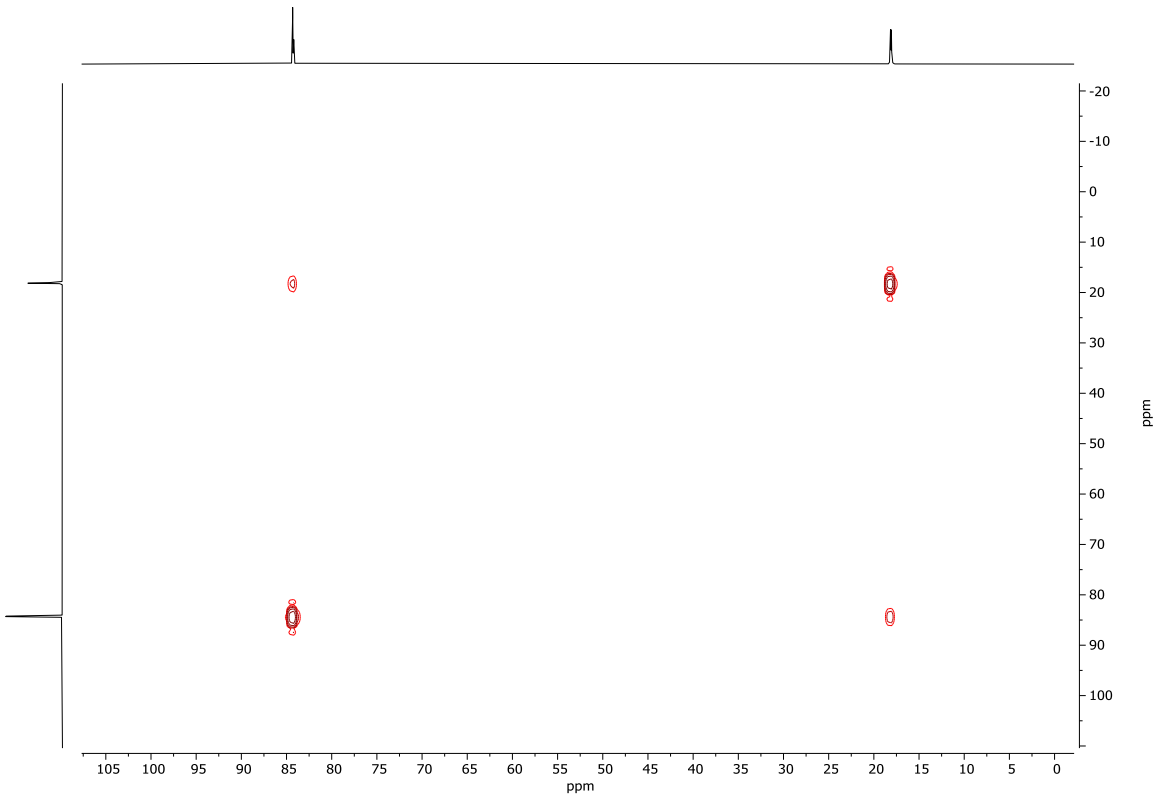

Figure 4.35: COSY ^{31}P NMR of **IV.J** in THF-d_8 at 293 K.

Exploration of the oxidative addition of different allylic precursors to Ni^0(L$_{JP}$)(COD) IV.I

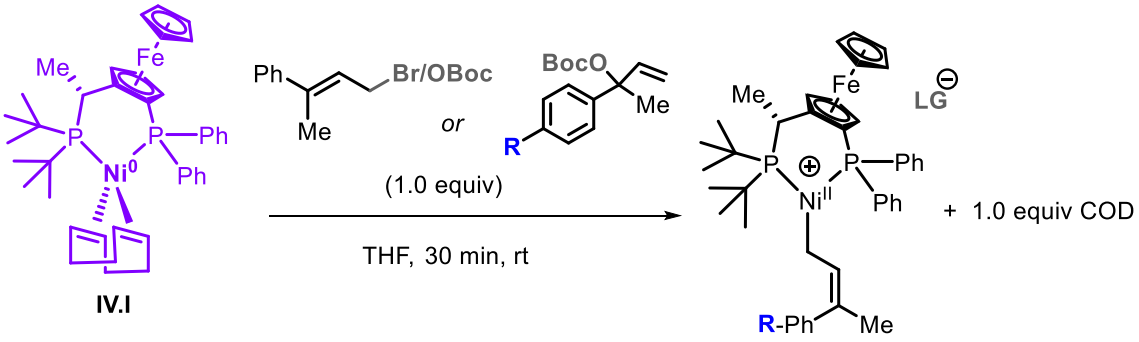

Figure 4.36: Reaction scheme for the synthesis of different Ni^{II}(L$_{JP}$)(allyl) complexes.

Procedure: First **IV.I** was prepared in situ; in a 2 mL screwed vial, Ni(COD)$_2$ (5.5 mg, 0.02 mmol) and **L$_{JP}$** (10.8 mg, 0.02 mmol) were dissolved in 0.5 mL of THF. The reaction mixture was stirred at room temperature for a total amount of 16 h and it was transferred to a NMR tube equipped with an acetone-d_6 capillary. When the complexation to obtain Ni^0(**L$_{JP}$**)(COD) complex **IV.I** was confirmed by ^{31}P{^{1}H} NMR, 1.0 equiv of allyl precursor (0.02 mmol) was added to the NMR tube with a Hamilton syringe or a glass pipet. Then, the evolution of the second transformation was evaluated by ^{31}P{^{1}H} NMR after 30 min of reaction time.

Observations: While the OA of allyl bromide with complex **IV.I** gives a clean and quantitative conversion (see Figure 4.30), di-substituted Me,Ph-allyl bromide **IV.8** probably undergoes a SET as indicated by the silent NMR (entry 5, Figure 4.37) delivering Ni^I(**L$_{JP}$**)Br complex **IV.B** (Ni^I signal was detected by EPR in this same transformation). Curiously, when the di-substituted Me,Ph-allyl carbonate **IV.7** is used as substrate, the two electron based OA reaction is extremely slow (entry 2, Figure 4.37). The signal of complex **IV.I** remains stable until the mixture is heated at 50 ºC, which at that moment produces new signals (*spectra not reported here*).

On the other hand, when the branched allylic carbonates **IV.1a** and **IV.1e** are used, the OA towards with complex **IV.I** produces new spectral signals but with low conversion. In the case of the benchmark allylic surrogate **IV.1a**, complex **IV.I** is converted at around 50% (entry 4). Longer reaction times do not further help the reaction evolution, but promote comproportionation pathways delivering Ni^I(**L$_{JP}$**)Br complex **IV.B** (the signal of this complex was again detected by EPR). Curiously the

p-OMe-substituted allyl carbonate **IV.1e** shows higher stability of the target Ni^{II}(**L**$_{JP}$)(allyl) complex (entry 3) compared to the use of **IV.1a** (entry 4). Therefore, substrate **IV.1e** was used as the standard precursor for the mechanistic studies.

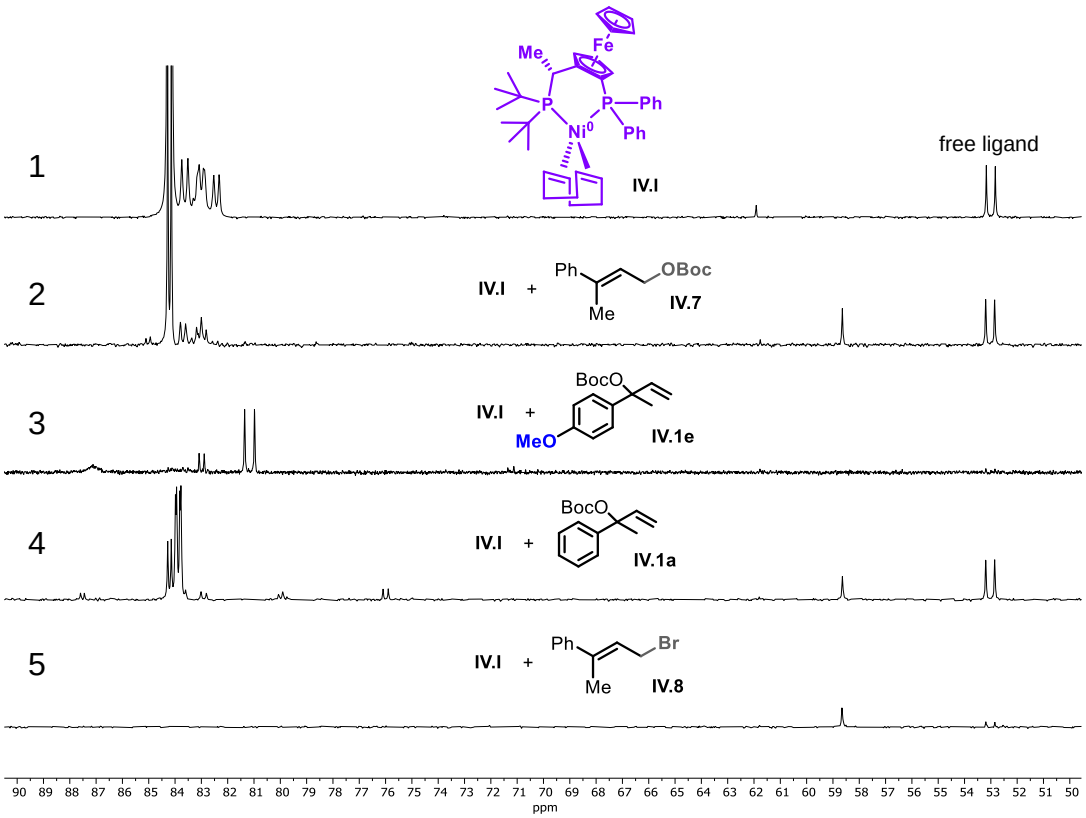

Figure 4.37: ^{31}P NMR spectra of different Ni^{II}(**L**$_{JP}$)(allyl) complexes in THF-d_8 at 293 K.

Synthetic procedure of complex IV.K

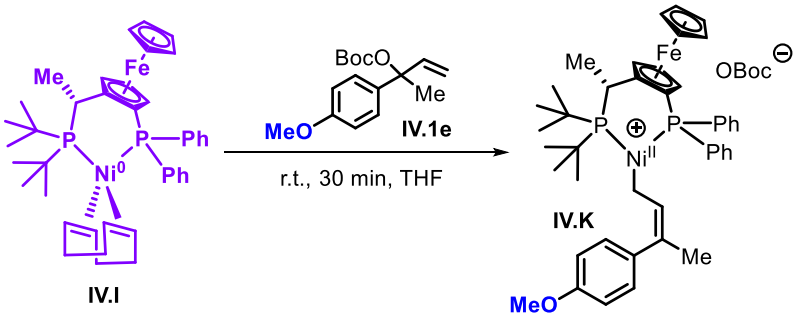

Figure 4.38: Reaction scheme for the synthesis of complex **IV.K**.

Procedure: In a 2 mL screwed vial, $Ni(COD)_2$ (5.5 mg, 0.02 mmol) and $\mathbf{L}_{JP}$ (10.8 mg, 0.02 mmol) were dissolved in 0.5 mL of THF. The reaction mixture was stirred at room temperature for a total amount of 16 h and it then was transferred to a NMR tube equipped with an acetone-d_6 capillary. When the complexation to obtain $Ni^0(\mathbf{L}_{JP})(COD)$ complex **IV.I** was confirmed by $^{31}P\{^1H\}$ NMR, substrate **IV.1e** (5.6 mg, 0.02 mmol, 1.0 equiv) was added to the NMR tube with a glass pipet. Then, the evolution of the OA was analyzed by $^{31}P\{^1H\}$ NMR after 20 min of reaction time (Figure 4.39).

Observations: The reaction of **IV.I** to form complex **IV.K** does not show full conversion. An amount of Ni(0) **IV.I** remains as can be observed in the ^{31}P NMR spectrum. Nonetheless, if pure complex **IV.K** is pursued, the crude mixture can be washed with pentane, eliminating the unreacted complex **IV.I** and (slight) excess of chiral ligand $\mathbf{L}_{JP}$.

Although several attempts were done to grow crystals of complex **IV.K**, it was not possible to characterize the compound by X-ray crystallography.

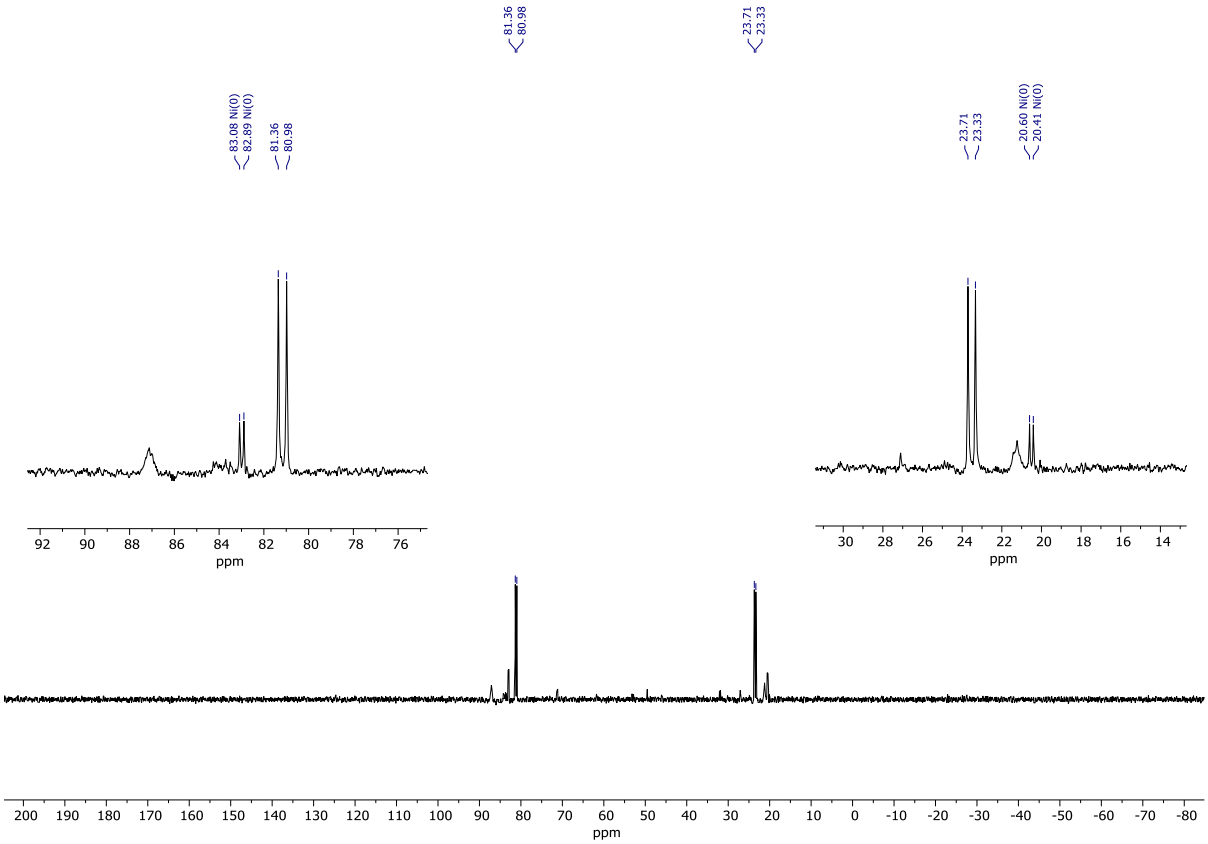

Figure 4.39: $^{31}P\{^{1}H\}$ NMR of **IV.K** in THF at 293 K.

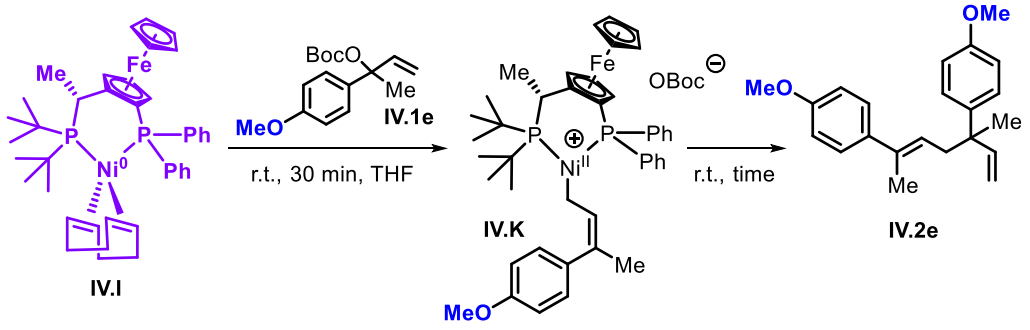

Figure 4.40: Reaction scheme for the reaction of complex **IV.I** with substrate **IV.1e** forming complex **IV.K** and releasing the branched product **IV.2e**.

A complimentary experiment was done following the procedure related to Figure 4.38. In this case, the sample was monitored by ^{1}H NMR for two days to see the conversion of substrate **IV.1e** into product **IV.1e** (see Figure 4.41).

Observations: In Figure 4.41, it can be observed that the formation of branched-product **IV.2e** can be obtained from the conversion of complex **IV.K** at room

temperature and without the use of any external additive. However, this non-promoted reaction is slower than the benchmark catalytic reaction. The investigation of the role of additives will be discussed below.

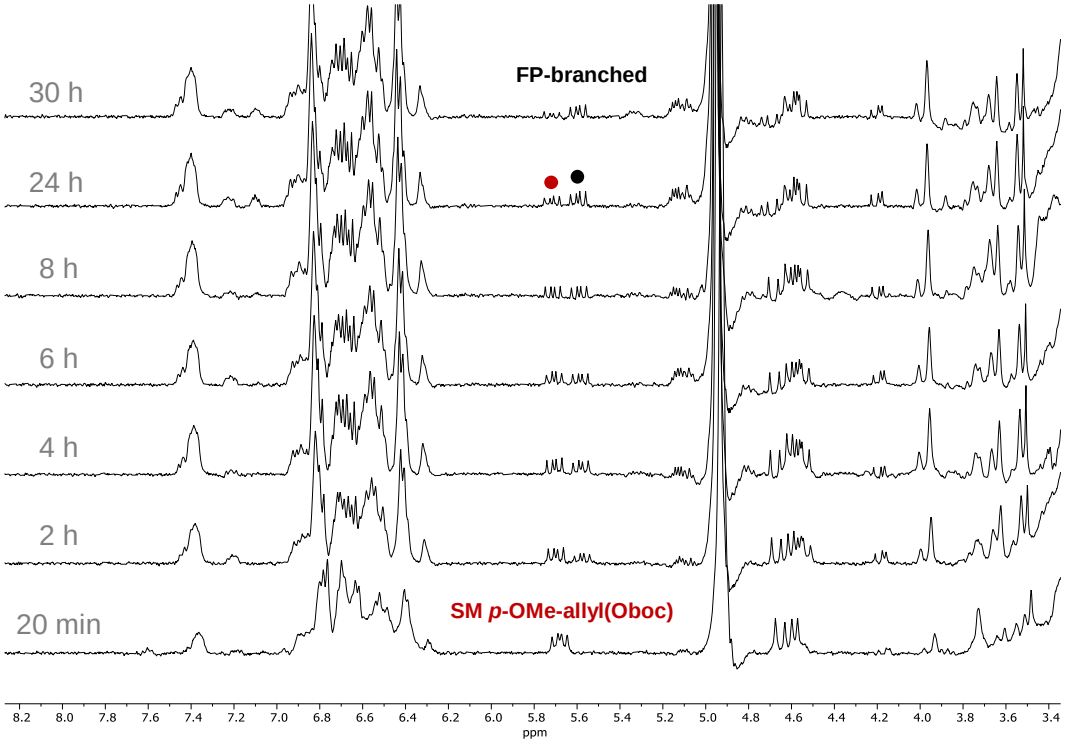

Figure 4.41: ^{1}H NMR stacked spectra of the reaction monitoring between complex **IV.I** and substrate **IV.1e** in THF at 293 K.

4.5.5 $^{31}P\{^{1}H\}$ NMR study of $Ni^{II}(L_{JP})$(allylic) species obtained through different approaches

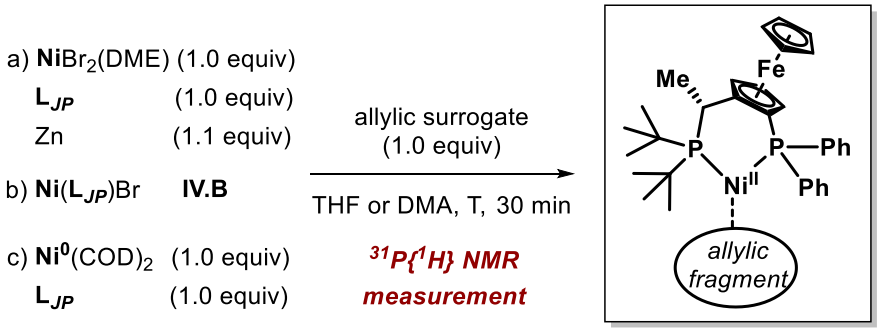

Figure 4.42: Reaction scheme for the formation of Ni(II)($\mathbf{L_{JP}}$)(allyl) species using different conditions and Ni precursors.

Conditions under **a**: In a 2 mL screwed vial, $Ni(DME)Br_2$ (6.1 mg, 0.02 mmol, 1.0 equiv), $\mathbf{L_{JP}}$ (10.8 mg, 0.02 mmol, 1.0 equiv) and Zn (1.4 mg, 0.022 mmol, 1.1 equiv) were mixed in 0.5 mL of THF. The reaction mixture was stirred at room temperature for 5 min and the allylic precursor (1.0 equiv) was added. The reaction mixture was transferred to an NMR tube equipped with an acetone-d_6 capillary and measured after 30 min (entries 2, 3 and 8, see next page Figure 4.43).

Conditions under **b**: In a 2 mL screwed vial, Ni($\mathbf{L_{JP}}$)Br complex **IV.B** (13.6 mg, 0.02 mmol, 1.0 equiv) was dissolved in 0.5 mL of THF. Then, the allylic precursor (1.0 equiv) was added and the reaction mixture was transferred to an NMR tube equipped with an acetone-d_6 capillary. The sample was measured after a 30 min reaction time.

Conditions under **c**: In a 2 mL screwed vial, $Ni(COD)_2$ (5.5 mg, 0.02 mmol, 1.0 equiv) and JosiPhos^{tert} (10.8 mg, 0.02 mmol, 1.0 equiv) were dissolved in 0.5 mL of THF. The reaction mixture was stirred at room temperature for 16 h and it was then transferred to an NMR tube equipped with an acetone-d_6 capillary. When the complexation to obtain Ni^0($\mathbf{L_{JP}}$)(COD) complex **IV.I** was confirmed by $^{31}P\{^{1}H\}$ NMR (entry 5, Figure 4.43), 1.0 equiv of allylic precursor was added to the NMR tube and the transformation was analyzed by $^{31}P\{^{1}H\}$ NMR after a 30 min reaction time (entries 6 and 7 in Figure 4.43).

On the next page - Figure 4.43: Stacked NMR spectra of different stoichiometric reactions using different Ni(0), Ni(I) and Ni(II) complexes and comparing them with the benchmark catalytic reaction in THF at 298 K.

Chapter 4

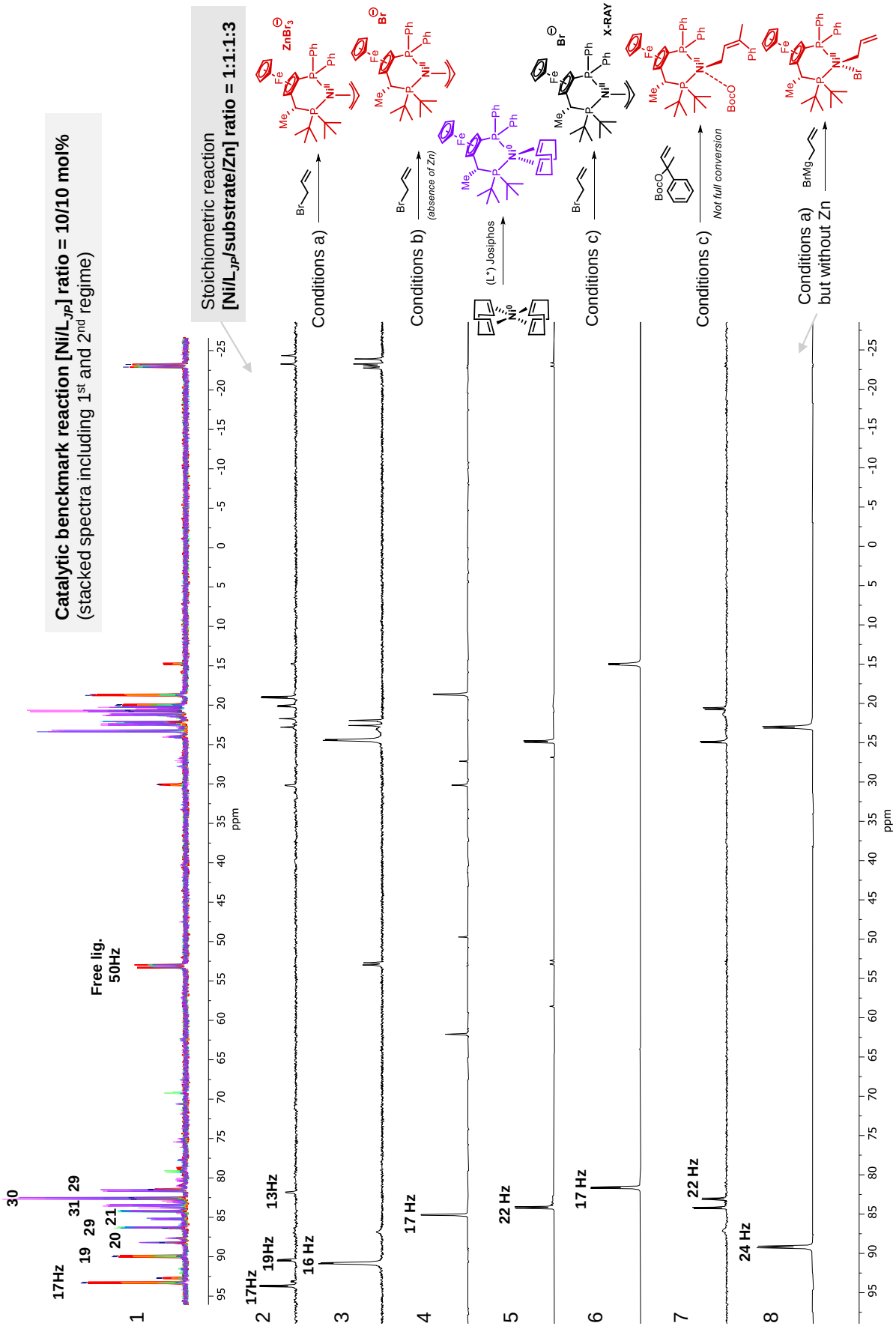
Catalytic benckmark reaction [Ni/L_JP] ratio = 10/10 mol%
(stacked spectra including 1st and 2nd regime)
Free lig.
50Hz
Stoichiometric reaction
[Ni/L_JP/substrate/Zn] ratio = 1:1:1:3
Conditions a)
Conditions b)
(absence of Zn)
(L*) Josiphos
Conditions c)
X-RAY
Conditions c)
Not full conversion
Conditions a)
but without Zn
ppm

4.5.6 $^{31}P\{^{1}H\}$ NMR study of catalysis pre-activation stage: evaluation of stoichiometric reactions to understand the influence of LG and aryl substituents during the initial turnovers

Benchmark reaction

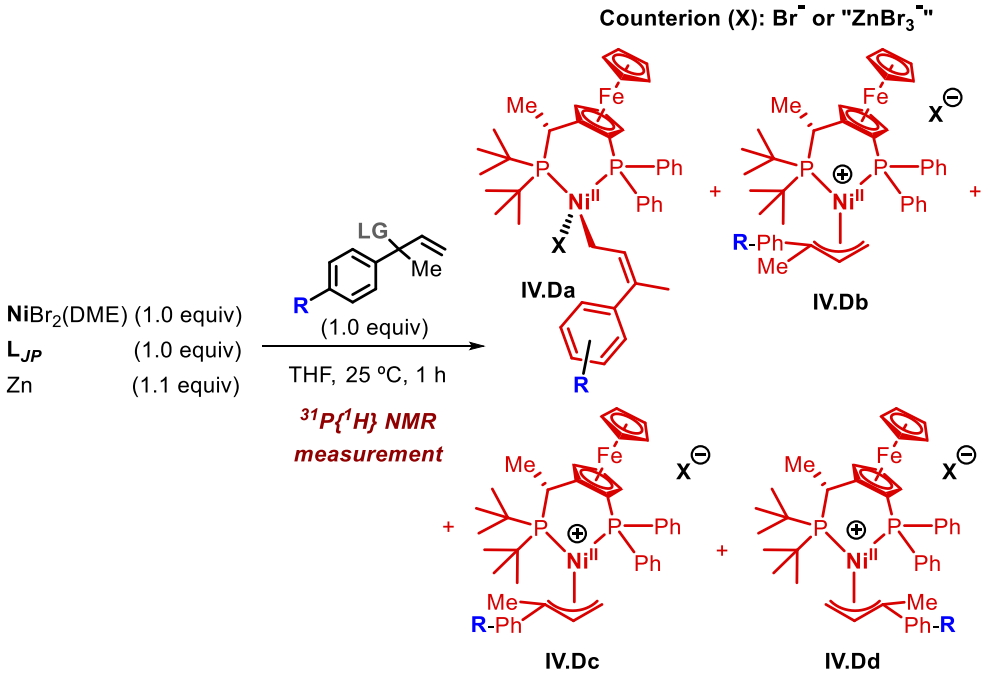

Figure 4.44: Reaction scheme for the NMR analysis of the formation of Ni(II)**L**$_{JP}$(allyl) using different allylic precursors. Proposed structures of complexes **IV.Da** to **IV.Db** representing different hapticity and/or *endo*/*exo* isomers.

Procedure: In a 2 mL screwed vial, Ni(DME)Br$_2$ (6.1 mg, 0.02 mmol), **L**$_{JP}$ (10.8 mg, 0.02 mmol) and Zn (1.4 mg, 0.022 mmol, 1.1 equiv) were mixed in 0.5 mL of THF. The reaction mixture was stirred at room temperature for 5 min, the allylic precursor (1.0 equiv) was added and the reaction mixture was then transferred to an NMR tube equipped with an acetone-d_6 capillary. The sample was measured after a 1 h reaction.

Observations: Taking entry 3 (Figure 4.45) as the benchmark stoichiometric reaction, four different species can be observed with different coupling constants here reported in ppm: 93.3 (d, $^{3}J_{P,P}$ = 17.3 Hz), 92.7 (d, $^{3}J_{P,P}$ = 14.5 Hz), 89.7 (d, $^{3}J_{P,P}$ = 19.5 Hz) and 81.5 (d, $^{3}J_{P,P}$ = 12.6 Hz). The aryl-substituent has an influence on the population of each Ni(II)(**L**$_{JP}$)(allyl) species formed in solution, as well as on the chemical shift of these species (entry 3 vs entries 1 and 2). Allylic precursors with EWG such as the

para-substituted–CF_3 branched allylic carbonate do not display reactivity. The LG does not influence the nature of the Ni(II)**L**$_{JP}$(allyl) species, as noted in entries 3, 4 and 5. Lastly, the presence of a linear allylic bromide reproduces the signals of entry 3 (see entry 6), but curiously the use of a linear allylic carbonate does not show observable reactivity.

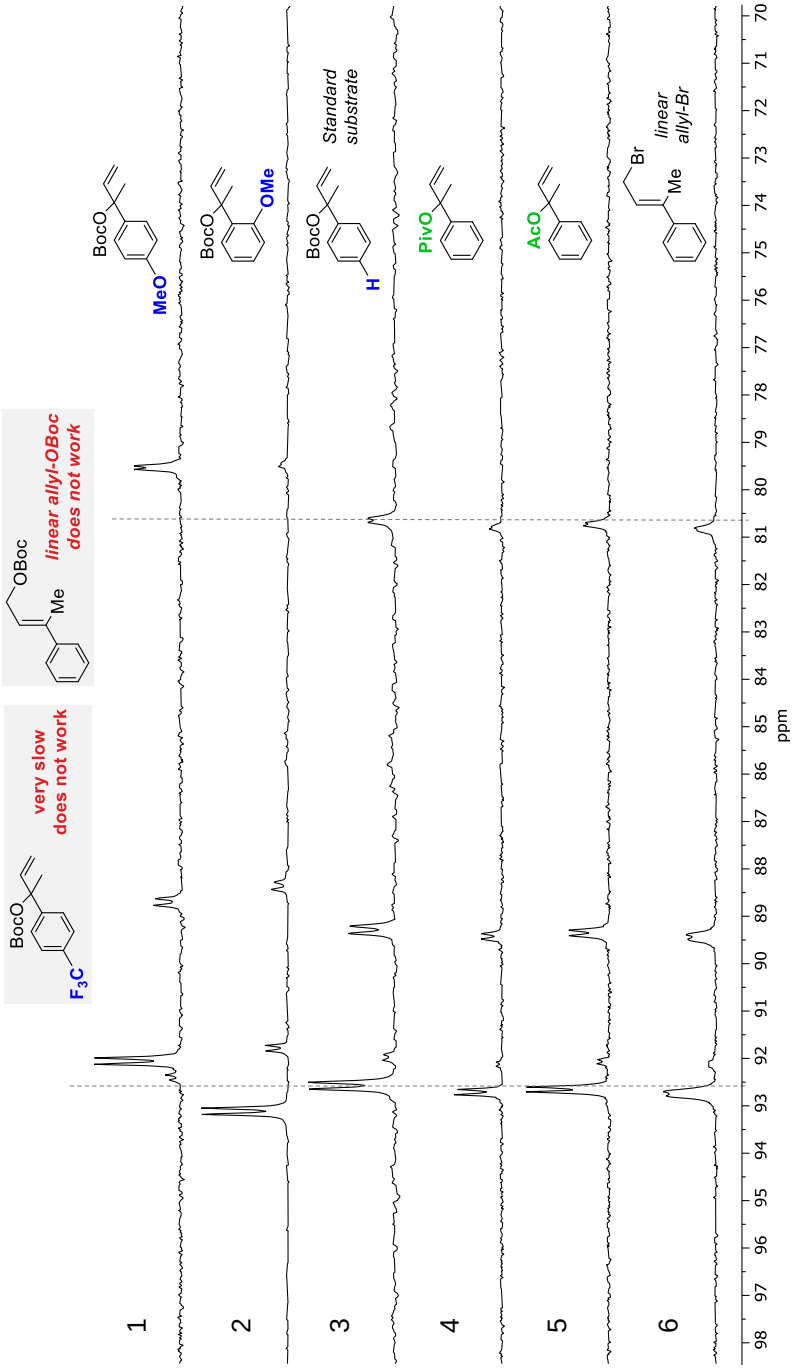

Figure 4.45: Stacked NMR spectra of different Ni(II)allyl species formed from aryl-substituted allylic carbonates and related precursors measured in THF at 298 K.

*Ni(**L**$_{JP}$)Br complex **IV.B** as Ni source*

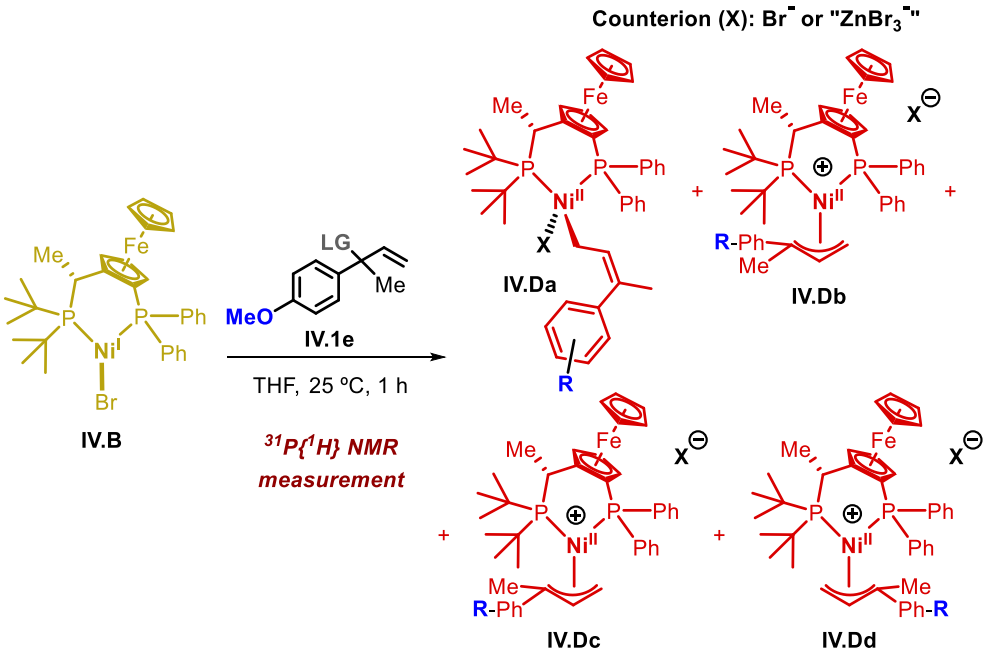

Figure 4.46: Reaction scheme for the study of Ni(II)(**L**$_{JP}$)(allyl) species formation using Ni(I)(**L**$_{JP}$)Br as precursor.

Procedure: In a 2 mL screwed vial, Ni^{I}(**L**$_{JP}$)Br complex **IV.B** (13.6 mg, 0.02 mmol, 1.0 equiv) was dissolved in 0.5 mL of THF. Then, the allylic precursor (1.0 equiv) was added and the reaction mixture was transferred to an NMR tube equipped with an acetone-d_6 capillary. **After first confirming that the addition of IV.1e in the presence of IV.B remained NMR silent, 1.0 equiv of $ZnBr_2$ (4.5 mg, 0.02 mmol) was added to the same mixture.** The sample was measured after 30 min confirming the formation of a mixture of Ni(II)(**L**$_{JP}$)(allyl) species.

Observations: As seen in entry 1 (Figure 4.47), the formation of Ni(II)(**L**$_{JP}$)(allyl) species is not observed until 1.0 equiv of $ZnBr_2$ is added as an additive to the reaction mixture. With this experiment we can confirm that the formation of Ni(II)(**L**$_{JP}$)(allyl) isomers is promoted by divalent Zn and can be derived from the Ni(I) complex **IV.B**. Entry 2 serves as a comparison representing the formation of **IV.2e** under optimized reaction conditions (same as in entry 2 in Figure 4.43).

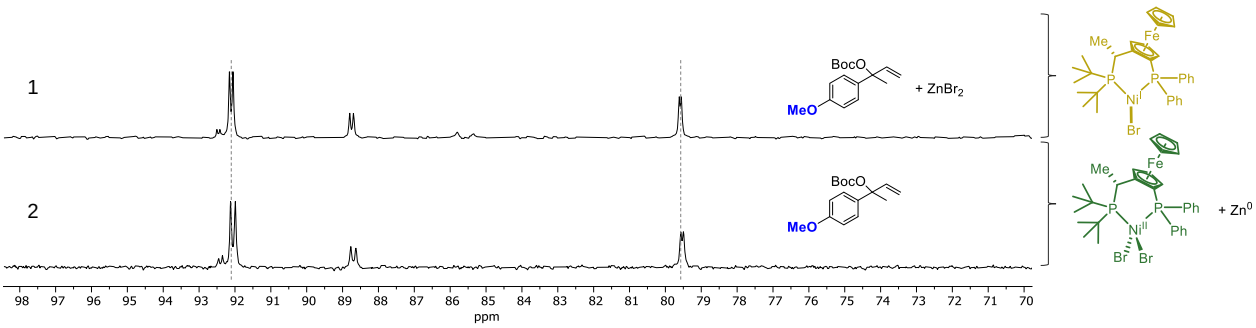

Figure 4.47: Stacked NMR spectra of stoichiometric reactions using allylic precursor **IV.1e** using Ni(I) complex **IV.B** as precursor in THF at 293 K. Entry 2 reports the Ni(II) speciation under standard catalytic conditions starting from Ni(II)**L*JP*** **IV.A** and Zn.

4.5.7 HRMS experiments of the stoichiometric reaction mixture

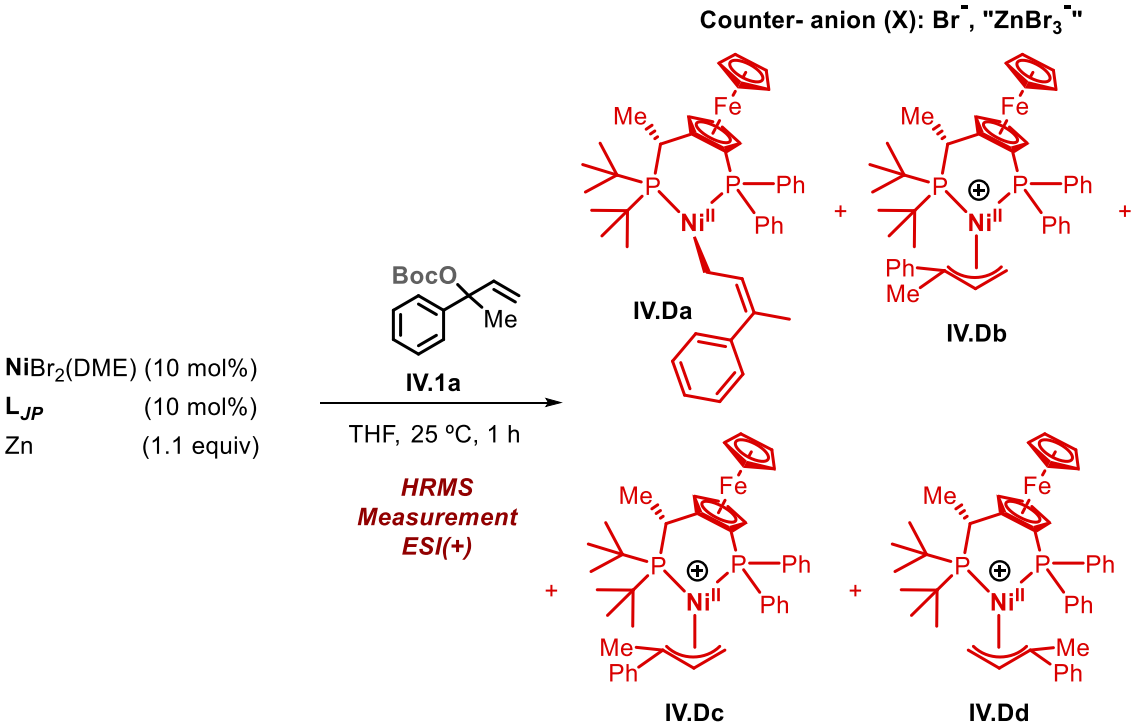

Figure 4.48: Reaction scheme for the mass spectrometric experiment performed on a stoichiometric benchmark reaction with substrate **IV.1a**.

Procedure: The sample was prepared following the same procedure as described in Figure 4.48. After 1 h of reaction time an aliquot of the mixture was diluted in MeOH and analyzed by mass spectrometry.

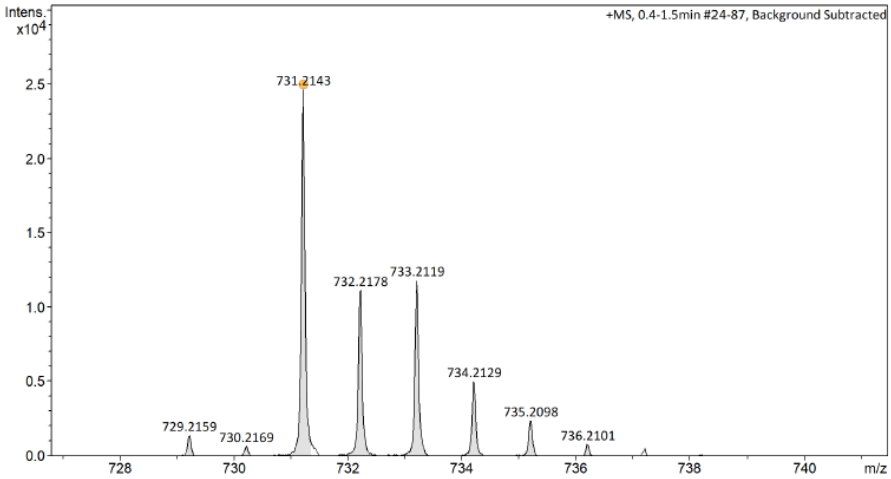

Figure 4.49: HRMS spectrum of the Ni(II)**L*JP***(allyl) species identified in the reaction mixture of a stoichiometric reaction.

4.5.8 Control experiments: chemo and regio-selectivities using different solvent, additives and Ni precursor

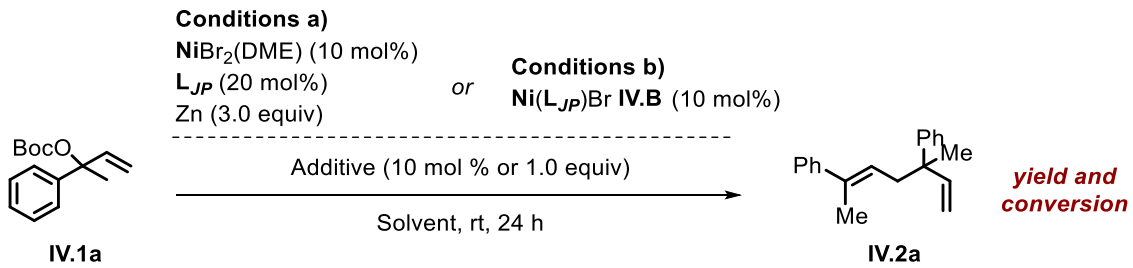

Figure 4.50: Reaction scheme for the catalytic transformation under different conditions a and b. Conversion and yields were calculated by ^{1}H NMR using mesitylene as internal standard.

Procedure for entries 1 to 7 (Table **IV.II**): In a 2 mL screwed vial, Ni(DME)Br$_2$ (6.1 mg, 0.02 mmol, 1.0 equiv), **L*JP*** (10.8 mg, 0.02 mmol, 1.0 equiv) and Zn (1.4 mg, 0.022 mmol, 1.1 equiv) were mixed in 0.5 mL of solvent. The reaction mixture was stirred at room temperature for 5 min and substrate **IV.1a** (49.6 mg, 0.2 mmol, 1.0 equiv) was added. The reaction was stopped and analyzed by ^{1}H NMR after 24 h.

Procedure for entries 6 to 8 (Table **IV.II**): In a 2 mL screwed vial, **Ni(L*JP*)Br** complex **IV.B** (13.6 mg, 0.02 mmol, 1.0 equiv) was dissolved in 0.5 mL of THF. The reaction mixture was stirred at room temperature for 5 min and substrate **IV.1a** (49.6 mg, 0.2 mmol, 1.0 equiv) was added. The reaction was stopped and analyzed by ^{1}H NMR after 24 h.

Observations: DMA generally helps to maintain high chemo- and regio-selectivity in this transformation compared to the use of THF (entry 1 vs 3). When ZnBr$_2$ is used in combination with DMA, the reactivity pattern can be reproduced with an even enhanced regio-selectivity towards the branched product (entry 1 vs 2). ZnBr$_2$ and allylZnBr as additives help to reduce the H-elimination product, whose amount is more pronounced when THF is used (entry 3 vs 4 and 5). On the other hand, when complex Ni(L$_{JP}$)Br IV.B is used as the pre-catalyst, there is no conversion of substrate IV.1a (entry 6 vs 1). However, when ZnBr$_2$ and allylZnBr are used as additives, the reaction leads to 41 % NMR yield of branched IV.2a product (entry 6 vs 7 and 8).

Table IV.II: Catalytic results of some conditions screening of the benchmark transformation (solvent, [Ni] source and additives). **B** = branched, **L** = linear.

En-try	**[Ni] source**	**Solvent**	**Additive**	**B (IV.2a)**	**L (IV.2a)**	**B/L**	***E/Z***	**H-elim**	**SM**
1	**a**	**DMA**	**-**	**0.96**	**0.04**	**1/0**	**-**	**-**	**-**
2	a	DMA	$ZnBr_2$ (*10 mol%)*	0.98	0.02	1/0	**-**	**-**	**-**
3	a	THF	-	0.27	0.32	1/1	5/1	0.36	0.05
4	a	THF	allylZnBr (*1 equiv)*	0.48	0.31	1.5/ 1	3.5/ 1	0.1	0.1
5	a	THF	$ZnBr_2$ (*10 mol%)*	0.36	0.63	1/1. 7	2.3/ 1	-	-
6	b	THF	-	-	-	-	-	-	1
7	b	THF	allylZnBr (*1 equiv)*	0.41	0.41	1/1	8/1	0.36	0.36
8	b	THF	$ZnBr_2$ (*1 equiv*)	*Decomposition and mixture of branched products*					

Divalent zinc and other Lewis acids based control experiments

Kinetic profile comparison with and without the addition of Lewis acids

Procedure: Following the same procedure as Figure 4.50 (conditions a), two catalytic experiments were prepared using LiBr and $ZnBr_2$ as reaction additives (1.0 equiv). The reactions were stopped and analyzed by ^1H NMR after 3 h and the results were plotted to compare them with the general reaction kinetic profile (Figure 4.16).

Table IV.III: Catalytic results using $ZnBr_2$ and LiBr as additives (1.0 equiv), using standard reaction conditions for 3 h. **SM** is the standard allyl(OBoc) substrate **IV.1a**.

Entry	3 h	SM (%)	Branched (IV.2a) (%)	Linear (IV.2b) (%)	□-H (%)
1	$ZnBr_2$	27	55	10	7
2	LiBr	78	20	1	1
3	none	82	18	<1	<1

Observations: When the results were interpolated in our transformation's kinetic profile we found out that the presence of $ZnBr_2$ significantly accelerates the formation of branched desired product **IV.2a** (Figure S31). $ZnBr_2$ speeds up the reaction but compromises somewhat the chemo- and regio-selectivities. On the other hand, LiBr does not substantially influence the rate of the reaction (**Table IV.III**).

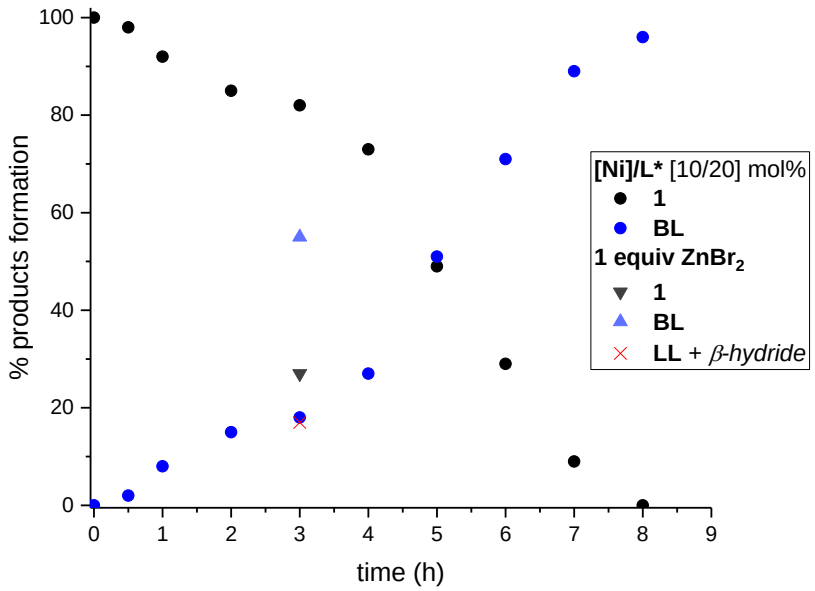

Figure 4.51: Kinetic profile of the catalytic transformation using ^1H NMR analysis of different reaction crudes. Entry 1 of Table **IV.III** is plotted at 3 h of reaction time.

*Reaction progress from **IV.K** onwards and the influence of $ZnBr_2$ as additive*

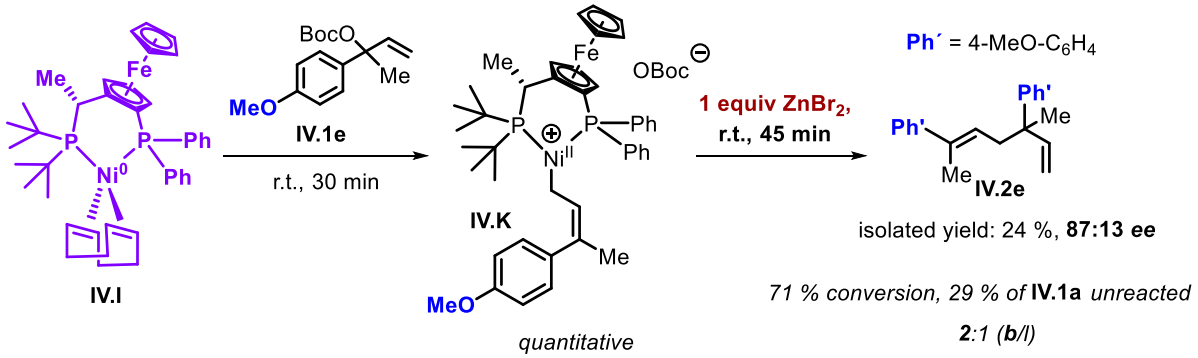

Figure 4.52: Reaction scheme for the stoichiometric control reaction using complex **IV.I** and substrate **IV.1e** and influence of the addition of 1.0 equiv of $ZnBr_2$ to the reaction mixture.

Procedure: In a 2 mL screwed vial, $Ni(COD)_2$ (5.5 mg, 0.02 mmol) and JosiPhos^{tert} (10.8 mg, 0.02 mmol) were dissolved in 0.5 mL of THF. The reaction mixture was stirred at room temperature for a total amount of 16 h and it was then transferred to a NMR tube equipped with an acetone-d_6 capillary. Substrate **IV.1e** (5.6 mg, 0.02 mmol, 1.0 equiv) was added to the NMR tube with a glass pipet and after 30 min of reaction 1.0 equiv of $ZnBr_2$ were added (4.5 mg, 0.02 mmol). After 45 min, the reaction mixture was extracted with hexanes and diethyl ether, the ^1H NMR analysis ($CDCl_3$) of the combined extract showed a 71 % conversion of **IV.1e** and 29% of starting linear allyl carbonate **IV1e**. From the 71% of the product mixture, 24% of **IV.2e** could be isolated while the b/l ratio of 1,5-diene product in the crude was 2:1.

Observations: If we compare in Figure 4.41 the ^1H NMR spectra for this transformation, we can clearly notice that the addition of $ZnBr_2$ accelerates the formation of diene product.

*Reaction progress from **IV.K** onwards and the influence of allylZnBr and allylMgBr as additives*

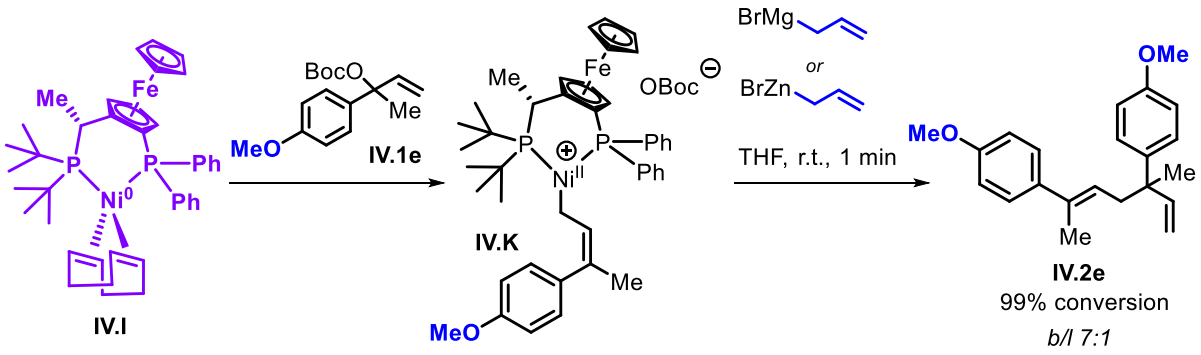

Figure 4.53: Reaction scheme for the stoichiometric control reaction using complex **IV.I** and substrate **IV.1e** and a subsequent addition of 1.0 equiv of allylZnBr or allyl-MgBr into the reaction mixture.

Procedure: The preparation of these experiments was done following a similar procedure related to Figure 4.52.

Observations: The hetero-cross-coupling product between substrate **IV.1e** and both organometallic reagents could not be observed. Instead, the formation of the branched product **IV.2e** was observed with a 7:1 (b:l) regio-selectivity in both cases. The conversion of this transformation was quantitatively confirmed by ^{1}H NMR after isolating the reaction crude by extraction with Et_2O.

Radical scavenging experiments and Zn-dependency of the reaction

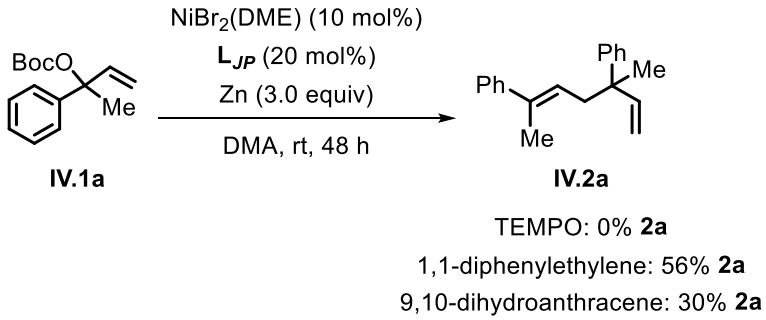

Figure 4.54: Reaction scheme for the catalytic control experiments using several radical scavengers.

Procedure: In a sealed tube $NiBr_2$(DME) (10.0 mol%, 3.1 mg), **L*JP*** (20.0 mol%, 11 mg) and Zn (0.3 mmol, 20 mg) were mixed in DMA (0.2 mL). The tube was degassed three times and filled with argon. The mixture was firmly stirred for approximately 15 min. Then, **IV.1a** (0.1 mmol, 24.8 mg) and TEMPO (0.1 mmol, 15.6 mg) or 1,1-diphenylethylene (0.12 mmol, 21.6 mg) or 9,10-dihydroanthracene (0.1 mmol, 18 mg) were added to mixture and stirred at 25 ºC. After 48 h, the reaction mixture was passed through a short Celite pad, which was further rinsed with EtOAc (three times). The organic phase was concentrated and evaporated under reduced pressure. The crude reaction mixture was purified by flash chromatography on silica gel impregnated with $AgNO_3$ to furnish product **IV.2a** in 0%, 56% (7.3 mg) and 30% (4 mg) yield, respectively.

Benzaldehyde as a competing electrophile

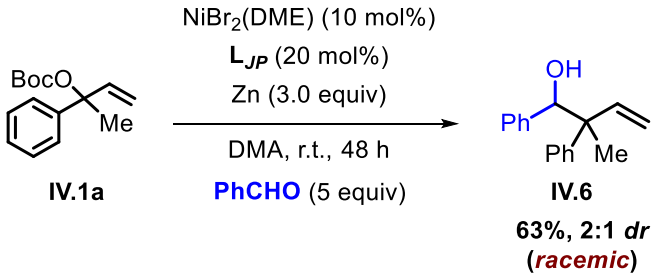

Figure 4.55: Reaction scheme for the catalytic control expiring using benzaldehyde as a competing electrophilic coupling partner.

Procedure: In a sealed tube $NiBr_2$(DME) (10.0 mol%, 3.1 mg), **L*JP*** (20.0 mol%, 11 mg) and Zn (0.3 mmol, 20 mg) were mixed in DMA (0.2 mL). The tube was degassed three times and filled with argon. The mixture was firmly stirred for approximately 15 min. At

that moment, **IV.1a** (0.1 mmol, 24.8 mg) and benzaldehyde (0.5 mmol, 53 mg, 5 equiv) was added to mixture and stirred at 25 ℃. After 48 h, the reaction mixture was passed through short Celite pad, which was further rinsed with EtOAc (three times). The organic phase was concentrated and evaporated under reduced pressure. The crude reaction mixture was purified by flash chromatography on silica gel to furnish product **IV.6** in 63% (15 mg) yield.

4.5.9 Crystallographic data

The measured crystals were air and moisture sensitive. The samples were treated under inert conditions immersed in perfluoro-polyether as protecting oil for manipulation. Data collection was made following the procedure stated in section 2.6.1.

Crystal data for **IV.A**:

$C_{32}H_{40}Br_2FeNiP_2$, *M*r = 760.69, orthorhombic, $P2_12_12_1$, *a* = 9.3145(15) Å, *b* = 16.103(3) Å, *c* = 20.486(3) Å, α = 90°, β = 90°, γ = 90°, *V* = 3072.9(8) Å^3, *Z* = 4, ρ = 1.645 mg·M^{-3}, μ = 3.810 mm^{-1}, λ = 0.71073 Å, *T* = 100(2) K, *F(000)* = 1544, θ(min) = 1.645°, θ(max) = 32.103°, 56643 reflections collected, 10566 reflections unique (R_{int} = 0.0726), GoF = 0.991, R_1 = 0.0334, wR_2 = 0.0576 [$I>2\sigma(I)$], R_1 = 0.0490, wR_2 = 0.0613 (all indices), min/max residual density = -0.483/0.534 [e·Å^{-3}], Completeness to θ(32.103°) = 99.3 %.

Crystal data for **IV.B**:

$C_{32}H_{40.5}BrFeNiP_2$, *M*r = 681.51, monoclinic, $P2_1$, *a* = 9.363(4) Å, *b* = 15.681(7) Å, *c* = 20.958(10) Å, α = 90°, β = 92.332(9)°, γ = 90°, *V* = 3075(2) Å^3, *Z* = 4, ρ = 1.472 mg·M^{-3}, μ = 2.507 mm^{-1}, λ = 0.71073 Å, *T* = 100(2) K, *F(000)* = 1406, θ(min) = 1.622°, θ(max) = 26.476°, 32017 reflections collected, 11671 reflections unique (R_{int} = 0.2090), GoF = 0.962, R_1 = 0.0853, wR_2 = 0.1474 [$I>2\sigma(I)$], R_1 = 0.2122, wR_2 = 0.1899 (all indices), min/max residual density = -0.943/1.045 [e·Å^{-3}], Completeness to θ(26.476°) = 98.9 %.

Crystal data for **IV.C**:

$C_{45}H_{65}BrFeNiO_{2.5}P_2$, *M*r = 902.38, monoclinic, $P2_1$, *a* = 10.602(3) Å, *b* = 14.130(4) Å, *c* = 28.192(9) Å, α = 90°, β = 94.130(6)°, γ = 90°, *V* = 4212(2) Å^3, *Z* = 4, ρ = 1.423 mg·M^{-3}, μ = 1.854 mm^{-1}, λ = 0.71073 Å, *T* = 100(2) K, *F(000)* = 1896, θ(min) = 0.724°, θ(max) = 26.631°, 34983 reflections collected, 17108 reflections unique (R_{int} = 0.1074), GoF = 1.020, R_1 = 0.0843, wR_2 = 0.1954 [$I>2\sigma(I)$], R_1 = 0.1493, wR_2 = 0.2297 (all indices), min/max residual density = -0.854/1.638 [e·Å^{-3}], Completeness to θ(26.631°) = 99.2 %.

Chapter 4

Chapter 5.

Summary and General Conclusions

Chapter 5

To summarize this doctoral thesis, it is important to reflect on the initial objectives set out and the obtained results and insights reported in the various (experimental) chapters. The PhD research discussed in this dissertation aimed at a better and detailed mechanistic understanding of metal-promoted asymmetric synthesis of compounds that feature a sterically challenging quaternary or similar stereocenter. In particular, focus has been on chemical transformations that are enabled through either allylic or propargylic substitution chemistry, which is a core competence of our group. Small organic scaffolds that have such a stereocenter integrated in their structure are highly interesting in the realm of advancing and diversicating synthons for fine chemical and pharma-related discovery and development programs. Three separate chapters discuss the results and key achievements attained, and in each of these sections a fundamentally different conversion (molecular target and/or catalysis approach) is presented.

In **Chapter 2**, the analysis of a **Cu**-mediated asymmetric propargylic sulfonylation of alkyne-functionalized cyclic carbonates is presented. We previously reported a methodology that allows for the synthesis of propargylic sulfones with high regio- and enantio-control, and with a clearly observable NLE. The mechanistic studies that were undertaken had various objectives, including the elucidation of the manifold responsible for the high levels of regio- and enantio-induction, providing an explanation for the strong positive NLE in this conversion and finding further evidence how the initial Cu(II) precursor advances to an active Cu(I) catalyst at the pre-activation stage. Various reaction intermediates could be isolated and structurally characterized creating a rather complete picture of the pre-activation stage. The requisite Cu(I) intermediate is formed in a reductive environment, and once entering the productive cycle it empowers the formation of the desired product through a catalyst-controlled, though unexpected regio- and enantio-selective proto-demetalation step rather than an anticipated control at the stage where attack of the sulfonate nucleophile onto a Cu(allenylidene) intermediate occurs. Furthermore, the positive NLE could be explained at the Cu(I) oxidation state level using Kagan´s model, with heterochiral $Cu(L)_2$ type complexes being relative inactive for the investigated transformation.

Chapter 3 presents the findings for a **Pd**-catalyzed allylic amination process that involves linear type carbonate precursors and aliphatic amines as reaction partners.

During catalyst activation, we were able to gather information on the Pd(0) intermediates that are derived from $Pd_2(dba)_3$ in the presence of a chiral phosphoramidite ligand. The Pd(0) speciation is believed to control the overall rate of this allylic amination process. Further along the reaction pathway, various Pd(II)allyl species could be observed and assigned illustrating important moments during catalysis. With the help of ^{31}P NMR analysis, HRMS and computational support, we were able to identify an important intermediate linked to an inner-sphere pathway before finally reductive elimination of the product occurs. Altogether, the collected data point at mechanistic divergence when sterically congested carbon stereocenters are formed.

Finally, in **Chapter 4** a **Ni**-catalyzed allyl cross-coupling process is outlined that delivers chiral branched-linear type 1,5-dienes with high regio- and enantio-induction. Analogously to the processes studied in chapters 2 and 3, efforts were made to provide a detailed picture on catalyst activation (starting from a Ni(II) precursor and Zn as reductant) and the productive cycle. Different catalysis regimes were noted in the kinetic studies, and various intermediates could be identified on the basis of EPR, NMR and X-ray crystallographic studies complemented by mechanistic control experiments. In the main catalysis regime, a Ni(0)/Ni(II) redox couple is responsible for substrate turnover, with a key role for a bimetallic manifold that is assisted by divalent Zn acting as a co-factor. Based on several experimental evidences, the role of Lewis acidic Zn(II) is connected to its ability to induce isomerization of the preferred η^1-allyl to a less preferred η^3-allyl Ni(II) complex by formation of an –ate species, thereby providing the necessary combination of an electrophile and nucleophile for allyl cross-coupling. The information gathered in this latter chapter further helps to uncover and explore the unique and unpredictable influence of divalent Zn in Ni-based cross-coupling chemistry.

As a **general conclusion** from this thesis, a deep understanding of complex and challenging asymmetric transformations promoted by various transition metal catalysts has been achieved that in each of the case studies has provided new and more detailed insight in their modus operandi. More importantly, this thesis demonstrates that detailed and elaborative mechanistic investigations have great merit as to (1) more completely understand the formation of compounds with sterically frustrated stereocenters, (2) to discover unprecedented steps and catalysis

intermediates typically overlooked in organic/organometallic chemistry, and (3) to provide new reactivity frameworks that can inspire the community to design efficient and above all selective protocols for medicinal compounds and pharmaceutical intermediates that contain tetra-substituted tertiary or quaternary carbon centers.

Chapter 5

Chapter 5


UNIVERSITAT
ROVIRA i VIRGILI
ICIQ